ABSTRACT

Title of Dissertation: *IN SITU* ENRICHMENT AND EPITAXIAL GROWTH OF ^{28}Si FILMS VIA ION BEAM DEPOSITION

Kevin Joseph Dwyer, Doctor of Philosophy, 2017

Directed By: Professor John Cumings, Department of Materials Science and Engineering

Isotopically enriched ^{28}Si is an ideal material for solid state quantum computing because it interacts weakly with the spin states of embedded qubits (quantum bits) resulting in long coherence times. This is the result of eliminating the roughly 4.7 % ^{29}Si isotopes present in natural abundance Si, which possesses nuclear spin $I = 1/2$ that is disruptive to qubit operation. However, high-quality ^{28}Si is scarce and the degree to which it improves the performance of a qubit is not well understood. This leads to an important question in the Si-based quantum information field, which can be stated as "how good is good enough?" regarding the perfection of ^{28}Si as a host medium for qubits. The focus of this thesis is to engineer a material that can address this question, specifically in terms of the enrichment. Secondary requirements for ideal ^{28}Si films that are also pursued are crystalline perfection and high chemical purity.

I report on the production and characterization of ^{28}Si thin films that are the most highly enriched of any known ^{28}Si material ever produced with a maximum

^{28}Si enrichment of 99.9999819(35) % and a residual ^{29}Si isotopic concentration of $1.27(29) \times 10^{-7}$. A hyperthermal energy ion beamline is used to produce this extreme level of enrichment starting from a natural abundance silane gas (SiH_4) source. The Si is enriched *in situ* by mass separating the ions in a magnetic field just before deposition onto Si(100) substrates. Initial proof of principle experiments enriching ^{22}Ne and ^{12}C were also conducted. In the course of achieving this ^{28}Si enrichment, I also pursue the epitaxial deposition of ^{28}Si thin films. Characterizations of the film morphology and crystallinity are presented showing that smooth, epitaxial ^{28}Si films are achieved using deposition temperatures between 349 °C and 460 °C. Crystalline defects present in these films include {111} stacking faults. When using higher deposition temperatures, I find that trace impurity compounds such as SiC cause step pinning and faceting of the growth surface leading to severely rough films. Assessments of the chemical purity of ^{28}Si films are also presented, which show major impurities N, C, and O are present in the purest film at an atomic concentration of approximately 1×10^{19} cm^{-3}, resulting in a Si purity of 99.96(2) %.

Additionally, I introduce a model that describes the residual ^{29}Si and ^{30}Si in ^{28}Si films, i.e. the enrichment, as the result of adsorption of diffusive natural abundance SiH_4 gas from the ion source into the ^{28}Si films during deposition. This model correlates the measured enrichments of ^{28}Si films with the SiH_4 partial pressures during deposition. An incorporation fraction for SiH_4 adsorption at room temperature of $s = 6.8(3) \times 10^{-4}$ is extracted. Finally, the temperature dependence of the sample enrichment is analyzed using a thermally activated incorporation model that gives an activation energy of $E_c = 1.1(1)$ eV for the reactive sticking coefficient of SiH_4.

IN SITU ENRICHMENT AND EPITAXIAL GROWTH OF ^{28}Si FILMS VIA ION BEAM DEPOSITION

by

Kevin Joseph Dwyer

Dissertation submitted to the Faculty of the Graduate School of the
University of Maryland, College Park in partial fulfillment
of the requirements for the degree of
Doctor of Philosophy
2017

Advisory Committee:
Professor John Cumings, Chair/Advisor
Dr. Joshua Pomeroy, Co-Advisor
Professor Lourdes Salamanca-Riba
Professor Ichiro Takeuchi
Professor Neil Goldsman

Acknowledgments

The path that led me to become a Ph.D. candidate studying materials science and engineering (MSE) at the University of Maryland, College Park began as I was an undergraduate physics major at Maryland and sought to join a lab to gain research experience. I contacted Professor Gottlieb Oehrlein, who invited me to work in his lab, for which I am grateful. His lab was a materials science lab researching plasma-surface interactions. Later, when applying to graduate programs, Professor Oehrlein's graduate student, Robert Bruce, suggested that I apply to the Materials Science and Engineering Department at Maryland. I did apply, and, after being accepted, I decided to become a materials scientist.

While taking first year classes in graduate school, my professor, John Cumings, put me in touch with a scientist at the National Institute of Standards and Technology (NIST) looking for a graduate student. That scientist was Dr. Joshua Pomeroy, and I soon joined his group at NIST in Gaithersburg after an impressive tour. Josh became my co-advisor and John my official MSE advisor for the duration of a fruitful six year collaboration that produced the work in this thesis. I thank John for not only introducing me to Josh and being the "guy that signs my forms", but also for his practical advice for achieving academic milestones as well as the growth of my scientific career. Working with Josh at NIST has been pivotal in my development as a scientist, and I thank him for his role in guiding that development. The combination of practical engineering and analytical science knowledge imparted by Josh has made a strong impression on me and will no doubt serve me well moving

forward. Additionally, Josh's do-it-yourself attitude and adage that "data talks and everything else walks" will always stick with me. I am very proud of what we have accomplished and look forward to collaborating with him again.

I want to thank Dr. Russell Lake, Josh's first graduate student, for making me feel welcome after transitioning from Maryland to Josh's group at NIST and for many insights and scientific discussions. I thank Josh's current group members, Dr. Aruna Ramanayaka and Ke Tang for helpful discussions, and especially Hyun soo Kim, with whom I spent countless hours in the lab (breaking and fixing things) in the pursuit of data. I have had the fortune and pleasure of working with numerous other smart people at NIST. Thank you to former and current members of the Quantum Processes and Metrology group at NIST including Dr. Neil Zimmerman, Dr. Ted Thorbeck, Dr. Panu Koppinen, Dr. Justin Perron, Dr. Michael (Stew) Stewart, Dr. Roy Murray, Dr. Hamza Shakeel, and Zac Barcikowski for numerous helpful discussions and brainstorming sessions over the years. Interactions with these colleague have led to valuable scientific relationships and even more valuable friendships. Additionally, thank you to Dr. Garnett Bryant for paying my stipend during my tenure.

I gratefully acknowledge the Laboratory for Physical Sciences for partially funding this work and look forward to joining them as a postdoctoral researcher.

Other collaborators at NIST I want to thank include Terry Moore, Dr. Rick Silver, Dr. Kai Li, Dr. Pradeep Namboodiri, Xiqiao Wang, Dr. Kristen Steffens, Dr. June Lau, Dr. Vald Oleshko, Dr. Joshua Schumacher, and Dr. Alline Myers. I extend a special thank you to the most important collaborator I had the pleasure

of working with, Dr. Dave Simons, whose expertise in isotope measurements and willingness to push the boundaries of his work played a critical role in this thesis.

Thank you to the fellow students of my MSE Ph.D candidate class including Alex, Jen, Amy, Colin, Elliot, Ben, and Jeff for helping me survive my first year of graduate school. Thank you to the GRA NIST solfball team led by our fearless leader Jack for helping me blow off steam at the plate and on the pitching mound in between experiments. We may not have won any championships, but it was fun nonetheless! Thank you also to my roommates Dana, Somak, and Evan for putting up with my crazy hours while writing this thesis.

Most crucially, I want to acknowledge and extend a very warm thank you to my parents Eddie and Linda and brother John as well as the rest of my family for their endless love and support over the years! Thank you to my parents for cultivating, encouraging, and enabling my scientific curiosity as a child. Lego building, physics and chemistry kits, model rockets, a telescope, trips to the Franklin Institute, and numerous other activities and discussions about science topics provided by my parents formed the foundation for the scientist that I have become. Further financial and emotional support from them throughout the years as I progressed through high school, college, and finally, graduate school is greatly appreciated. Ultimately, the work presented in this thesis would not have been possible without them.

Finally, thank you to my committee members Josh, John, Professor Lourdes Salamanca-Riba, Professor Ichiro Takeuchi, and Professor Neil Goldsman for their careful consideration of this thesis.

Table of Contents

List of Tables

List of Figures

Chapter 1

Introduction

1.1 ^{28}Si for Quantum Information

1.1.1 Si-Based Solid State Quantum Information

Major technological advances are often driven by or require development of new or improved materials [1]. Development of visible light LEDs and lasers in the 1960s was possible due to improvements in GaAs crystals with engineered compositions. Carbon-based materials have played an important role in both manufacturing advances and basic physics research. Carbon fibers and carbon reinforced plastics were first developed in the 1960s and have found a wide variety of manufacturing applications as strong, lightweight materials. At the microscopic level, carbon nanotubes have spurred a tremendous amount of research into their unique and impressive physical and electrical properties with numerous potential applications. Although they were initially discovered in 1952, interest in carbon nanotubes increased after further observations in the 1990s. The widespread use of small, high-energy density, rechargeable batteries for portable electronics was made possible by

the development and engineering of lithium ion-based electrodes such as $LiCoO_2$ or later $LiFeO_2$ starting in the 1980s. Another major materials-based technology that has made portable electronics and, more broadly, all modern computers possible is the transistor. Developed initially in the 1950s, the ubiquitous use of semiconductor transistors as the base computing component in integrated circuits in the microelectronics industry first required the engineering of extremely high purity, single-crystalline silicon material. Further advances in silicon processing for metal-on-semiconductor transistor technology would come to be guided on a large scale by the International Technology Roadmap for Semiconductors. The engineering of the properties of silicon has also been integral to the development of photovoltaic solar cells since the 1970s and silicon cells account for the majority of solar panels in use. High-quality, i.e. nearly perfect, silicon has perhaps been the most important material to the modern and increasingly computer oriented world.

In solid state quantum information (QI), isotopically enriched ^{28}Si is a critical material for the further development of Si-based quantum computing architectures. The abundance of high-quality (unenriched) Si and the established microelectronics infrastructure make Si an attractive medium for quantum computing, which holds the promise of significant increases in computing speed for certain tasks over classical computers. For quantum coherent devices, both the classical aspects of device operation and the states of the qubits (quantum bits) utilize the electronic band structure of crystalline semiconductors like Si. A great deal of experimental QI research has leveraged these advantages with a high degree of success, as described by Zwanenburg *et al.* in a review article [2]. Si-based quantum computing architectures

include electron spin qubits in quantum dots defined electrostatically by gate electrodes. Quantum dots can be formed in a variety of structures including undoped Si surfaces, Si nanowires, and Si quantum wells in Si/SiGe heterostructures.

Another popular quantum computing architecture is based on a proposal by Kane to use the nuclear spins of an array of single donor ^{31}P atoms in Si as qubits [3]. In this design, metal "A-gates" on the surface manipulate the individual donor spins and they interact via electron-mediated coupling, which is controlled by "J-gates". The proposal makes clear that for this scheme to be successfully implemented in a quantum computer, a host material for the donors needs to be free of nuclear spins ($I = 0$). This basic design principle of gate-controlled donors and dots has been adapted to produce architectures including implanted ^{31}P atoms in Si transistor devices or in combination with quantum dots and ^{31}P single atom transistors or quantum dots in Si produced by scanning tunneling microscopy H-lithography. A schematic of Kane's architecture as well as examples of two physical implementations of these types of Si quantum computing devices are shown in Fig. 1.1. Panel (a) is the Kane schematic from Ref. [3] showing the relation between the ^{31}P donors and the surface control gates. Panel (b) is a false colored top-down scanning electron microscope (SEM) micrograph of a Si quantum dot device from an experiment in Ref. [4] defined by electrostatic metal gates on a ^{28}Si epilayer. The location of the quantum dot is shown by the representation of the cartoon electron spin (circle with arrow). A single electron transistor (SET) is formed by the gates at the bottom of the micrograph. A transmission line for sending microwave pulses to the dot to manipulate the qubit spin states is seen at the left. A schematic cartoon of the quantum dot system is

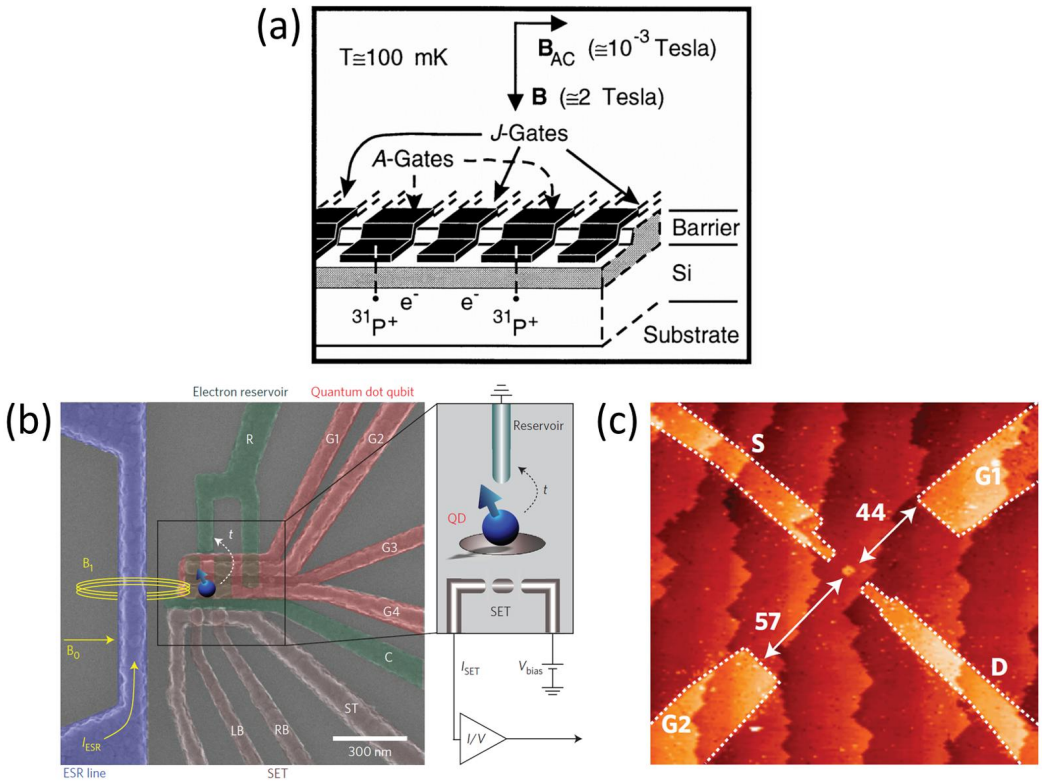

Figure 1.1: Si-based quantum dot and P-donor devices. (a) Schematic for a proposed quantum computing architecture for ^{31}P donors in Si. ^{31}P nuclear spin qubits are manipulated by metal "A-gates" and interact via their electrons, controlled by "J-gates" (from Ref. [3]). (b) False colored SEM micrograph of a Si quantum dot (cartoon arrow) defined electrostatically by metal gates on ^{28}Si epilayer. Gates defining a single electron transistor are seen below the quantum dot and a transmission line for ESR pulses is at the left. A cartoon schematic of the quantum dot is at the right (from Ref. [4]). (c) STM image of a H-terminated Si(100) surface with areas selectively depassivated for ^{31}P dosing that will define electric gates and a quantum dot with single or multiple ^{31}P donors (from Ref. [5]).

shown at the right. Panel (c) is a scanning tunneling microscope (STM) image of a H-terminated Si(100) surface from Ref. [5] with electrostatic gates and a dot defined by selectively removing H in the bright and outlined areas of the image. These areas of bare Si substrate will be dosed with ^{31}P atoms, producing conductive wires and a dot formed of one or several ^{31}P atoms.

Interest in ^{31}P nuclear and electron spins as qubits (or memory) in Si has also

spurred research in electron spin resonance (ESR) and nuclear magnetic resonance (NMR) of ^{31}P spin ensembles in Si crystals. One of the key performance metrics of spin qubits, which is measured in bulk ESR experiments, is their dephasing or coherence time, T_2. This is the time that coherent spins comprising the qubit maintain their quantum phase before the information they encode is lost to the environment. For a continuous wave ESR measurement, T_2 is inversely related to the ESR signal linewidth. For a viable quantum computer, the T_2 time must be sufficiently long as to be approximately 1×10^6 times longer than the average single gate operation time to account for dephasing errors. This is a general design rule which depends on a number of factors including use of error reduction codes. Two qubit gate operations with gate times of the order of 100 ns have been demonstrated [6]. If the spin interacts with local inhomogeneities in the magnetic field, enhanced dephasing will occur and the resulting coherence time is denoted as T_2^*. Certain manipulations of the spins using specific pulse sequences such as a Hahn echo or dynamical decoupling can reduce the effects of dephasing due to environmental noise and will result in a T_2 echo signal measurement. The dephasing of spins in an ensemble is measured, for example, by projecting the spin states as spin-up (aligned to an external magnetic field) or spin-down (anti-aligned to an external magnetic field) and the probability of the spin being in those projected states over time gives the decay characterised by T_2. Other more complicated projections to states not aligned to the magnetic field are also possible. Figure 1.2 shows a cartoon schematic of the Bloch sphere construction for a spin qubit as well as a schematic of a T_2 determination from measurements of such a spin. Panel (a) shows the Bloch sphere for a

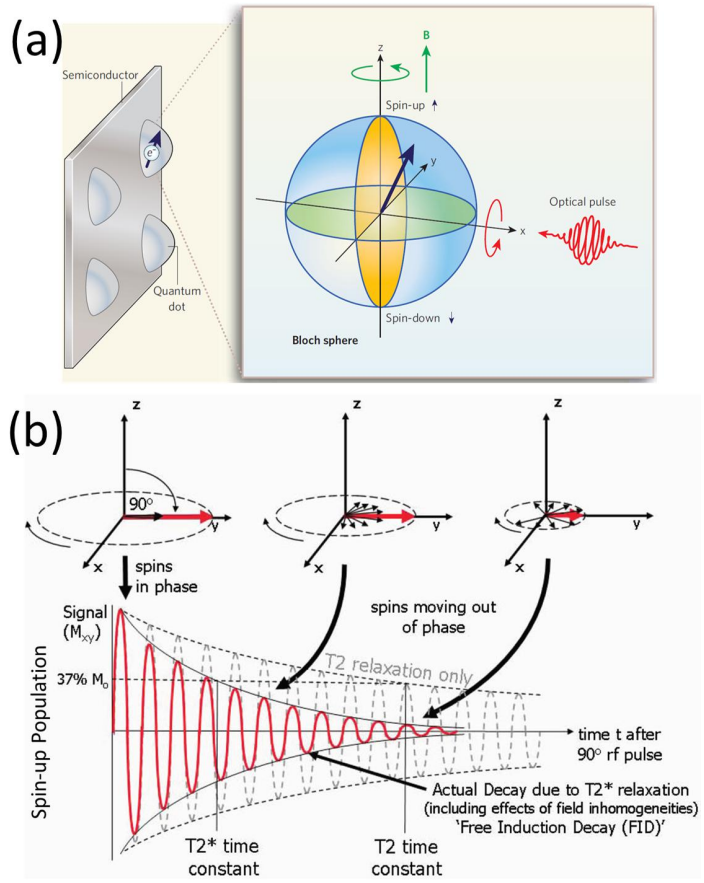

Figure 1.2: Schematic diagrams of the Bloch sphere for a qubit spin and the T_2 coherence time due to spin dephasing (a) The Bloch sphere for two level quantum system. The state of an electron spin qubit in a semiconductor quantum dot exists as a vector on the sphere and is projected as spin-up or spin-down. A "σx" optical control pulse rotates the qubit spin around the x-axis to perform gate control operations (from Ref. [7]). (b) Diagram of a T_2 coherence time determination showing the decay of measurements of the spin-up probability after gate control operations. The T_2^* decay is caused by the dephasing of the spin ensemble (adapted from Ref. [8]).

two level quantum system from Ref. [7]. The state of an electron spin qubit in a semiconductor quantum dot exists as a vector on the sphere and is projected by a measurement onto a basis state such as spin-up or spin-down. ESR or NMR control pulses rotate the qubit spin around an axis, e.g. the "σx" rotation shown in panel (a), to perform gate control operations. When the spin vector with a basis state aligned with the magnetic field in the positive z direction lies in the x-y plane, the

strongest dephasing can occur. Panel (b) shows how T_2^* is determined from many measurements of a spin where the spin-up population oscillates with varying spin evolution time, adapted from Ref. [8]. The spin evolution when the spin is dephasing is shown for three representations of the Bloch sphere at the top of the figure. The spin-up oscillations exhibit a certain decay related to T_2 and environmental inhomogeneities.

In Si, a significant source of inhomogeneous magnetic field noise is the Overhauser field generated by nuclear and impurity spins in the crystal. Natural abundance Si is comprised of three stable isotopes, ^{28}Si, ^{29}Si, and ^{30}Si, which have abundances of approximately 92.2 %, 4.7 %, and 3.1 %, respectively. The ^{29}Si isotope has a nuclear spin $I = 1/2$, while ^{28}Si and ^{30}Si isotopes have no net nuclear spin. By eliminating ^{29}Si nuclei, pure, isotopically enriched ^{28}Si becomes an ideal spin-free environment in which to place the electron and nuclear spins of qubits. Without a randomly fluctuating global Overhauser field present, spins in ^{28}Si interact with their environment far less than in unenriched material leading to a greatly enhanced T_2^* coherence time. Consequently, ^{28}Si has been dubbed a "semiconductor vacuum" and is analogous to the isolation of trapped atoms in a vacuum chamber [9]. A cartoon model depicting the composition of ^{28}Si and natural abundance Si (^{nat}Si) is shown in Fig. 1.3, adapted from Ref. [10].

Theoretical modeling and bulk ESR experiments predicted the enhancement in T_2^* to be proportional to the reduction in ^{29}Si concentration [11,12], which further spurred interest in exploiting ^{28}Si experimentally. Numerous research groups have shown through bulk ESR and NMR experiments of ^{31}P spins in ^{28}Si that nuclear

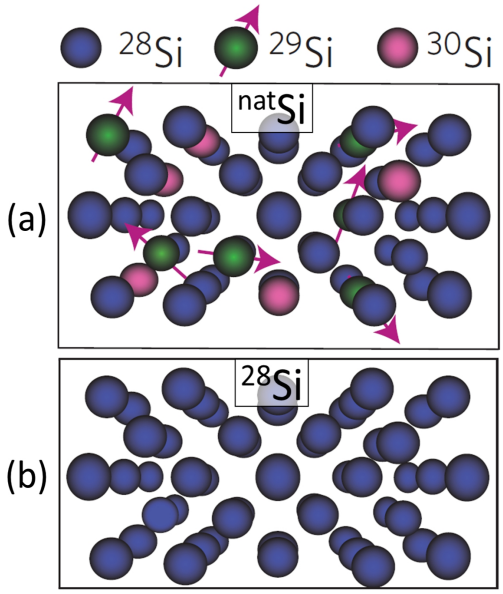

Figure 1.3: Cartoon depictions of natural abundance Si and enriched ^{28}Si crystals. (a) Natural abundance Si contains ^{29}Si atoms that possess nuclear spins as well as nuclear spin-free ^{28}Si and ^{30}Si atoms. (b) The ^{28}Si is free of nuclear spins. (adapted from Ref. [10])

and electron spin coherence T_2 times can exceed seconds [9, 10, 13, 14]. A recent measurement of the T_2 time of a single ^{31}P electron spin resulted in a value of 559 ms [10]. Two examples of T_2 measurements of spins in ^{28}Si for both bulk NMR and in the single spin regime are presented in Fig. 1.4. Panel (a) shows the measurement results from Ref. [10] mentioned above for a single ^{31}P atom implanted into a ^{28}Si quantum dot device. The dynamic decoupling pulse sequence used for this measurement is referred to as CPMG [15]. The ^{31}P nuclear spin measured in this experiment was determined to have a $T_2 = 35.6$ s. Those measurements were done at cryogenic temperatures. Panel (b) shows a T_2 determination measurement from Ref. [14] of the nuclear spins of an ensemble of ^{31}P atoms in ^{28}Si in a bulk NMR experiment. When using a so-called XY-16 decoupling pulse sequence [16], the measurement resulted in a coherence time of $T_2 = 39$ min, measured at room

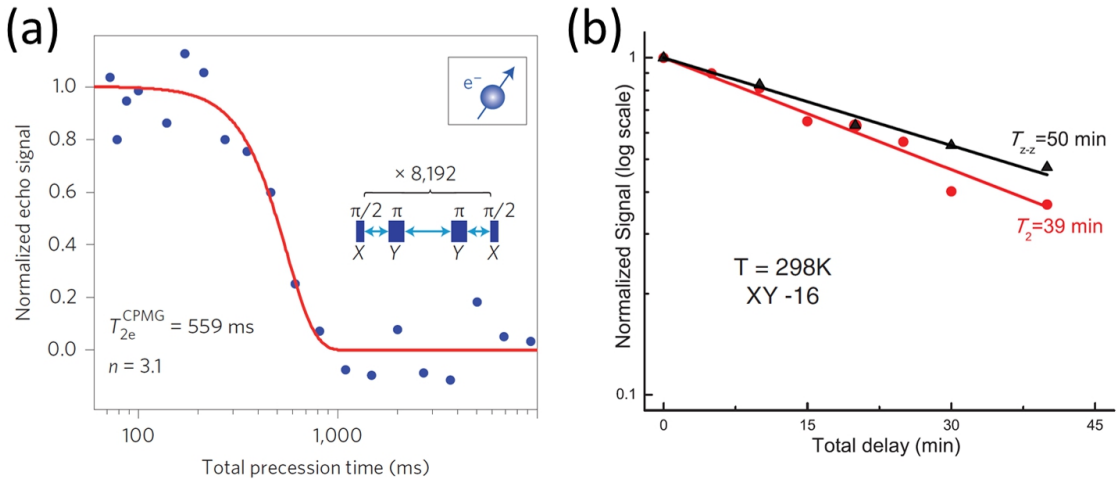

Figure 1.4: T_2 coherence time measurements of spins in ^{28}Si. (a) An electron spin of a single ^{31}P atom in ^{28}Si has a T_2 = 559 ms after dynamical decoupling (from Ref. [10]). (b) An ensemble of ^{31}P atoms in ^{28}Si have a nuclear spin T_2 = 39 min at room temperature (from Ref. [14]).

temperature.

Quantum computing architectures that stand to benefit from or already have demonstrated benefits from using enriched ^{28}Si include STM hydrogen lithography Si:P devices [17–20], single dopant qubits implanted near SETs [2,21–23], ^{28}Si quantum wells in Si/Ge heterostructures [24,25], and fabrication of transistors (FinFETs) for QI [26]. A few of these groups have shown both long T_2 times and coherent manipulation in ^{28}Si for bulk donor spins [27] as well as single spins in quantum wells [24] and quantum dots [10, 28].

In addition to long coherence times, using ^{28}Si as a medium for ^{31}P opens up the possibility of optical manipulation of the qubit system through the use of hyperfine transitions, which are unresolvable in natural Si. Typically in solid state QI systems, in the absence of optical addressability, electrostatic control gates are needed in close proximity to the dot to manipulate the qubit states and have the

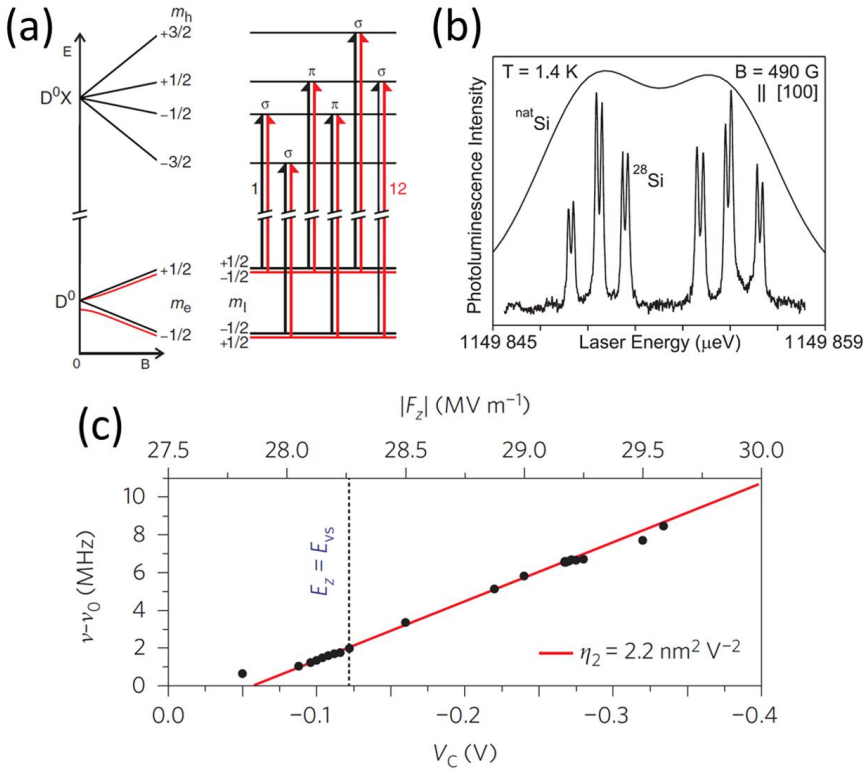

Figure 1.5: Examples of experimental capabilities for qubit control in ^{28}Si (a) ^{31}P in Si energy level diagram for 12 optical transitions between the neutral donor (D^0) and the donor bound exciton (D^0X) (from Ref. [14]). (b) Photoluminescence spectra (bound exciton no-phonon) of ^{31}P atoms in natural abundance Si and ^{28}Si showing hyperfine splitting only resolvable in ^{28}Si, making optical addressing possible (from Ref. [29]). (c) ESR frequency tuning of a ^{31}P electron spin in ^{28}Si using a control gate voltage to induce a Stark shift. This is due to the very narrow ESR linewidth of spins in ^{28}Si (from Ref. [4]).

possibility of introducing charge noise into the system [30]. Additionally, qubit manipulation schemes, which have been proposed for arrays of quantum dot qubits, and which involve tuning the qubit ESR frequency through Stark or Zeeman shifts, have been demonstrated in single quantum dots in ^{28}Si [4]. The ability to tune the qubit ESR frequency relies on qubit spins that have very narrow inhomogeneous ESR linewidths of a few kHz, which are only achievable in a material with homogeneous mass such as highly enriched ^{28}Si with exceptionally small strain fields [9,31].

Examples of the ^{31}P hyperfine splitting and the tuning of a ^{31}P ESR frequency are shown in Fig. 1.5. Panel (a) shows an energy level diagram for 12 hyperfine-split optical transitions of a ^{31}P in Si from Ref. [14]. The transitions are between the neutral donor (D^0) levels and the donor bound exciton (D^0X) levels and can be excited with optical control pulses. Panel (b) shows the photoluminescence spectra (bound exciton no-phonon) of ^{31}P atoms in natural abundance Si and ^{28}Si from Ref. [29]. The 12 transitions of the hyperfine splitting are clearly resolvable only in the ^{28}Si sample, which makes it possible to address the spins with the optical pulse in panel (a). Panel (c) shows experimental data from Ref. [4] displaying the change in the ESR frequency of a ^{31}P electron spin in ^{28}Si due to a Stark shift induced by a gate voltage. Multiple qubits can be addressed by one pulse signal using such a technique by bringing only one at a time into resonance with the control pulse.

1.1.2 Sources of ^{28}Si

Despite the demonstrated advantages of ^{28}Si for solid state quantum information, only a very limited amount of highly enriched ^{28}Si is available within the solid state quantum computing community for use in QI experiments. ^{28}Si is primarily produced at great cost and effort through international collaborations requiring large centrifuge facilities. This lack of readily available ^{28}Si is one of the prime motivations for using ion beam enrichment and deposition to produce ^{28}Si films in this work.

The majority of the ^{28}Si bulk crystals and epitaxial films that have been produced are grown from chemical vapor deposition (CVD) of enriched $^{28}SiH_4$. The

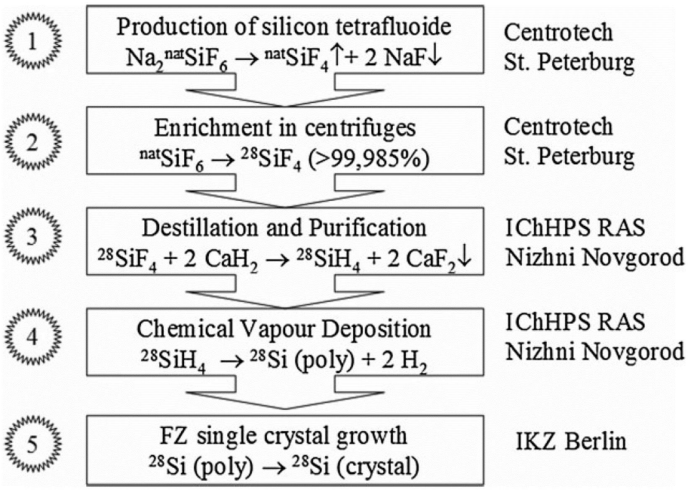

Figure 1.6: Process flow chart for the production of a ^{28}Si bulk crystal at IKZ by $^{28}SiH_4$ CVD, generated from centrifugation of natural abundance SiF_4 at Centrotech. (from Ref. [32])

production of this $^{28}SiH_4$ has predominately started at the Centrotech facility in St. Petersburg, Russia. There, natural abundance SiF_4 is enriched using industrial gas centrifuges. The enriched $^{28}SiF_4$ is then converted chemically into the silane ($^{28}SiH_4$) used to grow ^{28}Si crystals at the Leibniz Institute (IKZ) in Berlin, Germany [32]. A process flow chart for this production of ^{28}Si is shown in Fig. 1.6.

Production of ^{28}Si early on in the 1990s in these efforts was spurred on by interest in the thermal conductivity of ^{28}Si. Evidence existed that ^{28}Si had a higher thermal conductivity than natural abundance Si. A higher thermal conductivity was advantageous because heat dissipation was a major problem in the microelectronics industry at the time. This early ^{28}Si had a ^{28}Si enrichment of about 99.9 %. Measurements of the thermal conductivity of ^{28}Si revealed that it significantly exceeded that of natural abundance Si, but only at cryogenic temperatures [33]. This meant that ^{28}Si was not a viable option to solve the heat dissipation crisis and thus

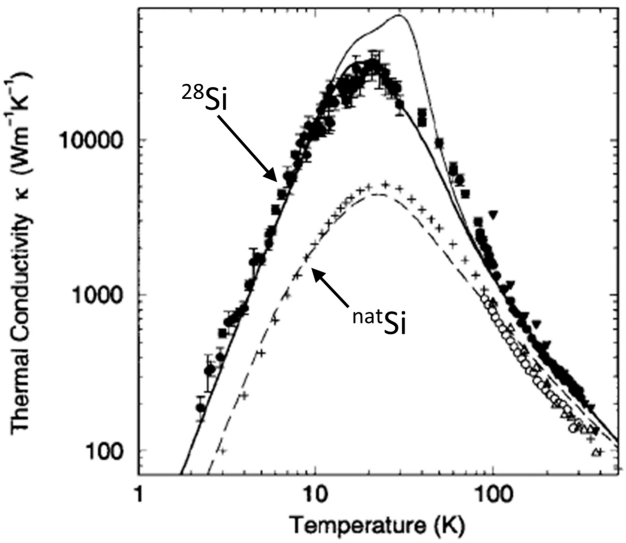

Figure 1.7: Thermal conductivity measurements of natural abundance Si and ^{28}Si as a function of temperature showing a large enhancement in thermal conductivity for ^{28}Si compared to natural abundance Si at low temperatures. (adapted from Ref. [33])

demand for ^{28}Si plummeted. The thermal conductivity measurements of ^{28}Si and natural abundance Si are shown in Fig. 1.7, adapted from Ref. [33].

Multiple ^{28}Si bulk crystals were grown by CVD and zone refinement from enriched $^{28}SiH_4$ at IKZ. The largest of these crystals were grown as part of the International Avogadro Coordination (IAC), which seeks to use single crystal ^{28}Si spheres as a standard to measure the Avogadro constant, N_A, by counting the number of atoms in a kg of ^{28}Si [32,34,35]. This effort is also related to the redefinition of the kg unit using the kg ^{28}Si sphere. The accuracy of the measurements of N_A using these spheres relies on them being very nearly perfect 1 kg ^{28}Si spheres. Measurements of their properties show that they are almost perfect single crystals with no detectable dislocations. They have chemical impurity concentrations, including C and O, of approximately 5 $\times 10^{14}$ cm^{-3}, and they have a ^{28}Si enrichment of approx-

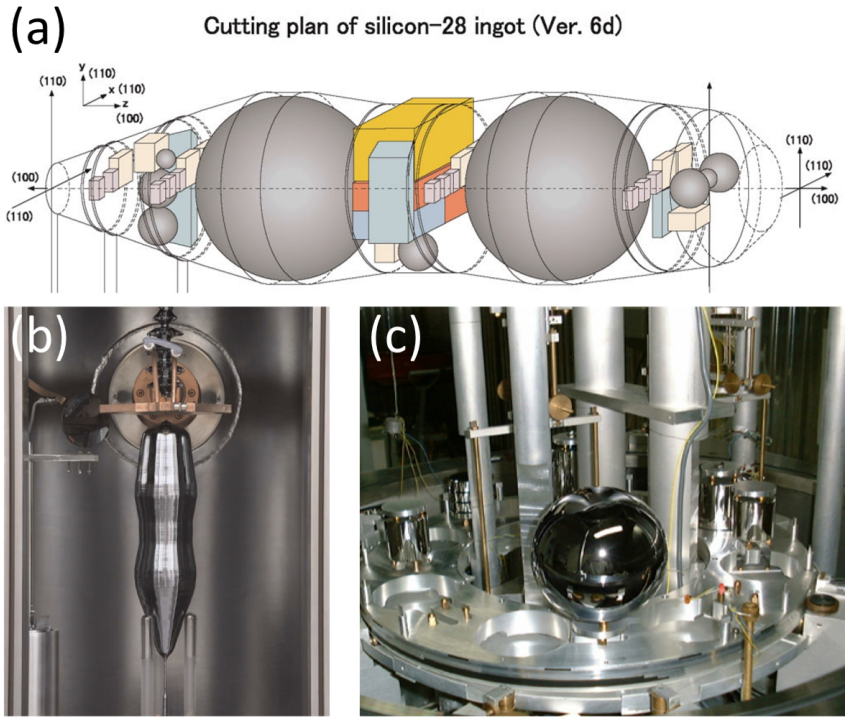

Figure 1.8: ^{28}Si bulk crystals produced by the International Avogadro Coordination. (a) Schematic of the cutting plan to produce two ^{28}Si spheres from a single-crystal boule and (b) a photograph of the ^{28}Si boule (from Ref. [32]). (c) Photograph of one the final ^{28}Si spheres on a weighing apparatus (from Ref. [34]).

imately 99.995 % with a residual ^{29}Si isotopic concentration, i.e. the concentration among the three Si isotopes, of approximately 50 ppm (parts per million, equal to the isotopic concentration times 10^6) [32]. A schematic cutting plan for producing two ^{28}Si spheres from the ^{28}Si boule produced for the IAC is shown in Fig. 1.8 (a) from Ref. [32]. Panel (b) shows a photograph from Ref. [32] of the IAC single-crystal ^{28}Si boule and panel (c) shows a photograph from Ref. [34] of one of the final spheres sitting on a weighing apparatus.

An effect of producing this much ^{28}Si is that the pieces leftover after forming the spheres from the boule as well as from other bulk crystals produced at IKZ were then able to be used for research in the QI community. This of course is a

limited supply of ^{28}Si and producing more in this manner using centrifuges is both extremely expensive and time consuming.

Some enriched $^{28}SiH_4$ was also acquired by the Isonics Corporation, USA as well as Dr. Kohei Itoh in the early 2000s who collaborated to grow CVD epilayer ^{28}Si films on natural abundance Si substrates. Itoh has also grown bulk ^{28}Si crystals from this source. The ^{28}Si enrichment of these materials was measured to be approximately 99.927 % with a residual ^{29}Si isotope concentration of approximately 730 ppm [36, 37]. The epilayers and other material from Itoh have been used by research groups for QI experiments as well [10], although this material is also limited in supply. Some other less abundant sources of ^{28}Si have also been used in QI research although the exact details of those sources are difficult to verify.

1.1.3 Single Spin Measurements in ^{28}Si

In addition to there being a general need for ^{28}Si in semiconductor quantum computing research, a specific need exists for material with targeted levels of enrichment to map the dependence of T_2 on ^{29}Si concentration in the few-spin or single-spin regime. Recent ESR measurements of T_2^* for single ^{31}P spins in ^{28}Si [10, 28] have disagreed with both the theoretical predictions for the same systems made by Witzel *et al.* [12], as well as each other. These theoretical predictions are shown in Fig. 1.9. The T_2 and T_2^* coherence times for quantum dots and ^{31}P electron spin qubits in Si are shown vs. the concentration of ^{29}Si in the system. Solid and dashed lines represent T_2 times for ^{31}P-donor and quantum dots, respectfully, i.e. the two architectures shown in Fig. 1.1. The theory predicts that for every order of magnitude

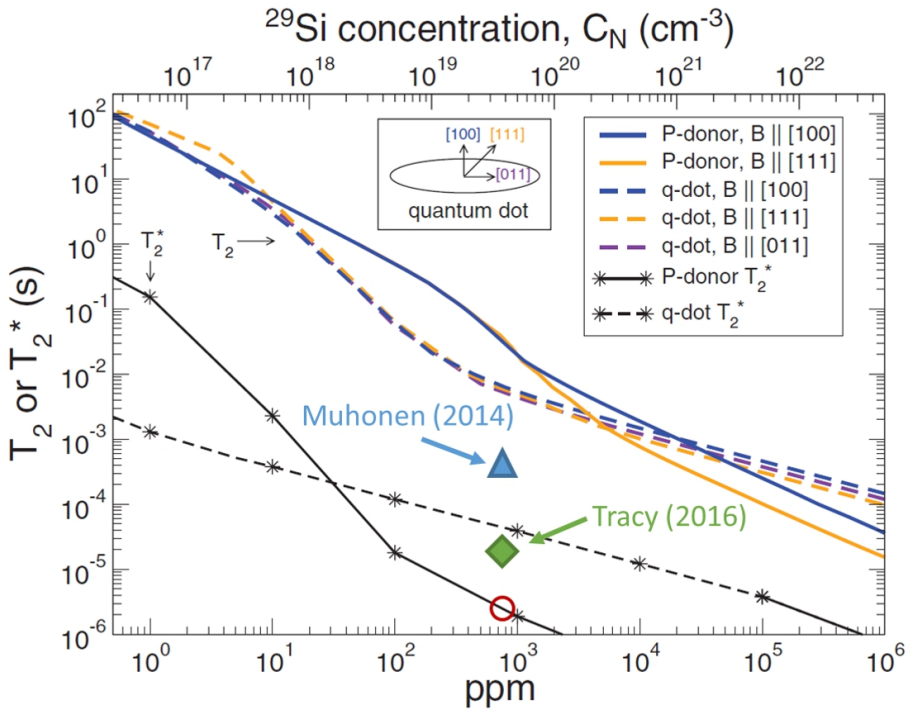

Figure 1.9: Predicted electron T_2 (solid and dashed lines) and T_2^* (solid and dashed line and symbols) coherence time dependance on ^{29}Si concentration for qubits in Si including quantum dots and ^{31}P-donor atoms. Experiments measuring T_2^* for single ^{31}P electron spins in ^{28}Si represented by the triangle (from Ref. [10]) and diamond (from Ref. [28]) do not agree with the prediction value (open circle). (figure adapted from Ref. [12])

decrease in ^{29}Si concentration, there is roughly an order of magnitude increase in the T_2 time. Bulk electron paramagnetic resonance (EPR) and ESR experiments of ^{31}P spins in Si with various enrichments including Si enriched in ^{28}Si to Si enriched in ^{29}Si [11] have agreed with this theoretical work over a large portion of the predicted curve, as discussed by Witzel *et al.* in Ref. [12]. The dashed line with symbols shows the T_2^* times for a quantum dot, and the solid line with symbols shows the T_2^* times for ^{31}P electron spins in Si. Also shown are the two results from the previously mentioned ESR experiments (triangle and diamond) measuring a ^{31}P electron spin T_2^* in ^{28}Si with residual ^{29}Si isotopic concentrations of approximately 800 ppm.

Both of these experiments involve a single ^{31}P atom implanted in a ^{28}Si SET device, which is used for readout, and manipulated with a nearby ESR line. One result by Muhonen *et al.* [10] gave a value of $T_2^* = 268$ μs, and the result by Tracy *et al.* [28] gave a value of $T_2^* = 18$ μs, which was believed to be limited by experimental non-idealities, e.g. magnetic field noise. The value predicted by the theory of $T_2^* \approx 2$ μs is highlighted by the open circle, which lies below both experimental results. Although the experimental results give longer and thus more desirable coherence times than the theory, this outcome shows the fundamental mechanisms limiting coherence at the single-spin level require further study.

In order for the field of solid state quantum computing, especially utilizing ^{31}P or other donor spin qubits, to continue to progress, the effects of nuclear spins such as ^{29}Si isotopes near a single qubit spin needs to be better understood. This requires further measurements of coherence times in the few or single-spin regime with varying concentrations of ^{29}Si in the host material around the qubit atoms. The goal of such a measurement would be to recreate the ^{31}P T_2^* curve from Fig. 1.9 with additional experimental data and compare it to the existing theoretical curve. ^{28}Si material with ^{29}Si concentrations as low as 1 ppm would make the measurement more robust and complete. The ability to measure single spins and predict coherence times may ultimately be required for a viable quantum computer. This concept is highlighted by a schematic ESR measurement phase space diagram of ^{29}Si concentration vs. number of measured spins, N_s, in Fig. 1.10. Ovals represent ESR measurements that have been demonstrated already in QI research. These include bulk EPR experiments on a large number of donor spins (e.g. $> 10^{10}$) for a range

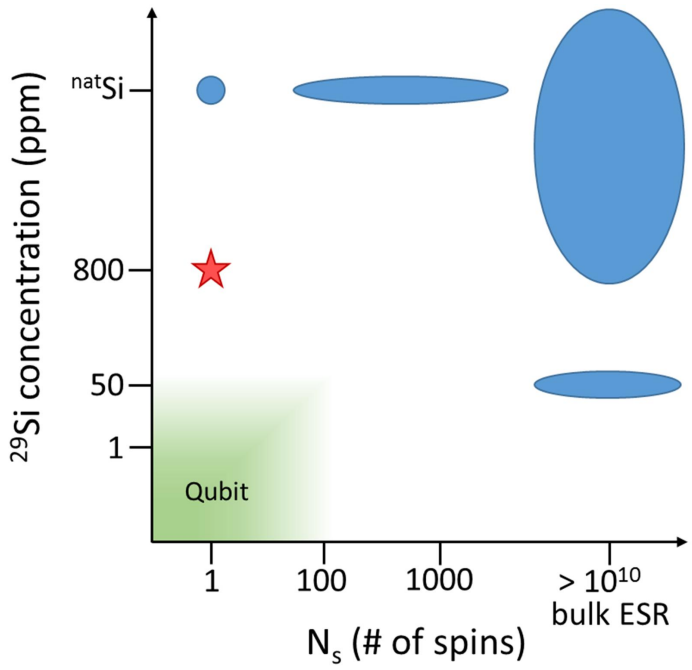

Figure 1.10: ESR measurement phase space diagram of ^{29}Si concentration vs. number of measured ^{31}P spins, N_s, in Si. Ovals represent ESR measurements that have been made in the QI field including bulk ESR (i.e. $> 10^{10}$ spins) for ^{31}P in Si with a range of enrichments (^{29}Si concentrations), a large number of ESR measurements of hundreds or thousands of ^{31}P in natural abundance Si, and single spin ESR measurements in natural abundance Si. Only two single spin measurements are known to have been made of ^{31}P in ^{28}Si, represented by the star. These two measurements are the two shown in Fig. 1.9. For a viable quantum computer, it is probable that single spin measurements in highly enriched ^{28}Si is necessary, represented by the shaded region of the phase space.

of ^{29}Si concentrations down to approximately 800 ppm [11, 27, 38], represented by the large oval on the right. Bulk ESR experiments have also been done on ^{28}Si with an approximately 50 ppm ^{29}Si concentration [39]. Experiments on smaller numbers of donor spins ranging from 100s to 1000s have also been done but only in natural abundance Si [40, 41], which is represented by the oval at the top. In the single spin regime, a large number of QI experiments have measured ^{31}P spin coherence times in natural abundance Si, but only the two previously mentioned experiments have used enriched ^{28}Si with a residual ^{29}Si concentrations of approximately 800 ppm,

represented by the star. These two measurements are the two shown in Fig. 1.9 from Ref. [28] and [12]. The far bottom left corner of the phase space is where it is suspected that measurements required for a viable quantum computer will reside when considering scale-up, represented by the shaded region. It is this region of single ^{31}P spins in ^{28}Si with 1 ppm ^{29}Si concentrations where further research is required. Enabling such measurements through production of highly enriched ^{28}Si epitaxial films with targeted enrichments is another aspect of the goals of this work.

1.2 Ion Beam Enrichment and Deposition

Si thin film epitaxial deposition can proceed by several techniques including CVD using SiH_4, molecular beam epitaxy (MBE) by thermal evaporation, ion assisted deposition (IAD) which uses a separate source of ions to enhance deposition, and direct ion beam deposition or ion beam epitaxy (IBE). IBE has two advantages over the other methods. First, the energy of the ions can be used to enhance the deposition process leading to higher quality epitaxy [42, 43]. Typically, hyperthermal energies below 200 eV are used, and this will be discussed further in Chapter 5. Second, ions can be mass filtered in a magnetic field to select a single isotope of an atom for deposition. This means that ion beam deposition can be used to isotopically enrich a material during the deposition process itself starting from a natural abundance source. This is referred to here as *in situ* enrichment because the enrichment occurs along the flight path of the ions from the source before being deposited on a substrate to grow a film of enriched material, e.g. ^{28}Si. Mass sepa-

rated ion beam deposition and epitaxy is the technique used in this work to produce highly enriched ^{28}Si films.

One of the earliest and most well known uses of ion beam enrichment was in the calutron mass spectrometer developed by Ernest Lawrence for the the Manhattan Project in the United States in the 1940s [44]. The calutron was used to generate enriched quantities of the isotope ^{235}U for use as fissile material in the development of nuclear weapons. This was accomplished by ionizing natural abundance U containing over 99 % ^{238}U, accelerating the ions using electric fields, and then deflecting the ion trajectory using a magnetic field as in a mass spectrometer. The magnetic field separates the ions by mass, which generates an enriched ion beam of ^{235}U that is collected at a target. In order for this process to produce significant quantities of enriched ^{235}U, large, industrial scale apparatus were required, which were produced at great cost and effort during the Manhattan Project.

Laboratory scale ion beam deposition systems have been studied and developed since the early 1970s. Fair developed an ion beam deposition system and demonstrated deposition of thin In films with energies between 100 eV and 500 eV [45]. Around the same time, Aisenberg and Chabot demonstrated deposition of diamond-like thin films at room temperature using a beam of C atoms with 40 eV of energy, which was transferred into the film to enhance the deposition [46]. Neither of these early experiments involved mass selecting the ions. Later, in the 1980s and 1990s, a number of other groups began experimenting with mass separated ion beam deposition and IBE. Shimizu *et al.* developed an ion beam deposition capable of producing mass separated ion beams with mA level current and ion energies down to 10 eV.

Ar ion beams and Ca deposition was demonstrated [47].

Various groups have also demonstrated enrichment and ion beam deposition of materials significant to quantum computing research including semiconductors such as Si and Ge, for production of enriched Si/SiGe heterostructures and quantum wells, and C, for nitrogen-vacancy centers in enriched diamond. Herbots et al. demonstrated deposition of both ^{30}Si and ^{74}Ge ions with energies of 40 eV at deposition temperatures including 400 °C [48]. Zalm and Beckers deposited mass separated ^{28}Si ions on both Si and Ge substrates [49], and Yagi *et al.* likewise deposited ^{28}Si as well as ^{74}Ge films with energies of 100 eV at deposition temperatures of 300 °C [50].

^{28}Si IBE was extensively studied by several groups including by Tsubouchi *et al.* [43] and Rabalais *et al.* [51] who both developed dual ion beam deposition systems for single and compound enriched materials [52, 53]. ^{28}Si epitaxial deposition was achieved by both groups using ions with energies of typically 20 eV at very low deposition temperatures of 100 °C to 400 °C. These parameters produced epitaxial thin films of ^{28}Si with low defect densities. The highest ^{28}Si enrichment reported by Rabalais *et al.* was a film enriched to approximately 99.99 %. Tsubouchi *et al.* reported a ^{28}Si sample with a higher enrichment of approximately 99.9982 % with a residual ^{29}Si isotopic concentration of approximately 16 ppm, which is more highly enriched than the material produced for the IAC. An isotope measurement of this enriched ^{28}Si sample as well as a schematic of the ion beam system used for deposition are shown in Fig. 1.11. Panel (a) shows a dual source ion beam deposition system schematic drawing from Ref. [53]. Two ion sources are seen connected to

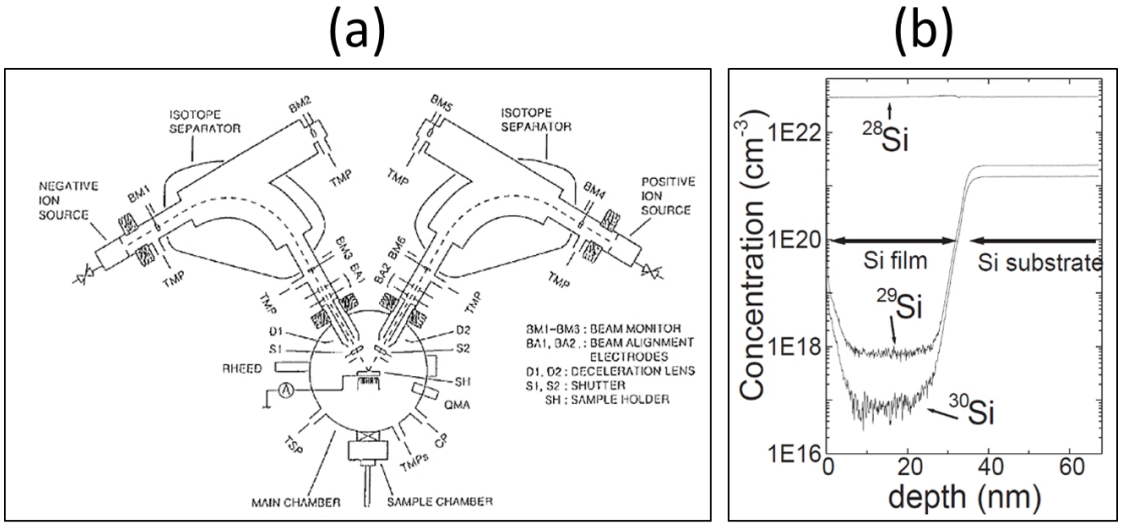

Figure 1.11: Ion beam enrichment by Tsubouchi *et al.* used for depositing ^{28}Si. Panel (a) Schematic drawing of a dual source ion beam deposition system for enriching and depositing single or multi-component materials (from Ref. [53]). Panel (b) Isotope depth profile of a ^{28}Si film deposited from the ion beam. The isotope concentrations of ^{28}Si, ^{29}Si, and ^{30}Si are shown vs. the depth from the surface into the film and Si substrate. The ^{28}Si film is clearly enriched with the ^{29}Si and ^{30}Si concentrations reduced to below 10^{18} cm^{-3}, or approximately 16 ppm for ^{29}Si (from Ref. [43]).

two 90° magnetic isotope separators that both feed into a deposition chamber. This system can be used to enrich and deposit single or multi-component materials. Panel (b) shows a depth profile measurement of the enrichment of a ^{28}Si film deposited with the system in (a) from Ref. [43]. The concentrations of isotopes ^{28}Si, ^{29}Si, and ^{30}Si are shown vs. the depth from the surface into the film and Si substrate. ^{29}Si and ^{30}Si concentrations in the ^{28}Si film are reduced to below 10^{18} cm^{-3}, resulting in the aforementioned enrichment values.

Rabalais *et al.* have also used their ion beam system to implant ^{74}Ge ions in SiO_2 to create enriched Ge quantum dots [54], and deposited $^{28}Si^{16}O_2$ using the dual beam setup with ^{28}Si and ^{16}O [55]. Tsubouchi *et al.* have used the dual beam

system to deposit enriched compounds including $^{28}Si^{12}C$ and $^{12}C^{14}N$ [56, 57].

Finally, the work presented here relies heavily on the previous work done using this same ion beam deposition system by the lead researcher of this effort, Dr. Joshua Pomeroy. This system was used to deposit thin films of Cu using mass separated ions and observe the effects of the ion energy on the epitaxial quality of the film using STM [58, 59].

1.3 Objectives and Outline

1.3.1 Project Goals

Enrichment and thin film deposition of ^{28}Si is pursued here with the objective of producing high-quality enriched material for solid state quantum computing. ^{28}Si of sufficiently high quality (i.e. high enrichment, crystallinity, and purity) provides an ideal solid state environment to host qubit spins, as discussed previously. Unwanted deviations from ideal ^{28}Si material can be classified as three types of defects: isotopic defects, structural defects, and chemical defects. Controlling and limiting these defects is critical for successful integration of ^{28}Si into quantum computing architectures. The ^{28}Si materials goals of this work are stated as follows:

(1) high enrichment in ^{28}Si with a residual ^{29}Si isotopic concentrations less than 50 ppm,

(2) single-crystalline and smooth epitaxial structure with a low dislocation density below 1×10^6 cm^{-3}, and

(3) high chemical purity including C and O with atomic concentrations below 2×10^{15} cm^{-3}.

These are believed (but not known) to be the criteria needed for the ^{28}Si to be comparable to single-crystalline electronic grade (EGS) natural abundance Si as well as the enriched Si currently available in the QI research community from the IAC. Electronic grade Si that is purified and crystallized into single-crystalline boules of Si can have dislocation densities below roughly 1×10^6 cm^{-3} [60]. Float zone refinement also produces Si with atomic concentrations of most residual impurities below 5×10^{13} cm^{-3} and atomic concentrations of some impurities such as O below 1×10^{18} cm^{-3} [61]. As mentioned previously, Si produced for the IAC has C and O concentrations below roughly 5×10^{14} cm^{-3}. The crystallinity of this material is nearly perfect with no detectable dislocations and a vacancy related defect density of roughly 3×10^{14} cm^{-3} [35]. Additionally, the IAC ^{28}Si has a residual ^{29}Si isotopic concentration as low as 50 ppm. Producing ^{28}Si with ^{29}Si isotopic concentrations as low as 1 ppm is necessary to enable a robust and systematic study measuring electron coherence times vs. ^{29}Si concentration in the single spin regime and compare it to the theoretical predictions discussed previously.

Ultimately, the goal of this work is to produce ^{28}Si material that can answer the question "how good is good enough?" for quantum information. This means determining the levels of enrichment, purity, and crystallinity that are necessary to satisfy the materials needs of QI and solid state quantum computing devices. These goals will be achieved using processing methods that are both common (e.g. vacuum deposition, sample heating) and fairly unique (e.g. mass selected ion beam deposition) to engineer the properties, such as enrichment in ^{28}Si and chemical purity, and structure (crystallinity) of Si thin films.

1.3.2 Strategy and Impact of Results

The experimental strategy used to achieve the materials goals described above for this work is to use an ultra-high vacuum (UHV) ion beam deposition system to prepare and deposit ^{28}Si thin films several hundred nm in thickness. A hyperthermal energy ion beam is used to achieve *in situ* enrichment to very high levels from a natural abundance silane gas (SiH_4) source and deposit it on Si(100) substrates. Clean substrates are prepared *in situ* in a UHV environment for minimal incorporation of chemical impurities and heated during deposition to facilitate epitaxial deposition. Proof of principle experiments enriching Ne and C are used to establish experimental techniques.

Characterization methods used to support this effort include *in situ* analysis of the surface and crystallinity of ^{28}Si films by reflection high energy electron diffraction (RHEED) and STM. These are used for quick feedback to fine tune the deposition parameters. *Ex situ* characterization used to assess the quality of the films includes secondary ion mass spectrometry (SIMS) to analyze the enrichment as well as the chemical purity, x-ray photoelectron spectroscopy (XPS) to determine chemical purity, SEM to inspect the surface morphology, and transmission electron microscopy (TEM) to inspect the crystallinity of the films. These characterization methods are used for feedback on the deposition process to make informed decisions on experimental changes leading to higher quality ^{28}Si films.

The main impact on the QI field of this work is that ^{28}Si was produced with extremely high levels of enrichment. The most highly enriched sample produced

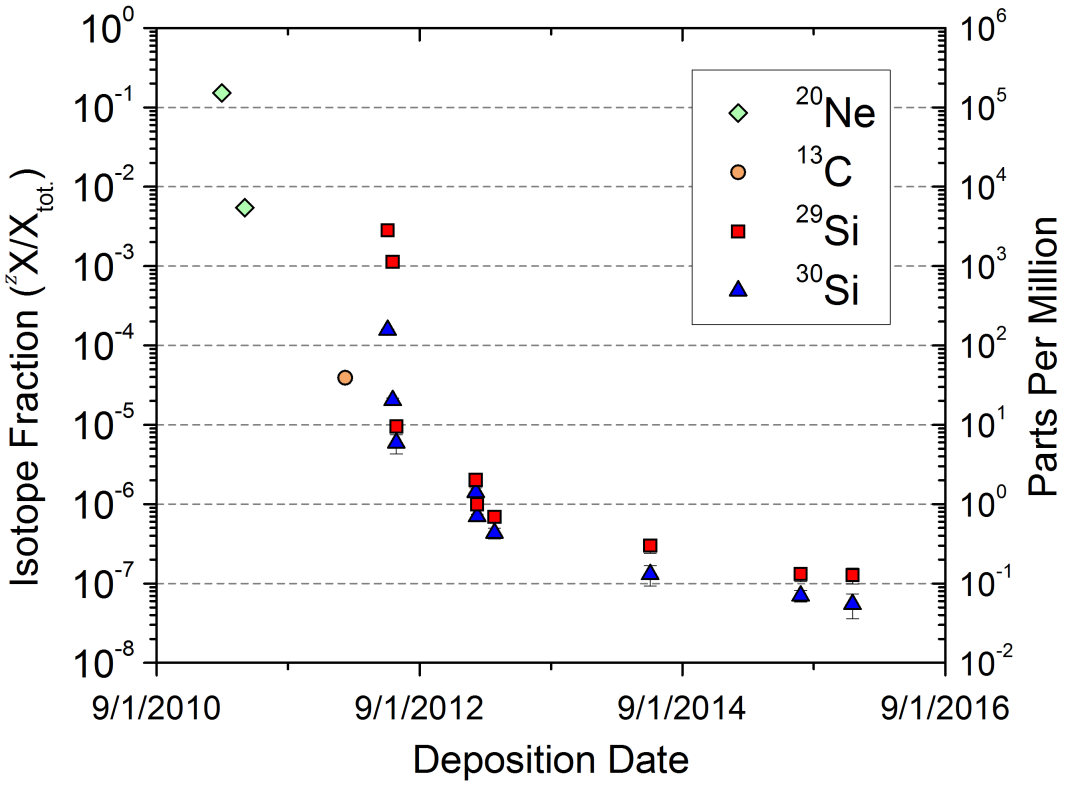

Figure 1.12: Enrichment progression timeline. A timeline of the progression of samples with the lowest residual isotope fractions of ^{20}Ne (diamonds), ^{13}C (circle), ^{29}Si (squares), and ^{30}Si (triangles), as measured by SIMS. These were achieved for ^{22}Ne, ^{12}C, and ^{28}Si samples produced over approximately five years.

by this work had an overall enrichment in ^{28}Si of 99.9999819(35) % with a residual ^{29}Si isotopic concentration of 127(29) ppb (parts per billion, equal to the isotopic concentration times 10^6). This level of enrichment exceeds that of all other known sources of ^{28}Si by a factor of approximately 125. The enrichment of this sample and other highly enriched samples is seen in the enrichment progression timeline in Fig. 1.12 showing the best isotope fractions, which are a measure of the sample enrichment, measured by SIMS for the minor isotopes ^{29}Si (squares) and ^{30}Si (triangles) vs. the deposition date for selected samples produced throughout this work. Isotope fractions of a particular isotope are defined in a SIMS measurement as the

detected counts of that isotope divided by the total counts of the measurement. Also shown in this figure are measurements of the isotope fractions of ^{20}Ne (diamonds) and ^{13}C (circles). These measurements were part of initial proof of principle experiments producing enriched ^{22}Ne and ^{12}C samples done in preparation for enriching and depositing ^{28}Si. The isotope fractions here are written generally as $^{z}\mathrm{X}/\mathrm{X}_{\mathrm{tot.}}$, where z refers to the mass number of a particular isotope, e.g. 28 for ^{28}Si, X refers to a particular element, and therefore ^{z}X is the counts of a particular isotope in the measurement. $\mathrm{X}_{\mathrm{tot.}}$ is the sum of the counts of all isotopes being measured. Uncertainties in the isotope fractions are shown for all samples and are derived from isotope measurements described in later chapters. The samples depicted here in this enrichment timeline are those that had the best enrichments of any sample produced up to that point. In other words, Fig. 1.12 is a timeline of the record enrichments achieved in this work.

1.3.3 Outline

- **Chapter 2:** The experimental apparatus and methods used to produce ^{28}Si thin films are presented. Descriptions of the hyperthermal energy ion beamline used for *in situ* isotopic enrichment, as well as descriptions of the UHV deposition and analysis chamber used for substrate preparation and *in situ* sample analysis are included.

- **Chapter 3:** Initial proof of principle experiments enriching ^{22}Ne and ^{12}C are discussed. ^{22}Ne is implanted into Si while ^{12}C thin films are deposited

on Si substrates. Three ^{22}Ne and three ^{12}C samples were produced. SIMS enrichment measurements are presented showing a maximum achieved ^{22}Ne isotope fraction of 99.455(36) % and a maximum achieved ^{12}C isotope fraction of 99.9961(4) %.

- **Chapter 4:** Phase I of ^{28}Si deposition is discussed involving two experimental configurations. First, ^{28}Si thin films are deposited in a proof of principle experiment for Si enrichment producing five ^{28}Si samples out of 61 total ^{28}Si samples produced in this work. Adjustments of the deposition parameters are discussed for improved depositions producing 16 ^{28}Si films. SIMS measurements of the enrichments and chemical purity are presented. A maximum ^{28}Si isotope fraction of 99.999888(10) % was achieved with a residual ^{29}Si isotope fraction of 0.691(74) ppm.

- **Chapter 5:** Phase II of ^{28}Si deposition is discussed involving an experimental configuration that leverages the capabilities of the full system while depositing 40 ^{28}Si samples. SIMS enrichment measurements are presented showing a maximum achieved ^{28}Si isotope fraction of 99.9999819(35) % with a residual ^{29}Si isotope fraction of 127(29) ppb for the most highly enriched sample in this work. New substrate preparation procedures are discussed as is substrate heating to enable epitaxial deposition. RHEED, STM, and SEM analysis of ^{28}Si film morphology and TEM analysis of film crystallinity is presented. Finally, chemical purity analysis of ^{28}Si films by SIMS is presented. Smooth, epitaxial ^{28}Si films were achieved for deposition temperatures between about

349 °C and 460 °C. These samples contain atomic concentrations of N, C, and O slightly below 1 $\times 10^{19}$ cm^{-3}.

- **Chapter 6:** A model describing the adsorption of natural abundance SiH_4 into ^{28}Si films during deposition is presented and discussed. SIMS enrichment values and SiH_4 partial pressures are correlated using the model to extract a room temperature incorporation fraction, $s = 6.8(3) \times 10^{-4}$. The temperature dependance of the sample enrichment is explored and an activation energy for reactive SiH_4 adsorption is determined to be $E_c = 1.1(1)$ eV.

- **Chapter 7:** A summary of the main scientific results is presented. Then, experimental proposals enabled by this work are discussed including ^{28}Si samples with targeted levels of enrichment for measuring T_2, deposition of enriched $^{28}Si/^{28}Si^{74}Ge$ quantum well heterostructures, ^{28}Si re-deposition, Al dopant devices, and several electrical measurements.

Chapter 2

Experimental Apparatus and Methods

2.1 Context

2.1.1 Ultra-High Vacuum Deposition

These experiments involving the deposition of ^{28}Si from a mass selected ion beam are conducted primarily in an ultra-high vacuum chamber. This provides the cleanest possible environment to prepare clean, flat surfaces on substrates before deposition. While the ion beam itself is not UHV, a gate valve separates it from the UHV deposition chamber and the bulk of the higher pressures gases generated by the ion source are differentially pumped before reaching the sample position. The surfaces of ^{28}Si samples are also inspected in UHV after deposition, which is critical to prevent contaminants from adsorbing that would obscure the measurements. A top-down schematic of the UHV and ion beamline deposition system is shown in Fig. 2.1. The deposition system consists of four connected but isolated vacuum chambers. The hyperthermal energy ion beamline is pictured at the left. The UHV deposition and analysis chamber is at the right with a load lock branching

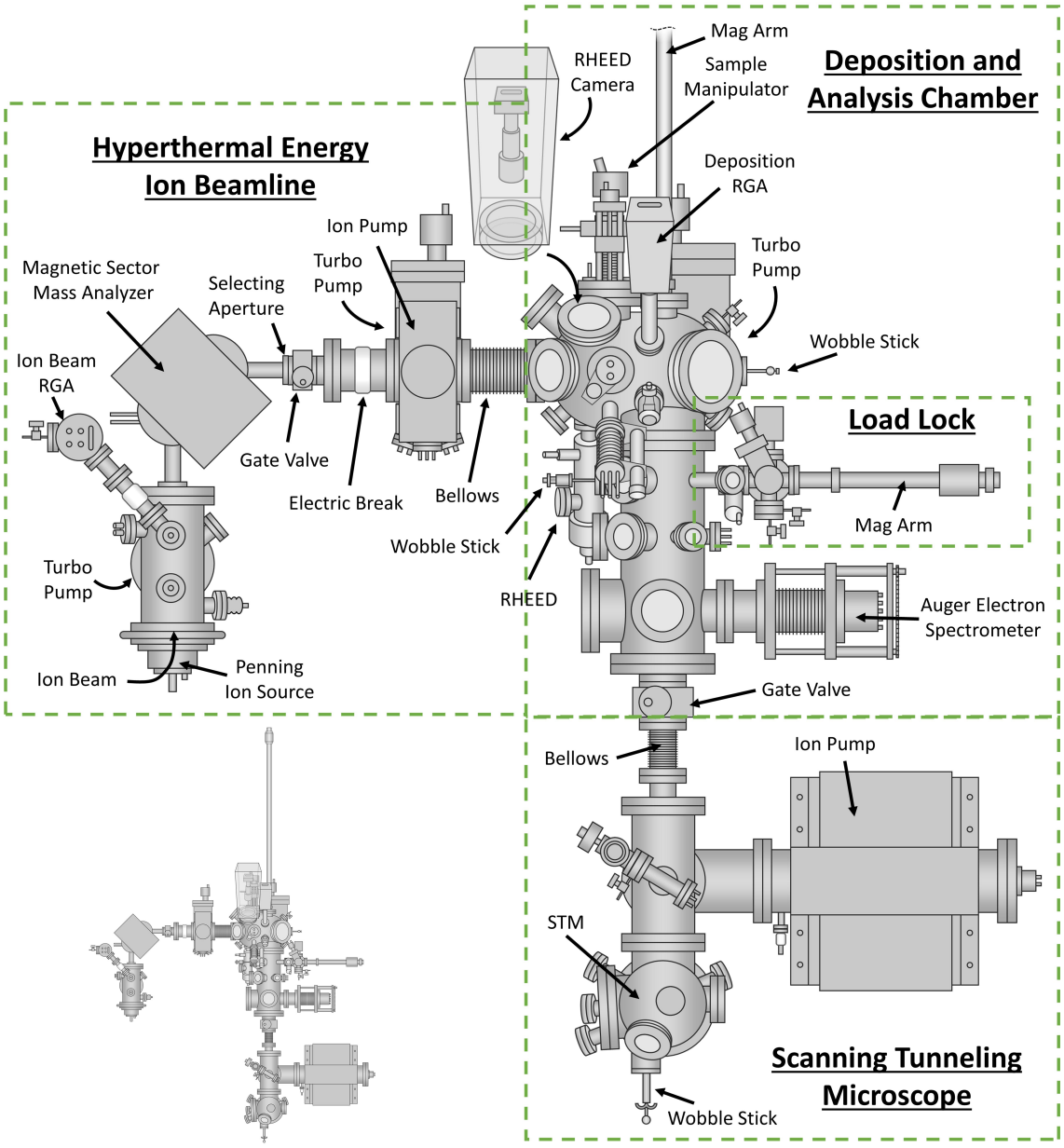

Figure 2.1: Top-down schematic of the ion beam deposition system including the hyperthermal energy ion beamline pictured at the left, the UHV deposition and analysis chamber at the upper right, the load lock used for sample loading into the deposition chamber at the right, and the scanning tunneling microscope pictured at the bottom. These four sections roughly separate four vacuum environments. A smaller scale schematic showing the full length of the magnetic transfer arm used to move samples from the deposition chamber into the STM is in the lower left.

off further to the right for sample loading. Separated from this chamber is the scanning tunneling microscope pictured at the bottom, which is separated from the deposition chamber by a gate valve. Photographs of the system are shown in Fig. B.1 in Appendix B.

2.1.2 Previous Operation

This work relies heavily on the previous work done using this same ion beam deposition system by the lead researcher of the broader enriched Si project, of which this work is a part, Dr. Joshua Pomeroy. This system was used by Pomeroy at Cornell University to deposit thin films of Cu using mass separated ions and observe the effects of the ion energy on the epitaxial quality of the film using STM [58,59], as previously mentioned. Additionally, Baumann and Bethge have extensively tested and utilized the same type of Penning ion source used in these experiments [62–64], and one study in particular served as a reference for the operation of the source in this work under various settings [65]. These tests showed the dependence of the ion current on the gas flow, ion source magnetic field, and anode and cathode voltages. Versions of similar ion source parameter tests generated using the ion source in this work are shown in Fig. A.2 in Appendix A. Other references of previous operation of the ion source used here include studies by Nouri *et al.* [66] and the *Handbook of Ion Sources* by Wolf [67].

2.2 Hyperthermal Energy Ion Beamline

2.2.1 Apparatus

Much of the hyperthermal energy ion beamline used in this work was obtained from Physicon Corporation (MA, USA) including two ion sources, the first section of the beamline and housing chamber, and the magnetic sector mass analyzer. The first element of the ion beamline is the Penning-type ion source, also called a Penning Ionization Gauge (PIG) ion source. The principle of gas discharge, which is the basis of this type of ion source, was first investigate by Phillips [68]. The Penning source generates a plasma from a working gas in an electric field generated by a high voltage between the anode and the cathode that is contained radially by a magnetic field. This plasma ionizes and cracks gas molecules that are injected into the ion source. Mostly singly charged ions are then extracted by a high voltage applied to the extractor electrode, V_{Ext}, into the beamline. An einzel lens with the focus electrode, V_F, focuses and transports the ions at the transport voltage, V_T, which is typically about -4 kV. The transport voltage is applied to the entire ion beam vacuum chamber, which is isolated from the chamber frame and ground. This high transport voltage is needed in order to minimize the effect of space charge repulsion of the positively charged beam, which would cause the beam to expand and become unfocused. A schematic of the ion beamline is shown in Fig. 2.2 (from Ref. [59]). This diagram shows the electrostatic elements of the beamline. Inset is a schematic of the gas-mode Penning ion source showing the anode, cathodes, electromagnet,

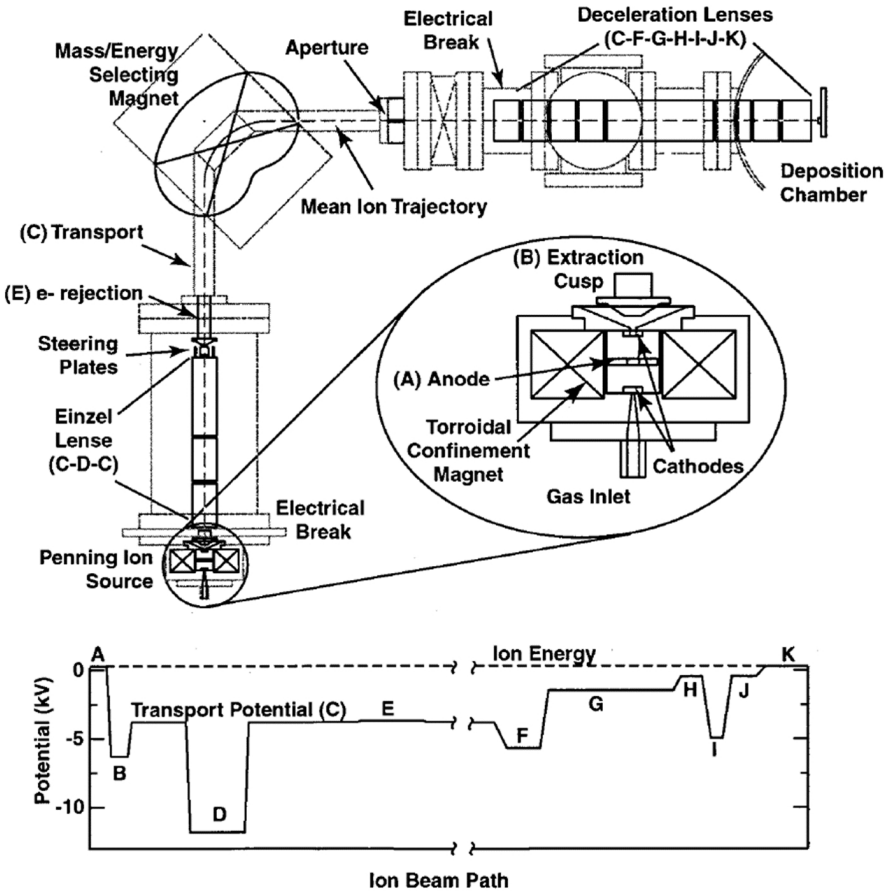

Figure 2.2: Ion beamline schematic showing the electrostatic lens elements used to focus and control an ion beam. Inset is a schematic of the gas-mode Penning ion source showing the anode, cathodes, electromagnet, and extraction cusp (extractor). The gas plasma forms in the anode between the cathodes. The potential energy landscape seen by ions in the beamline is represented at the bottom of the figure with labels A through K referencing the electrostatic elements in the beamline. Ions are created in the source at close to the anode potential (A) and extracted with a large negative potential by the extractor (B). Ions are then focused by an einzel lens (D) and transported at a large negative potential (C). Deceleration lenses (C to K) lower the ion kinetic energy to their starting energy for deposition at a grounded target sample. (from Ref. [59])

and extraction cusp (extractor). At the bottom of the figure is a representation of the potential energy landscape seen by ions in the beamline with labels A through K corresponding to lens elements. A is the anode potential and the potential at which the ions are created, B is the extractor, C is the transport potential, D is the

focus, E is an electron suppression (rejection) electrode that has a potential fixed at approximately 100 V more negative than V_T. Before the electron suppressor, there are X-Y deflectors for steering the ion beam and a skimmer element with monitoring current, I_{sk}. F through K are the individual elements of the deceleration lenses that focus and slow the ions to deliver them onto the sample, which is at ground potential. Six lens elements are independently tunable and are referred to as lenses A2, A3, B2, B3, B4, and X. A typical voltage applied to some of these lenses is roughly -1 kV. Voltages for the deceleration lenes that were used when depositing a ^{28}Si sample are given in Table A.3 in Appendix A. Additionally, a schematic circuit diagram of the power supplies and wiring of the various lens elements within the beamline is presented there in Fig. A.1.

In order to isolate the transport voltage of the ion beam chamber and the cathode voltage applied to the housing of the ion source, an insulating flange is used to connect the two. While most components and flanges comprising the ion beam chamber use UHV seals, the insulating flange uses o-rings to form the vacuum seals. The components of the ion source itself are also sealed using o-rings. This means that these components of the vacuum chamber containing the beamline are only rated to high vacuum, i.e. a minimum achievable pressure of roughly 1.3×10^{-7} Pa (1.0×10^{-9} Torr). The ion beam chamber is pumped using a 350 L/s turbo pump (Pfeiffer Vacuum). The base pressure of the ion beam chamber ranged from approximately 2.7×10^{-6} Pa to 1.3×10^{-5} Pa (2.0×10^{-8} Torr to 1.0×10^{-7} Torr) throughout the work presented here. While initially at the higher end of this range, the base pressure was reduced at one point by removing a gate valve that was also

only rated to high vacuum. The components of the vacuum for the first and second achieved base pressures can be observed using the residual gas analyzer (RGA) in the ion beam chamber. Residual gas mass spectra representative of these base pressures are shown in Fig. 2.3. Base pressure 1 (line) corresponds to the earlier base pressure before removing the gate valve. Base pressure 2 (diagonal line fill) corresponds to the lower achieved base pressure after removing the gate valve. Common vacuum components are observed in both spectra as peaks vs. their mass un u (unified atomic mass unit) including H_2, C, N, H_2O, CO and N_2 at 28 u, O_2, and CO_2. Ar is also observed due to it being used to vent the chamber previously. When a lower base pressure was achieved, the partial pressures of N at 14 u, N_2 and CO at 28 u, and O_2 at 32 u were all reduced within the chamber.

After the ions are extracted and focused into a beam, they are transported into a re-focusing magnetic sector mass analyzer, which bends the ion trajectories in a 90° arc. The sector mass analyzer is a large electromagnet that is used to separate the ions according to their mass-to-charge ratio, m/q. Ions of different mass-to-charge ratios have different resulting trajectories. When the sector mass analyzer is tuned to transmit ions with a particular value of m/q, that value is referred to in discussions and in graphical representations of data only by the mass number, e.g. the mass analyzer is said to be tuned to a mass of 28 u for ^{28}Si ions with m/q = 28 u/e. This is because ions generated from the ion beam and discussed in this work are assumed to be singly charged, unless otherwise noted. This mass analyzer is used to select a particular mass, u, and propagate those ions down the beamline.

At the exit of the mass analyzer is the mass-selecting aperture. Nominally,

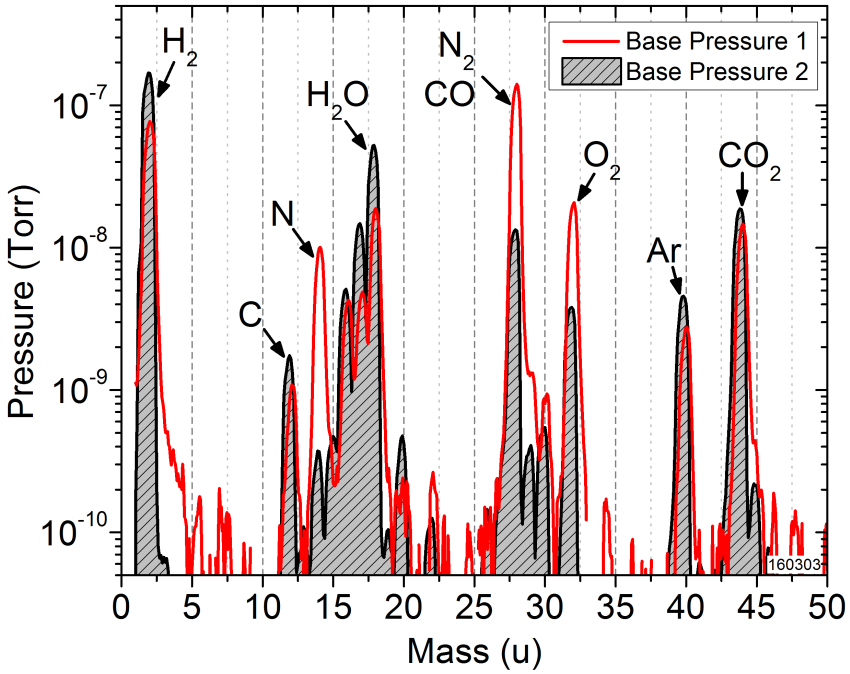

Figure 2.3: Residual gas mass spectra collected from the RGA in the ion beam chamber for two achieved base pressures. Partial pressure peaks of typical components of the vacuum are seen including H_2, C, N, H_2O, CO and N_2 at 28 u, O_2, and CO_2. Ar is also observed due to it being used to vent the chamber previously. The initial base pressure 1 (line) corresponds to the use of a gate value only rated to high vacuum, while a later base pressure 2 (diagonal line fill) was achieved after removing that gate valve. The partial pressures of N, N_2 and CO, and O_2 were reduced with base pressure 2.

ions of a single mass pass through the aperture, while those with other masses are rejected. Three mass-selecting apertures were used in the work presented here. Initially, an aperture that consisted of a circular hole approximately 5 mm in diameter in a stainless steel spacer that was 16 mm thick was used to produce ^{22}Ne and ^{12}C samples. Then, a much thinner Cu gasket aperture in the shape of a slit approximately 1 mm in width, i.e. the same direction that different mass ion beams are spatially separated, was used for initial ^{28}Si depositions. The aperture was also approximately 15.25 mm tall and 2 mm thick. Finally, a second Cu slit approximately 2 mm in width and 12 mm tall with a beveled slit opening to reduce ion scattering

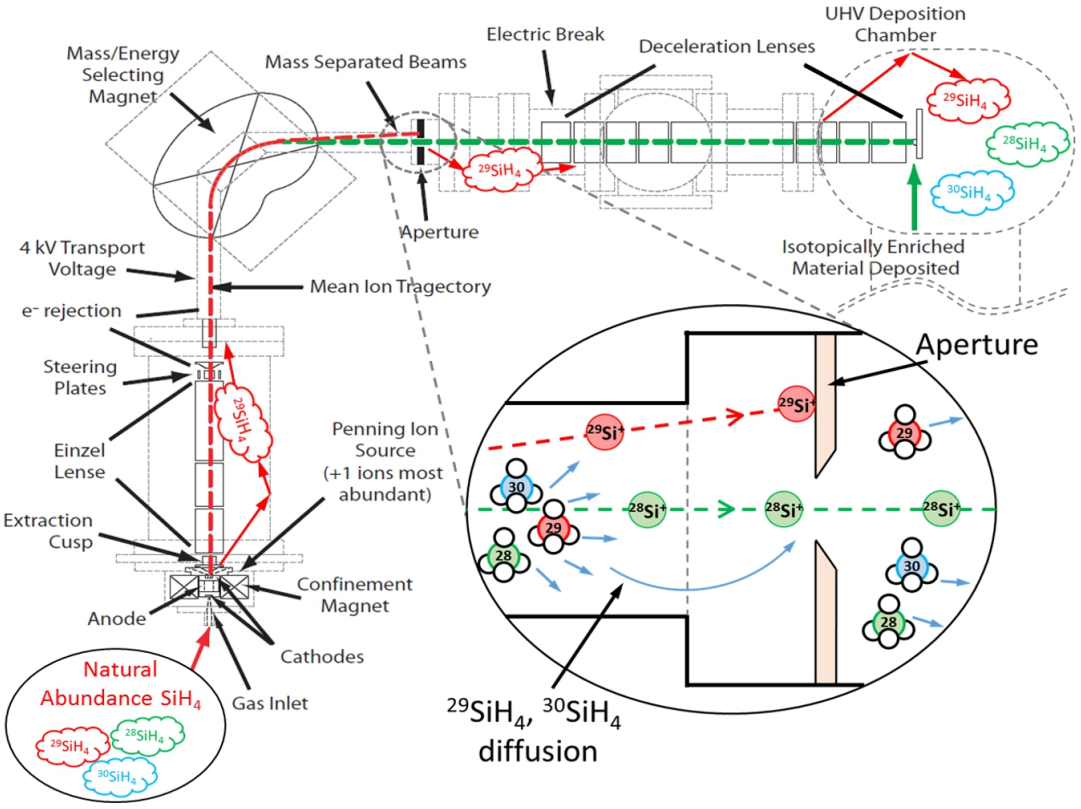

Figure 2.4: Ion beamline schematic showing the diffusion path of natural abundance SiH_4 ("clouds"), including $^{29}SiH_4$, from the ion source inlet (lower left), through the magnetic sector mass analyzer (top left), past the mass-selecting aperture and into the deposition chamber where the sample is located (upper right). The inset cartoon shows a magnification of the aperture area with mass separated Si ions. ^{29}Si ions are blocked by the aperture while the ^{28}Si ions as well as $^{29}SiH_4$ (and other) gas molecules pass into the depositions chamber.

off of the aperture was used to deposit the remaining ^{28}Si samples. Photos of these three mass-selecting apertures are shown in Fig. B.5 to B.7 in Appendix B.

Simultaneous with ions passing through the aperture, gas from the ion source diffuses along the beam path and through the aperture as well. This source gas is natural abundance and results in a partial pressure of unwanted isotopes at the sample, which may be incorporated into the sample during deposition. This phenomenon is discussed in great detail in Chapter 6. Figure 2.4 shows a schematic

of the ion beamline with a cartoon representation of the mass selection and gas diffusion for the case of ^{28}Si deposition. Natural abundance silane gas (SiH_4) is used as the source for generating Si ions in this work. This gas has a purity of 99.999 % according to the gas vendor (Matheson Tri-Gas). Gas is injected into the ion source using a UHV leak valve from a gas manifold used to regulate different gases used for operation of the ion source. A photograph of the gas manifold is shown in Fig. B.2 in Appendix B. When depositing ^{28}Si, the natural abundance SiH_4 diffuses from the ion source down the beamline and to the sample location in the deposition chamber, as represented by the "clouds" in the figure. The inset shows a magnification of the mass selection process occurring at the mass-selecting aperture. ^{29}Si (and ^{30}Si) ions are blocked by the aperture while the ^{28}Si ions and SiH_4 gas molecules pass into the deposition chamber.

Beyond the mass-selecting aperture are the deceleration lenses. As mentioned, the purpose of these einzel lenses is to maintain the focus or de-focus of the ions while decelerating them from the transport voltage mentioned above to ground potential at the sample. The final kinetic energy of the ions depends on the voltage at which they were created in the ion source (plasma potential), which is typically similar to the positive voltage applied to the anode. This is discussed in more detail later in this chapter. Photographs of the electrostatic and magnetic elements comprising the ion beamline are shown in Fig. B.4 in Appendix B.

2.2.2 Theory of Magnetic Mass Separation

When charged ions with different masses but otherwise equal properties traverse a region of magnetic field, they will follow circular motion. Each ion of a particular mass will follow different circular trajectories, resulting in a physical separation of the ions by mass. This principle of magnetic mass separation of ions used in mass spectrometers relies primarily on the magnetic Lorentz force, $\mathbf{F_B}$, which is the force exerted on a charged particle in a magnetic field. The magnetic Lorentz force is given by

$$\mathbf{F_B} = q\mathbf{v} \times \mathbf{B}, \tag{2.1}$$

where q is the charge state of the particle, here an ion, $\mathbf{v}$ is the ion velocity, and $\mathbf{B}$ is the magnetic field experienced by the ion. The cross product results in a force, $\mathbf{F_B}$, acting on the ion in a direction perpendicular to the direction of motion. This force thus results in circular motion of the ion.

In order to determine how ions of different masses are separated as a function of the magnetic field in terms of the radii of curvature of their trajectories, a general equation for circular motion is used. Circular motion of any object can be described as being the result of a centripetal force, $\mathbf{F_c}$, which acts on the object in the direction of the center of the circular path. $\mathbf{F_c}$ is given by

$$\mathbf{F_c} = \frac{m\mathbf{v}^2}{r}, \tag{2.2}$$

where m is the mass of the object, $\mathbf{v}$ is the velocity, and r is the radius of curvature of the circle defining the object's trajectory. The centripetal force and the magnetic

Lorentz force can then be equated, $\mathbf{F_B} = \mathbf{F_c}$, because they both describe circular motion. This expression is solved to get the radius of curvature of the ion trajectory, r, in terms of the mass, velocity, charge state, and magnetic field, yielding

$$r = \frac{m\mathbf{v}}{q\mathbf{B}}. \tag{2.3}$$

This means that for ions with different masses but equal charge states and velocities, the radius of curvature of the ion's motion is proportional to its mass. However, for ions with different masses generated in a beamline and accelerated by electric fields, their velocities will not be equal.

An expression for the ion velocity in a beamline can be determined from considering the ion kinetic energy, E_K, due to acceleration by an electric field generated from an applied voltage. For this scenario, the potential energy, E_P, of the ion in the electric field is transformed into its kinetic energy. Thus, setting $E_K = E_P$ gives the expression

$$\frac{m\mathbf{v}^2}{2} = qV, \tag{2.4}$$

with the kinetic energy term on the left side of the equation and the potential energy on the right. V is the accelerating voltage used to generate the ion beam. Then, solving for $\mathbf{v}$ yields

$$\mathbf{v} = \sqrt{\frac{2qV}{m}}. \tag{2.5}$$

This expression for $\mathbf{v}$ is substituted into Eq. (2.3) yielding a general expression for the mass dependance of the radius of curvature of an ion trajectory given by

$$r_i = \frac{1}{\mathbf{B}}\sqrt{\frac{2m_iV}{q}}. \tag{2.6}$$

Here, r_i is the radius for an ion with index i corresponding to a mass of m_i. In other words, Eq. (2.6) shows that for ions with equal charge states of q and accelerated with voltage V that pass through a magnetic field of $\mathbf{B}$, different masses, m_i, will follow trajectories with different radii of curvature, r_i. It is from this equation that the mass-to-charge ratio, m/q, is seen to be the important parameter for mass separation in an ion mass spectrum.

In a mass spectrometer and in the ion beamline used in this work, the radius of curvature of the sector mass analyzer is fixed, giving a single value of the radius for selected (transmitting) ions, r_0. Rearranging Eq. (2.6) to get an expression for $\mathbf{B}$ and substituting $q = 1$ e and $r_0 = 97.9$ mm gives

$$\mathbf{B} = (1.47 \times 10^{-3})\sqrt{mV}, \tag{2.7}$$

which is the magnetic field in units of T required for selecting ions with a given mass, m, in units of u using a given acceleration voltage, V, in units of V for the beamline used in this work. The quoted value of r_0 is an approximation determined from analysis similar to Eq. (2.6) using experimental values. A plot of $\mathbf{B}$ vs. m calculated from Eq. (2.7) is shown in Fig. 2.5 (a). This calculation uses a value for the accelerating voltage into the sector mass analyzer of $V = 4040$ V, which is a typical value for the operation of the beamline in this work. $\mathbf{B}$ ranges from 0.09 T at 1 u to 0.84 T at 80 u. For ^{28}Si at 28 u, $\mathbf{B} = 0.49$ T in this calculation.

Panel (b) of Fig. 2.5 shows the relation between the current applied to the sector mass analyzer magnet and the resulting mass of the ions being selected for accelerating voltage values of 4040 V (line) and 4740 V (dashed line). An accel-

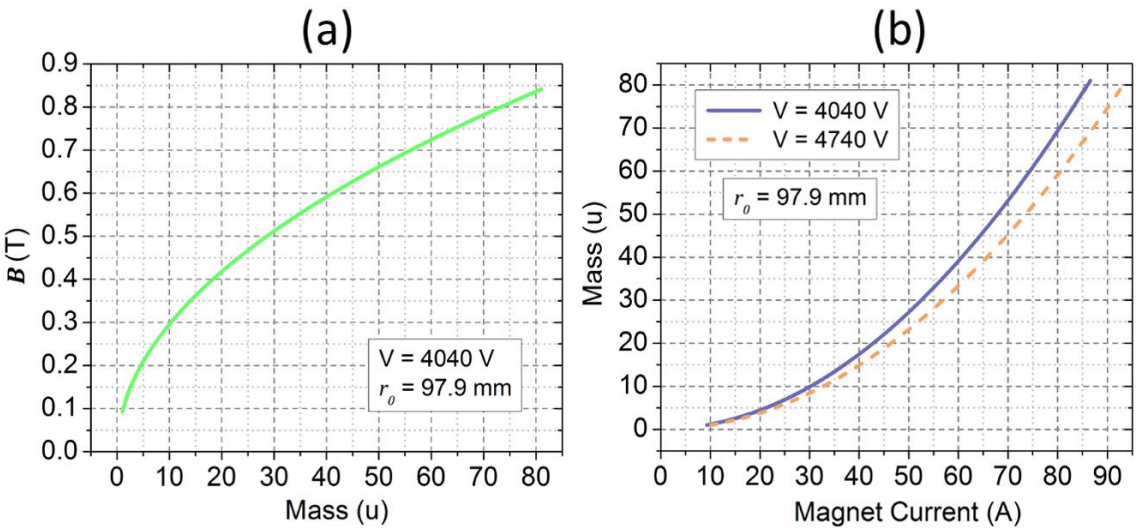

Figure 2.5: Calculated relation of the sector mass analyzer magnetic field and applied current to the selected mass in the ion beam. These calculations are for singly charged ions and use a value for the sector mass analyzer radius of curvature of $r_0 =$ 97.9 mm. (a) The magnetic field required to select a certain mass (line) is calculated from Eq. (2.7) as a function of mass. This calculation uses an accelerating voltage V = 4040 V, typical of the operation of the beamline. (b) The selected mass is shown as a function of the current applied to the mass analyzer magnet for accelerating voltages of V = 4040 V (line) and V = 4740 V (dashed line). These curves are calculated from Eq. (2.9), which is an experimentally derived conversion from the calculated field to the current.

erating voltage of $V \approx 4740$ V is also used for operation of the ion beamline in addition to 4040 V. These curves are determined from the curves in panel (a), by converting the calculated values of $\mathbf{B}$ into the applied current based on experimental measurements. $\mathbf{B}$ and the applied magnet current, I_{mag}, are linearly related, as given by

$$\mathbf{B} = (9.69 \times 10^{-3}) I_{\text{mag}} + (3.43 \times 10^{-3}). \tag{2.8}$$

The slope and intercept of this linear equation were experimentally determined. Here, I_{mag} is in units of A and $\mathbf{B}$ is in units of T. Substituting Eq. (2.8) for $\mathbf{B}$ in Eq. (2.7) and solving for m yields an expression relating the selected mass and the

applied current given by

$$m = \frac{((6.59)I_{\text{mag}} + 2.33)^2}{V}, \tag{2.9}$$

where, I_{mag} is in units of A, V is in units of V, and m is in units of u. In Fig. 2.5 (b), values of I_{mag} between approximately 10 A and 90 A are needed to select ions with masses from 1 u up to about 80 u. Inverting Eq. (2.9) yields an expression for I_{mag} as a function of m and V given by

$$I_{\text{mag}} = (0.15)\sqrt{mV} - 0.35. \tag{2.10}$$

Again, m is in units of u, V is in units of V, and I_{mag} is in units of A. This equation gives the applied current needed for the mass analyzer in this work to select ions with a particular mass for a given accelerating voltage. The mass analyzer current needed for ^{28}Si at 28 u for $V = 4040$ V is $I_{\text{mag}} \approx 50.1$ A.

For a mass analyzer with a 90° bend, the physical separation, λ_1, at a mass-selecting aperture of the trajectories of ions with different masses can be calculated using geometry and trigonometric relations. The two parameters that are required for the calculation are the radius of curvature of the analyzer, r_0, and the distance, Y, from the exit of the analyzer to the aperture where mass selection occurs. An expression for λ_1 as a function of r_0, Y, and two masses is given by

$$\lambda_1 = r_0 \left(\left\{ \frac{m_1}{m_0} \right\}^{\frac{1}{2}} \cos \left\{ \sin^{-1} \left[1 - \left(\frac{m_0}{m_1} \right)^{\frac{1}{2}} \right] \right\} - 1 \right) + Y \tan \left\{ \sin^{-1} \left[1 - \left(\frac{m_0}{m_1} \right)^{\frac{1}{2}} \right] \right\}, \tag{2.11}$$

where m_0 is the mass of the ions being selected and passing through the aperture and m_1 is the mass of another ion not being selected. For this equation, $m_1 >$

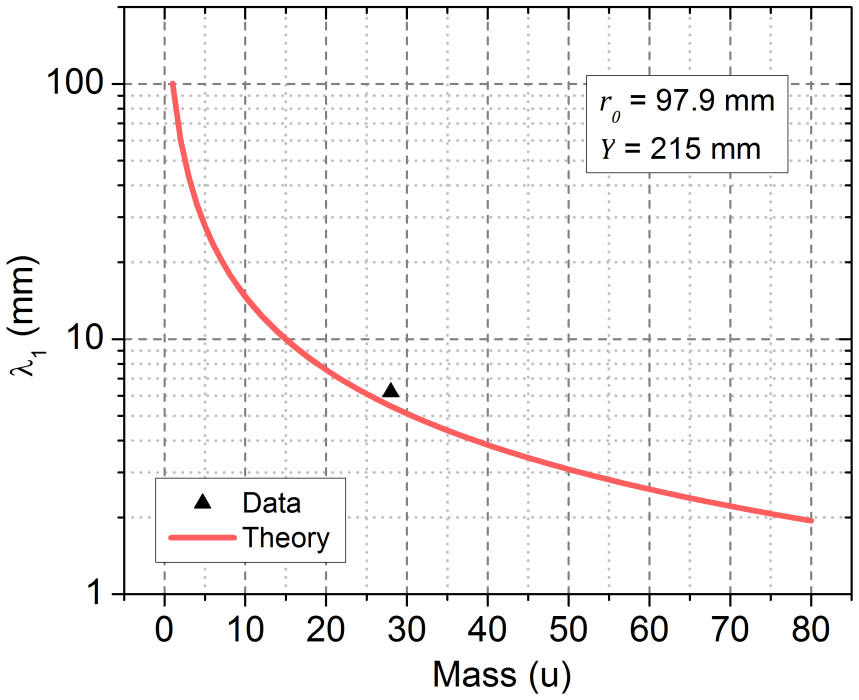

Figure 2.6: Calculated mass dependance of the spatial separation, λ_1, of ions with adjacent mass number in a mass separated ion beam at the mass-selecting aperture. These calculations (line) use values for the physical parameters of the ion beamline including the sector mass analyzer radius of curvature of $r_0 = 97.9$ mm and the distance from the analyzer outlet to the mass-selecting aperture of $Y = 215$ mm. The spatial separation between ions of a given mass and ions of one mass unit, u, higher decreases with increasing mass number from about 100 mm between masses 1 u and 2 u to about 2 mm between masses 80 u and 81 u. This calculated curve is derived from Eq. (2.11). The datum (triangle) is the result of measuring the distance between the aperture center and a deposited mark on the aperture due to the 29 u ion beam.

m_0 in general, and in this case, m_1 is adjacent to m_0, i.e. $m_1 = m_0 + 1$ u. λ_1, the distance between m_0 and m_1 ion trajectories, depends only on the physical parameters (geometry) of the system and the two masses, and it is independent of the energy of the ions or the magnetic field used.

The dependance calculated from Eq. (2.11) of λ_1 as a function of mass, m_0, is shown in Fig. 2.6. A measured value for the distance to the aperture of $Y \approx$ 215 mm was used for this calculation along with a value for the analyzer radius of

curvature of $r_0 = 97.9$ mm. The calculated λ_1 values (line) are highest at lower masses, decreasing with increasing mass. This shows that the physical distance between trajectories at the aperture of ions with adjacent mass numbers ranges from approximately 100 mm between 1 u and 2 u to approximately 2 mm between 80 u and 81 u. For ^{28}Si at 28 u, the calculated distance to the ^{29}Si beam at 29 u is $\lambda_1 \approx$ 5.5 mm. A 2 mm wide mass-selecting aperture then allows a mass-to-charge range of approximately $\pm$ 0.18 u/e when selecting 28 u/e ions. This distance is compared to a measurement of the distance between these two beams (triangle), which has a similar value of approximately 6.2 mm. This measurement was made from the center of the aperture to the center of a visible deposition spot on the aperture created from the 29 u ion beam after depositing ^{28}Si samples. A photograph of this measured aperture is shown in Fig. B.6 in Appendix B. The significance of λ_1 being larger at lower masses is that ions at those masses have a better isolation with ions at adjacent masses leading to larger geometric selectivites for a selected mass.

Ions with the same mass but different kinetic energies due to different accelerating voltages will also have different radii of curvature in a mass analyzer. The physical separation of these ion trajectories at the aperture can be calculated in a similar manner as Eq. (2.11). For the case of a small kinetic energy spread amongst otherwise identical ions due to slight variations in the accelerating voltage, ΔV, a slight spreading of the ion trajectories would result. The physical size of this spreading of trajectories at the mass-selecting aperture, λ_E, from a selected ion to an ion

of the same mass but with a slightly higher kinetic energy is given by

$$\lambda_E = r_0 \left(\left\{ 1 + \frac{\Delta V}{V} \right\}^{\frac{1}{2}} \cos \left\{ \sin^{-1} \left[1 - \left(1 + \frac{\Delta V}{V} \right)^{-\frac{1}{2}} \right] \right\} - 1 \right) + Y \tan \left\{ \sin^{-1} \left[1 - \left(1 + \frac{\Delta V}{V} \right)^{-\frac{1}{2}} \right] \right\}. \quad (2.12)$$

This expression shows that the spreading of ion trajectories due to an energy spread, λ_E, for ions of a given mass depends only on the physical parameters of the system and the accelerating voltage and is independent of mass or magnetic field. A plot of λ_E calculated from Eq. (2.12) as a function of the accelerating voltage, V, for different values of the variation in accelerating voltage, ΔV, is shown in Fig. 2.7. Values in this calculation for the distance to the aperture ($Y = 215$ mm) and the analyzer radius of curvature ($r_0 = 97.9$ mm) were the same as previously used. λ_E is calculated for $\Delta V = 5$ V (line), $\Delta V = 7.5$ V (dotted line), and $\Delta V = 7.5$ V (dashed line). For ions accelerated with a nominal voltage of 4040 V with a typical $\Delta V =$ 6 V, $\lambda_E \approx 0.23$ mm. It is observed from these calculations that λ_E decreases with increasing V, and although the effect is relatively small, it is therefore advantageous to transport ions in the beamline at higher voltages. For V increased to 4740 V in the previous calculation, λ_E is reduced to approximately 0.20 mm. For $\lambda_E =$ 0.23 mm, the total width of the trajectories due to this spread is 0.46 mm, which is equivalent to a mass range of 0.08 u at a mass of 28 u.

From the calculated values of λ_1, the mass resolving power, $\frac{m}{\Delta m}$, of the ion beam system and sector mass analyzer can be calculated as

$$\frac{m}{\Delta m} = \frac{m_0 \lambda_1}{(m_1 - m_0)\Delta\lambda}, \quad (2.13)$$

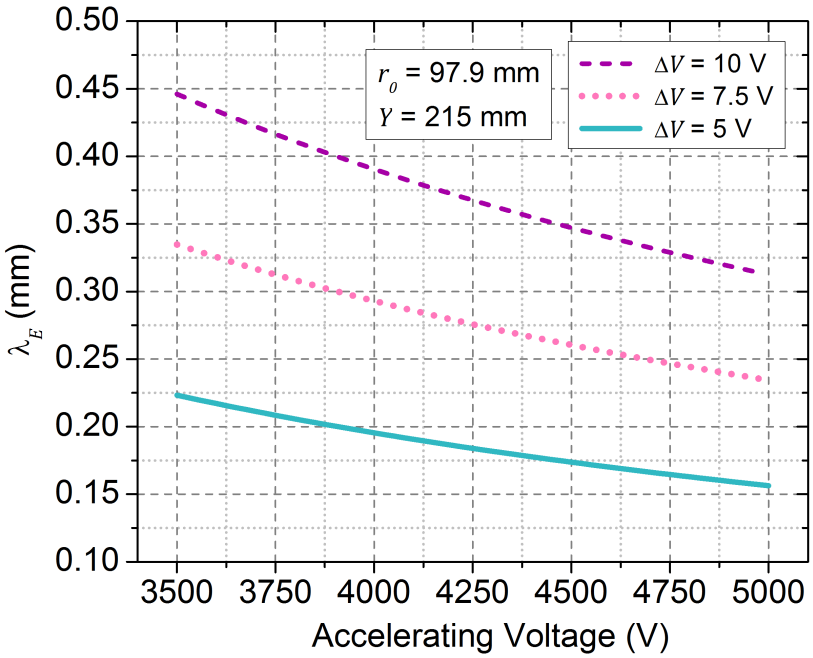

Figure 2.7: Calculated accelerating voltage dependance of the spatial separation, λ_E, of ions accelerated with voltages differing by ΔV in the ion beam at the mass-selecting aperture. These calculations use values for the physical parameters of the ion beamline including the sector mass analyzer radius of curvature of $r_0 =$ 97.9 mm and the distance from the analyzer outlet to the mass-selecting aperture of $Y = 215$ mm. λ_E is calculated for ΔV values of 5 V (line), 7.5 V (dotted line), and 10 V (dashed line). λ_E decreases with increasing accelerating voltage by about 35 % from 3500 V to 5000 V. These calculated curves are derived from Eq. (2.12).

where $\Delta\lambda$ is the width of the selected ion beam at mass m_0. m_1 is the larger mass used in the calculation of λ_1 in Eq. (2.11) and here, $m_1 - m_0 = 1$ u. For the mass resolving power of a mass spectrometer, the numerator represents the selected mass, here m_0, and the denominator, Δm, is a variant of the width of the selected ion beam. Calculated mass resolving power values from Eq. (2.11) and (2.13) are shown as a function of mass in Fig. 2.8. Values in this calculation for the distance to the aperture ($Y = 215$ mm) and the analyzer radius of curvature ($r_0 = 97.9$ mm) were the same as previously used. Additionally, a value of the beam width of $\Delta\lambda =$ 2 mm was used, which is equal to the aperture width used for much of this work.

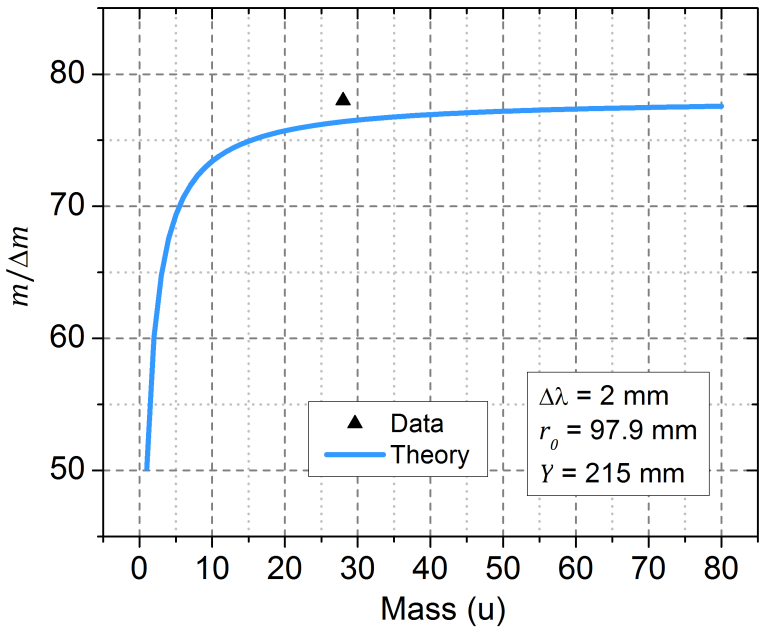

Figure 2.8: Calculated mass dependance of the mass resolving power, $\frac{m}{\Delta m}$, of the ion beamline. These calculations (line) use values for the physical parameters of the ion beamline including the sector mass analyzer radius of curvature of $r_0 = 97$ mm, and the distance from the analyzer outlet to the mass-selecting aperture of $Y = 215$ mm. Additionally, they use an ion beam width, $\Delta\lambda = 2$ mm. This calculated curve is derived from Eq. (2.13). The datum (triangle) is the highest measured mass resolution for a ^{28}Si ion current peak.

The calculated values of $\frac{m}{\Delta m}$ (line) increase with increasing mass, which is counter intuitive because the ion beams of lower masses are better separated than those at higher masses. $\frac{m}{\Delta m}$ increases sharply from a value of approximately 50.2 at a mass of 1 u to approximately 73.4 at 10 u and then increases much slower at higher masses up to approximately 77.6 at 80 u. A single experimental value of $\frac{m}{\Delta m}$ (triangle) for the best mass resolving power measured in this work is shown for comparison. Although other experimental data exists, it can be problematic comparing them if the total ion beam current at various masses is very different because the beam widths can depend on the total current, which is often the case.

2.2.3 Operating Parameters

Two versions of the Penning ion source were used in this work. One with a thin disc-like anode that is efficient at producing ions by sputtering the cathode material, and another with a longer cylindrical anode that is more efficient at ionizing atoms of the working gas. Schematic diagrams of the two ion sources are shown in Fig. 2.9. These schematics are viewed as a cross-section through the middle of the ion sources in a plane parallel to the axis of the ion beamline. Panel (a) shows a schematic obtained from Physicon Corp. of the gas-mode ion source with the gas inlet at the right and the ion beam exit facing the left with an outlet cone. This source uses an anode that is long and cylindrical that is surrounded on either side by the inlet and outlet cathodes. These cathodes have holes through their middles to allow gas to enter the source at the inlet side and ions to exit at the outlet. The anode and cathodes are isolated from each other by a ring shaped insulator seen inside the back plate. As mentioned, the voltage between the anode and cathodes, V_{arc}, was typically about 3 kV, and it was used to generate the gas plasma between the cathodes and inside the anode (shaded oval). Surrounding the anode and cathode region is the source electromagnet solenoid. The anode is in the middle of the solenoid in this source. The source magnet provides a magnetic field (dashed curves) of typically 60 mT that radially confines the ions in the plasma within the anode. Ions are extracted from the plasma by an electric field generated by the high voltage applied to the extractor electrode, V_{ext}. Photographs of the anodes and cathodes of the two ion sources are shown in Fig. B.3 in Appendix B.

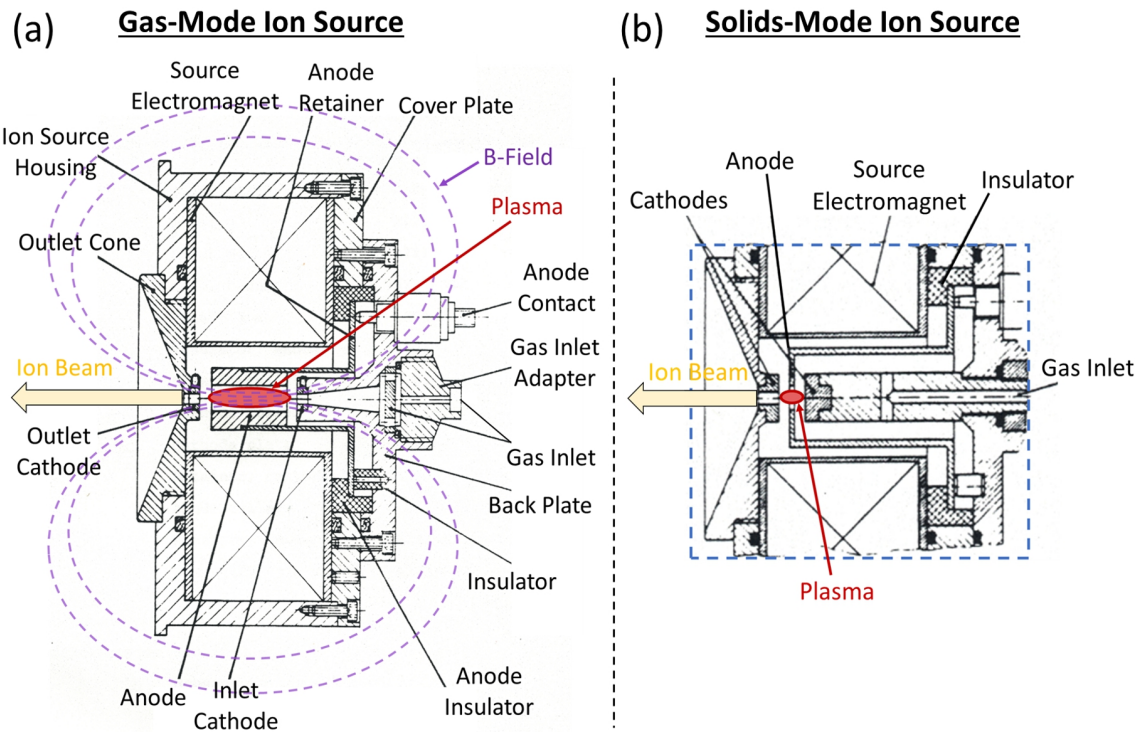

Figure 2.9: Schematic diagrams of the gas-mode and solids-mode Penning ion sources. These sources are distinguished primarily by the size and configuration of the anode and cathodes. (a) The gas-mode ion source is viewed in cross-section through the middle with the gas inlet at the right and the ion beam exit at the left (from Physicon Corp.). This source uses a long cylindrical anode surrounded by inlet and outlet cathodes with holes through each. The voltage between the anode and cathodes, V_{arc}, was typically 3 kV and was used to generate the plasma between the cathodes (shaded oval). The source electromagnet solenoid surrounds the anode and cathode section, providing a magnetic field (dashed curves) of typically 60 mT to radially confine the ions in the plasma. (b) The solids-mode ion source is viewed in cross-section in a similar orientation to the schematic in (a) but with only the middle area visible (from Ref. [62]). This source uses a short anode in the shape of a disk with a hole in the center surrounded by an outlet cathode with a hole on the left and a solid inlet cathode at the right. The plasma (shaded oval) is confined between the cathodes in a smaller volume than in the source in (a). Although the magnetic field is not shown, the electromagnet is used in a similar manner as in (a).

Panel (b) of Fig. 2.9 shows a schematic cross-section from Ref. [62] of a portion of the solids-mode ion source in the same orientation as the source in (a). This source uses an anode that is in the shape of a thin disk with a hole in the center. As with the gas-mode source, the anode is surrounded by the inlet and outlet cathodes. The

outlet cathode on the right of the diagram is the same used for the outlet of the gas-mode source with a hole through it for ions to escape. The inlet cathode is larger and is solid without a hole in order to provide a surface for sputtering. Gas is injected into this source through holes at the base of the inset cathode support. Although not shown, the magnetic field used is similar to that of panel (b) but with anode and cathodes offset from the center of the solenoid. The plasma region is again between the cathodes and within the anode (shaded oval), however, the volume is much smaller in this source than for the gas-mode source.

The solids-mode ion source was used to produce both ^{22}Ne and ^{12}C samples in this work. Working pressures of the source gas injected into the ion source ranged from 1.1×10^{-3} Pa to $\approx 1.0 \times 10^{-2}$ Pa (8.0×10^{-6} Torr to 7.8×10^{-5} Torr). The anode voltage, V_A, was typically about 500 V or more and the cathode was typically about -500 V. The source electromagnet typically current ranged between 1.0 A and 1.5 A. Arc currents, I_{arc}, between 15 mA and 30 mA were observed.

The gas-mode ion source was used to produce ^{28}Si in this work. There are two operating regimes of the gas-mode ion source. These are the typical "low pressure" plasma mode operating condition used to deposit the majority of ^{28}Si samples in this work, as well as a "high pressure" mode that was used to deposit several samples. The typical working pressure used when injecting gas into the source for the low pressure mode was between 1.0×10^{-4} Pa and 3.3×10^{-4} Pa (7.5×10^{-7} Torr to 2.5×10^{-6} Torr). The operating pressure of the high pressure plasma mode was typically 1.3×10^{-3} Pa (1.0×10^{-5} Torr). Anode voltages, V_A, between +30 V and +700 V were used for various depositions throughout this work to generate ions with

a similar range of final ion kinetic energies, E_i. The voltage of to the cathode, V_C, was between -1 kV and -4 kV. This voltage was floating on top of the anode voltage, and the applied difference between the two was referred to as the "arc" voltage, V_{arc}. The source electromagnet typically requires 1.5 A to 2 A to enable ignition of the plasma, which corresponds to magnetic fields of approximately 40 mT to 80 mT. A typical arc current, I_{arc}, of 0.5 mA was observed for this source. Additional operating parameters for both ion sources including those used to deposit the most highly enriched ^{28}Si sample produced in this work are shown in Tables A.1 to A.3 in Appendix A.

The operation and tuning procedures used with the ion beamline to produce a stable and focused ion beam are described in the following steps.

1. Inject the source gas into the ion source using the leak valve at an appropriate pressure, depending on the source and plasma mode being used,
2. set the anode voltage, V_A, to a small positive voltage and the arc voltage, V_{arc}, negative with reference to V_A to define the cathode voltage, V_C,
3. set the transport voltage, V_T, to typically -4 kV,
4. set the extractor voltage, V_{Ext}, which floats on and is more negative than V_T, and
5. set the focus voltage, V_F, which also floats on and is more negative than V_T and V_{Ext}.
6. With these voltages set, turn on the source electromagnet and as the current, I_{SM}, is increased, watch the current reading on the transport power supply, I_T. This will ignite a plasma in the source and then set I_{SM} for when I_T is observed to increase and stabilize.
7. Then, set the magnetic sector mass analyzer to a current corresponding to the desired ion mass and power on the deceleration lenses, monitoring the ion current at the target.

8. Tune the ion beam by adjusting each control element starting from the ion source and moving down the beamline to the deceleration lenses, including the source pressure, I_{SM}, V_{arc}, V_{Ext}, V_F, and the X-Y deflectors, all while maximising the total detected ion current.

9. Finally, tune the deceleration lenses by adjusting the voltages of lenses A2, A3, B2, B3, B4, and X in order while maximising the ion beam current through the sample aperture.

2.2.4 Ion Beam Characterization

2.2.4.1 Ion Beam Mass Spectra

Several techniques were used to characterize each ion beam in preparation for deposition of enriched materials. The components of the ion beam can be observed by sweeping the current, and thus the magnetic field, of the sector mass analyzer magnet, which corresponds to sweeping the selected mass, and recording the measured ion current at the sample location. This type of measurement generates a mass spectrum of the components of the ion beam. Ion currents are measured using a picoammeter with a typical noise floor of 10 pA for the range setting typically used. Several working gases are used in the ion source throughout this work including Ne, carbon dioxide (CO_2), and SiH_4 for ^{28}Si deposition. Mass spectra for Ne and CO_2 are discussed in Chapter 3, and mass spectra for SiH_4 are discussed later in this chapter and throughout this work. Collecting and analyzing a mass spectrum is an important aspect to preparing a mass separated ion beam for deposition. The mass spectrum is used for tuning the mass analyzer to the desired ion, assessing the isolation of that ion beam from adjacent beams, and detecting contaminants within

the vacuum system, among other things.

The mass spectra collected while using several other working gases of Ar, N_2, and methane (CH_4) in the ion source are shown in Fig. 2.10. The measured ion currents (circles and line) are shown as a function of the ion mass-to-charge ratio, m/q. As discussed previously, in this work, mostly singly charged ions are produced, so the mass-to-charge ratio is simply referred to and represented as the ion mass when discussing mass spectra. The current applied to the sector mass analyzer used for the magnetic field sweep is shown on the top axes. The spectra in panels (a) and (b) were acquired using the gas-mode ion source, while the spectrum in panel (c) was acquired using solids-mode source. Panel (a) is a portion of a mass spectrum for Ar showing current peaks corresponding to ^{36}Ar (36 u), ^{38}Ar (38 u), and ^{40}Ar (40 u). The relative sizes of these peaks are similar to the natural abundance of Ar, which is comprised of approximately 0.33 % ^{36}Ar, 0.07 % ^{38}Ar, and 99.6 % ^{40}Ar.

Panel (b) of Fig. 2.10 is a portion of a mass spectrum for N_2 showing current peaks corresponding to ^{13}C (13 u), ^{14}N (14 u), ^{15}N (15 u), and ^{16}O (16 u). The presence of C and O in the beam is due to partial pressures of molecular species containing those elements within the vacuum chamber or possibly contamination in the N_2 gas itself. The peak at 14.5 u likely corresponds to a doubly-charged ion of mass 29 u. A large shoulder peak is seen on the lower mass side of the ^{14}N peak and is likely a result of poor ion beam focusing causing ion scattering from a lens element. The relative sizes of the 14 u and 15 u peaks are similar to the natural abundance of N, which is comprised of approximately 99.6 % ^{14}N and 0.4 % ^{15}N.

Panel (c) of Fig. 2.10 is a portion of a mass spectrum for CH_4 showing current

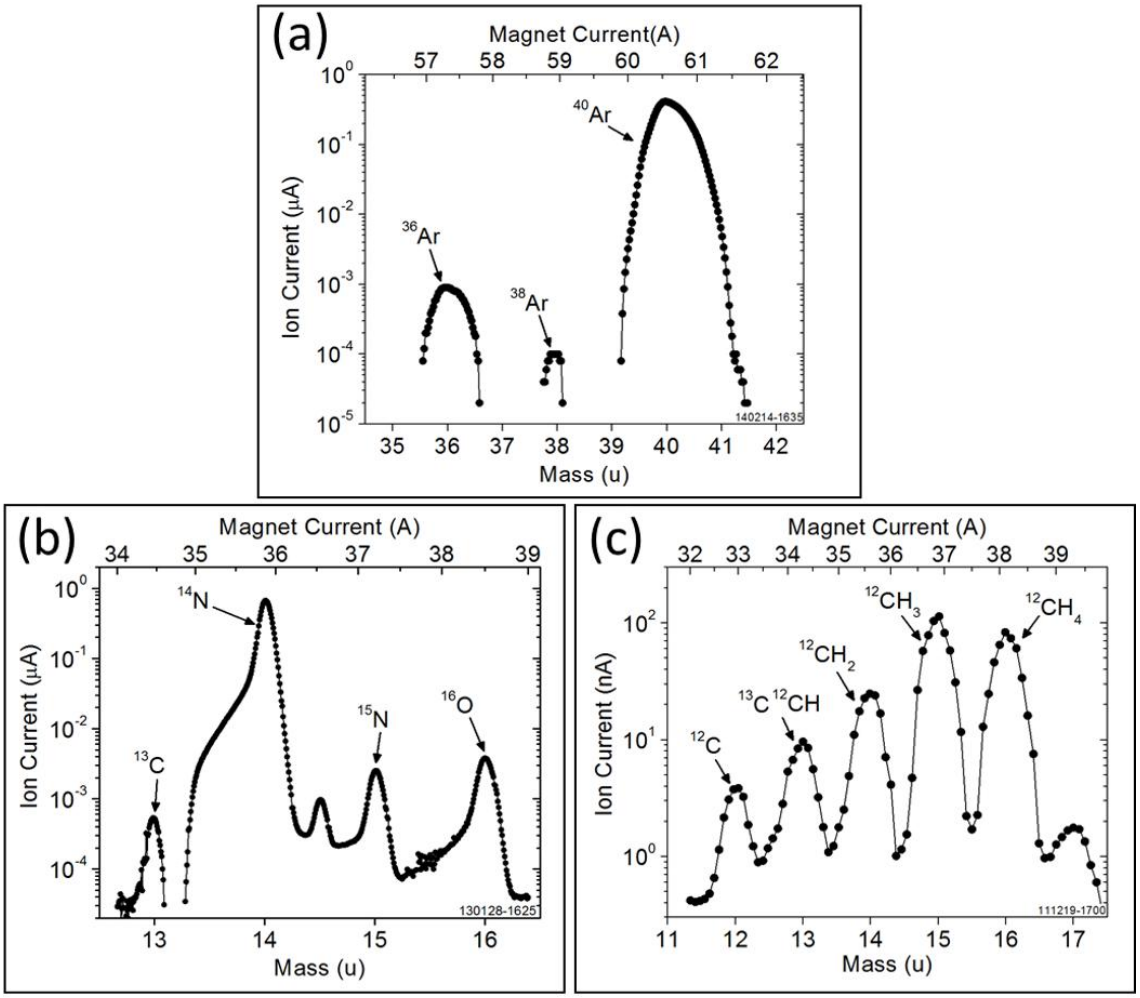

Figure 2.10: Ion beam mass spectra for different working gases used in the ion source. Ion currents (circles and line) are recorded while sweeping the mass analyzer current, and thus the magnetic field (top axes) (a) Ar mass spectrum showing current peaks corresponding to ^{36}Ar (36 u), ^{38}Ar (38 u), and ^{40}Ar (40 u). The relative sizes of these peaks are similar to the natural abundance of Ar. (b) N_2 mass spectrum showing current peaks corresponding to ^{13}C (13 u), ^{14}N (14 u), ^{15}N (15 u), and ^{16}O (16 u). The peak at 14.5 u likely corresponds to a doubly-charged ion of mass 29 u. A large shoulder peak is seen on the lower mass side of the ^{14}N peak due to poor ion beam focusing causing scattering from a lens element. The relative sizes of the 14 u and 15 u peaks are similar to the natural abundance of N. (c) CH_4 mass spectrum showing current peaks corresponding to ^{12}C (12 u) and various C hydrides that are cracked in the ion source plasma. The peak at 13 u is mostly ^{12}CH with a small amount of ^{13}C. Likewise, the peaks at 14 u, 15 u, 16 u are mostly $^{12}CH_2$, $^{12}CH_3$, $^{12}CH_4$, respectively.

peaks corresponding to ^{12}C (12 u) as well as various C hydrides that are the result of different numbers of H atoms being removed when CH_4 is cracked in the ion source plasma. The ion current peak at 13 u is mostly ^{12}CH with a small amount of ^{13}C. Similarly, the peak at 14 u is mostly $^{12}CH_2$ and possibly ^{14}N, the peak at 15 u is mostly $^{12}CH_3$, and the peak at 16 u is mostly $^{12}CH_4$ and possibly ^{16}O.

As mentioned, natural abundance SiH_4 gas is used for ^{28}Si deposition and several spectra representing various deposition conditions for different samples will be presented in chapters 4, 5, and 6. Figure 2.11 shows a portion of a mass spectrum of the ion beam collected while using SiH_4 as the working gas. The corresponding magnetic sector mass analyzer current used for the field sweep is shown on the top axis. This spectrum was generated while using the gas-mode ion source. Ion current peaks (circles) corresponding to ^{28}Si, and various Si hydrides are observed from 28 u to 33 u. The ion current peak at 28 u is ^{28}Si, and the ion current peak at 29 u is mostly ^{28}SiH containing ≈ 5 % ^{29}Si. This estimated relative ^{29}Si is based on the peak heights of 28 u and 29 u being similar and the expected natural abundance of ^{29}Si relative to the ^{28}Si at 28 u. Similar to the peak at 29 u, the peak at 30 u is mostly $^{28}SiH_2$, the peak at 31 u is mostly $^{28}SiH_3$, and the peak at 32 u is mostly $^{28}SiH_4$. The peak at 33 u is likely a combination of $^{30}SiH_3$ and $^{29}SiH_4$. These molecular species are formed by SiH_4 being cracked in the ion source and losing different numbers of H atoms. The overall efficiency of generating ^{28}Si is fairly low as it makes up roughly 10 % of the total SiH_4 ion current. The ^{28}Si ion current observed in this spectrum is $I_i \approx = 620$ nA, which is typical for ^{28}Si depositions.

The 28 u peak and the 29 u peaks in Fig. 2.11 show a high degree of separa-

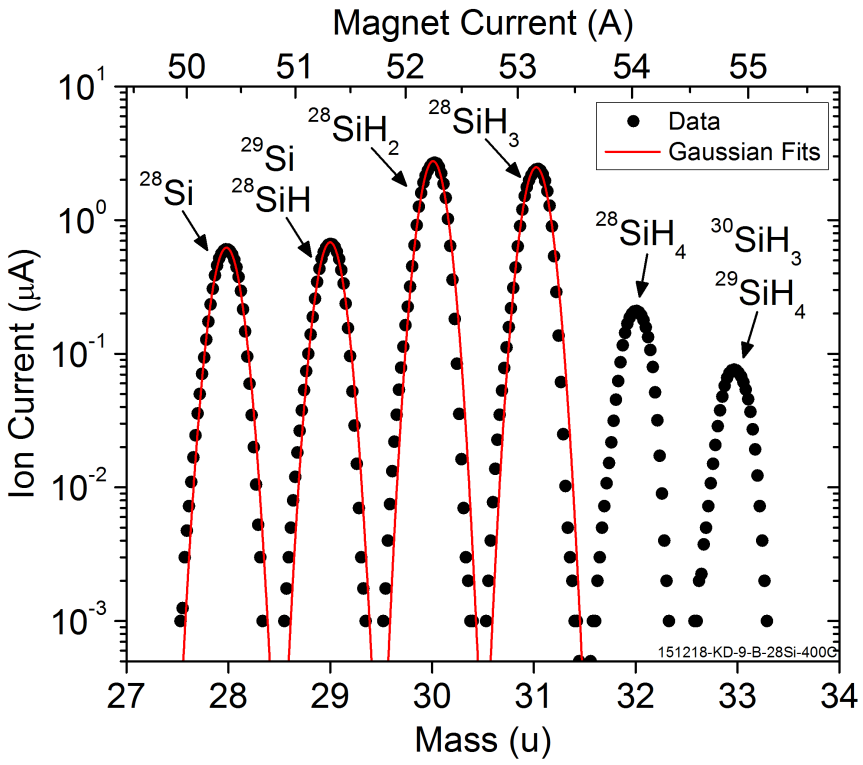

Figure 2.11: SiH_4 mass spectrum representative of the ion beam settings for deposition of many ^{28}Si samples. The ion current (circles) is recorded while sweeping the mass analyzer current, and thus the magnetic field (top axis). Gaussian fits (line, Eq. (2.14)) to the 28 u, 29 u, 30 u, and 31 u peaks are superimposed on the data. The peak at 28 u is ^{28}Si and the peak at 29 u peak is ^{28}SiH and $\approx$ 5 % ^{29}Si. Several higher order hydrides are also observed corresponding to mostly $^{28}SiH_2$ (30 u), $^{28}SiH_3$ (31 u), and $^{28}SiH_4$ (32 u). These molecular species are cracked in the ion source plasma. The centers of the 28 u and 29 u fits are separated by $\approx 10\ \sigma$.

tion with no detectable ion current signal occurring between the peaks. Secondary electrons generated by the ion beam cause the current between the peaks to be $\approx$ -0.5 nA. Also shown is a sum of Gaussian fits to the data (line) of the form

$$I_i = I_i^0 + \frac{B}{\sigma\sqrt{2\pi}} \exp\left(-\frac{1}{2}\left(\frac{m - m_c}{\sigma}\right)^2\right), \tag{2.14}$$

where I_i is the measured ion current, I_i^0 is an offset to the current due to the noise floor of the measurement, B is the area of the Gaussian, σ is the standard deviation, m is the mass, and m_c is the center mass of the peak. The value of

I_i^0 used for fits to ion current peaks is typically 10 pA, which is the noise of the picoammeter mentioned previously. One can see that the data matches the form of a Gaussian very well. This indicates a symmetric and optimally tuned beam shape with minimal perturbations such as scattering. The ion current peaks generated in this system are expected to be approximately Gaussian due to several factors. A Gaussian shaped current peak can result only if the width of the ion beam is greater than the aperture width, which is the case for this system. For a beam with a width smaller than the aperture width, the current peak would have a flat top as the full beam traversed the aperture. The approximately Gaussian shaped profile represents a spacial distribution of beam fluxes that likely originates at the ion source where a higher flux of ions is extracted from the center of the source exit and a smaller distribution coming from the edges.

For this mass spectrum in Fig. 2.11, the centers of the 28 u and 29 u fits are separated by $\approx 10\ \sigma$ (standard deviation). The mass resolving power of the system in this configuration can also be derived from this mass spectrum as $\frac{m}{\Delta m} \approx 58$ at 28 u. Δm in this calculation is determined by taking the full width of the fit to the 28 u peak at 10 % of the peak height, which is approximately 0.48 u. This width is equivalent to a physical width at the mass-selecting aperture of 2.6 mm. As mentioned previously, for a typical ion energy spread of $\pm$ 6 eV due to a spread of accelerating voltages in the beam of $\Delta V = 6$ V, the width in mass due to the energy spread at mass 28 u is approximately 0.08 u. This width due to the energy spread is therefore approximately 17 % of the total width of the ^{28}Si beam as measured in this mass spectrum. The more significant contribution to the full width is likely related

to the width of the ion beam exiting the ion source and may be an intrinsic width for the system, although there may be different focusing conditions which could reduce this width. The hole in the exit cathode of the ion source is approximately 2.54 mm, which is perhaps not coincidentally very similar to the measured ^{28}Si beam width. Ions with a small spread of angles entering the sector mass analyzer could contribute to this width as well. If the total width was only due to the mentioned energy spread, then the resulting mass resolving power would be $\frac{m}{\Delta m} \approx 350$.

An example of a SiH_4 mass spectrum where the ion current peaks are not symmetric and cannot be described by single Gaussian fits is presented in Fig. 2.12. This spectrum shows four ion current peaks (circles) including ^{28}Si at 28 u and a combination of ^{29}Si and ^{28}SiH at 29 u. The corresponding magnetic sector mass analyzer current used for the field sweep is shown on the top axis. Unlike the peaks in the mass spectrum in Fig. 2.11, the peaks here are not symmetric. Shoulders appear on the current peaks to the lower mass side. This is likely due to imperfect tuning and focusing of the ion beam causing a small amount of ion scattering from a lens element. This type of asymmetry decreases the isolation of adjacent peaks, which could possibly affect the realized selectivity and enrichment of a sample. Gaussian fits (line, Eq. (2.14)) to the 28 u and 29 u peaks are superimposed on the data. An additional Gaussian fit of a shoulder peak (dotted line) of the 29 u main peak is also shown, which is needed to accurately determine the peak separation. In this case, the separation from the 29 u main peak to 28 u is $\approx 13\ \sigma$, however, when considering the shoulder peak, that separation drops to $\approx 10\ \sigma$. This value is still very large, but it illustrates the effects of non-ideal beam tuning. Much more

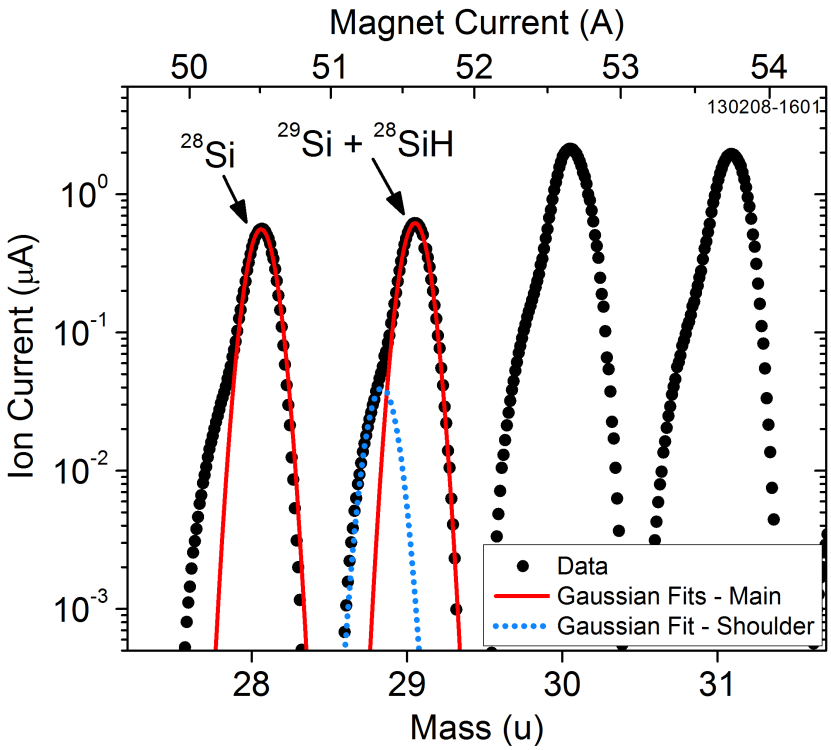

Figure 2.12: SiH_4 ion beam mass spectrum showing shoulder peaks on the main ion current peaks to lower mass side. The ion current (circles) is recorded while sweeping the mass analyzer current, and thus the magnetic field (top axis). The peak at 28 u is ^{28}Si and the peak at 29 u peak is ^{28}SiH and $\approx$ 5 % ^{29}Si. Gaussian fits (line, Eq. (2.14)) to the 28 u and 29 u peaks are superimposed on the data. A Gaussian fit of the shoulder peak (dotted line) of the 29 u main peak is also shown.

significant shoulder peaks are sometimes observed as well.

Other elements and contaminants in the ion beam generated from the chamber or the gas being used can be observed in the mass spectra as well. Typically, when analyzing the mass spectrum of SiH_4, several other mass regions of the full spectrum that contain common contaminants are inspected and recorded. Four of these ion beam contaminant mass spectra acquired when using SiH_4 as the working gas are shown in Fig. 2.13. In each of these spectra, the ion current (circles and lines) is recorded while sweeping the mass analyzer current, and thus the magnetic field,

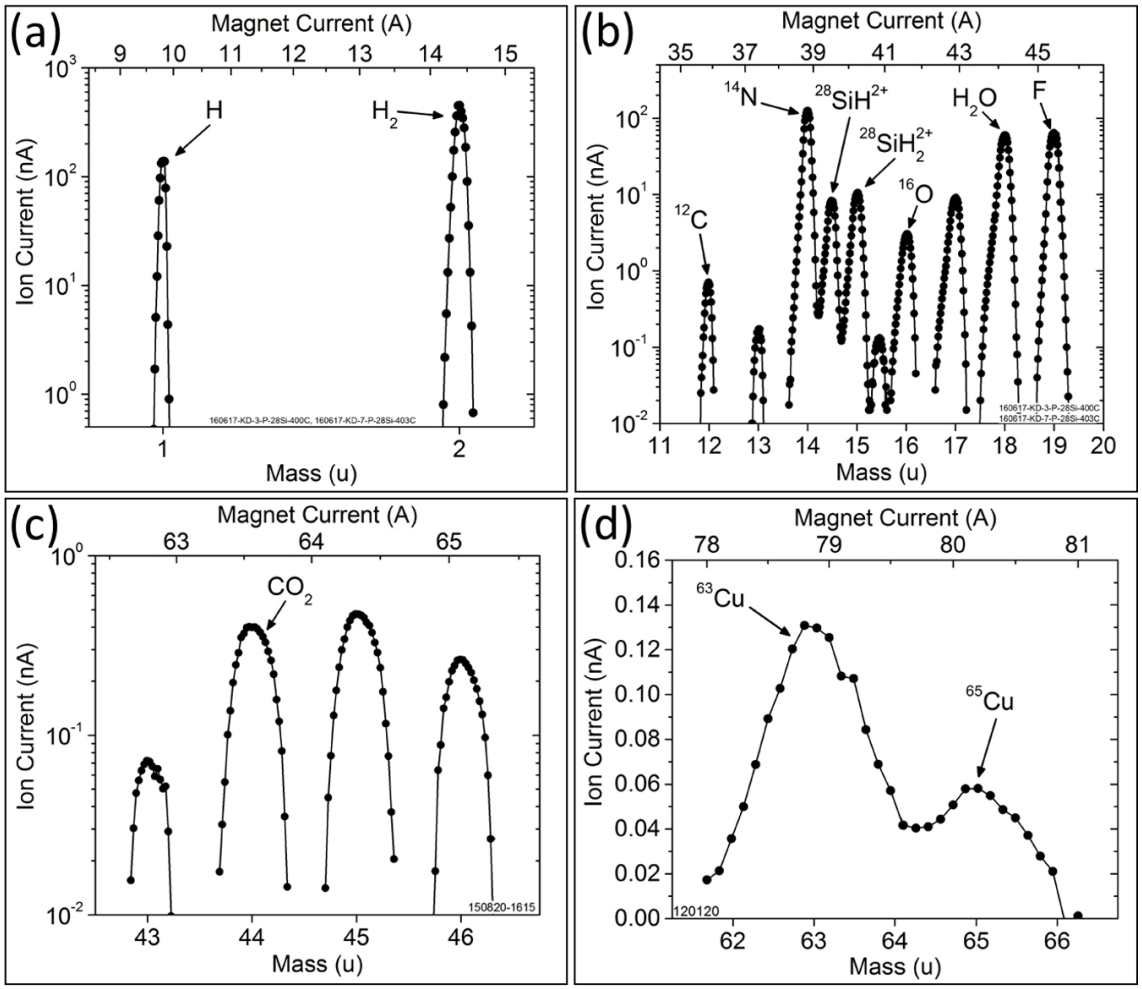

Figure 2.13: Ion beam mass spectra of several chemical contaminants in the ion beam. These spectra were acquired while using SiH_4 as the working gas. In each of these spectra, the ion current (circles and line) is recorded while sweeping the mass analyzer current, and thus the magnetic field (top axes). (a) H (1 u) and H_2 (2 u) current peaks are typically observed in the ion beam. (b) Most of the contaminants have masses between 11 u and 20 u, as seen here. These current peaks correspond to elements including ^{12}C (12 u), ^{14}N (14 u), ^{16}O (16 u), H_2O at mass 18 u, and F (19 u). Doubly charged Si-hydride peaks $^{28}SiH^{2+}$ and $^{28}SiH_2^{2+}$ are also present at masses 14.5 u and 15 u, respectively. Other unknown peaks appear as well. (c) A CO_2 current peak is also typically observed at 44 u, although usually at much lower current levels than other peaks in (a) and (b). The species corresponding to the other three peaks observed within this range are not known. (d) ^{63}Cu (63 u) and ^{65}Cu (65 u) ion current peaks are observed due to ions generated through sputtering of the Cu cathodes in the ion source. The relative peak heights are similar to the natural abundance of Cu.

which is shown on the top axes. The spectra in panels (a), (b), and (c) were acquired while using the gas-mode ion source and the spectrum in panel (c) was acquired while using the solids-mode source. Panel (a) shows H (1 u) and H_2 (2 u) current peaks, which are typically observed in the ion beam. These can originate from vacuum chamber, which always contains H_2, or from the ion source which is cracking SiH_4 and releasing H_2. Panel (b) shows a spectrum with a mass range between 11 u and 20 u containing the most common and abundant contaminants observed. These current peaks correspond to elements including ^{12}C (12 u), ^{14}N (14 u), ^{16}O (16 u), H_2O at mass 18 u, and F (19 u). Doubly charged Si-hydride peaks $^{28}SiH^{2+}$ and $^{28}SiH_2^{2+}$ are also present at masses 14.5 u and 15 u, respectively. If a large ^{14}N or ^{12}C is present, it could indicate the presence of N_2 or CO, which both would appear at approximately 28 u along with ^{28}Si.

Panel (c) of Fig. 2.13 shows a mass range beyond the SiH_4 peaks where several peaks are present. The current peak at 44 u is likely CO_2, which is also typically observed, although with lower currents than the peaks in panels (a) and (b). It is not obvious what ionic species correspond to the other three peaks in this spectrum. Panel (d) shows ^{63}Cu (63 u) and ^{65}Cu (65 u) ion current peaks, which are due to ions generated through sputtering of the Cu cathodes in the ion source. The relative peak heights are similar to the natural abundance of Cu, which is comprised of approximately 69.2 % ^{63}Cu and 30.8 % ^{65}Cu. Note the linear scale of panel (d).

As previously mentioned, a low pressure plasma mode and an high pressure plasma mode of the ion source were used to deposit ^{28}Si samples in this work. These working modes result in qualitatively and quantitatively different SiH_4 ion beam

mass spectra. To demonstrate the transition between these two pressure modes, SiH_4 mass spectra were acquired for several different ion source pressures. These spectra are presented in Fig. 2.14. Note that these spectra are shown on a linear scale to emphasize the differences. Four current peaks are shown comprised of ^{28}Si at 28 u, ^{28}SiH and ^{29}Si at 29 u, primarily $^{28}SiH_2$ at 30 u, and primarily $^{28}SiH_3$ at 31 u. Initially, a typical working pressure for the low pressure mode of 1.2×10^{-4} Pa (9.0×10^{-7} Torr) is used. This pressure results in a standard low pressure mode spectrum (open circles and line), with the 28 u peak appearing smaller than the 30 u and 31 u peaks. This is qualitatively similar to the spectrum shown in Fig. 2.11 on a semi-log scale. When the pressure of the ion source is increased to 6.7×10^{-4} Pa (5.0×10^{-6} Torr), the relative peak heights of the ion peaks in the spectrum shift (open squares and lines). The 28 u peak increases as the 29 u, 30 u, and 31 u peaks decrease. This is because the cracking efficiency of the plasma mode increases with higher pressures and additional H atoms are being cracked from the hydrides, producing more ^{28}Si. This trend continues for the spectrum corresponding to a pressure of 1.1×10^{-3} Pa (8.0×10^{-6} Torr), which shows the 28 u peak even larger (dotted line) but still lower than the 30 u and 31 u peaks. Finally, when the working pressure of the source is increased to 1.3×10^{-3} Pa (9.5×10^{-6} Torr), the mass spectrum (line) appears as a nominal spectrum for the high pressure mode. Here the 28 u peak is the largest of the four peaks resulting from a further increase in the cracking efficiency of hydrides into ^{28}Si. In these spectra, the total efficiency for producing ^{28}Si increased from approximately 8 % to 33 %. The highest efficiency for producing ^{28}Si observed for a high pressure mode spectrum was approximately

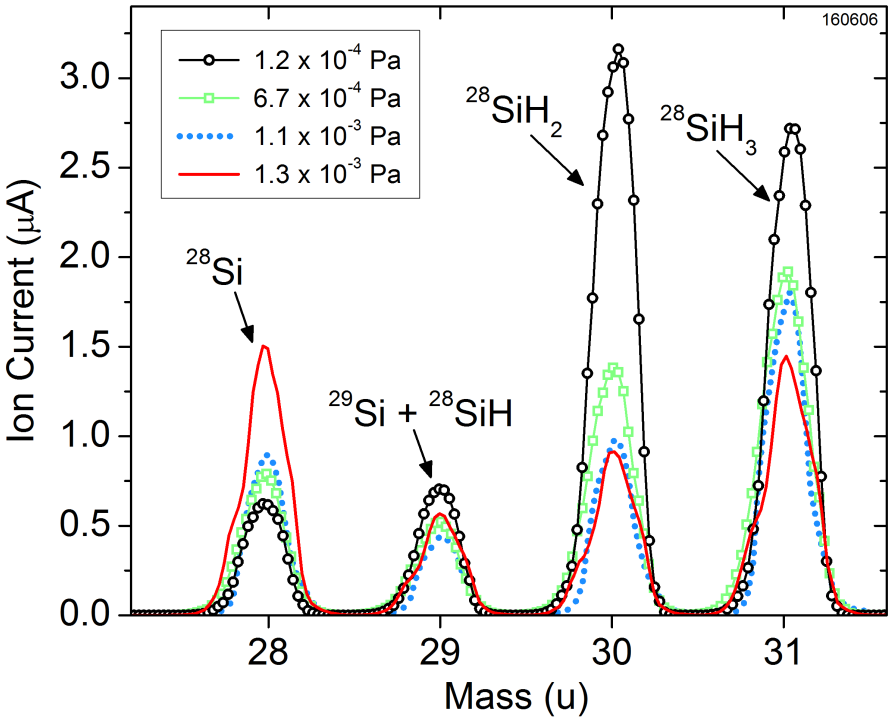

Figure 2.14: SiH_4 ion beam mass spectra for several working pressures showing the transition of the relative peak heights from the low pressure mode of the ion source to the high pressure mode. Note the linear scale. The four current peaks are comprised of ^{28}Si at 28 u, mostly ^{28}SiH and ≈ 5 % ^{29}Si at 29 u, primarily $^{28}SiH_2$ at 30 u, and primarily $^{28}SiH_3$ at 31 u. For a typical pressure used for the low pressure mode of 1.2×10^{-4} Pa, a standard low pressure mode spectrum is observed (open circles and line) with the 28 u peak appearing smaller than the 30 u and 31 u peaks. As the pressure of SiH_4 in the source is increased, leading to a higher cracking efficiency, the 29 u, 30 u, and 31 u peaks decrease in height while the 28 u peak increases. For a pressure of 1.3×10^{-3} Pa, typical of the high pressure mode, the spectrum has fully transitioned to a high pressure mode spectrum (line) with the 28 u peak larger than the other peaks.

47 %. Note also that the total ^{28}Si ion current increased roughly a factor of 2.7 up to approximately 1.5 μA. The high pressure mode is thus able to produce the highest ^{28}Si ion currents, which leads to the highest growth rates and thickest films.

While all ^{28}Si samples produced in this work were deposited using SiH_4 as the Si source, the viability of using solid Si cathodes in the ion source that are sputtered to generate ions was explored. Tests with Si cathodes were conducted using the gas-

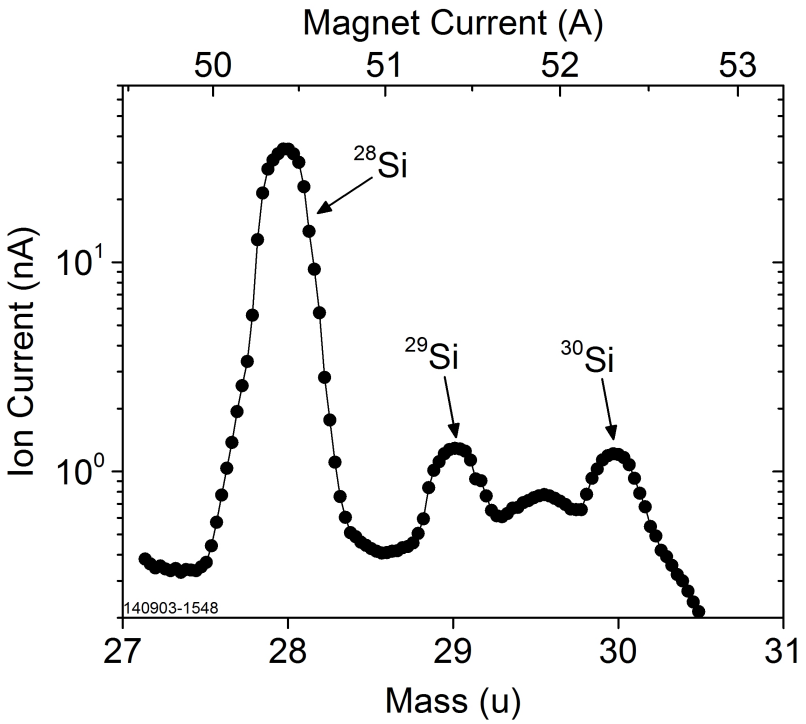

Figure 2.15: Ion beam mass spectrum of Si ions generated by sputtering natural abundance Si cathodes while using Ar as the working gas in the gas-mode ion source. The ion current (circles and line) is recorded while sweeping the mass analyzer current, and thus the magnetic field (top axis). Ion current peaks corresponding to ^{28}Si (28 u), ^{29}Si (29 u), and ^{30}Si (30 u) are observed. The relative heights of the three peaks are similar to the natural abundance of Si.

mode ion source instead of the solids-mode source because the gas-mode source was deemed more reliable at the time. To sputter the Si cathodes, Ar was used as the working gas. A Si mass spectrum acquired when using Si cathodes is shown in Fig. 2.15. The ion current (circles and line) is recorded while sweeping the mass analyzer current, and thus the magnetic field, which is shown on the top axes. Ion current peaks corresponding to ^{28}Si (28 u), ^{29}Si (29 u), and ^{30}Si (30 u) are seen. There also appears to be a small peak at 29.5 u, but the origin of this peak is not known. The relative heights of the three peaks approximately match the natural abundance of Si. With only approximately 35 nA of ^{28}Si ion beam current, which

is at least a factor of ten lower than when using SiH_4 as a source, this approach was abandoned in favor of continuing to use SiH_4.

2.2.4.2 Ion Beam Energy, E_i

The average ion energy, E_i, of ions in the beam at the target can be determined in a measurement referred to as a "roll-off" curve. In this measurement, a positive bias voltage, V_{bias}, is applied to the target to repel the incoming ions and is increased in steps while the ion current, I_i, is recorded. The ion current will drop significantly at a voltage equal to the average ion energy. An example of a roll-off curve produced in this work is shown in Fig. 2.16 (a). This roll-off curve is for Ar ions while using an anode voltage $V_A = 30$ V. The Ar ion current (circles and line) initially has a value over 1.5 μA and initially decreases slowly as V_{bias} is increased. The current then drops much more sharply from approximately 1.25 μA to near 0 μA between 20 V and 30 V. Finally, beyond 30 V, the ion current levels off and again degreases slowly with further increasing V_{bias}. Note that the ion current becomes negative for voltages above 30 V. This is because electrons are attracted to the positively biased target. Panel (b) is the numerical derivative of the current signal in (a) with respect to the bias voltage, $|dI_i/dV_{bias}|$. The absolute value of the derivative is taken for clarity in the figure. The derivative (circles) shows the peak change in ion current at the average ion energy. $|dI_i/dV_{bias}|$ is then fit to a Gaussian (line) of the same form as Eq. (2.14) but with different variables given by

$$\left|\frac{dI_i}{dV_{bias}}\right| = C_0 + \frac{B}{\sigma\sqrt{2\pi}} \exp\left(-\frac{1}{2}\left(\frac{V_{bias} - E_i/q}{\sigma}\right)^2\right), \tag{2.15}$$

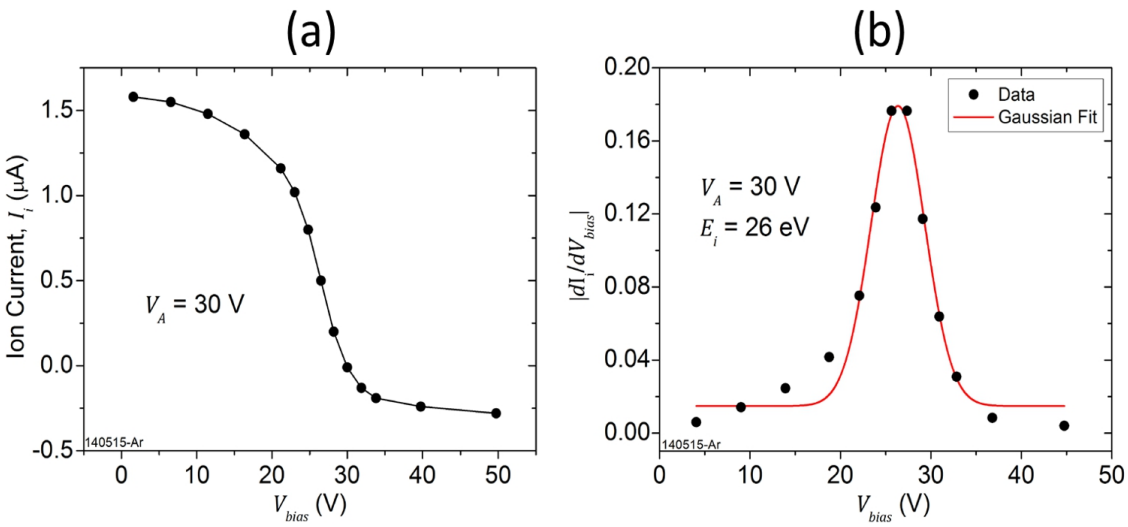

Figure 2.16: Average ion energy measurement for Ar ions using a roll-off curve. (a) Roll-off curve for an anode voltage, $V_A = 30$ V. As the positive bias voltage on the sample, V_{bias}, is increased, positively charged Ar ions are repelled and the ion current, I_i, decreases (circles and line). At a bias voltage corresponding to the average ion energy, E_i, I_i decreases significantly. The measured current becomes negative as electrons are attracted into the target. (b) The absolute value of the derivative, $|dI_i/dV_{bias}|$, of the data in (a) (circles) shows a peak in the derivative at the average ion energy. The data is fit to a Gaussian (line, Eq. (2.15)) giving a peak center $E_i \approx 26$ eV.

where C_0 is the vertical offset from zero of the derivative, B is again the area of the Gaussian, and the ion charge state, $q = 1$, is needed as a conversion of the voltage value of the peak center to ion energy. From this fit, the average ion energy, i.e. the energy corresponding to the peak center, is determined to be $E_i \approx 26$ eV, which is close to the 30 V applied to the anode, as expected for ions created at the plasma potential defined by the anode in the source.

E_i can be mapped as a function of anode voltage, V_A, to determine their relationship. The plasma potential is also affected by the cathode voltage, however, and so the relation between E_i and V_A will change depending on the cathode voltage, or rather the arc voltage between the anode and cathode, V_{arc}. Experimental

measurements of the dependance of E_i on V_A and V_{arc} is shown in Fig. 2.17. The values of E_i are determined in roll-off curve measurements such as the one shown in Fig. 2.16. These measurements are repeated for several values of V_A to get their relationship while keeping the value of V_{arc} constant. This measurement was repeated for different values of V_{arc} including 1.74 kV (circles), 2 kV (squares), 3 kV (triangles), and 4 kV (diamonds). The resulting values of E_i are always smaller than V_A. Additionally, for a given value of V_A, E_i increases with increasing values of V_{arc}. The data for each V_{arc} value is fit to a line (solid, dashed, and dotted lines) given by

$$E_i = \alpha V_A + \beta, \tag{2.16}$$

with slope α and offset β. These fits give values of $\alpha \approx 1$ e, and in general α should ideally be the ion charge state, q. This means that the offset fit parameter, β, approximately describes the difference between the applied V_A and the resulting E_i of ions, written as $\beta \approx E_i - qV_A$. β is plotted as a function of V_{arc} in the inset of Fig. 2.17, which shows that the magnitude of β becomes smaller, i.e. less negative, with increasing V_{arc}.

The energy spread of the ions can also be determined from the fits to the derivatives of the roll-off curves. The energy spread, ΔE, is determined as half the peak width at half the height, with the full range of expected energies being twice this value. For the measurements of E_i in Fig. 2.17, ΔE varies between approximately 17 eV for the highest values of V_A and 4 eV for the lowest ones. The relative energy spread of the ion is then calculated as $\Delta E/E_i$, which is plotted vs.

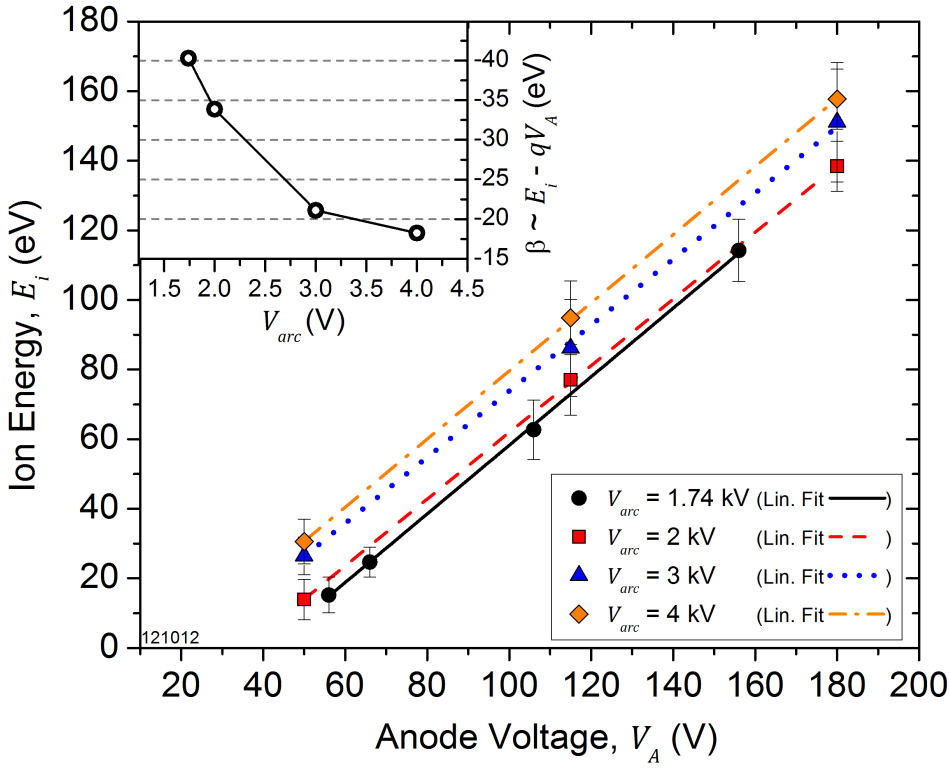

Figure 2.17: Dependance of the average ion energy, E_i, on the anode voltage, V_A, and arc voltage, V_{arc}. Measured values of E_i are plotted vs. V_A for a four values of V_{arc}: 1.74 kV (circles), 2 kV (squares), 3 kV (triangles), and 4 kV (diamonds). The data for each arc voltage value are fit to a line (solid, dashed, and dotted lines, Eq. (2.16)). The inset shows the dependance of the intercept fit parameter of the linear fits, β, on V_{arc}. With slopes of $\alpha \approx 1$ e for the linear fits, $\beta \approx E_i - qV_A$, the magnitude of which becomes smaller, i.e. less negative, with increasing V_{arc}.

E_i in Fig. 2.18. The measured values of $\Delta E/E_i$ (circles) increase with decreasing ion energy from roughly 0.1 at 160 eV to 0.35 at 15 eV. This means that nominally 15 eV ions will have an approximate range of energies between 4.5 eV and 25.5 eV. The uncertainty on the values of $\Delta E/E_i$ come from the standard error of the fit values. This data is fit using a power low plus a constant given by

$$\frac{\Delta E}{E_i} = (4.5)E_i^{-1} + 0.04, \tag{2.17}$$

where the prefactor and the constant are the fit values, E_i is in units of eV, and

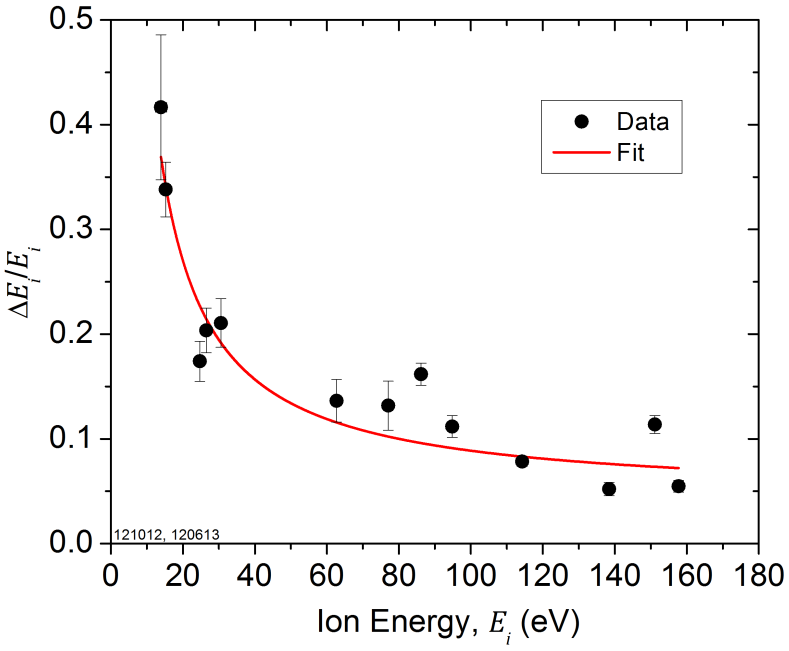

Figure 2.18: Dependance of the relative energy spread $\Delta E/E_i$ of ions on the average ion energy, E_i. $\Delta E/E_i$ (circles) increases from below 0.1 at about 150 eV to above 0.3 at lower ion energies below about 20 eV. A fit to the data of the form of a power law plus a constant (line, Eq. (2.17)) is also shown.

$\Delta E/E_i$ is unitless. This fit equation is derived by first fitting ΔE vs. E_i to a line. These quantities are expected to be proportional with a constant offset from an intrinsic energy spread possibly due to other potentials near the source. The resulting linear equation is then divided by E_i to get a fit for $\Delta E/E_i$. For deposition of ^{28}Si, ions with average energies of $E_i \approx 35$ eV were typically used, and these ions would have a ΔE of approximately 5.9 eV and range in energy from approximately 29 eV to 41 eV. Additionally, at 28 u, a ΔE of 5.9 eV would represent a physical width of of the beam at the mass-selecting aperture of approximately 0.23 mm and a width in mass of approximately 0.08 u, as mentioned previously.

The ion energy is an important parameter in hyperthermal energy ion beam deposition because ions with these energies will sputter the film as they are deposited.

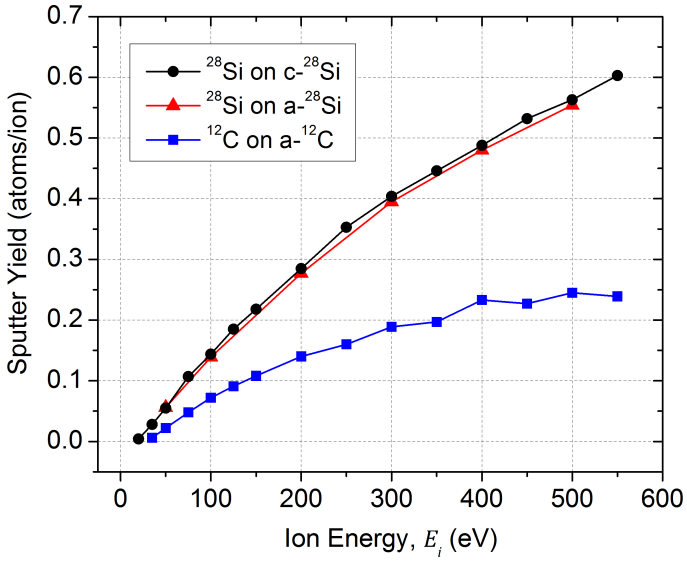

Figure 2.19: Calculated sputter yields for ^{28}Si ions bombarding a crystalline ^{28}Si surface (circles and line) and an amorphous ^{28}Si surface (triangles and line) are shown vs. the ion energy. Sputter yields for ^{12}C ions bombarding an amorphous ^{12}C surface (squares and line) are also shown. Sputter yield values are based on TRIM calculations [69]. The ^{28}Si sputter yield decreases from about 0.6 sputtered atoms per ion down to about 0.05 when decreasing the ion energy from 550 eV to 50 eV. ^{12}C sputter yields are lower and only reach about 0.25 at an ion energy of 550 eV.

If the sputter rate is too large, then the efficiency of the deposition decreases. Sputter yields for ^{28}Si and ^{12}C deposition have been calculated using TRIM [69] and are shown in Fig. 2.19. Sputter yields for the average number of atoms sputtered for every incident ion were calculated for ^{28}Si ions bombarding an amorphous ^{28}Si film (triangles and line), ^{28}Si ions bombarding a crystalline ^{28}Si film (circles and line), and ^{12}C ions bombarding an amorphous ^{12}C film (squares and line). These calculated sputter yields are shown as a function of the ion energy, E_i. As one would expect, the sputter yields decrease with decreasing ion energy. The ^{28}Si sputter yield decreases from approximately 0.6 sputtered atoms per ion down to approximately 0.05 when decreasing the ion energy from 550 eV to 50 eV. ^{12}C sputter yields are

lower and only reach approximately 0.25 at an ion energy of 550 eV, showing that the issue of sputtering is more significant for Si deposition. For ^{28}Si ions with $E_i \approx$ 35 eV, the sputter yield is approximately 0.03, which means that for every 100 ^{28}Si ions bombarding the surface, roughly 3 ^{28}Si atoms on the surface are sputtered off. This results in a very high deposition efficiency.

2.2.4.3 Ion Beam Spot Size

The beam spot shape and ion distribution can be mapped using a small detector at the sample position that is scanned in two dimensions. The detector consists of a collector plate behind an aperture referred to as the sample aperture. At the detector, the ion beam passes through the roughly 3 mm diameter aperture and is collected. The measured ion current through aperture is typically used for assessing the beam flux to estimate the expected deposition rate when producing a sample. A 2D current current map of an Ar ion beam spot is shown in Fig. 2.20. The maximum current measured in the map is approximately 550 nA. The size of the spot is approximately 5 mm by 7 mm with a resulting area of approximately 35 mm^2. This spot size is convolved with the size of an aperture at the detector used for this measurement. The aperture is a roughly 3 mm diameter circular hole, which is large compared to the beam spot size. A simple estimate of the true beam spot size can be made by subtracting half of the aperture diameter from each size of the spot. This give dimensions for the ion beam spot size of roughly 2 mm by 4 mm with a resulting area of roughly 8 mm^2. 2D maps such as these can help to tune the beam

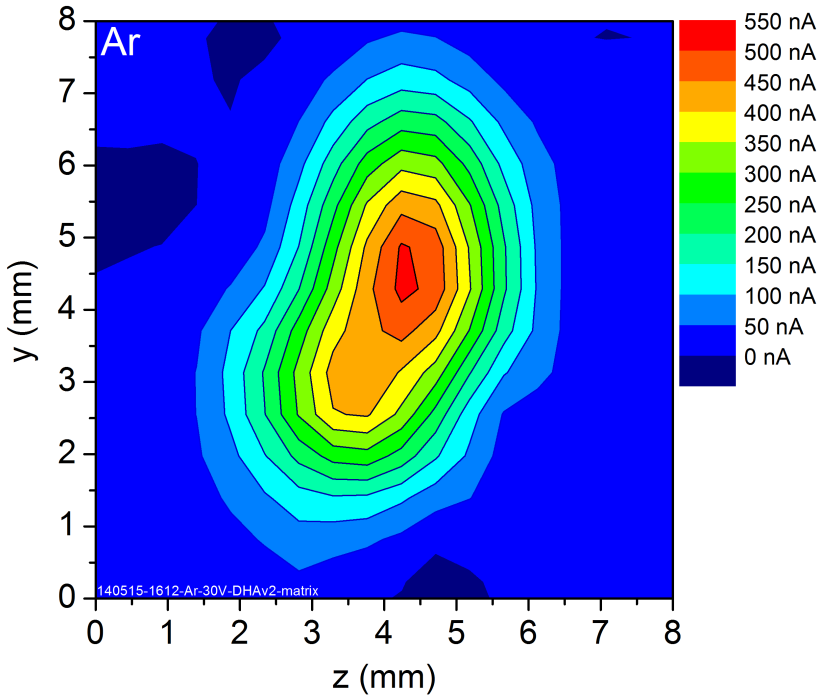

Figure 2.20: Ar ion beam spot 2D current map. The ion current is recorded while moving the detector in two directions, y and z, perpendicular to the axis of the ion beam to produce a 2D grid of data. The maximum current measured in the map is about 550 nA. The area of the spot in this measurement is about 35 mm^2, although the spot size is convolved with the 3 mm diameter of the detector.

better and produce a more circular shape for deposition so the spot location on the sample is better known.

While mass analyzed ion beam currents are typically of the order of 1 μA, the ion source actually generate as much as 1.5 mA of ion current. This total current can be measured on the power supply for the transport voltage, because all ions exiting the ion source must be neutralized in the ion beam chamber except those ions that pass through the mass-selecting aperture. This loss of ion current (fluence) from the total output to the analyzed current at the target was investigated by measuring ion currents on various electrostatic lens elements along the beamline. These investigation found that for a total of 1.3 mA, 0.56 mA was captured on the

extractor, 0.11 mA was captured on the focus, 0.2 mA was captured on the skimmer, and 0.02 mA was captured on the electron suppressor. A total of 0.28 mA was transmitted into the sector mass analyzer. As previously mentioned, approximately 10 % of the total current of SiH_4 ions is ^{28}Si when using the low pressure mode, so one would expect about 28 μA of ^{28}Si current to be transmitted, which is much larger than typical. This may be because the re-focusing properties of the analyzer only affect ion trajectories in the plane of the bend of the analyzer and so ions are perhaps spreading out in a vertical direction perpendicular to the bend of the analyzer. Some modeling using SIMION ion trajectory software was used to model the electrostatic lenes of the ion beamline to try to find better settings for transmitting more ions, but a suitable solution was not found.

2.3 UHV Deposition and Analysis Chamber

2.3.1 Apparatus

The deposition and analysis chamber pictured in the right part of Fig. 2.1 consists of a UHV system connected to the ion beamline on one side and the STM chamber on another. Samples can be loaded into the deposition chamber through the load lock, which can accommodate up to four samples. The load lock is pumped by a 67 L/s turbo pump (Agilent Technologies), which results in a base pressure of approximately 1.3×10^{-7} Pa (1.0×10^{-9} Torr). Typically, the load lock must be pumped out for one day before samples can be transferred into the deposition chamber. At that time, the pressure is about 1.3×10^{-6} Pa (1.0×10^{-8} Torr). The

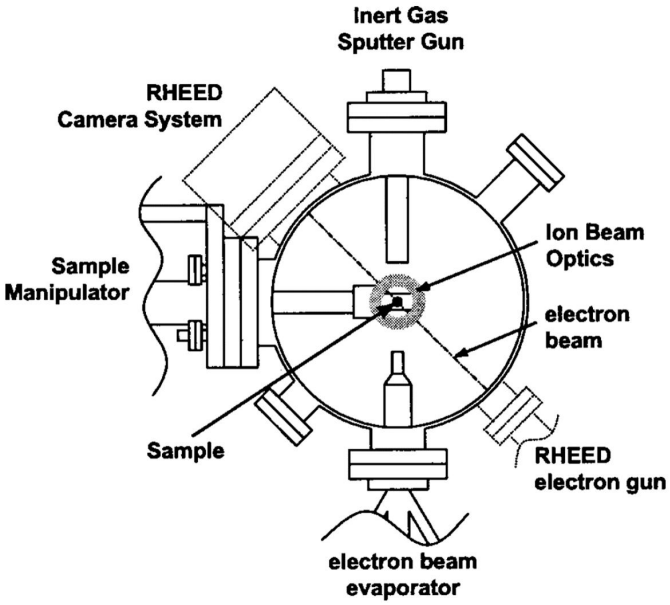

Figure 2.21: Schematic cross section through the deposition chamber in the plane of the sample normal to the ion beam. The sample location on the manipulator and instruments are shown including the ion beam lenses, the RHEED gun and screen, and the natural abundance Si evaporator. Samples facing the ion beam during deposition can simultaneously be monitored with RHEED. (from Ref. [59])

deposition chamber also contains a 5-axis sample manipulator, where the samples sit during deposition. Several other analytic instruments are also present in the chamber including UHV ion gauges, a residual gas analyzer (RGA), reflection high energy electron diffraction (RHEED), a natural abundance Si electron beam thermal evaporator, and an Auger electron spectrometer (Physical Electronics), which was not used significantly in this work. Figure 2.21 shows a schematic cross section through the deposition chamber at the sample location normal to the ion beam, i.e. from the perspective of the ion beam (from Ref. [59]). The sample manipulator is pictured at the right of the schematic with the sample at the center. Normal to the sample (on the manipulator) are the deceleration lenses of ion beam optics, and aligned in the plane of the sample are the RHEED gun and screen and the Si

evaporator. Samples facing the ion beam during deposition can simultaneously be monitored with RHEED. The Si thermal evaporator (Omicron) is a model EFM 3 and is used for natural abundance Si (^{nat}Si) deposition. The EFM is capable of producing deposition rates of typically 0.1 nm/min. The Si source used was either standard Si wafer pieces in a crucible or a high purity Si rod.

Throughout the experiments discussed here, the deposition chamber has also contained other instruments including a sputter gun for Ar sputter cleaning, an Al-deposition source, a STM tip preparation tool, a H-passivation cracking filament, and a quartz crystal microbalance (QCM). These components were also not significantly used in the work reported here. Two external infrared pyrometers, one from Omega and the other from Process Sensors, were used to measure the temperature of samples through a window. The Process Sensors pyrometer has a measurement range between 300 °C and 1300 °C, while the Omega pyrometer can only measure temperatures above 600 °C. When comparing the reading from the two pyrometers, a correction is applied to the Omega pyrometer, which can differ from the Process Sensors readings by $\approx$ 25 °C. A long magnetic transfer rod is used to transport samples between the manipulator, the load lock, and the STM chamber. Additionally, wobble sticks are used to manipulate samples in vacuum at sample stations.

2.3.2 Vacuum Analysis

The deposition chamber is pumped using two turbo pumps and two ion pumps. The turbo pumps are a 300 L/s pump (Edwards Vacuum) located at the deceleration lens section, and a 685 L/s pump (Pfeiffer Vacuum) located at the main

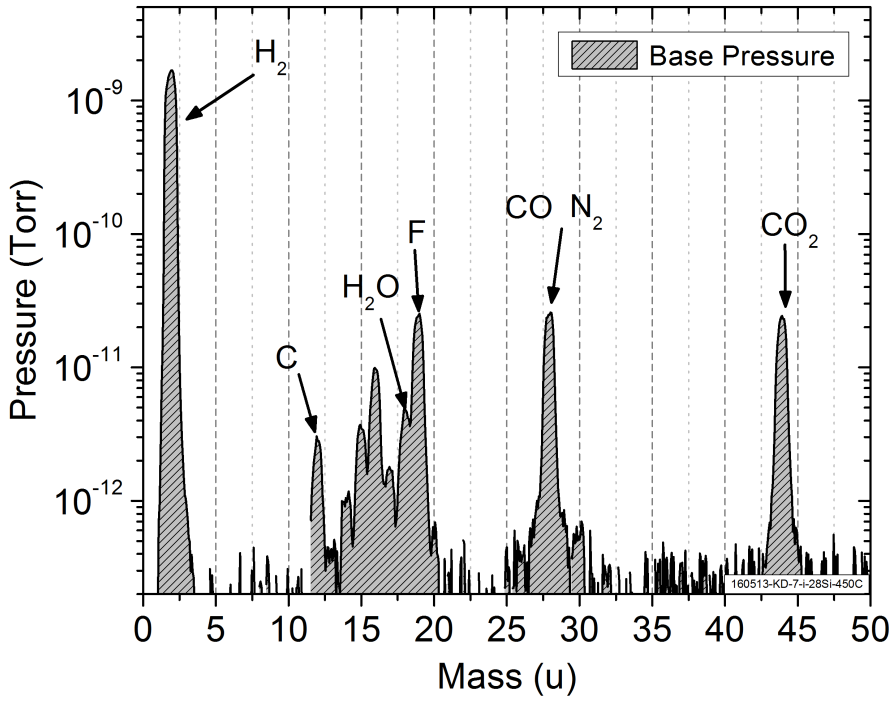

Figure 2.22: Residual gas mass spectrum collected from the RGA in the deposition chamber for a base pressure of 8.3×10^{-9} Pa obtained after baking out the chamber to UHV conditions. Partial pressure peaks of typical components of the vacuum are seen including H_2, C, a very small H_2O peak, CO and N_2, and CO_2. F is also seen in this system.

deposition chamber below the manipulator. Typically, the base pressure of the deposition chamber for the experiments discussed in this work has been between 6.7×10^{-9} Pa (5.0×10^{-11} Torr) and about 1.3×10^{-8} Pa (1.0×10^{-10} Torr). This UHV environment is achieved by heating the chamber to around 150 °C for several days, commonly referred to as baking out. This process removes water and other impurities from inside the chamber, which otherwise get pumped very slowly. The RGA (SRS Vacuum Instruments) can detect the components of the vacuum as partial pressures, giving insight into possible contaminants within the chamber. A residual gas mass spectrum collected from the RGA of the deposition chamber

at a base pressure of approximately 8.3×10^{-9} Pa (6.2×10^{-11} Torr) is shown in Fig. 2.22. Typical components of the vacuum are seen including H_2, C, a very small H_2O peak, CO and N_2, and CO_2. F is also seen in this system. This indicates that some component in the chamber is outgassing F, which may act as a contaminant in the deposition of thin films. The impurities and vacuum pressures do increase from these base values when the deposition chamber is exposed to the ion beam chamber and ion beam. Another RGA residual gas mass spectrum from the deposition chamber collected while the ion beam was being operated with SiH_4 will be shown and discussed in Fig. 6.4 in Chapter 6.

2.3.3 Sample Manipulation

As mentioned previously, a 5-axis manipulator is used to position samples within the deposition chamber for various purposes. The manipulator itself was produced by VG Scienta, but a sample stage from Omicron was attached to the end. It has motion in x, y, and z directions as well as rotation about two axes. One rotation axis is aligned with the insertion axis of the manipulator and is used to face a sample towards or away from the ion beam as well as other instruments. The other rotation axis is an azimuthal rotation about the normal to the sample surface. This rotation is used to position the sample so that particular crystallographic directions of the substrate can be aligned with the RHEED electron beam. The sample manipulator also provides heating capabilities to samples, which are held by sample holders that are loaded onto the manipulator. Sample holders are made of Mo and clamp the Si chips between clips, one of which is electrically iso-

lated from the base. Two methods of sample heating include radiative heating from a tungsten wire back heater, which is referred to as "RH", and direct current resistive heating where current is passed through the Si substrate resistively heating it, which is referred to as "DH". Heating of the substrates and samples are used for several purposes. Deposition at elevated temperatures is critical for facilitating epitaxial deposition of the films. Additionally, substrates can be prepared *in situ* to have clean surfaces by flash annealing them using the DH method for heating. Flash annealing involves rapidly increasing the temperature of the substrate typically from approximately 600 °C to as high as 1250 °C in a few seconds. This high temperature anneal step removes oxide from the substrate surface and reconstructs the surface to form the well known Si(100) (2×1) dimer rows. The oxide typically present on substrates introduced into the vacuum chamber in this work was either a native SiO_2 or a deliberately grown oxide. After remaining at a high temperature for typically 10 s, the substrate is cooled quickly back to 600 °C. This flash annealing method produces flat, nominally clean surfaces on the Si(100) substrates.

A wiring diagram on a photograph of the sample stage on the manipulator is shown in Fig. 2.23 indicating the current path for the two heating methods. A Si(100) substrate with dimensions of approximately 10 mm wide by 4 mm long is seen mounted in a sample holder that is being held on the manipulator. The sample is mounted in the holder *ex situ* using two Mo foil clips that clamp either end of the substrate chip, as mentioned. The Si(100) substrate is glowing due to it being at a temperature of roughly 1000 °C. This demonstrates the DH heating method where current is being driven through the sample to resistively heat it. The DH

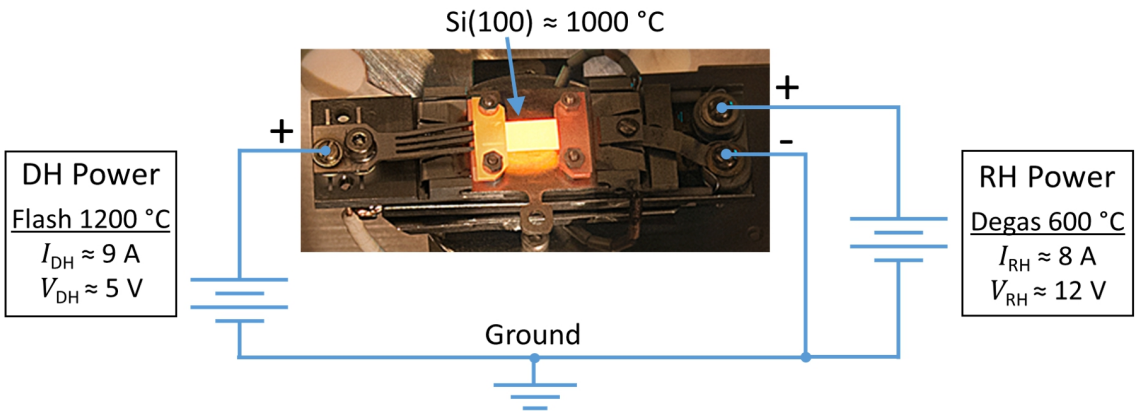

Figure 2.23: Photograph and wiring diagram for heating a Si(100) substrate on the sample manipulator. The Si(100) substrate shown is heated to about 1000 °C using the DH power supply to drive current through the substrate. The DH supply connects to "finger" contact on the left of the sample holder and the grounded base of the sample stage. The current and voltage of the DH supply used for sample flashing to 1200 °C are $I_{\mathrm{DH}} \approx 9$ A, and $V_{\mathrm{DH}} \approx 5$ V, respectively. The RH power supply connects to terminals of a tungsten wire heater beneath the sample, one of which is grounded to the sample stage base. The RH supply uses a current and voltage of $I_{\mathrm{RH}} \approx 8$ A, and $V_{\mathrm{RH}} \approx 12$ V, respectively, for sample degassing at about 600 C.

power supply is represented on the left side of the diagram with the positive lead being connected to the "finger" contact on the left side of the sample stage. The finger is isolated from the rest of the sample stage and contacts the left sample holder mounting clip, which is also isolated from the rest of the sample holder. Therefore, when a voltage, V_{DH} is applied to the finger, a current, I_{DH} flows through the substrate. The other (right) side of the substrate is grounded through the sample holder to the sample stage so that the current flows to the negative terminal pictured on the right. The current and voltage of the DH supply used for sample flashing to 1200 °C are $I_{\mathrm{DH}} \approx 9$ A, and $V_{\mathrm{DH}} \approx 5$ V, respectively.

The RH tungsten back heater shares the negative terminal on the right side of the sample stage in Fig. 2.23. The positive lead of the RH power supply represented

on the right connects to the positive terminal above the negative terminal at the right. The positive terminal of the RH heater is isolated from the sample stage, unlike the negative one. The tungsten wire is connected to these two terminals and runs beneath the sample location in a snaking pattern. The RH supply uses a current and voltage of $I_{\mathrm{RH}} \approx 8$ A, and $V_{\mathrm{RH}} \approx 12$ V, respectively, for degassing samples at approximately 600 C. The RH heater is also typically required to pre-heat the Si substrate before the DH method can be used. This is because the resistance of the substrate is often too large at room temperature to begin flowing current. As the sample is heated by the RH back heater, the resistance of the substrate drops and the Si can then be heated using DH. Photographs of the manipulator and sample stage are shown in Fig. B.12 in Appendix B.

When depositing a ^{28}Si film while simultaneously heating the substrate, a different wiring setup is used in order to be able to monitor the ion beam current on the sample. In this setup, the RH leads are disconnected and the DH power supply is isolated from ground with its leads remaining connected to the sample stage as shown in Fig. 2.23. The input of a picoammeter, which is itself grounded, is then connected to the negative terminal of the sample stage. This setup allows for the ion beam current to flow from the sample through the picoammeter to be measured. There is some leakage current of typically about -10 μA registered using this setup, which produces an offset in the ion current measurement.

In order to achieve the sample heating procedures discussed in this section including rapidly changing the sample temperature as well as using precise deposition temperatures, accurate temperature measurements are important. As was

mentioned previously, an infrared pyrometer is used in this work to measure the temperature of samples. The pyrometers are external to the deposition chamber and view the sample surface through a window. The temperature reading of the pyrometer depends on the value of the emissivity, e, to which it is referenced. Therefore, the emissivity of the Si substrates, which is a temperature dependant quantity, needs to be determined for the temperature range being measured. An indication of the emissivity values for Si can be taken from literature, however, differences in experimental setups such as the type of window that the pyrometer views the sample through require calibration to the system being used. The pyrometer from Process Sensors, which was used for the most samples, was calibrated for the work reported here, while the Omega pyrometer was not. Experimental data and calculations show that for Si at temperatures above approximately 800 °C, e $\approx$ 0.68 and below 100 °C, e can be as low as 0.1 [70, 71].

To calibrate the pyrometer and determine e, two Si eutectics were used. These Si compounds have melting temperatures that are much lower than the Si melting temperature of approximately 1414 °C. By forming a Si eutectic in a small region on a Si substrate, the substrate temperature can be brought to the melting point of the eutectic while the Si substrate remains solid. To calibrate the pyrometer, it is used to monitor the temperature of the substrate while the eutectic is heated until it melts. With the temperature adjusted so that the eutectic is held at its melting point, the emissivity of the pyrometer is adjusted until the temperature that it reads matches the known melting temperature of the eutectic. This gives a calibration for the pyrometer at a specific temperature for the experimental setup being used.

The two Si eutectic systems that were used in this work to calibrate the Process Sensors pyrometer are Au-Si, which has a melting temperature of approximately 363 °C and Al-Si, which has a melting temperature of 577 °C. The Au-Si eutectic phase diagram is shown in Fig. 2.24 taken from Ref. [72]. The phase boundary for the liquid phase is shown as a function of Si atomic concentration as a percentage. The eutectic forms at a Si concentration of approximately 18.6 % where the melting temperature is at a minimum of approximately 363 °C.

The Au-Si eutectic was formed here by pressing a small Au wire onto the edge of a Si substrate. The substrate was then heated in the vacuum chamber using the DH method. The substrate temperature was increased until part of the Au wire was seen to melt. This signified a Au-Si eutectic being formed due to a small amount of Si diffusing into the Au where it contacting the substrate. Upon repeated cycling of the temperature above and below the the point that the (mostly) Au wire melts, the temperature at the melting point is observed to decrease as the Si concentration equilibrates to the optimal eutectic Si concentration of 18.6 %. When this occurs, the temperature reading at the melting and freezing of the wire remains constant. This temperature is then known to be approximately the 363 °C melting temperature of Au-Si and the pyrometer emissivity was adjusted to match this temperature, yielding a value of e = 0.25. A similar procedure was followed for the Al-Si eutectic although instead of a Al wire, an approximately 2 mm by 2 mm square of Al approximately 500 nm thick was deposited on the Si substrate. This method was found to be less reliable than using a larger wire. For the Al-Si calibration at 577 °C, an emissivity value of e = 0.42 was determined. These

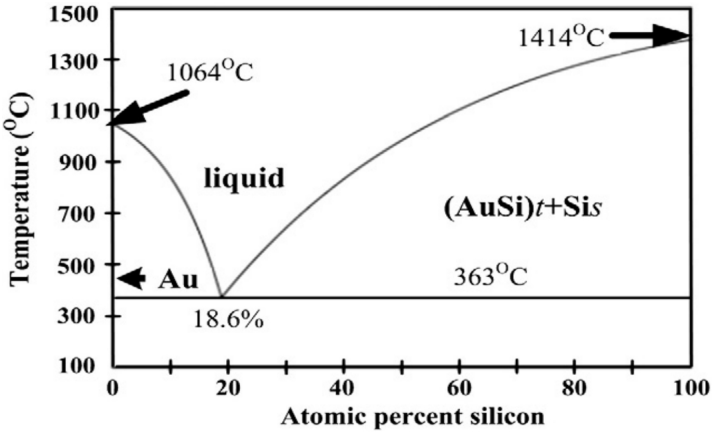

Figure 2.24: Au-Si eutectic phase diagram showing the phase boundaries as a function of Si concentration. The melting temperature of a Au-Si system is lowest for a Si atomic concentration of 18.6 %. This corresponds to the eutectic melting temperature of 363 °C. (from Ref. [72])

measured values were then combined with the literate value for temperatures above approximately 800 °C of e $\approx$ 0.68 to get an approximate function of e vs. T used for experiments here. In this function, e = 0.25 is used for Si substrates temperatures between room temperature and 470 °C, e = 0.42 is used between temperatures of 470 °C and 625 °C, and e = 0.68 is used for temperatures above 625 °C. These crossover points were chosen based on both the measured e values and literature values of e for a range of temperatures [70, 71].

The calibrated pyrometer was then used to determine a calibration curve for the current applied for DH sample heating and flashing. This control curve of substrate temperature as a function of the substrate current using the DH, I_{DH}, is shown in Fig. 2.25. To generate this control curve, the temperature of the substrate was recorded for different values of I_{DH} using the three previously discussed values of e in their appropriate temperature ranges. These data are seen appearing in three distinct curves (circles) marked with each value of e. Note that the current is shown

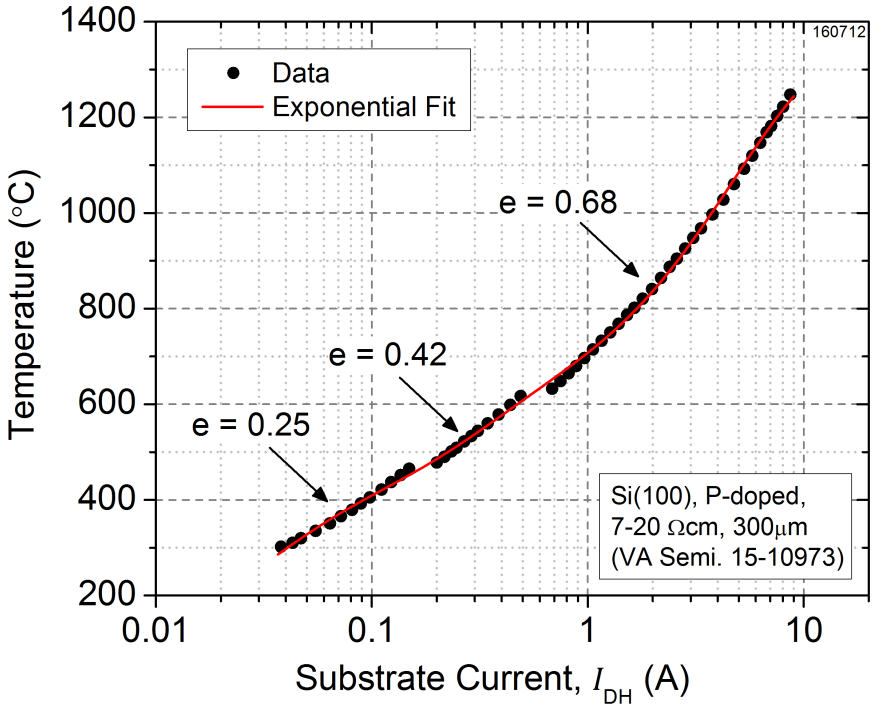

Figure 2.25: Experimental control curve for the DH power supply used for sample heating. Temperature measurements (circles) are shown vs. DH current, I_{DH}, applied through the substrate. Note that the current axis is shown as a log scale. Temperatures are measured using an infrared pyrometer for three emissivity values, 0.25, 0.42, and 0.68. These three values correspond to measurements in three temperature ranges with crossover points between the ranges at 470 °C and 625 °C. To transition smoothly between the three regions, the data is fit to a sum of three exponentials (line, Eq. (2.18)), which is then used for sample heating. This data is for a Si(100), phosphorous-doped substrate 300 μm thick with a resistivity between 7 $\Omega \cdot$ cm and 20 $\Omega \cdot$ cm.

on a log axis. This data is for a Si(100), phosphorous-doped substrate 300 μm thick with a resistivity between 7 $\Omega \cdot$ cm and 20 $\Omega \cdot$ cm acquired from Virginia Semiconductor. Substrates with different specifications, especially the thickness, will have different control curves. In order to smoothly transition between the three ranges, the data is fit to a sum of three exponentials (line) given by

$$T = 1360 - (290)\exp\left(\frac{-I_{\mathrm{DH}}}{0.026}\right) - (240)\exp\left(\frac{-I_{\mathrm{DH}}}{0.024}\right) - (810)\exp\left(\frac{-I_{\mathrm{DH}}}{4.7}\right), \quad (2.18)$$

which shows the fit parameters. I_{DH} is in units of A and T is in units of °C.

This fit allows for the substrate temperature to be controlled continuously using the applied DH current for both sample degassing and flash annealing. Including the uncertainties from the pyrometer calibration, the temperature readings of the substrate are estimated to have a 5 % relative uncertainty due to fluctuations in the current used for sample heating as well as temperature gradients across the sample.

2.3.4 *In situ* Sample Analysis

After flash annealing a Si(100) substrate to clean and prepare it *in situ*, the surface can be inspected by RHEED. This and other capabilities including STM are used to produce ^{28}Si thin films and analyze them *in situ*. The RHEED system (STAIB Instruments) used here typically uses an electron energy of approximately 15 keV, and an electron gun filament current of approximately 1.55 mA. As mentioned previously, Si(100) substrates are positioned using the manipulator to be able to do RHEED during deposition. The sample can be rotated about its azimuth normal to the surface to align the RHEED electron beam along different crystallographic directions, but typically the beam was aligned with the $\langle 110 \rangle$ direction. The other axis of rotation of the manipulator can be used to adjust the angle of incidence of the RHEED electron beam, and typically, an angle of approximately 2° was used for capturing diffraction patterns although angles as high as 5° were sometimes used. The RHEED diffraction patterns are captured using a camera in a dark enclosure that images the patterns produced by diffracted electrons on a phosphorous screen.

An example RHEED diffraction pattern of a flashed Si(100) surface showing

diffraction corresponding to the (2×1) surface reconstruction is shown in Fig. 2.26, which was acquired with the surface at approximately 600 °C. The observed semi-circle of spots is the zeroth Laue zone, which is typically imaged. The outer diffraction spots are due to the bulk Si diffraction and the inner two spots are due to the reconstruction. The reflected specular spot appears in the middle. As this pattern is a representation of reciprocal space, the distance from the central (00) spot to the bulk Si (11) spots are inversely related to the atomic spacing of atoms on the Si(100) surface. Knowing the physical spacing of these spots on the screen and the working distance to the sample, the Si lattice constant can be extracted. The spacing of Si(100) (2×1) dimer rows on the surface is double the atomic spacing, and so the (2×1) spots appear at a distance from the central spot that is half of that to the bulk spots.

These diffraction spots and a lack of a diffuse background indicate a crystalline surface that is fairly clean, i.e. free of oxide, although RHEED is not sensitive to trace impurities. The observed diffraction patterns in RHEED are the result of the combined diffraction from a macroscopic area on the sample (≈ 0.25 mm^2) due to an elongated electron beam spot on the surface of several mm resulting from the low incidence angle. Typically, diffraction from a flat surface produces long vertical streaks in the pattern, which can be seen in Fig. 2.26. Stronger intensity spots in the middle of the streaks are the result of the finite and relatively large size of atomic terraces (e.g. 100 nm) on the Si(100) surface with the streak length being inversely proportional to the terrace size. Kikuchi lines are also seen running diagonally through the pattern, which are due to surface resonances.

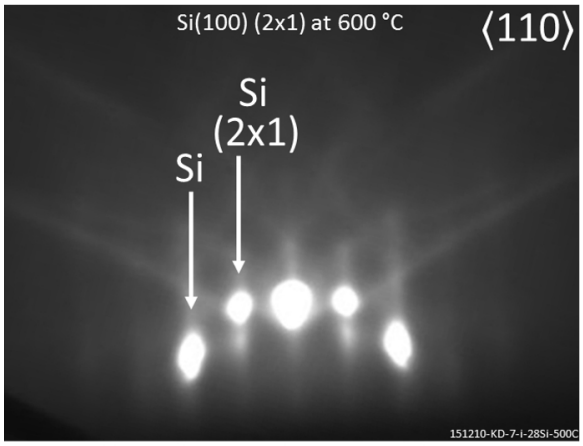

Figure 2.26: RHEED diffraction pattern of a clean, flash annealed Si(100) substrate showing bulk Si diffraction spots and (2×1) reconstruction spots. A lack of a bright diffuse background and the presence of the (2×1) spots indicates that the native oxide has been removed. This pattern was acquired with the substrate at about 600 °C and the electron beam in the ⟨110⟩ direction.

RHEED is used during deposition of ^{28}Si films to monitor the growth structure, i.e. smooth crystalline vs. rough crystalline vs. amorphous, as a function of film thickness. Additionally, by inspecting different areas of the substrate, the location of the deposition spot, which is typically smaller than the substrate chip, can be roughly located. This is because the diffraction pattern of a deposited film is never exactly the same as the diffraction pattern of the bare Si(100) substrate. Thus the spot can be located based on the changing pattern and by comparing those patterns to the patterns of the substrate before deposition.

After depositing ^{28}Si films, samples are typically moved into the STM chamber for inspection of the film surface. As previously mentioned, the STM resides in a UHV chamber separated from the deposition chamber by a gate valve. A magnetic transfer arm was used to transfer samples between the two. The STM chamber has a typical base pressure of approximately 6.7×10^{-9} Pa (5.0×10^{-11} Torr) and

was pumped by a 500 L/s ion pump (Varian) and a Ti sublimation pump (TSP). A sample holding area in this chamber can store up to 12 samples at a time. The STM used here is an Omicron variable temperature model. STM images were typically acquired using a tip bias of -2 V for Si substrates and -1.8 V for ^{28}Si samples. Tunneling currents used were typically 150 pA for Si substrates and 100 pA for ^{28}Si samples. STM was used to assess the cleanliness and surface quality of Si(100) substrates prepared *in situ* by flashing before deposition. Scanning was typical done in an area on the surface of 100 nm by 100 nm where contaminants, residual surface oxide, adsorbates, or other surface defects are clearly visible. The quality of the visible Si(100) (2×1) dimer rows can also give an indication of the presence of contaminants. After depositing ^{28}Si films, STM was also used to image the film surface morphology to gain qualitative information about island formation or other features as well as determine some qualitative parameters such as the total local height variation of a film surface. STM images presented in this work were acquired in collaboration with Hyun soo Kim.

Chapter 3

Initial Experiments Enriching ^{22}Ne and ^{12}C

3.1 Context and Experimental Setup

Before depositing ^{28}Si films, proof of principle experiments were conducted involving the enrichment of ^{22}Ne, which was implanted into Si substrates, and ^{12}C, which was deposited as thin films onto Si. These experiments helped establish the experimental practices needed for later adapting the system to ^{28}Si deposition. Additionally, they showed that a high enough level of enrichment was possible to warrant investment in ^{28}Si enrichment and deposition, as can be seen on the enrichment progression timeline in Fig. 1.12 in Chapter 1.

The experiments discussed in this chapter were conducted with an experimental setup where the ion beamline was disconnected from the deposition chamber. A schematic of the ion beam and lens chambers in this setup is shown in the upper right section of Fig. 4.1 and is discussed further in Chapter 4. The mass-selecting aperture used in these experiments was a circular hole that was approximately 5 mm

in diameter and 16 mm thick. In this configuration, samples were located after the deceleration lenses, and they were mounted on the end of an electrical vacuum feedthrough which acted as a sample stage. A sketch of the sample stage feedthrough and sample location is shown in the blowup of the schematic of the "LC–2" setup in Fig. 4.1. Samples were mounted using a strip of conductive carbon tape on the back side of the chip. The purpose of the feedthrough was to isolate the sample electrically from the chamber so that the ion beam current could be monitored during beam tuning and deposition. Additional electrical feedthroughs on the sample stage were used to mount a masking element above the sample location consisting of a metal shim for collecting current. This was positioned between the sample and the path of the ion beam and had a small circular aperture directly above the sample. This mask and aperture was fixed in place for the duration of a deposition. The fixed sample aperture was approximately 3 mm in diameter and provided a mechanism to monitor the focusing of the ion beam on the sample by maximizing the ion current detected on the sample while minimizing the current detected on the sample mask.

Additionally, the mask and sample aperture allowed for precise location of the ion beam spot on the sample substrate. The feedthrough (and sample) were positioned on axis with the ion beamline optics, and the sample aperture allowed for the ion beam to be tuned and steered onto the exact sample location under the aperture. A photograph of a sample mounted on the vacuum feedthrough on this intermediate sample stage with the sample mask is shown in Fig. B.11 in Appendix B. A lack of sample motion in this setup means that the ion beam was constrained to be on

axis, which may not have been the optimal tuning position. There was no method for sample heating in this setup.

One difference between the ^{12}C and ^{22}Ne experiments is that, as a gas at room temperature, Ne needs to be implanted into a substrate as a means of capturing it so that the enrichment can be measured later. Ne implantation required much higher ion kinetic energies than the carbon deposition. To accomplish this, a bias voltage as high as approximately -4 kV was applied to the substrates during deposition to attract the positively charged $^{22}Ne^{+}$ ions into the substrate. The final energy of the ^{22}Ne ions would then be the energy due to the bias potential plus the starting energy of the ions, which was approximately 500 eV for Ne ions, for a total energy of roughly 4.5 keV. As will be discussed below, this high energy was needed to achieve an implantation depth of at least 10 nm for a reliable SIMS measurement of the enrichment. A sample bias of -4 kV was the highest bias achievable for the experimental setup used in Ne implantation experiments.

Section 3.2 of this chapter will discuss the enrichment and implantation of ^{22}Ne. Section 3.3 will discuss the enrichment and deposition of ^{12}C. Finally, Section 3.4 will summarize those results.

3.2 ^{22}Ne Implantation and Characterization: Proof of Principle

3.2.1 Sample Preparation

For these ^{22}Ne implantation tests, there was very little *ex situ* sample preparation. Substrates consisted of "lightly doped" natural abundance commercial Si(100) wafers that were cleaved by hand into approximately 1.5 cm by 1.5 cm chips. The chips were handled with clean teflon tweezers and mounted on the end of the feedthrough using a strip of carbon tape on the back of the wafer, and they were loaded into the vacuum chamber with a native oxide. No further sample preparation occurred *in situ*. The role of these substrates is to simply be a "catcher foil" to collect the ^{22}Ne ions. Typically, after being loaded, samples sat several day in the vacuum chamber before deposition.

3.2.2 ^{22}Ne Implantation

For Ne implantation experiments, the solids-mode Penning ion source was used (see discussion and Fig. 2.9 in Chapter 2). While the gas-mode ion source should be more efficient for generating Ne ions, it was not yet purchased at the time of this experiment. Natural abundance Ne gas was used to generate mostly singly charged Ne ions with a working pressure in the ion source of $\approx 1.0 \times 10^{-2}$ Pa (7.8×10^{-5} Torr). Sweeping the magnetic field of the mass analyzer and monitoring the ion current onto the vacuum feedthrough and sample through the fixed sample

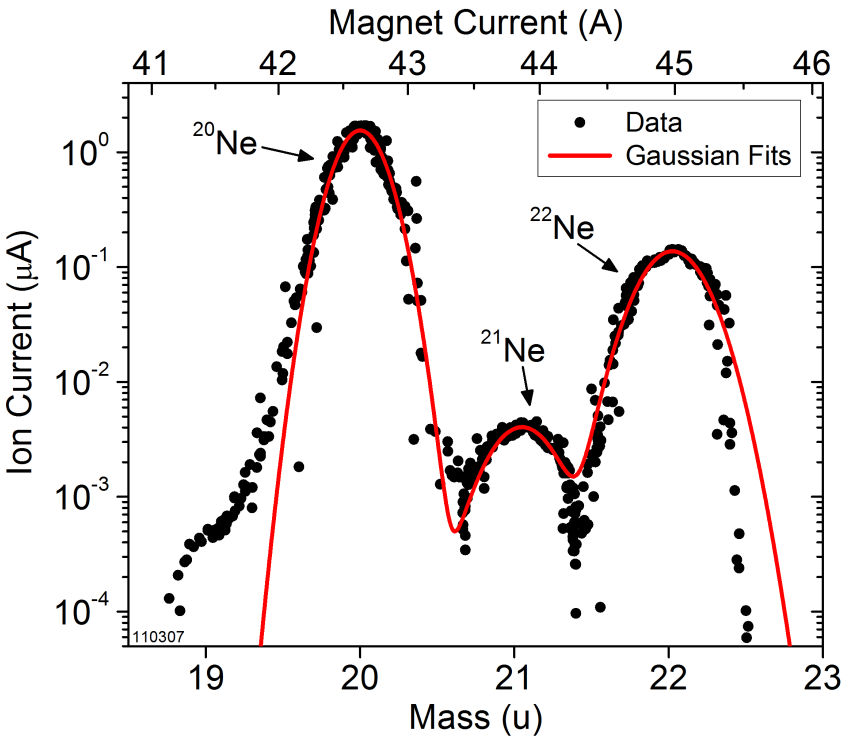

Figure 3.1: A mass spectrum obtained using Ne as a working gas shows ion current peaks (circles) corresponding to atomic species of ^{20}Ne (20 u), ^{21}Ne (21 u), and ^{22}Ne (22 u). The ion current is recorded while sweeping the mass analyzer current, and thus the magnetic field (top axis). Gaussian fits (line, Eq. (2.14)) to the Ne peaks are superimposed on the data. The centers of the 20 u and 22 u fits are separated by $\approx 14\ \sigma$.

aperture at the end of the ion beamline, a mass spectrum of the individual molecular and atomic species is generated. Figure 3.1 shows a portion of the mass spectrum obtained using Ne as a source gas with ion current peaks (circles) at masses of 20 u, 21 u, and 22 u corresponding to atomic species of ^{20}Ne, ^{21}Ne, and ^{22}Ne, respectively. The top axis shows the applied current used to sweep the magnetic field of the analyzer. The three stable Ne isotopes have a natural abundance of approximately 90.5 % ^{20}Ne, 0.3 % ^{21}Ne, and 9.2 % ^{22}Ne, and the relative peak heights of the three peaks in Fig. 3.1 fairly accurately reflect this abundance. A sum of Gaussian fits (line, Eq. (2.14)) to the Ne peaks are superimposed on the data and show

fairly good agreement with some divergence to the low mass side in the tails of the peaks, indicating possible ballistic scattering of a small portion of the ion beam. As discussed in Chapter 2, the spacial distribution of ions in the beam is expected to be roughly Gaussian for this system. The minor isotope, ^{22}Ne, was chosen for enrichment in these experiments because enriching in the minor isotope and rejecting the major isotope is a stronger proof of principle demonstration of the enriching power of the ion beam system than enriching the more abundant major isotope. The Gaussian fits to the mass spectrum peaks can be used to indicate the separation of the 22 u peak from the 20 u peak. From the fits, the 20 u peak has a standard deviation of $\sigma \approx 0.14$, resulting in a separation to the major isotope ^{20}Ne at 20 u of approximately 14 σ. The mass resolving power at the ^{22}Ne peak of the ion beam in this configuration is derived from the mass spectrum to be $\frac{m}{\Delta m} \approx 26$ (measured at 10 % of the peak height). This fairly low mass resolution and the presence of an ion current of roughly 1 nA between the peaks indicates that the beam may not be optimally focused at the mass-selecting aperture. Tuning the mass analyzer to a mass of 22 u (unified atomic mass units) results in the ^{22}Ne ion beam passing through the mass-selecting aperture, through the focusing lenses, and to the sample for implantation.

The ^{22}Ne sample discussed below in the analysis of the sample enrichment here was implanted with the substrate at room temperature with an unknown background pressure. This pressure was possibly around 6.5×10^{-5} Pa (5.0×10^{-7} Torr) based on later experiments. This partial pressure during growth was mostly Ne leakage from the ion source as the base pressure of the deceleration lens chamber before

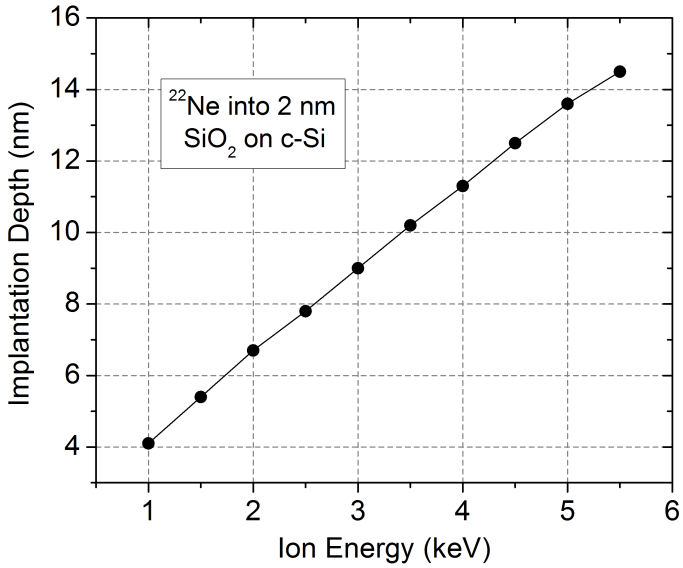

Figure 3.2: ^{22}Ne stopping range (implantation depth) vs. ion energy (circles and line) based on TRIM calculations [69]. In the calculation, the ions hit a crystalline Si target with a 2 nm SiO_2 surface layer.

implanting this sample was $\approx 3.1 \times 10^{-6}$ Pa (2.8×10^{-8} Torr). The anode voltage used for generating Ne ion beams in these experiments was approximately 500 V resulting in an initial energy of the ions in the ion source of 500 eV. As mentioned previously, the sample was biased with a negative high voltage to achieve implantation. The starting energy of the ions is added to the energy gained from the sample bias voltage of approximately -4 kV. The total average ion energy at the target was then approximately 4.5 keV, as discussed previously. This high energy was required to achieve an implant depth of at least 10 nm, which was needed for the SIMS measurements of the enrichment to separate the Ne signals of the implant from that of surface contaminants.

Calculations of the stopping range of energetic ions based on TRIM [69] predict that 4.5 keV ^{22}Ne ions will implant into Si with a native oxide at a peak implantation

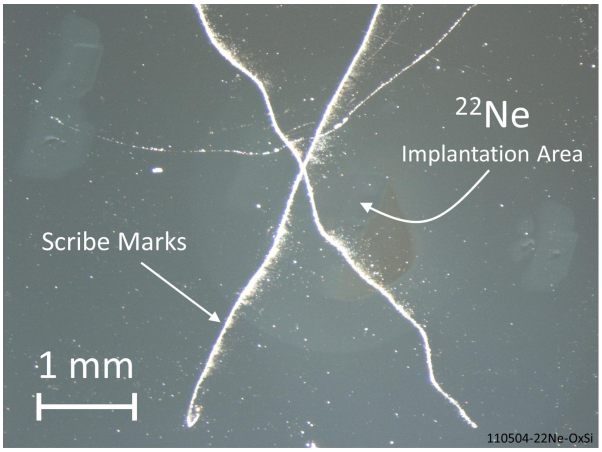

Figure 3.3: Optical micrograph of an implanted ^{22}Ne sample produced at room temperature at LC–2. The Si(100) substrate is seen with scribe marks used to align the chip to the expected ion beam spot location. The ^{22}Ne implanted area is not clear but is likely to the right of the crossing of the scribe marks in an expected area of about 2 mm^2. Other marks visible on the chip are due to sputtering from the SIMS measurement.

depth of approximately 12.5 nm. The stopping range, i.e. the peak implantation depth, of ^{22}Ne ions hitting a Si target (circles and line) is shown for a range of ion energies in Fig. 3.2. The Si target used in these calculations is crystalline and has a 2 nm SiO_2 surface layer representing the native oxide on the substrates used in these experiments. The implantation depth varies between approximately 4 nm for an ion energy of 1 keV to approximately 14.5 nm for an ion energy of 5.5 keV.

The ion current of ^{22}Ne achieved for implantation was approximately 140 nA over an implantation area, estimated from other samples, of approximately 2 mm^2. The associated ion dose for these parameters is approximately 7.7×10^{16} cm^2, resulting in an atomic concentration of ^{22}Ne in the Si substrate of approximately 4.9×10^{22} cm^{-3}, based on TRIM calculations. This means the implantation volume in the Si substrate was roughly 50 % ^{22}Ne.

An optical micrograph of the ^{22}Ne sample analyzed for enrichment here is

shown in Fig. 3.3. The Si(100) substrate is seen in the micrograph with scribe marks used to align the chip to the expected ion beam spot location just under the fixed sample aperture. It is not obvious where the ^{22}Ne-implanted area is, although it is believed to be just to the right of the crossing of the scribe marks. Other marks visible on the chip are due to sputtering from the SIMS measurement. A total of three ^{22}Ne samples were produced in this work, and two were analyzed for enrichment, the second of which is discussed below.

3.2.3 Enrichment Measurements via SIMS

SIMS was used to determine the enrichment of two ^{22}Ne-implanted samples, both of which are represented on the enrichment progression timeline in Fig. 1.12. For the SIMS measurement of these samples, the primary ion sputter beam was composed of Cs^+ ions with a current of 40 nA and an energy of 10 keV. The sputter beam was raster-scanned over a nominal 280 μm by 430 μm area on the sample, although the actual area sputtered was considerably larger because of the finite size of the ion beam. Measurements of the counts of the major isotope, ^{20}Ne, and the minor isotope chosen for enrichment, ^{22}Ne, were made after each sputter cycle, producing a "depth" profile of the isotope ratios (assuming a constant sputter rate). Isotope ratios are then used to determine the isotope fractions, which indicate the enrichment level. As mentioned in Chapter 1, isotope fractions of a particular isotope are defined as the counts of that isotope divided by the total counts of the measurement. The isotope fractions of Ne can be written as $^{z}\mathrm{Ne}/\mathrm{Ne}_{\mathrm{tot.}}$, where z is the mass number denoted as 20 for ^{20}Ne counts and 22 for ^{22}Ne counts and $\mathrm{Ne}_{\mathrm{tot.}}$ is

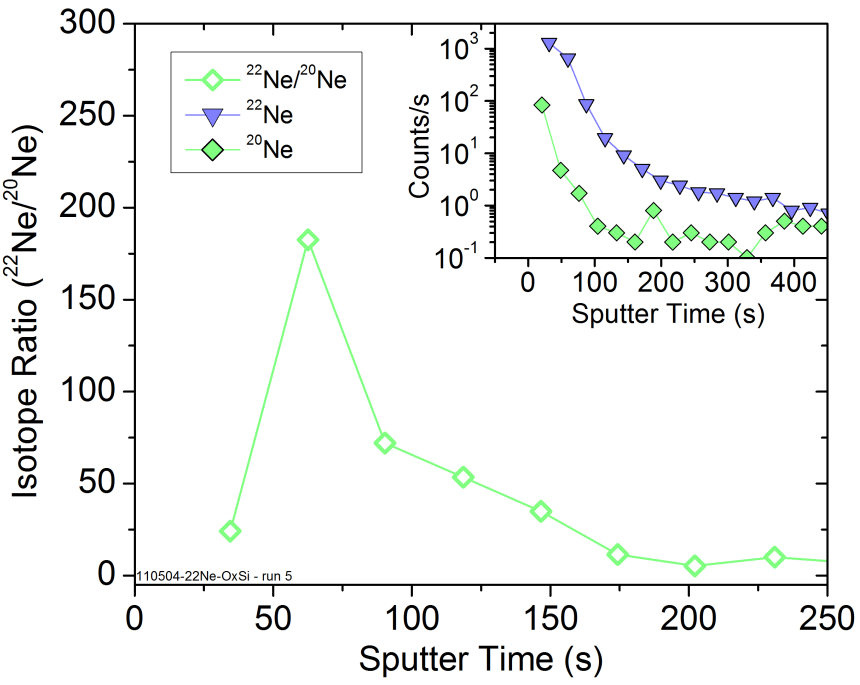

Figure 3.4: SIMS "depth" profile of a ^{22}Ne-implanted sample produced at room temperature at LC–2. ^{22}Ne was implanted into Si(100) with an energy of about 4.5 kV. Isotope ratios of ^{22}Ne/^{20}Ne (open diamonds and line) are shown vs. the sputter time. The second point at 63 s is the largest ratio value (183), representing the maximum enrichment in ^{22}Ne. The inset shows the raw count rates vs. sputter time for ^{22}Ne (triangles and line) and ^{20}Ne (diamonds and line).

the sum of ^{20}Ne and ^{22}Ne counts.

The first ^{22}Ne sample produced, which was also the first enriched sample of any kind produced in this work, had a lower level of enrichment than the second one. This first sample had a ^{22}Ne isotope fraction of 84.4(10) %, seen on the enrichment progression timeline as the highest residual isotope fraction of those samples. The second ^{22}Ne sample was also analyzed by SIMS, and the resulting "depth" profile is shown in Fig. 3.4. The isotope ratios of ^{22}Ne/^{20}Ne (open diamonds and line) are shown vs. the sputter depth into the sample. At a sputter time of 63 s, which likely corresponds to the peak implantation depth of the ^{22}Ne (expected to be ap-

proximately 12.5 nm), the isotope ratio has a maximum value of 183. This value represents a ^{22}Ne isotope fraction (assumes no ^{21}Ne is present) of 99.455(36) % and a residual ^{20}Ne isotope fraction of 0.545(36) %, as seen on the enrichment progression timeline. The inset of Fig. 3.4 shows the raw count rates vs. sputter time of ^{22}Ne (triangles and line) and ^{20}Ne (diamonds and line) for reference. Another useful parameter that describes the measured enrichment of a sample is the isotope reduction factor, which gives the amount by which an excluded isotope is reduced from the natural abundance. This reduction factor is determined by dividing the natural abundance of an isotope of an element by the measured isotope fraction described previously. The natural abundance of an isotope is represented by a_z, where z again is the mass number of the isotope. For the reduction factor of the excluded isotope ^{20}Ne, a_z is a_{20}, i.e. the natural abundance of ^{20}Ne. The reduction factor for ^{20}Ne is thus written as $a_{20}/(^{20}\mathrm{Ne}/\mathrm{Ne}_{\mathrm{tot.}})$. The measured isotope fractions discussed here give an isotope reduction factor for ^{20}Ne of 166(1), i.e. the ^{20}Ne in the sample is approximately 166 times lower than in natural abundance Ne. These measurements indicate a realized mass selectivity of 1785:1 for the ion beam system in this configuration. This value gives a sense of the performance of the system independent of the natural abundance of Ne.

3.3 ^{12}C Deposition and Characterization: First Enriched Thin Films

3.3.1 Context

Solid state QI using spin states of atoms or quantum dots as qubits is limited by the need for host materials that are as minimally-interacting as possible, e.g., ^{28}Si. Another potential host material for QI devices is diamond. Natural abundance diamond has isotopes possessing a non-zero nuclear spin, and so isotopic enrichment can increase the coherence time of qubits in diamond by reducing the density of randomly fluctuating spins in their local environment. Qubits in ^{12}C enriched diamond have received a lot of attention in this context [73]. Isotopic enrichment eliminates the ^{13}C nuclear spins $I = 1/2$ present in natural abundance C (natural stable isotope abundances: 98.9 % ^{12}C, 1.1 % ^{13}C). Nitrogen-vacancy (NV) centers in enriched, highly pure diamond can have electron spin T_2 coherence times of milliseconds [74, 75]. Additionally, qubits with long nuclear spin coherence times approaching a second have been demonstrated for isolated ^{13}C atoms coupled to NV centers in ^{12}C diamond [73]. This chapter describes the enrichment and deposition of ^{12}C films as a potential host for qubits, but it also serves as a demonstration for the production of ^{28}Si films. Significant portions of the data and analysis presented in this section was previously published in Ref. [76].

The ^{12}C reported here has an enrichment in the solid state comparable to that of commercially available methane (up to 99.999 % $^{12}CH_4$) used as a source

gas to grow enriched diamond by CVD [73, 77, 78], where enrichment and purity may be diminished in processing. CVD diamonds grown from enriched $^{12}CH_4$ can suffer from incorporation of excess N (^{14}N has nuclear spin $I = 1$) that can also limit coherence times. Several groups growing enriched ^{12}C diamond by CVD have made efforts to reduce the atomic concentration of paramagnetic impurities like N below 1×10^{-9} cm^{-3} [74, 75, 78, 79]. The mass selecting method used here isolates the ^{12}C to avoid contaminants such as N and O. N may still be physisorbed from the background vacuum but vacuum improvements and heated substrates could mitigate this liability. As previously mentioned, some work has been done depositing enriched C materials including ^{12}C, $^{28}Si^{12}C$ and $^{12}C^{14}N$ [56, 57, 80]. The numerous research efforts utilizing enriched diamond and other C allotropes [74, 81, 82] can also benefit from the availability of ^{12}C films.

3.3.2 Sample Preparation

Similar to the Ne samples, for these ^{12}C deposition tests, there was very little *ex situ* sample preparation. Substrates consisted of "lightly doped" natural abundance commercial Si(100) wafers that were cleaved by hand into approximately 1.5 cm by 1.5 cm chips. Clean teflon tweezers were used to mount these substrates onto the end of the same electrical vacuum feedthrough used in Ne implantation experiments using a strip of carbon tape on the back of the wafer. Substrates were loaded into the vacuum chamber with a native oxide. No further sample preparation occurred *in situ* before the deposition of ^{12}C films. Similar to the substrates used in the Ne experiments, these substrates serve as a simple "catcher foil" to collect the ^{12}C ions

as a film in these experiments. Typically, after being loaded, substrates sat several days in the vacuum chamber before deposition occurred.

3.3.3 Deposition of ^{12}C

In this experiment, natural abundance CO_2 is used as the carbon source to generate ^{12}C ions and grow ^{12}C films. CH_4 gas was also tested but was found to produce a lower ion beam flux than CO_2 (see Fig. 2.10 in Chapter 2). The solids-mode Penning ion source was used in these experiments (see Fig. 2.9 and discussion in Chapter 2). The working pressure of the ion source used in these experiments was between approximately 1.1×10^{-3} Pa (8.0×10^{-6} Torr) and 1.3×10^{-3} Pa (1.0×10^{-5} Torr). CO_2 molecules are cracked and ionized by the plasma in the ion source to generate the ion beam. By scanning the magnetic sector mass analyzer and monitoring the ion current through the mass-selecting aperture onto the sample stage, a mass spectrum of the individual molecular and atomic species is generated. Figure 3.5 shows a portion of the mass spectrum acquired using CO_2 as a source gas that is representative of the ion beam conditions used to deposit samples discussed in this section. Ion current peaks (circles) are visible at masses of 12 u, 13 u, 14 u, and 16 u corresponding to atomic species of ^{12}C, ^{13}C, ^{14}N, and ^{16}O, respectively. The ^{14}N peak is due to a small amount of residual nitrogen background pressure present in the ion source chamber. The top axis shows the applied current used to sweep the magnetic field of the analyzer. The relative peak heights of the ^{12}C and ^{13}C peaks fairly accurately reflect the natural abundance of stable C isotopes. The 12 u and 13 u mass peaks are fitted to Gaussian functions (line, Eq. (2.14)), which are super-

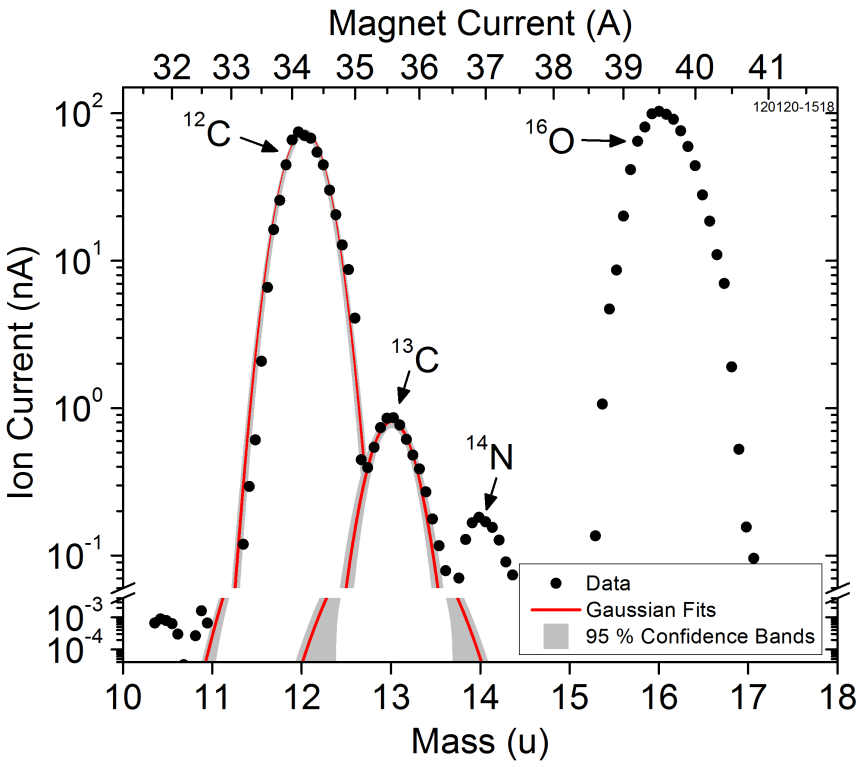

Figure 3.5: A mass spectrum obtained using CO_2 as a working gas shows current peaks (circles) corresponding to atomic species of ^{12}C (12 u), ^{13}C (13 u), ^{14}N (14 u), and ^{16}O (16 u). The ion current is recorded while sweeping the mass analyzer current, and thus the magnetic field (top axis). Gaussian fits (line, Eq. (2.14)) to the ^{12}C and ^{13}C peaks with 95 % confidence bands are superimposed on the data. The centers of the fits are separated by $\approx 4\ \sigma$.

imposed on the data along with 95 % confidence bands (shaded area). The peaks are fairly symmetric and the data can be seen to match the form of a Gaussian, indicating minimal scattering of ions by lens elements.

The mass resolving power of the ion beam at the ^{12}C peak is derived from the fits to the mass spectrum to be $\frac{m}{\Delta m} \approx 13.5$ (measured at 10 % of the peak height). This mass resolution is fairly low and the presence of a measurable ion current of roughly 0.4 nA between the 12 u and 13 u peaks indicates that the beam may not be optimally focused at the mass-selecting aperture. The separation of the

peaks can also be estimated from the Gaussian fits, which show that the center of the ^{13}C peak is $\approx 4\ \sigma$ away from the center of the ^{12}C peak. The overlap of the 13 u peak on the 12 u peak due to this high level of separation can be determined using the parameters $G_{12}(m)$ and $G_{13}(m)$. These are the values (calculated at mass m in units of u) of the Gaussian fits to the current peaks at 12 u and 13 u. The geometric selectivity of the system for ^{12}C relative to ^{13}C for the conditions used when producing a ^{12}C beam is then determined from the ratio of the Gaussian fit functions at 12 u, given by

$$\frac{G_{12}(12)}{G_{12}(12) + G_{13}(12)} = 99.9999(3)\ \%\ ^{12}\mathrm{C}, \tag{3.1}$$

where $m = 12$ for the above parameters signifying that the values of the Gaussian fits are calculated at a mass of 12 u. The uncertainty is found in a similar manner using the 95 % confidence bands of the fits. By further tuning the ion beam and adjusting the parameters of the electrostatic lenses, better isolation of the masses can be achieved in this setup at the expense of beam flux. This analysis sets an upper bound for a sample enrichment grown under these conditions. By tuning the magnetic field to the center of the peak at 12 u, ^{12}C ions are transmitted with a high degree of selectivity to the target substrate for deposition. Thus, the enrichment should not be limited by the geometric mass selectivity of the beamline but by other sources of contamination, e.g. neutral ^{13}C from un-ionized source gas diffusing to the sample during deposition or gas scattering of ions.

^{12}C samples were grown with typical beam currents ranging from 600 nA to 900 nA over a ≈ 1 mm^2 beam spot, resulting in deposition rates between approxi-

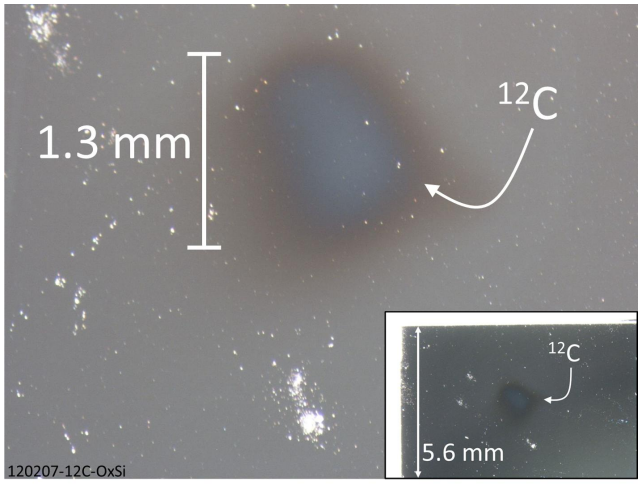

Figure 3.6: Optical micrograph of a ^{12}C sample deposited at room temperature at LC–2. The Si(100) substrate is seen with the ^{12}C deposition spot near the upper center appearing darker. The spot is roughly 1.3 mm in diameter. Lighter dust is also visible on the substrate surface. Inset is a lower magnification image with the edges of the chip visible.

mately 0.5 nm/min and 0.75 nm/min. An optical micrograph of a ^{12}C sample after deposition is shown in Fig. 3.6. The Si(100) substrate is seen with the ^{12}C deposition spot visible near the upper center appearing darker than the substrate. The spot is roughly 1.3 mm in diameter. Lighter dust is also visible on the substrate surface from handling the chip. Inset is a lower magnification image of the sample with the edges of the chip visible giving an indication of the chip size. The sample discussed in the analysis of this section was deposited with an average ion energy of ≈ 560 eV in a background pressure of $\approx 2.1 \times 10^{-5}$ Pa (1.6×10^{-7} Torr). This partial pressure during growth was mostly CO_2 leakage from the ion source and the typical base pressure for the deposition chamber is $\approx 1.3 \times 10^{-7}$ Pa (1.0×10^{-9} Torr). A total of three ^{12}C samples were produced in this work, and two samples were analyzed for enrichment, one of which is the focus of the analysis below.

SEM was used to inspect one of the deposited ^{12}C films in cross-section and

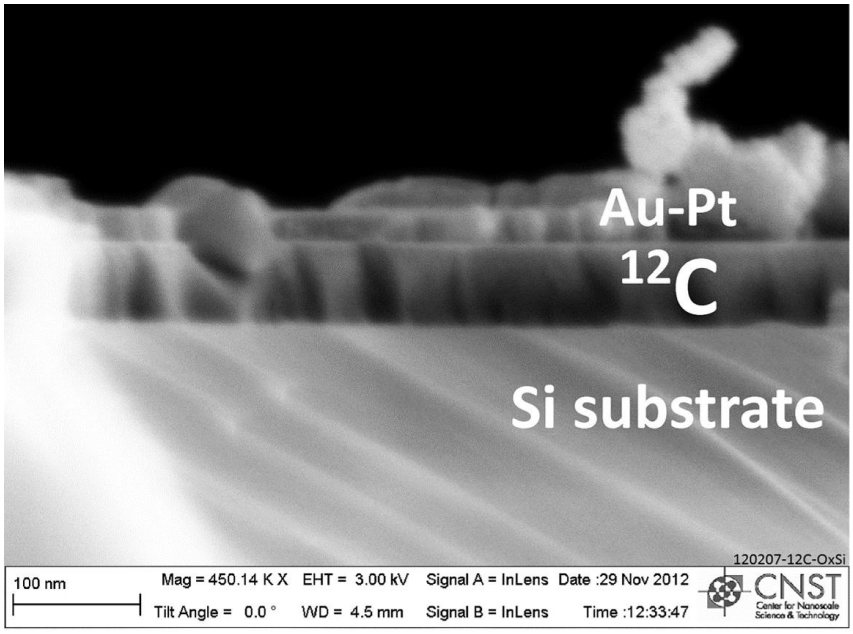

Figure 3.7: SEM cross-sectional micrograph of a ^{12}C sample deposited at room temperature at LC–2. The top layer is ≈ 27 nm of Au-Pt deposited for imaging. The middle layer is the deposited ^{12}C film which is ≈ 66 nm thick. Below that is the crystalline Si(100) substrate.

measure the thickness. Figure 3.7 is a cross-sectional SEM micrograph of a cleaved edge of the analyzed ^{12}C sample. The micrograph shows the crystalline silicon substrate on the bottom that has diagonal lines going from upper left to lower right, which are a consequence of the cleaving. On top of the silicon is the deposited ^{12}C film, which also shows lines running vertically through the entire thickness of the film. These lines suggest continuity and uniformity throughout the material that would not be expected if the sample is more polycrystalline consisting of multiple grains from the bottom to the top of the film. In the area of the sample shown in the micrograph, the film is ≈ 66 nm thick. Above the ^{12}C film is ≈ 27 nm of Au-Pt deposited for imaging. The upper and lower edges of the carbon film are nearly parallel, indicating smooth growth. While there are no obvious signs that the film

is amorphous, it is not expected that a crystalline film can be deposited at room temperature on a substrate with a surface oxide layer.

3.3.4 Enrichment Measurements via SIMS

The enrichment in ^{12}C and the residual ^{13}C in the carbon films were determined using SIMS. One of these analyzed samples is represented on the enrichment progression timeline in Fig. 1.12 in Chapter 1. For the SIMS measurements, a Cs^+ primary ion beam with an impact energy of 20 keV was raster-scanned to sputter a 150 μm by 150 μm area of the sample. Secondary negative ions of ^{12}C and ^{13}C sputtered from the surface were alternately directed by magnetic peak-switching into a secondary electron multiplier where the counts were recorded. Under the measurement conditions, the instrument has a mass resolving power $\frac{m}{\Delta m} \approx 5000$, allowing it to distinguish between ^{13}C and ^{12}CH peaks, which are separated by approximately 0.0045 u. A set of measurements were made by pre-sputtering the target area with an 8 nA primary ion current and then recording counts of 40 isotopic ratio pairs with a sputter beam current of 23 pA.

Isotope fractions of ^{12}C and ^{13}C were determined from the averages of the 40 ratios by calculating $^{z}C/C_{tot.}$, where z is the mass number denoted as 12 for the ^{12}C average counts and 13 for the ^{13}C average counts. $C_{tot.}$ is the sum of the ^{12}C and ^{13}C average counts. The isotope fractions of ^{12}C and ^{13}C from eight sets of SIMS isotopic ratio measurements after successive pre-sputter cycles are presented in Fig. 3.8. The ^{12}C (squares and line) and ^{13}C (circles and line) isotope fractions are shown in a semi-log plot of the "depth" profile vs. the cumulative pre-sputter

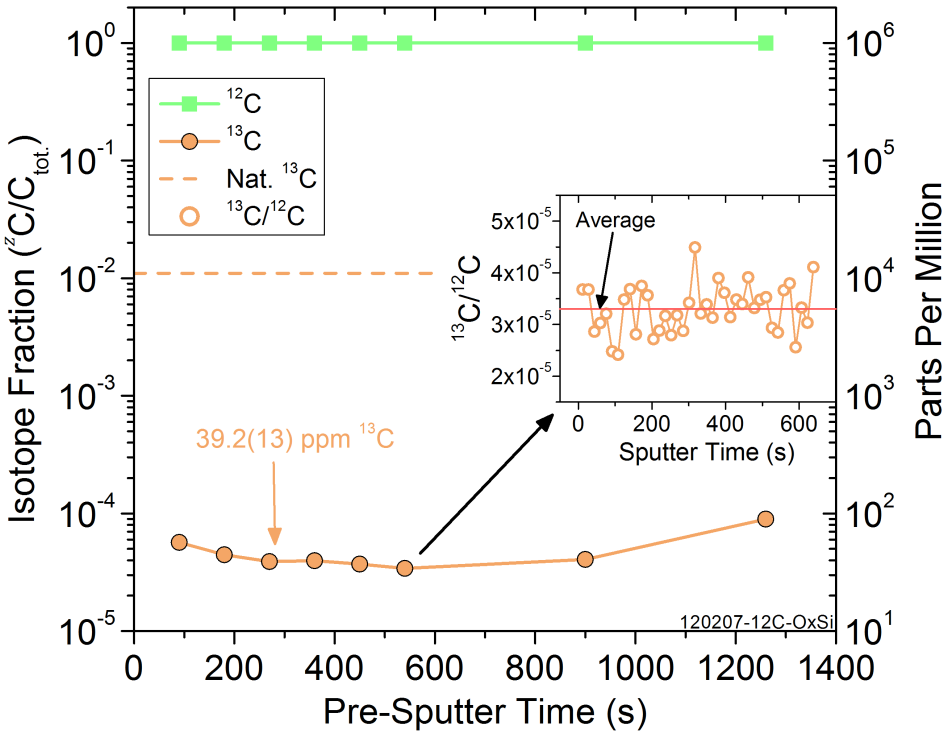

Figure 3.8: SIMS "depth" profile of a ^{12}C sample deposited at room temperature at LC–2. Isotope fractions of ^{12}C (squares and line) and ^{13}C (circles and line) representing eight successive data runs as the primary SIMS beam sputtered through the film are shown vs. the pre-sputter time. The inset shows 40 measurements of ^{13}C/^{12}C ratios (open circle and line) vs. sputter time, which are averaged (line) to determine the values of the isotope fractions of the sixth points at a pre-sputter time of 540 s. The middle six points between 180 s and 900 s were averaged for the final enrichment and ^{13}C isotope fraction of 39.2(13) ppm. Also shown is the natural abundance value for ^{13}C (dashed line) as a reference.

time, i.e. different depths into the film. The inset shows one set of 40 isotopic ratio measurements of ^{13}C/^{12}C (open circles and line) vs. sputter time into the film for the sixth data points of the isotope fractions at a pre-sputter time of 540 s. The average (line) of the 40 measurements is used to determine the ^{13}C and ^{13}C isotope fractions. The natural abundance of ^{13}C (dashed line) is also shown for reference highlighting the reduction of ^{13}C. To determine the average isotope fractions of the film, only the middle six data between pre-sputter times of 180 s and 900 s were

averaged, excluding the first and last data points. The first datum at 90 s shows a lower enrichment that is likely due to natural abundance carbon contamination on the film surface. The last datum at 900 s has lower enrichment but also corresponds to a dramatic drop in absolute ^{12}C counts indicating that the interface between the carbon film and the Si(100) substrate had likely been reached. This depth was later estimated to be roughly 100 nm. For the remaining six points, the average measured $^{13}C/^{12}C$ ratio is $3.79(5) \times 10^{-5}$. After accounting for an instrumental mass fractionation for carbon, the average measured ^{12}C isotope fraction in the film was determined to be 99.99608(13) %. The average residual isotope fraction of ^{13}C in the film was measured to be $39.2(13) \times 10^{-6}$ or 39.2(13) ppm, as seen in the enrichment progression timeline. The isotope reduction factor for ^{13}C based on the isotope fraction is written as $a_{13}/(^{13}C/C_{tot.})$. The isotope fraction of the measurement here represents an isotope reduction factor for ^{13}C of 270(20), i.e. the ^{13}C in the film is approximately 270 times lower than in natural abundance C.

The data from Fig. 3.8 is also shown on a linear scale and over a smaller isotope fraction range in Fig. 3.9 to highlight the structure of the "depth" profile. Here, the ^{12}C isotope fractions (squares and line) corresponding to the left axis and ^{13}C isotope fractions (circles and line) in ppm corresponding to the right axis are shown again vs. the pre-sputter time. Small changes in the isotope fractions throughout the film are clearly visible with the sixth points at a pre-sputter time of 540 s representing the highest local enrichment within the film. As mentioned, the first datum at a pre-sputter time of 90 s and the last datum at 1260 s (crosses) were discarded when the averages were determined. The middle six points between 180 s and 900 s represent

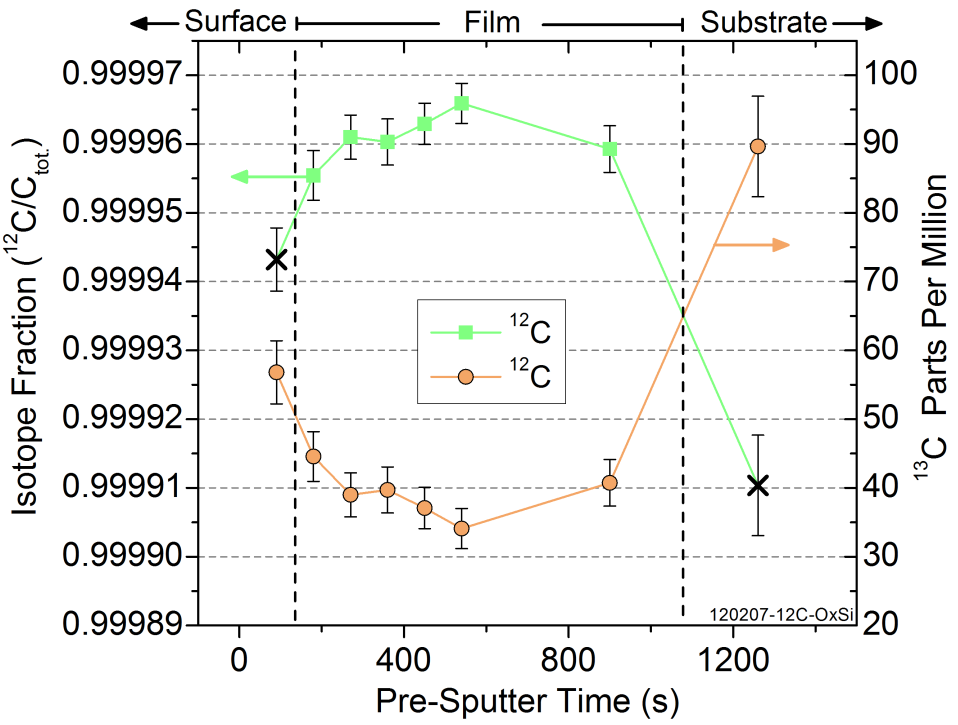

Figure 3.9: SIMS "depth" profile of a ^{12}C sample deposited at room temperature at LC–2. The data from Fig. 3.8 is shown on a linear scale. Isotope fractions of ^{12}C (squares and line, left axis) and ^{13}C (circles and line, right axis) representing eight successive data runs as the primary SIMS beam sputtered through the film are shown vs. the pre-sputter time. The middle six points between 180 s and 900 s were averaged for the final enrichment. The outside points of the ^{12}C isotope fractions (crosses) at 90 s and 1260 s were discarded due to surface contamination and a loss of signal moving into the Si(100) substrate, respectively, represented by vertical dashed lines. The average ^{13}C isotope fraction of the middle six points is 39.2(13) ppm.

the bulk of the deposited film, represented by the vertical dashed lines, with surface contamination and the Si(100) substrate on either side. Each error bar is derived from the standard deviation of the mean of the 40 individual measurements at each data point. The enrichment of this sample is comparable to that of CVD grown ^{12}C diamonds used for NV center QI experiments [74, 78]. A second ^{12}C sample was also analyzed by SIMS as a check on the reproducibility, and it was found to have a nearly identical ^{12}C enrichment. These ^{12}C enrichment measurements represent a

realized mass selectivity of 276:1 for ^{12}C in this system. This value gives a sense of the performance of the system independent of the natural abundance of C. The ^{12}C realized mass selectivity is less than that achieved for ^{22}Ne, but that may be due to the estimated spatial peak separation between ^{12}C and ^{13}C at the mass-selecting aperture (12.4 mm) being smaller than that between ^{20}Ne and ^{22}Ne (14.7 mm).

As mentioned above, it is believed that the limiting factor for the enrichment of these samples is not the ultimate mass selectivity of the ion beam system, but rather other sources of unwanted isotopes such as background CO_2 gas diffusing from the ion source. Therefore, the contribution to the ^{13}C concentration from this CO_2 partial pressure is considered. Using the deposition conditions of a CO_2 partial pressure of 2.1×10^{-5} Pa (1.6×10^{-7} Torr) and a natural ^{13}C abundance in the gas of 1.1 %, an incorporation fraction, s, of about 0.037 is needed to account for the measured isotope fraction of ^{13}C in the film of $\approx$ 39 ppm. Representative sticking coefficients found in the literature range from values that are similar in magnitude to several times lower [83]. The former case provides a reasonable explanation for the ^{13}C observed while the latter may indicate an additional source of contamination such as scattered ions in the beam path. These sources of ^{13}C can be mitigated by reducing the background pressure during deposition. For ^{13}C due to adsorption from the vacuum, every order of magnitude decrease in background pressure would correspond to an order of magnitude increase in the enrichment of the deposited material. Reducing the background gas in the above estimate to 2×10^{-6} Pa (1.5×10^{-8} Torr) would lower the isotope fraction of ^{13}C to $\approx 4 \times 10^{-6}$ (4 ppm) under the same deposition conditions. An improved vacuum would also

reduce chemical impurities incorporated during deposition, which could be paramagnetic. Increasing the beam flux and therefore deposition rate will further reduce the effect of unwanted background gases adsorbing into the films by reducing the relative ^{13}C gas flux compared to the deposition rate.

Time-of-Flight SIMS (TOF-SIMS) was also used to look at chemical contaminants present in a sample similar to the one analyzed for enrichment. All signals of organic and inorganic species being monitored for analysis were near the noise floor of the measurement and at least 100 times lower than the ^{12}C signal. The derived concentrations of chemical impurities in the film are unreliable because the sample was not being efficiently sputtered and ionized for detection. Any signal from O adsorbed during deposition from a CO_2 background partial pressure is below the detection of this measurement. Further assessment needs to be done to determine the concentrations of spin and chemical impurities present in these films.

3.4 Chapter 3 Summary: Outlook for ^{28}Si

This chapter demonstrated successful proof of principle enrichment by implanting the minor isotope ^{22}Ne enriched with an isotope fraction of 99.455(36) % into Si as well as depositing thin films of ^{12}C enriched to an isotope fraction of 99.9961(4) % onto Si using the mass selected ion beam system. A total of three ^{22}Ne and three ^{12}C were produced. The isotope fractions of ^{20}Ne and ^{13}C from these measurements can be seen in the enrichment progression timeline in Fig. 1.12. Realized mass selectivities of 1785:1 for ^{22}Ne (selection between masses separated by

2 u) and 276:1 for ^{12}C (selection between masses separated by 1 u) were achieved. While these selectivities are not directly translatable to ^{28}Si because the peaks of Si are spatially closer than for Ne or C, these experiments do show that very high levels of *in situ* enrichment are possible in thin film deposition using this system. Similar levels of ^{28}Si enrichment are likely possible, especially if background gas adsorption has a more significant effect on the realized sample enrichment than does the mass selectivity.

Chapter 4

^{28}Si Thin Film Deposition and Characterization Phase I: *In Situ* Enrichment

4.1 Introduction

4.1.1 Context

In this chapter as well as Chapter 5, the ion beam deposition of ^{28}Si films enriched *in situ* is discussed as well as the characterization of their properties, particularly their enrichment level. Chapter 3 demonstrated successful proof of principle enrichment experimenubots by implanting ^{22}Ne enriched to 99.455(36) % into Si as well as depositing thin films of ^{12}C enriched to 99.9961(4) % using the mass selected ion beam system. Realized mass selectivities of 1785:1 for ^{22}Ne (selection between masses separated by 2 u) and 276:1 for ^{12}C (selection between masses separated by 1 u) were achieved. Because the 28 u and 29 u mass peaks are spatially closer together at the mass-selecting aperture than the Ne or C peaks, the selectivity for

Si deposition is lower than these values. Nevertheless, these experiments showed that high levels of isotopic enrichment can be achieved with this method, laying the groundwork for adapting the system for ^{28}Si deposition.

As stated in Chapter 1, enrichment and thin film deposition of ^{28}Si is pursued here with the objective of producing high-quality enriched material for Si based solid state quantum computing. ^{28}Si of sufficiently high quality (i.e. high enrichment, crystallinity, and purity) provides an ideal solid state environment to host qubit spins. The minimal interactions between ^{28}Si and nuclear and electron spins of qubits result in a level of isolation akin to a trapped atom in a vacuum chamber. This leads to extremely long coherence times which have earned ^{28}Si the moniker of "semiconductor vacuum" [9]. Unwanted deviations from ideal ^{28}Si material can be classified as three types of defects: isotopic defects, structural defects, and chemical defects. Controlling and limiting these defects is critical for successful integration of ^{28}Si into quantum computing architectures. The ^{28}Si materials goals of this work are discussed in Chapter 1 and can be restated as follows:

(1) high enrichment in ^{28}Si with a residual ^{29}Si isotopic concentration less than 50 ppm,

(2) single-crystalline and smooth epitaxial structure with a low dislocation density below 1×10^6 cm^{-3}, and

(3) high chemical purity including C and O with atomic concentrations below 2×10^{15} cm^{-3}.

These are believed to be the criteria needed for the ^{28}Si to be comparable to electronics grade natural abundance Si as well as the enriched Si currently available

in the QI research community. The bulk of that ^{28}Si is produced by the International Avogadro Coordination [32], which has a residual ^{29}Si isotopic concentration as low as 50 ppm. Producing ^{28}Si with ^{29}Si isotopic concentrations as low as 1 ppm is necessary to enable a robust and systematic study measuring electron coherence times vs. ^{29}Si concentration in the single spin regime and compare it to theoretical predictions (see Fig. 1.9), as discussed in Chapter 1 [12].

The experiments producing ^{28}Si discussed in this chapter and Chapter 5 rely not only on prior work using this ion beam deposition system, such as the Ne and C experiments of Chapter 3 and previous thin metal film deposition experiments [59], but also on previous work by other groups that have deposited Si via an ion beam [43, 48–51]. The results from these groups were reviewed in Chapter 1 showing that they demonstrated both enrichment in ^{28}Si to approximately 99.9982 % in one experiment [43] as well as epitaxial deposition using hyperthermal energy ions and a range of substrate temperatures [51].

The experiments described in this chapter and Chapter 5 seek to use processing methods that are both common (e.g. vacuum deposition, sample heating) and fairly unique (e.g. mass selected ion beam deposition) to engineer the properties, such as enrichment in ^{28}Si and chemical purity, and structure (crystallinity) of Si thin films. Characterization methods including SIMS for assessing sample enrichment and chemical purity, STM, RHEED, and SEM for inspecting the film surface and crystallinity, TEM to inspect the bulk crystallinity of films, and XPS for detecting chemical impurities are used to assess the ^{28}Si films in terms of the materials goals and guide the experimental adjustments needed to improve their quality. The

experiments discussed in this chapter focus on achieving very high levels of ^{28}Si enrichment. The experiments of Chapter 5 will focus on maintaining a high enrichment while assessing and improving the chemical purity and crystallinity of ^{28}Si samples.

4.1.2 Experimental Configurations for ^{28}Si Deposition

Three distinct experimental configurations were used for deposition of ^{28}Si films in this work. Experiments involving the first two will be discussed in this chapter, and experiments involving the third one will be discussed in Chapter 5. These experimental configurations are defined partly by the location of samples during deposition at three positions in the vacuum system. Additionally, they are defined as a chronology of initial, intermediate, and final experimental configurations with materials characterizations and subsequent experimental improvements occurring between segments of ^{28}Si deposition at each one. The final configuration is the final (last) setup used in this work, although not necessarily the final setup used in the larger enriched Si project of which this work is a part. These three setups are illustrated in Fig. 4.1, which shows top down schematics of the ion beam chamber, deceleration lens chamber, and deposition and analysis chamber in the three experimental configurations used to deposit ^{28}Si samples. Schematic drawings of these chambers were previously shown in Fig. 2.1 in Chapter 2 and described in detail there. Highlighted here are the three sample locations used in each of the setups, which are discussed further below.

The initial experimental configuration was one in which samples were located

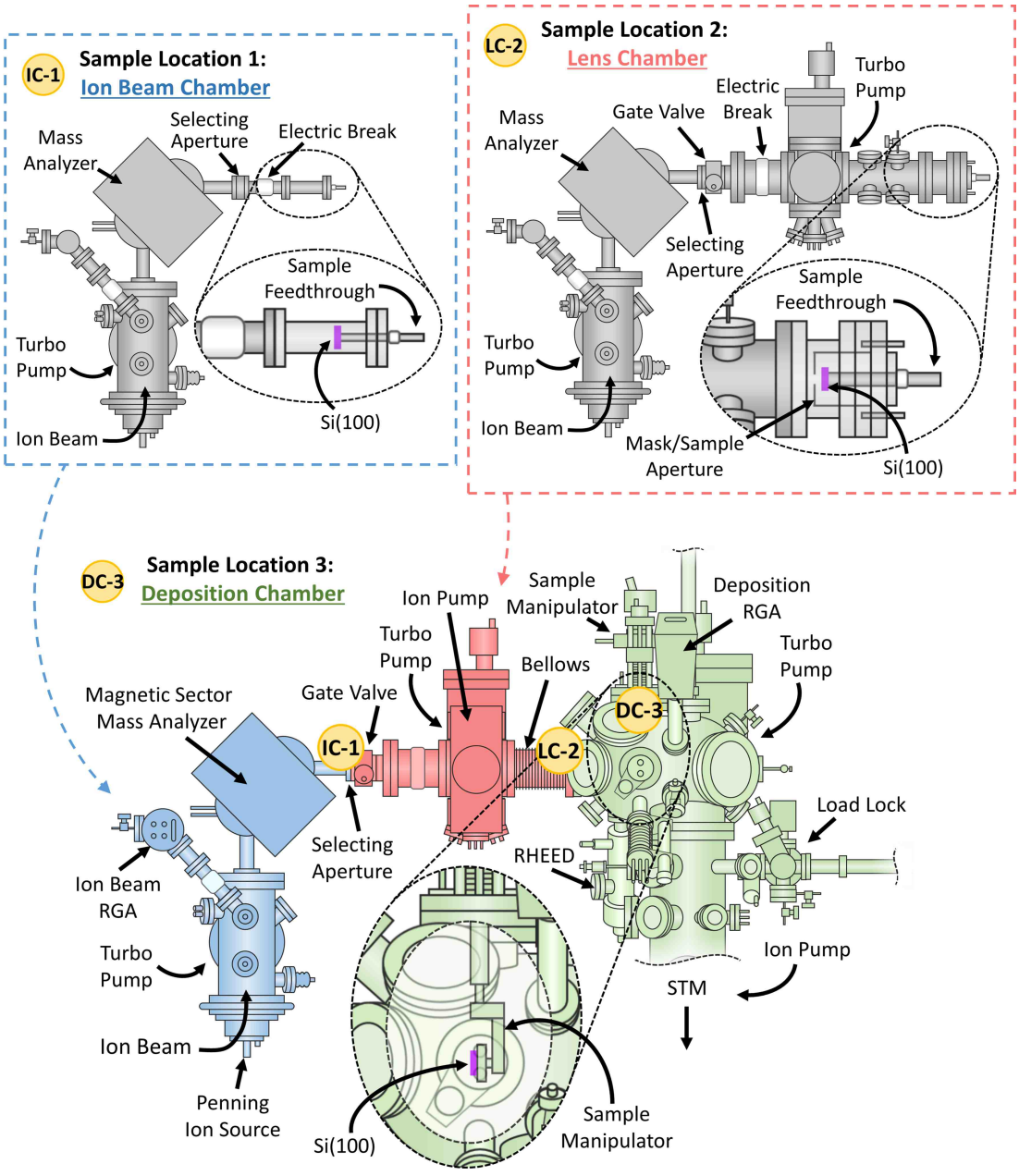

Figure 4.1: Schematic top down drawings of the ion beam chamber, lens chamber, and deposition chamber experimental configurations used to deposit ^{28}Si samples. The top left shows the setup for Sample Location 1 in the ion beam chamber (IC–1). This setup consists of the ion beam with the sample located on a feedthrough at the end of the beamline, shown in the blowup. The top right shows the setup for Sample Location 2 in the lens chamber (LC–2). This setup consists of the ion beam chamber connected to the lens chamber with the sample located on a feedthrough at the end of the deceleration lenses, shown in the blowup. The bottom shows the setup for Sample Location 3 in the deposition chamber (DC–3). This setup consists of the ion beam and lens chambers connected to the deposition chamber with the sample located on the manipulator, shown in the blowup.

just after the mass analyzer and mass-selecting aperture at the end of the ion beam chamber. This is the location corresponding to the schematic setup shown in the upper left section of Fig. 4.1 marked as "Sample Location 1: Ion Beam Chamber", which will be referred to as IC–1. The sample was mounted on an electrical vacuum feedthrough for deposition, which is shown in the transparent blowup of this schematic. It consists of an isolated metal rod connecting two sides of a vacuum flange. For the samples deposited at IC–1, the ion beamline was separated from the other vacuum chambers just after the mass-selecting aperture. Initially this setup was designed to maximize the total ion current onto the sample by positioning the sample before the electrostatic deceleration lenses. Additionally, this simple configuration facilitated changing the mass-selecting aperture relatively quickly to test apertures with different dimensions in an effort to optimize ion beam fluence through it. This setup also had a higher background pressure during deposition due to the beamline being disconnected from the rest of the vacuum system, which normally differentially pumps the sample location. Only a single turbo pump, marked in Fig. 4.1, pumps this setup.

Next, the intermediate experimental configuration was used to deposit ^{28}Si samples in the deceleration lens chamber. This is the sample location corresponding to the schematic setup shown in the upper right section of Fig. 4.1 marked as "Sample Location 2: Lens Chamber", which will be referred to as LC–2. In this configuration, the ion beam chamber was reconnected to the deceleration lens chamber (separated by a gate valve), and the samples were placed on a new sample stage just after the lenses. This sample stage consisted, in part, of an electric feedthrough

to mount the sample, which is shown in the transparent blowup in this schematic. This setup was used for almost all the samples deposited at room temperature. It enabled better control of the ion beam by providing a means of focusing the beam using the deceleration lenses. The lens chamber also has additional vacuum pumping in the form of a second turbo pump, marked in Fig. 4.1 which differentially pumped the sample location compared to the ion beam chamber. This resulted in depositions at lower background pressures. This setup is also the same one used in the Ne and C deposition experiments from Chapter 3. Depositing samples at LC–2 was advantageous because it provided relatively easy access to the sample stage. This enabled moderately quick sample exchanges as well as the ability to perform quick modifications to the sample stage in efforts to optimize the deposition process. Photographs of the experimental setups for IC–1 and LC–2 are shown in Fig. B.9 and B.10 in Appendix B.

Lastly, the final experimental configuration used for depositing ^{28}Si in this work is one where the entire ion beamline, including the ion beam chamber and the deceleration lens chamber, is connected to the deposition and analysis chamber. This is the sample location corresponding to the schematic setup in the lower section of Fig. 4.1 marked as "Sample Location 3: Deposition Chamber", which will be referred to as DC–3. In this setup, samples were placed on the 5-axis manipulator for deposition of ^{28}Si, shown in the transparent blowup of this schematic. This configuration enabled lower background pressures, sample heating, and use of analytic instruments, and it is discussed further in Chapter 5. This lower schematic in Fig. 4.1 also marks the approximate locations of samples on the full combined

system for each of the three experimental configurations for depositing ^{28}Si.

In Chapter 1, the timeline progression of the best sample enrichment values achieved throughout this work using the ion beam deposition system was shown in the enrichment progression timeline in Fig. 1.12. This timeline will be discussed throughout this chapter as well as Chapter 5 in terms of the experimental changes that led to improvements in the ^{28}Si enrichment. A version of this timeline showing the isotope fractions measured by SIMS of ^{29}Si (squares) and ^{30}Si (triangles) vs. deposition date for just the ^{28}Si samples is presented in Fig. 4.2 along with indicators of the sample location during deposition. As mentioned in Chapter 1, isotope fractions of a particular isotope are defined in a SIMS measurement as the average detected counts of that isotope divided by the total average counts of the measurement. The isotope fractions of Si are written as $^{z}\mathrm{Si}/\mathrm{Si}_{\mathrm{tot.}}$, where z is the mass number denoted as 29 for ^{29}Si average counts and similarly for ^{30}Si and ^{28}Si and $\mathrm{Si}_{\mathrm{tot.}}$ is the sum of ^{28}Si, ^{29}Si, and ^{30}Si average counts. Uncertainties in the isotope fractions are derived from uncertainties in the SIMS measurements of those samples. Nine ^{28}Si samples out of a total of 61 produced in this work are represented on this timeline. Each of the nine samples were the most highly enriched of any samples produced up to that point on the timeline, that is, they represent new record enrichments for ^{28}Si samples achieved for this work. One can see that overall, the ^{29}Si isotope fraction was reduced from 2822(18) ppm in the initial sample, down to a minimum of 127(29) ppb with an overall enrichment in ^{28}Si of 99.9999819(35) % for the most highly enriched sample produced in this work. This level of enrichment exceeds that of all other known sources of ^{28}Si and will be discussed in Chapter 5. This chapter

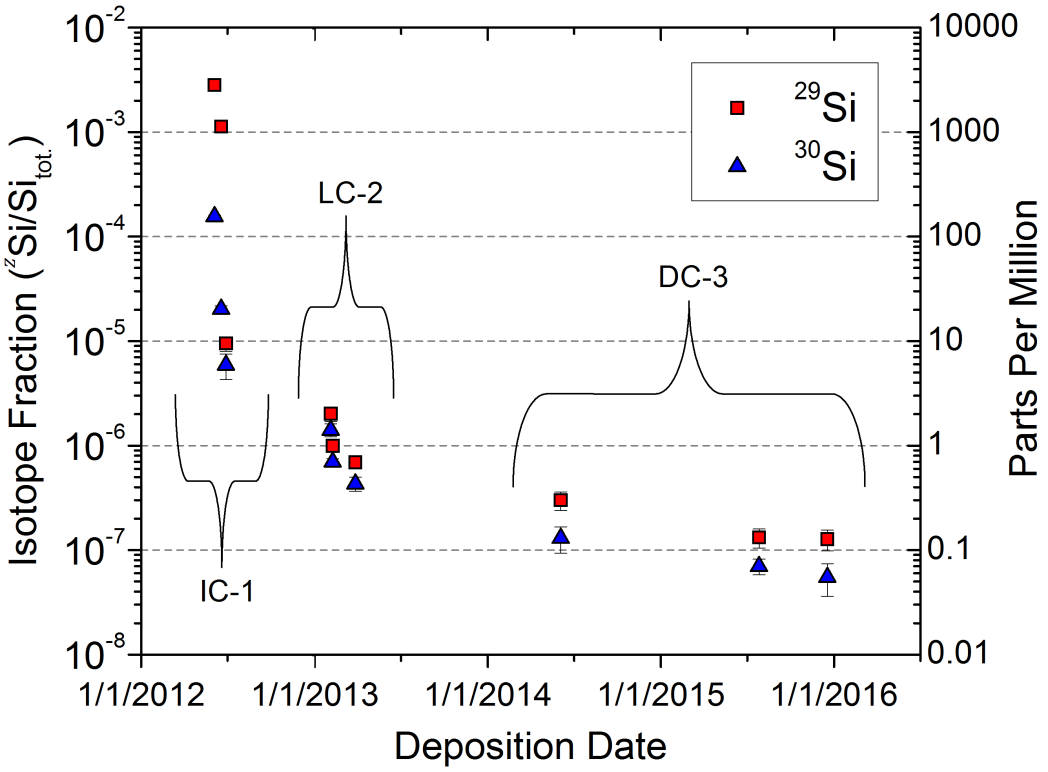

Figure 4.2: Enrichment progression timeline. A timeline of the progression of the lowest residual isotope fractions of ^{29}Si (squares) and ^{30}Si (triangles), as measured by SIMS. These were achieved for ^{28}Si samples deposited over approximately three and one half years. Groups of samples are labeled based on their deposition locations, IC–1 in the ion beam chamber, LC–2 in the lens chamber, and DC–3 in the deposition chamber.

will focus on the enrichment of the samples in the first two sections of this timeline. In total, 21 ^{28}Si samples were deposited at IC–1 and LC–2 combined.

Section 4.2 of this chapter will discuss samples deposited at IC–1 in the initial experimental configuration and SIMS measurements of their enrichment. Section 4.3 will discuss samples deposited at LC–2 in the intermediate configuration, SIMS measurements of their enrichment, and initial characterizations of their crystallinity by TEM and chemical purity by SIMS and XPS. Finally, Section 4.4 will give a brief summary of this chapter and the achieved enrichment values in the context

of the enrichment progression timeline. Some data presented in this chapter was previously published in Ref. [84].

4.2 Si Deposition Proof of Principle: Ion Beam Chamber Samples

4.2.1 Experimental Setup

This section discusses the initial deposition of ^{28}Si samples in an experimental configuration with the sample located in the ion beam chamber at IC–1 during deposition. A schematic of the ion beam chamber in this setup is shown in the upper left section of Fig. 4.1. Depositing ^{28}Si at IC–1 was a proof of principle experiment for the adaptation from depositing enriched C films to depositing enriched Si. One experimental change implemented for the transition from C deposition to Si deposition was the initial use of the gas-mode Penning ion source described in Chapter 2. This source was designed to more efficiently crack and ionize gas to generate an ion beam as opposed to ions being generated by sputtering a solid target. Using this ion source, an increase in the mass analyzed ion beam fluence was achieved from an average of 0.55 μA for ^{12}C depositions to an average of 0.92 μA for the initial ^{28}Si samples described in this section. Additionally, the gas-mode source allows a reduction in the source working pressure of nearly an order of magnitude from $\approx 1.3 \times 10^{-3}$ Pa (1.0×10^{-5} Torr) used for the ^{12}C deposition to $\approx 1.7 \times 10^{-4}$ Pa (1.3×10^{-6} Torr) for better integration with UHV deposition environments.

Samples at IC–1 were located immediately after the mass-selecting aperture,

and they were mounted on the end of an electrical feedthrough using a strip of conductive carbon tape on the back of the chip. This feedthrough and the sample location of IC–1 are shown in Fig. 4.1 in the blowup of the upper left section of the figure. A ceramic electric break was used to isolate the mounting flange of the electric vacuum feedthrough from the high voltage ion beam chamber. The feedthrough and sample are both on axis with the ion beamline optics, but there was no sample motion available in this configuration. Therefore, the ion beam must be precisely tuned to be on axis as well. The purpose of this feedthrough was to isolate the sample electrically from the chamber so that the ion beam current could be monitored during beam tuning and deposition. A photograph of a sample mounted on the vacuum feedthrough after a ^{28}Si deposition is shown in Fig. B.9 in Appendix B.

Using a small feedthrough to mount the sample in this way is advantageous in that its simplicity allows for quick and easy sample loading and unloading. However, it is disadvantageous in that there is no way to shield the sample substrate before deposition, which means that it is exposed to and accumulates material from the ion beam during initial tuning procedures and sweeps of the ion beam mass spectrum. Additionally, no sample heating capabilities are available when using this setup, which precludes *in situ* sample annealing and makes crystalline growth unlikely. The mass-selecting aperture consisted of a slit approximately 1 mm in width, i.e. the same direction that different mass ion beams are spatially separated. The aperture was also approximately 15.25 mm tall and 2 mm thick. This aperture was expected to provide an improvement in mass resolving power over the aperture used for the Ne

and C samples described in Chapter 3, which was an approximately 5 mm diameter circular hole that was 16 mm thick.

As mentioned, the sample location was not differentially pumped in this configuration, and so the base pressure and deposition pressures were that of the ion beam chamber itself. The base pressure of the ion beam chamber for these samples ranged from approximately 6.5×10^{-6} Pa to 1.3×10^{-5} Pa (4.9×10^{-8} Torr to 1.0×10^{-7} Torr) before deposition. A residual gas mass spectra of the base pressure of this chamber was shown in Fig. 2.22 in Chapter 2. This high base pressure is due to ambient air leakage through the o-rings used to seal the ion source as well as a gate valve, which are only rated for high vacuum, i.e. a minimum pressure of roughly 1.3×10^{-7} Pa (1.0×10^{-9} Torr). As previously mentioned, SiH_4 was used as the source gas for ^{28}Si deposition. SiH_4 was injected into the ion source via a UHV leak valve to generate a plasma that cracks and ionizes the SiH_4, producing the Si ion beam. The SiH_4 gas used for these samples and all ^{28}Si samples in this work had a natural abundance of isotopes and a purity of 99.999 % according to the gas vendor (Matheson Tri-Gas). During operation of the ion source, a working pressure for the low pressure plasma mode typically around 1.7×10^{-4} Pa (1.3×10^{-6} Torr) was chosen, as measured by the ion gauge. It should be noted that because there is no differential pumping at the sample location and thus no outlet for gas diffusion, there may be a slightly higher local pressure at the sample location. This is because the ion beam itself carries a lot of hydrogen in the form of a H_2^+ beam as well as H from SiH_4 fragments. This fluence of particles is delivered close to the sample before being blocked at the aperture where it can increase the local partial

pressures of H_2 and SiH_4. It is estimated that this effect may only contribute a 15 % higher total pressure at the sample, but it is nevertheless undesirable to have the sample in an environment with unknown partial pressures which may lead to increased adsorbates in the deposited film. SiH_4 adsorption is of particular concern in this work because, as described in Chapter 2, naturally abundant SiH_4 (including $^{29}SiH_4$) adsorbed onto the deposition surface becomes incorporated into the film resulting in higher concentrations of ^{29}Si and ^{30}Si in the sample. This subject is explored in great detail in Chapter 6.

4.2.2 Sample Preparation

For the initial ^{28}Si deposition tests, very little *ex situ* sample preparation occurred. Substrates consisted of "lightly doped" natural abundance commercial Si(100) wafers that were cleaved by hand into approximately 1 cm by 1 cm chips. The chips were handled with clean teflon tweezers and mounted on the end of the feedthrough using a strip of carbon tape on the back of the wafer, and they were loaded into the vacuum chamber with a native oxide. No further sample preparation occurred *in situ*. The role of these substrates is to simply be a "catcher foil" to collect the ^{28}Si ions, and one substrate used here actually was a Ag foil. Typically, after being loaded, samples sat several days in the vacuum chamber before deposition.

4.2.3 Deposition of ^{28}Si

The background deposition pressure for these samples was roughly the operating pressure of the ion source, and so during deposition, the pressure in the chamber

rose to between approximately 1.6×10^{-4} Pa and 2.3×10^{-4} Pa (1.2×10^{-6} Torr to 1.7×10^{-6} Torr), as measured by an ion gauge in a different section of the chamber. ^{28}Si ions were deposited onto the Si(100) substrates at room temperature. This temperature was not measured but assumed to be similar to the ambient temperature outside of the vacuum chamber, which was typically measured to be 21 °C ± 2 °C. Initially, an average ion energy, E_i, at the sample of approximately 455 eV was used. This value of E_i was chosen to be similar to the ion energy previously used for ^{12}C deposition. The energy was lowered to around 64 eV for the remainder of these samples to reduce the sputter yield during deposition. Sputter yield values for Si are shown in Fig. 2.19 in Chapter 2, as determined from TRIM calculations [69]. For Si ions striking a Si target, the sputter yield is around 53 % at 455 eV. This means that on average, every incident ion sputters 0.53 atoms from the surface leading to a deposition rate that is effectively reduced by half. The sputter yield for Si at an energy of 64 eV is reduced to only about 8 %. Sputtering is more significant for Si deposition than for C deposition, which has sputter yields that are about half the value of those of Si for a given ion energy.

The other significant aspect of the incident ion energies used here is that they are in the hyperthermal energy regime, as discussed in Chapter 2. The energy possessed by the ions can be transferred into the depositing film promoting epitaxial deposition. However, only amorphous deposition is expected for the samples discussed in this section due to the low substrate temperature and the presence of a surface oxide on the substrates. For these samples, ^{28}Si ion beam currents, I_i, ranged from 770 nA to 1.1 μA. A mass spectrum from the measured ion current for

^{28}Si and other SiH_4 ions, which is representative of the configuration and ion beam settings for samples deposited at sample location IC–1, is shown in Fig. 4.3. The corresponding magnetic sector analyzer current used for the field sweep is shown on the top axis of this figure. Ion current peaks on this semi-log plot (circles) are observed between 28 u and 32 u. As discussed in Chapter 2, the 28 u current peak is ^{28}Si, and the 29 u current peak is ^{28}SiH and approximately 6 % ^{29}Si based on the peak heights and the expected natural abundance. Ions of other Si hydrides up to $^{28}SiH_4$ are also generated in the ion source. A sum of Gaussian fits to the peaks (line, Eq. (2.14)) are also shown superimposed on the data, which they match fairly well. As discussed in Chapter 2, the spacial distribution of ions in the beam is expected to be roughly Gaussian for this system. The mass resolving power of the ion beam in this configuration derived from this mass spectrum is $\frac{m}{\Delta m} \approx 38$ (measured at 10 % of the peak height). The high ion current level between peaks of more than one tenth of the 28 u maximum (630 nA vs. 75 nA) possibly indicates a poorly focused beam leading to a large overlap between peaks. This could limit the separation of the ^{28}Si ion beam from the ^{29}Si ion beam and reduce the enrichment that is achieved with the settings used for these samples. The separation of the peaks can also be determined from the Gaussian fits, which give a standard deviation of the 29 u peak of $\sigma \approx 0.14$. This results in a peak separation between the 28 u and 29 u peaks of approximately 7 σ.

The ^{28}Si ion beam in this setup had a fairly large average spot size leading to a deposition spot on the substrate of about 20 mm^2. The ^{28}Si spot is easily visible on the substrates due to the difference in color from the underlying native oxide. This

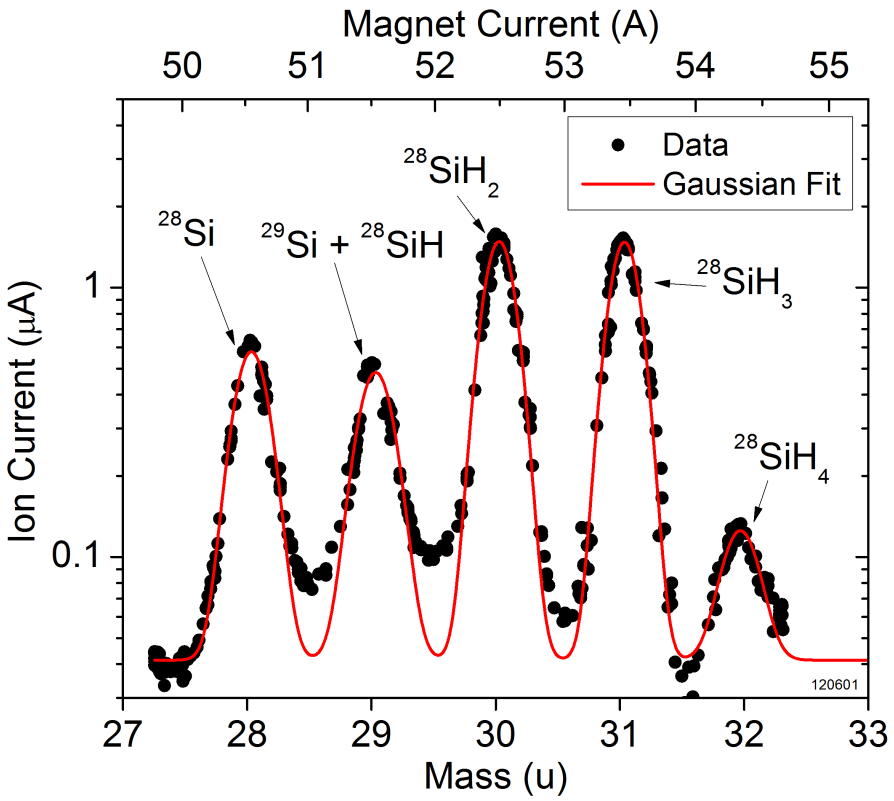

Figure 4.3: SiH_4 mass spectrum representative of the ion beam settings for samples deposited at room temperature at IC–1. The ion current (circles) is recorded while sweeping the mass analyzer current, and thus the magnetic field (top axis). The 28 u peak is ^{28}Si and the 29 u peak is both ^{28}SiH and ≈ 6 % ^{29}Si. Other higher order hydrides are also observed. Gaussian fits (line, Eq. (2.14)) to the peaks are shown superimposed on the data. The centers of the 28 u and 29 u fits are separated by $\approx 7\ \sigma$.

large spot size is a result of not being able to use the focusing deceleration lenses in this configuration. Despite relatively high ion currents achieved in this configuration, the large spot size reduces the achievable growth rate for a given ion fluence, as compared to a more compact spot. The resulting thickness, d, of one deposited film was about 85 nm with a deposition rate, R, of 0.41 nm/min derived from dividing the thickness by the deposition time. The thickness was measured by SEM cross-sectional microscopy. A SEM micrograph of this ^{28}Si sample is shown in Fig. 4.4. A photograph of the sample as deposited is inset showing the Si(100) substrate with

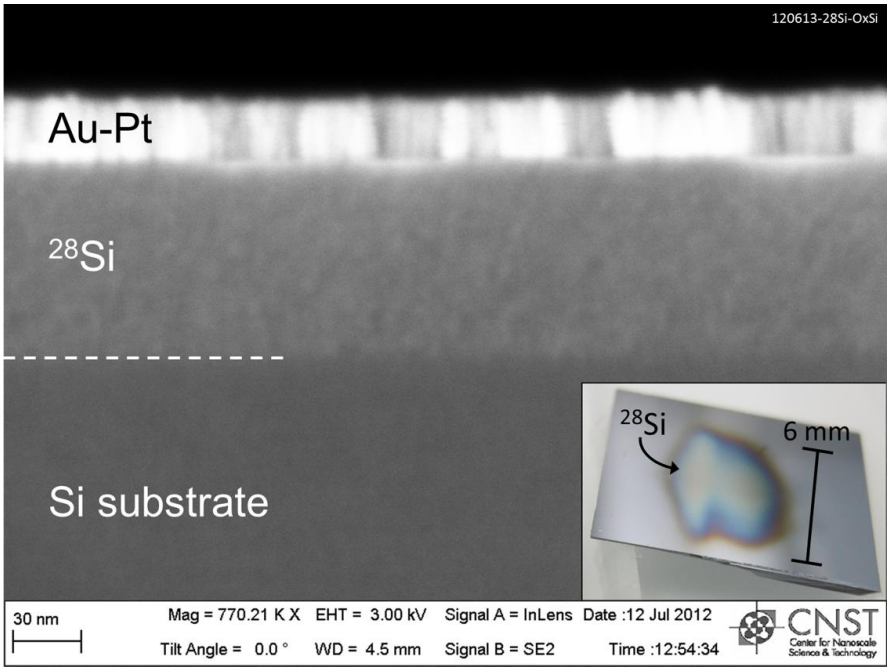

Figure 4.4: SEM cross-sectional micrograph of an amorphous ^{28}Si thin film deposited at room temperature at IC–1. The Si(100) substrate is seen in the lower portion of the image and the ^{28}Si film is above it. A dashed line marks the interface between the film and substrate. The thickness of the ^{28}Si film here is approximately 86 nm. Au-Pt is deposited on the top surface of the sample to to protect the film during sample cleaving. Inset is a photograph of the sample after deposition showing the roughly 6 mm wide ^{28}Si spot on the substrate.

the ^{28}Si deposition spot, which is roughly 6 mm wide. This SEM micrograph was acquired in collaboration with Dr. Michael Stewart (NIST). The Si(100) substrate is seen in the lower portion of the micrograph with the ^{28}Si film appearing as a slightly lighter region above it. A dashed line marks the interface between the film and substrate. The thickness of the ^{28}Si film seen here is approximately 86 nm. The ^{28}Si appears to have a different texture and possibly structure than the substrate, possibly indicating grains about 10 nm in size, although it is more likely that the film is amorphous. Amorphous deposition is expected for these samples because the presence of a native oxide prevents crystalline registration of the atoms in the

depositing film which could otherwise lead to epitaxy. Additionally, depositing at room temperature means that the likelihood of forming polycrystalline grains is low [85]. The thickness of two other samples was inferred from the calibration of the SIMS depth profiles (discussed below). The thickness of one sample was estimated to be only about 15 nm with a corresponding deposition rate of 0.07 nm/min, and the other sample thickness ranged from approximately 75 nm to 92 nm across the deposition spot with deposition rates between 0.33 nm/min and 0.40 nm/min.

To summarize, the typical deposition procedure for samples deposited at IC–1 was as follows:

1. a substrate is cleaved before being mounted onto the electrical feedthrough and loaded into the ion beam chamber, which is pumped out for > 12 h,
2. SiH_4 is then introduced into the chamber and the ion source is turned on. The beam is tuned including characterization of the mass spectrum by collecting the ion current on the substrate,
3. the ion beam is then tuned to the 28 u peak to commence deposition of ^{28}Si while monitoring the ion current onto the sample as a measure of the deposition rate,
4. after typically three to four hours of deposition, the ion source is turned off to end deposition, and the SiH_4 leak valve is closed to reduce the ion beam chamber pressure back to its base, and
5. the sample is then removed from the vacuum chamber for *ex situ* analyses by venting the ion beam chamber.

A total of five ^{28}Si samples were deposited at IC–1 and all used this procedure.

4.2.4 Enrichment Measurements via SIMS for IC–1 Samples

The enrichment of these samples and all samples discussed in this work were measured *ex situ* by SIMS using a CAMECA IMS-1270E7 large geometry spectrometer as mentioned in Chapter 3. ^{28}Si, ^{29}Si, and ^{30}Si isotopes were measured in collaboration with Dr. David Simons (NIST) and Dr. Shinichiro Muramoto (NIST). Dr. Simons collected the depth profile data for all but one of the samples discussed in this thesis. The raw data was then mostly analyzed by myself. The basic SIMS process for measuring Ne and C isotope ratios and isotope fractions was introduced in Chapter 3, and the measurement is similar for Si isotope fractions.

^{28}Si samples are bombarded with a primary ion beam of O_2^+ which sputters the sample at a constant rate and is rastered across an area typically 50 μm across. Ejected Si ions are collected into a secondary ion beam for analysis in a mass spectrometer. ^{28}Si, ^{29}Si, and ^{30}Si ions are collected separately using an electron multiplier and the counts are recorded for a given time interval, or SIMS cycle, to get a count rate. With a mass resolving power $\frac{m}{\Delta m} = 6000$ (measured at 10 % of the peak height) for this instrument, ^{28}SiH is easily distinguished from ^{29}Si in these measurements. An example SIMS mass spectrum (line) of these two separated peaks is shown in Fig. 4.5. The ion masses are separated by only approximately 0.008 u, but are well resolved in the SIMS instrument. This resolution is necessary for an accurate measurement of the ratio of ^{29}Si to ^{28}Si. The count rates are used to determine the isotope ratios ^{29}Si/^{28}Si and ^{30}Si/^{28}Si. To reduce discrete counting noise, isotope

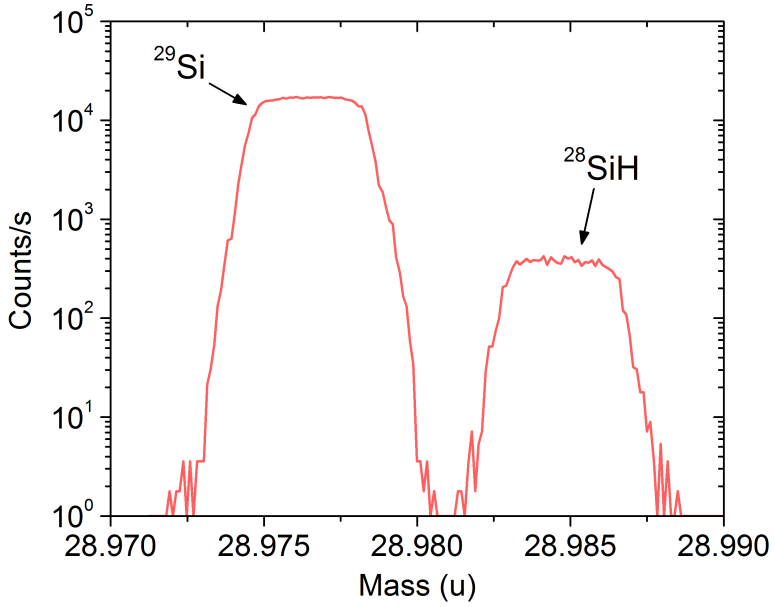

Figure 4.5: SIMS mass spectrum of ^{29}Si and ^{28}SiH ion currents (line) showing that the two peaks, which are separated by about 0.008 u, are well resolved in the SIMS instrument. This resolution is necessary for an accurate measurement of the ratio of ^{29}Si to ^{28}Si.

ratios for each cycle are then averaged together from the highly enriched portion of the ^{28}Si films after confirming no systematic trend to calculate the total average isotope ratios for that measurement. Isotope count ratios are converted into isotope fractions of the form (^{z}Si/Si$_{\mathrm{tot.}}$), which was previously described. The uncertainty of the isotope fractions was determined from the standard deviation of the mean of the measurements.

The depth profiles are calibrated by measuring the depth of the crater formed from sputtering the sample during the measurement. Crater depths were measured using a stylus profilometer, and then this value was used to determine the depth at each cycle by assuming a constant sputter rate. Because the measurement area is much smaller than the typical deposition area, multiple SIMS measurements are

sometimes made on the same sample. Measurements are typically made in the thickest portion of the ^{28}Si film because better measurement statistics result from analyzing more material within a single measurement. The results corresponding to the highest individual enrichment measured in each sample is presented in this work instead of an average of the multiple measurements. This is because the average of multiple measurements depends on factors such as the number of measurements and their location across the deposition spot, which are not consistent between different samples. Different locations across the deposition spot have different enrichments because the deposition rate and thus relative SiH_4 adsorption is not constant across the sample, which will be discussed further later. The multi-spot averages are therefore not a reliable metric for comparing the overall enrichments of samples, although they can give an idea of the variation in enrichment across a single sample. Additionally, the best measured enrichment for a sample is a preferred metric because it gives a lower bound on the best possible enrichment achievable by the deposition system. Further details of the specific SIMS measurements used for the different sets of samples discussed in this chapter can be found in Appendix E.

Of the five samples deposited at IC–1, three are represented on the enrichment progression timeline in Fig. 4.2 and will be discussed here. A SIMS depth profile for a ^{28}Si sample deposited at IC–1 is shown in Fig. 4.6. ^{28}Si (circles), ^{29}Si (squares), and ^{30}Si (triangles) isotope fractions are shown vs. sputter depth into the sample. This measurement as done using a TOF-SIMS instrument. At very shallow depths below the sample surface (0 nm to 10 nm), the isotope ratios are inflated to higher values due primarily to surface contamination from the sample being exposed to the ambi-

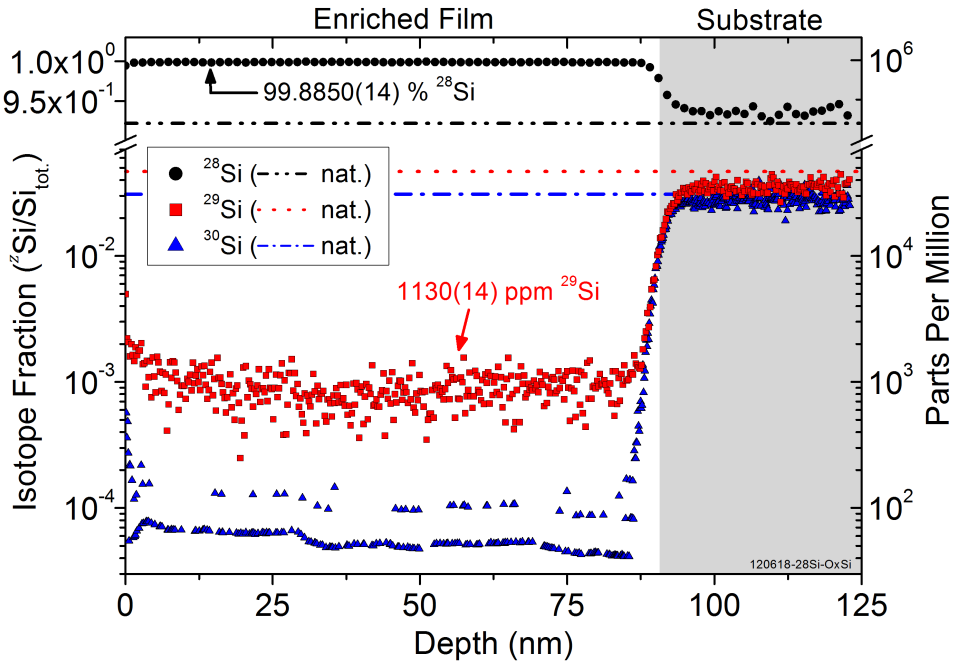

Figure 4.6: SIMS depth profile for a ^{28}Si sample deposited at room temperature at IC–1. ^{28}Si (circles), ^{29}Si (squares), and ^{30}Si (triangles) isotope fractions are shown vs. sputter depth into the sample. The average ^{29}Si isotope fraction is 1130(14) ppm. The natural abundance values for each isotope (dotted and dashed lines) are also shown for reference. The ^{30}Si data fluctuates between two values due to either zero (not shown), one, or two counts being detected in each measurement cycle. At 92 nm, the isotope fractions return to their natural abundance values indicating the interface with the substrate (shaded region). This measurement was done using a TOF-SIMS instrument.

ent environment before the SIMS measurements. This initial "surface tail" artifact is typical of SIMS and is seen in all the measurements discussed here. Isotope ratios from each measurement cycle were averaged together from about 20 nm to 80 nm to determine total isotope fractions for this sample. At a depth of around 92 nm, the isotope fractions return to their natural abundance values (dotted and dashed lines) indicating the interface with the natural abundance Si substrate (shaded region) and giving an estimate of the ^{28}Si film thickness. This value for the depth of the substrate interface is determined as the point at which the ^{29}Si and ^{30}Si isotope fractions re-

turn to half of their natural abundance values. It is difficult to infer any quantitative information about the width of the interface between the film and substrate from the depth profile because SIMS measurements tend to exaggerate interface widths. This can be due to interface roughness, which can be intrinsic to the sample or caused by the SIMS sputtering process itself [86]. For the sample measured in Fig. 4.6, the average measured ^{28}Si isotope fraction in the ^{28}Si film is 99.8850(14) %. The average ^{29}Si isotope fraction is $1.130(14) \times 10^{-3}$ (1130(14) ppm), and the average ^{30}Si isotope fraction is $2.03(14) \times 10^{-5}$ (20.3(14) ppm). The ^{30}Si signal appears in two bands because of discrete counting fluctuations between one and two counts in each SIMS data cycle and most ^{30}Si data being zero counts in some cycles. This measurement was the more highly enriched of two SIMS measurements performed on different spots on this sample. The average ^{29}Si isotope fraction of the two spots for this sample is 1332(13) ppm.

As previously discussed in Chapter 3, the isotope reduction factor is another useful parameter that describes the measured enrichment of a sample and, more specifically, gives the amount by which an excluded isotope is reduced from the natural abundance of that element. The reduction factor is determined by dividing the natural abundance of an isotope of an element by the measured isotope fraction. a_z represents the natural abundance of an isotope and, again, z is the mass number of the isotope denoted as 29 for ^{29}Si and 30 for ^{30}Si. The isotope reduction factors of the minor Si isotopes in the film are thus written as $a_z/(^z\mathrm{Si}/\mathrm{Si}_{\mathrm{tot.}})$. In the SIMS measurement discussed here, the isotope reduction factor for ^{29}Si is determined to be 41.5(5) (i.e. approximately 41 times lower than the natural abundance of ^{29}Si).

The reduction factor of ^{30}Si in this measurement is higher than that of ^{29}Si, having a value of $1.5(1) \times 10^3$. This is likely due to the 30 u peak being farther away spatially from the 28 u peak at the mass-selecting aperture. These measurements indicate a realized mass selectivity for this configuration of approximately 45:1 for ^{29}Si, which is lower than what was achieved for ^{12}C. This sample is less enriched than the ^{12}C samples by a factor of about 30 despite the mass resolving power determined from the mass spectrum being similar. This is perhaps not surprising considering that the 28 u and 29 u peaks have a spatial separation (5.5 mm) at the mass-selecting aperture approximately 44 % that of the 12 u and 13 u peaks (12.4 mm). Additionally, the natural abundance of ^{29}Si relative to ^{28}Si is higher than the natural abundance of ^{13}C relative to ^{12}C, so a ^{28}Si sample deposited with a given ion peak separation would be less enriched than a ^{12}C sample deposited with the same peak separation. A second ^{28}Si sample deposited at IC–1 was measured by SIMS as well, but it showed a ^{29}Si isotope fraction of 2822(18) ppm, which is approximately twice as large as the previous sample. This is potentially due to slightly different beam tuning parameters and a slightly lower mass selectivity achieved at the time of deposition.

After depositing these two samples and reviewing the SIMS data, a third ^{28}Si sample was deposited in an effort to better tune the ion beam parameters and increase the mass spectrum geometric selectivity, i.e. reduce the overlap of the 29 u peak onto the 28 u peak. This effort resulted in a lowering of the residual ^{29}Si isotope fraction by nearly a factor of 200. A SIMS depth profile of the most highly enriched spot measured for this sample is shown in Fig. 4.7. ^{28}Si (circles), ^{29}Si (squares),

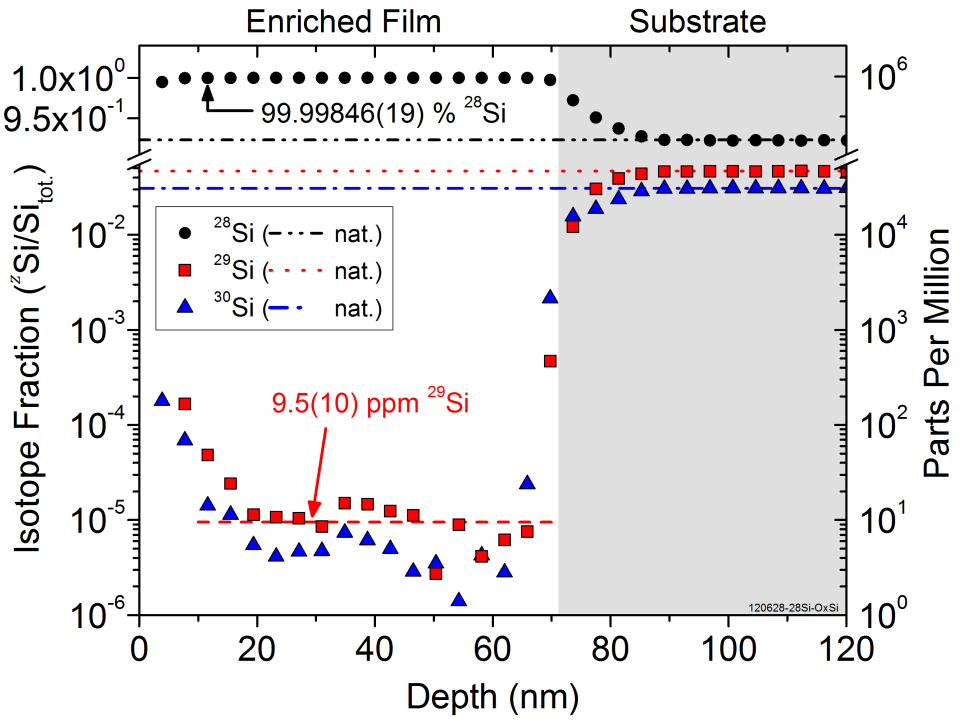

Figure 4.7: SIMS depth profile for the most highly enriched ^{28}Si sample deposited at room temperature at IC–1. ^{28}Si (circles), ^{29}Si (squares), and ^{30}Si (triangles) isotope fractions are shown vs. sputter depth. The average ^{29}Si isotope fraction is 9.5(10) ppm. The natural abundance values for each isotope (dotted and dashed lines) are also shown for reference. At a depth of 75 nm, the isotope fractions return to their natural abundance values indicating the interface between the film and the substrate (shaded region).

and ^{30}Si (triangles) isotope fractions are shown vs. sputter depth. At a depth of around 70 nm, the isotope fractions return to their natural abundance values (dotted and dashed lines) giving an estimate of the ^{28}Si film thickness. The substrate is marked by the shaded region. The average measured ^{28}Si isotope fraction in the ^{28}Si film is 99.99846(19) %. The average ^{29}Si isotope fraction is $9.5(10) \times 10^{-6}$ (9.5(10) ppm), and the average ^{30}Si isotope fraction is $5.9(16) \times 10^{-6}$ (5.9(16) ppm). Isotope fractions were determined by averaging the data from depths between 20 nm to 65 nm. The isotope fraction of ^{29}Si in this measurement is a nearly a factor of 120 lower than that of the previous sample. These measurements indicate a much

larger average isotope reduction factor of approximately $5.1(8) \times 10^3$ for ^{29}Si and ^{30}Si. The large improvement in ^{29}Si reduction factor but modest improvement in ^{30}Si reduction factor shows that the ion beam was indeed tuned better for ^{29}Si rejection during deposition of this sample. For this sample, a total of four areas across the deposition spot were measured by SIMS with similar results to the most highly enriched one mentioned above. The average ^{29}Si isotope fraction of the four measurements from this sample is 11.28(54) ppm. This result shows that a very high level of enrichment in ^{28}Si is achievable, which surpasses the enrichment goal stated at the beginning of this chapter.

It is difficult to determine the exact cause of the large reduction in the ^{29}Si isotope fraction, as seen in the enrichment progression timeline in Fig. 4.2. Presumably, the peak separation between the 28 u and 29 u ion current peaks in the mass spectrum was significantly larger for this final sample than for earlier samples resulting in a realized selectivity, although that data was not recorded.

4.2.5 Summary of Results for IC–1 Samples

The ^{28}Si samples deposited at IC–1 in the initial experimental configuration showed that the mass selected ion beam deposition method, demonstrated first in in Chapter 3, could be adapted to produce enriched ^{28}Si thin films. It established the experimental parameters and methods needed for depositing ^{28}Si from a natural abundance SiH_4 source gas and subsequently characterizing the enrichment. The most highly enriched ^{28}Si sample produced in this configuration has an average measured ^{28}Si isotope fraction of 99.99846(19) %, an average residual ^{29}Si isotope

fraction of 9.5(10) ppm, and an average ^{30}Si isotope fraction of 5.9(16) ppm, similar to that of the previous ^{12}C samples. This level of enrichment not only matches the enrichments of ^{28}Si produced by other sources currently available in the QI community, such as the IAC [32], but it surpasses them and meets the enrichment goal stated at the beginning of this chapter. The ^{28}Si enrichment of this sample also surpasses the best reported enrichment of previous ^{28}Si ion beam deposition by Tsubouchi *et al.* [43]. However, the enrichment of some samples was significantly worse, probably due to a lower geometric mass selectivity achieved for ^{28}Si in these experiments. It is obvious from these initial depositions that the geometric selectivity of the ion beam needs to be consistently larger in order to, at a minimum, consistently and predictably match the residual ^{29}Si isotope fractions of ^{28}Si material produced by other sources including the IAC. Large variations and uncertainty in the mass selectivity of the ion beam system is a clear drawback of this experimental configuration. A cross section of a ^{28}Si film was also analyzed using SEM as a secondary method for measuring the film thickness, and it showed that the film likely has a different structure than the substrate.

4.3 Achieving Highly Enriched ^{28}Si: Lens Chamber Samples

4.3.1 Experimental Setup

This section discusses the deposition of ^{28}Si samples in an experimental configuration with the sample located in the lens chamber at LC–2 during deposition.

A schematic of the ion beam and lens chambers in this setup is shown in the upper right section of Fig. 4.1. These experiments expand upon the work of the previous section by implementing a number of experimental improvements including reconnecting the deceleration lens chamber to the ion beam chamber. The mass-selecting aperture used between the ion beam and the lens chamber was the same 1 mm wide slit discussed in the previous section.

In this configuration, samples were located after the deceleration lenses, and they were mounted on the end of an electrical feedthrough which acted as a sample stage for this intermediate experimental setup. A sketch of the sample stage feedthrough and sample location is shown in the blowup of the schematic of the LC–2 setup in Fig. 4.1. Samples were mounted using a strip of conductive carbon tape on the back side of the chip. As was the case with the previous setup, the purpose of the feedthrough was to isolate the sample electrically from the chamber so that the ion beam current could be monitored during beam tuning and deposition. Unlike the previous setup, additional electrical vacuum feedthroughs on the sample stage were used to mount a masking element above the sample location consisting of a metal shim for collecting current. This was positioned between the sample and the path of the ion beam and had a small circular aperture directly above the sample. This mask and aperture was fixed in place for the duration of a deposition. The fixed sample aperture was approximately 3 mm in diameter and provided a mechanism to monitor the focusing of the ion beam on the sample by maximizing the ion current detected on the sample while minimizing the current detected on the sample mask. Additionally, the mask and sample aperture allowed for precise loca-

tion of the ion beam spot on the sample substrate. The feedthrough (and sample) were positioned on axis with the ion beamline optics, and unlike the previous setup, IC–1, the sample aperture allowed for the ion beam to be tuned and steered onto the exact sample location under the aperture. However, a lack of sample motion in this setup means that the ion beam was constrained to be on axis, which may not have been the optimal tuning position. A photograph of a sample mounted on the vacuum feedthrough on this intermediate sample stage with the sample mask is shown in Fig. B.11 in Appendix B. As was the case with the previous setup, no method for sample heating exists on this sample stage here. This precludes *in situ* sample preparation and limits the available experimental phase space for achieving epitaxial deposition.

For these experiments, the ion source was operated in the low pressure mode with a working pressure of SiH_4 similar to that which was used for the previous setup of around 2.7×10^{-4} Pa (2.0×10^{-6} Torr). An additional turbo pump in the lens chamber provides differential pumping at the sample location, which results in lower partial pressures during deposition. Unlike the ion beam chamber, the lens chamber is rated to UHV, although it was never baked prior to these experiments. The base pressure of the lens chamber for these samples ranged from approximately 3.6×10^{-8} Pa to 1.3×10^{-6} Pa (2.7×10^{-10} Torr to 1.0×10^{-8} Torr) before deposition, although for the majority of samples, the base pressure was typically around 1.3×10^{-7} Pa (1.0×10^{-9} Torr).

The decelerating lenses themselves are described in detail in Chapter 2. As was mentioned previously, the benefit of the lenses is that they provide focusing of the

^{28}Si ion beam as it exits the mass-selecting aperture. The lenses help maintain a tight beam spot as the ions are smoothly decelerated from the transport voltage (-4 kV) to ground potential at the sample. A more focused beam spot is advantageous because it corresponds to a higher ion flux, F_i, on the substrate and a higher deposition rate. This results in a lower relative rate of adsorption of gaseous species from the vacuum into the ^{28}Si film for a given background pressure.

Another significant experimental change implemented for the experiments of this section is the replacement and reconfiguration of several power supplies that controlled the voltages of various electrostatic lens elements in the ion beamline. These include the "arc" voltage, which defines the potential between the anode and cathode in the source, the "extractor" element voltage, and the "focus" element voltage. The additional control and degrees of freedom provided by this reconfiguration allowed for better ion beam tuning to maximize ion fluence as well as produce a more confined beam before mass separation. This improved ion beam tuning yielding a more consistent geometric selectivity similar to and exceeding that which was achieved with the final sample deposited at IC–1. The circuit diagram of the power supplies controlling the ion beam lens elements up to the sector mass analyzer is shown in Fig. A.1 in Appendix A and discussed in Chapter 2.

4.3.2 Sample Preparation

Substrates used for depositing ^{28}Si in this section consisted primarily of "lightly doped" natural abundance commercial Si(100) wafers that were cleaved by hand into approximately 1 cm by 1 cm chips. Additionally, several ^{28}Si samples were

deposited onto silicon-on-insulator (SOI) chips which had a 40 nm Si "device" layer on top of 400 nm of buried thermal oxide. The motivation for using these SOI wafers was to address a potential difficulty in using electron microscopy to measure the properties of a Si film deposited onto Si. If perfect epitaxy is achieved, then the ^{28}Si film would become indistinguishable from the substrate except by means of isotope measurements such as SIMS. By introducing the buried oxide below an ultra-thin Si surface layer of known thickness, the ^{28}Si film-substrate interface, and thus the film, would always be easily located in microscopy studies. Before being loaded into the vacuum chamber, substrates were pre-treated with hydrofluoric acid (HF) to remove the native oxide and provide a clean surface for deposition. This treatment was necessary to enable the possibility of epitaxial deposition because *in situ* substrate heating was not available to thermally desorb the surface oxide before deposition. The substrates were only handled with clean teflon tweezers and were mounted on the end of the sample feedthrough using a strip of carbon tape on the back of the wafer. No further sample preparation occurred *in situ*. Typically, after being loaded into the chamber, samples sat several days in the vacuum chamber before deposition.

4.3.3 Deposition of ^{28}Si

After tuning and focusing the ion beam according to the procedures described in Chapter 2, ^{28}Si ions were deposited onto the Si(100) substrates at room temperature ($\approx$ 21 °C, see Section 4.2.3). For the deposition of one ^{28}Si sample, a different sample stage was used that had a tungsten wire back heater for sample

heating. This was used to to deposit the ^{28}Si film with a substrate temperature of approximately 550 °C. This experiment, however, did not have a significant impact on the work presented here and will not be discussed further. During deposition of the ^{28}Si films at room temperature, the pressure in the chamber rose to between 3.3×10^{-6} Pa and 7.2×10^{-6} Pa (2.5×10^{-8} Torr to 5.4×10^{-8} Torr) due to gas diffusion from the operation of the ion source. These pressures are more than a factor of 20 improvement over the previous setup. Ions were deposited with a range of average ion energies at the sample between 50 eV and 170 eV. A lower value of E_i generally produced a larger geometric selectivity as observed in mass spectra during the tuning procedures prior to each deposition. For these samples, ^{28}Si ion beam currents ranged from 200 nA to 800 nA. A mass spectrum for an ion beam with an average ion energy energy $E_i \approx 122$ eV collected through the fixed sample aperture prior to deposition of a ^{28}Si sample is shown in Fig. 4.8. The corresponding magnetic sector mass analyzer current used for the field sweep is shown on the top axis. Ion current peaks (circles) corresponding to ^{28}Si and Si hydrides are observed from 28 u to 33 u. The ^{28}Si ion peak at 28 u and the ion peak at 29 u, containing ≈ 5 % ^{29}Si, show a high degree of separation on this semi-log plot with no detectable ion current signal occurring between the peaks. Secondary electrons generated by the ion beam cause the current between the peaks to be ≈ -0.5 nA. Gaussian fits to the data (line, Eq. (2.14)) are also shown for the 28 u and 29 u current peaks, and one can see that the data matches the form of a Gaussian very well. This indicates a symmetric and optimally tuned beam shape with minimal perturbations such as scattering off of lens elements. The Gaussian fits give a separation of the 28 u peak

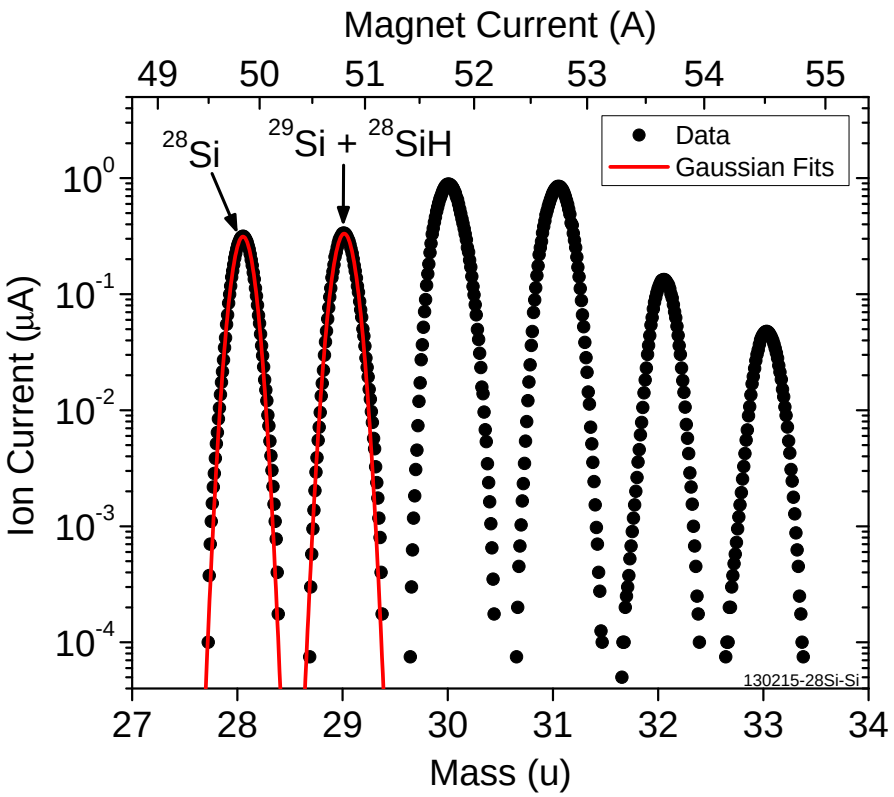

Figure 4.8: SiH_4 mass spectrum representative of the ion beam settings for samples deposited at LC–2. The ion current (circles) is recorded while sweeping the the analyzer current, and thus the magnetic field (top axis). The peak at 28 u is ^{28}Si and the peak at 29 u peak is ^{28}SiH and $\approx$ 5 % ^{29}Si. Several higher order hydrides are also observed. Gaussian fits (line, Eq. (2.14)) to the 28 u and 29 u peaks are superimposed on the data. The centers of the 28 u and 29 u fits are separated by $\approx 11\ \sigma$.

from the 29 u peak of approximately 11 σ. The mass resolving power of the ion beam in this configuration derived from this mass spectrum is $\frac{m}{\Delta m} \approx 78$ (measured at 10 % of the peak height), which is significantly better than for the mass spectrum shown in the previous section.

Focusing the ^{28}Si ion beam with the deceleration lenses resulted in a more compact beam spot size and an average deposition area of about 6 mm^2. The beam spot focusing procedure was not yet optimized for the initial sample deposited here resulting in a larger deposition area of 16 mm^2. The ^{28}Si spots on these samples are

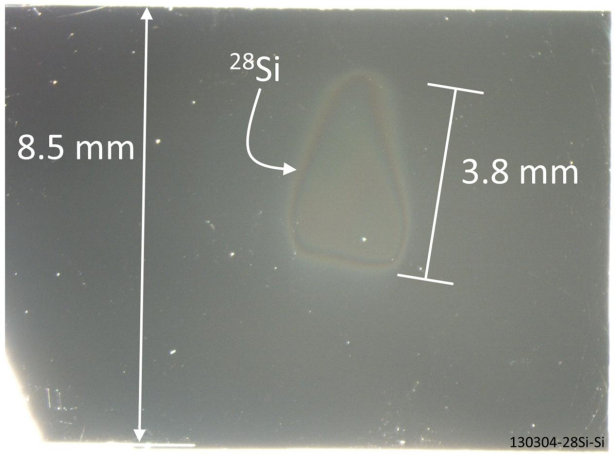

Figure 4.9: Optical micrograph of a ^{28}Si sample deposited at room temperature at LC–2. The Si(100) substrate consisting of a roughly 8.5 mm wide chip is seen with the ^{28}Si spot measuring about 3.8 mm long.

still visible to the naked eye although they appear different from the samples in the previous section likely due to the native oxide being stripped prior to deposition. A visible deposition spot indicates that the ^{28}Si film is structurally different from the substrate and probably not epitaxial. A representative optical micrograph of a ^{28}Si sample deposited at LC–2 is shown in Fig. 4.9. The Si(100) substrate is approximately 8.5 mm wide and the ^{28}Si spot is approximately 3.8 mm long. The resulting thicknesses of these ^{28}Si films ranged from approximately 50 nm to 350 nm as inferred from SIMS depth profiles with corresponding deposition rates between 0.51 nm/min and 1.49 nm/min.

To summarize, the typical deposition procedure for samples deposited at LC–2 was as follows:

1. a substrate is cleaved and dipped in HF immediately before being mounted onto the sample stage feedthrough and loaded into the deceleration lens chamber which is pumped out for $>$ 12 h,
2. after turning on the ion source, the gate valve to the ion beam chamber is

opened and the ion beam is tuned and characterized on the substrate using the fixed sample aperture on the feedthrough. The mass spectrum, ion beam energy, and beam spot focusing are analyzed and recorded,

3. the ion beam is then tuned to the 28 u peak to commence deposition of ^{28}Si while monitoring the ion current onto the sample as a measure of the deposition rate,

4. after typically three to five hours of deposition, the gate valve to the ion beam chamber is closed to end deposition and reduce the lens chamber pressure back to its base, and

5. the sample is then removed from the vacuum chamber for *ex situ* analyses by venting the lens chamber.

In total, 16 ^{28}Si samples were deposited at LC–2 under these conditions.

4.3.4 Enrichment Measurements via SIMS for LC–2 Samples

SIMS was used to assess the enrichment of several samples deposited at LC–2 to determine if the experimental improvements including the higher degree of control over the ion beam, which were discussed at the beginning of this section, yielded more consistent and lower overall ^{29}Si and ^{30}Si isotope fractions. Of the 16 samples produced at LC–2, three are represented on the enrichment progression timeline in Fig. 4.2, and will be discussed in this section. A SIMS depth profile of the highest enrichment measured for the first ^{28}Si sample deposited at LC–2 is shown in Fig. 4.10. Measurements of the ^{28}Si (circles), ^{29}Si (squares), and ^{30}Si (triangles) isotope fractions are shown vs. the sputter depth into the sample. At a depth of around 80 nm, the isotope fractions begin to increase to their natural abundance

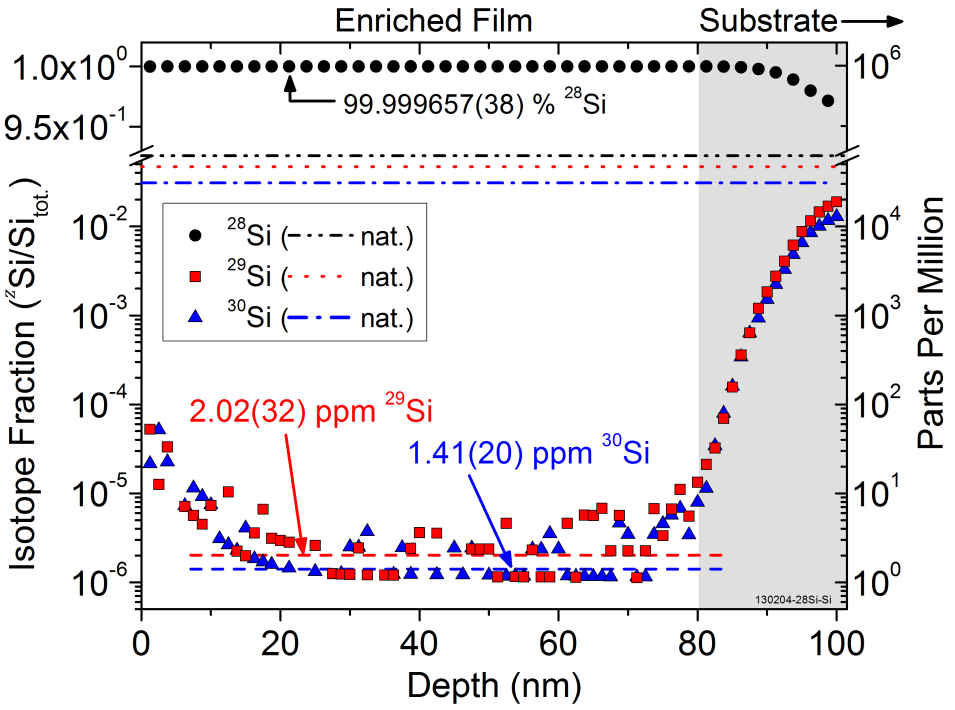

Figure 4.10: SIMS depth profile of a ^{28}Si sample deposited at room temperature at LC–2. ^{28}Si (circles), ^{29}Si (squares), and ^{30}Si (triangles) isotope fractions are shown vs. sputter depth. The average ^{29}Si isotope fraction is 2.02(32) ppm, and the average ^{30}Si isotope fraction is 1.41(20) ppm. The natural abundance values for each isotope (dotted and dashed lines) are also shown for reference. At a depth of 80 nm, the isotope fractions increase to their natural abundance values in the transition into the Si(100) substrate (shaded region). The film-substrate interface is estimated to be at a depth of 105 nm (not shown).

values (dotted and dashed lines) in the transition into the Si(100) substrate, marked by the shaded region. This relatively gradual increase in isotope fraction over 25 nm is partially an artifact of the SIMS measurement, which was described in the previous section. It is also probably due to beam tuning, including mass spectrum sweeps, which would deposit all three Si isotopes on the substrate before ^{28}Si deposition. The film thickness is determined from the location of the interface between the film and substrate, which is estimated to be at a depth of 105 nm (not shown).

The average measured ^{28}Si isotope fraction in the ^{28}Si film is 99.999657(38) %.

The average residual ^{29}Si isotope fraction is $2.02(32) \times 10^{-6}$ (2.02(32) ppm), and the average ^{30}Si isotope fraction is $1.41(20) \times 10^{-6}$ (1.41(20) ppm). These measurements indicate an average isotope reduction factor for ^{29}Si and ^{30}Si of nearly $2.3(2) \times 10^4$. A second area on this sample was also measured by SIMS giving an average ^{29}Si isotope fraction of these two measurements of 2.16(21) ppm. This level of ^{29}Si isotope fraction is nearly a factor of five lower than for sample with the highest enrichment achieved at IC–1, as seen in the jump from IC–1 to LC–2 in the enrichment progression timeline in Fig. 4.2. The similar reduction factors for ^{29}Si and ^{30}Si indicate that the upgraded ion beam tuning control introduced in this section enables more consistent geometric selectivites similar to and surpassing those achieved for the final sample deposited at IC–1 in the last section. This sample was deposited with a background pressure 20 times lower than previous samples, and the resulting enrichment appears to support the conjecture discussed previously that the enrichment is partially a consequence of the adsorption of SiH_4 from the background gas. Despite this improvement in enrichment, this initial sample had a relatively large deposition spot size as was mentioned previously. This resulted in the lowest deposition rate of any of the samples discussed in this section, which may limit the enrichment that was achieved. This is because a lower ^{28}Si deposition rate will result in a higher relative adsorption rate of gaseous species for a given background pressure during deposition. As was mentioned previously in Chapter 2 and in this chapter, part of this background pressure is natural abundance SiH_4, which, if adsorbed into the film, will result in a lower ^{28}Si enrichment in the sample.

After depositing this initial sample, another ^{28}Si sample was deposited under

similar conditions except with a more focused beam spot resulting in a smaller deposition spot size of about 7 mm^2. The SIMS measurement of the most highly enriched region of this second sample is shown as a depth profile in Fig. 4.11. ^{28}Si (circles), ^{29}Si (squares), and ^{30}Si (triangles) isotope fractions are shown vs. sputter depth. At a depth of around 340 nm, the isotope fractions begin to increase due to ion beam tuning and mass spectrum sweeps prior to deposition of ^{28}Si. Beyond this, the isotope fractions continue to rise to their natural abundance values (dotted and dashed lines) in the transition into the substrate, marked by the shaded region. The film-substrate interface is estimated to be at a depth of 384 nm, giving a value for the ^{28}Si film thickness. The data appears to reside in two main bands because of discrete counting fluctuations in the measurement, as mentioned for previous SIMS measurements.

The average measured ^{28}Si isotope fraction in the ^{28}Si film for this sample is 99.9998308(82) %. The average ^{29}Si isotope fraction is about a factor of two lower than the previous sample at a value of $0.993(64) \times 10^{-6}$ (0.993(64) ppm). The average ^{30}Si isotope fraction is $0.699(51) \times 10^{-6}$ (0.699(51) ppm). These measurements indicate an average isotope reduction factor for ^{29}Si and ^{30}Si of $4.6(2) \times 10^4$. Achieving this very high enrichment potentially enables a robust measurement of the dependance of electron coherence times on ^{29}Si concentration in the single spin regime, as discussed at the beginning of this chapter. Four other areas of the deposition spot of this sample were also measured by SIMS giving an average ^{29}Si isotope fraction for the five measurements of this sample of 1.388(38) ppm.

This result again indicates that the measured enrichment could be due to the

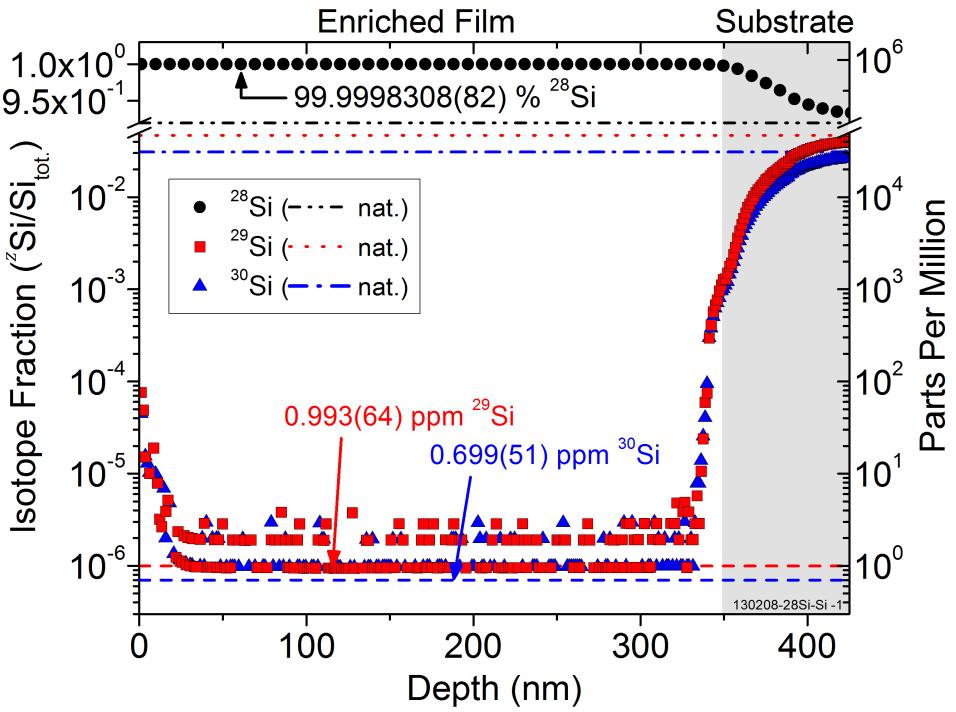

Figure 4.11: SIMS depth profile of a ^{28}Si sample deposited at room temperature at LC–2. ^{28}Si (circles), ^{29}Si (squares), and ^{30}Si (triangles) isotope fractions are shown vs. sputter depth. The average ^{29}Si isotope fraction in the film is 0.993 ppm, and the average ^{30}Si isotope fraction is 0.699 ppm. The natural abundance values for each isotope (dotted and dashed lines) are also shown for reference. At 340 nm, the isotope fractions begin to increase to their natural abundance values in the transition to the substrate (shaded region). The film-substrate interface is estimated to be at a depth of 384 nm.

presence of a SiH_4 background gas at the sample. The smaller spot size of this sample led to the highest deposition rate for any of the samples discussed in this section, and one that is almost three times higher than the previously discussed sample. The higher deposition rate of this second sample results in a shorter time for gaseous species to adsorb into the film for a given volume of material being deposited and thus lower ^{29}Si and ^{30}Si residual isotope fractions.

This effect is evident not just when comparing the previous sample to this one, but also within the five SIMS measurements of this sample. Due to the ^{28}Si

ion beam flux being nonuniform throughout the beam spot with a roughly Gaussian spatial distribution, the five areas on the deposition spot were measured to have different thicknesses and thus different corresponding deposition rates. The SIMS measurements of ^{29}Si from this sample are shown vs. the deposition rate in Fig. 4.12. As expected, the residual ^{29}Si isotope fraction (squares) varies inversely with the deposition rate for these five measurements. These deposition rates are derived from the film thickness at each spot (top axis), which are inferred from the SIMS depth profiles. The uncertainty of the deposition rates are determined from uncertainty in the SIMS depth scales and deposition times. This shows that improvements to either the background pressure during deposition or the deposition rate can improve the enrichment of these ^{28}Si samples.

Having establishing the experimental procedures and processes to produce this last ^{28}Si film with a residual ^{29}Si isotope fraction of 0.993 ppm, several other ^{28}Si samples were deposited with isotope fractions of ^{29}Si and ^{30}Si consistently at or below 1 ppm. One of these samples was deposited on a SOI substrate and was measured by SIMS to have an average ^{28}Si isotope fraction of 99.999863(16) %. The average residual ^{29}Si isotope fraction is $0.77(11) \times 10^{-6}$ (0.77(11) ppm), and the average ^{30}Si isotope fraction is $0.60(11) \times 10^{-6}$ (0.60(11) ppm). The most highly enriched of these samples deposited at LC–2 has an average measured ^{28}Si isotope fraction of 99.999888(10) %. The average residual ^{29}Si isotope fraction in this sample is $0.691(74) \times 10^{-6}$ (0.691(74) ppm), and the average ^{30}Si isotope fraction is $0.432(67) \times 10^{-6}$ (0.432(67) ppm). The SIMS depth profile of this sample is shown in Fig. 4.13. The isotope fraction values were determined by averaging the data be-

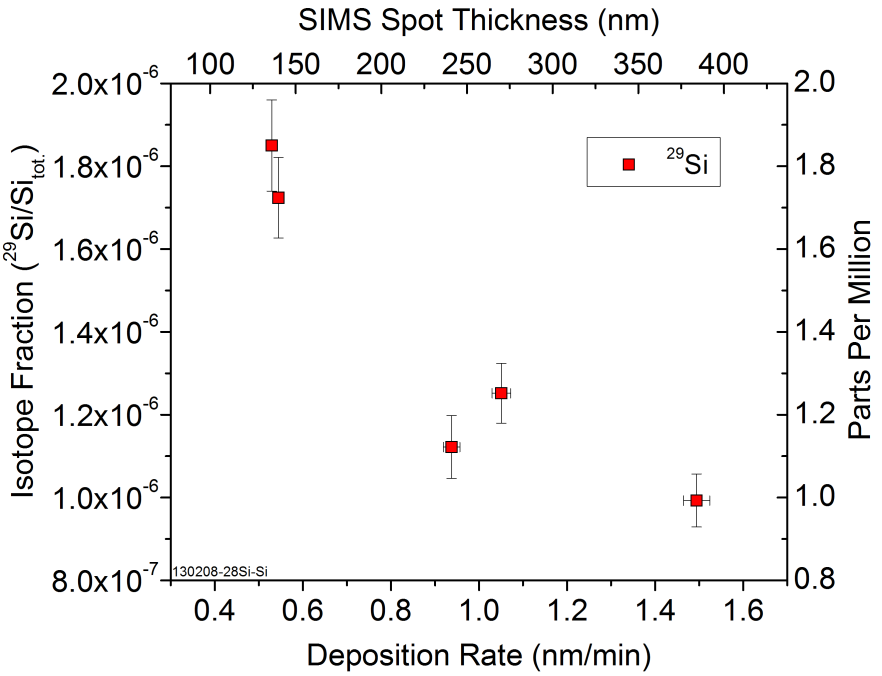

Figure 4.12: ^{29}Si isotope fractions vs. the deposition rate for multiple SIMS measurements made on a sample deposited at room temperature at LC–2. Five different areas across the deposition spot experienced different deposition rates due to an inhomogeneous ion beam flux. These rates were derived from the thickness at each spot (top axis) inferred from the SIMS depth profiles. The ^{29}Si isotope fractions (squares) vary inversely with the deposition rate across the sample.

tween 25 nm and 100 nm. The data from the rest of the ^{28}Si film was not included because during the first half of the deposition, the pressure at LC–2 was being varied as part of a separate experiment resulting in slightly increased ^{29}Si and ^{30}Si isotope fractions due to SiH_4 adsorption. The average isotope reduction factor for ^{29}Si and ^{30}Si in this sample is $7.0(7) \times 10^4$. At a depth of around 225 nm, the isotope fractions begin to increase to the natural abundance values in the substrate (dotted and dashed lines). The interface between the film and the substrate is estimated to be at a depth of 249 nm and is marked by the shaded region.

Overall, SIMS measurements of samples deposited at LC–2 show that a reduction of nearly a factor of 14 in the ^{29}Si isotope fraction of the most highly enriched

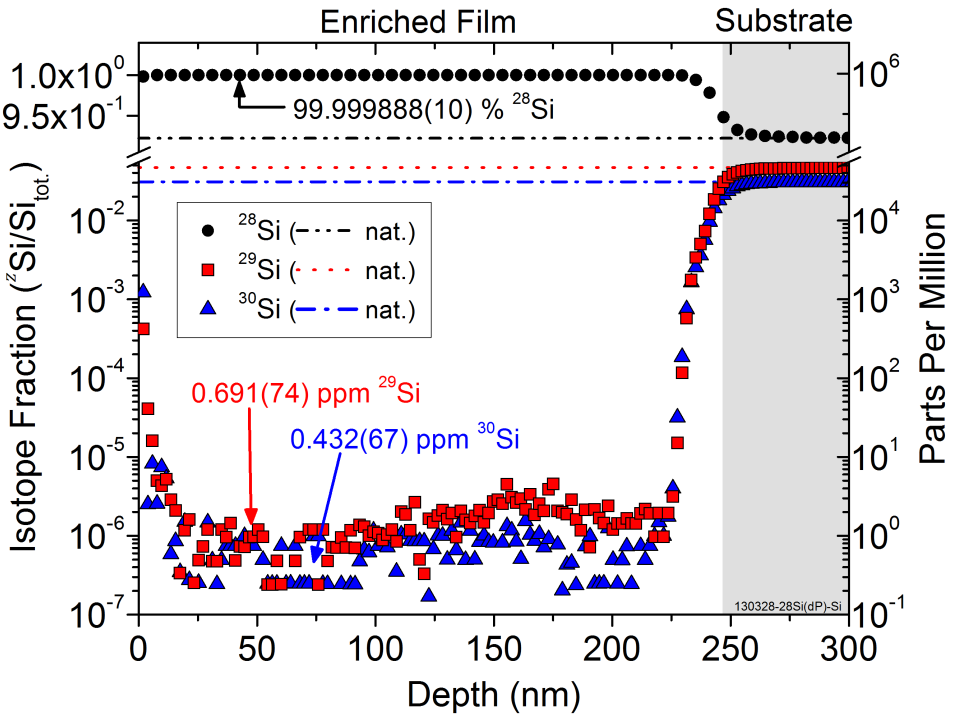

Figure 4.13: SIMS depth profile of the most highly enriched ^{28}Si sample deposited at room temperature at LC–2. ^{28}Si (circles), ^{29}Si (squares), and ^{30}Si (triangles) isotope fractions are shown vs. sputter depth. The average ^{29}Si isotope fraction in the film is 0.691 ppm, and the average ^{30}Si isotope fraction is 0.432 ppm. The natural abundance values for each isotope (dotted and dashed lines) are also shown for reference. At a depth of 225 nm, the isotope fractions begin to increase to their natural abundance values in the substrate (shaded region). The interface between the film and the substrate is estimated to be at a depth of 249 nm.

sample was achieved compared to that of the previous most highly enriched sample deposited at IC–1, which can be seen in the enrichment progression timeline in Fig. 4.2. Additionally, the ^{28}Si enrichment values of these samples are consistently high unlike those of the samples deposited at IC–1, which varied a great deal.

4.3.5 Crystallinity

Substrates were stripped of their native oxide *ex situ* in the experiments described in this section to facilitate the possibility of polycrystalline or epitaxial

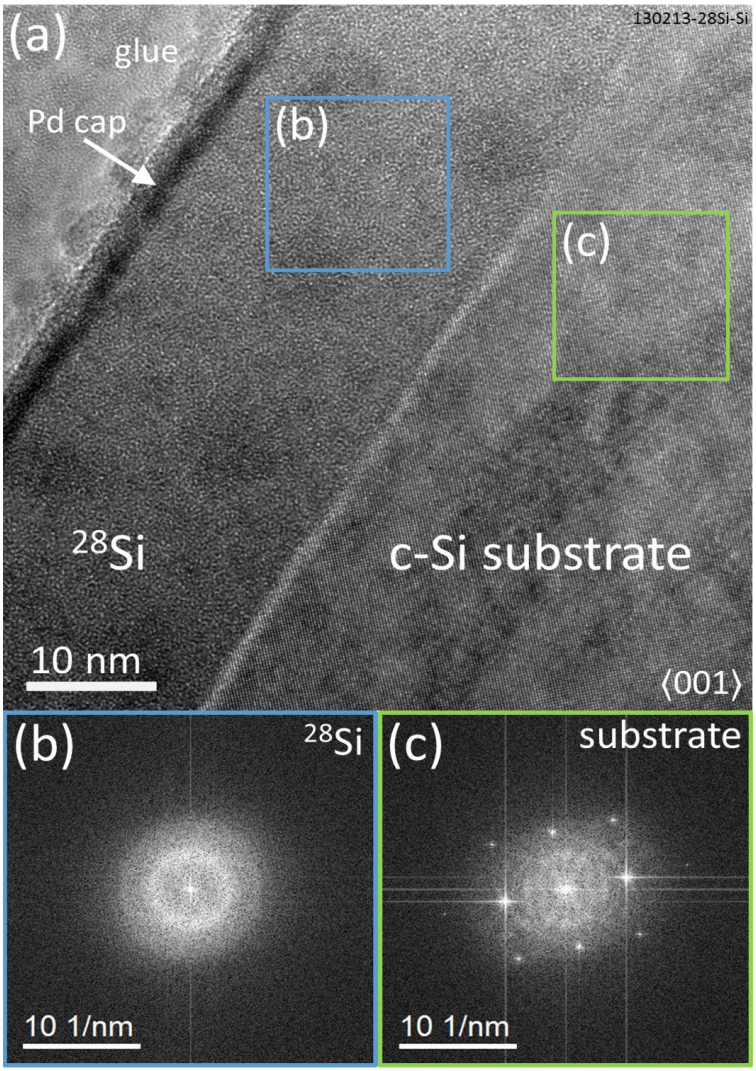

Figure 4.14: HR-TEM cross-sectional micrograph of a ^{28}Si film deposited at room temperature at LC–2. The Si substrate is seen in the lower right area of the image in (a), a layer of glue (light) and Pd cap (dark) are seen in the upper left, and the deposited ^{28}Si film resides between them. (b) is a FFT of the ^{28}Si region from box (b) and shows that it is amorphous. By comparison, (c) is a FFT of the Si(100) substrate from box (c) and it clearly shows a crystalline pattern. This image was taken on the ⟨001⟩ zone axis.

deposition. However, depositing at room temperature severely limits Si epitaxy to very thin layers if it occurs at all [55, 87], and Si solid phase epitaxy (SPE) is expected to be negligible [88] making the formation of crystalline grains unlikely. The suspected amorphous nature of these ^{28}Si films is verified using TEM. A cross-

sectional TEM micrograph of a ^{28}Si sample deposited at LC–2 is shown in Fig. 4.14. This microscopy was done in collaboration with Dr. June Lau (NIST), and the TEM specimen was prepared by mechanical polishing. Panel (a) is a high resolution (HR-TEM) image showing the deposited ^{28}Si film between the substrate and a Pd capping layer. The Si(100) substrate is the region in the lower right of the micrograph and to the left of that is the ^{28}Si film. In this area of the film, the ^{28}Si layer thickness is about 20 nm and the average thickness over all the areas surveyed was 37 nm. Just to the left of the ^{28}Si layer is a thin dark Pd capping layer deposited to protect the film during the TEM specimen thinning process by Ar milling. In the upper left of the micrograph is glue, also from specimen preparation. The sample was tilted to the $\langle 001 \rangle$ silicon zone axis in this micrograph. One can see that the ^{28}Si film is amorphous because the lattice rows of the substrate do not continue into the film region. This is made more clear by the fast fourier transform (FFT) analysis of the film and substrate. Panel(b) in Fig. 4.14 is a FFT of the ^{28}Si region (box (b) in panel (a)) and corresponds to an amorphous pattern. In contrast, panel (c), which is the FFT of the Si(100) substrate (box (c) in panel (a)), corresponds to a crystalline pattern.

4.3.6 Chemical Purity

4.3.6.1 SIMS

To begin to assess the chemical purity of the ^{28}Si samples in the context of the materials goals laid out at the beginning of this chapter, SIMS was used to detect

C contamination in two samples deposited at LC–2. ^{12}C and ^{13}C were monitored in the ^{28}Si samples both as a marker for general chemical contaminants in the films, but also because ^{13}C possesses nuclear spin ($I = 1/2$), which will cause decoherence of qubit spins in a quantum computing device in the same way that ^{29}Si does. A SIMS depth profile of the C atomic concentrations in a ^{28}Si sample is shown in Fig. 4.15. ^{12}C (solid line) and ^{13}C (circles and line) are plotted vs. sputter depth into the sample. A profile of ^{30}Si (triangles and line) measured at the same time is shown as a reference to the boundary between the deposited ^{28}Si film and the natural Si(100) substrate (shaded region). The film-substrate interface is estimated to be at a depth of around 425 nm. It is difficult to precisely determine the atomic concentration of carbon in the silicon film because the carbon background due to the SIMS instrument is not precisely known under the measurement conditions, however it must be a factor of 10 lower than in the film because the C concentration drops by that much in the substrate. For simplicity, C was monitored using the same measurement conditions as for Si detection, and so the measurement was not optimized for accurate C measurements. The slow roll off observed for the carbon signals moving into the substrate is probably a measurement artifact. After applying a value obtained from literature of 0.007 for the relative sensitivity factor of carbon to silicon for SIMS under similar analytical conditions [89], the average measured atomic fraction of ^{12}C (measuring only Si and C isotopes) in the film is found to be approximately 3.39(8) %. Considering the nominal atomic concentration for amorphous Si ($\approx\ 4.9 \times 10^{22}$) [90], the measured atomic fraction of ^{12}C represents an atomic concentration of $1.66(4) \times 10^{21}$ cm^{-3}. The average measured ^{13}C atomic

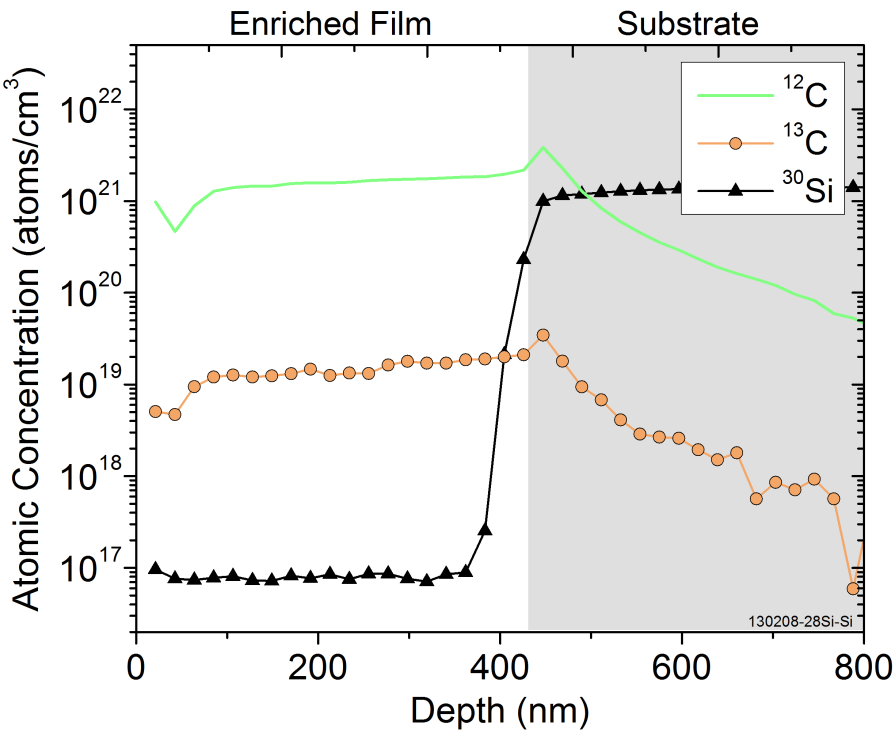

Figure 4.15: SIMS depth profile showing the atomic concentration of ^{12}C (solid line), ^{13}C (circles and line), and ^{30}Si (triangles and line) in a ^{28}Si sample deposited at room temperature at LC–2. The sharp rise in ^{30}Si concentration marks the boundary between the deposited ^{28}Si film and the natural Si(100) substrate (shaded region). The slow roll off of the carbon profiles into the substrate is an artifact of the SIMS measurement.

fraction is 0.031(1) % (310(10) ppm), which is about 110 times smaller than the ^{12}C fraction and close to the natural abundance fraction of about 1.1 %. For reference, the ^{30}Si atomic concentration in this particular measurement is approximately 1.6 ppm in the film.

The concentration of spins in the ^{28}Si film due to ^{13}C is over 300 times larger than the residual ^{29}Si spin concentration in this sample. The source of this C contamination is probably predominately gaseous carbon containing compounds in the vacuum such as CO and CO_2, which can adsorb into the ^{28}Si film during deposition. A buildup of gaseous C compounds is also likely the source of the small spike in

C concentration which can be seen at the interface with the substrate because the sample sat approximately one day in the chamber before deposition. In this experimental configuration there is no residual gas analyzer available to measure the relative abundance of such compounds. It is also possible that some C adsorbs into the amorphous film from the ambient environment after the sample is removed from vacuum.

To examine the dependance of the C contamination in the ^{28}Si film on background pressure, a sample was deposited using the nominal procedure described above except that during deposition, the pressure in the chamber was raised for about one third of the deposition time. This was achieved by closing the gate valve to the turbo pump in the lens chamber. This caused the pressure in the chamber to rise almost two orders of magnitude, which was partially due to SiH_4 gas from the ion source, but also probably due to an increase in partial pressures of typical residual gasses found in high vacuum systems such as H_2, CO, N, and CO_2.

The C contamination of this sample was measured by SIMS in the same manner as the last sample. A SIMS depth profile of the C concentration in this sample is shown in Fig. 4.16. ^{12}C (solid line) and ^{13}C (circles and line) are plotted vs. sputter depth into the sample. A profile for ^{30}Si (triangles and line), which was measured separately, is shown as a reference to the boundary between the deposited ^{28}Si film and the natural Si(100) substrate. The film-substrate interface, marked by the shaded region, is estimated to be at a depth of 240 nm. Also plotted is the ratio of ^{28}SiH/^{28}Si (dotted line), which is typically monitored during SIMS measurements and corresponds to the right axis in the figure. The ^{28}SiH signal gives

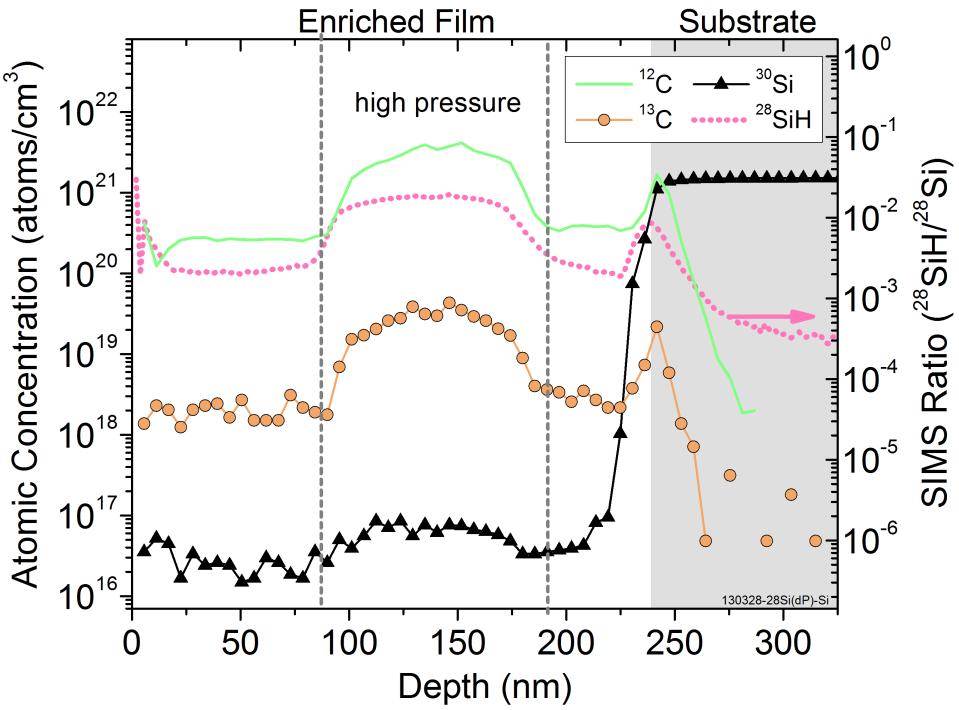

Figure 4.16: SIMS depth profile showing the atomic concentration of ^{12}C (solid line), ^{13}C (circles and line), and ^{30}Si (triangles and line) in a ^{28}Si sample deposited at room temperature at LC–2. The sharp rise in ^{30}Si concentration marks the boundary between the deposited ^{28}Si film and the natural Si(100) substrate (shaded region). Also shown is the measured SIMS ratio of ^{28}SiH/^{28}Si (dotted line) corresponding to the right hand axis. The chamber pressure was increased almost two orders of magnitude during the portion of the deposition bounded by the vertical dashed lines between approximately 80 nm and 190 nm. The ^{12}C, ^{13}C, and ^{28}SiH concentrations increase in this region.

a qualitative idea of relative amounts of H in the different layers of the film. The region of the film corresponding to the higher pressure during deposition is approximately between 80 nm and 190 nm, bounded by the vertical dashed lines. In this portion of the film, one can see that the C concentrations increase more than an order of magnitude and the ^{28}SiH signal increases slightly less than that. A spike in C concentration is observed at the interface between the film and the substrate due to carbon containing adsorbates accumulating when the sample sat for about three days in vacuum before deposition.

In the low pressure region of the film, i.e. the top layer from 0 nm to 80 nm, the average ^{12}C atomic concentration is determined to be 2.67(3) $\times$ 10^{20} cm^3, which is 0.545(6) %, and the average ^{13}C atomic concentration is 42(3) ppm. These values are around six times lower for this sample than for the previous one, probably due in part to the deposition pressure being slightly lower for this second sample. In the high pressure region of the film, the ^{12}C atomic concentration increases to 3.2(2) $\times$ 10^{21} cm^3 (6.6(4) %). The ^{13}C atomic concentration increases to 610(40) ppm. For reference, the ^{30}Si atomic concentration throughout the enriched film is approximately 0.9 ppm. A lower bound on the total achievable Si chemical purity for samples deposited at LC–2 can be determined from the low pressure region of this second sample to be approximately 99.451(6) %. This sample shows that adsorption and incorporation of chemical contaminants from the vacuum background pressure into the depositing ^{28}Si film is a significant issue in this experimental configuration.

4.3.6.2 XPS

In addition to the chemical purity analysis provided by SIMS for the C concentrations in ^{28}Si films, XPS was used to search for a broader range of chemical contaminants. XPS spectra were acquired and analyzed in collaboration with Dr. Kristen Steffens (NIST). The ^{28}Si sample used for XPS analysis was deposited at LC–2 under similar conditions as the previous samples described in this chapter. Additionally, a control chip accompanied the sample through the deposition pro-

cess but was not irradiated by the ion beam. XPS spectra were collected after sputter-cleaning the samples with Ar to remove surface contamination from the environment. Both low resolution survey scans (pass energy 160 eV, step size 0.5 eV) and high resolution region scans (20 eV pass energy, step size 0.1 eV) for C 1s, N 1s, Si 2p, and O 1s were performed on a Kratos Axis-Ultra DLD Photoelectron Spectrometer with a monochromated Al Kα x-ray source (1486.6 eV). Multiple spots were measured on each sample to ensure consistency. Peak positions were calibrated to the Si $2p_{1/2}$ peak at 99.3 eV.

Initially, prior to sputter cleaning, the ^{28}Si film showed C, N and O peaks in the XPS spectrum. However, after sputter cleaning, the N and the adventitious C disappeared, but a C 1s peak due to SiC persisted. This ^{28}Si XPS spectrum is shown in Fig. 4.17 (upper spectrum) as a plot of count rate vs. electron binding energy. The data for the ^{28}Si sample was shifted up for clarity. The C 1s peak indicates a relatively constant atomic fraction of approximately 3 %, consistent with the first SIMS result. After sputtering, two small O 1s peaks also remain at 531.4 eV and 532.5 eV, corresponding to an atomic fraction of approximately 4 %. Also shown are references for relevant elemental orbital level positions. In the Si 2p region, a SiO_2 peak from the native oxide was no longer present after sputtering, however, in addition to the elemental Si peaks, a small shoulder attributed to SiC is seen in finer scans. The control Si sample (lower spectrum) shows reduced C and O peaks corresponding to atomic fractions of approximately 1 % to 2 % each. These values are taken as upper limits which can give an indication of the instrumental background because the actual C and O content of the wafer is expected to be

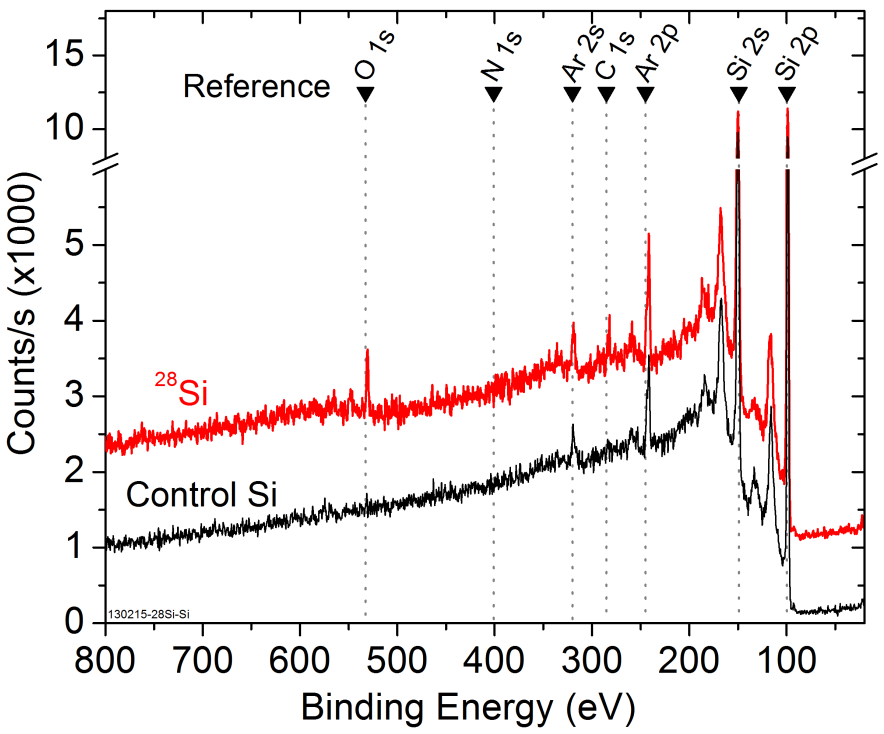

Figure 4.17: XPS spectra of a ^{28}Si sample deposited at room temperature at LC–2 and a control Si sample. Count rates vs. electron binding energy for survey scans are shown for the ^{28}Si sample after Ar sputter cleaning (upper spectrum) and the control chip (lower spectrum). The data for the ^{28}Si sample was shifted up for clarity. References for elemental orbital level positions are included above relevant peaks. O 1s and C 1s peaks are visible with larger amplitudes in the ^{28}Si film than the control sample.

much lower. Both the ^{28}Si and control scans show Ar peaks due to the Ar sputter cleaning process. This XPS analysis agrees with the SIMS result that at least some samples deposited at LC–2 can have as much as 3 % C throughout the ^{28}Si film, and in addition they can also contain an approximately equal amount of O. The Si chemical purity for this sample measured by XPS is roughly 95 %. Although the previous SIMS measurement showed that a sample can have lower level of C, it is not known if the O contamination is similarly reduced in that sample, and so it is difficult to place a bound on the total Si purity that is achievable for these samples.

4.4 Chapter 4 Summary

The ^{28}Si samples deposited at IC–1 served as a successful proof of principle for the adaptation of the *in situ* enrichment and ion beam deposition method from ^{12}C deposition to ^{28}Si. Experimental procedures for deposition using a natural abundance SiH_4 source gas and the characterization of the enrichment via SIMS were established. The samples deposited at LC–2 showed that ^{28}Si films could be deposited with residual ^{29}Si and ^{30}Si isotope fractions consistently below 1 ppm. A total of five ^{28}Si samples were produced at IC–1 and 16 were produced at LC–2. The overall improvement in ^{28}Si enrichment achieved from the initial samples deposited at IC–1 to the samples deposited at LC–2 can be seen in the enrichment progression timeline in Fig. 4.2. The residual ^{29}Si isotope fractions of these samples was reduced from 2822(18) ppm to 0.691(74) ppm. This most highly enriched sample deposited at LC–2 had a ^{28}Si isotope fraction of 99.999888(10) %. The achieved reduction in ^{29}Si and ^{30}Si isotope fractions in samples deposited at LC–2 was likely due to several factors. First, better control of the ion beam tuning lead to consistently higher geometric selectivities. Additionally, the lens chamber has significantly lower background pressures resulting in less SiH_4 adsorption during deposition. Finally, the deceleration lenses enabled focusing of the ion beam spot resulting in smaller deposition spots, higher growth rates, and less SiH_4 adsorption. The enrichment values of these samples meet the enrichment materials goal laid out at the beginning of this chapter to achieve ^{28}Si enrichments that surpass those of any other known sources of ^{28}Si including the IAC, and they do it consistently. Additionally, they

attain enrichments sufficient to enable a robust measurement of the dependance of electron coherence time on ^{29}Si concentration in the single spin regime and compare it to theoretical predictions (see Fig. 1.9), as proposed in Chapter 1.

However, initial observations of ^{28}Si film crystallinity and chemical purity show that these samples deposited at IC–1 and LC–2 do not meet the second and third materials goals stated at the beginning of this chapter of being crystalline and highly chemically pure. SEM and TEM cross-sectional micrographs of two samples show that the films are unsurprisingly amorphous, probably due to deposition occurring at room temperature. Chemical analysis of several samples deposited at LC–2 by both SIMS and XPS show that both C and O are present in these films at relatively high atomic concentrations up to approximately 3 %. Achieving both single crystal epitaxial deposition and eliminating chemical contaminants require further experimental improvements, and will be the subject of Chapter 5.

Chapter 5

^{28}Si Thin Film Deposition and Characterization Phase II: Crystallinity and Chemical Purity

5.1 Introduction

Chapter 4 demonstrated that extremely high levels of ^{28}Si enrichment ($<$ 1 ppm ^{29}Si) were achievable for thin film samples produced via ion beam deposition at LC–2. The most highly enriched sample deposited at LC–2 had a ^{28}Si isotope fraction of 99.999888(10) % and a residual ^{29}Si isotope fraction of 0.691(74) ppm. However, these samples were found to be amorphous, likely due to them being deposited at room temperature, and they were measured to contain C and O in atomic concentrations up to approximately 3 %. In order for the ^{28}Si to be viable for use in Si based solid state quantum computing, it must be of very high quality and meet the three materials goals of this work discussed in Chapters 1 and 4. The experiments in Chapter 4 produced samples which surpassed the first materials goal of achieving enrichments with residual ^{29}Si isotopic concentrations below 50 ppm

to match other sources of ^{28}Si including the International Avogadro Coordination. The residual ^{29}Si isotope fractions of these samples was also potentially low enough to facilitate a robust measurement of the dependence of electron coherence times on ^{29}Si concentration in the single spin regime, also discussed in Chapters 1 and 4. Assessments of samples produced in the experiments discussed in Chapter 4 were done in the context of the second and third materials goals of single-crystalline, epitaxial thin films with dislocation densities below 1×10^6 cm^{-3} and chemical impurity concentrations below 2×10^{15} cm^{-3}, however these goals were not pursued further in those experiments.

Discussion of the ion beam deposition of ^{28}Si films enriched *in situ* and the characterization of their properties including enrichment, crystallinity, and chemical purity is continued in this chapter. The experiments discussed here seek to maintain and improve upon the already high level of achieved ^{28}Si enrichment while depositing samples in the final experimental configuration for this system used in this work, which enables epitaxial deposition. This continued improvement in enrichment and reduction in residual ^{29}Si and ^{30}Si isotope fractions is illustrated in Fig. 4.2, the enrichment progression timeline. As previously described in Chapter 1, the measured isotope fractions of Si are written as $^{z}\mathrm{Si}/\mathrm{Si}_{\mathrm{tot.}}$, representing the average detected counts of an isotope divided by the total average counts of the SIMS measurement. It shows the ^{29}Si isotope fraction reduction at LC–2 from 0.691(74) ppm down to a minimum at DC–3 of 127(29) ppb with an overall enrichment in ^{28}Si of 99.9999819(35) % for the most highly enriched sample produced in this work. SIMS measurements of the enrichment of ^{28}Si presented in this chapter will be discussed in

terms of the progression of samples at DC–3 in Fig. 4.2 and the experimental factors that resulted in those higher enrichments. The experiments discussed here also seek to leverage the improved capabilities of this new experimental setup to facilitate high-quality epitaxial deposition as well as study chemical contaminants to improve the purity of the ^{28}Si films. Chemical impurities present in ^{28}Si films can act as or induce scattering sites and charge traps [91, 92]. This reduces electron mobility and other electronic properties that are important for the successful operation of QI devices. Additionally, chemical impurities can possess nuclear spin, which will cause decoherence of qubit spins in a quantum computing device in a similar manner as the nuclear spin of ^{29}Si in natural abundance Si. A total of 40 ^{28}Si samples were produced at DC–3.

The experimental configuration used for depositing samples in this chapter is the third setup discussed in Chapter 4 where samples are located at DC–3 in the deposition chamber, as shown in the deposition chamber schematic in Fig. 4.1. This setup had several advantages over the previous two including a further reduction in the background pressure during deposition due to additional differential pumping. In addition to a third turbo pump and an ion pump present in the deposition chamber, an ion pump was added to the lens chamber for this setup, which are all marked in Fig. 4.1. Lower partial pressures of gaseous species containing C and O should result in higher chemical purities of the film. Depositing samples at DC–3 crucially enabled heating of the Si substrate for *in situ* preparation and heating of the sample during ^{28}Si deposition to facilitate epitaxial growth. This setup also enables the use of the analytic instruments in the deposition chamber in conjunction

with ^{28}Si deposition including RHEED, RGA, and STM, as discussed in Chapter 2. These features will be discussed further in the next section.

Epitaxial deposition of ^{28}Si thin films with a high degree of crystallinity, i.e. a low defect density similar to electronics grade Si, is a key achievement towards producing material suitable for use with solid state quantum computing devices. The crystallinity of a film and the roughness of its surface depend on the characteristics of the deposition and growth. Si MBE is ideally categorized as either Volmer-Weber growth or Frank-van der Merwe growth [93]. Volmer-Weber growth is characterized by the formation of 3D islands consisting of multiple layers growing at once as islands coalesce into a continuous film. This type of growth is the result of the ratio of the depositing atomic flux to the surface diffusivity being large such that it is more likely that adatoms will cluster with each other and form islands before they can diffuse to and over step edges [94]. These islands result in the buildup of roughness on the surface. Conversely, Frank-van der Merwe growth is characterized by smooth layer-by-layer growth where single layer 2D islands merge to ideally form a continuous first monolayer before the second layer begins to form [95]. This type of growth is the result of the ratio of atomic flux to surface diffusivity being small such that adatoms are more likely to reach step edges as well as diffuse down to lower steps before clustering to form second layer islands. With the presence of atomic steps on the substrate, this growth mode can also lead to so-called step flow growth where no islands form and all adatoms can diffuse to step edges before any other interactions. In reality, most thin film deposition occurs between these two ideal cases. In general, deposition dominated by 3D island growth can lead to

rougher films with more crystalline defects than deposition dominated by smooth layer-by-layer growth.

Crystalline defects such as vacancies, dislocations, and stacking faults can degrade the performance of semiconductor electronic devices because they can act as charge traps and scattering sites which reduces electron mobility. Additionally, these types of defects have been theoretically predicted and experimentally shown using electric dipole spin resonance (EDSR), EPR, and deep-level transient spectroscopy (DLTS) to introduce electric defect states in the band gap of Si [96–99]. Si divacancies can exist in multiple charge states and have multiple deep electronic levels in the band gap, and stacking faults in a Si crystal lead to a defect state in the band gap which is approximately 100 meV above the valence band [100].

Crystalline defects in ^{28}Si are potentially more detrimental to quantum coherent devices because they introduce scattering centers and local time varying electric and magnetic fields in the crystal that can contribute to the decoherence of a quantum system nearby. Crystalline defects also introduce local strain fields which are known to cause the appearance of unintentional quantum dots in Si wires due to strain induced conduction band modulation [101]. Local strain fields around a qubit, such as a ^{31}P donor in Si, can also cause internal electric fields which have been shown to Stark shift the donor's electron energy levels and make the qubit spin more sensitive to electric field noise [102, 103]. The nature and magnitude of the effect of local crystalline defects on the performance of quantum coherent devices is still an open area of research and a question that will need to be addressed as this field progresses.

In any device comprised of multiple layers, smooth interfaces can be important in addition to a low level of structural defects within the bulk of the layer. At a basic level, fabricating additional layers or electric gates on top of a device layer that has a rough surface can be challenging and is generally undesirable. Dangling bonds and other defects present at a rough surface may result in an increased density of interface charge traps typically seen at oxide interfaces. Surface or interface roughness has also been predicted to affect the valley states of electrons in Si quantum dots and Si/SiGe quantum wells by causing mixing of valley, spin, and orbital states as well as random fluctuations in the phase of the valley-orbit coupling [104–108]. These effects would vary across devices and be impossible to predict, making operation of quantum devices utilizing the valley degree of freedom more difficult. The overall smoothness or roughness of a deposited film can also be a general indicator of their epitaxial quality or crystallinity, and so it is presented here as an important aspect of the ^{28}Si films discussed in this chapter.

Section 5.2 of this chapter discusses the specifics of the experimental setup for samples produced at DC–3 in the final experimental configuration. Sections 5.3 and 5.4 go over the experimental methods for *in situ* and *ex situ* sample preparation as well as the deposition conditions used for ^{28}Si samples at DC–3. Section 5.5 discusses the results of SIMS measurements of the enrichment of significant ^{28}Si samples deposited at DC–3. Sections 5.6 explores experiments to deposit films epitaxially at elevated temperatures and characterize their morphology by RHEED, STM and SEM. Section 5.7 discusses measurements of the chemical purity of these samples as measured by SIMS and XPS. Section 5.8 discusses the crystallinity of

deposited ^{28}Si films observed by TEM. Finally, Section 5.9 summarizes these results.

5.2 Experimental Setup for Improving Crystallinity and Chemical Purity: Deposition Chamber Samples

This chapter discusses the deposition of ^{28}Si samples in the final experimental configuration for this ion beam deposition system as it was designed as a whole and used in previous work [59]. In this experimental setup, samples are located at DC–3 as shown in Fig. 4.1. A number of experimental improvements and use of new analytic capabilities are enabled by connecting the ion beamline (including the deceleration lens chamber) to the deposition chamber.

In this configuration, samples were located after the deceleration lenses, but in the deposition chamber. As described in Chapter 2, the lenses protrude into the deposition chamber and stop approximately 1 cm before the sample location. As a consequence, the lens chamber and the deposition chamber are actually a single connected vacuum environment. The ion beam chamber is separated from these chambers just before the deceleration lenses by a gate valve. The mass-selecting aperture used between the ion beam and the lens chamber here had a slightly different geometry than the one used for the depositions in Chapter 4. The mass-selecting aperture slit width was increased to 2 mm to allow a larger ^{28}Si ion fluence to pass into the deceleration lens section. Previously, a thinner slit width was chosen to limit the range of mass values that can pass through from the beam thus increasing

the mass resolving power. However, the experiments at LC–2 in Chapter 4 demonstrated better beam tuning and very high geometric selectivity as represented by both SIMS measurements and mass spectra. Higher geometric selectivities allow for the aperture slit width to be increased without impacting the realized selectivity. The height of the slit was decreased from 15.25 mm to 12 mm. This was done to decrease the conductance of gas from the higher pressure ion beam chamber into the deposition chamber while maintaining the fluence of the ion beam, which has a typical spot size at the aperture of < 10 mm in the slit height direction. The thickness of the aperture was reduced to a knife edge at the opening to reduce potential scattering of ions as well as sputtering of the aperture as they pass through.

A secondary aperture with dimensions 12.7 mm by 6.4 mm was also installed at the beginning of the deceleration lenses for this configuration. This functioned as a gas aperture to block the gas diffusing past the mass-selecting aperture from entering the deceleration lens column. The only outlet for this gas would be at the sample, but with the gas aperture in place, it is instead diverted around the lens column where it may be better pumped away in the lens chamber. A photograph of this secondary gas aperture is shown in Fig. B.8 in Appendix B.

Samples were mounted onto sample holders which were then introduced into the vacuum chamber via the load lock and placed onto the 5-axis manipulator, all of which are described in more detail in Chapter 2. The manipulator and sample are positioned to face the deceleration lenses prior to deposition of ^{28}Si. Similar to the sample mounting setup described of Chapter 4 using an electrical vacuum feedthrough at LC–2, samples discussed in this section are electrically isolated from

the chamber as they sit in the sample holder on the manipulator. This isolation allows for the ion beam current to be monitored during deposition while controlling the sample potential. In the previous experimental setup with samples at LC–2, the fixed sample aperture that sat over the sample allowed for current collection and focusing of the ion beam through the sample aperture (see Section 4.3.1). Here, an interchangeable sample aperture, which can be inserted into the sample position and then removed prior to deposition, provides similar capabilities. One advantage of the interchangeable sample aperture is that the sample can be completely removed from the path of the ion beam while beam tuning, focusing, and mass spectrum sweeps are performed on the aperture, thus keeping the sample pristine prior to deposition. A sample aperture which was 2.2 mm in diameter was used for most samples, although other diameters including 3 mm, 2.5 mm, and 1 mm were also used. Additionally, the 5-axis manipulator allows for sample motion in three spacial dimensions and precise positioning in the vacuum chamber relative to the ion beam optics. The advantage of this is that, unlike in the setups of Chapter 4, the ion beam can be optimally tuned and the sample repositioned so that the beam spot is located at any desired location on the sample, typically at the center. A photograph of a sample mounted in a sample holder and on the manipulator at DC–3 was shown in Fig. 2.23 in Chapter 2. Photographs of the interchangeable sample apertures can be found in Fig. B.13 in Appendix B.

A significant experimental improvement enabled by this experimental configuration with samples located at DC–3 is sample heating. As described in Chapter 2, the 5-axis manipulator provides two methods of sample heating. First is a tungsten

wire back heater that sits behind the sample holder and can radiatively heat it up to around 900 °C, although with a relatively slow response time of several minutes. This is the RH method of sample heating referred to in Chapter 2. The second method uses electrical contacts on the manipulator that interface with the sample holder and provide the ability to pass current directly through the Si substrate, heating it resistively. This is the DH method of sample heating referred to in Chapter 2, and it can be used to heat the Si chip as high as its melting point with a very fast response time of less than a second. Sample heating crucially enables *in situ* substrate preparation and cleaning, deposition at elevated temperatures, and post-deposition sample annealing. These abilities allow for control over a critical experimental degree of freedom for achieving high-quality epitaxial deposition of ^{28}Si [51] and will be discussed later in this chapter.

Connecting the ion beam and lens chambers to the deposition chamber provides additional differential pumping at the sample location from a turbo pump and an ion pump, which result in a lower chamber base pressure and a lower background pressure during deposition. Additionally, for this configuration, an ion pump was added to the lens chamber. The typical base pressure of the deposition chamber for the experiments described in this chapter was approximately 6.7×10^{-9} Pa (5.0×10^{-11} Torr). Heating the sample before deposition usually causes some degassing that results in slightly elevated pressures. Typically, the pressure immediately before starting deposition was approximately 2.6×10^{-8} Pa (2.0×10^{-10} Torr), although it varied almost an order of magnitude from approximately 7.1×10^{-9} Pa to 5.7×10^{-8} Pa (5.3×10^{-11} Torr to 4.3×10^{-10} Torr). Additionally, the depo-

sition chamber and lens chamber, being of all UHV construction, were baked to approximately 150 °C prior to these experiments to reduce the partial pressures of water as well as carbon and oxygen containing compounds. The remaining dominant partial pressure in these chambers was H_2. The RGA in the deposition chamber gives insight into the specific atomic and molecular species that make up the base background and deposition pressures in this chamber. An example of the residual gas mass spectrum corresponding to the base pressure of the deposition chamber was shown in Fig. 2.22 in Chapter 2. For the experiments described in this chapter, the ion source was operated with a working pressure of SiH_4 between 1.0×10^{-4} Pa and 3.3×10^{-4} Pa (7.5×10^{-7} Torr to 2.5×10^{-6} Torr), similar to that of samples deposited at LC–2 in Chapter 4. The most common working pressure used was approximately 2.0×10^{-4} Pa (1.5×10^{-6} Torr). In addition to these typical low pressure operating conditions, the high pressure mode of the ion source plasma was also explored in which the typical operating pressure was approximately 1.3×10^{-3} Pa (1.0×10^{-5} Torr). In this experimental setup, another RGA was also installed in the ion beam chamber to diagnose the base pressure gas components and contaminants in the SiH_4 gas, both of which may diffuse into the deposition chamber. A residual gas mass spectrum of the base pressure from the ion beam chamber was shown in Fig. 2.3 in Chapter 2.

Another significant experimental advantage to depositing ^{28}Si samples at DC–3 vs. at IC–1 or LC–2 is having access to the various analytical and other features of the deposition and analysis chamber, which are described in Chapter 2. The load lock allows for quicker loading of multiple samples while maintaining the very high

vacuum level of the deposition chamber. Sample heating is critical for epitaxial deposition and feedback mechanisms in the form of analysis tools in the deposition chamber are necessary for developing the correct experimental procedures to achieve epitaxy. RHEED and the STM provide information on the state of the pre-deposition substrate, the growth mode during deposition, and surface characteristics of the deposited sample. The RGA and AES can provide ambient and surface chemical information for samples. Finally, deposition parameters for ^{28}Si can be modified to produce higher quality films by comparing them to the natural abundance Si films deposited from the electron beam evaporator (i.e. the EFM) in the same system.

5.3 Sample Preparation

5.3.1 *Ex Situ* Cleaning

A variety of Si substrates were used for the ^{28}Si samples discussed in this chapter, but they were all natural abundance, electronic grade, single crystalline commercial Si(100) wafers. A complete table of substrates used here is given in Table C.1 in Appendix C. Si(100) has been shown to facilitate higher quality epitaxial deposition at lower temperatures than other Si surface orientations such as Si(113), Si(111) or Si(110) [87,109,110]. N-type, p-type, and undoped (intrinsic) wafers were used. The p-type Si wafers were all boron-doped with resistivities between 1 $\Omega \cdot$ cm and 20 $\Omega \cdot$ cm and thicknesses between 300 μm and 380 μm. These wafers were used to deposit 22 samples at DC–3 and were obtained from both ITME and University

Wafer. Substrates from University Wafer have an unknown history because they are reclaimed wafers. The n-type wafers were all phosphorous-doped, mostly with resistivities of between 1 $\Omega \cdot$ cm and 10 $\Omega \cdot$ cm, and were 300 μm thick, although the substrate used for one sample originated from 600 μm thick stock. These wafers were used with eight samples and were obtained from University Wafer. Five samples were deposited on intrinsic Si wafers in these experiments, and they were obtained from University Wafer, were 380 μm thick, and had a resistivity of > 20 k$\Omega \cdot$ cm. The ^{28}Si samples that were deposited using the high pressure plasma deposition mode (a total of five) were deposited onto phosphorous-doped wafers with a resistivity between 7 $\Omega \cdot$ cm and 20 $\Omega \cdot$ cm. They were 300 μm thick with a minimal misalignment or miscut angle relative to the (100) plane of $\pm$ 0.05° and were obtained from Virginia Semiconductor. The wafers from Virginia Semiconductor were float-zone refined with an atomic concentration of O of $< 9 \times 10^{17}$ cm^{-3} and an atomic concentration of C of $< 5 \times 10^{13}$ cm^{-3}.

Initially, for about one quarter of the samples deposited at DC–3, there was no *ex situ* cleaning performed on the substrates, which were loaded into the vacuum chamber with a native oxide. This oxide was then thermally desorbed *in situ* in a process described below. As a comparison to those samples with no cleaning, two samples were treated with HF to strip off the oxide immediately prior to loading them into the vacuum chamber. These initial samples were cleaved by hand into approximately 5 mm by 12 mm chips, which is the approximate maximum sample size that can be accepted by the sample holders used in these experiments. The substrates used for the remainder of the samples deposited at DC–3 were cut using

a dicing saw into 4 mm by 10 mm chips after depositing a thin photoresist layer to protect the surface from the accumulation of Si dust during dicing. Individual chips were then cleaned using a more rigorous cleaning procedure designed for complementary metal-oxide-semiconductor (CMOS) technology to remove metals and organics from Si surfaces. This clean consists of a piranha etch, HF strip, and "Standard Clean 2" (SC–2) [111], and it was adopted to improve the substrate surface cleanliness and quality after feedback from analysis of earlier samples. The full cleaning procedure is as follows:

1. photoresist remover (PG Remover) at 70 °C for 10 min,
2. fresh PG Remover at room temperature for 5 min,
3. isopropanol (IPA) rinse for 1 min,
4. deionized water rinse, and N_2 blow dry,
5. 6:1 H_2SO_4:H_2O_2 for 12 min with no deliberate heating (piranha etch),
6. deionized water rinse, and N_2 blow dry,
7. 50:1 H_2O:HF for 10 s,
8. deionized water rinse and, and N_2 blow dry,
9. 5:1:1 H_2O:HCl:H_2O_2 at 80 °C for 12 min (SC–2),
10. deionized water rinse, and N_2 blow dry.

PG Remover is a standard solvent used to remove the protective photoresist from the substrates here. That is followed by a rinse in IPA and deionized water to remove residual photoresist and PG Remover residue and prepare the substrate surface for chemical cleaning. The first clean is a piranha etch designed to remove organics from the surface through oxidation. This was chosen over the "Standard Clean 1"

(SC–1) solution, which also cleans organics, because (SC–1) is known to sometimes roughen the wafer surface. A water rinse and N_2 blow dry is used between each cleaning step to remove chemical residues. The substrates are next etched with HF to remove the surface oxide containing contaminants and also remove some ionic metal contaminants. Finally, SC–2 solution is used to remove remaining ionic metal contaminants from the surface before a final deionized water rinse. As a result of the SC–2 clean, the chips are left with a thin protective oxide before being mounted onto sample holders and loaded into the vacuum chamber via the load lock. This protective oxide has been shown to reduce carbon contamination on the Si(100) surface as compared to a substrate which was treated with HF to strip the oxide prior to loading [112], and that result was confirmed in this work and will be discussed later in this chapter. Substrates were only handled with clean teflon tweezers. Typically, after being loaded, samples sat about a week in the vacuum chamber while being prepared before deposition.

5.3.2 *In Situ* Preparation

After substrates are introduced into the vacuum chamber via the load lock, they are prepared *in situ* using the degassing and flash annealing procedures first described in Chapter 2. This well known UHV high temperature Si "flashing" procedure is used to prepare an atomically clean Si(100) (2×1) reconstructed surface [113,114], enabling epitaxial deposition. Before flashing, samples are loaded into the deposition chamber after sitting in the load lock for approximately one day until the pressure drops to around 1.3×10^{-6} Pa (1.0×10^{-8} Torr). Sample substrates

and the sample holders next need to be degassed slowly and thoroughly before they can be flashed to high temperature in order to limit the pressure increase during the flashing procedure. The magnitude of the pressure spike that occurs during a high temperature flash is a critical parameter for forming a clean Si surface. A bare Si surface should not be exposed to a background pressure higher than roughly 1.3×10^{-7} Pa (1.0×10^{-9} Torr), or it will become contaminated and more defective. This pressure is based on experience from this work and communications with other labs as well as the literature [114]. Substrates are degassed using both the RH back heater to heat the sample holder and DH power to heat the chip itself. Degassing occurs at temperature of approximately 600 °C for at least 12 hours, and the pressure in the deposition chamber is monitored during the temperature ramp up to ensure that the pressure stays below 1.3×10^{-7} Pa. This pressure criteria is only precautionary for the degassing step if the substrate has a protective oxide.

After degassing, the DH power is used to rapidly flash anneal the sample in a few seconds up to higher temperatures for a short period of time. Typically, a 1 min flash to 1050 °C is initially used to desorb the thin oxide layer (if one is present) that was either a native oxide or remained from the *ex situ* cleaning process [115]. This initial flash also degasses the sample holder more thoroughly before further flashes to higher temperatures. After each flash anneal, the sample temperature is dropped rapidly back to around 600 °C. The flash temperature is then sequentially increased during the next several (one to five) flashes depending on the level of outgassing during flashing. These initial higher temperature flashes have a duration of approximately 15 s. The pressure spike that occurs from the higher temperature

outgassing (mostly from the sample holder) determines the duration and number of times that each flash is repeated at a certain temperature. If the pressure during flashing reaches the critical 1.3×10^{-7} Pa value, the flash is interrupted to reduce the pressure. This cycle is repeated until a final flash temperature of approximately 1150 °C to 1200 °C is reached. The sample sits at these higher temperatures for a max of 10 s each. The purpose of the higher temperature flashes is to desorb any trace amounts of oxide or other contaminants remaining on the surface and anneal surface defects such as missing or buckled dimers to produce a clean, well ordered Si(100) (2×1) surface. After the final flash, the sample is cooled slowly at a rate of approximately 1 °C/s, which additionally helps to recrystallize the surface, down to either the deposition temperature or near room temperature. Typically, as few as five total flashes are needed to prepare a substrate, although some samples/sample holders outgas more, requiring tens of flashes. A typical flash-anneal sequence for substrates used for many of the ^{28}Si samples deposited at DC–3 is as follows:

1. degas initially at ≈ 400 °C for 1 h,
2. degas at ≈ 600 °C for > 12 h,
3. flash to ≈ 1050 °C for 1 min then return to 600 °C,
4. flash to ≈ 1150 °C for 15 s then return to 600 °C,
5. repeat step 3,
6. flash to ≈ 1200 °C for 10 s then return to 600 °C,
7. repeat step 5,
8. flash to ≈ 1150 °C for 10 s then return to 850 °C,
9. ramp down the temperature at 1 °C/s to the desired final temperature.

Again, each flashing step is repeated until the pressure in the chamber remains less than 1.3×10^{-7} Pa for the maximum duration of the flash before the next flash step proceeds.

In order to provide feedback on this high temperature *in situ* substrate preparation process and assess its effectiveness for each sample before deposition, two analysis techniques are used: RHEED and STM. RHEED is used during the flashing process to identify oxide remaining on the surface and verify the (2×1) reconstruction of the Si surface. RHEED images are typically captured between flashes when the substrate is at ≈ 600 °C, but not typically after step 6 above so as to not introduce possible contamination due to the RHEED electron beam interacting with the surface. The number of flashes required to prepare a sample is dictated by the quality of the RHEED pattern in addition to the amount of outgassing. The highest temperature flash may be repeated until a sufficient RHEED pattern typical of a clean Si (2×1) surface is observed (discussed below). RHEED is also used to screen for samples contaminated with silicon carbide (SiC) or those with particularly rough surfaces. Figure 5.1 shows two RHEED images of a Si substrate before and after flash annealing at DC–3 to prepare a clean surface. Panel (a) shows the diffraction pattern from an intrinsic Si(100) substrate before flashing. Faint spots are seen in a (1×1) pattern originating from diffraction to rods in reciprocal space, but the image is dominated by the diffuse background caused by the amorphous native SiO_2 layer. This image was acquired at a substrate temperature of ≈ 600 °C with the electron beam in the ⟨110⟩ direction. Panel (b) shows the sample substrate after flash annealing seven times to a maximum temperature of ≈ 1197 °C for 8 s.

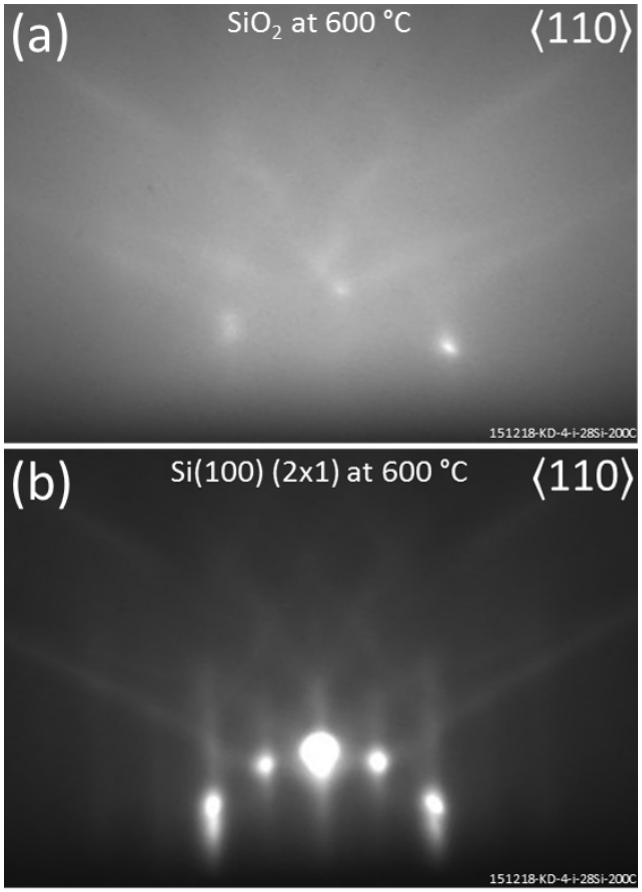

Figure 5.1: RHEED diffraction patterns showing the transition from Si with a native oxide to a reconstructed Si(100) (2×1) surface during the substrate flash annealing procedure. (a) Before flashing the substrate, a diffraction pattern showing weak Si (1×1) spots on a diffuse background is seen which indicates the presence of the SiO_2 surface layer. (b) After flashing the substrate to ≈ 1197 °C, the diffraction pattern shows strong Si(100) (2×1) spots indicating a clean, reconstructed surface. Both images were acquired at a substrate temperature of about 600 °C with the electron beam in the ⟨110⟩ direction.

After flashing, strong Si (2×1) diffraction spots appear in the pattern between the outer (1×1) spots, and the diffuse background is gone. These features plus the absence of additional spots due to chemical contaminants such as C indicates that the substrate has a reasonably clean, crystalline, and reconstructed Si(100) surface.

RHEED serves as a quick feedback mechanism during the substrate flashing procedure by indicating the general state and quality of surface, and a high-quality

RHEED pattern corresponding to a clean Si surface is a necessary condition for producing an atomically clean Si(100) ideal for epitaxial deposition. A RHEED pattern indicating a clean surface is not, however, a sufficient condition because the RHEED pattern is an amalgam resulting from diffraction over a macroscopic area (≈ 0.25 mm^2) on the substrate. RHEED is thus insensitive to trace surface defects and contaminants. To assess the surface quality of prepared substrates on an atomic scale, STM imaging is used. The STM used in this system was briefly described in Chapter 2.

After samples are flashed and cooled at a deliberate rate to approximately 250 °C using the DH power, they cool radiatively for at least 10 min to $>$ 50 °C before being transferred into the STM chamber. The typical base pressure in the STM chamber is approximately 6.7×10^{-9} Pa (5.0×10^{-11} Torr), and it is separated from the deposition chamber by a gate valve. The samples remain protected in the isolated UHV environment of the STM during ion beam tuning in the deposition chamber. The substrates are typically scanned both on relatively large areas (1 μm $\times$ 1 μm) and smaller areas (50 nm $\times$ 50 nm) to screen for both larger particulates or other features as well as atomic scale defects. Most STM images shown in this chapter were acquired in conjunction with Hyun soo Kim, who assisted with some aspects of these experiments. Several typical STM images of three different substrate types after flash annealing are shown in Fig. 5.2. These STM topography images all show clean Si(100) (2×1) reconstructed surfaces with atomic steps and atomically flat terraces of various widths. Panels (a) and (b) show images of boron-doped Si substrates with a relatively small average terrace width of approximately

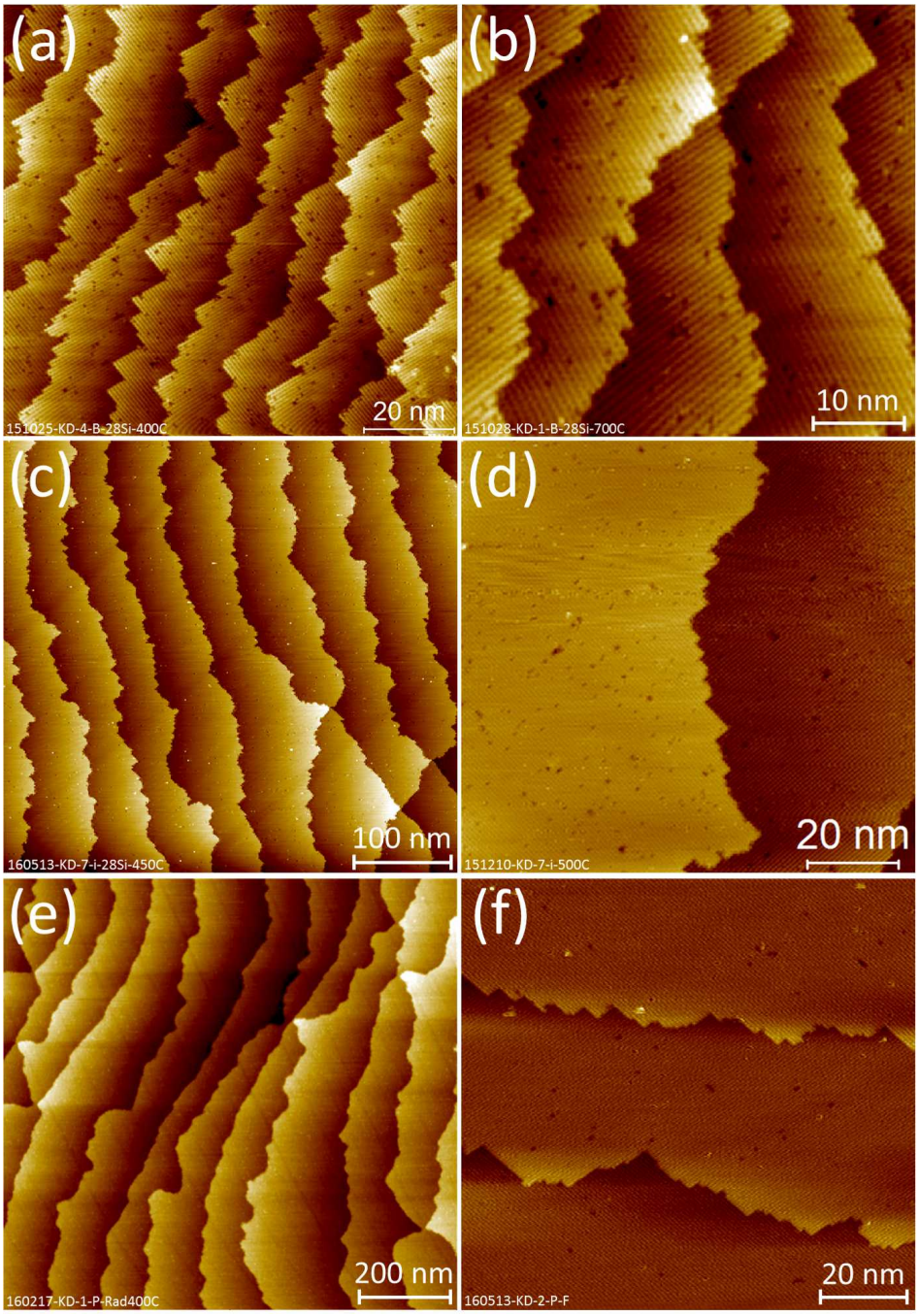

Figure 5.2: STM topography filled state images of clean Si(100) (2×1) surfaces for three substrate types prepared *in situ* by flash annealing. Images were typically acquired with a tip bias ≈ -2 V and a tunneling current ≈ 100 pA. These images show atomic steps on the Si surface and flat terraces of varying widths. Si (2×1) dimer rows are also seen in (a), (b), (d), and (f) with a minimal density of dimer defects (dark spots). (a) and (b) are boron-doped Si substrates with an average terrace width of around 15 nm. (c) and (d) are intrinsic Si substrates with an average terrace width of around 55 nm. (e) and (f) are phosphorous-doped Si substrates with an average terrace width of about 100 nm.

15 nm. The terrace size is a result of a misalignment during manufacturing of the cut direction of the wafer and the (100) crystal plane. When this miscut angle is small, larger terraces result. Panels (c) and (d) show images of intrinsic Si substrates with an average terrace width of approximately 55 nm. Finally, panels (e) and (f) show images of the phosphorous-doped Si substrates with a small miscut angle of $\pm$ 0.05° resulting in a large average terrace width of approximately 100 nm. The increase in average terrace width is apparent when noting the difference in scale between panels (a), (c), and (e). Panel (c) shows an area roughly 25 times larger than (a), and panel (e) shows an area four times larger than (c). Si (2×1) dimer rows are also seen predominantly in panel (b) and are just visible in (a), (d), and (f). A minimal density of dimer row defects (dark spots) are seen, which confirms that the surface cleaning procedures were sufficient. These defects can simply be missing surface atoms or due to chemical contaminants [116].

After the substrate surface is inspected via STM, and the ion beam is tuned for deposition, the sample is moved back to the deposition chamber and flashed a final time to remove possible adsorbates which may have accumulated during STM scanning. The substrate temperature is then lowered to the deposition temperature before ^{28}Si deposition commences. This cool down typically takes around 30 min as the substrate comes into equilibrium.

5.4 Deposition of ^{28}Si

Once substrates are prepared and ion beam tuning similar to that of Chapter 4 is complete, ^{28}Si is deposited in the deposition chamber at DC–3 using a range of deposition conditions. As was mentioned previously, one of the critical degrees of freedom for achieving epitaxial deposition that is enabled in this final experimental setup is the substrate temperature. ^{28}Si samples were deposited using a range of substrate temperatures, T, from room temperature ($\approx$ 21 °C) up to a maximum of 1080 °C and many temperatures in between. Depositing at room temperature allows for comparison between these samples and those deposited in the previous setup at LC–2. The most common sample deposition temperatures used were either around 450 °C or 700 °C. The range of temperatures was used to determine the effect of temperature on both the epitaxial quality of the ^{28}Si films and the adsorption of SiH_4 gas into samples, which then increases the ^{29}Si and ^{30}Si isotopic concentrations. The first of these effects is described in a later section of this chapter, and the second is described in Chapter 6.

For the samples deposited at DC–3, both the nominal low pressure working mode of the ion source as well as the high pressure working mode were used, which led to a range of deposition parameters. When using the low pressure mode, during deposition, the pressure in the deposition chamber rose to between 1.6×10^{-7} Pa and 1.5×10^{-6} Pa (1.2×10^{-9} Torr to 1.1×10^{-8} Torr) due to the SiH_4 gas diffusion from the ion beam chamber. Most samples, however, were deposited in a background pressure of about 1.1×10^{-6} Pa (8.0×10^{-9} Torr). This pressure is a factor of three

lower than the low end of the range of background pressures measured during deposition of samples at LC–2 in Chapter 4. The RGA in the deposition chamber is routinely used to monitor the partial pressures of various chemical contaminants present in the deposition chamber during ^{28}Si deposition. A typical RGA mass spectrum recorded while depositing a ^{28}Si sample with a substrate temperature of 705 °C at DC–3 is shown in Fig. 5.3. H_2 dominates the spectrum and is the result of both residual H_2 in the deposition chamber and also cracking of SiH_4 gas in the ion source releasing H_2 which diffuses to the deposition chamber. SiH_4 gas also diffuses into the chamber, however, cracking from the RGA itself reduces the SiH_4 signal to mostly just the 28 u peak. This peak also contains N_2 and CO. ${SiH_4}^{2+}$ hydride peaks do appear between 14 u and 16 u at 0.5 u increments. Partial pressures of other chemicals of interest can be seen including C, H_2O, F, and CO_2. The peak appearing at 26 u is not known, but it may be related to an alcohol. When using the high pressure mode, the pressure in the deposition chamber rose to approximately 4.0×10^{-6} Pa (3.0×10^{-8} Torr), which is comparable to the samples deposited at LC–2.

Ions were deposited with a range of average ion energies, E_i, at the sample between 20 eV and 40 eV. This energy range is smaller with lower overall values than the samples discussed in Chapter 4 in order to standardize the deposition process and minimize sample sputtering. The estimated sputter yield for 30 eV ^{28}Si ions hitting a crystalline Si surface is approximately 2 % (see Fig. 2.19 in Chapter 2). The most common average ion anergy used here was approximately 35 eV. For the low pressure mode, the average ion beam current achieved was approximately

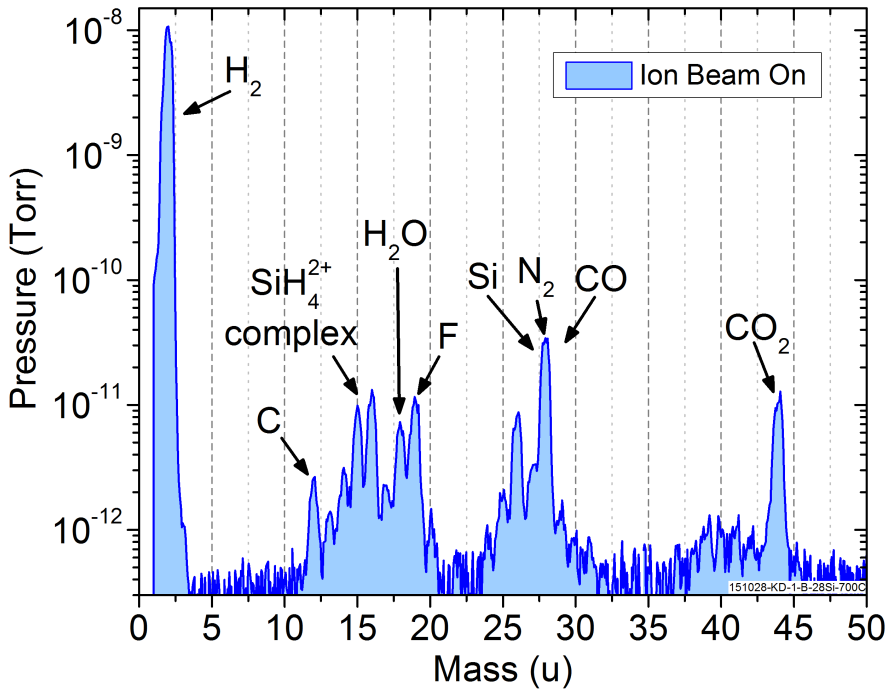

Figure 5.3: Residual gas mass spectrum collected from the RGA in the deposition chamber while operating the ion beam and depositing a ^{28}Si sample at 705 °C at DC–3. The spectrum is dominated by H_2 which diffuses from the ion beam chamber as SiH_4 gas is cracked in the ion source. The SiH_4 complex of peaks normally is reduced to only the 28 u peak due to cracking of the molecules by the RGA itself. N_2 and CO also make up the 28 u peak. Doubly charged SiH_4 hydrides do appear at around 15 u. Other potential chemical contaminants are present including C, F, H_2O, and CO_2.

0.55 μA. One major advantage of the high pressure plasma mode is that it yields a much larger ion current on average, and for these samples, an ion current of approximately 2.5 μA was achieved.

A mass spectrum for a Si ion beam with an ion energy of 37 eV generated using the low pressure mode of the ion source is shown in Fig. 5.4. This spectrum was collected using the interchangeable sample aperture at DC–3 prior to depositing a ^{28}Si sample. The corresponding magnet current used for the field sweep of the magnetic sector mass analyzer is shown on the top axis. Ion current peaks (circles)

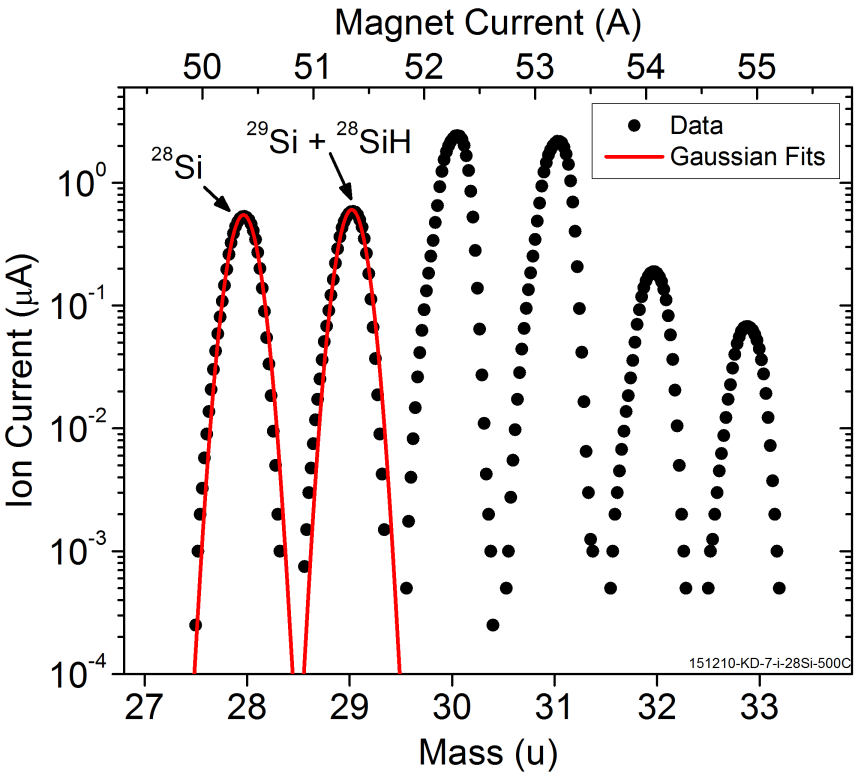

Figure 5.4: SiH_4 mass spectrum representative of the ion beam settings for samples deposited at DC–3 using the low pressure mode of the ion source. The ion current (circles) is recorded while sweeping the the analyzer current, and thus the magnetic field (top axis). The 28 u peak is ^{28}Si and the 29 u peak is both ^{28}SiH and $\approx$ 5 % ^{29}Si. Several higher order hydrides are also shown. Gaussian fits (line, Eq. (2.14)) to the 28 u and 29 u peaks are shown superimposed on the data. The centers of the 28 u and 29 u fits are separated by $\approx 10\ \sigma$.

corresponding to ^{28}Si and Si hydrides are observed between 28 u and 33 u. The ion current peaks in this spectrum appear qualitatively similar to the mass spectrum acquired in the previous experimental configuration (Fig. 4.8). The ion peak at 28 u is ^{28}Si and the ion peak at 29 u contains $\approx$ 5 % ^{29}Si based on the similar peak height to that of 28 u and the expected natural abundance, as discussed in Chapter 2. These peaks show a high degree of separation with no detectable ion current signal occurring between the peaks. Gaussian fits to the peaks (line, Eq. (2.14)) are also shown superimposed on the data, and one can see only a slight asymmetry in

the beam profile and no shoulder peaks, which indicates a fairly optimally tuned beam with minimal scattering off of lens elements. The mass resolving power of the ion beam in this configuration derived from this mass spectrum is $\frac{m}{\Delta m} \approx 57$ (measured at 10 % of the peak height). This value is similar to but slightly lower than the mass resolving power achieved in the previous experimental configuration perhaps due to the wider mass-selecting aperture used in this setup. However, no current is detected between the peaks, and the geometric selectivity is still expected to be sufficient to produce highly enriched ^{28}Si films comparable to those produced at LC–2. The Gaussian fits give a separation of the 28 u peak from the 29 u peak of approximately 10 σ.

A mass spectrum for a Si ion beam with an ion energy of 31 eV generated using the high pressure mode of the ion source is shown in Fig. 5.5. This spectrum was also collected using the interchangeable sample aperture prior to depositing a ^{28}Si sample. Again, the corresponding current used for the field sweep for the magnetic sector mass analyzer is shown on the top axis. The ion current peaks (circles) observed between 28 u and 33 u show the peak shapes typical of the high pressure mode. This spectrum shows a dramatic increase in the ^{28}Si ion current over the low pressure spectrum and a decrease in the 30 u and 31 u peaks. The ^{28}Si ion current becomes larger while the hydride peaks become smaller. This is because the hydrides are cracked more efficiently in the high pressure ion source plasma mode, as discussed in Chapter 2. The ^{28}Si ion current peak at 28 u and the ion current peak at 29 u show a fairly good separation but with a current level between the peaks of about 8 nA, which is higher than for the low pressure mode. Using the high pressure

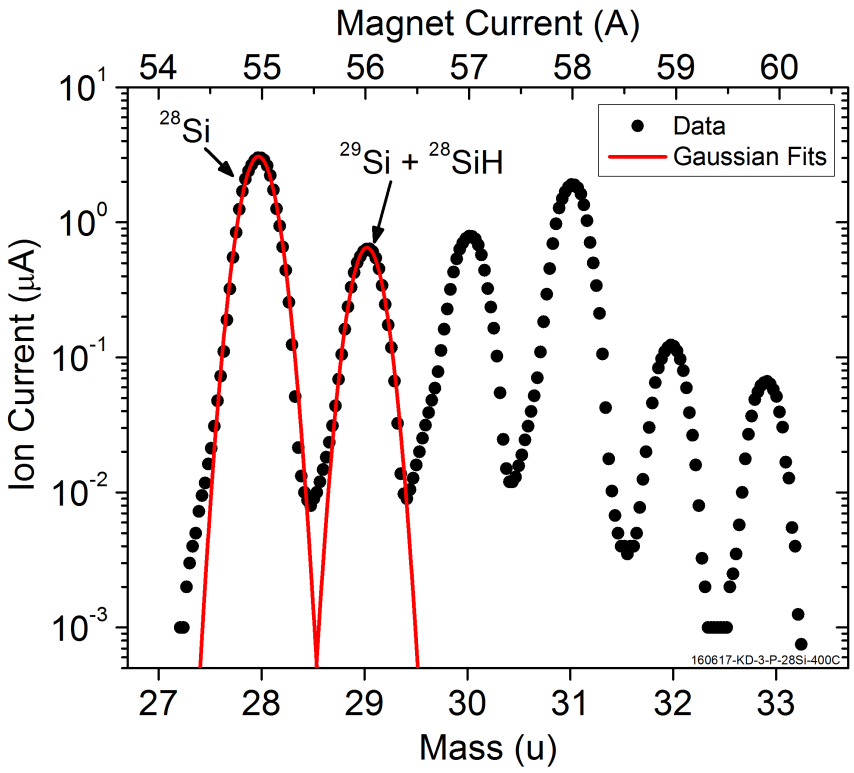

Figure 5.5: SiH_4 mass spectrum representative of the ion beam settings for samples deposited at DC–3 using the high pressure mode of the ion source. The ion current (circles) is recorded while sweeping the mass analyzer current, and thus the magnetic field (top axis). The 28 u peak is ^{28}Si and the 29 u peak is both ^{28}SiH and $\approx$ 24 % ^{29}Si. Several higher order hydrides are also shown. Gaussian fits (line, Eq. (2.14)) to the 28 u and 29 u peaks are shown superimposed on the data. The centers of the 28 u and 29 u fits are separated by $\approx 8\ \sigma$.

mode, ^{29}Si makes up approximately 24 % of the 29 u peak based on the peak heights and the expected natural abundance, as discussed in Chapter 2. Gaussian fits to the peaks (line, Eq. (2.14)) are also shown superimposed on the data as a sum. An asymmetry in the lower portion of the peaks possibly indicates some beam scattering to the lower mass side. The mass resolving power derived from this mass spectrum is $\frac{m}{\Delta m} \approx 48$ (measured at 10 % of the peak height), which is reduced further from the previous low pressure mode mass spectrum. The asymmetric peak and the lower mass resolving power may reduce the geometric selectivity and lower the achievable

enrichment level in ^{28}Si samples deposited using this mode. However, the roughly factor of five increase in ^{28}Si current compared to the 29 u peak containing ^{29}Si may offset any deleterious effects of a lower observed peak separation. The Gaussian fits give a separation of the 28 u peak from the 29 u peak of approximately 8 σ.

Tuning and focusing the ion beam onto the interchangeable sample aperture on the sample manipulator resulted in deposition spot sizes similar to those of samples deposited at LC–2. The average deposition area for samples deposited at DC–3 was approximately 6 mm^2 and as small as 2 mm^2 for a few samples. During deposition, RHEED was typically used to periodically monitor the structure of the depositing film and verify the location of the deposition spot on the chip. The appearance of the ^{28}Si deposition spot on the substrate of samples deposited at DC–3 varied depending on the deposition temperature. Optical micrographs of three samples deposited at three different temperatures at DC–3 are shown in Fig. 5.6. These micrographs show the Si(100) substrates with the ^{28}Si deposition spot appearing at the center as three visually distinct areas. Panel (a) shows ^{28}Si deposited on an intrinsic Si chip with a substrate temperature of approximately 249 °C in an area about 4.7 mm long. The deposition spot is clearly visible as a discolored patch on the chip and is visually similar to the samples deposited at room temperature at LC–2 in Chapter 4. This may indicate poor epitaxial quality. Panel (b) shows ^{28}Si deposited on a phosphorous-doped Si chip at a substrate temperature of about 421 °C in an area approximately 2.6 mm wide. The deposition spot is nearly indistinguishable from the substrate and only a faint outline is visible. This may indicate that the film is structurally similar to or even epitaxially matched with the substrate. The

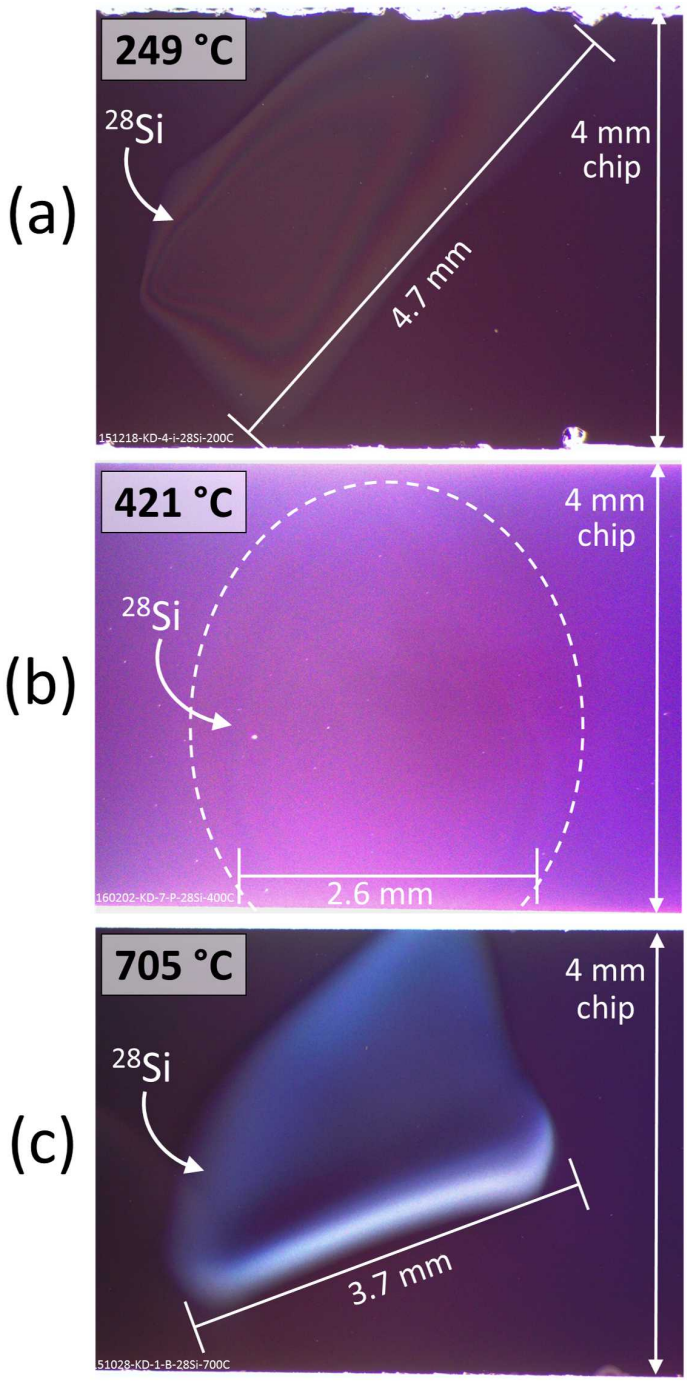

Figure 5.6: Optical micrographs of three ^{28}Si samples deposited at DC–3 at three different temperatures. The Si(100) substrates are seen in all three micrographs with the ^{28}Si deposition spot at the center. (a) ^{28}Si deposited on an intrinsic Si chip at 249 °C in an area 4.7 mm long is clearly visible. (b) ^{28}Si deposited on a phosphorous-doped Si chip at 421 °C in an area 2.6 mm wide is nearly indistinguishable from the substrate. (c) ^{28}Si deposited on a boron-doped Si chip at 705 °C in an area 3.7 mm wide is clearly visible.

brightness and contrast of this micrograph was altered to highlight the edges of the deposition spot, which is why the substrate appears lighter. Panel (c) shows ^{28}Si deposited with a substrate temperature of approximately 705 °C on a boron-doped Si chip in an area approximately 3.7 mm wide. The deposition spot is clearly visible on the chip and appears as a diffuse whitish color. Light scattering from the surface of the deposited area is probably due to a higher degree of surface roughness, which will be discussed later in this chapter.

The thicknesses of these ^{28}Si films ranged from around 45 nm to 370 nm as measured by TEM and/or inferred from SIMS depth profiling. The corresponding deposition rates for samples deposited using the low pressure mode of the ion source were between 0.32 nm/min and 1.41 nm/min with the most common deposition rate around 0.80 nm/min. The high pressure mode of the ion source resulted in a higher range of rates between 2.2 nm/min and 4.6 nm/min. These higher rates are desirable because they enable production of thicker samples in a typical deposition time (assuming similar spot sizes), and they lessen the relative adsorption rate of gaseous species from the background pressure into the ^{28}Si film during deposition.

To summarize, the typical deposition procedure for samples deposited at DC–3 was as follows:

1. a substrate is diced from a wafer and chemically cleaned *ex situ* before being mounted onto a sample holder and loaded into the load lock which is pumped out for $>$ 12 h,
2. the substrate is moved into the deposition chamber and degassed on the sample manipulator at 600 °C for $>$ 12 h,
3. the substrate is flash annealed to $\approx$ 1200 °C to prepare a clean (2×1) surface

which is inspected by RHEED,

4. after a deliberate temperature ramp down to ≈ 250 °C following flash annealing, the substrate cools radiatively for at least 10 min to ≈ 50 °C and is then transferred to the STM surface inspection,

5. with the sample in the STM, the ion beam is tuned and characterized using the interchangeable sample aperture on the manipulator. The mass spectrum, ion beam energy, beam spot focusing, and the deposition chamber RGA are all analyzed and recorded,

6. the substrate is transferred back to the deposition chamber after the gate valve to the ion beam is closed to reduce the background pressure where it is flashed once and set to the deposition temperature and position,

7. the gate valve to the ion beam is opened to commence deposition of ^{28}Si while monitoring the ion current onto the sample as a measure of the deposition rate,

8. RHEED is periodically used to monitor the crystallinity of the deposition and locate the deposition spot,

9. after typically three to five hours of deposition, the gate valve to the ion beam is closed to end deposition and reduce the deposition chamber pressure back to its base, then the sample is cooled to room temperature,

10. the sample is then transferred to the STM to inspect the surface morphology of the deposited ^{28}Si film, and finally,

11. the sample may be annealed at around 600 °C back on the manipulator and later inspected by STM again before ultimately being removed from the vacuum chamber via the load lock for *ex situ* analyses.

In total, 40 ^{28}Si samples were deposited at DC–3 including one room temperature sample, 32 samples deposited at elevated temperatures using the low pressure mode, and seven samples deposited at elevated temperatures using the high pressure mode.

5.5 Enrichment Measurements via SIMS for DC–3 Samples

5.5.1 Initial Tests at DC–3

SIMS was used to assess the enrichment of a large number of samples deposited at DC–3. The basic procedure for SIMS isotope measurements of ^{28}Si samples was discussed in Chapter 4. Isotope ratio measurements by SIMS were used to calculate the isotope fractions ($^{z}\mathrm{Si}/\mathrm{Si}_{\mathrm{tot.}}$). SIMS depth profiles presented in this chapter were acquired in collaboration with Dr. David Simons (NIST). Initial SIMS measurements were done to verify that the high levels of ^{28}Si enrichment achieved for samples deposited at LC–2 in Chapter 4 were reproducible for samples deposited at DC–3 after the significant experimental reconfiguration of connecting the ion beam to the deposition chamber. Recall the mass-selecting aperture width was increased, which may decrease the realized mass selectivity. Additionally, lower partial pressures of SiH_4 during deposition reduced the potential for adsorption of SiH_4 into the ^{28}Si films, which results in increased ^{29}Si and ^{30}Si isotope fractions. Along those same lines, it must be determined what role the substrate temperature plays in the enrichment of the samples. While the substrate deposition temperature is increased to facilitate epitaxial deposition, it may also change the kinetics and chemistry of any possible SiH_4 adsorption into the samples. Higher temperatures may reduce gaseous adsorption or perhaps the added energy may enhance incorporation into the depositing films. Addressing this topic required many SIMS measurements of

samples deposited at a large range of temperatures (some of which are shown here) and is the subject of Chapter 6.

Depositing a sample at room temperature should exclude any potential substrate temperature effects on the enrichment and provide a SIMS measurement more comparable to those of the samples deposited at LC–2 to verify the enrichment level of samples is no worse for this setup. A SIMS depth profile for a ^{28}Si sample deposited at room temperature (≈ 21 °C) using the low pressure mode of the ion source at DC–3 is shown in Fig. 5.7. Measurements of the ^{28}Si (circles), ^{29}Si (squares), and ^{30}Si (triangles) isotope fractions are shown vs. the sputter depth into the sample. This sample was relatively thin, and so the data density of the measurement is lower than for other samples. Also, a fairly short region (≈ 20 nm) exists where the isotope fractions reach a minimum and are averaged for the measurement. The count rate for a number of SIMS measurement cycles in this region was zero and thus that data does not appears on this semi-log plot. At a depth of around 40 nm, the isotope fractions begin to increase to their natural abundance values (dotted and dashed lines) in the transition into the Si(100) substrate, which is marked by the shaded region. The interface between the film and the substrate is estimated to be at a depth of about 53 nm, which is also the film thickness.

The average measured ^{28}Si isotope fraction in this sample is 99.999898(35) %. After some initial surface contamination, the average residual ^{29}Si isotope fraction measured between 13 nm and 41 nm is $0.58(26) \times 10^{-6}$ (0.58(26) ppm), and the average ^{30}Si isotope fraction is $0.44(23) \times 10^{-6}$ (0.44(23) ppm). Not only is the measured level of enrichment not diminished after the experimental transition to

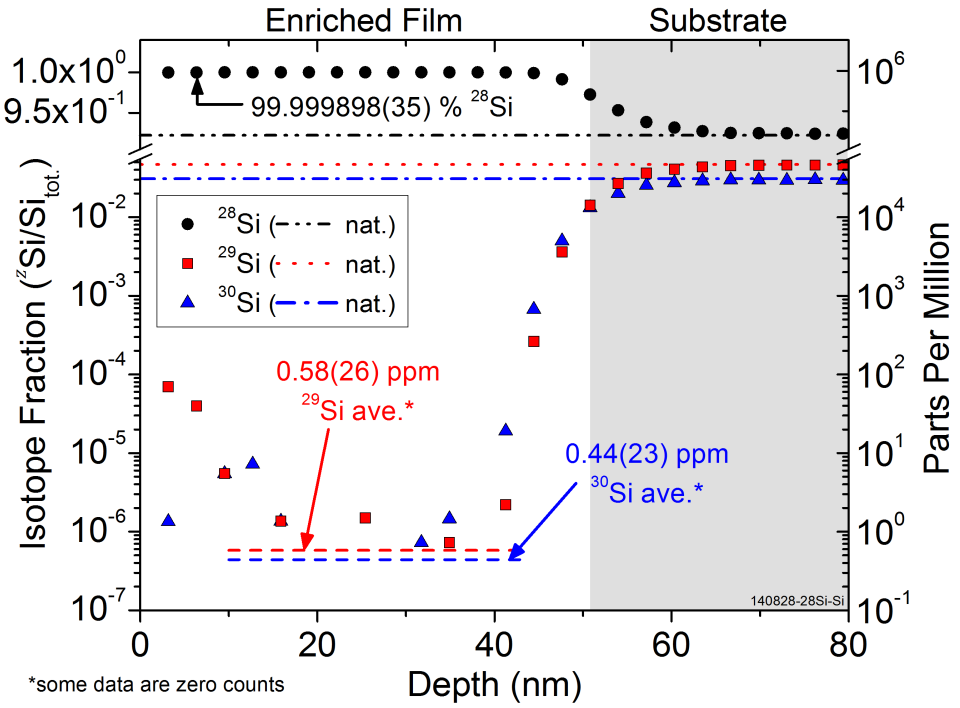

Figure 5.7: SIMS depth profile of a ^{28}Si sample deposited at room temperature using the low pressure mode at DC–3. ^{28}Si (circles), ^{29}Si (squares), and ^{30}Si (triangles) isotope fractions are shown vs. sputter depth. The average ^{29}Si isotope fraction in the film is 0.58 ppm, and the average ^{30}Si isotope fraction is 0.44 ppm (dashed lines). Note that data are zero counts in some SIMS cycles. The natural abundance values for each isotope (dotted and dashed lines) are also shown for reference. At a depth of 40 nm, the isotope fractions begin to increase to their natural abundance values in the Si(100) substrate. The interface between the film and the substrate (shaded region) is estimated to be at a depth of 53 nm.

this final experimental configuration, it is slightly better than the most highly enriched sample deposited at LC–2 (0.691(74) ppm ^{29}Si). This may be the result of a combination of the background pressure during deposition of this sample being roughly a factor of three lower than that of the sample deposited at LC–2 and the deposition rate being nearly a factor of three higher. These counter acting conditions would in fact result in only a slightly better enrichment. Also, apparently the widening of the mass-selecting aperture did not measurably decrease the realized selectivity in the ^{28}Si samples.

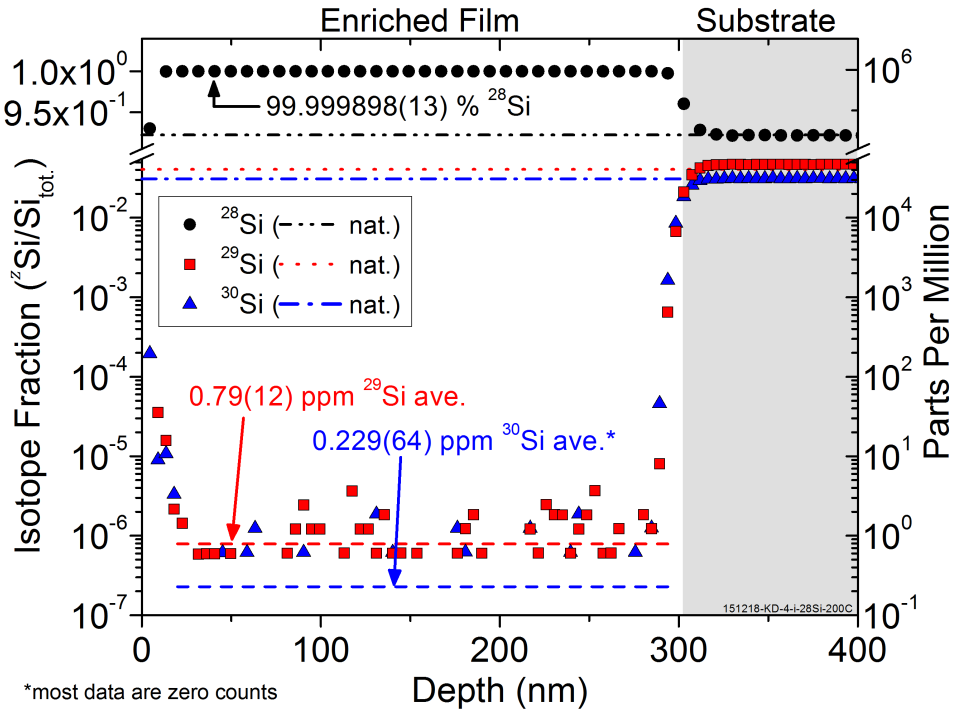

Figure 5.8: SIMS depth profile of a ^{28}Si sample deposited at 249 °C using the low pressure mode at DC–3. ^{28}Si (circles), ^{29}Si (squares), and ^{30}Si (triangles) isotope fractions are shown vs. sputter depth. The average ^{29}Si isotope fraction in the film is 0.79 ppm, and the average ^{30}Si isotope fraction is 0.229 ppm (dashed lines). Note that most data are zero counts in particular SIMS cycles for ^{30}Si. The natural abundance values for each isotope (dotted and dashed lines) are also shown for reference. At a depth of about 280 nm, the isotope fractions begin to increase to their natural abundance values in the substrate (shaded region). The interface between the film and the substrate is estimated to be at a depth of 305 nm.

The room temperature sample can also be compared with samples deposited at elevated temperatures. Figure 5.8 shows a SIMS depth profile for a sample deposited at approximately 249 °C at DC–3 using the low pressure mode. The ^{28}Si (circles), ^{29}Si (squares), and ^{30}Si (triangles) isotope fractions are shown vs. the sputter depth into the sample. This much thicker sample shows a large flat region in the isotope fraction profile and an abrupt increase up to the natural abundance values in the substrate indicating a sharp interface. At a depth of about 280 nm, the isotope fractions begin to increase to their natural abundance values (dotted and dashed

lines) in the transition into the substrate, which is marked by the shaded region. The interface between the film and the substrate is estimated to be at a depth of approximately 305 nm, giving a value for the film thickness.

For this sample, the average measured ^{28}Si isotope fraction in the film is 99.999898(13) %. After sputtering through some initial surface contamination, the average residual ^{29}Si isotope fraction is $0.79(12) \times 10^{-6}$ (0.79(12) ppm), and the average ^{30}Si isotope fraction is $0.229(64) \times 10^{-6}$ (0.229(64) ppm). For the ^{30}Si data, most of the SIMS measurement cycles in this region contained zero counts and thus the data does not appears on this semi-log plot. These averages were calculated using the data between 32 nm and 285 nm. The level of enrichment of this sample is very similar to that of the room temperature sample. In fact, the ^{28}Si isotope fraction is identical with slightly different proportions of ^{29}Si and ^{30}Si. When this result is combined with a SIMS measurement of a second area of this sample, the average ^{29}Si isotope fraction of the two measurements is 0.90(10) ppm. These measurements shows that ^{28}Si samples can successfully be deposited at elevated temperatures using the low pressure mode of the ion source at DC–3 while maintaining a very high level of enrichment.

5.5.2 Enrichment Progression Timeline Samples

Out of the 40 samples produced at DC–3, three are represented on the enrichment progression timeline (Fig. 4.2) in Chapter 4 as new record enrichments achieved in this work at the time of their deposition, and they will be discussed in this section. In fact, these samples achieved the highest enrichments of any samples

produced in this work. A SIMS depth profile for the first of these ^{28}Si samples deposited using the low pressure mode of the ion source at DC–3 with a higher level of enrichment than the previous ones deposited at LC–2 is shown in Fig. 5.9. This sample was deposited at a substrate temperature of approximately 610 °C using the low pressure mode of the ion source. The ^{28}Si (circles), ^{29}Si (squares), and ^{30}Si (triangles) isotope fractions are shown vs. the sputter depth into the sample. Beyond some initial surface contamination, there is only a relatively thin region between 20 nm and 70 nm over which the ^{29}Si isotope fraction reaches a sustained minimum value. In this region of the film, the isotope fractions were averaged. At a depth below 70 nm, the ^{29}Si isotope fraction increases more than two orders of magnitude. This increase is likely a result of extended ion beam tuning off of the 28 u peak after deposition had commenced. At a depth of around 125 nm, the ^{29}Si and ^{30}Si isotope fractions together begin to increase to their natural abundance values (dotted and dashed lines) in the transition into the substrate, which is marked by the shaded region. The interface between the film and the substrate is estimated to be at a depth of approximately 162 nm, giving a value for the total film thickness. The length over which the isotope fractions return to their natural abundance values is relatively wide in this sample compared to the previous sample, possibly indicating a larger degree of surface roughness.

Within the highly enriched portion of this sample, the average measured ^{28}Si isotope fraction is 99.9999570(70) %. The average residual ^{29}Si isotope fraction in the film is $3.00(60) \times 10^{-7}$ (300(60) ppb), and the average ^{30}Si isotope fraction is $1.30(37) \times 10^{-7}$ (130(37) ppb). Some of the SIMS measurement cycles in this region

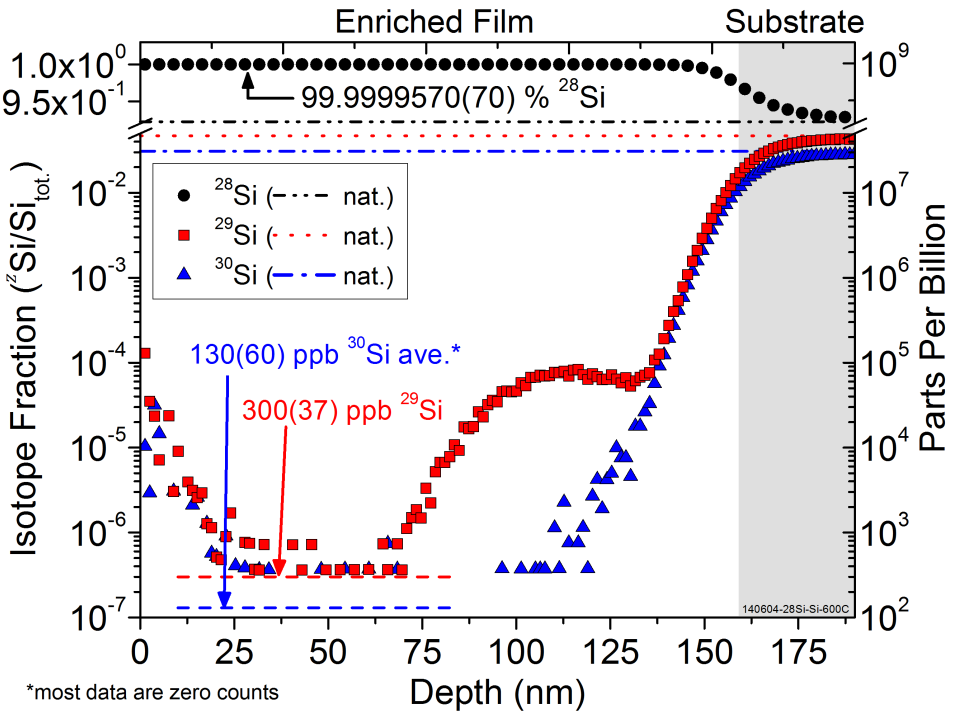

Figure 5.9: SIMS depth profile of a ^{28}Si sample deposited at 610 °C using the low pressure mode at DC–3. ^{28}Si (circles), ^{29}Si (squares), and ^{30}Si (triangles) isotope fractions are shown vs. sputter depth. The isotope fraction values were averaged between 20 nm and 70 nm. The average ^{29}Si isotope fraction in this part of the film is 300 ppb, and the average ^{30}Si isotope fraction is 130 ppb (dashed lines). Note that most data are zero counts in particular SIMS cycles. The natural abundance values for each isotope (dotted and dashed lines) are also shown for reference. At a depth of about 70 nm, the ^{29}Si isotope fraction increases two orders of magnitude likely as a result of ion beam tuning off of the 28 u peak. At a depth of 125 nm, the ^{29}Si and ^{30}Si isotope fractions begin to increase to their natural abundance values. The interface between the film and the substrate (shaded region) is estimated to be at a depth of 162 nm.

for the ^{29}Si data and most of the measurement cycles for the ^{30}Si data contained zero counts and thus the data does not appears on this semi-log plot. These measurements indicate an isotope reduction factor ($a_z/(^z\mathrm{Si}/\mathrm{Si}_{\mathrm{tot.}})$, discussed in Chapter 4) for ^{29}Si of $1.6(3) \times 10^5$, i.e. the ^{29}Si is approximately $1.6(3) \times 10^5$ times lower than in natural abundance Si. The isotope reduction factor for ^{30}Si is slightly higher at $2.4(4) \times 10^5$, although it is similar to that of ^{29}Si within the uncertainty of the

values. The ^{29}Si isotope fraction of this sample is a little more than a factor of two less than that of the most highly enriched sample deposited at LC–2 in Chapter 4, as seen in the jump from LC–2 to DC–3 in Fig. 4.2. This decrease in ^{29}Si and ^{30}Si isotope fractions was probably due to the significantly lowered background deposition pressure for these samples, which would result in a lower amount of adsorbed SiH_4. Additionally, this result shows that very high enrichments continue to be achieved while the substrate deposition temperature is increased further compared to the previous sample discussed in this section. Despite the high level of enrichment achieved in a portion of the film, this sample is clearly not ideal due to the region of elevated ^{29}Si. Additional SIMS measurements of samples deposited under similar conditions show the elevated ^{29}Si to be an anomaly.

The second sample represented on the enrichment progression timeline in Fig. 4.2, which was deposited at DC–3 and achieved an even higher level of enrichment over the previous sample is one that was deposited with a substrate temperature of approximately 712 °C using the low pressure mode. A SIMS depth profile of the area of highest enrichment of this sample is shown in Fig. 5.10. The ^{28}Si (circles), ^{29}Si (squares), and ^{30}Si (triangles) isotope fractions are shown vs. the sputter depth into the sample. Beyond the initial signal due to surface contamination, the ^{29}Si and ^{30}Si isotope fractions show an extended minimum. At a depth of around 227 nm, the isotope fractions begin to increase to their natural abundance values (dotted and dashed lines) in the transition into the substrate, which is marked by the shaded region. The interface between the film and the substrate is estimated to be at a depth of approximately 256 nm, giving a value for the film thickness.

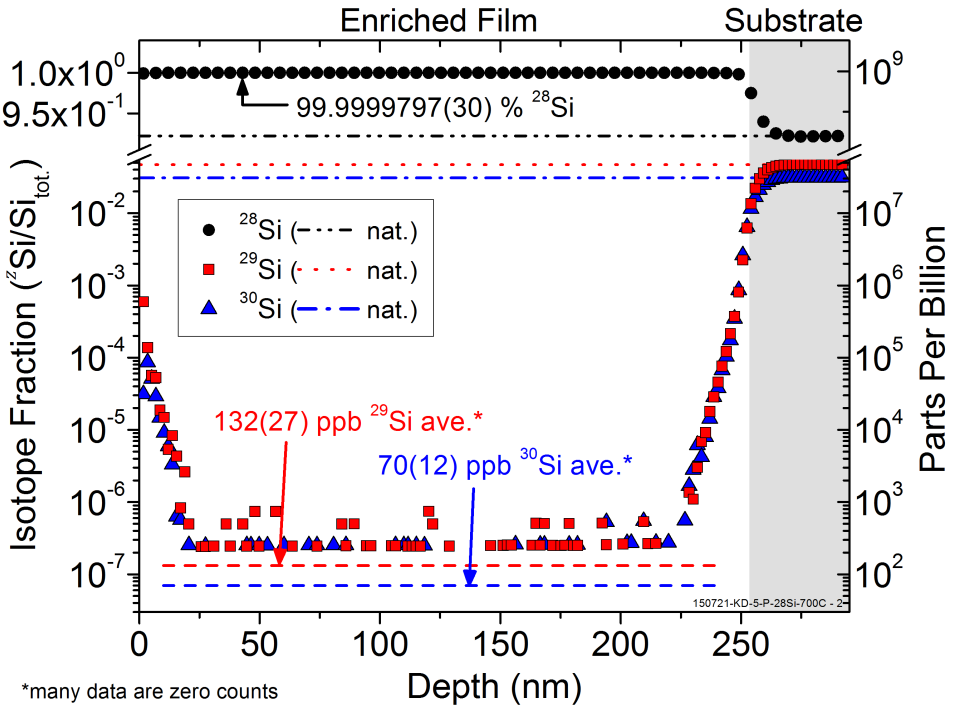

Figure 5.10: SIMS depth profile of a ^{28}Si sample deposited at 712 °C using the low pressure mode at DC–3. ^{28}Si (circles), ^{29}Si (squares), and ^{30}Si (triangles) isotope fractions are shown vs. sputter depth. The average ^{29}Si isotope fraction in the film is 132 ppb, and the average ^{30}Si isotope fraction is 70 ppb (dashed lines). Many data in this region are zero counts in the SIMS cycles. The natural abundance values for each isotope (dotted and dashed lines) are also shown for reference. The isotope fraction values were averaged between 21 nm and 227 nm, where the ^{29}Si and ^{30}Si isotope fractions begin to increase to their natural abundance values. The interface between the film and the substrate (shaded region) is estimated to be at a depth of 256 nm.

The average measured ^{28}Si isotope fraction in the highly enriched portion of the film is 99.9999797(30) %. The average residual ^{29}Si isotope fraction is measured to be $1.32(27) \times 10^{-7}$ (132(27) ppb), and the average ^{30}Si isotope fraction is $7.0(12) \times 10^{-8}$ (70(12) ppb) (dashed lines). Many of the SIMS measurement cycles in this region contained zero counts and thus the data does not appears on this semi-log plot. The averages were calculated from the data between 21 nm and 227 nm. These measurements indicate an isotope reduction factor for ^{29}Si of $3.5(7) \times 10^5$.

The isotope reduction factor for ^{30}Si is slightly higher at $4.4(8) \times 10^5$, although they are similar within the uncertainty of the values. A second area of this sample was also measured by SIMS giving an average ^{29}Si isotope fraction of the two measurements of 163(18) ppb. As mentioned in Chapter 4, this variation between measurements on the same sample is likely due to a difference in deposition rate at the two areas of the film.

The enrichment of this sample represents yet another decrease of more than a factor of two in the isotope fraction of ^{29}Si from the 610 °C sample, which can be seen in Fig. 4.2, the enrichment progression timeline. This reduction is possibly due to a lower rate of incorporation of SiH_4 into the film from a slight decrease in deposition background pressure and also a nearly twofold increase in deposition rate for this sample compared to the previous one. The deposition was approximately 1.22 nm/min, which is fairly high compared to other samples deposited using the low pressure mode. This was a result of both a slightly higher average ion beam current of about 740 nA and better beam spot tuning that led to a more compact than average deposition spot of about 4.2 mm^2. A complicating factor which may effect the enrichment of this sample is an anomalous amount of nitrogen observed in the ion beam mass spectrum before depositing this sample. This matter will be addressed in the later sections of this chapter.

The third and final sample represented on the enrichment progression timeline in Fig. 4.2 that was deposited at DC–3 is a sample deposited at approximately 502 °C using the low pressure mode. This ^{28}Si sample is the most highly enriched sample produced in this entire work. A SIMS depth profile of the area of highest

enrichment within this sample is shown in Fig. 5.11. The ^{28}Si (circles), ^{29}Si (squares), and ^{30}Si (triangles) isotope fractions are shown vs. the sputter depth into the sample. Beyond the initial signal due to surface contamination, the ^{29}Si and ^{30}Si isotope fractions show an extended minimum with very little variation in value. At a depth of around 290 nm, the isotope fractions begin to increase to their natural abundance values (dotted and dashed lines) in a fairly abruptly transition into the substrate, which is marked by the shaded region, indicating a sharp interface. The interface between the film and the substrate is estimated to be at a depth of approximately 321 nm, which also gives a value for the film thickness.

The average measured ^{28}Si isotope fraction in this highly enriched film is 99.9999819(35) %. This value is the highest enrichment of any sample measured in this work. Additionally, the average residual ^{29}Si isotope fraction is the lowest for any sample with a value of $1.27(29) \times 10^{-7}$ (127(29) ppb), and the average ^{30}Si isotope fraction is $5.5(19) \times 10^{-8}$ (55(19) ppb) (dashed lines). The averages were calculated from the data between 30 nm and 290 nm. They lie well below where the data appears because many of the SIMS measurement cycles in this region contained zero counts and thus the data is not represented on this semi-log plot. These enrichment measurements of ^{29}Si and ^{30}Si represent the best isotope reduction factors for this entire work. The isotope reduction factor for ^{29}Si is $3.7(8) \times 10^5$, and the isotope reduction factor for ^{30}Si is higher with a value of $5.6(19) \times 10^5$. These values are actually similar to each other to within their uncertainties due to a large relative uncertainty in the measurement of the isotope fraction of ^{30}Si in this sample. The level of enrichment of this sample is similar to that of the 712 °C sample, and while

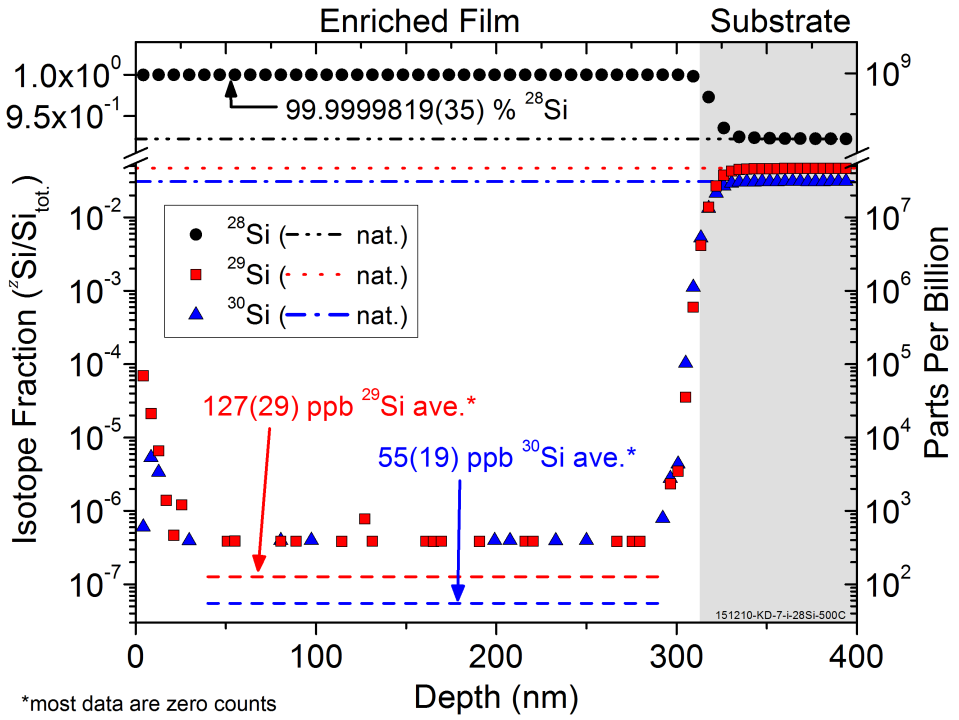

Figure 5.11: SIMS depth profile of the most highly enriched ^{28}Si sample deposited at DC–3. This sample was deposited with a substrate temperature of 502 °C using the low pressure mode. ^{28}Si (circles), ^{29}Si (squares), and ^{30}Si (triangles) isotope fractions are shown vs. sputter depth. The average ^{29}Si isotope fraction in the film is 127 ppb, and the average ^{30}Si isotope fraction is 55 ppb (dashed lines). Many data in this region are zero counts in the SIMS cycles. The natural abundance values for each isotope (dotted and dashed lines) are also shown for reference. The isotope fraction values were averaged between 21 nm and 292 nm, where the ^{29}Si and ^{30}Si isotope fractions begin to increase to their natural abundance values. The interface between the film and the substrate (shaded region) is estimated to be at a depth of 321 nm.

the center value of this measurement is lower than that of the previous sample, they agree within their uncertainties as seen in the enrichment progression timeline in Fig. 4.2. Like the 712 °C sample, the extremely low isotope fractions of ^{29}Si and ^{30}Si observed in this sample are likely due to a lower rate of incorporation of SiH_4 into the film. This is probably due in part to a relatively high deposition rate of 1.41 nm/min, which is actually the highest deposition rate for samples deposited using the low pressure mode at DC–3. Again, the deposition temperature may also

be playing a part in the reduction of ^{29}Si and ^{30}Si although it is not clear from this data alone.

A total of three SIMS measurements were made on different areas of this sample resulting in an average ^{29}Si isotope fraction for the three areas of 233(39) ppb. The single area best value of 127(29) ppb ^{29}Si residual isotope fraction is given more weight in this discussion than the multiple measurement average because the average depends on the distribution of the measurement areas across regions of the film with different deposition rates. The single area best value also gives a lower bound on the best possible enrichment achievable by the deposition system for the specific ion beam selectivity, deposition rate, background pressure, and substrate temperature used.

The samples already described in this chapter, which were deposited with elevated substrate temperatures, demonstrate enrichment levels similar to or better than those of the highly enriched room temperature samples deposited at LC–2, i.e. isotope fractions < 1 ppm of ^{29}Si. However, some samples deposited at DC–3 with elevated substrate temperatures showed significantly higher isotope fractions of ^{29}Si and ^{30}Si. One sample deposited at approximately 357 °C using the low pressure mode was measured by SIMS to have a average ^{28}Si isotope fraction of 99.999405(93) %. The average residual ^{29}Si isotope fraction in the film is measured to be $4.18(70) \times 10^{-6}$ (4.18(70) ppm), and the average ^{30}Si isotope fraction is $1.77(61) \times 10^{-6}$ (1.77(61) ppm). These higher isotope fractions are likely due in part to a low deposition rate for this sample of 0.33 nm/min and a higher background pressure during deposition of approximately 1.5×10^{-6} Pa (1.1×10^{-8} Torr), which

equals the highest pressure for any sample deposited at DC–3 using the low pressure mode of the ion source.

Another sample deposited with a substrate temperature of 421 °C using the low pressure mode was measured in one area to have an average ^{28}Si isotope fraction of 99.999812(25) %. The average residual ^{29}Si isotope fraction measured for this sample is $1.30(22) \times 10^{-6}$ (1.30(22) ppm), and the average ^{30}Si isotope fraction is $5.8(12) \times 10^{-7}$ (0.58(12) ppm). Averaging the measurements of three areas on the deposition spot of this sample gives an overall average ^{29}Si isotope fraction of 1.48(13) ppm. The average deposition rate corresponding to the three measured areas of this sample was also lower than average at approximately 0.46 nm/min. The background deposition pressure was similar to that of the 357 °C sample.

5.5.3 Samples with Deposition $T > 600$ °C

The highest residual ^{29}Si and ^{30}Si isotope fractions were measured in samples deposited with a substrate temperature above 600 °C, suggesting that higher substrate deposition temperatures effect the enrichment. This temperature dependence will be discussed in Chapter 6. SIMS measurements of a sample deposited at approximately 705 °C using the low pressure mode show a maximum average ^{28}Si isotope fraction of 99.999488(48) %. The average residual ^{29}Si isotope fraction is $3.30(25) \times 10^{-6}$ (3.30(25) ppm), and the average ^{30}Si isotope fraction is $1.82(42) \times 10^{-6}$ (1.82(42) ppm). The ^{29}Si isotope fraction averaged between two measurements on this sample is 4.06(37) ppm. Unlike the 357 °C and 421 °C samples, this 705 °C sample had a higher estimated average deposition rate of approxi-

mately 0.74 nm/min, which is average for samples deposited at DC–3. This sample was also deposited in a slightly lower background deposition pressure than the previous two sample. These results are counter intuitive when comparing them to past results discussed throughout Chapter 4 and this chapter, and thus they seem to provide supporting evidence for the substrate temperature having an affect the enrichment.

Another similar sample with elevated ^{29}Si and ^{30}Si isotope fractions was deposited with a substrate temperature of approximately 812 °C using the low pressure mode. The average ^{28}Si isotope fraction measured by SIMS for this sample is 99.99907(10) %. The average residual ^{29}Si isotope fraction in the film is $4.32(46) \times 10^{-6}$ (4.32(46) ppm), and the average ^{30}Si isotope fraction is slightly higher at $4.96(93) \times 10^{-6}$ (4.96(93) ppm). This sample was deposited in a slightly lower background pressure than the 705 °C sample and had a slightly higher estimated deposition rate of 0.90 nm/min, which is again counter intuitive because higher deposition rates were seen to lower the residual isotope fractions previously.

In addition to higher deposition temperatures, other differences exist between these samples and others discussed in this chapter that may affect the measurement of the isotope fractions. Unlike the SIMS measurements of the lower temperature samples, the measurements of some of the samples deposited above 600 °C result in only a very short range in the depth profile where the isotope fractions reach a minimum value. A SIMS depth profile of the 812 °C sample discussed above is shown in Fig. 5.12 and exhibits this effect. The ^{28}Si (circles), ^{29}Si (squares), and ^{30}Si (triangles) isotope fractions are shown vs. the sputter depth into the sample.

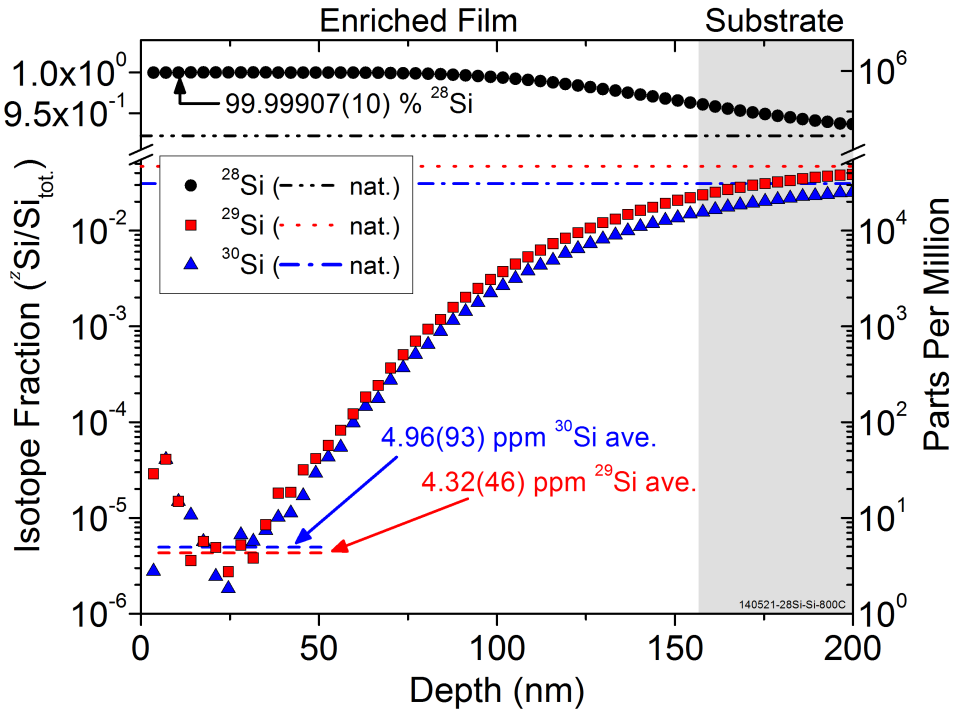

Figure 5.12: SIMS depth profile of a ^{28}Si sample deposited at 812 °C using the low pressure mode at DC–3. ^{28}Si (circles), ^{29}Si (squares), and ^{30}Si (triangles) isotope fractions are shown vs. sputter depth. After some surface contamination, the ^{29}Si and ^{30}Si isotope fractions reach a minimum at a depth of 25 nm and then gradually increase through the rest of the film to the natural values in the substrate. The natural abundance values for each isotope (dotted and dashed lines) are shown for reference. The ^{29}Si and ^{30}Si isotope fractions are averaged at this minimum between 14 nm and 32 nm. The average ^{29}Si isotope fraction at the film minimum is 4.32 ppm, and the average ^{30}Si isotope fraction is 4.96 ppm (dashed lines). The interface between the film and the substrate (shaded region) is estimated to be at a depth of 158 nm.

This depth profile is qualitatively very different from previously shown SIMS depth profiles. After sputtering through the typical surface contamination, the ^{29}Si and ^{30}Si isotope fractions reach a minimum value at a depth of about 25 nm and then gradually and immediately increase through the remaining 133 nm of deposited film up to the natural values in the substrate (dotted and dashed lines). The interface between the film and the substrate is estimated to be at a depth of approximately 158 nm, marked by the shaded region. The ^{29}Si and ^{30}Si isotope fraction averages

(dashed lines) were calculated for a small region where the signals reach its minimum between 14 nm and 32 nm. SIMS depth profiles of other samples deposited at temperatures of approximately 708 °C, 759 °C, 804 °C, and 1041 °C also exhibit the same qualitative depth profile seen in Fig. 5.12.

The apparent gradual increase in ^{29}Si and ^{30}Si isotope fractions throughout the enriched film of these samples may be explained by considering self-diffusion of ^{29}Si and ^{30}Si isotopes from the naturally abundant Si substrate into the deposited film. As the ^{28}Si film is depositing, it is effectively being annealed by the elevated temperature of the substrate. At deposition temperatures of about 700 °C and above, the thermal activation of Si self-diffusion may be enough to produce the isotope fraction gradients seen in the SIMS depth profiles. To explore this hypothesis, Si diffusion profiles are calculated and compared to the measured SIMS depth profiles. Si self-diffusion is believed to be dominated by self-interstitials above 800 °C with an activation energy of approximately 4.75 eV [117]. The concentration of ^{29}Si or ^{30}Si in an enriched ^{28}Si film, $C(x)$, at a depth below the film surface, x, due to Si isotope diffusion is given by

$$C(x) = \frac{C_{sub} + C_{film}}{2} + \frac{C_{sub} - C_{film}}{2} \text{ erf}\left(\frac{x-d}{2(D_{Si}^{SD}t)^{0.5}}\right), \tag{5.1}$$

where C_{sub} is the concentration of ^{29}Si or ^{30}Si in the substrate, C_{film} is the concentration of ^{29}Si or ^{30}Si in the enriched film without diffusion, d is the film thickness, t is the deposition time (annealing time), and the Si self-diffusion coefficient, D_{Si}^{SD}, is given by

$$D_{Si}^{SD} = (530)\exp\left(-\frac{E_a}{k_B T}\right). \tag{5.2}$$

Here, E_a is the activation energy, mentioned above. Equations (5.1) and (5.2) as well as the exponential prefactor of Eq. (5.2), 530 $cm^2 \cdot s^{-1}$, were taken from Ref. [117]. These equations are used to calculate the expected concentration of ^{29}Si from diffusion into enriched ^{28}Si films and compare it to the measured SIMS depth profile shown in Fig. 5.12. The calculated concentration profiles for ^{29}Si in a ^{28}Si film resulting from several different deposition temperatures are shown in Fig. 5.13. In these calculations, ^{29}Si diffuses from the natural abundance Si substrate (shaded region) into the ^{28}Si film during deposition with elevated substrate temperatures which anneal the film. The film thickness and thus film/substrate interface is arbitrarily set at a depth of 100 nm below the film surface. Calculated ^{29}Si concentration profiles are shown for deposition temperatures of 700 °C (solid line), 750 °C (dotted line), 800 °C (dash-dot line), 850 °C (dash-dot-dot line), and 900 °C (dashed line). These calculations also used a total deposition time of 4 h, which is an average deposition time for samples produced at DC–3, and a nominal ^{29}Si isotope fraction in the ^{28}Si film of 1 ppm. The ^{29}Si profiles show that there is relatively little diffusion expected from the substrate into the ^{28}Si film for these time and temperature combinations. Most of the samples deposited with substrate temperatures within the range of these calculation were deposited at around 700 °C or 800 °C, and the profiles for these temperatures show significant concentrations of ^{29}Si only within approximately 1 nm of the interface. Even for the 900 °C profile, the ^{29}Si concentration drops to less than double the nominal film concentration beyond a distance of 10 nm from the substrate interface. This small amount of diffusion would be not even be detected in the SIMS depth profiles because it is still smaller

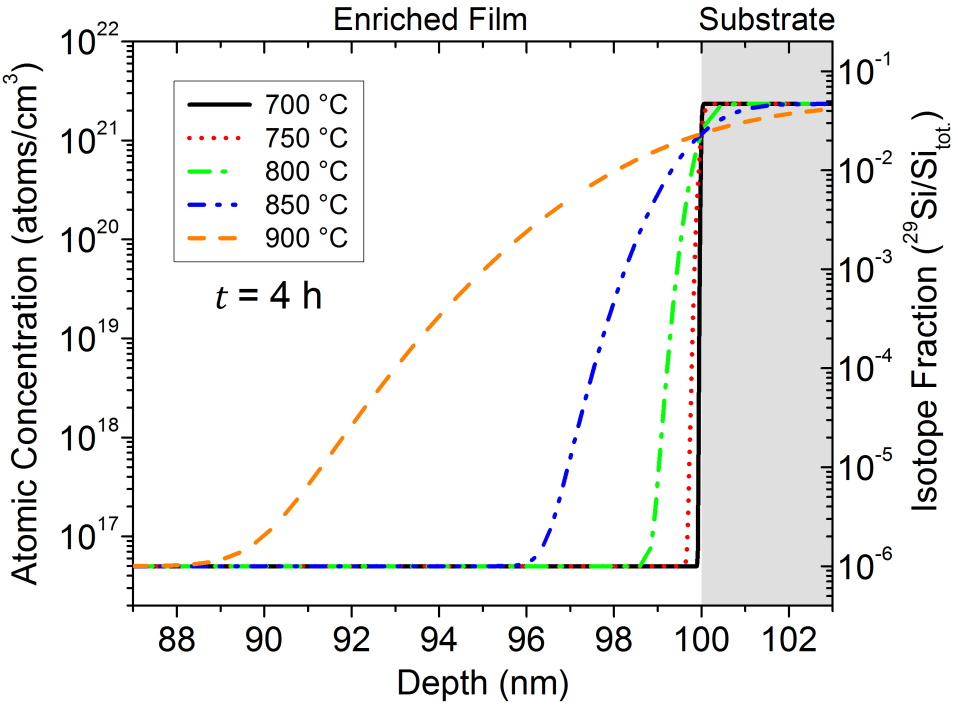

Figure 5.13: Calculated ^{29}Si concentration profiles in a ^{28}Si film from isotope diffusion at elevated temperatures. ^{29}Si diffuses from the natural abundance Si substrate (shaded region) at a depth of 100 nm into the ^{28}Si film during deposition. Atomic concentration profiles for five deposition temperatures from 700 °C (solid line) to 900 °C (dashed line). These profiles were calculated from Eq. (5.1) for a deposition time of 4 h and a nominal ^{29}Si isotope fraction in the ^{28}Si film of 1 ppm.

than the typical 25 nm region over which the isotope signals transition from low isotope fractions in the film to high isotope fractions in the substrate. Figure 5.13 shows that isotope self-diffusion from the substrate into the depositing ^{28}Si films is not responsible for the SIMS depth profile shape in Fig. 5.12.

Another possible explanation for the apparent gradual increase in ^{29}Si and ^{30}Si isotope fractions throughout the films of some samples deposited at higher temperatures is that a large amount of surface roughness is causing an artifact in the SIMS measurement. Producing an accurate SIMS depth profile relies on the assumption that all of the sputtered atoms contributing to the signal at a given time

in the measurement originated from the same plane in the sample relative to the film-substrate interface. The presence of surface roughness invalidates this assumption because it results in the SIMS beam sputtering atoms from different depths at the same time. Here, surface roughness is characterized by a surface width, Δz, which is the total width of the region at the surface between the highest peak and lowest valley. This surface roughness will be transferred down through the film during the SIMS measurement, and when the sputter beam reaches the interface between the ^{28}Si film and the substrate, it will begin sampling the substrate in some areas while still sampling the film in other areas. This effect artificially inflates the measured ^{29}Si and ^{30}Si isotope fractions near the substrate interface by mixing the higher ^{29}Si and ^{30}Si signals from the substrate with the lower signals from the ^{28}Si film. The relationship between Δz and the total film thickness, d, determine whether a reliable SIMS measurement is possible. The range over which this artifact will manifest is always similar to the size of Δz, and it only manifests near the substrate interface. So, for $\Delta z \ll d$, the effect does not impact the ability to make a good measurement of the film. However, for $\Delta z \sim d$, the signal from the measurement artifact would be comparable or dominant to the signal of the true measurement of the film.

Surface roughness appears to be a reasonable explanation for the ^{28}Si samples deposited at higher temperatures that exhibit a SIMS depth profile qualitatively similar to the one in Fig. 5.12, with a gradual ^{29}Si and ^{30}Si isotope fraction increase through the depth profile of the film. Many of these samples are observed to have much rougher surfaces as deposited than samples deposited at lower temperatures, and for several samples, Δz was of the order of d, as determined by SEM and

TEM cross-sectional microscopy. Details of this observed roughness is discussed in a later section. A tilted SEM cross-sectional micrograph of a sample deposited with a substrate temperature of approximately 708 °C using the low pressure mode is shown in Fig. 5.14. This micrograph was acquired in collaboration with Dr. Joshua Schumacher (NIST). The Si(100) substrate and the ^{28}Si film both appear dark in the lower half of this micrograph with the substrate at the bottom and the film above it. The ^{28}Si film is indistinguishable from from the substrate in this image without obvious grains or other features. A dashed line represents the approximate location of the interface between the substrate and the ^{28}Si film, determined from TEM cross-sectional microscopy. The light region above the film is Pt deposited to protect the sample, which was cross-sectioned using a focused ion beam (FIB). The top surface of the Pt is also visible because the sample is viewed at a tilt angle of 52°. The surface of the ^{28}Si appears very rough with a maximum Δz of approximately 80 nm. The thickest areas of the film are approximately 120 nm. The inset shows a cartoon of a rough ^{28}Si film on a substrate being sputtered by SIMS in an isotope measurement. SIMS sputter beams (vertical arrows) sample both a thick and thin region of the film. Sputtering in the thick region results in isotope signals from the ^{28}Si film, while sputtering at the same time in the thin region results in isotope signals partially originating from the natural abundance substrate. This is the process that leads to the measurement artifact which inflates the ^{29}Si and ^{30}Si isotope fractions above the nominal film values as the measurement approaches the interface.

The measured ^{28}Si enrichment values for all samples that exhibit the roughness

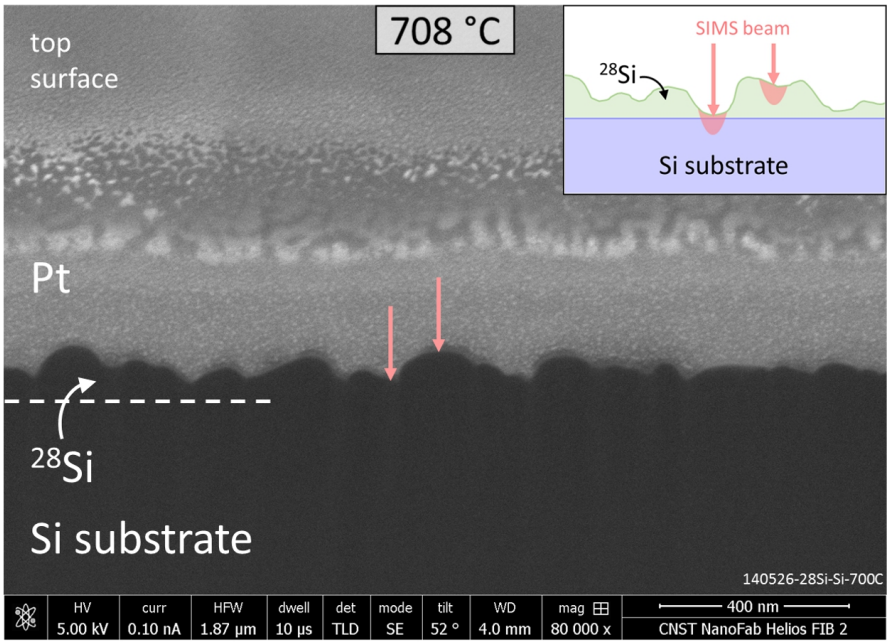

Figure 5.14: SEM tilted cross-sectional micrograph of a ^{28}Si film deposited at 708 °C at DC–3. The tilt angle is 52°. The Si(100) substrate and ^{28}Si film are indistinguishable and appear dark in the lower half of this micrograph with a dashed line representing the film-substrate interface. The light region above the film is Pt deposited to protect the sample. The top surface of the Pt is visible in this tilted image. The surface of the ^{28}Si film appears very rough with a maximum surface width $\Delta z \approx 80$ nm. The thickest areas of the film are almost 120 nm. Sputtering this surface in a SIMS measurement introduces a measurement artifact. The inset shows a cartoon of a rough ^{28}Si film being sputtered by SIMS beams (arrows) in a thick and thin region of the film. Sputtering in the thick region results in isotope signals from the ^{28}Si film, while sputtering in the thin region results in isotope signals partially from the substrate.

induced SIMS measurement artifact need to be considered as a lower bound on the true film enrichment. Conversely, the measured ^{29}Si and ^{30}Si isotope fraction for these samples are an upper bound. This means that the isotope fractions are not larger than the measured values, but they may be smaller due to the SIMS artifact inflating the results. In this work, however, only SIMS measurements which are believed to show an accurate minimum value for ^{29}Si and ^{30}Si isotope fractions are reported.

The accuracy of the reported enrichment values of the 812 °C sample shown above in Fig. 5.12 can be evaluated by comparing them to those of another sample similar sample which does not show evidence for a large amount of surface roughness. A sample deposited with a substrate temperature of approximately 808 °C using the low pressure mode of the ion source was measured by SIMS and showed a more typical depth profile without obvious effects from a measurement artifact. Also, large scale roughness was not observed in a top down SEM micrograph of this sample due to it being mostly amorphous from a higher than usual N content, which will be discussed later. The SIMS depth profile of area of highest enrichment for this sample is shown in Fig. 5.15. The ^{28}Si (circles), ^{29}Si (squares), and ^{30}Si (triangles) isotope fractions are shown vs. the sputter depth into the sample. Beyond the initial signal due to some surface contamination, the ^{29}Si and ^{30}Si isotope fractions do show an extended minimum between a depth of 22 nm and 81 nm. The average isotope fraction values were calculated by averaging the data in this region. Beyond a depth of about 81 nm, the isotope fractions begin to increase to their natural abundance values (dotted and dashed lines) in the transition into the substrate, which is marked by the shaded region. The interface between the film and the substrate is estimated to be at a depth of approximately 112 nm, which also gives a value for the film thickness.

Also shown for comparison is the ^{29}Si isotope fraction depth profile (squares and solid line) from the 812 °C sample shown above in Fig. 5.12. The depth scale of this profile was shifted by compressing it so that the locations of the substrate interfaces of this profile and the depth profiles of the 812 °C sample were aligned

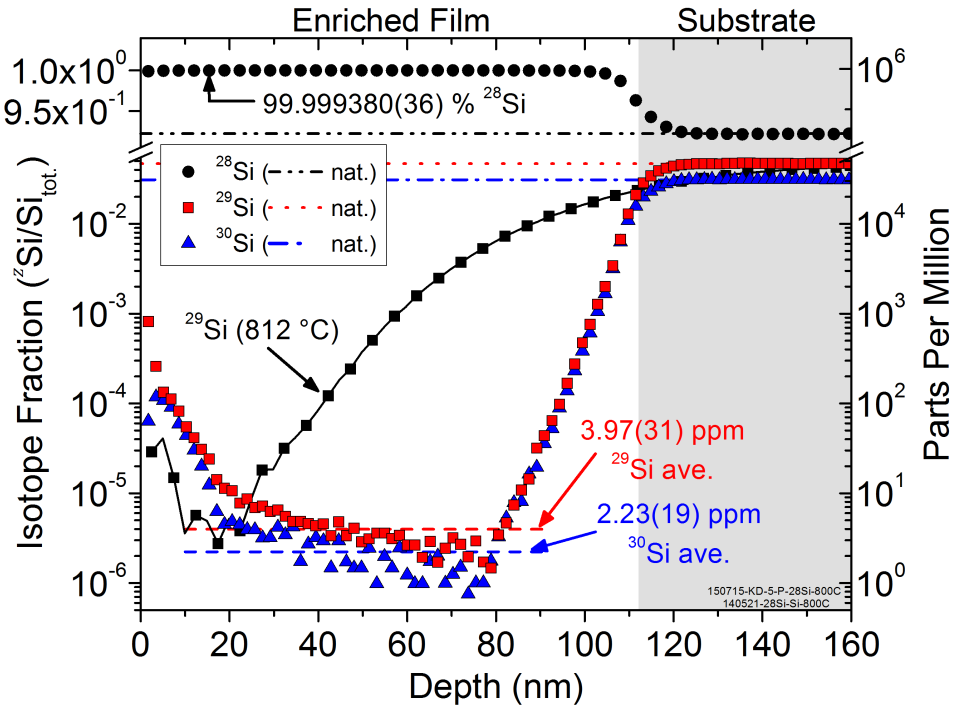

Figure 5.15: SIMS depth profile of a ^{28}Si sample deposited at 808 °C using the low pressure mode at DC–3. ^{28}Si (circles), ^{29}Si (squares), and ^{30}Si (triangles) isotope fractions are shown vs. sputter depth. After some surface contamination, the ^{29}Si and ^{30}Si isotope fractions reach an extended minimum between a depth of 22 nm and 81 nm where they are averaged. The average ^{29}Si isotope fraction in the film is 3.97 ppm, and the average ^{30}Si isotope fraction is 2.23 ppm (dashed lines). At a depth of 81 nm the ^{29}Si and ^{30}Si isotope fractions increase to their natural abundance values in the substrate (shaded region). The natural abundance values for each isotope (dotted and dashed lines) are also shown for reference. The interface between the film and the substrate is estimated to be at a depth of 112 nm. For reference, the ^{29}Si depth profile for the 812 °C sample (squares and solid line) is plotted showing the effect of surface roughening on the SIMS measurement. The depth scale of this profile was shifted to match the film thickness of the 808 °C sample.

with each other. Clearly, the depth profiles of the two sample are qualitatively different. The ^{29}Si and ^{30}Si profiles of the 808 °C sample do not show signs of the surface roughness induced SIMS measurement artifact. Unlike the 812 °C sample, the ^{29}Si and ^{30}Si isotope fraction values of the 808 °C sample remain low through most of the film thickness. These depth profiles seem to support the conclusion that the depth profiles with elevated isotope fractions throughout the film, such

as those of the 812 °C sample, are not due to Si isotope self-diffusion at elevated temperatures.

Despite the qualitative differences of the depth profiles of the two samples, the minimum in ^{29}Si isotope fractions for the two samples appears to be similar. The average measured ^{28}Si isotope fraction in this film is 99.999380(36) %. The average residual ^{29}Si isotope fraction is $3.97(31) \times 10^{-6}$ (3.97(31) ppm), and the average ^{30}Si isotope fraction is $2.23(19) \times 10^{-6}$ (2.23(19) ppm) (dashed lines). A second area of this sample was also measured giving an average ^{29}Si isotope fraction for the two areas on the sample of 4.33(23) ppm. The average ^{29}Si isotope fraction in the more highly enriched area of this sample is quite similar in value to the average measured value of the 812 °C samples, which is 4.32(46) ppm, and they agree within their uncertainties. This agreement is possibly partially coincidental because they were deposited with slightly different deposition parameters. However, this result does show that SIMS measurements of samples exhibiting the roughness induced measurement artifact can give accurate enrichment values, with the caveat that they still may be bounds on the true film enrichment values.

5.5.4 High Pressure Mode Sample

All of the previous samples discussed in this chapter were deposited using the low pressure working mode of the ion source, but as mentioned in a previous section discussing the deposition parameters of ^{28}Si at DC–3, it is not clear if the benefit of a significantly increased ^{28}Si ion beam current produced in the high pressure mode is offset by a lower mass resolving power. Figure 5.5 showed that the total ^{28}Si current

of the high pressure mode was typically a factor of five larger than the currents produced in the low pressure mode. An increased current is beneficial because it allows for faster growth rates which enables production of thicker samples in a typical deposition, and it reduces the relative adsorption rate of gaseous species into the ^{28}Si film, including SiH_4. However, Fig. 5.5 also showed that the mass resolving power was lower than had been observed using the low pressure mode with a measurable ion current signal between the 28 u peak and the 29 u peaks of approximately 8 nA. This current level may result in a lower geometric selectivity and thus lower realized enrichments. Additionally, the high pressure mode requires higher pressures in the ion source that result in a background pressure during deposition three times higher than the highest pressures experienced by samples deposited using the low pressure mode. Higher partial pressures of SiH_4 may also decrease the enrichment level in the samples.

In order to examine the viability of the high pressure mode as a source of highly enrich ^{28}Si and compare its effectiveness to the low pressure mode, SIMS was used to measure the isotope fractions of a sample deposited with a substrate temperature of approximately 421 °C at DC–3 using the high pressure mode of the ion source. A SIMS depth profile of the area of highest enrichment of this sample is shown in Fig. 5.16.

The ^{28}Si (circles), ^{29}Si (squares), and ^{30}Si (triangles) isotope fractions are shown vs. the sputter depth into the sample. Beyond an initial signal due to a small amount of surface contamination, the ^{29}Si and ^{30}Si isotope fractions show an extended minimum with very little variation in value. At a depth of around 290 nm,

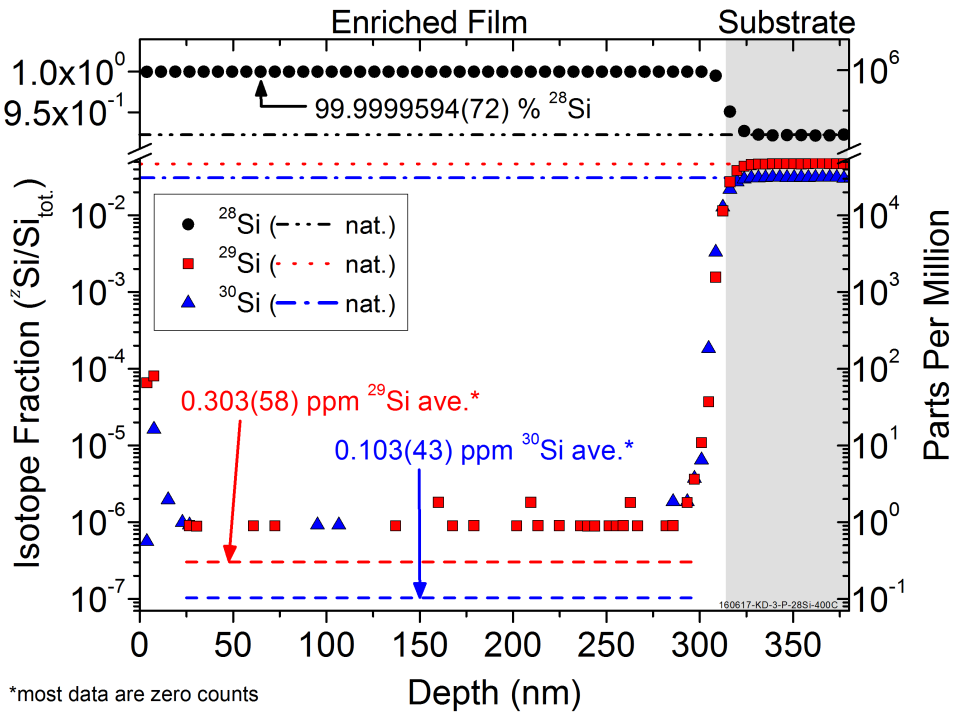

Figure 5.16: SIMS depth profile of a ^{28}Si sample deposited at 421 °C at DC–3 using the high pressure mode. ^{28}Si (circles), ^{29}Si (squares), and ^{30}Si (triangles) isotope fractions are shown vs. sputter depth. The average ^{29}Si isotope fraction in the film is 0.303 ppm, and the average ^{30}Si isotope fraction is 0.103 (dashed lines). Many data in this region are zero counts in the SIMS cycles, especially for ^{30}Si. The natural abundance values for each isotope (dotted and dashed lines) are also shown for reference. The isotope fraction values were averaged between 11 nm and 290 nm, where the ^{29}Si and ^{30}Si isotope fractions begin to increase to their natural abundance values. The interface between the film and the substrate (shaded region) is estimated to be at a depth of 315 nm.

the isotope fractions begin to increase to their natural abundance values (dotted and dashed lines) in a fairly abruptly transition into the substrate, which is marked by the shaded region. The interface between the film and the substrate is estimated to be at a depth of approximately 315 nm, which also gives a value for the film thickness.

The average measured ^{28}Si isotope fraction in the film is 99.9999594(72) %. The average residual ^{29}Si isotope fraction is $3.03(58) \times 10^{-7}$ (0.303(58) ppm), and

the average ^{30}Si isotope fraction is $1.03(43) \times 10^{-7}$ (0.103(43) ppm) (dashed lines). These averages lie below where the data appears because many of the SIMS measurement cycles in this region contained zero counts and thus the data does not appears on this semi-log plot. This is especially true of the ^{30}Si data. The averages were calculated from the data between 11 nm and 290 nm. The enrichment level of this sample is comparable to that of the most highly enriched samples deposited at DC–3 that appear on the enrichment progression timeline in Fig. 4.2. The ^{29}Si isotope fraction of this sample is nearly identical to that of the 610 °C sample, although the ^{30}Si isotope fraction of this sample was lower, which resulted in the ^{28}Si isotope fraction for this 421 °C high pressure sample being slightly higher than that of the 610 °C sample. A second area on this sample was measured by SIMS also which resulted in an average ^{29}Si isotope fraction between the two measurements of 0.355(41) ppm.

The ^{28}Si ion current achieved for this sample was approximately 3.00 μA, which is the highest for any sample in this work. This ion current, which was only achieved using the high pressure mode, combined with a relatively small deposition spot size of approximately 3.7 mm^2 resulted in a high deposition rate of 3.94 nm/min. This high rate led to the very low ^{29}Si and ^{30}Si isotope fractions measured in this sample despite the higher background pressure during deposition. Additionally, the lowered mass resolving power and high overlap current between peaks in the mass spectrum do not appear to reduce the realized mass selectivity and enrichment in any significant (or at least measurable) way. This measurement showed that the high pressure mode of the ion source is not only viable for pro-

ducing highly enriched ^{28}Si films, but from the perspective of enrichment, it is the preferred deposition mode because of the high deposition rates that are achievable while maintaining extremely high levels of ^{28}Si enrichment, and conversely, extremely low levels of ^{29}Si isotope fractions. These enrichments are comparable to the most highly enriched ^{28}Si samples produced in this work and are potentially suitable for QI experiments such as a measurement of the dependance of electron coherence times on ^{29}Si concentration in the single spin regime, which was discussed at the beginning of Chapter 4.

SIMS measurements of samples deposited at DC–3 show that overall, a reduction of more than a factor of five in the ^{29}Si isotope fraction of the most highly enriched sample was achieved compared to that of the previous most highly enriched sample deposited at LC–2, which can be seen in the enrichment progression timeline in Fig. 4.2. These SIMS measurements also shows that these extremely high enrichments are achievable both for samples deposited with elevated substrate temperatures, and for samples deposited using the high pressure mode of the ion source.

5.6 Epitaxial Deposition

5.6.1 Context

Epitaxial deposition of Si and other semiconductors at low temperature has been extensively studied and characterized via molecular beam epitaxy (MBE) experiments. Eaglesham *et al.* showed for the first time in 1990 that there exists a

critical thickness for epitaxy, h_{epi}, at a given deposition temperature [118]. Beyond this thickness, epitaxy breaks down and the film becomes amorphous. That study found that for a deposition rate of around 0.4 nm/min and a substrate temperature of 200 °C, $h_{\text{epi}} = 25$ nm for Si(100). At a deposition temperature of 300 °C, h_{epi} increased to 120 nm. h_{epi} was found to increase exponentially with increasing deposition temperature with an activation energy of about 0.4 eV, although this value is dependent on the deposition rate. The concept of a critical epitaxial thickness is only valid for these lower temperatures and typical deposition rates of a few nm/min. Above a temperature of 500 °C, solid phase epitaxy (SPE) begins to dominate the growth because the recrystallization front propagates faster (4.2 nm/min) than the deposition rate, which effectively extends h_{epi} to be infinite. This regime is sometimes referred to as unlimited epitaxy.

Numerous research groups later studied low temperature Si epitaxy phenomena, and some of these efforts were nicely summarized by Eaglesham [119]. For low temperature MBE of Si and Ge and other similar deposition methods including sputter deposition and ion assisted deposition (IAD), it is observed that an amorphous phase eventually develops after epitaxial growth. Prior to this amorphous phase, an epitaxial but highly defective region forms in the film [109, 110, 120–122]. In this intermediate layer before amorphization occurs, the most apparent defects observed by TEM are stacking faults and microtwins. The epitaxial, defective, and amorphous regions of a Si film from Ref. [109] are seen in a cross-sectional TEM micrograph in Fig. 5.17, separated by dashed lines. This Si(100) film was deposited at 270 °C by IAD. The bottom of the film (I) is epitaxial and defect free, then the film

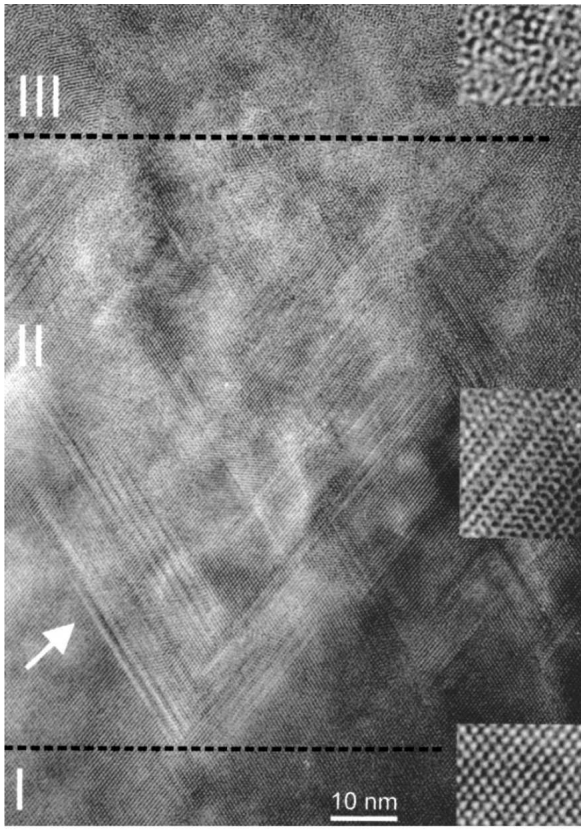

Figure 5.17: TEM cross-sectional micrograph of a Si(100) film deposited at 270 °C by IAD. Three visible regions are separated by dashed lines and include an epitaxial region (I) above the substrate (substrate not shown), a defective region (II) approximately 80 nm thick with visible stacking faults, and an amorphous region (III) with nanocrystallites. The arrow indicates several stacking faults on {111} planes. Insets show magnified views of each region. (from Ref. [109])

becomes defective above that in the middle region (II). Stacking faults are visible in this region (marked by the arrow) running along the {111} planes. The film then becomes amorphous beyond h_{epi} in the top region (III). The insets show magnified views of the three regions where the crystallinity is clearly visible. The density of stacking faults has been seen to generally increase with increasing deposition temperature [110] until h_{epi} becomes unlimited at higher temperatures. Another morphological feature frequently seen in similar TEM micrographs of epitaxial thin films is the formation of pyramidal structures bounded by the {111} stacking faults,

which result in a large roughness at the interface between the defective region and the amorphous region. Locally, the transition to the amorphous region is fairly abrupt, however.

There have been several proposed explanations for the existence of h_{epi} and the breakdown of an epitaxial layer into a defective layer and finally an amorphous layer in low temperature Si deposition, which are summarized in Ref. [119]. One model attributes the formation of the expitaxial layer to H incorporation during deposition [123]. H then could segregate and accumulate at the growth surface and disrupt the epitaxy by altering the nominal bonding pattern of the lattice. The critical concentration of H for breakdown to occur is expected to be around 2×10^{19} cm^{-3}. Experimental observations of the effect of H coverage on epitaxy seem to indicate, however, that H cannot solely be responsible for the epitaxial breakdown in thin films [119, 124] because epitaxy is possible on H terminated surfaces. Another explanation for the epitaxial breakdown is the accumulation of defects in the depositing film until epitaxy is not sustainable [125]. This mechanism, however, requires very large defect densities, possibly as high as 1×10^{14} cm^{-2}. Estimates of the density of extended defects in Si(100) put the number much lower at around 1×10^{7} cm^{-2} [119], which seems to rule out defect buildup as the cause of the amorphous transition. Finally, Eaglesham *et al.* propose that roughening of the growth surface itself is the cause of the breakdown of an epitaxial film into an amorphous one in low temperature Si epitaxy [126]. Roughening of the surface during deposition may be due to several factors including the presence of impurities, anisotropic surface diffusion, or faceting of the surface.

Si low temperature epitaxial deposition by MBE can be augmented using energetic (i.e. hyperthermal energy) ions with tens of eV of kinetic energy, as briefly discussed in Chapter 1. The Si source target can be sputtered by ions to produce a flux of Si with hyperthermal energy, or ions such as Ar or Xe can be used to bombard the surface of the sample during Si epitaxial deposition. In addition to ion assisted deposition, mentioned above, these techniques are also sometimes referred to as ion beam assisted deposition, ion enhanced deposition, or ion enhanced epitaxy, but they will be collectively referred to as IAD here. These techniques use hyperthermal energy ions to impart energy mostly in the form of momentum into the sample during deposition, which has the effect of enhancing the epitaxial quality of the film. Epitaxial deposition of Si and other elements has been demonstrated using IAD with qualitatively similar results to MBE in terms of a limiting epitaxial thickness and stacking fault formation, discussed above. However, IAD has been shown to extend h_{epi} to larger thicknesses for a given deposition temperature and rate. Conversely, IAD can achieve the same h_{epi} as MBE but at a lower temperature [109, 120, 121, 127–129]. Experimental examples of the benefits of IAD include extending h_{epi} to approximately 1 μm for a deposition at 300 °C and a growth rate of 6 nm/min [120], and lowering the temperature required for achieving unlimited epitaxy to around 390 °C, even at very high deposition rates of 300 nm/min [109].

While Si IAD achieves enhanced epitaxy using a flux of hyperthermal ions of a different element, ion beam epitaxy (IBE) achieves a similar enhancement of epitaxial deposition using ions of the material being deposited. This technique, which typically generates the ions from an ion beamline, has been studied and used for de-

position of Si, Ge, and other materials, as discussed in Chapter 1. Research groups studying IBE of ^{28}Si have demonstrated epitaxial deposition of varying crystalline quality on Si(100) with similar results to IAD. Al-Bayati *et al.* demonstrated IBE of ^{28}Si with 50 eV ions [42]. Films deposited using a substrate temperature of 400 °C were shown by TEM to be epitaxial but defective with stacking faults and twins. Tsubouchi *et al.* used 40 eV ions and a deposition temperature of 600 °C [43] to demonstrate epitaxy. TEM analysis showed that the films were epitaxial but likely contained a high density of dislocations.

Rabalais *et al.* extensively studied the relationship between the epitaxial quality of ^{28}Si films and the ion energy and substrate temperature [51]. They demonstrated epitaxial deposition of varying quality with deposition temperatures between 40 °C and 290 °C and ion energies between 8 eV and 50 eV. RHEED and TEM analysis showed that for 15 eV ions deposited at 160 °C and below, h_{epi} was limited to less than 15 nm. ^{28}Si films deposited at 160 °C but an increased ion energy of 20 eV were found to be epitaxial with no visible stacking faults. Additionally, films deposited with 15 eV ions but an increased substrate temperature of 290 °C were also epitaxial. Their research showed that for a given deposition temperature, high-quality epitaxial deposition occurred when using ions with energies within a certain optimal range. The ^{28}Si ion energy that resulted in the lowest temperature epitaxial deposition was 20 eV.

Other IBE experiments also show optimal epitaxial deposition with ion energies around 20 eV including Matsuoka and Tohno, who observed that the highest quality epitaxial growth occurred with 25 eV Si ions deposited at 400 °C, accord-

ing to RHEED measurements [130]. 50 eV ions produced epitaxial films, but with stacking fault densities around 1×10^{10} cm^{-2}. Deposition using higher ion energies produce more defective films, even at elevated deposition temperatures. Depositing Si at 740 °C with 200 eV ions resulted in epitaxial but highly defective films with TEM showing stacking faults and twin structures [131]. Molecular Dynamics simulations have also been used to predict a Si ion energy window for optimal epitaxial deposition on Si(100) [132]. These simulations showed that epitaxial deposition should be possible even for deposition temperatures below 200 °C when using ions with energies between 20 eV and 25 eV. These theoretical results along with the experimental results from Ref. [51] are represented on epitaxy phase diagrams in Fig. 5.18. The quality of the epitaxy is represented in these figures by several regions that occupy different portions of the deposition phase space of substrate temperature, T, vs. ion energy, E_i.

Figure 5.18 (a) shows an epitaxy phase diagram from Ref. [132] for the behavior of Si epitaxy as predicted my molecular dynamics simulations. Regions of unlimited epitaxy (I) and high-quality ion enhanced epitaxy (III) as well as regions where epitaxy is defective and limited (i.e. a finite h_{epi}) by lattice registry errors (II) and vacancy formation (IV). T_{epi} is the temperature above which unlimited epitaxy is achievable with conventional MBE. T^*_{epi} is the temperature above which hyperthermal ions can enhance the films epitaxial quality, for a given deposition rate. The phase boundary between limited and enhanced epitaxy at T^*_{epi} occurs near E_d, which is the energy threshold for lattice damage due to the ions and is about 25 eV for Si deposited on Si(100). This indicates that damage caused by ions is beneficial

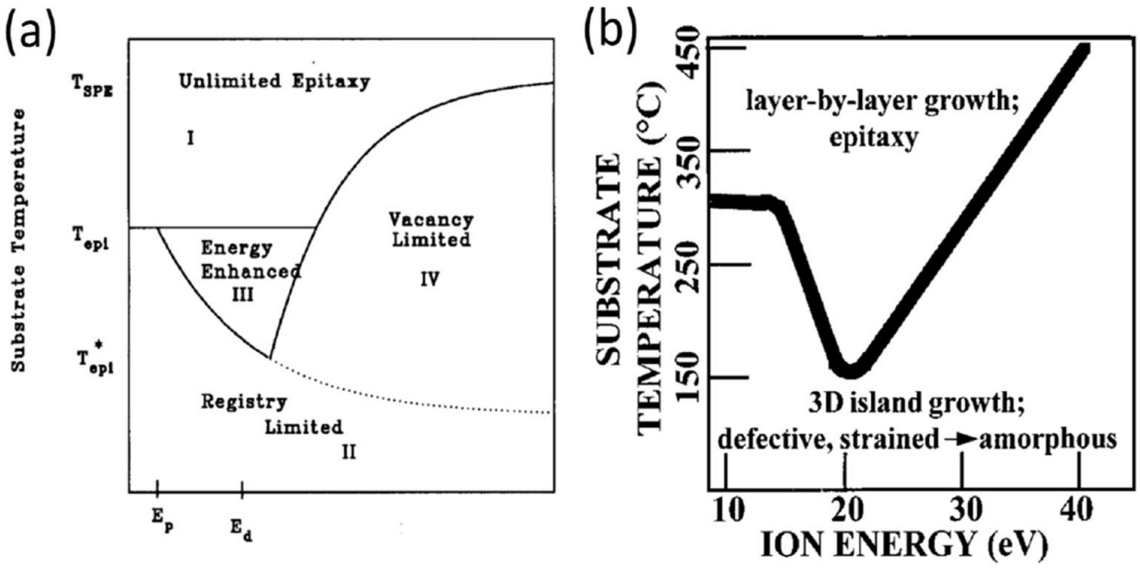

Figure 5.18: Theoretical, (a), and experimental, (b), phase diagrams for Si ion beam epitaxy in the deposition phase space of substrate temperature, T, vs. ion energy, E_i. (a) Si epitaxy phase diagram based on molecular dynamics simulations of the qualitative behavior of the epitaxy for regions of unlimited (I) and high-quality ion enhanced epitaxy (III) as well as regions of limited, defective epitaxy (II and IV). $T_{\rm epi}$ is the temperature above which unlimited epitaxy is achievable with MBE, and $T^*_{\rm epi}$ is the temperature above which hyperthermal ions enhance epitaxy. E_d is the energy threshold for lattice damage due to ions (from Ref. [132]). (b) Qualitative Si epitaxy phase diagram based on experimental results. TEM and RHEED analysis of ^{28}Si films deposited using various ion energies and substrate temperatures were used to categorize deposition as either high-quality epitaxy (upper region) or defective growth leading to an amorphous phase (lower region) (from Ref. [51]).

to the epitaxial quality.

Panel (b) of Fig. 5.18 shows an epitaxy phase diagram from Ref. [51] that is similar to the one in (a) and is based on experimental results. TEM and RHEED analysis of ^{28}Si films deposited onto Si(100) using various ion energies and substrate temperatures were used to define the phase boundary between high-quality and defective epitaxy. The epitaxial deposition was categorized as either high-quality epitaxy (upper region) or defective, limited epitaxy (lower region) with a finite $h_{\rm epi}$ leading to an amorphous phase. The boundary between the two epitaxial growth

modes is qualitatively similar to the one in panel (a) and shows a kink where high-quality epitaxy is possible at a minimum substrate temperature of 160 °C and an ion energy of 20 eV.

The energy deposited into the growth surface by hyperthermal ions produces several effects beneficial to epitaxy. Ions can transfer energy to the film through neutralization, which should be approximately the ionization potential, 8.15 eV [51]. This energy can excite nearby atoms and enhance their mobility. Molecular dynamics simulations show that hyperthermal ions can create vacancies that facilitate adatom incorporation [133] during MBE and also suppress the formation of 3D islands and step pinning from impurities [127,128]. The optimal ion energy of around 20 eV, observed to lead to higher quality epitaxy, seems to match both the critical energy for defect formation in Si of 20 eV to 40 eV as well as an average Si displacement energy of 13 eV to 15 eV [58,134,135]. Calculations show that approximately 70 % of 10 eV Si ions impinging on Si(111) surfaces penetrate about two layers into the surface and stop in an intersticial site before diffusing to the surface to participate in the film growth. The impact and transfer of momentum from the ions leads to the formation of dangling bonds and mobile defects such as Frenkel pairs. When the concentration of these defects is high enough, they can facilitate ordered recrystallization and epitaxial growth [136]. Simulations also show that ions with energies greater than 50 eV begin to create more permanent defects and less of the mobile, epitaxy-enhancing defects [51], which is supported by the experimental observations mentioned previously.

5.6.2 Morphology of Films with Deposition $T > 600$ °C

^{28}Si samples were deposited at sample location DC–3 with a range of substrate temperatures, as was mentioned previously in this section. Initially, deposition temperatures between 610 °C and 1041 °C were chosen in order to facilitate high-quality epitaxial growth on Si(100) substrates. Depositing at these temperatures using ions with a typical average ion energy $E_i \approx 33$ eV for these samples should result in a growth mode dominated by smooth layer-by-layer growth, in accordance with the epitaxy phase diagram for IBE in Fig. 5.18 (b). Ten of these initial samples, of which there were 12 in total, were deposited on boron-doped (University Wafer) substrates that were not cleaned *ex situ* and were loaded into the vacuum chamber with a native oxide. The final two ^{28}Si samples deposited in this initial group were prepared *ex situ* using an HF etch, and one of them was deposited on a phosphorous-doped substrate.

5.6.2.1 RHEED

RHEED was used as an initial check on the epitaxial nature and surface morphology of these samples immediately after deposition. The RHEED patterns of all of the samples deposited with a substrate temperature above 600 °C showed that they were crystalline and epitaxially aligned to the substrate due to the presence of Si(100) diffractions spots. RHEED can only provide a limited view of the overall epitaxial quality of the samples because it is only sensitive to the top few layers, however, it was often used intermittently throughout the deposition to monitor the

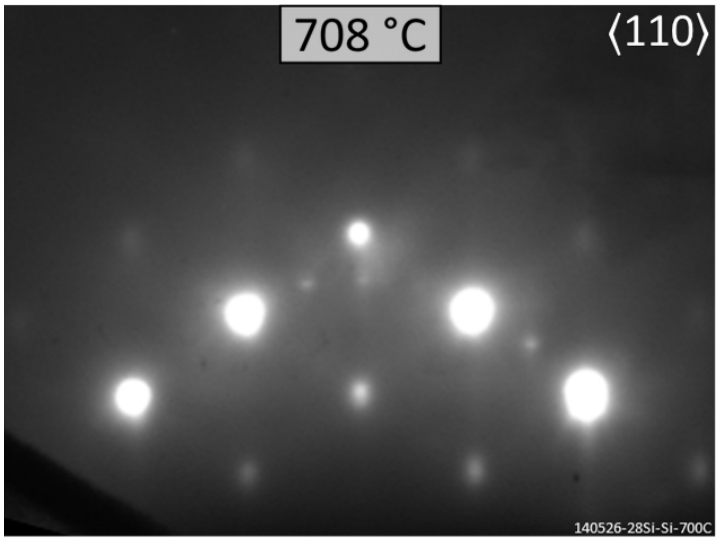

Figure 5.19: RHEED diffraction pattern of a ^{28}Si sample deposited at 708 °C at DC–3. This image was acquired with the sample at the deposition temperature and the electron beam in the ⟨110⟩ direction. The presence of (1×1) bulk Si diffraction spots in this pattern indicate that the film is crystalline and aligned to the Si(100) substrate. Additionally, this pattern of spots corresponds to a 3D transmission-type pattern for diffraction from a rough surface. Faint (2×1) spots between some of the (1×1) spots are visible and are likely due to part of the electron beam diffracting from the substrate outside of the deposition spot.

crystallinity as a function of deposition thickness. The same crystalline RHEED pattern was typically seen from the initial stages of deposition through to the end for these samples. A typical RHEED pattern for these higher temperature ^{28}Si samples is shown in Fig. 5.19. This sample was deposited at 708 °C and is about 120 nm at its thickest. The image was acquired with the substrate at the deposition temperature and the electron beam in the ⟨110⟩ direction. It is clear from the presence of (1×1) bulk Si diffraction spots that the ^{28}Si film is crystalline and aligned with the Si(100) surface of the substrate. However, this pattern is quite different from the RHEED pattern shown in Fig. 5.1 for a (2×1) reconstructed Si(100) surface where each diffraction streak collapses into a point for a flat surface. This pattern

(Fig. 5.19) corresponds to a 3D transmission-type diffraction pattern where diffraction occurs not at rods, but at a 3D matrix of reciprocal space points. 3D diffraction indicates that the surface of the deposited film is rough such that there is significant transmission of the electron beam through raised features such as mounds or large islands on the surface. Also seen in this RHEED pattern are faint (2×1) spots between some of the (1×1) spots, which are likely due to part of the RHEED electron beam diffracting from an area of the substrate outside of the ^{28}Si deposition spot concurrent with diffraction from the film. A SEM cross-sectional micrograph of this 708 °C sample was previously shown in Fig. 5.14 where the rough surface is obvious. The surface roughness of these samples observed by RHEED and then by SEM, which is discussed further below, is unexpected considering the phase diagrams for smooth epitaxy in Fig. 5.18 and the comparatively high deposition temperatures (i.e. $>$ 600 °C) used for this initial set of samples.

RHEED also shows that the rough surfaces of these samples deposited with substrate temperatures above 600 °C develop higher index microfacets. Figure 5.20 shows RHEED images for two ^{28}Si samples deposited at DC–3 with clear signs of faceting on a rough surface. The (1×1) bulk Si diffraction spots present in the patterns of both of these samples indicate that the films are crystalline and aligned to the Si(100) surface, similar to the sample represented in Fig. 5.19. The 3D transmission patterns here indicate a rough surface. Figure 5.20 (a) is the diffraction pattern for a sample deposited at 610 °C, and it was acquired with the sample at the deposition temperature and the RHEED electron beam in the ⟨110⟩ direction. This sample was measured to be approximately 162 nm thick. In the pattern, diffraction

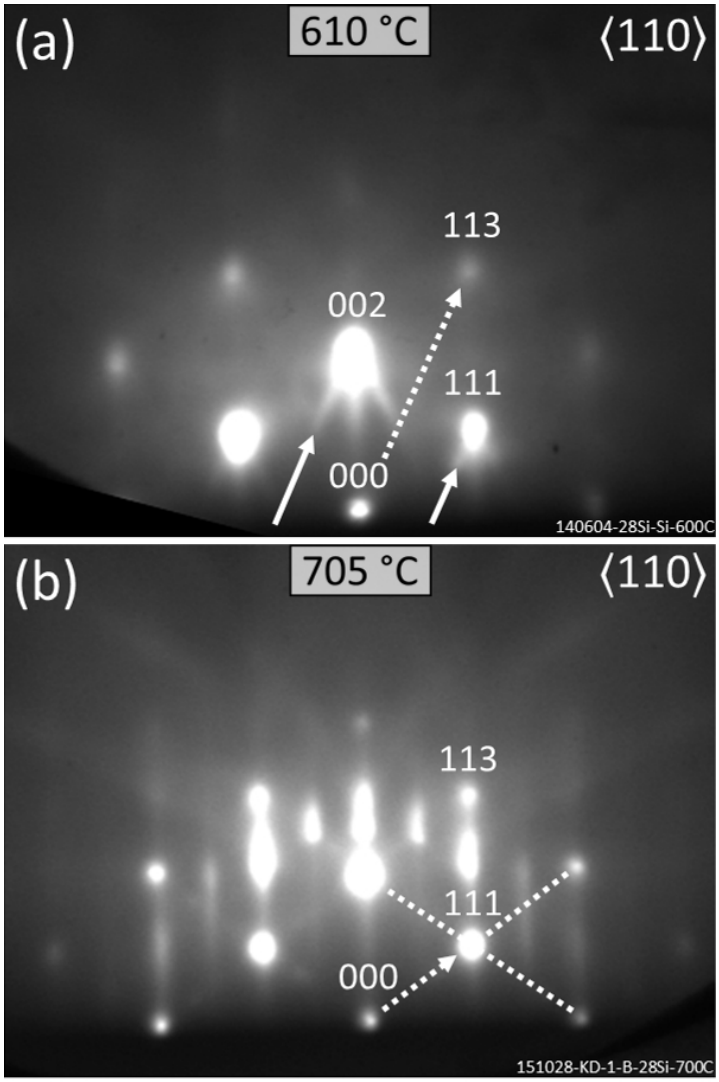

Figure 5.20: RHEED diffraction patterns of two ^{28}Si samples deposited at 610 °C, (a), and 705 °C, (b), at DC–3. Both images were acquired with the samples at the deposition temperatures and the electron beam in the ⟨110⟩ direction. The (1×1) bulk Si diffraction spots present in both patterns indicate that the films are crystalline and aligned to the Si(100) surface. They are also 3D transmission patterns indicating a rough surface. In (a), additional lines forming a "chevron" pattern emanate from several of the spots (solid arrows) indicating diffraction from microfacets in the {113} family of planes. These lines are parallel to the dashed arrow pointing from the (000) spot to the (113) spot, indicating the direction of the facet face. In (b), additional lines can be seen connecting diffraction spots, highlighted on the right by the dashed lines. These lines run along ⟨111⟩ directions, as indicated by the arrow pointing from the (000) spot to the (111) spot, and they are due to diffraction from {111} microfacets. Si(100) (2×1) spots are also seen in (b) likely due to part of the electron beam diffracting from the substrate outside of the deposition spot.

intensity from additional lines are observed emanating down and outward from some of the spots, marked by the solid arrows. These lines form "chevron" patterns and indicate diffraction from microfacets in the {113} family of planes. This classification is evident when noting that these lines run parallel to the dashed arrow pointing from the (000) spot to the (113) spot, indicating the plane of the facet face to be {113}. These same {113} facet "chevron" patterns are seen on a number of other RHEED patterns for samples deposited with deposition temperatures above 600 °C.

Panel (b) of Fig. 5.20 is the diffraction pattern for a sample deposited at 705 °C. It was acquired with the sample at the deposition temperature and the RHEED electron beam in the ⟨110⟩ direction. This sample was measured to be approximately 144 nm at its thickest. Similar to the pattern in panel (a), this pattern shows diffraction intensity from additional lines connecting some of the adjacent 3D diffraction spots. These lines are visible in the left side of the image and are highlighted by the dashed lines in the right side of the image. The arrow pointing from the (000) spot to the (111) spot indicates that these diffraction lines run along ⟨111⟩ directions and are due to diffraction from {111} microfacets. Superimposed on the 3D pattern in this image is the nominal Si(100) (2×1) spot and rod pattern, which is likely due to part of the electron beam diffracting from an area of the substrate outside of the ^{28}Si deposition spot. It should be noted that this sample was actually deposited later and with a different preparation procedure than the other high deposition temperature samples discussed so far in this section, but the RHEED pattern of this sample is presented here because it is more illustrative of {111} faceting than those of other samples. The presence of microfacets and their

orientation on the surfaces of these ^{28}Si films are important pieces of information that provide insight on the growth mechanisms leading to the unexpected surface roughness.

5.6.2.2 STM

After deposition, the surface morphology of these samples was investigated by *in situ* STM and *ex situ* SEM as a primary means of evaluating the quality of the epitaxial growth as well as confirming and measuring the extent of the surface roughness observed by RHEED. Figure 5.21 shows an example of a filled state STM topography image of a ^{28}Si sample deposited at approximately 708 °C at DC–3, which had a RHEED pattern corresponding to a rough surface. The ^{28}Si film was measured by TEM to be 155 nm at the thickest. The roughness indicated in the RHEED pattern of this and similar samples is supported by the presence of large grain-like features visible in this micrograph. These features are approximately 200 nm wide and at least 1 μm long running diagonally from the bottom left to the top right of the image. A measure of the roughness of this surface is given by the total peak-to-valley surface width, i.e. the difference in height values between the highest peak and lowest valley in the STM topography. This surface width in this image is $\Delta z \approx 12.8$ nm. Other measurements of the value of the surface width for this sample including those from a SEM cross-sectional micrograph show that it is as much as 60 nm. The STM derived value may be smaller because the STM tip is too large to fit in between the valleys seen in the image and thus it

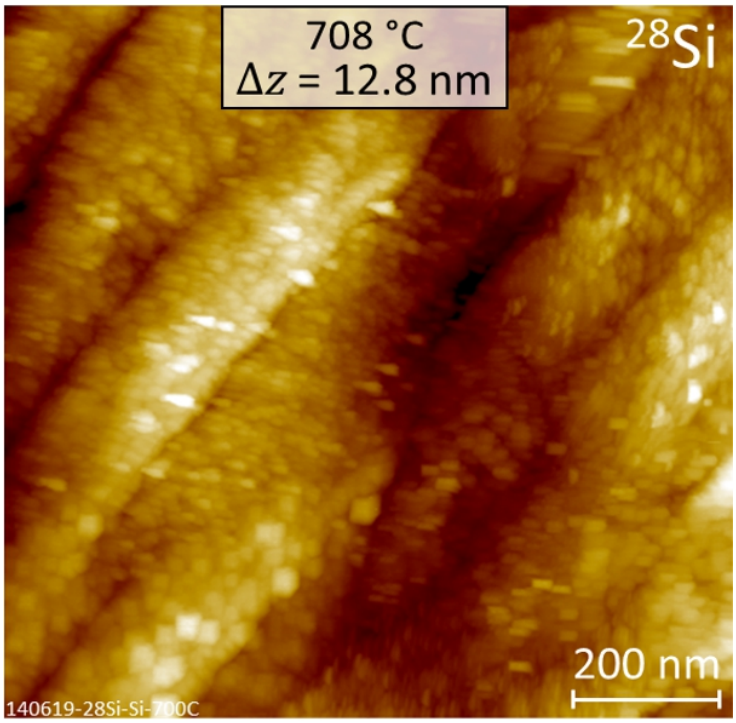

Figure 5.21: STM topography filled state image of a ^{28}Si sample deposited at 708 °C at DC–3. The image was acquired with a tip bias ≈ -1.8 V and a tunneling current ≈ 100 pA. This film is about 155 nm at its thickest and was deposited on a Si(100) substrate with no *ex situ* cleaning. Large grain-like features ≈ 200 nm wide are visible on the surface running diagonally from the bottom left to the top right of the image. The surface width determined from the topography is $\Delta z \approx 12.8$ nm.

cannot accurately measure the full range between valley and peak. Alternatively, it may be that the film is thinner in the region scanned by the STM. The difficulty STM has with accurately measuring the topography of very rough surfaces limits its usefulness compared to SEM for evaluating the morphology of these samples.

5.6.2.3 SEM

SEM was used *ex situ* to survey the surface morphology of numerous ^{28}Si samples deposited with a substrate deposition temperature above 600 °C at DC–3. SEM images presented in this section were acquired in collaboration with Dr. Joshua

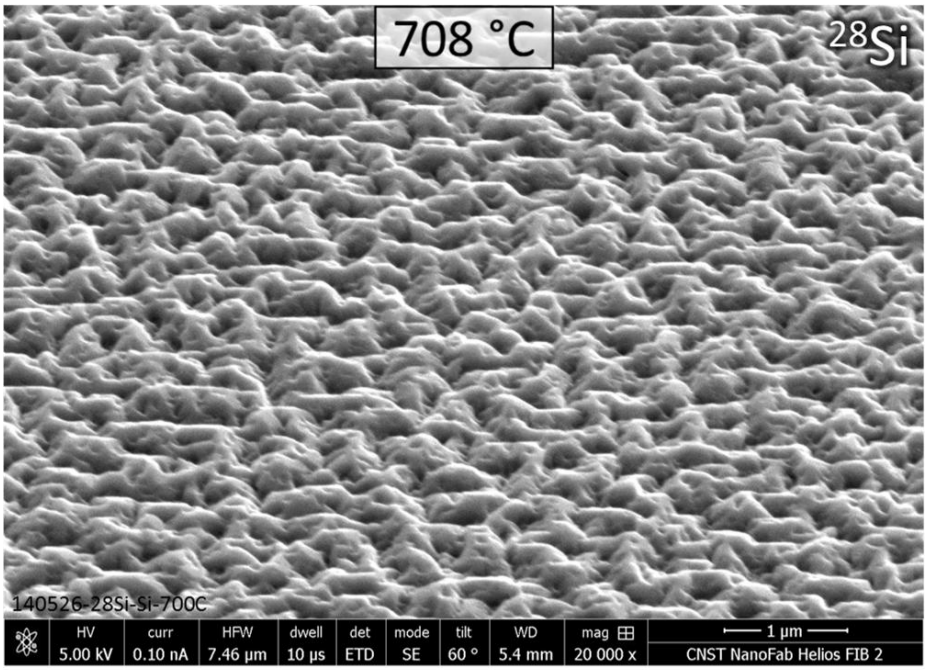

Figure 5.22: SEM tilted micrograph of the surface of a ^{28}Si film deposited at 708 °C at DC–3. The tilt angle of this micrograph is 60°. The substrate used for this sample was not cleaned *ex situ* and was loaded into the chamber with a native oxide. This film is almost 120 nm at its thickest. The surface morphology of the deposited film appears to be extremely rough with mounds or grain-like features that have an average length ≈ 440 nm. The longer side of some of the mounds appear to run left-to-right in the image indicating orientation with a ⟨110⟩ direction.

Schumacher (NIST) and Dr. Vladimir Oleshko (NIST). A tilted SEM micrograph of one of the first ^{28}Si samples deposited at DC–3 is shown in Fig. 5.22. The tilt angle of the image is 60°. The substrate used for this deposition was boron-doped and was not cleaned *ex situ* before being loaded into the vacuum chamber with a native oxide and being prepared *in situ* in the usual manner. This sample was deposited with a substrate temperature of approximately 708 °C and is almost 120 nm at its thickest, as measured in cross-section. A SEM cross-sectional micrograph of this sample was previously shown in Fig. 5.14. It is obvious from Fig. 5.22 that the surface morphology of this sample is extremely rough. The surface of the film is

covered with large mounds or grain-like features. The rough surface indicated by the RHEED image (Fig. 5.19) is clearly confirmed and understood to be due to these tall mounds visible in the micrograph. The tilt of the image makes it difficult to estimate the height of the mounds and their size in the direction running top-to-bottom in the image, but their estimated average size in the direction running left-to-right is approximately 440 nm. The longer side of some of the mounds appear to directly run left-to-right in the image possibly indicating orientation with a ⟨110⟩ direction. The crystallographic directions in SEM micrographs presented here are determined from the positioning of the samples in the SEM. This orientation of mounds or grains on the surface of the films is consistent with the indication from the RHEED images (Fig. 5.20) that {111} and {113} microfacets are present on the surface.

All of the ^{28}Si samples produced in this initial batch with substrate temperatures above 600 °C which were inspected with SEM showed similarly rough surfaces with mound formation, although with slightly varying morphologies. SEM micrographs of six of these samples deposited at various temperatures are shown in Fig. 5.23. The deposition temperatures for the samples in panels (a)–(f) were 610 °C, 708 °C, 804 °C, 812 °C, 920 °C, and 1041 °C respectively. All substrates used for these samples were boron-doped except for the sample in panel (c), which was phosphorous-doped. No *ex situ* cleaning was performed on the substrates used for these samples except for the sample in panel (c), which was etched with HF prior to being loaded into the vacuum chamber. Large mounds are visible on the surface of the 610 °C sample in the top-down micrograph in panel (a). The thickness of

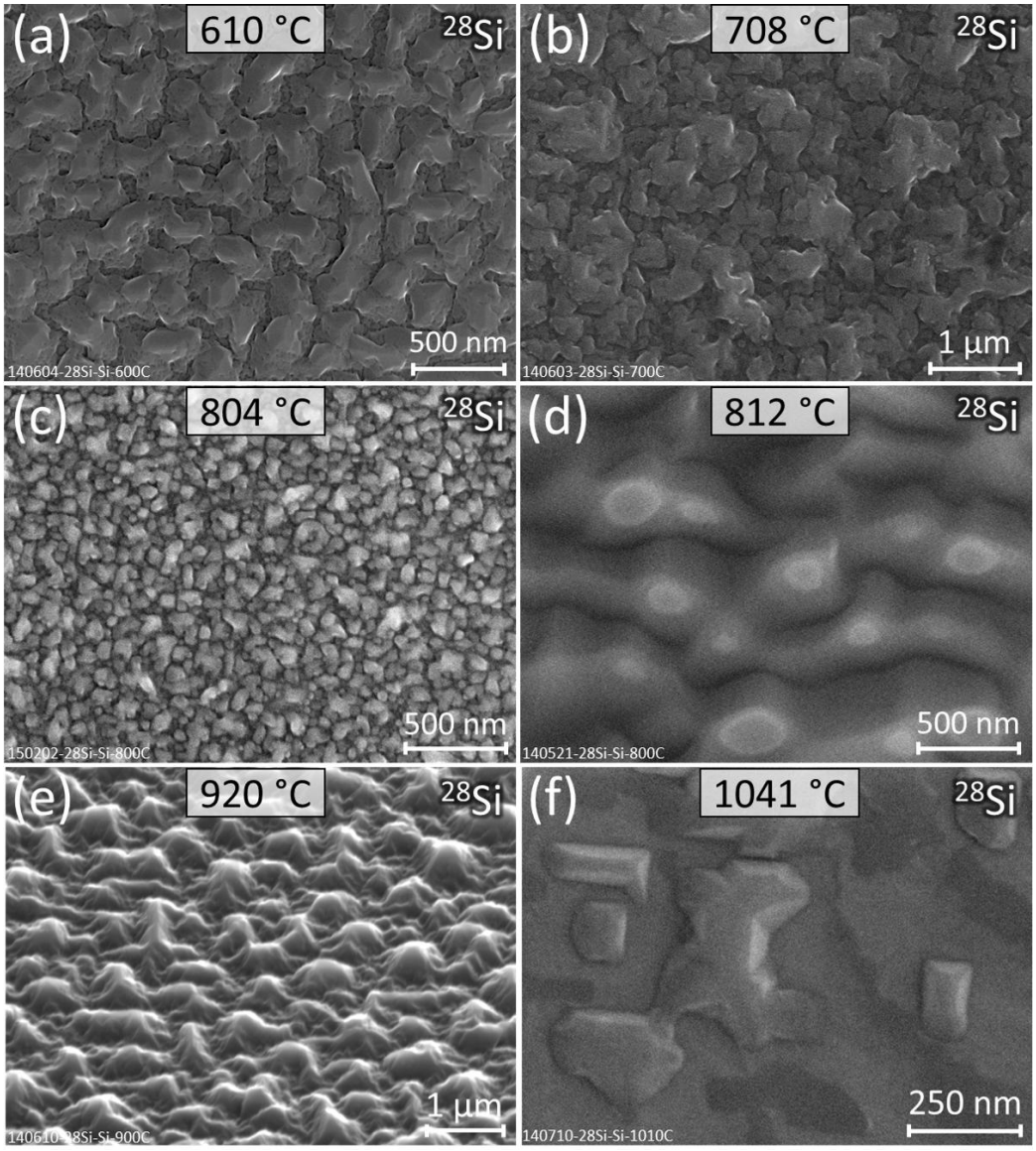

Figure 5.23: SEM top-down micrographs of the surface morphology of six ^{28}Si films deposited at DC–3 at 610 °C, (a), 708 °C, (b), 804 °C, (c), 812 °C, (d), 920 °C, (e), and 1041 °C, (f). No *ex situ* cleaning was performed on these substrates except for (c), which was etched with HF. (a) Mounds are apparent on a very rough surface with an average length $\approx$ 320 nm and faceted sides oriented top-to-bottom or left-to-right in $\langle 110 \rangle$ directions. (b) Irregularly shaped mound features are apparent with an average size $\approx$ 450 nm. (c) Smaller grains are apparent with an average length $\approx$ 180 nm. (d) Mounds are visible with an average length $\approx$ 780 nm and align in rows running left-to-right in a $\langle 110 \rangle$ direction. The larger grains in (d) compared to (c) may be due to the different cleaning procedures, despite similar temperatures. (e) 60° tilted image of hut-like mounds with faceted sides and an average length $\approx$ 1105 nm. (f) Several hut-like mounds are apparent on a smooth surface with sizes between $\approx$ 200 nm and 500 nm. These mounds have faceted sides oriented in $\langle 110 \rangle$ directions.

this sample measured by SIMS depth profiling was determined to be approximately 162 nm. The mounds appear generally elongated and are measured to have an average length $\approx$ 320 nm and an average width $\approx$ 175 nm. The length of the mounds is defined as the longer dimension here. The length and width of mounds in the SEM micrographs are determined from software analysis of the images using an autocorrelation function for finding repeating patterns. The values determined from multiple images were then averaged together to produce the values reported here, which have a 10 % relative uncertainty. Many of the mounds in panel (a) appear to be aligned in similar directions. They also appear to have faceted sides where the edges of the microfacets run top-to-bottom or left-to-right in the image indicating orientation with $\langle 110 \rangle$ directions. This observation of the presence of microfacets confirms the indications from the RHEED images (Fig. 5.20). The observed orientation is consistent with the microfacets being on {111} and {113} planes.

Panel (b) in Fig. 5.23 is a top-down micrograph showing the morphology of the surface of the 708 °C sample, which consists of irregularly shaped mound features with an average size $\approx$ 450 nm. The maximum thickness determined from SIMS depth profiles of this sample is approximately 126 nm. Note that the area of panel (b) is roughly four times larger than the area shown in (a). The mounds in panel (b) do not seem to be oriented in any particular direction. The surface of the 804 °C sample is shown in the top-down micrograph in panel (c). Smaller grain-like features are seen covering the surface of the film. The scale of panel (c) is the same as that of (a) and the average length of the grains in (c) is $\approx$ 180 nm. As mentioned above, the substrate used for the 804 °C sample in panel (c) was the only one in Fig. 5.23 which

was etched with HF. Panel (d) shows a top-down micrograph of a sample deposited at 812 °C, which has a maximum thickness determined from a SIMS depth profile to be approximately 158 nm. Despite the similar deposition temperature to that used for the sample in panel (c), the surface morphology of this sample is clearly qualitatively different, possibly due to the different cleaning procedure. Much larger mounds are seen on the surface, the edges of which are not as well defined as the features of the other samples in the other micrographs. The mounds on this sample appear to run together much more giving the surface more of a wavy appearance as opposed to the granular appearance of the other micrographs. This could indicate that the surface of this film is smoother than the others, however, the SIMS depth profile of this sample (Fig. 5.12) showed the characteristic measurement artifact for rough surfaces of a gradual increase in minor isotopes throughout the profile, as determined in a previous section in this chapter. Although the boundaries of the mounds in panel (d) are not as well defined as in the other micrographs in Fig. 5.23, the autocorrelation of this image gives an average width $\approx$ 250 nm and an average length $\approx$ 780 nm. These mounds also appear to approximately align in rows running left-to-right in the image, which is consistent with alignment to a $\langle 110 \rangle$ direction.

Figure 5.23 (e) is a 60° tilted micrograph showing the surface morphology of a sample deposited at 920 °C. Many hut-like mounds are visible on the surface with an average width $\approx$ 560 nm and an average length $\approx$ 1105 nm. These measurements were corrected for the tilt of the image. The thickness of this film was not directly measured, but the height of some of the mounds is estimated from the image to be roughly 400 nm. Many of these mounds do appear to have faceted sides giving

them the hut-like shape, and the long direction of several of them are clearly aligned either top-to-bottom or left-to-right in the image. It can be reasonably presumed that like in several of the other SEM micrographs shown here, the mounds in panel (e) are aligned to a ⟨110⟩ direction, although this cannot be confirmed because the positioning of the sample inside the SEM is not known. Finally, panel (f) is a top-down micrograph showing the surface morphology of the 1041 °C sample. The surface of this sample appears very different from the other samples shown here in that the film does not appear to be continuous. Several hut-like mounds are seen on an otherwise smooth surface. These mounds range in size from approximately 200 nm to 500 nm and were measured to be about 50 nm tall from a SIMS depth profile and TEM cross-sectional imaging. The mounds have clearly faceted sides with edges running from top-to-bottom and left-to-right in the image, indicating orientation with ⟨110⟩ directions, as expected for {111} and {113} microfacets.

5.6.2.4 Step Pinning Induced Roughness

The results presented in Fig. 5.23 are not only unexpected because they show that ^{28}Si deposition at temperatures above 600 °C yields films with very rough surfaces, but also because despite depositing over a range of temperatures up to 1041 °C, the surface roughness not only persists but appears to increase at higher temperatures. Generally, in epitaxial deposition and growth, including Si MBE and chemical vapor deposition (CVD), higher deposition temperatures result in higher quality epitaxy and smoother films. Si CVD commonly uses deposition temperatures

above 600 °C or even in excess of 1100 °C both to achieve high growth rates from decomposition from silane gas and to facilitate high-quality epitaxial growth of thin films [137]. For Si MBE, above a deposition temperature of approximately 500 °C, SPE is expected to dominate the growth [118], and IAD has been shown to produce smooth, unlimited epitaxy at a deposition temperature as low as 390 °C [109]. As mentioned previously, the epitaxy phase diagrams for IBE in Fig. 5.18 also predict that higher deposition temperatures should lead to higher quality and unlimited epitaxy, and IBE experiments have demonstrated epitaxial deposition of ^{28}Si films dominated by smooth, layer-by-layer growth [51]. Smooth, epitaxial growth proceeds in these cases because the dominant growth mode at higher temperatures is 2D layer-by-layer growth. The dominant growth for a given deposition flux is controlled by the surface diffusivity, which is a thermally activated process. A high surface diffusivity-to-flux ratio ideally leads 2D layer-by-layer or step flow growth producing a smooth surface.

An explanation for the rough morphology characterized by large mounds seen on the ^{28}Si samples deposited at high temperature is presented here and is based on the presence of contaminants interfering with smooth deposition. Contaminants such as SiC or SiO_2 can act as pinning sites for step movement during deposition in a layer-by-layer growth mode at elevated temperatures. This leads to the formation of pits in the growth surface, which are a manifestation of step pinning in the early stages of thin film deposition. The continued movement of new steps around a pit will lead to local step bunching, and inevitably a high enough step density will form into larger microfacets in the film surface such as {111} and {113} microfacets. The

presence of strain in the substrate can also lead to increased roughness and step bunching after thermal processing. Flash annealing strained SOI (sSOI) substrates to between 900 °C and 1110 °C has been shown to produce a rough crosshatch pattern of step bunching on the surface [138]. For nominally unstrained substrates, strain can arise from the mounting of the chip in the sample holder. Strain could also arise in a deposited ^{28}Si film due to a small lattice constant mismatch between ^{28}Si and a natural abundance Si substrate. The lattice constant of ^{28}Si is larger than that of natural abundance Si by a relative value of roughly 1×10^{-6} [29, 139, 140]. The strain due to this difference is quite small compared to the typical strain of a sSOI wafer of approximately 1 %, and so is unlikely to result in a large amount of surface roughening. However, any lattice constant mismatch between a film and substrate will still need to be accounted for by the development of dislocation in the film. As step bunching and microfacets build up on the surface of a film, the roughness increases, and they will come to dominate the growth and morphology of the film. This process leads to the formation of mounds as raised microfacets meet forming larger structures, similar to the faceted mounds seen in the SEM micrographs of ^{28}Si samples deposited above 600 °C.

Numerous groups have studied the effects of roughness and faceting on the critical thickness, h_{epi}, and epitaxial quality of films produced by Si MBE, and IBE [109, 110, 119, 120, 122]. h_{epi} is found to be smallest on Si(111) surfaces, larger on Si(113) surfaces, and significantly larger on Si(100) surfaces [109]. These studies typically focus on the role of {111} microfacets in defect formation and transition of the growth from epitaxial to amorphous. While they do not directly address

the crystalline growth of mounds on a film surface, they do show the critical effect microfacets can have on the evolution of a depositing film and the important link between {111} planes and defects. General roughness on a Si(100) surface is known to develop into {111} microfacets [119], and both {111} and {113} microfacets are commonly observed in low temperature Si epitaxy [122]. {111} planes have been shown to form more easily on smaller terraces on and around islands, and here it may be that the decreased terrace sizes at step bunches have the same effect. Furthermore, incomplete filling of lattice sites by adatoms on step bunches or existing {111} microfacets can lead to the growth of {113} or {115} planes during deposition [110]. Thus, it is no surprise that {111} and {113} microfacets were found on the ^{28}Si samples discussed above.

One study showed that C contamination on a Si(100) surface can directly lead to the formation of {113} microfacets after annealing the sample to above 950 °C. This study concluded that impurities can effect formation of faceting, and that SiC, for example, can act as a pinning site to step motion [141]. Moreover, once pinning sites are formed from trace amounts of SiC, other C may migrate to the pinning site and form larger, more stable clusters. In general, C and O impurities can cause defects in a film during deposition that lead to pinning sites [122]. Experiments of Si growth confined in bare opening of a patterned SiO_2 surface layer have shown that near boundaries, similar to step bunches but in this case the edge of the SiO_2 pattern, {113} and sometimes {111} develop from the formation of rebonded double steps (D_B) in the Si(100) surface [142,143]. Once {111} and {113} planes are established in the growth surface, they tend to endure and subsequently expand because they

are more stable, i.e. energetically favorable, than the Si(100) surface. The Si(111) surface is known to be the most stable with the lowest Si surface energy, and although the Si(113) surface has a higher surface energy than Si(100), it becomes stable when formed by the D_B steps [143]. These surfaces are also more stable with the presence of C contamination.

In addition to the {111} and {113} microfacets being highly stable, molecular dynamics simulations show that the surface diffusion constant of surfaces such as Si(111) is smaller than for Si(100) [144]. Similarly, total-energy calculations predict that adatoms diffusing on a {113} surface encounter energy barriers at the rebonded double steps which increases the activation energy for adatom diffusion and a lower reactivity at the D_B steps [143]. The result of this may be that the growth rate of new layers on the Si(100) surfaces is higher because adatoms on the {111} and {113} surfaces will preferentially hop to a neighboring {100} surface where movement is easier and they are more likely to diffuse away from the facet boundary. The more stable {111} and {113} surfaces may also inhibit new layer formation compared to a {100} surface. A higher growth rate of the {100} surface would actually result in the shrinking of that surface and simultaneous expansion of adjacent microfacet surfaces as each new {100} layer encounters the {111} or {113} edges and adds to them, expanding those surfaces. The {111} or {113} microfacets would grow in time and come to dominate the surface morphology as the {100} surfaces shrink, producing faceted mounds like those observed on the ^{28}Si films deposited at high temperature in this work. A similar explanation was used to describe the preferential growth of {113} microfacets on Si(100) surfaces during Si CVD, where the {113}

surface has a slower CVD epitaxial growth rate than the {100} surface [142].

To better understand the mechanisms driving the observed rough morphology, experiments were carried out to explore the different aspects of the proposed sequence for mound formation. The development of step bunching and roughness around pinning sites on a ^{28}Si sample can be observed by inspecting a film thin enough to exhibit the initial formation of these features in the form of pits on the surface. A STM topography filled state image of a ^{28}Si film deposited with a substrate temperature of around 709 °C at DC–3 which exhibits pit formation is shown in Fig. 5.24. The substrate used for this sample was prepared *ex situ* by an HF etch. The film is estimated to be approximately 10 nm thick based on the ion flux at the center of the deposition spot, although there is a large uncertainty on this value. Thickness estimates of particular regions of very thin films in STM images presented here may not be accurate because the ion flux across a deposition spot is not uniform and the position of the STM scan area was not well known relative to the center of the deposition spot.

A large area scan of the deposited film is shown in panel (a) of Fig. 5.24 with a large number of dark, round, pit-like features in the surface. Large, flat, single terraces roughly 100 nm wide appear bounded by the pits that act as pinning sites to step movement and create step bunching. The single terraces between pits indicate a predominantly layer-by-layer growth mode. Multiple bright spots are seen within and around the pits and are probably clusters of chemical contaminants such as SiC, SiO, or Si_3N_4. The average areal pit density of this sample is determined to be 340 μm^{-2} $\pm$ 18 μm^{-2}, and the total height scale of this image is about 2.1 nm.

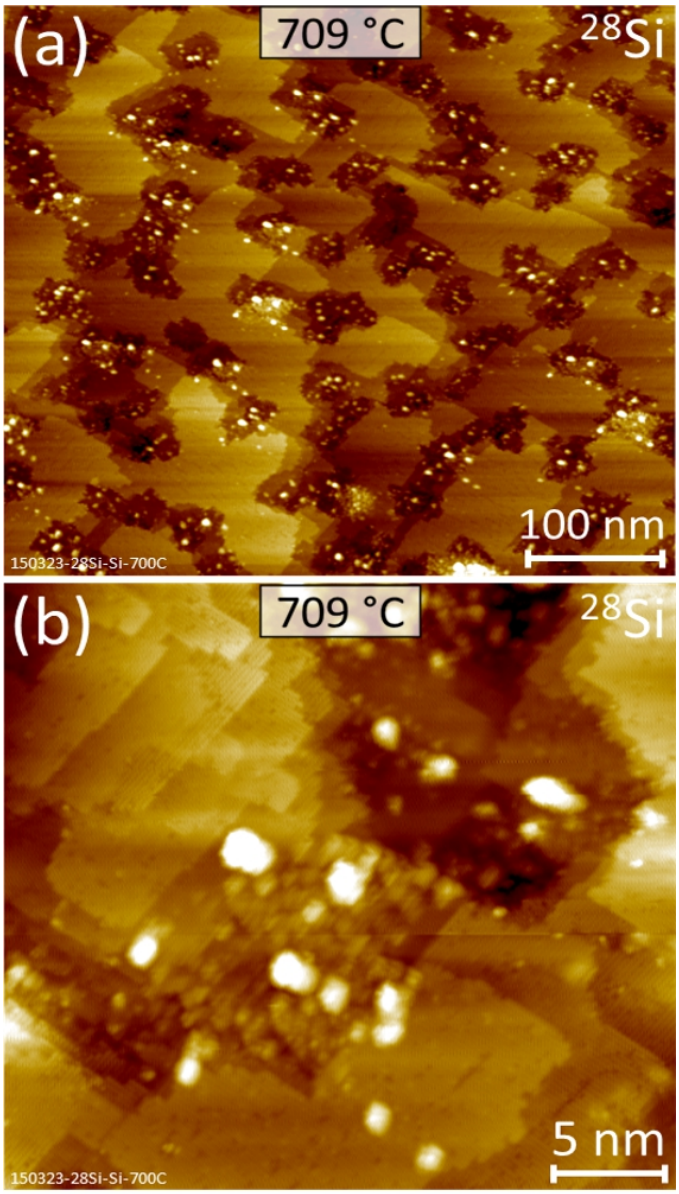

Figure 5.24: STM topography filled state images of a ^{28}Si film deposited at 709 °C at DC–3 showing pits. The images were acquired with a tip bias ≈ -1.8 V and a tunneling current ≈ 100 pA. This film was deposited after an *ex situ* HF etch of the substrate, and it is estimated to be 10 nm thick. (a) Large area scan of the film showing dark pits in the surface. Bounded by the pits and step bunching are large, flat, single terraces about 100 nm wide. Bright spots are seen inside the pits and are probably clusters of chemical contaminants, possibly SiC. The average areal pit density of this sample is ≈ 340 μm^{-2} ± 18 μm^{-2}. The total height scale of this image is about 2.1 nm. (b) Small area scan of a pit on this sample. Numerous contaminant clusters are seen in and near the pit and step bunching can be seen around the pit, resulting in increased roughness. The height scale is about 1.5 nm. Si (2×1) dimer rows can be seen on several terraces.

Panel (b) is a small area scan of a region near a pit from another area of this ^{28}Si sample showing numerous contaminant clusters in and near the pit. Step bunching resulting from the pinning of steps by the clusters can be seen, resulting in increased roughness. The total height scale of panel (b) is about 1.5 nm, which is mostly accounted for by the apparent height of the clusters themselves. Si(100) (2×1) dimer rows can be seen on several terraces surrounding the pit in this image.

To determine if the step pinning and pit formation in the initial stages of deposition is related to certain aspects of the ion beam deposition process, a thin natural abundance Si (^{nat}Si) film was deposited using the Si electron beam evaporator (i.e. the EFM). Aspects of the ion beam excluded from the ^{nat}Si deposition which may affect the growth include the hyperthermal energy ions, the presence of chemical contaminants in the ion beam that are transported ballistically as ions to the sample, and the presence of SiH_4 or other gases which diffuse from the ion beam chamber during deposition. STM topography filled state images of a ^{nat}Si thin film deposited with a substrate temperature of approximately 713 °C at DC–3 are shown in Fig. 5.25. Numerous dark pits are apparent on this sample, similar to the pitting on the ^{28}Si sample in Fig. 5.24. Panel (a) of Fig. 5.25 is a large area scan of the film, which is estimated to be approximately 13 nm thick. Note that the scan area of panel (a) is about four times larger than the displayed area of the ^{28}Si film in Fig. 5.24 (a). The pits in the ^{nat}Si film are more ordered and square shaped than the pits seen in the ^{28}Si film. Bounded by the pits and step bunching are large, flat, single terraces roughly 200 nm wide. The presence of these single terraces between pits indicates a predominantly layer-by-layer growth mode. Clearly the pits

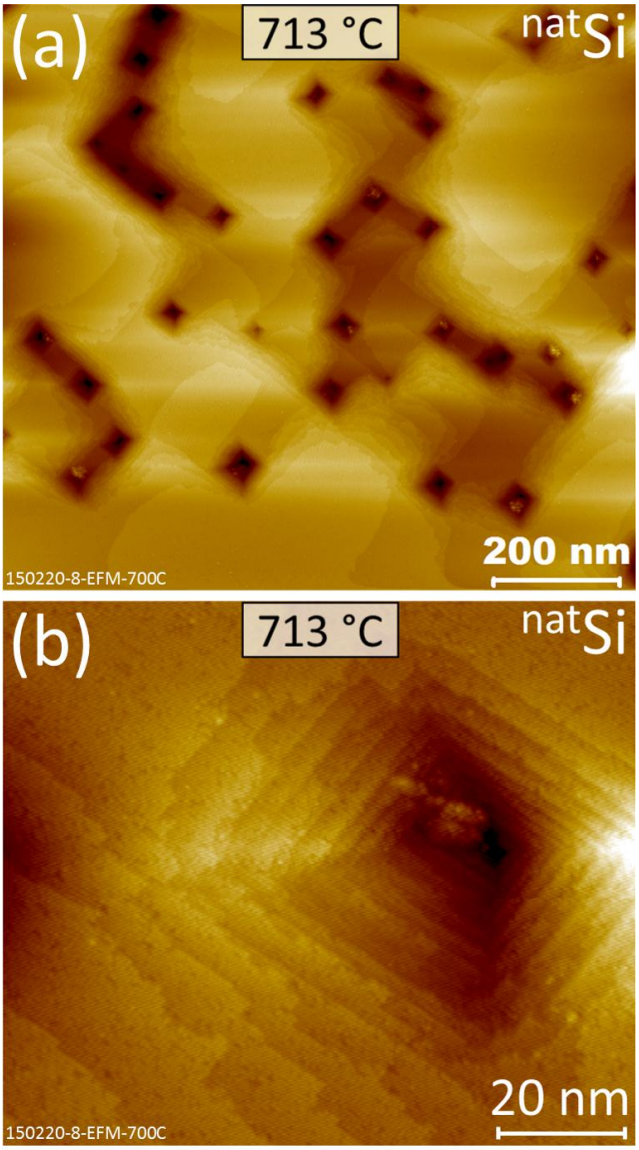

Figure 5.25: STM topography filled state images of a natural abundance Si film deposited at 713 °C at DC–3 showing pits. These images were acquired with a tip bias ≈ -2 V and a tunneling current ≈ 150 pA. This film was deposited from the natural abundance Si source after an *ex situ* HF etch of the substrate, and it is estimated to be 13 nm thick. (a) Large area scan showing dark, square pits in the film bordering large, flat, single terraces about 200 nm wide. Step bunching, seen around the pits, results in increased surface roughness. Contaminant clusters are seen as bright spots in several pits. The average areal pit density of this sample is $\approx 40\ \mu\text{m}^{-2} \pm 6\ \mu\text{m}^{-2}$. The total height scale is about 5.6 nm. (b) Small area scan of a pit in (a). The pit resembles an inverted pyramid with sides aligned with the $\langle 110 \rangle$ directions. A contaminant cluster, possibly SiC, can be seen at the bottom of the pit with a height scale of about 3 nm. Si(100) (2×1) dimer rows can be seen on the terraces.

are located at step pinning sites where step bunching during deposition has led to increased roughness. The total height scale of this image is approximately 5.6 nm, which is accounted for mostly by the pits and gives a reference for their depth. Several of the pits in panel (a) contain brighter features at their center which are probably contaminant clusters and possibly SiC. The average areal pit density of this sample is determined to be 40 $\mu m^{-2} \pm 6\ \mu m^{-2}$. This pit density is almost nine times lower than that of the ^{28}Si sample in Fig. 5.24 indicating that the roughness observed in thicker films may be partially due to some factor inherent to the ion beam deposition process. Clearly, though, the presence of any pits on the ^{nat}Si film shows that other factors not specific to the deposition sources also contribute to development of pinning sites and roughness on these films.

Panel (b) in Fig. 5.25 is a small area scan of a pit in (a). The pit resembles an inverted pyramid in the surface and is larger than the pit of the ^{28}Si film in Fig. 5.24 (b). Note that the scan area is approximately one quarter of the scan area of image showing the ^{nat}Si film in Fig. 5.25 (b). The sides of the pit can be seen to align parallel or perpendicular with the Si (2×1) dimer rows that are visible on the terraces surrounding the pit, i.e. the pit sides are aligned with ⟨110⟩ directions. A contaminant cluster, possibly SiC, can be seen at the bottom of the pit in panel (b) and is likely the source of the step pinning that formed this pit. The total height scale of this image is about 3 nm from the bottom of the pit to the surrounding terraces, making the pit quite shallow compared to its lateral size. The pits in both the ^{28}Si and ^{nat}Si films as well as in other thin samples have a variety of depths. This indicates that while some pits likely originate at the substrate surface, other

pits form during the deposition at different depths in the films. This indicates that the deposition process itself can generate more pits.

It seems likely that the step pinning and pit formation observed in both the thin ^{28}Si (Fig. 5.24) and ^{nat}Si (Fig. 5.25) films do lead to increased surface roughness and eventually large scale mound formation for deposition occurring at higher temperatures, i.e. above 600 °C. The step bunching and terrace formations that develop around pinning sites and pits qualitatively resemble the shape, distribution, and orientation of the mounds observed in SEM micrographs of the thicker ^{28}Si films (Fig. 5.23). These STM images suggest that mounds may form from the continued growth of the large flat terraces which separate from other nearby terraces by groupings of pits where further growth is inhibited. Groups of pits may then form the valleys between the mounds observed in SEM. It is also clear from the STM image of the ^{nat}Si film in Fig. 5.24 (a) and, to a lesser extent, the image showing the ^{28}Si film in Fig. 5.25 (a) that the edges of the large terraces are aligned with ⟨110⟩ directions forming rectangular sections. This is consistent with the observation that many of the large mounds visible in the SEM micrographs of ^{28}Si samples have edges oriented in ⟨110⟩ directions.

The features observed inside pits in STM images of both thin ^{28}Si and ^{nat}Si films, which are presumed to be clusters of contaminants, likely act as nucleation sites for the formation of the pits by pinning step motion. Several different types of contaminants may play a role in step pinning during deposition, such as SiC. It is important to identify contaminants in this system in order to better understand and ultimately ameliorate the cause of mound formation and roughness on ^{28}Si films.

Carbon contamination on substrates can originate from a number of sources including the ambient environment before the substrate is loaded into the chamber, carbon-containing adsorbates produced inside the vacuum chamber, or even *ex situ* chemical cleaning procedures not targeted to remove organic compounds, such as HF etching. SiC contamination in the form of clusters can be observed on the surface of substrates directly by STM imaging, or it can be detected via the RHEED pattern of substrates during *in situ* preparation by flash annealing. While the STM can observe individual SiC clusters in very small areas on the substrate, observing the signature of SiC in RHEED generally requires a significant amount of contamination over a large area. SiC is indeed found to be present on substrates used for samples deposited at DC–3 and is most often detected by RHEED during the flashing process. An example of a RHEED image of a flashed Si(100) substrate displaying the signature of SiC contamination is shown in Fig. 5.26. This substrate was prepared *ex situ* by an HF etch. The RHEED image in panel (a) was acquired with the sample at 600 °C and the electron beam in the ⟨110⟩ direction. A typical Si(100) (2×1) diffraction pattern is seen consisting mainly of the five central streaks as well as bulk Si and reconstruction spots indicated by the two inner arrows. Superimposed on the Si pattern in this image is a SiC pattern. This pattern first appeared after flashing the substrate to approximately 1040 °C for 20 s. Additional diffraction spots are also visible just outside the bulk Si streaks, which correspond to SiC as indicated by the two outer arrows. Other spots comprising the SiC pattern are visible on the central rod as well as the far left and right edges of the image. This SiC pattern is a transmission-type pattern, which indicates the SiC exists on the surface in 3D

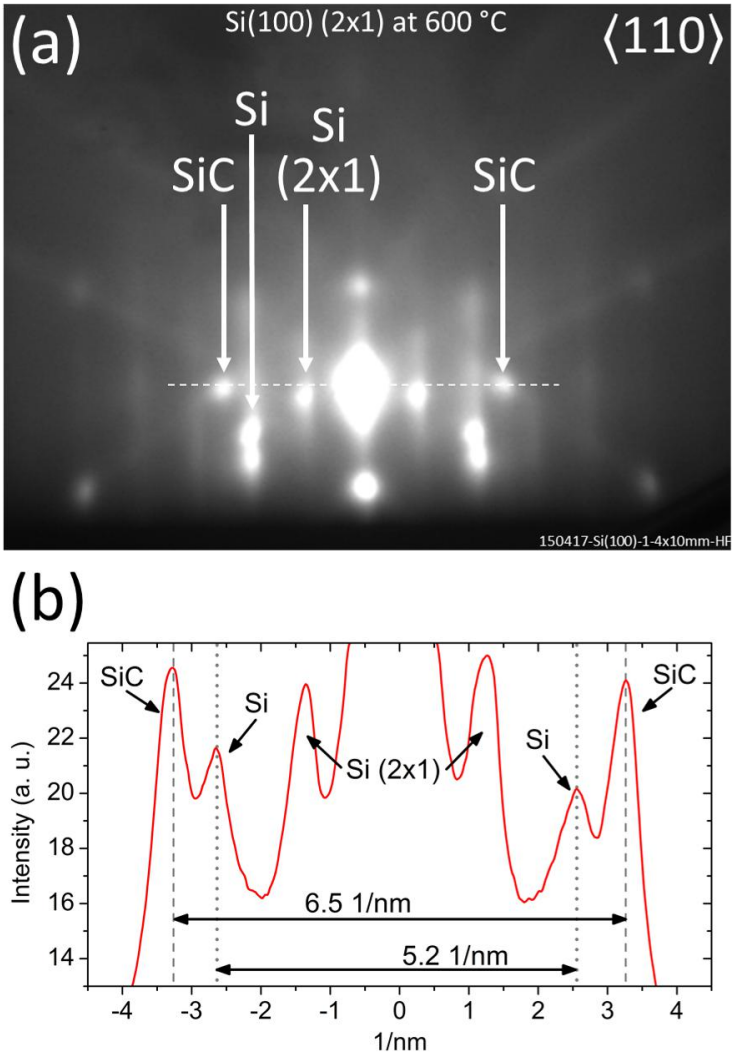

Figure 5.26: RHEED diffraction pattern of a Si(100) substrate after an *ex situ* HF etch and *in situ* flash annealing, which shows SiC contamination. (a) The RHEED image was acquired with the sample at 600 °C and the electron beam in the ⟨110⟩ direction. A Si(100) (2×1) diffraction pattern is seen consisting of streaks and bulk Si and reconstruction spots indicated by the two inner arrows. SiC diffraction spots are also visible outside the bulk Si streaks, indicated by the outer arrows, as well as on the central Si streak and the far left and right edges of the image. The transmission-type pattern of the SiC spots indicates 3D clusters. (b) A line profile of the diffraction intensity in arbitrary units is shown corresponding to the dashed line in (a). The reciprocal space mapping of the profile was calibrated from the separation of the bulk Si spots (dotted lines). The separation of the SiC spots (dashed lines) is then calculated to be about 6.5 1/nm, corresponding to the 3C-SiC lattice constant.

clusters aligned to the Si(100) surface.

Panel (b) of Fig. 5.26 shows a line profile of the RHEED diffraction intensity in arbitrary units corresponding to the horizontal dashed line in (a). This profile is plotted in reciprocal space in order to deduce the lattice constant of the SiC clusters from the spacing of the diffraction spots. The reciprocal space mapping was calibrated using the known separation of the bulk Si spots, indicated by the dotted lines in panel (b). In reciprocal space, these spots should be separated by approximately 5.2 1/nm, which is calculated from the distance between Si lattice planes in the $\langle 110 \rangle$ direction and the Si lattice constant, $a_0 = 0.543$ nm [145]. The separation of the outer SiC spots, indicated by the dashed lines is then calculated to be approximately 6.5 1/nm. Taking half of this value gives a distance of 3.25 1/nm between one SiC spot and the central streak, which is difficult to measure directly in this image. Then, inverting this value gives a real space distance between lattice planes of the SiC cluster in the $\langle 110 \rangle$ direction of 0.31 nm. Multiplying this spacing by $2/\sqrt{2}$ gives the $\langle 100 \rangle$ lattice constant, 0.44 nm. This value agrees quite well with the lattice constant of the 3C-SiC polytype, $a_0 = 0.436$ nm [146]. 3C-SiC has a zincblende crystal structure making it able to align to the Si diamond cubic lattice, and this alignment is clear in the RHEED pattern of Fig. 5.26.

SiC diffraction spots in the RHEED patterns of substrates were commonly seen during the flash annealing process of many samples in this work. This prevalence highlights the need for *ex situ* cleaning procedures to mitigate C and other contaminants. Typically, indications of SiC appear after exceeding a temperature of about 1000 °C, which is usually the minimum temperature of the initial flash in

the flashing sequence after keeping the substrate at about 600 °C or below (see the *in situ* substrate preparation discussion in an previous section of this chapter). This observation matches well with the known temperatures associated with SiC cluster formation on Si surfaces [119]. SiC CVD experiments have shown that stoichiometric SiC begins to form on Si(100) at substrate temperatures above 700 °C [147], and annealing C_{60} films on Si(100) substrates produces crystalline SiC between 800 °C and 900 °C [148]. Other experiments studying SiC contamination during vacuum preparation of Si surfaces have seen similar results to those observed in this work. Becker *et al.* used RHEED to demonstrate that SiC typically takes the form 3C-SiC when clusters form on Si(100) and Si(111) surfaces [149]. Samples were cleaned *ex situ* using HF and flashed *in situ* to between 800 °C and 1000 °C with background pressures as high as 1.3×10^{-5} Pa (1.0×10^{-7} Torr) resulting in SiC contamination. This study concluded that the contaminants originated from carbon-containing adsorbates from the vacuum chamber which dissociate to release C during flashing, including at lower pressures. Similarly, Henderson *et al.* showed that 3C-SiC forms on Si(111) surfaces above temperatures of 800 °C and likely originates from both carbon-containing adsorbates and the *ex situ* chemical cleaning procedure, which included an HF etch [150]. These results indicate that SiC formation is not only likely due to the flashing process, but that it possibly forms throughout a deposition occurring at higher temperatures such as the ones described here above 600 °C.

Further, experiments by Mol *et al.* showed that pre-treating Si(100) substrates with HF can directly result in SiC contamination [112]. Figure 5.27 shows a STM topography filled state image from that work of a Si(100) substrate prepared *ex*

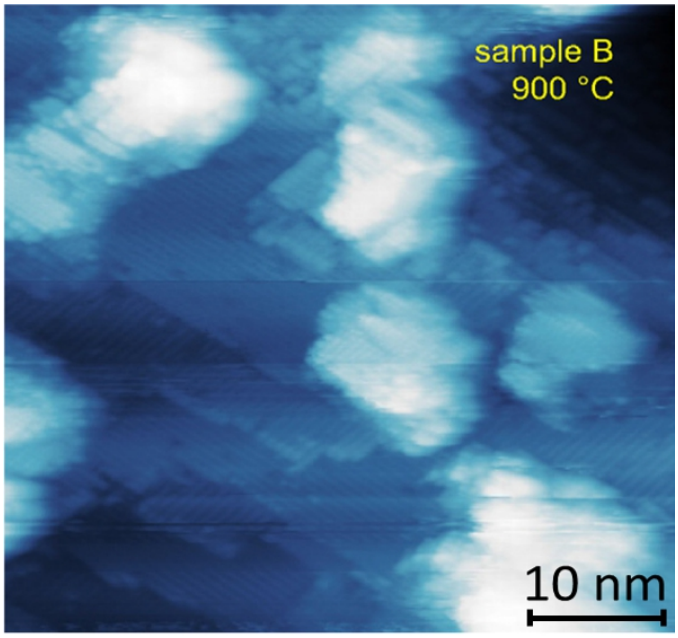

Figure 5.27: STM topography filled state image of a Si(100) substrate which was prepared *ex situ* by an HF etch and *in situ* by a 900 °C anneal. The image was acquired with a tip bias of -1.5 V and a tunneling current of 100 pA. Bright SiC clusters about 15 nm across are seen covering the (2×1) reconstructed surface. Step bunching is apparent in the upper left and lower right of the image. (from Ref. [112])

situ by an HF etch. The sample was loaded into the vacuum system with just the H passivation layer from the etch before being annealed at approximately 900 °C. Several bright SiC clusters approximately 15 nm wide can be seen on the annealed surface. Below the clusters can be seen (2×1) dimer rows on short terraces with steps appearing highly bunched in the upper right and lower left of the image, likely due to the presence of the SiC. Another sample in this study was prepared with a protective oxide layer resulting from the oxidation during *ex situ* cleaning with HNO_3. After the same anneal to 900 °C to remove the oxide, the surface was found to be flat and free of contaminants. Another group has shown that IBE deposition of ^{28}Si onto a substrate treated with HF produced a defective film with stacking

faults present [42].

Some of these previous experimental results regarding SiC discussed above were reproduced in this current work. Approximately 90 % of substrates prepared *ex situ* with an HF etch in this work showed signs of SiC contamination in the RHEED pattern after initial flashes. Most of these patterns were completely dominated by the SiC diffraction spots and showed only weak bulk Si spots or streaks, unlike the more balanced combination of patterns observed in Fig. 5.26. This suggests that the contamination was such that the surfaces of these substrates were mostly if not completely covered in SiC clusters. By contrast, approximately 32 % of the substrates which had no *ex situ* cleaning and were loaded into the chamber with a native oxide showed signs of SiC in the RHEED pattern. Furthermore, the RHEED patterns of these substrates typically only showed weak SiC diffraction spots with much stronger Si (2×1) spots, likely indicating only trace amounts of SiC on the surface. Another potential issue with cleaning substrates using only HF is that F atoms in the solution or left behind as residue can etch the Si surface, leading to roughening and potential pinning sites in film growth [150, 151]. These observations of the prevalence of SiC on substrates as well as the results of the experiment shown in Fig. 5.27 highlight both the potential benefit of alternate chemical cleaning combined with a protective oxide layer on substrates before *in situ* preparation as well as the ineffectiveness of HF etches alone to mitigate contaminants.

After the appearance of SiC on the surface of prepared substrates, further heat treatments in the form of higher temperature flash annealing typically results in the disappearance of the SiC diffraction pattern. For almost all of the samples where a

RHEED diffraction pattern corresponding to SiC appears after initial flashing to at least 1000 °C, flashing to between approximately 1150 °C and 1200 °C was required to remove the SiC spots and recover a nominal Si (2×1) pattern. Experimental results from other groups support this observation showing that SiC can be removed from Si(100) and Si(111) surfaces only by heating it to between 1100 °C and 1200 °C [150,152]. It is also suggested that upon heating to these temperatures, the C from the clusters goes into solution in the Si substrate, although it is not known how this C may affect the growth of a film.

After RHEED is used to identify substrates with SiC contamination, STM imaging is used to directly observe and inspect the SiC clusters to confirm their presence and view their effect on the substrate. Additionally, STM inspection of nominally clean substrates can reveal small contaminant clusters or other particulates in trace amounts below the detection capability of RHEED. These trace contaminants may still result in pinning sites during film growth. Figure 5.28 shows STM topography filled state images of two Si(100) substrates prepared *in situ* by flash annealing that show contaminant clusters. Both these substrates were prepared *ex situ* by an HF etch. These images were acquired with a tip bias ≈ -2 V and a tunneling current ≈ 150 pA. Panel (a) shows a phosphorous-doped Si substrate flashed to approximately 1150 °C. This substrate was nominally clean after flashing and although the RHEED pattern showed indication of SiC initially, no SiC signal was present after the final, higher temperature flashes. Unknown contaminants appear as bright spots in a cluster approximately 30 nm across on otherwise normal (2×1) reconstructed terraces. SiC, SiO_2, or other particulates are possible explanations

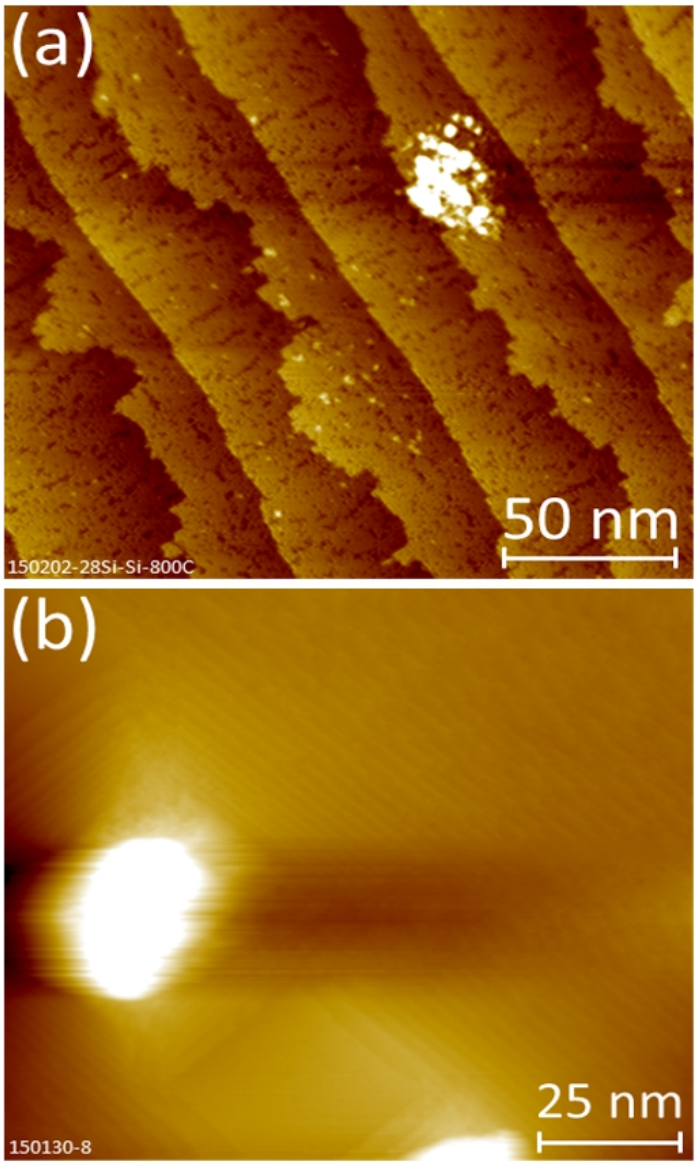

Figure 5.28: STM topography filled state images of Si(100) substrates prepared *ex situ* by an HF etch and *in situ* by flash annealing. These images were acquired with a tip bias ≈ -2 V and a tunneling current ≈ 150 pA. (a) Phosphorous-doped Si(100) substrate flashed to around 1150 °C with contaminants appearing as a cluster of bright spots on otherwise normal terraces. This substrate was nominally clean and free of SiC as determined by RHEED. The height scale of this image is about 1.3 nm. (b) Boron-doped Si(100) substrate flashed to around 1130 °C with two clusters of contaminants appearing as bright areas. The RHEED pattern of this substrate showed significant SiC contamination. The clusters act as step pinning sites causing step bunching around them, which forms small mounds. The height scale of this image is about 15 nm.

for clusters commonly seen during STM inspection on nominally clean substrates such as that in panel (a). These features may also be due to Si atoms stuck on the tip. During deposition of a thin film on such a surface, steps may become pinned at this cluster, causing a buildup of roughness nearby. The total height scale of this image is approximately 1.3 nm, which is mostly accounted for by the height of the cluster. Some dark dimer row defects are also seen on this surface. Panel (b) shows a boron-doped Si substrate flashed to around 1130 °C. The RHEED pattern of this substrate showed significant SiC contamination. Two clusters of SiC appear as bright areas approximately 25 nm across. The total height scale of this image is approximately 15 nm. These clusters clearly act as step pinning sites causing significant step bunching around them, which has resulted in the formation of small mounds that the SiC clusters sit atop.

The *in situ* prepared Si(100) substrates used for the initial set of ^{28}Si films deposited above 600 °C can not only have SiC and other clusters of contaminants and particulates on their surface, they can additionally exhibit signs of metal contamination. Metal atoms on or just below Si(100) surfaces produce patterns of dimer row defects observable in the STM, which are most often attributed to Ni contamination [116, 153–157]. The presence of Ni or possibly other metal impurities including In, Ga, and Al on the Si(100) surface produces long chains or lines of ordered dimer defects after high temperature heat treatments such as the typical flash annealing process. Ni atoms are thought to reside just below the surface and disrupt local bonds generating surface defects. These dimer vacancy lines (DVLs) run perpendicular to the Si dimer rows on each terrace, forming $(2\times n)$ patterns

where typically $n \approx 8$ and represents the number of normal Si dimers between the DVLs [153,154,157]. Si surfaces with DVLs present appear striped in STM imaging. The ordering of vacancies in DVLs is due to repulsive interactions between vacancies along a dimer row and attractive interactions between vacancies in adjacent dimer rows, which may be related to strain relaxation [153,158].

Figure 5.29 (a) shows an example of a STM topography filled state image of a Si(100) surface with Ni contamination from Ref. [153]. This image was acquired with a tip bias ≈ -2 V and a tunneling current ≈ 30 pA. This sample was deliberately contaminated with Ni by contacting it with stainless steel tweezers *ex situ* before it was loaded into the STM. That simple handling of the sample was enough to contaminate the surface with Ni. After it was flash annealed to 1150 °C, the sample then exhibited a highly ordered (2×n) reconstructed surface. Dark DVLs due to the Ni contamination are ubiquitous on this surface and are seen running perpendicular to the dimer row directions on each terrace. Typically, a surface coverage of < 1 % Ni can produce the (2×n) surface seen in panel (a). A similar example of metal contamination on a prepared substrate from this work is shown in Fig. 5.29 (b), which is a STM topography filled state image of a Si(100) surface prepared by flash annealing to approximately 1130 °C. This image was acquired with a tip bias ≈ -2 V and a tunneling current ≈ 150 pA. Although this boron-doped substrate was not intentionally contaminated with Ni or other metals, its surface appears very similar to the Si surface shown in panel (a). The surface has a (2×n) reconstruction with dark DVLs running perpendicular to the dimer row directions, although the concentration and length of DVLs is less than in panel (a).

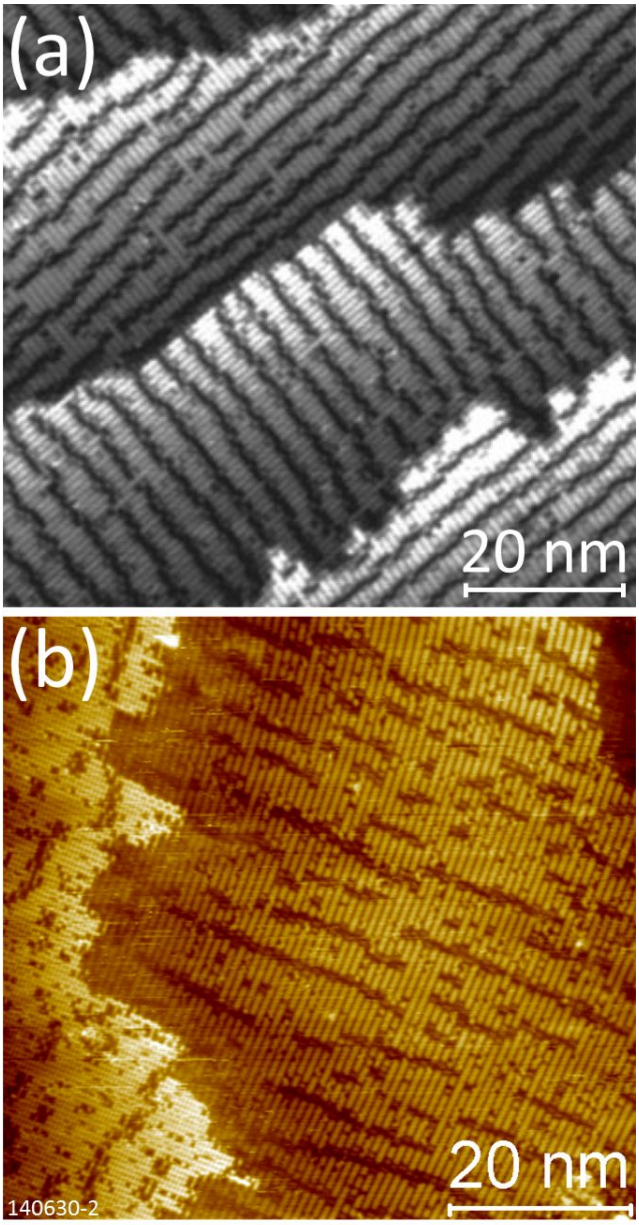

Figure 5.29: STM topography filled state images of Si(100) substrates prepared *in situ* by flash annealing. (a) A Si(100) substrate flash annealed to 1150 °C has a (2×n) reconstructed surface with dark dimer vacancy lines due to Ni contamination. Vacancy lines run perpendicular to the dimer row direction on each terrace. The substrate was intentionally contaminated by contacting it with stainless steel tweezers *ex situ*. This image was acquired with a tip bias ≈ -2 V and a tunneling current ≈ 30 pA (from Ref. [153]). (b) A boron-doped Si(100) substrate flash annealed to around 1130 °C has a (2×n) reconstructed surface with dark dimer vacancy lines due to metal although the substrate was not intentionally contaminated. This image was acquired with a tip bias ≈ -2 V and a tunneling current ≈ 150 pA.

The concentration of DVLs seen in Fig. 5.29 (b) is around the highest observed for substrates discussed to this point in this section, which were not chemically cleaned *ex situ*. Much more frequently, flashed substrates will exhibit a more moderate concentration of DVLs with shorter lengths. Some substrates have had a large number of individual or small clusters of dimer vacancy defects present on their surface, although not aligned in DVLs. It is not obvious if all dimer vacancies are related to metal contamination or what causes the dimer vacancies to form lines on some substrates while remaining disordered on others. The formation of DVLs is probably related to the level of contamination as well as differences in the specific heating times and temperatures that each substrate experiences. It has been found in this work that a minimal number of flashes to around 1200 °C followed by a quick cool down to below 800 °C can eliminate DVLs from a surface. Other groups have used similar procedures to reduce or eliminate DVLs [114, 154]. It is also observed that prolonged annealing to temperatures between 600 °C and 800 °C can result in the reappearance of DVLs even after their elimination by higher temperature flashing. The solid solubility limit of Ni in Si at a temperature of around 1200 °C is 5.8×10^{17} cm^{-3} [159]. So, at concentrations below this, Ni likely diffuses into the Si bulk at higher temperatures and can return to the surface during lower temperature annealing. While it is not ultimately desirable from a device point of view for ^{28}Si films to contain Ni or other metal impurities, it is not known exactly how this type of contamination may effect the growth morphology or epitaxy of deposited ^{28}Si films. Clearly, Ni atoms disrupt the bonding structure of the surface potentially creating strain and defects which may result in the formation of pinning sites or defects in

the epitaxy.

In addition to SiC or other particulates and metal contamination, there are other candidates for contaminants on Si(100) substrates prepared by *in situ* flash annealing which may lead to step pinning sites during deposition and ^{28}Si film growth. For the substrates which are not cleaned before they enter the vacuum chamber with a native oxide, removal of the oxide may be incomplete during flash annealing. The remaining, possibly non-stoichiometric, silicon oxide (SiO_x) may form clusters similar to the observed SiC, or molecules may remain isolated being very difficult to detect using the STM. Even a small amount of SiO_x on the surface of a substrate may act as a pinning site. Within the deposition chamber, N_2 is one of the major residual components of the vacuum after H_2 and CO_2, as seen in the RGA mass spectrum in Fig. 2.22 in Chapter 2. N-containing adsorbates on a Si substrate may dissociate during thermal processes potentially leading to the formation of silicon nitride clusters (Si_3N_4). As will be discussed in a following section, chemical analysis shows that ^{28}Si samples deposited after the ones discussed in this section contain a relatively high concentration of N, originating from the vacuum or the ion beam itself. Si_3N_4 clusters are thus a candidate for the nucleation of pinning sites during deposition. The solid solubility limits of N, C, and O in Si are shown in Fig. 5.42 and discussed in a later section. These solid solubility limits show, however, that the measured concentrations of N, C, and O in the films can lead to contaminant clusters that cause step pinning. The presence of H_2 on Si surfaces is believed to lead to increased roughness during epitaxial deposition [119]. Surface interaction with H_2 is nearly unavoidable in a vacuum system especially when increased amounts of H_2

and SiH_4 are introduced into the deposition chamber from the ion beam chamber. Finally, another potential contaminant coming from the vacuum during deposition is F, as seen in the deposition chamber RGA mass spectrum in Fig. 5.3. As mentioned previously, F atoms can also contaminate a substrate which was treated with HF and etch the surface when they desorb with thermal processes in the vacuum [151]. Small areas etched by F on a Si substrate and the resulting defects may lead directly to step pinning and increased roughness.

Another aspect to the formation of faceted mounds is the deposition temperature. To restate from a previous discussion, the rough ^{28}Si samples discussed thus far in this section were deposited with substrate temperatures between 610 °C and 1041 °C. At these temperatures, one would expect the deposition to occur in a predominantly layer-by-layer 2D growth mode. Despite the extreme roughness of these samples and morphology dominated by facet formation, the primary mechanism of mass transport and step motion is likely still akin to layer-by-layer growth, especially in the early stages of deposition when the surface is still fairly smooth. The high temperature layer-by-layer growth likely enhances some aspects of the mound formation. For example, the defects that form on {111} planes during Si epitaxy are found to increase in quantity as the deposition temperature is increased [120]. In general, layer-by-layer growth is much more likely to lead to the formation of microfacets, especially the rebonded D_B steps required for more stable {113} planes [143]. It also leads to faster growth of {111} and {113} planes while the {100} planes diminish, as mentioned previously. Probably the most important role of predominantly layer-by-layer growth is that it allows for the flow of steps around

pinning sites which leads to the step bunching required for microfacet formation.

If layer-by-layer growth and Si surface diffusion are in fact important driving aspects to the formation of mounds on the surface of ^{28}Si samples, then the characteristics of the mounds should reflect that. Another characteristic of the mounds besides faceting which can inform on their origin is their size. Using the analysis method described previously, the length and width of mounds on several samples was analyzed from the SEM micrographs of the surface. Here, the length is defined as the longer dimension of mounds (if applicable), while the width is the shorter dimension. An autocorrelation function was used to determine these values for each sample analyzed including several of the sample micrographs shown in Fig. 5.23 as well as others.

The results of this analysis are shown in Fig. 5.30. The average length (triangles) and width (squares) of mounds is plotted vs. the deposition temperature. Both the length and width of mounds increase with increasing temperature. The widths vary from approximately 175 nm for the 610 °C sample to approximately 560 nm for the 920 °C sample. The mound lengths vary from approximately 320 nm for the 610 °C sample to approximately 1105 nm for the 920 °C sample. The relative uncertainty in the lengths and widths is determined to be about 10 % from comparing measurements of multiple SEM images from a single sample. The uncertainty in the deposition temperature is due to uncertainty in the pyrometer readings and its calibration, as discussed in Chapter 2. The length-to-width aspect ratio of mounds formed on different samples is shown in the inset in Fig. 5.30 (open circles) to be between 1.5:1 and 3.5:1. The average aspect ratio of the mounds from all samples

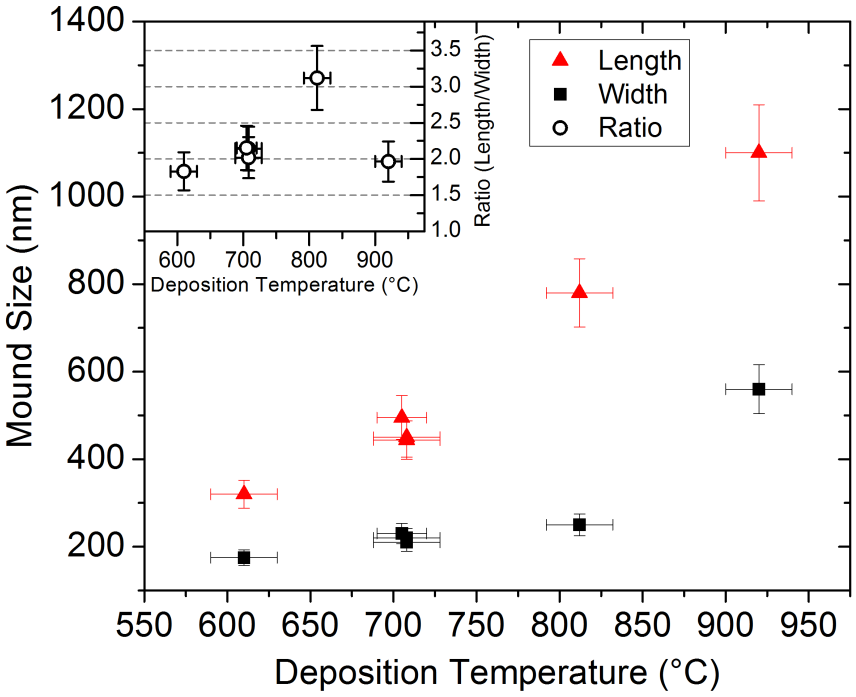

Figure 5.30: Average mound size vs. deposition temperature for rough ^{28}Si films deposited above 600 °C. The length (triangles) and width (squares) of large mounds formed on the films increase with increasing temperature as calculated from SEM micrographs of the surface morphology. The inset shows the ratios of the lengths to the widths (open circles) of the mounds for the different samples, most of which are about 2:1.

analyzed in this section is found to be ≈ 2:1. This value is similar to the aspect ratio reported by Mo *et al.* of 2D Si islands deposited on Si(100) [160]. That study used STM imaging to determine that the aspect ratio of the islands close to their equilibrium shape was between 2:1 and 3:1, and attribute it to differences in adatom incorporation and diffusion along the island edges.

The increase in mound size with increasing temperature suggests that the mounds are formed from a process or mechanism that is thermally activated, such as surface diffusion. Surface diffusion constants have the standard exponential form

of a thermally activated process:

$$D = D_0 \exp\left(-\frac{E_a}{k_B T}\right), \tag{5.3}$$

where D_0 is the exponential prefactor, k_B is the Boltzmann constant, E_a is the activation energy, and T is the substrate temperature. As the Si surface diffusion constant increases exponentially with increasing temperature, the mechanisms involving both the flow of steps leading to faceting and competing diffusion on different microfacets may be enhanced causing an increase in the characteristic size of the mounds at a given temperature. Increased temperature also leads to increased diffusion of adatoms over steps. This may lead to merging of different facets around pinning sites at a higher rate and the formation of larger mounds at higher temperatures.

It is important to note that other factors besides temperature may affect the mound size. The deposition time, deposition rate, or more likely the final film thickness may lead to different size mounds for a given temperature. However, the mound sizes do not seem to vary as a function of film thickness and most of the samples analyzed in Fig. 5.30 have similar thicknesses between approximately 110 nm and 160 nm. The thickness of the 920 °C sample was not measured, but it is roughly estimated to be larger than the other samples at around 400 nm, and this sample also exhibits the largest mounds. Another factor that may affect the mound size independent of the temperature is the amount of contaminants present on the substrate that would lead to pinning sites. A sample with a higher density of contaminants and pinning sites may result in smaller mounds because the area

between pinning sites where mounds may form would be smaller. However, most of the samples involved in this analysis were not cleaned *ex situ*, which should lead to similar amounts of contaminants. So, contaminants and thus the size of the mounds would not be expected to vary significantly across nominally similar samples. One sample deposited at 804 °C and shown in Fig. 5.23 (c) was not included in the mound size analysis because it was etched with HF, which is known to produce more SiC contamination, and it exhibited smaller grains than the other samples. This suggests that the amount of contaminants or other factors that lead to pinning do affect the size of mounds or grains that form on the surface.

The link between mound size and surface diffusion is explored further by plotting dependance of the mound size on deposition temperature in an Arrhenius form. An effective activation energy can then be extracted that results from the activation energy of the diffusion constant. This assumes that the change in the mound size is proportional to the change in the diffusion constant over the temperature range of the data. This proportionality makes sense when considering that an increased surface diffusion would lead to an increase in adatom flux to the growing faceted sides of the mounds and thus an increased area. In order to simplify this determination and not favor one particular dimension of the mounds, the mounds are treated as rectangular and the lengths and widths are combined to yield the average mound area, A. Then, taking $A \propto D$ and substituting A for D and a new exponential prefactor for the mound area, A_0, for D_0 in Eq. (5.3), the area data can be plotted to extract E_a. Taking the natural log of Eq. (5.3) with the aforementioned

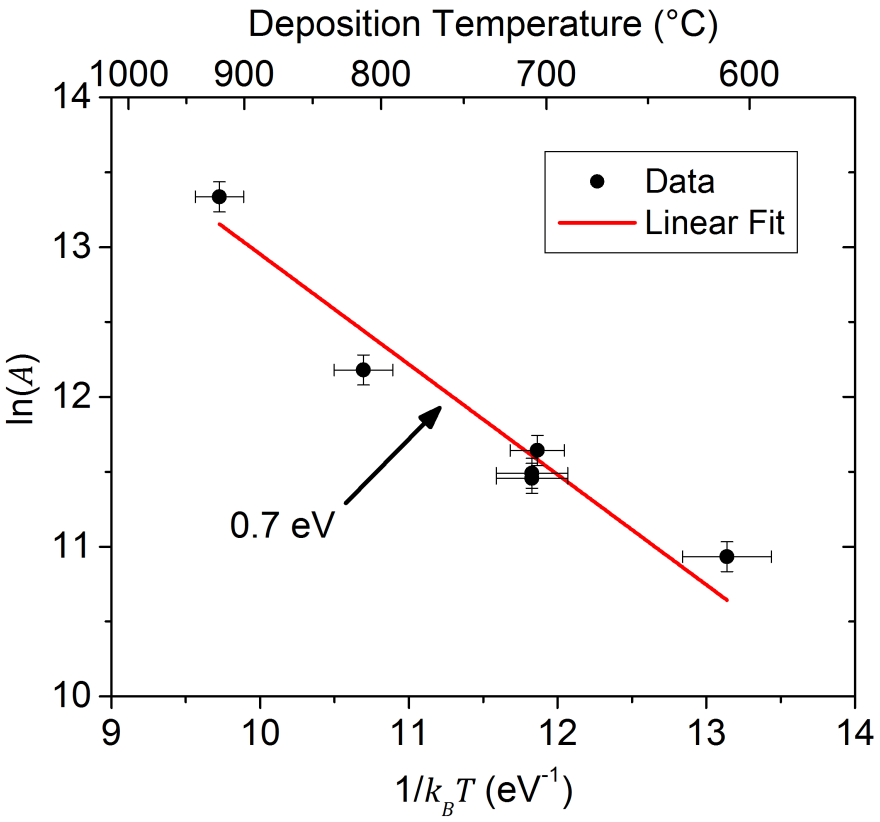

Figure 5.31: Arrhenius plot of $\ln(A)$, the natural log of the average mound area (circles), vs. inverse temperature in energy units for rough ^{28}Si samples deposited above 600 °C. The top axis shows the equivalent deposition temperature in °C. The data are fit to a line (Eq. (5.4)) whose slope gives an activation energy E_a = 0.7(3) eV.

substitutions gives a linear equation,

$$\ln(A) = \ln(A_0) - E_a \left(\frac{1}{k_B T} \right), \tag{5.4}$$

where the slope of $\ln(A)$ as function of $\frac{1}{k_B T}$ is equal to E_a. In Fig. 5.31, $\ln(A)$ is plotted vs. the inverse deposition temperature, which is modified by the Boltzmann constant to have units of eV^{-1}. The uncertainty in $\ln(A)$ is from the combined uncertainties of the lengths and widths. The data is fit to a line using Eq. (5.4), the slope of which gives a value for the activation energy for Si surface diffusion of E_a = 0.7(3) eV. The uncertainty in this value is the standard error from the fit. Again,

this assumes that the appropriate activation energy for diffusion would emerge from this analysis of A, the mound areas, because A changes with T in proportion to D. First-principles and experimental investigations of Si diffusion on Si(100) surfaces find activation energies of 0.6 eV and 0.67 eV respectively for diffusion along dimer rows, similar to the value reported here [161,162]. Those calculations also predict a value of $E_a = 1.0$ eV for diffusion perpendicular to dimer rows. However, another experiment found an average value of $E_a \approx 1.55$ eV for diffusion across steps of the Si(100) surface [163], and molecular dynamics simulations of Si diffusion on Si(100) along dimer rows give a value of $E_a = 0.2$ eV [144]. While there is a large range of values reported in the literature, it seems reasonable that the activation energy determined here from Fig. 5.31 can be attributed to Si surface diffusion, an important component in faceted mound formation.

5.6.3 Elimination Strategies for Step Pinning Sites

Several strategies were used to try to reduce the density of pinning sites on substrates, which manifest during deposition as pits and step bunching. New cleaning protocols were established to reduce chemical contaminants, such as SiC, on or near the substrates. An *ex situ* CMOS cleaning procedure was implemented for preparing Si(100) substrates. This is the sample preparation cleaning procedure described previously in this chapter in Section 5.3. This CMOS clean consists of etching the substrate first with piranha solution, then etching the oxide that forms with HF, and finally using SC–2 to clean and cap the substrate with a protective oxide. This clean is designed to remove both organic impurities containing C as well

as metals including Ni from the substrate. An HF etch alone, while a standard Si substrate preparation method for vacuum surface science experiments, was not chosen because of the ample evidence presented previously that it results in a substrate surface with far more SiC contamination than one that was protected with a native oxide before *in situ* heat treatments. Clean Si substrates were only ever handled with teflon tweezers that were also cleaned of metals using hydrochloric acid (HCl).

In addition to cleaning metal contamination off the substrates, the sample manipulator in the deposition chamber as well as the in vacuum sample holders were also cleaned. This was done to reduce cross-contamination onto the substrates of Ni and other metals, which can migrate from these parts during sample heating. While the sample holders are comprised of only Mo, several stainless steel components, which can spread Ni, were removed from the Mo section of the manipulator that gets hot during sample heating. Also, a chromel-alumel thermocouple, which is mostly Ni, was removed from the manipulator. The Mo parts were cleaned first in "base piranha", which is a 1:1:3 mixture of ammonium hydroxide (NH_4OH), hydrogen peroxide (H_2O_2), and water. This solution gently etches Mo surfaces removing contaminants, and it etches Group V elements. Then the Mo parts were treated with HCl to remove metals. Mo tools used for manipulating the sample holders were also cleaned in this manner. These vacuum component cleaning procedures were adopted from Richardson [164].

Despite these efforts to eliminate contaminants that cause step pinning, indications of the presence of contaminants on substrates persists. The CMOS cleaning procedure is either not sufficient at removing the offending contaminants from

the substrate surface, or the substrates pick up additional contaminants after the cleaning procedure. After preparing newly cleaned substrates *in situ* through flash annealing, inspection by RHEED shows that SiC was present more often than before CMOS cleaning, although the level of contamination was still much less than that of the substrates etched with HF alone. The frequency with which SiC was observed depended on the source of the wafers used for substrates. Wafers that were re-claimed wafers obtained from University Wafer and prepared with the CMOS cleaning procedure exhibited signs of SiC in the RHEED pattern approximately 66 % of the time. Virginia Semiconductor is generally seen as a source of higher quality wafers (e.g. lower impurities, smoother), and approximately 35 % of those wafers exhibited signs of SiC in the RHEED pattern. That frequency of SiC formation is similar to that of the older substrates which were not cleaned at all *ex situ*. It is not clear why the samples from University Wafer exhibit more contamination, but it is likely a combination of surface contamination from poor handling by the company and some contaminants in solution from previous processing of the re-claimed wafers.

Several samples were made to investigate any changes in contaminants, step pinning, or morphology of ^{28}Si samples deposited above 600 °C after implementing the above described cleaning procedures. To view the formation of pits due to step pinning sites, thinner films were deposited from both the ion beam and the natural abundance Si EFM source on Si(100) substrates prepared by the CMOS cleaning procedure. Figure 5.32 shows STM topography filled state images of thin films of ^{28}Si, (a) and (b), and ^{nat}Si, (c) and (d), which show the formation of pits in the

growth surface. Both of these films were deposited with substrate temperatures of approximately 712 °C at DC–3, and both are estimated to be approximately 10 nm thick. Panel (a) is a large area scan of the ^{28}Si film. Numerous square shaped pits can be seen in the growth surface surrounded by step bunching that bounds elevated areas with large, flat, single terraces roughly 50 nm wide. Single terraces between pits indicates a predominantly layer-by-layer growth mode. The pits are qualitatively different from the pits previously seen in the ^{28}Si film in Fig. 5.24 and are more similar to the square pits seen in the ^{nat}Si film in Fig. 5.25. The cause of the qualitative difference in the pits seen in the two ^{28}Si samples is not known, although it is perhaps related to the new cleaning procedure for substrates. Also, the native step density due to the wafer miscut of the substrate used for the second ^{28}Si sample was roughly five times higher than that of the first ^{28}Si sample. The average areal pit density of this ^{28}Si sample in Fig. 5.32 is determined to be 580 μm^{-2} $\pm$ 24 μm^{-2}, which is significantly more than the areal density of pits in the previous ^{28}Si sample (340 μm^{-2}) shown in Fig. 5.24, despite the more rigorous substrate cleaning procedure used for this latter sample. Panel (b) of Fig. 5.32 shows a small area scan of a pit in panel (a). Si (2×1) dimer rows are visible on terraces around the pit, which appears as an inverted pyramid in the surface with sides aligned with the ⟨110⟩ directions. The total height scale in panel (b) is approximately 1.4 nm, giving an indication of the pit depth.

Panel (c) in Fig. 5.32 is a large area scan of the ^{nat}Si film showing six pits in the growth surface. Note that the scan area in panel (c) is roughly 25 times larger than the area shown in panel (a). Surrounding the pits are triangular shaped

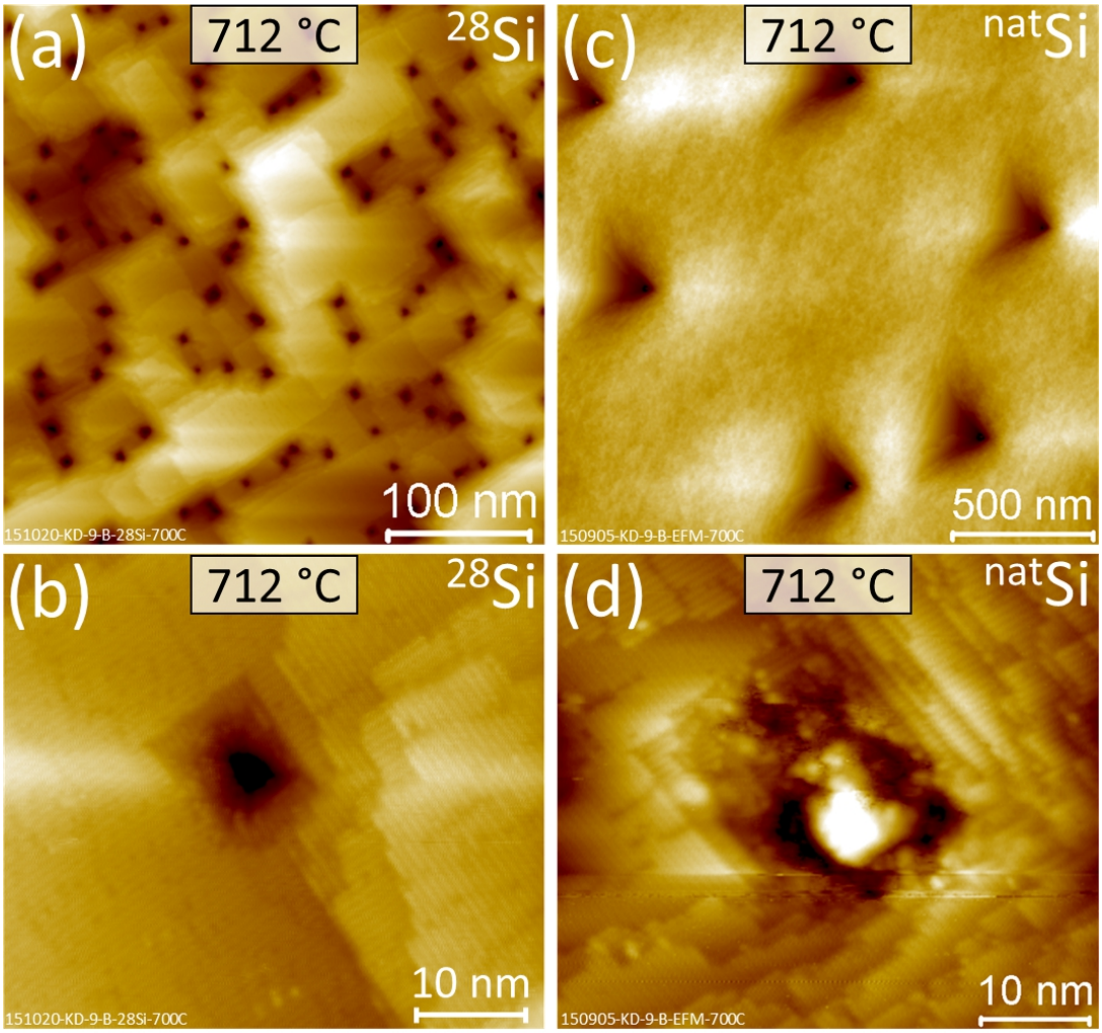

Figure 5.32: STM topography filled state images of ^{28}Si, (a) and (b), and natural abundance Si, (c) and (d), films deposited at 712 °C at DC–3. Si(100) substrates were prepared *ex situ* by CMOS cleaning. Both films are estimated to be about 10 nm thick. (a) Large area scan of the ^{28}Si film showing many dark, square pits and step bunching in the surface bounding large, single terraces about 50 nm wide. The average areal pit density of this sample is $\approx 580\ \mu\text{m}^{-2} \pm 24\ \mu\text{m}^{-2}$. (b) Small area scan of a pit in (a). Dimer rows are visible and the pit appears as an inverted pyramid with sides aligned with the $\langle 110 \rangle$ directions. Images (a) and (b) were acquired with a tip bias $\approx$ -1.8 V and a tunneling current $\approx$ 100 pA. (c) Large area scan of the $^{\text{nat}}$Si film showing six dark pits in the surface. Many steps < 50 nm wide are seen due to the wafer miscut, indicating step flow growth. Steps appear to flow around the pinning sites. The average areal pit density of this sample is $\approx 1.5\ \mu\text{m}^{-2}$. (d) Small area scan of a square pit in (c). Dimer rows are visible around the pit and a bright contaminant cluster, possibly SiC, appears at the center. Images (c) and (d) were acquired with a tip bias $\approx$ -2 V and a tunneling current $\approx$ 150 pA. Si (2×1) dimer rows are visible in (b) and (d), and their total height scales are about 1.4 nm and 1.6 nm respectively.

regions of step bunching where the step motion was pinned by and flowed around the pits during deposition. A large number of steps with widths < 50 nm are seen on the surface with step edges running top-to-bottom along the hypotenuse of the pits in the image. These are a consequence of a large miscut away from {100} in the plane of the wafer surface. The presence of steps matched to the underlying substrate indicates that deposition on this sample proceeded in a step flow growth mode. The average areal pit density of this sample is determined to be 1.5 μm^{-2} $\pm$ 1.2 μm^{-2}, which is less than the pit density of the previous ^{nat}Si film (40 μm^{-2}) shown in Fig. 5.25. For the approximately ten ^{nat}Si thin films deposited from the EFM evaporation source that exhibited pit formation and were cleaned with the CMOS procedure, the average areal density of pits varied between approximately 1 μm^{-2} and 30 μm^{-2}. Panel (d) on Fig. 5.32 is a small area scan of one of the pits in panel (a). Si (2×1) dimer rows are visible on terraces around the pit and a bright contaminant cluster approximately 10 nm across, possibly SiC, appears at the center. The flow of steps was right-to-left around the pit in this image with a high degree of step bunching seen to the right of the pit. The total height scale in panel (d) is approximately 1.6 nm, which is mostly accounted for by the height of the pit.

The ^{nat}Si films described above that exhibit step pinning and pits seem to show that the overall areal pit density and thus the amount of contaminants present on the substrates did decrease, if somewhat inconsistently, when implementing the CMOS and other cleaning procedures. However, the same is not true of the ^{28}Si film, which appears to have a higher amount of contaminants. Considering these results,

the one to two orders of magnitude larger areal pit density of the ^{28}Si films compared to the ^{nat}Si films suggests more strongly than before that many contaminants and pinning sites are due in part or exacerbated by something intrinsic to the ^{28}Si ion beam deposition process. Two possibilities are contaminants in the ion beam and contaminants in the gases that diffuse from the ion beam chamber to the sample.

To observe surface contaminants before thin film deposition, other Si substrates were prepared *ex situ* by the CMOS cleaning procedure, flash annealed *in situ*, and inspected with the STM. The normal flashing procedure of heating the substrate up to a temperature of around 1200 °C was not used, however. Instead, substrates were flashed to a lower temperature that should form SiC but not eliminate it from the surface, similar to the STM study of Si surface contaminants represented in Fig. 5.27 showing SiC clusters after a 900 °C anneal. Figure 5.33 shows STM topography filled state images of two Si(100) substrates prepared in this manner that show contaminant clusters. Panel (a) shows a phosphorous-doped Si substrate flashed to a temperature of approximately 1060 °C two times. The RHEED pattern of this sample did show faint signs of SiC on the surface after flashing. Multiple contaminant clusters, probably SiC, are seen on the surface, appearing as bright spots. Step movement during flashing caused the steps to recede around the clusters, which act as pinning sites causing step bunching nearby. The total height scale of this image is approximately 7.0 nm, which is mostly accounted for by the height of the clusters. Panel (b) shows a boron-doped Si substrate flashed to a temperature of approximately 1050 °C two times. It was unclear from the RHEED pattern of this sample if SiC was present or not. A bright contaminant cluster, pos-

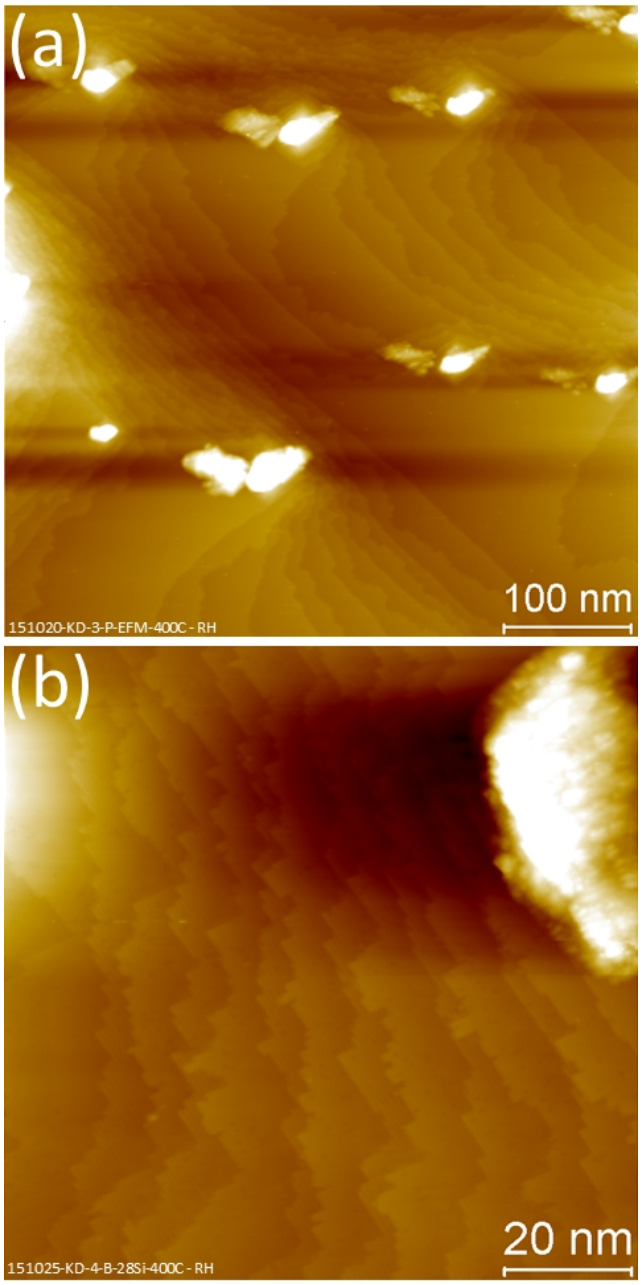

Figure 5.33: STM topography filled state images of Si(100) substrates prepared *ex situ* by CMOS cleaning and *in situ* by flash annealing. These images were acquired with a tip bias ≈ -2 V and a tunneling current ≈ 150 pA. (a) Phosphorous-doped substrate flashed to around 1060 °C with contaminant clusters, probably SiC, appearing as bright spots. Step flow due to flashing appears pinned at the clusters causing step bunching and increased roughness. The total height scale of this image is about 7.0 nm. (b) Smaller area scan of a boron-doped substrate flashed to around 1050 °C with a contaminant cluster appearing in the upper right corner. The height scale of this image is about 2.8 nm.

sibly SiC or SiO_x from incomplete desorption due to the lower flash temperature, is apparent in the upper right of the image. This cluster is approximately 20 nm wide and approximately 60 nm long. The total height scale of this image is approximately 2.8 nm, which is accounted for mostly by the height of the cluster. Short terraces are also seen with step bunching occurring near the cluster and Si (2×1) dimer rows visible on some terraces.

Finally, a thick ^{28}Si film was deposited onto a substrate prepared with the CMOS cleaning procedure to determine any changes in roughness or surface morphology compared to the previous ^{28}Si films shown in Fig. 5.23 that were not cleaned. Figure 5.34 is a top-down SEM micrograph of a thick ^{28}Si film deposited on a clean, boron-doped Si(100) substrate with a substrate temperature of approximately 705 °C at DC–3. The maximum thickness of this film found by SIMS depth profiling is approximately 144 nm. The surface morphology of the deposited film appears to be very rough, similar to SEM micrographs of the previous ^{28}Si films. Mounds cover the surface with an average width ≈ 230 nm and an average length ≈ 495 nm. The mounds have sharp, well defined, faceted edges predominantly running diagonally in the micrograph, indicating that they are oriented with the ⟨110⟩ directions as determined from the sample positioning in the SEM. The mounds on this sample appear qualitatively different from those of the previous ^{28}Si sample deposited with a similar substrate temperature of 708 °C, which had more rounded and randomly shaped mounds as opposed to the faceted, zig-zag pattern created by the mounds in the 705 °C sample. It is not known if the cause of this qualitatively different morphologies is due to the updated cleaning procedures.

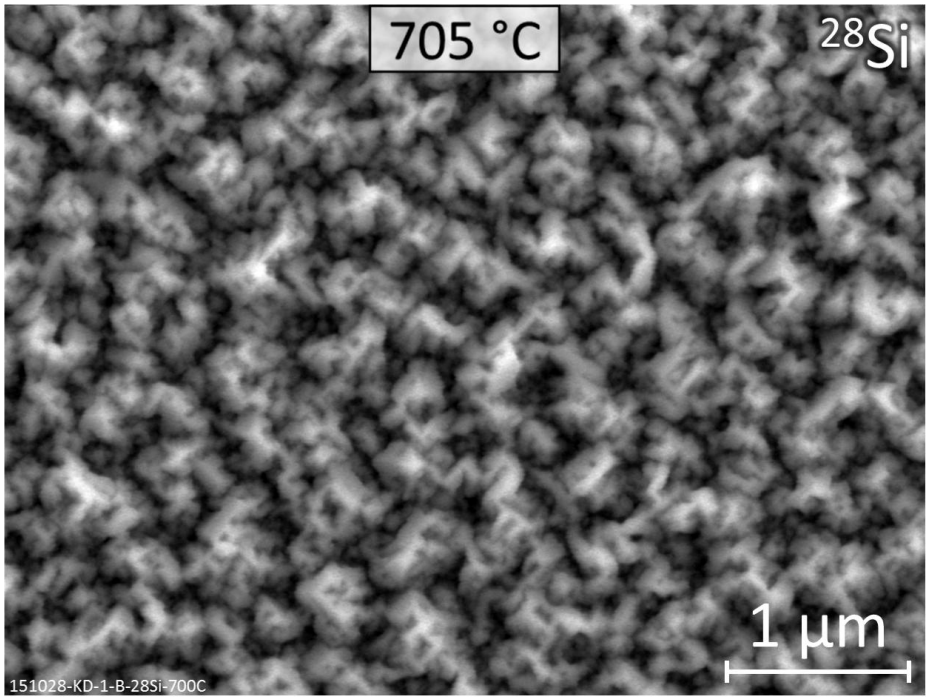

Figure 5.34: SEM top-down micrograph of the surface of a ^{28}Si film deposited at 705 °C at DC–3. The substrate used for this sample was prepared *ex situ* by CMOS cleaning. The thickness of this film determined from SIMS depth profiling is about 144 nm. The surface morphology of the deposited film appears very rough with mounds that have an average length $\approx$ 495 nm. The mounds have sharp, well defined, faceted edges predominantly running diagonally in the micrograph, indicating they are oriented with the $\langle 110 \rangle$ directions.

The above results show that the CMOS and other cleaning procedures implemented to reduce substrate contamination and thus step pinning that leads to mound formation and roughness were mostly unsuccessful. One notable aspect of the as-prepared quality of substrates that seemed improved by the new cleaning procedures was the presence of Si (2×1) dimer row defects. Although DVLs similar to those in Fig. 5.29 still appeared on some ^{28}Si samples after deposition, very few were seen on substrates prepared for deposition after flash annealing. Further, the surface density of isolated dimer row defects was reduced on prepared substrates after the new cleaning procedures. For substrates that were not cleaned *ex situ*, dimer row de-

fects were observed using STM to account for a wide range of areal densities between approximately 1 % and 34 % of the surface, with an average value of approximately 9 % being typical. These areal dimer defect densities were determined using particle detection software for the STM. By contrast, the higher quality substrates that were cleaned with the CMOS procedure and prepared after the manipulator and sample holder cleaning typically exhibited dimer row defects on approximately 2 % to 3 % of the surface.

While the CMOS and other cleaning procedures mentioned above are ultimately believed to be an important aspect in preparing clean substrates, it is apparent that a potentially monumental effort would be required to sufficiently reduce contaminants on substrates in this system. Considering this and the continued influence of contaminants and pinning sites on the growth morphology, surface roughness, and possibly epitaxial quality of ^{28}Si films deposited with substrate temperatures above 600 °C, a strategy of lower temperature deposition was adopted to limit the effects of the pinning sites. A predominantly layer-by-layer growth mode at higher temperatures is believed to facilitate and enhance the formation of step bunching at pinning sites and faceting at step bunching, as discussed previously. Depositing with a substrate temperature below 600 °C in a 3D island growth mode prevents step bunching and faceting from dominating the growth. While the formation of 3D multi-layer islands represents some intrinsic roughness in the growth surface, the merging of islands in this growth mode leads to an overall smoother surface.

Another strategy adopted to improve the epitaxial quality of films and heal potential defects resulting from deposition at lower temperatures is post-deposition

annealing. Thin film annealing has been used in both Si MBE and ^{28}Si IBE experiments to recrystalize amorphous layers and extend h_{epi}, the epitaxial critical thickness. Extending h_{epi} for a given deposition temperature was demonstrated by annealing at a minimum temperature of 500 °C, which is needed to break Si-H bonds that can form at crystalline defects [165]. Another experiment found that annealing at 600 °C results in SPE with a recrystallization front propagation speed of approximately 60 nm/min, allowing crystalline ^{28}Si layers to form from regions amorphized by high energy ion impacts [166]. Finally, annealing at 510 °C has been used to smooth thin films of Si deposited at low temperature and reduce roughness due to surface islands [167]. A post-deposition anneal of 600 °C for 1 h was chosen for most low temperature depositions in this work.

The strategy for eliminating pinning sites and producing smooth, epitaxial thin films of ^{28}Si consists primarily of preparing atomically clean Si substrates followed by depositing at temperatures below 600 °C. Although the elimination of contaminants on the substrates through *ex situ* cleaning is not fully experimentally realized, this strategy can be summarized as follows:

1. prepare Si substrates free of organics and metals *ex situ* with a CMOS cleaning procedure,
2. handle Si substrates with non-metal tools only,
3. manipulate and heat Si substrates *in situ* with only Mo parts cleaned of other metals,
4. flash anneal Si substrates to approximately 1200 °C to prepare a clean surface, verified by RHEED and STM,
5. deposit ^{28}Si in a 3D island growth mode below 600 °C to reduce pinning and step bunching,

6. and anneal the ^{28}Si film at 600 °C for 1 h.

5.6.4 Morphology of Films with Deposition $T < 600$ °C

A total of 18 ^{28}Si samples were deposited at sample location DC–3 with a range of substrate temperatures following the CMOS and other strategies laid out above for producing smooth, epitaxial films. Samples were deposited with substrate temperatures between approximately 249 °C and 502 °C on Si(100) substrates. Typical average ion energies, E_i, between approximately 35 eV and 40 eV were used. The epitaxy phase diagram for IBE in Fig. 5.18 predicts that a deposition temperature of approximately 350 °C is needed with these ion energies to produce high-quality epitaxial deposition, although the exact value would vary with deposition rate and other factors. These samples were deposited on a variety of Si(100) substrates including phosphorous-doped, boron-doped, and intrinsic wafers (University Wafer) initially before transitioning to higher quality phosphorous-doped wafers (Virginia Semiconductor).

5.6.4.1 RHEED

Initially, ^{28}Si samples deposited at low temperature (i.e. below 600 °C) were inspected using RHEED immediately following deposition to determine the epitaxial quality and morphology of the films. The first thicker sample produced at low temperature was a ^{28}Si film deposited at approximately 357 °C at DC–3. A RHEED diffraction pattern of this sample after deposition is shown in Fig. 5.35. This image was acquired with the sample at the deposition temperature and the

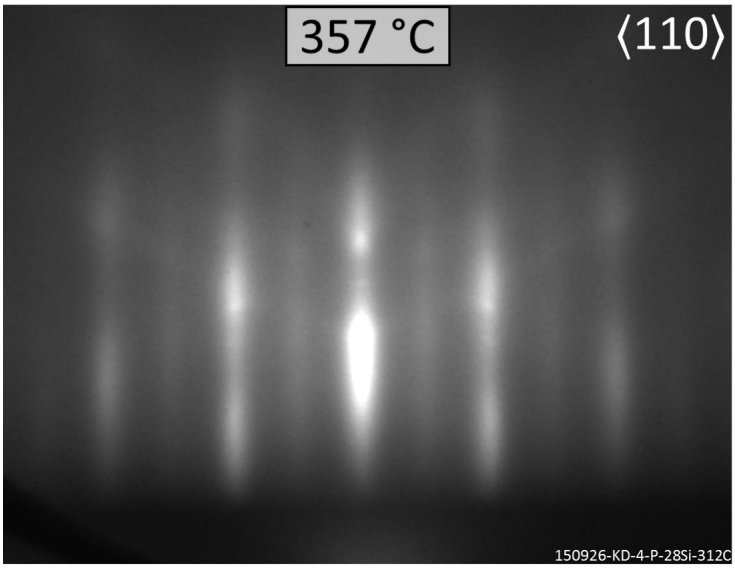

Figure 5.35: RHEED diffraction pattern of a ^{28}Si sample deposited at 357 °C at DC–3. This image was acquired with the sample at the deposition temperature and the electron beam in the ⟨110⟩ direction. The presence of (1×1) and weak (2×1) Si diffraction streaks indicate that the film is crystalline and aligned to the Si(100) substrate. Additionally, the streaks of this pattern corresponds to diffraction from very narrow terraces, likely due to a surface consisting of small, flat islands. A diffuse 3D transmission pattern is also visible superimposed on the streaks indicating some surface roughness.

electron beam in the ⟨110⟩ direction. The diffraction pattern is clearly different from those of the ^{28}Si samples deposited with substrate temperatures above 600 °C as in Fig. 5.19. In the pattern of this 357 °C sample, both (1×1) and (2×1) Si diffraction streaks are visible indicating that the film is crystalline and epitaxially aligned to the Si(100) substrate. The elongation of the nominal spots into streaks on this pattern corresponds to diffraction terraces that are narrow, e.g. about 20 nm wide, in two dimensions (parallel and perpendicular to the RHEED electron beam). This diffraction pattern is likely due to a predominantly 2D surface consisting of small, flat islands. This suggests that the low temperature deposition strategy was indeed successful at producing a smooth film free of large mounds.

Although the well defined 3D transmission spot pattern of the high temperature samples is absent from this image, there does appear to be a diffuse transmission diffraction characteristic visible superimposed on the streaks, which indicates the presence of some small amount of surface roughness, possibly due to the islands themselves. Additionally, there is no diffraction attributable to microfacets visible in this pattern, i.e. the "chevron" pattern or other lines connecting adjacent diffraction rods previously seen. With $E_i \approx 46$ eV for this sample, the epitaxy phase diagram for IBE in Fig. 5.18 would predict that a deposition temperature above 450 °C would be needed to produce the epitaxy seen in the RHEED pattern. However, this sample had a fairly slow growth rate of approximately 0.33 nm/min, which may offset the effect of a lower temperature, and it was quite thin at only approximately 50 nm as measured by SIMS depth profiling. This film may indeed have been deposited in the limited epitaxy regime as Fig. 5.18 suggests but was too thin to develop the amorphous phase at h_{epi}, which has been shown to be as large as 1 μm for deposition occurring above 300 °C [120].

Nearly all of the low temperature ^{28}Si samples had RHEED diffraction patterns similar to the one above in Fig. 5.35, although with varying intensities of the transmission aspects of the patterns, indicating varying degrees of roughness on the surface of the films. The most commonly used deposition temperatures for these samples were nominally 400 °C or 450 °C. A summary of the evolution of the RHEED diffraction patterns from these low temperature films to the high temperature films is shown for a series of eight ^{28}Si samples in Fig. 5.36. These samples were deposited at DC–3 on Si(100) substrates with substrate temperatures of ap-

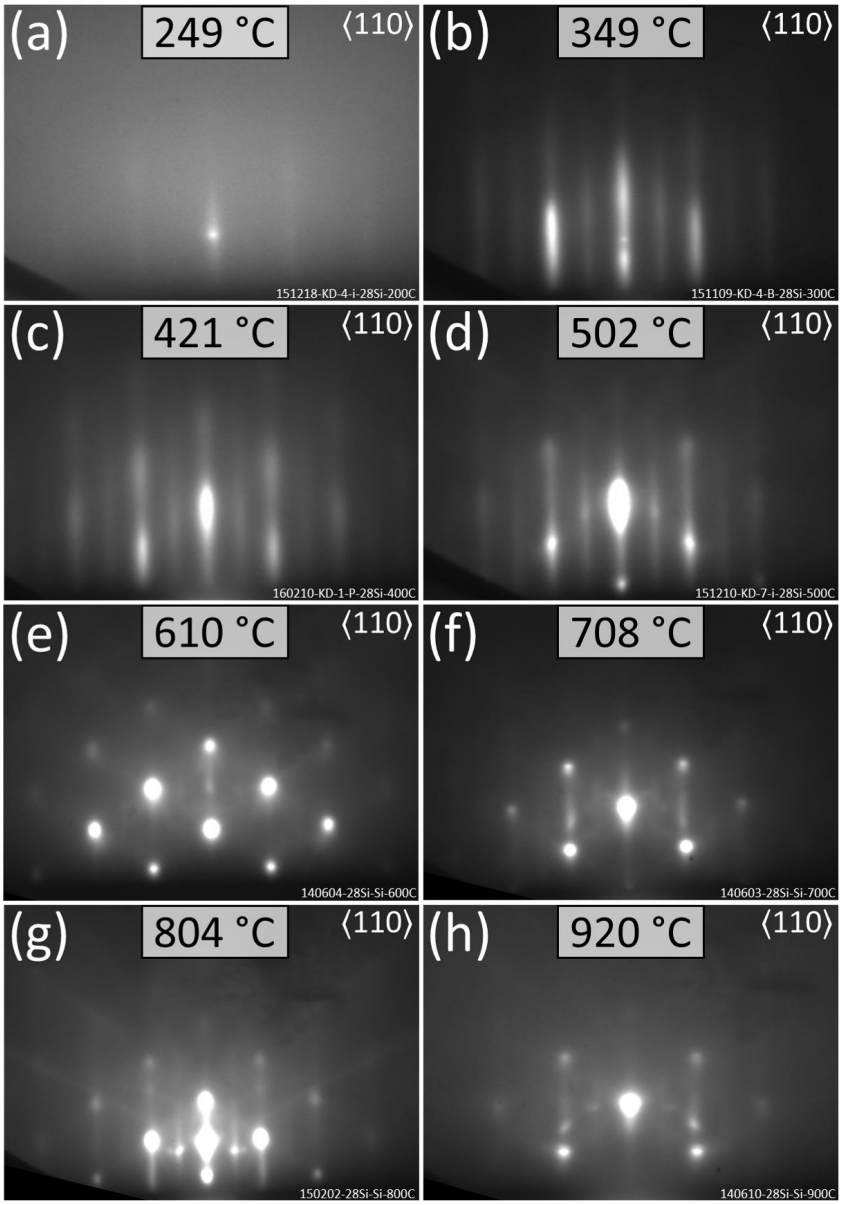

Figure 5.36: RHEED diffraction patterns of eight ^{28}Si films deposited at DC–3 at 249 °C, (a), 349 °C, (b), 421 °C, (c), 502 °C, (d), 610 °C, (e), 708 °C, (f), 804 °C, (g), and 920 °C, (h) on Si(100) substrates. These images were acquired with the samples at the deposition temperatures and the electron beam in the ⟨110⟩ direction. (a) The 249 °C film has a diffuse pattern with faint (1×1) bulk Si streaks indicating a partially disordered film and possibly a fully amorphous layer. (b)–(d) The patterns of films deposited between 349 °C and 502 °C have (1×1) and (2×1) Si diffraction streaks indicating crystalline films with small, flat islands on the surface. Diffuse 3D transmission spots superimposed on (c) indicates some surface roughness. (e)–(h) The patterns of films deposited between 610 °C and 920 °C show 3D transmission spots indicating rough, crystalline surfaces. A faint "chevron" pattern in (e) indicates diffraction from {311} microfacets. The (2×1) spots in (g) and (h) are likely due to diffraction from the substrate outside of the deposition areas.

proximately 249 °C, (a), 349 °C, (b), 421 °C, (c), 502 °C, (d), 610 °C, (e), 708 °C, (f), 804 °C, (g), and 920 °C, (h). These images were acquired with the samples at the deposition temperatures and the electron beam in the ⟨110⟩ directions. The diffraction pattern for the 249 °C sample in panel (a) is diffuse with faint (1×1) bulk Si streaks. This indicates that the film is at least partially disordered and possibly fully amorphous. The (1×1) streaks could be due to part of the RHEED electron beam diffracting from the substrate outside of the amorphous deposition area, although faint (2×1) streaks would probably be expected as well in that case. (1×1) streaks could also be due to diffraction of crystalline Si below a thin disordered layer or partial ordering within the film. This 249 °C sample was deposited with $E_i \approx 38$ eV and was determined by SIMS depth profiling to be approximately 305 nm in the thickest area measured. Given these parameters, the implication of the RHEED pattern agrees with the epitaxy phase diagram for IBE shown in Fig. 5.18 (b), which predicts limited epitaxy transitioning to an amorphous phase. This sample differs from the 357 °C sample in that it had a much higher deposition rate of approximately 1.25 nm/min, and it was much thicker.

The diffraction patterns of the films deposited with substrate temperatures between 349 °C and 502 °C in panels (b)–(d) of Fig. 5.36 show (1×1) and (2×1) Si diffraction streaks indicating crystalline films epitaxially aligned to the Si(100) substrates with small, flat islands on a predominantly 2D surface, similar to the pattern of the 357 °C sample in Fig. 5.35. Diffuse 3D transmission spots are visible superimposed on the pattern of the 421 °C sample in panel (c) of Fig. 5.36 and to a lesser extend on the pattern of the 502 °C sample in panel (d), indicates some small

surface roughness.

For samples with deposition temperatures higher than that of the 502 °C sample, there is an abrupt transition in the diffraction pattern from that of a 2D surface with islands, to that of a rough 3D surface, and this latter pattern persists to the highest deposition temperatures used here. The diffraction patterns of the films deposited with substrate temperatures between 610 °C and 920 °C in panels (e)–(h) of Fig. 5.36 show 3D transmission spots indicating very rough but crystalline surfaces, which known to be covered in mounds. These patterns are similar to that of the 708 °C sample shown in Fig. 5.19. A faint "chevron" pattern can be seen in panel (e) of Fig. 5.36 indicating diffraction from {311} microfacets. The (2×1) spots seen in panels (g) and (h) are likely due to diffraction from the substrate outside of the deposition areas.

5.6.4.2 STM

In addition to observing 2D island growth diffraction patterns in RHEED for ^{28}Si samples deposited at lower temperature, the STM was used to inspect the surface morphology of these samples. The surface of a ^{28}Si sample deposited at 357 °C at DC–3, corresponding to the RHEED diffraction pattern shown in Fig. 5.35, is shown in the STM topography filled state image in Fig. 5.37. This film is approximately 50 nm thick as determined from SIMS depth profiling, and it was deposited on a Si(100) substrate that was prepared *ex situ* by the CMOS cleaning procedure. After deposition and initial imaging in the STM, the sample was annealed at approx-

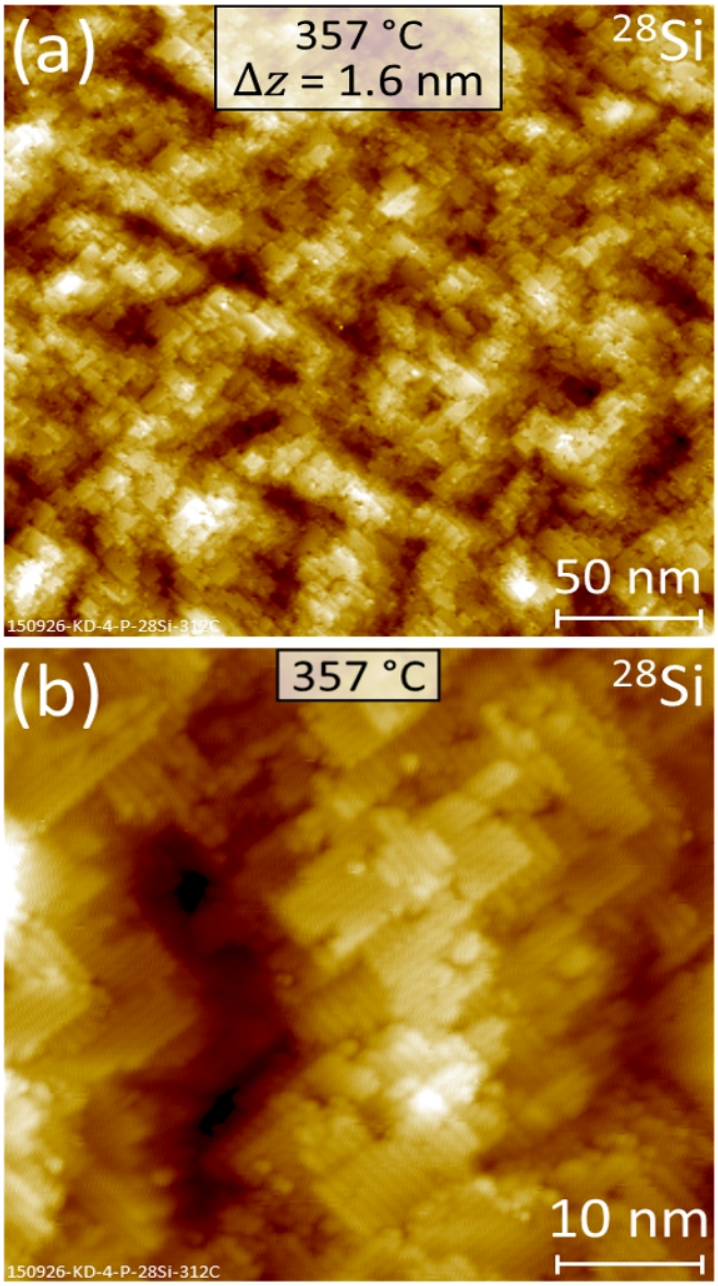

Figure 5.37: STM topography filled state images of a ^{28}Si sample deposited at 357 °C at DC–3. This film is about 50 nm thick determined from SIMS depth profiling and was deposited on a Si(100) substrate after CMOS cleaning. The sample was annealed at about 600 °C for 10 min. Images were acquired with a tip bias ≈ -1.8 V and a tunneling current ≈ 100 pA. (a) Large area scan of the sample showing small, multi-layer 3D islands comprising a smooth surface. Peaks and valleys are seen across the surface due to islands merging. The surface width determined from the topography is $\Delta z \approx 1.6$ nm or almost 12 monolayers. (b) Small area scan of an area in (a) showing multi-layer islands roughly 10 nm wide with many steps visible. Si (2×1) dimer rows are seen on the terraces making up the islands.

imately 600 °C for 10 min to form a more ordered surface before further imaging shown here. Panel (a) is a large area scan of the sample showing many small, multi-layer 3D islands comprising a relatively smooth, epitaxial surface. Peaks and valleys are seen across the surface likely the result of various islands merging during deposition. The topography of this image gives a surface width $\Delta z \approx 1.6$ nm for the film. The height of a single atomic layer on a Si(100) surface is approximately 0.136 nm, and so the measured surface width of this sample equates to there being approximately 13 crystalline layers exposed on the surface.

Panel (b) of Fig. 5.37 is a smaller scan of an area in panel (a). Again, multi-layer islands roughly 10 nm wide are seen covering the surface with many steps and terraces. Si (2×1) dimer rows are visible on the terraces forming the islands in this image indicating epitaxial alignment with the substrate. The morphology observed here matches the surface structure determined from the RHEED pattern for this sample (Fig. 5.35). Further, the lack of mounds, large areas of step bunching, or evidence of pinning sites visible in Fig. 5.37 affirms that lower temperature deposition, i.e. below 600 °C, does completely alter the growth morphology, resulting in a smooth film. The smooth morphology of sample is in contrast to the rough surface shown in Fig. 5.21 and the other samples with large mounds on the surface.

To replicate these results, several other ^{28}Si samples were deposited with a similar or slightly higher substrate temperature including nominal deposition temperatures of 400 °C and 450 °C, which were most commonly used. The smooth morphology of the 357 °C sample shown in Fig. 5.37 is generally found to be reproducible for all of these depositions, which produce films with surfaces that appear

qualitatively similar in the STM. Four STM topography filled state images of four different ^{28}Si samples deposited at DC–3 with substrate temperatures of approximately 349 °C, (a), 417 °C, (b), and 421 °C, (c) and (d), are shown in Fig. 5.38. These samples were deposited on Si(100) substrates that were prepared *ex situ* by the CMOS cleaning procedure. After deposition, these samples were all annealed at approximately 600 °C for 1 h to form more ordered surfaces. Similar to the 357 °C sample, all of these images (panels (a)–(d)) show multi-layer 3D islands comprising relatively smooth, epitaxial surfaces. Note that the scan areas in these four images are the same to facilitate comparisons between them.

The film shown in panel (a) is approximately 206 nm thick with islands that are roughly 20 nm wide. The surface width of this film determined from the STM topography is $\Delta z \approx 1.0$ nm, which is approximately eight atomic layers exposed to the surface. These eight layers are visible and can be counted in the image. The film shown in panel (b) is approximately 250 nm thick with islands that are roughly 15 nm wide. The surface width of this film determined from the topography is $\Delta z \approx 2.1$ nm, which is approximately 16 atomic layers. The film show in panel (c) is approximately 148 nm thick with islands that are roughly 30 nm wide. The surface width of this film determined from the topography is $\Delta z \approx 2.2$ nm, which is approximately 17 atomic layers. Finally, the film shown in panel (d) is approximately 320 nm thick with islands that are roughly 20 nm wide. The surface width of this film determined from the topography is $\Delta z \approx 1.0$ nm, which is, again, approximately eight atomic layers. The surface in panel (d) also shows some dark dimer row defects on the terraces at a higher concentration than the other samples, possibly indicating

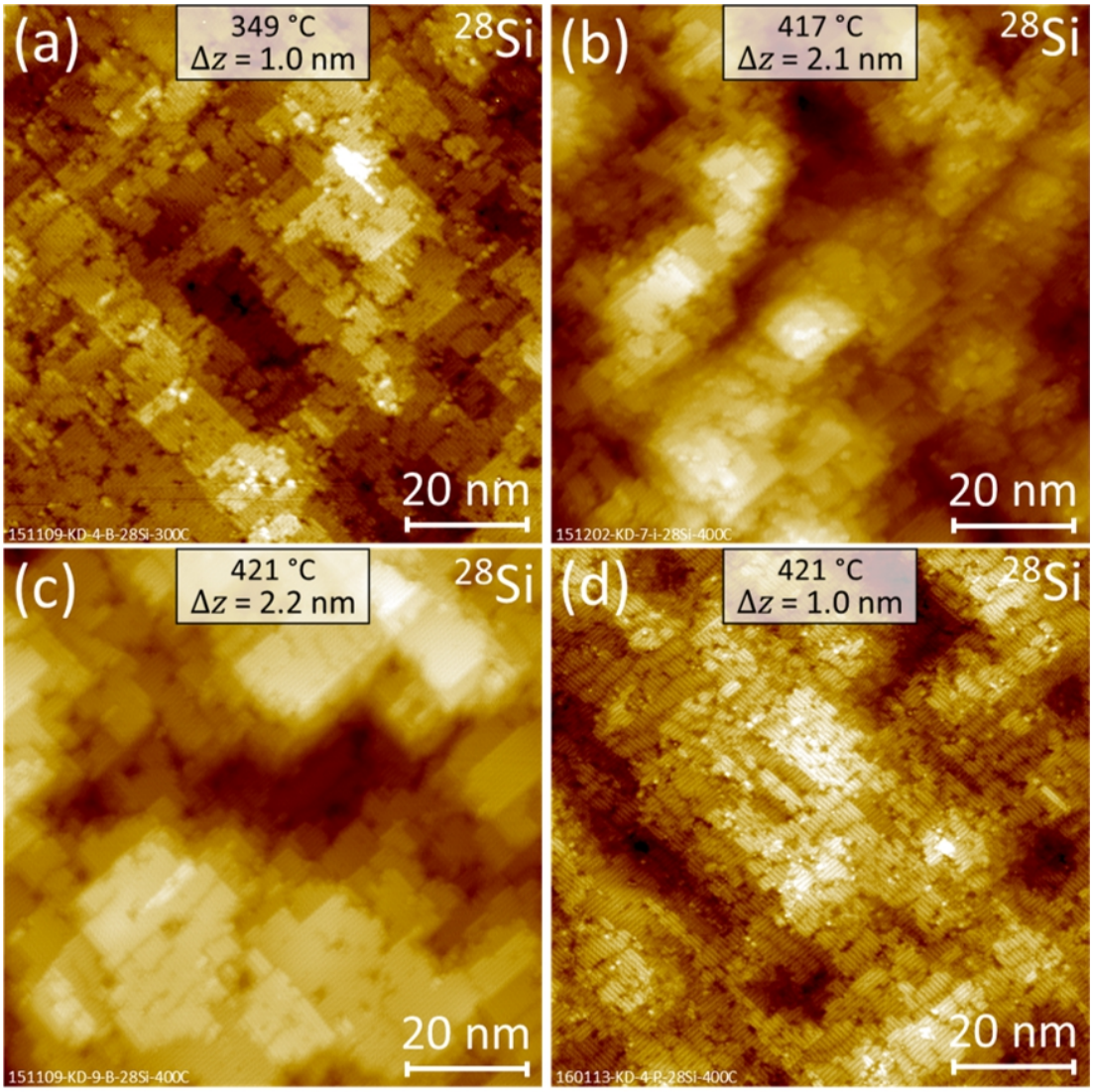

Figure 5.38: STM topography filled state images of four ^{28}Si samples deposited at DC–3 at 349 °C, (a), 417 °C, (b), and 421 °C, (c) and (d). These samples were deposited on Si(100) substrates after CMOS cleaning and were annealed at about 600 °C for 1 h. Images were acquired with a tip bias ≈ -1.8 V and a tunneling current ≈ 100 pA. Multi-layer 3D islands comprising smooth surfaces are seen on all samples. Peaks and valleys are seen due to islands merging. (a) This film is about 206 nm thick with islands roughly 20 nm wide and the surface width determined from the topography is $\Delta z \approx 1.0$ nm. (b) This film is about 250 nm thick with islands roughly 15 nm wide and a surface width of $\Delta z \approx 2.1$ nm. (c) This film is about 148 nm thick with islands roughly 30 nm wide and a surface width of $\Delta z \approx$ 2.2 nm. (d) This film is estimated to be about 320 nm thick with islands roughly 20 nm wide and a surface width of $\Delta z \approx 1.0$ nm. The surface in (d) also shows some dark dimer row defects on the terraces. Si (2×1) dimer rows are visible on the island terraces in (a)–(d). Film thicknesses were determined from SIMS depth profiling except for that of the sample in (d), which is an estimate.

the presence of impurities in the film. These film thicknesses were the maximum measured thicknesses determined from SIMS depth profiling except for that of the sample in panel (d), which is an estimate based on the measured ^{28}Si ion beam flux during deposition. Si (2×1) dimer rows are visible on the terraces forming the island in panels (a)–(d) indicating epitaxial alignment with the substrates.

The overall smoothness, i.e. the lack of extended step bunching and facet and mound formation, of these ^{28}Si films deposited with substrate temperatures below 600 °C is achievable for several reasons. As discusses previously, lower temperature deposition reduces step movement associated with higher temperature layer-by-layer growth. This step movement can facilitate the formation of step bunching and faceting, ultimately leading to mounds. Additionally, contaminants that cause pinning sites and step bunching may cluster or become active at higher temperatures. These effects are reduced during low temperature deposition in a 3D island growth mode. However, 3D island growth introduces some intrinsic roughness and step bunching around the islands, and defect formation that may act as pinning sites can result from merging islands. Despite these aspects of 3D island growth, films with a smooth morphology still occur due to the nature of island formation on Si surfaces. Si island growth is anisotropic due to the difference in the diffusion constants for adatom movement along or perpendicular to dimer rows. Anisotropic growth is believed to result in the growth surface being constrained to a limited number of atomic layers and thus a limited amount of surface roughness and step bunching [160, 168]. This appears to be the case for the ^{28}Si films deposited in a 3D island growth mode as in Fig. 5.38. The surface width of all of these samples is

fairly consistent with a typical value of $\Delta z \approx 2$ nm, which equates to approximately 16 atomic layers being exposed on the surface at any time. The surface width of these samples does not seem to vary with deposition temperature or film thickness, although there is not enough data to more strongly support these conclusions. This possibly indicates that the measured Δz values are indeed constant and intrinsic to Si island growth.

Additionally, the hyperthermal energy of the ^{28}Si ions may play a role in producing a smooth surface during 3D island growth. Energetic ions are known to suppress and dissociate 3D islands as well as defect clusters leading to smoother growth. Mobile adatoms formed in the break up of islands may continually fill in other inter-island trenches [120,127,169]. It is not clear if the ^{28}Si ion energy has any effect on the smoothing of films in this work because low temperature deposition using the natural abundance Si EFM evaporator, which produces Si atoms with only thermal energies, also results in smooth films. STM inspection of these ^{nat}Si films shows that they consist of small islands qualitatively similar to those of the ^{28}Si films.

While most of the ^{28}Si films deposited with substrate temperatures below 600 °C had surfaces that appear similar in the STM to those of the samples in Fig. 5.38, several had surface morphologies that appeared different including two samples with deposition temperatures of 502 °C and 249 °C. STM topography filled state images of these samples and four others are shown in Fig. 5.39, which serves to summarizes the variation in film morphology over the range of deposition temperatures used in this work. ^{28}Si samples were deposited at DC–3 with substrate

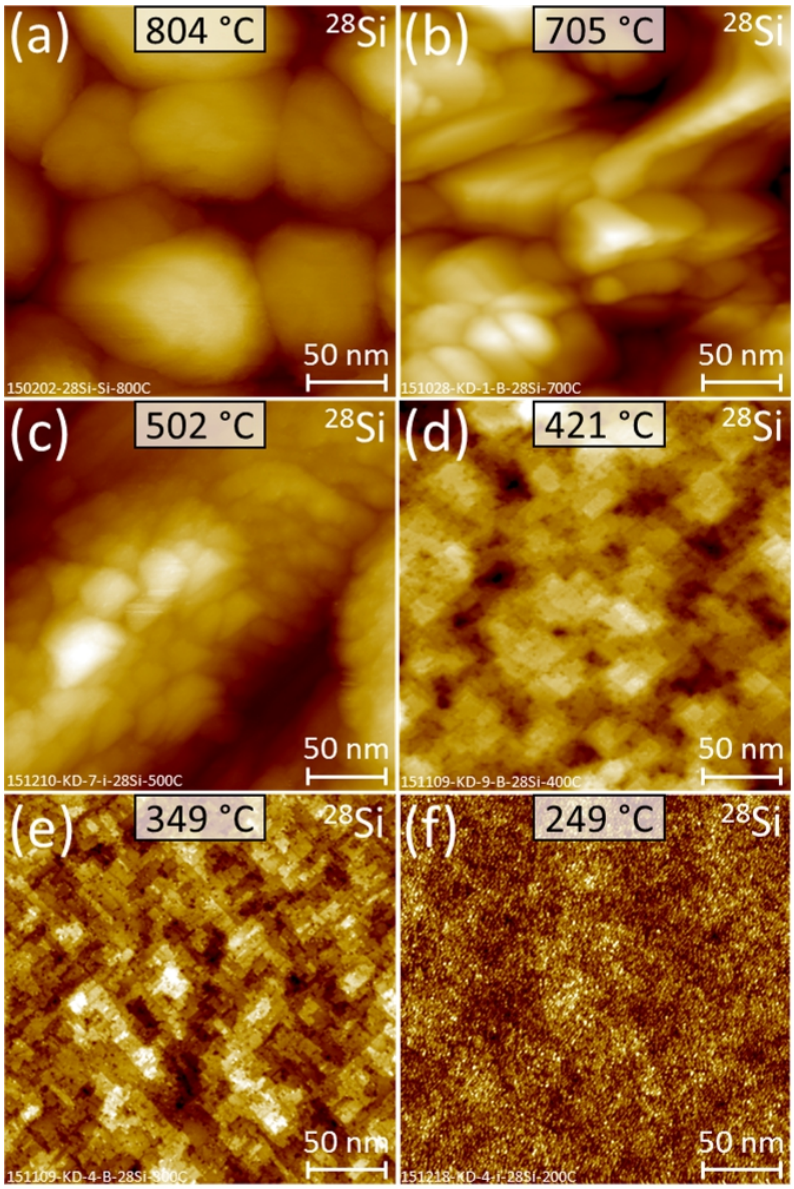

Figure 5.39: STM topography filled state images of six ^{28}Si samples deposited at DC–3 at 804 °C, (a), 705 °C, (b), 502 °C, (c), 421 °C, (d), 349 °C, (e), and 249 °C, (f). Images were acquired with a tip bias ≈ -1.8 V and a tunneling current ≈ 100 pA. All substrates used for these samples were prepared *ex situ* by CMOS cleaning except for the sample in (a), which was etched with HF. (a) and (b) The morphology of films deposited above 600 °C appear very rough with large mounds and grains. The total height scale in (a) and (b) is about 45 nm and 50 nm respectively. (c) The 502 °C sample morphology appears less rough with a large mound as well as small island-like features visible. The height scale is about 13 nm. (d) and (e) The morphology of films deposited between 349 °C and 421 °C appear smooth with small, multi-layer 3D islands. The height scales in (d) and (e) are about 1.3 nm and 3.6 nm respectively. (f) The 249 °C sample shows a smooth surface with small features ≈ 3 nm in size. The height scale is about 1.0 nm.

temperatures of approximately 804 °C, (a), 705 °C, (b), 502 °C, (c), 421 °C, (d), 349 °C, (e), and 249 °C, (f). All Si(100) substrates used for these samples were prepared *ex situ* by the CMOS cleaning procedure except for the sample in panel (a), which was etched with HF. Note that the scan area displayed in panels (a)–(f) are all the same to facilitate comparisons between them.

Panels (a) and (b) of Fig. 5.39 show the morphology of films deposited above 600 °C. These surfaces appear very rough with large mounds or grain-like features. The total height scale in panels (a) and (b) is approximately 45 nm and 50 nm respectively. For comparison, SEM micrographs of the 804 °C sample in panel (a) and the 705 °C sample in panel (b) were shown in Fig. 5.23 (c) and Fig. 5.34 respectively. Panel (c) of Fig. 5.39 shows the morphology of the 502 °C sample, which appears less rough than the samples in panels (a) and (b). This sample was annealed at approximately 600 °C for 1 h after deposition. A large mound is seen in the center of the image with smaller island-like features on it. The height scale of this image is approximately 13 nm. The RHEED pattern of the 502 °C sample (Fig. 5.36 (d)) indicated a smooth surface with small, flat islands, which does not seem to be the case from the STM image. The nature of this discrepancy is not known.

Panels (d) and (e) of Fig. 5.39 show the morphology of films deposited with substrate temperatures of 349 °C and 421 °C, but they represent relatively smooth films produces at deposition temperatures between 349 °C and 460 °C in this work. These samples were annealed after deposition at approximately 600 °C for 1 h. The surface of these samples appear smooth with small, flat, multi-layer 3D islands.

Smaller area scans of these samples show Si (2×1) dimer rows on the islands indicating epitaxial deposition. The height scales in panels (d) and (e) are approximately 1.3 nm and 3.6 nm respectively. Finally, panel (f) shows the morphology of the 249 °C sample, which has a smooth surface covered with small round features approximately 3 nm in size that do not appear epitaxial. The height scale of this image is approximately 1.0 nm. The RHEED pattern of this sample (Fig. 5.36 (a)) indicated an amorphous surface layer on the film, which may explain the round features on the surface and absence of larger epitaxial islands.

It appears from this work that the smoothest epitaxial ^{28}Si films are achieved with deposition temperatures between approximately 349 °C and 460 °C. However, although these smooth ^{28}Si films were achieved with an apparent disappearance of the pinning sites seen in the higher temperature samples, the defects and contaminants causing those pinning sites are likely still present in the film. While their effects do not manifest in the film morphology at low deposition temperatures, they may still affect the bulk crystallinity or even the electronic properties of the films.

5.7 Chemical Purity

5.7.1 Context

The ^{28}Si films produced in this work need to have a high chemical purity in order to be considered comparable to both commercially available electronics grade natural abundance Si as well as the enriched ^{28}Si available in the QI research community. As mentioned at the beginning of this chapter, the third materials goal

for these ^{28}Si films is to have chemical impurity concentrations including C and O below 2×10^{15} cm^{-3}. Chemical contaminates are undesirable in part because of their detrimental effect on the smooth morphology and bulk epitaxy of thin films, as discussed in detail above. Additionally, as mentioned previously, chemical impurities present in the bulk of a ^{28}Si film can act as or induce various scattering sites and charge traps. This reduces electron mobility and other electronic properties important for operating QI devices [91,92]. Further, chemical impurities can possess nuclear spin including ^{13}C, which has a nuclear spin $I = 1/2$, and ^{14}N, which has a nuclear spin $I = 1$. The presence of these nuclear spins will cause decoherence of qubit spins in a quantum computing device, just as ^{29}Si does.

Several sources of chemical contaminants exist within the deposition system that may contribute impurities that become incorporated into the ^{28}Si films. Contaminants can come from various molecular species comprising the background partial pressures in the deposition chamber. A residual gas mass spectrum of the base pressure of the deposition chamber acquired from the RGA is shown in Fig. 2.22 in Chapter 2 and gives insight into the contaminants present in the vacuum such as N, C, O, and F, although quantitative partial pressures are not reliable. The typical base pressure of the deposition chamber was approximately 6.7×10^{-9} Pa (5.0×10^{-11} Torr). Other gaseous contaminants may diffuse into the deposition chamber from the ion beam chamber during deposition. These can originate from either the background base pressure of the ion beam chamber, which was typically approximately 1.3×10^{-5} Pa (1.0×10^{-7} Torr), or the SiH_4 gas source used during deposition. Potential contaminants from the ion beam chamber including N, C, and

O can be seen in the residual gas mass spectrum of the base pressure acquired from the RGA in the ion beam chamber, shown in Fig. 2.3 in Chapter 2. While the SiH_4 source bottle has a purity of 99.999 % according to the gas vendor (Matheson Tri-Gas), the gas manifold used to load SiH_4 into the ion source may contain much higher levels of residual gas impurities because it is only pumped out to roughly 20 mTorr. When heating samples on the manipulator during deposition, the elevated temperatures of the sample holder and other parts of the manipulator can cause increases in the background pressure due to outgassing.

Probably the most significant source of chemical contaminants in the ^{28}Si films, specifically N, C, and O, is the ion beam itself. Selecting for $^{28}Si^+$ ions in the ion beam is the result of tuning the sector mass analyzer such that any ion with a mass-to-charge ratio ≈ 28 u/e $\pm$ 0.18 u/e (at 28 u) will pass through the mass-selecting aperture and propagate to the sample. The acceptance through the aperture of a range of masses approximately 0.36 u wide (for a singly charged ion) around 28 u is due to the width of the mass-selecting aperture (2 mm). This mass range is also similar to the mass resolution at 28 u of 0.35 u, which is the smallest mass that can be resolved by the system based on the maximum measured mass resolving power $\frac{m}{\Delta m} \approx 78$. Any ions with masses within this range will be transported to the sample along with ^{28}Si. Two ionic species that match this criteria are $^{14}N_2^+$ and $^{12}C^{16}O^+$. The mass of ^{28}Si is 27.97692653465(44) u, the mass of $^{12}C^{16}O$ is 27.99491461957(17) u, and the mass of $^{14}N_2$ is 28.00614800886(40) u [170]. Therefore, the separation in mass between ^{28}Si and $^{12}C^{16}O$ is approximately 0.018 u, and the separation in mass between ^{28}Si and $^{14}N_2$ is approximately 0.029 u, which are

both well within the range for transport past the aperture when the 28 u beam is centered on it. A mass resolving power of $\frac{m}{\Delta m} \approx 1600$ would be needed to significantly separate ^{28}Si from $^{12}C^{16}O$ and $^{14}N_2$. The maximum achievable mass resolving power for this system with an ion beam width due only to the energy spread from the ion source, i.e. with no intrinsic beam width, would be approximately 350 at mass 28 for a typical energy spread of $\Delta E = \pm$ 6 eV. This means that for this system, any N_2 and CO ions generated in the ion source will be passed into the deposition chamber and onto the sample along with ^{28}Si. Further, these contaminant species that have a mass separation below the mass resolution of the system are not detectable in an ion beam mass spectrum.

5.7.2 XPS

XPS was used as an initial check on the chemical purity of ^{28}Si samples deposited at elevated temperatures at DC–3 and to compare them to the previous sample measured with XPS, which was deposited at room temperature at LC–2 (Fig. 4.17). This measurement was a search for gross chemical contaminants that may have been introduced into the samples arising from the significant experimental switch from ^{28}Si deposition at LC–2 to DC–3 at elevated temperatures. XPS spectra shown in this section were acquired and analyzed in collaboration with Dr. Kristen Steffens (NIST). XPS spectra were collected after sputter-cleaning the sample with Ar to remove surface contamination from the environment. The measurement parameters for the spectra shown here are similar to those used for the previous sample (see Section 4.3.6.2).

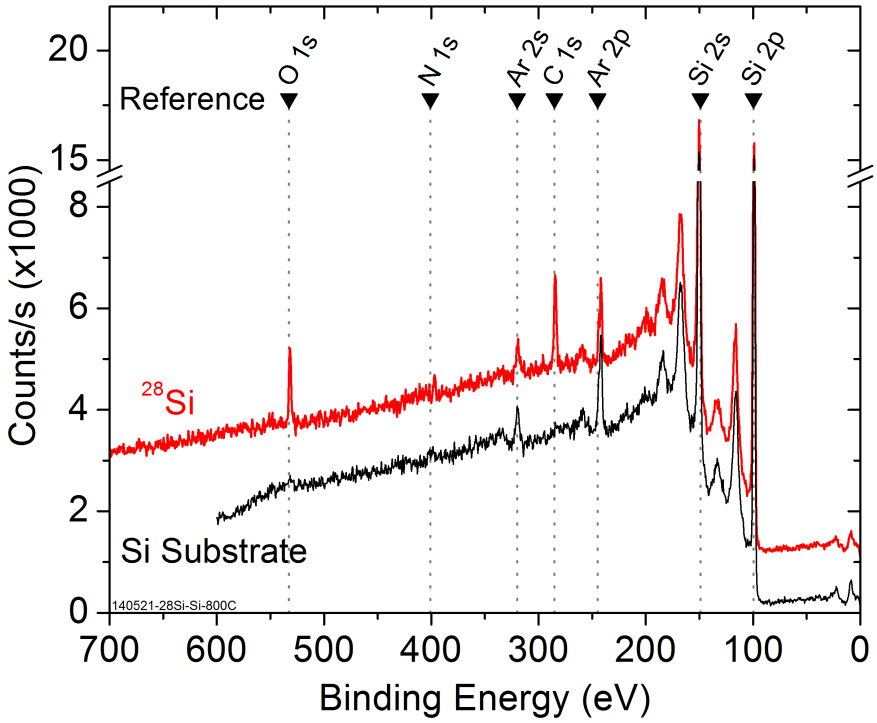

Figure 5.40: XPS spectra of a ^{28}Si sample deposited at 812 °C at DC–3. Count rates vs. electron binding energy for survey scans are shown for the ^{28}Si sample after Ar sputter cleaning (upper spectrum) as well as the substrate away from the deposition area (lower spectrum). The data for the ^{28}Si sample was shifted up for clarity. References for elemental orbital levels are included above relevant peaks. O 1s and C 1s peaks are visible with larger amplitudes in the ^{28}Si film than the substrate.

XPS spectra for the second ^{28}Si sample deposited at DC–3 with a deposition temperature of approximately 812 °C is shown in Fig. 5.40 (upper spectrum). Also shown is a reference spectrum of the Si substrate away from the deposition area (lower spectrum). References for relevant elemental orbital levels are shown at the top.

A C 1s peak is visible at 285.2 eV in the ^{28}Si spectrum corresponding to an atomic fraction of approximately 3.4 %. Additionally, a O 1s peak is visible at 532.7 eV corresponding to an atomic fraction of approximately 4.5 %. No C or O peaks are visible above the noise in the spectrum for the Si substrate. A

small N 1s signal is also present at 400.9 eV corresponding to an atomic fraction of approximately 1.7 %. Both the ^{28}Si and the substrate spectra show Ar peaks due to the Ar sputter cleaning process. The expected instrumental background for C and O in these scans is approximately 1 % to 2 %. This measurement is similar to the previous XPS measurement of a ^{28}Si sample deposited at LC–2 with similar atomic fractions of C and O. The small N concentration in the sample was not previously detected. No other major contaminants were detected in this sample. Given the large background signal for these measurements, it is difficult to place a bound on the expected Si purity for this sample.

5.7.3 SIMS

SIMS was used not only to get a more accurate measurement of N, C, and O concentrations in the ^{28}Si films than XPS can provide but to also analyze the films for a broad range of trace impurities. The SIMS measurements discussed here were performed at EAG Laboratories unless otherwise stated, and are of the major isotope of each element. A SIMS depth profile of the concentration of 22 different potential contaminants in a ^{28}Si film deposited with a substrate temperature of approximately 460 °C at DC–3 is shown in Fig. 5.41. Atomic concentrations of ^{28}Si (circles and line), ^{29}Si (squares and line), and ^{30}Si (triangles and line) are also shown vs. sputter depth as an indicator of the enriched film where the ^{29}Si and ^{30}Si values are reduced. The minimum detected ^{29}Si and ^{30}Si concentrations can only be taken as bounds on the enrichment of this sample because they are limited by the measurement noise floor. At a depth of approximately 145 nm they return to their

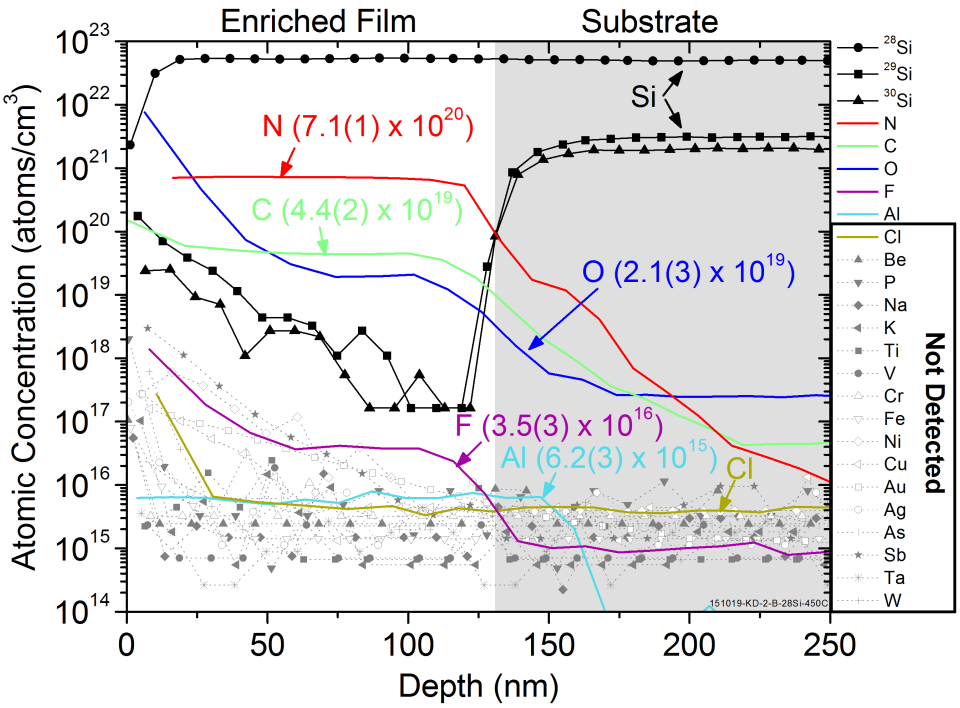

Figure 5.41: SIMS depth profile of the concentration of 22 atomic species in a ^{28}Si sample deposited at 460 °C at DC–3. Atomic concentrations of ^{28}Si (circles and line), ^{29}Si (squares and line), and ^{30}Si (triangles and line) are also shown vs. sputter depth as an indicator of the enriched film. The minimum detected ^{29}Si and ^{30}Si concentrations are limited by the measurement noise floor. At a depth of about 145 nm they return to their natural abundance values in the Si(100) substrate (shaded region), indicating the film thickness. Depth profiles of the atomic concentrations of many elements including light gases and metals (open and closed symbols and lines) in the enriched film and substrate are shown vs. sputter depth. N, C, O, F, and Al were detected in the film while the remaining elements were not, indicated by the box in the legend. The atomic concentration of N in the film is 7.1(1) $\times 10^{20}$ cm^{-3}, the concentration of C in the film is 4.4(2) $\times 10^{19}$ cm^{-3}, and the concentration of O in the film is 2.1(7) $\times 10^{19}$ cm^{-3}. The signals for these elements drop to the measurement detection limit in the substrate.

natural abundance values in the Si(100) substrate, which is marked by the shaded region. This indicates the film interface with the substrate and gives a value for the film thickness. Depth profiles of the atomic concentrations of many elements that are potential contaminants in the ^{28}Si films, including light gases and metals, are shown vs. the sputter depth. N, C, O, F, and Al (solid lines) were all detected

in the film. The remaining elements Cl, Be, P, Na, K, Ti, V, Cr, Fe, Ni, Cu, Au, Ag, As, Sb, Ta, and W (open and closed symbols and lines) were not detected in the film or substrate down to the measurement detection limit, which is an atomic concentration of approximately 1 $\times 10^{16}$ cm^{-3} for Sb, Au, As, and P, and is an atomic concentration of approximately 5 $\times 10^{15}$ cm^{-3} for the remaining elements.

The average atomic concentration of N within the film was measured to be 7.1(1) $\times 10^{20}$ cm^{-3}, or 1.42(2) %. The uncertainties of the values of atomic concentrations for the SIMS measurements discussed here are the standard deviations of the means. This value is similar to the value of the N concentration of a ^{28}Si sample determined from XPS of approximately 1.7 %. The average atomic concentration of C in the film was measured to be 4.4(2) $\times 10^{19}$ cm^{-3}, or 880(40) ppm, and the average atomic concentration of O in the film was measured to be 2.1(7) $\times 10^{19}$ cm^{-3}, or 420(140) ppm. These values are significantly less than the C and O values measured by XPS. This may be due in part to the high measurement background in XPS for C and O. The differences between the two samples is the *ex situ* cleaning procedure (none vs. CMOS) and the deposition temperatures (812 °C vs. 460 °C). It may be that an increase in the background pressure during deposition of the 812 °C sample due to the high temperature of the sample and holder is responsible for increased C and O concentrations. The signals for these elements drop to the detection limit of the measurement in the substrate.

The structural relation between chemical impurities and the surrounding Si crystal is dictated by the solid solubility of those impurities in Si. Small changes in the atomic concentration of an impurity can greatly influence its effect on the

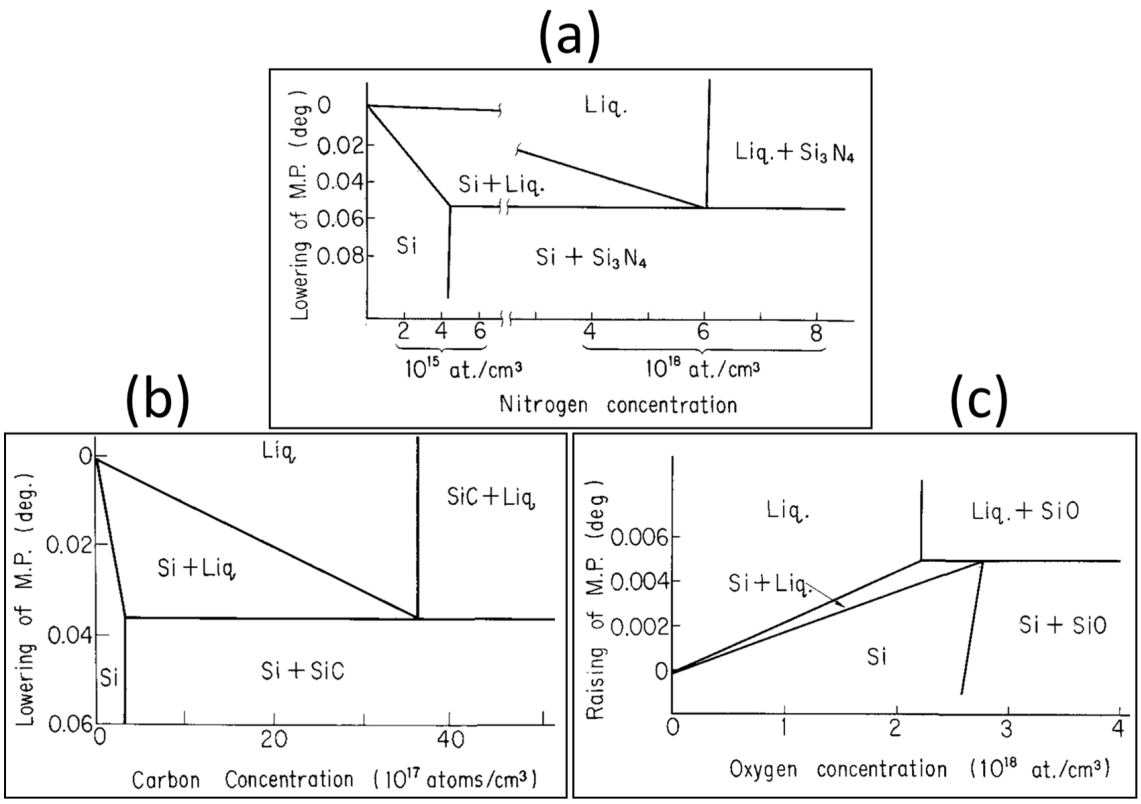

Figure 5.42: Phase diagrams for the N-Si, C-Si, and O-Si systems with low impurity concentrations near the solid solubility limit. (a) The N-Si phase diagram near the melting point shows the solid solubility of N in Si is about 4.5 $\times 10^{15}$ cm^{-3} and above this, Si_3N_4 forms. (b) The C-Si phase diagram near the melting point shows the solid solubility of C in Si is about 3.2 $\times 10^{17}$ cm^{-3} and above this, SiC forms. (c) The O-Si phase diagram near the melting point shows the solid solubility of O in Si is about 2.8 $\times 10^{18}$ cm^{-3} and above this, SiO forms. ((a) and (c) from Ref. [171], (b) from Ref. [172])

structural properties of the host Si. Phase diagrams for the N-Si, C-Si, and O-Si systems in the case of extremely low impurity concentrations near the solid solubility are shown in Fig. 5.42. The N-Si phase diagram from Ref. [171] in panel (a) shows that the solid solubility limit of N in Si is approximately 4.5 $\times 10^{15}$ cm^{-3}. At atomic concentrations of N that are higher than this, Si_3N_4 crystallites form in the Si. Similarly, the C-Si phase diagram from Ref. [172] in panel (b) shows that the solid solubility limit of C in Si is approximately 3.2 $\times 10^{17}$ cm^{-3}. At atomic concentrations

of C that are higher than this, SiC crystallites form in the Si. Finally, the O-Si phase diagram from Ref. [171] in panel (c) shows that the solid solubility limit of O in Si is approximately 2.8 $\times 10^{18}$ cm^{-3}. At atomic concentrations of O that are higher than this, SiO clusters form in the Si. Based on these values, the measured atomic concentrations of N, C, and O in the 460 °C sample analyzed in Fig. 5.41 are well beyond their respective solid solubility limits in Si and so those contaminants likely exist as Si_3N_4 and SiC crystallites, and SiO clusters in the ^{28}Si film.

The average atomic concentration of F in the 460 °C sample analyzed in Fig. 5.41 was measured to be 3.5(3) $\times 10^{16}$ cm^{-3}, or 0.70(6) ppm. This F is believed to originate from the background vacuum in the deposition chamber and incorporate into the depositing film. A partial pressure of F is always observed in the RGA mass spectrum at a level larger than H_2O, and can be seen in the RGA spectrum recorded while operating the ion beam in Fig. 5.3. Several instruments and apparatus components within the vacuum chamber contain teflon insulation (PTFE), which is suspected to outgas F in UHV environments and contribute to the observed partial pressure. These components include insulated wires on the manipulator that supply power for sample heating, insulated wires on the STM tip preparation tool, which heats STM tips, teflon support structures for the ion beam deceleration lenses, and Viton seals on gate valves. The STM tip preparation tool in particular was observed to significantly increase the partial pressure of F while in use. Eliminating F-containing compounds within the vacuum system can reduce the concentration of F in samples. The atomic concentration of Al detected in the film is 6.2(3) $\times 10^{15}$ cm^{-3}, or 0.12(2) ppm. The origin of this Al is an Al deposition

source sitting above the sample location that consists of an Al wire wrapped around a tungsten heating element.

The total purity of this ^{28}Si sample calculated from these measurements is approximately 98.45(2) %, which is quite low compared to commercial Si wafers. The concentrations of N, C, and O in the sample are far too high for the material to be viable for use in quantum coherent devices or other QI related experiments. The concentration of nuclear spins due to the ^{14}N ($I = 1$) in the sample is much larger than the residual ^{29}Si isotopic concentration and is only roughly a factor of three lower than that of ^{29}Si in natural abundance Si. It is difficult to determine if the N, C, and O detected in these films predominantly originates from the ion beam or the background vacuum. It is unlikely that the N concentration is due to adsorption from the vacuum because the partial pressure of N_2 needed to account for the measured concentration (with unity sticking) is higher than the measured partial pressure of N_2 in the chamber during deposition. This indicates that most, i.e. likely > 90 %, of the N in this sample was introduced through the ion beam.

A second ^{28}Si sample deposited at DC–3 was also analyzed by SIMS for chemical contaminants after the first sample. This second sample had a deposition temperature of approximately 421 °C. The only significant differences between the first sample and this second one are that the deposition rate of the second sample was roughly two times larger and the gas manifold was purged with Ar instead of N_2 before deposition. It was thought that the previous N_2 purge may have contributed to the high atomic concentration of N measured in the first sample, although this was not verified. The atomic concentrations of N, C, and O were all lower than

those of the first sample but not significantly, with slightly over half the total impurities. The average atomic concentration of N in this film was measured to be 4.16(5) $\times 10^{20}$ cm^{-3}, or 0.83(1) %. The average atomic concentration of C in the film was measured to be 1.81(2) $\times 10^{19}$ cm^{-3}, or 363(4) ppm, and the average atomic concentration of O in the film was measured to be 6.93(6) $\times 10^{18}$ cm^{-3}, or 139(1) ppm. The total Si purity of this second sample is approximately 99.12(1) %.

In total, three SIMS measurements were made on this sample in three different locations on the deposition spot. These three locations had three different measured film thicknesses, which also means that they had three different local deposition rates. The measurements of the chemical contaminants for the three locations can then be compared for different deposition rates while other variables including the background pressure are constant. Such an analysis can give insight into the source of the contaminants. For adsorption from the background vacuum, an increasing deposition rate would result in a decreasing contaminant concentration because the gas flux is decreasing relative to the ion beam flux. Contaminants incorporated from the ion beam, however, should remain constant for different deposition rates. The three deposition rates determined from the SIMS depth profiles of the three spots on this sample are approximately 0.11 nm/min, 0.32 nm/min, and 0.88 nm/min. The N concentrations were found to not decrease with increasing deposition rate and instead increased roughly 39 % from the area with the lowest deposition rate to that with the highest. This again indicates that the detected N is not significantly due to adsorption from the vacuum. C and O concentrations, however, were found to decrease with increasing deposition rate. The C concentration decreased by roughly

71 % from the area with the lowest deposition rate to that with the highest. This result indicates that the C and O concentrations measured in these films are due, at least partially, to adsorption from the vacuum.

To determine the minimum N, C, and O contamination that is contributed to samples by adsorption and incorporation during ^{28}Si deposition, any effects of the ion beam must be eliminated. To this end, a natural abundance Si sample was deposited in the deposition chamber at DC–3 and analyzed by SIMS for chemical contaminants. This sample was deposited by sublimating Si from a bare substrate held at approximately 1150 °C and positioned over the surface of the target substrate. The target Si(100) substrate was flash annealed before the deposition and was nominally at room temperature during it, although it may have been heated radiatively from the source substrate.

SIMS depth profiles of the atomic concentrations of N, C, and Cl (solid lines) in the ^{nat}Si film are shown vs. sputter depth in Fig. 5.43. An O profile did not yield usable results due to atmospheric contamination. The profiles show slightly increased values near the surface due to environmental surface contamination before leveling off through the bulk of the film. The atomic concentrations of N and C then dip just beyond 200 nm before peaking at approximately 227 nm. This peak corresponds to the interface between the film and the substrate, which is marked by the shaded region and indicates the film thickness. The N and C signals peak at the interface because adsorbates will accumulate on the surface from the vacuum before deposition begins. Initial heating of the sublimation source will also increase the partial pressures of adsorbates, increasing the contaminant concentrations in

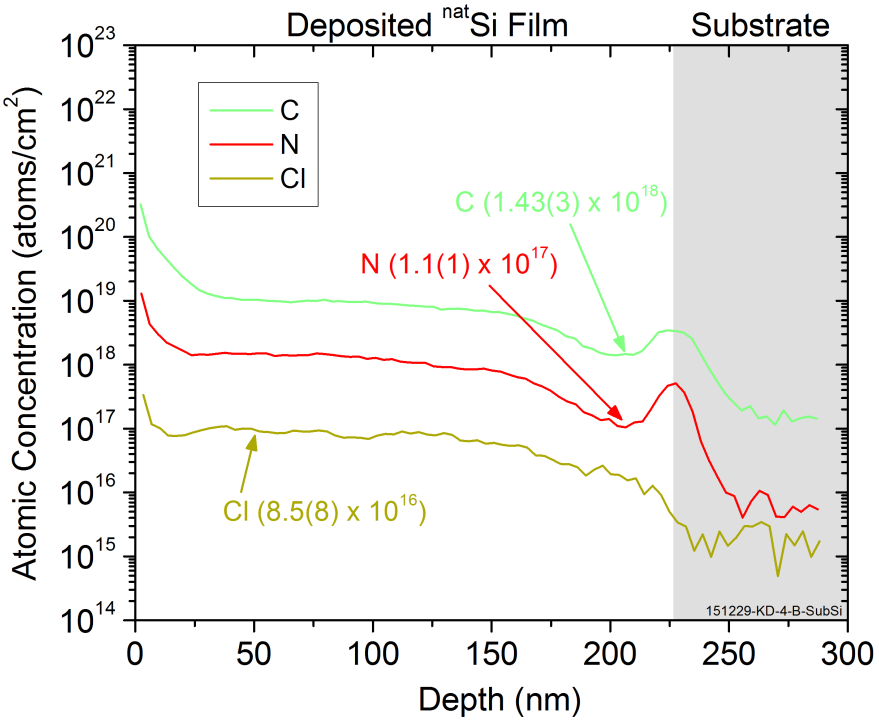

Figure 5.43: SIMS depth profile of a ^{nat}Si film deposited at room temperature at DC–3. This film was deposited on a Si(100) substrate by sublimating Si from a second wafer held over the surface. Atomic concentrations of N, C, and Cl in the deposited film and substrate are shown vs. sputter depth. The interface between the film and substrate (shaded region) is indicated by the peak in the N and O signals at a depth of about 227 nm, which also indicates the film thickness. The minimum atomic concentration of N in the film at about 206 nm is 1.1(1) $\times 10^{17}$ cm^{-3}, and the minimum atomic concentration of C in the film is 1.43(3) $\times 10^{18}$ cm^{-3}.

the film. The N, C, and Cl signals in the substrate are at the detection limit of the measurement. The dip in the atomic concentrations of N and C near the interface gives an upper bound on the minimum possible N and C concentrations that would be expected in a ^{28}Si film deposited without contamination from other sources such as the ion beam.

The minimum atomic concentration of N in the ^{nat}Si film was measured to be 1.1(1) $\times 10^{17}$ cm^{-3}, or 2.2(2) ppm. The minimum atomic concentration of C in the film was measured to be 1.43(3) $\times 10^{18}$ cm^{-3}, or 28.7(6) ppm. The higher

concentrations of N and C throughout the bulk of the film are likely due to increased outgassing of these elements when the target sample began to be heated by the source. While the detected atomic concentration of N in the ^{nat}Si film is roughly 6.5 $\times 10^3$ times lower than that measured in the first ^{28}Si film, it is still more than 10 times higher than the ^{29}Si isotopic concentration in the more highly enriched ^{28}Si samples produced in this work. Additional pumping or a faster growth rate may be needed to reduce contaminants from the vacuum to concentrations that meet the purity goal for ^{28}Si films of 2×10^{15} cm^{-3} stated at the beginning of this section.

Cl is also detected within this film with an average atomic concentration of 8.5(8) $\times 10^{16}$ cm^{-3}, or 1.7(2) ppm. This Cl may be outgassing from the sample holders or other elements near the sample that get hot because there is no peak in the concentration near the surface due to build up from the vacuum. This means that Cl only appears to be present once the sample heating was turned on to start the deposition. Evidence of Cl in the vacuum chamber can be seen in the residual gas mass spectrum of the RGA. During heating of samples and sample holders for either degassing or sample flashing, several mass peaks can appear that are not normally present in the chamber, particularly peaks at masses of 31 u and 50 u. An example of a residual gas mass spectrum from the RGA that was recorded while a Si substrate was being degassed is shown in Fig. 5.44. A spectrum of the base pressure of the deposition chamber (diagonal line fill) recorded at a later date is given for reference and shows major residual gas peaks corresponding to H_2 (2 u), F (19 u), CO and N_2 (28 u), and CO_2 (44 u). The Si substrate was degassed at approximately 600 °C while recording a RGA spectrum (solid fill). During degassing, the pressure

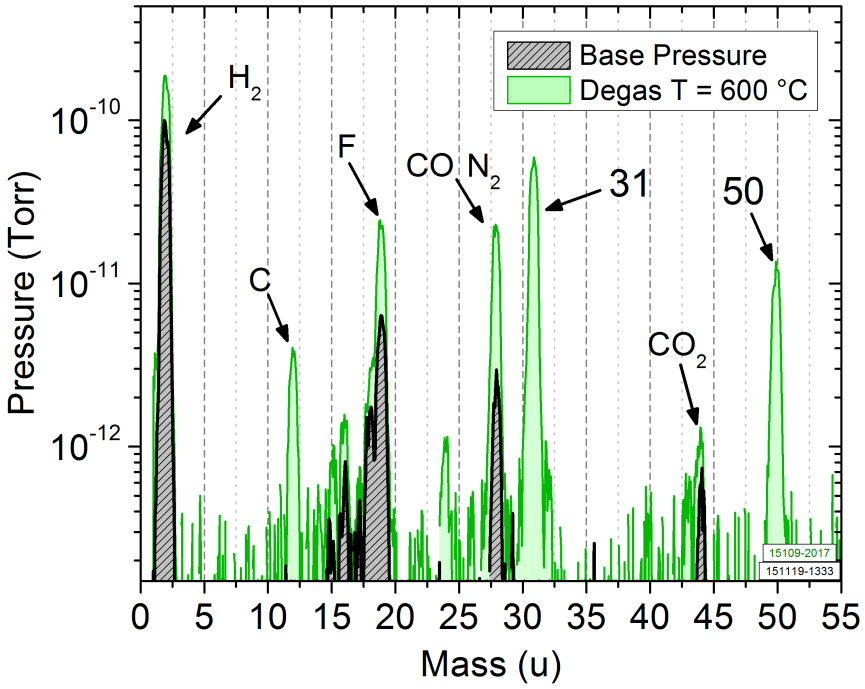

Figure 5.44: Residual gas mass spectra collected from the RGA in the deposition chamber while degassing a Si substrate at about 600 °C. The base pressure of the chamber (diagonal line fill) is shown for reference with peaks corresponding to H_2, F, CO and N_2, and CO_2 visible. When the substrate is heated for degassing, the pressure increases and several new peaks appear (solid fill) including C and those at masses 31 u and 50 u, which may indicate Cl-containing molecules.

rises from the typical base pressure, evidenced by the aforementioned peaks rising. Additionally, several other peaks appear in the spectrum that are not present or much smaller in the base pressure spectrum including a C peak as well as peaks at masses of 31 u and 50 u.

There are several chemical compounds that are likely candidates for being associated with these masses in a vacuum environment, some of which contain Cl. Chloromethane (CH_3Cl) and related molecules Cl_2F_2 and CF_3Cl all contribute significant signals to mass 50 u if present in a vacuum. CF_3Cl also appears at mass 31. The compounds containing F are possible because F is known to be present in the

system, as seen in the base pressure spectra. Other possible candidates for the peak at 31 u are ethanol and propanol. The source of these alcohols as well as Cl may be the *ex situ* chemical cleaning procedure used on the substrates. The SC–2 solution used contains HCl and so it may be that some residue from the clean resides on the chip and is then released in the chamber during degassing and flashing procedures as well as when samples are heated during deposition of Si films.

N_2 and CO contamination in the ^{28}Si ion beam can be measured in both the mass spectrum and in a deposited ^{28}Si sample if the concentrations are high enough. A demonstration of this resulted from the case of a leak from air in the gas manifold system that delivers SiH_4 to the ion source. An increase in the concentration of N_2 and O_2 in the ion source while it is running then leads to increased amounts of $^{14}N_2^+$ and $^{12}C^{16}O^+$ ions being created and extracted into the beamline. Tuning the sector mass analyzer to select for ^{28}Si then also selects these contaminants which are measured in the SiH_4 mass spectrum or deposited. ^{28}Si samples which were deposited with these conditions are referred to here as "N-contaminated" samples. A mass spectrum of SiH_4 that shows a large amount of N_2 and/or CO contamination in the ion beam is shown in Fig. 5.45. The ion currents shown in this figure (open and closed circles) were recorded while sweeping the mass analyzer current, and thus the magnetic field of the analyzer (top axes). Panel (a) shows a semi-log plot of a mass spectrum used for depositing a ^{28}Si sample at DC–3 using the low pressure plasma mode of the ion source. The typical SiH_4 current peaks are seen including the 28 u peak, which is ^{28}Si, and the 29 u peak, which is both ^{28}SiH and ^{29}Si. The 29 u peak is assumed to be ≈ 5 % ^{29}Si based on previous mass spectrums. Several

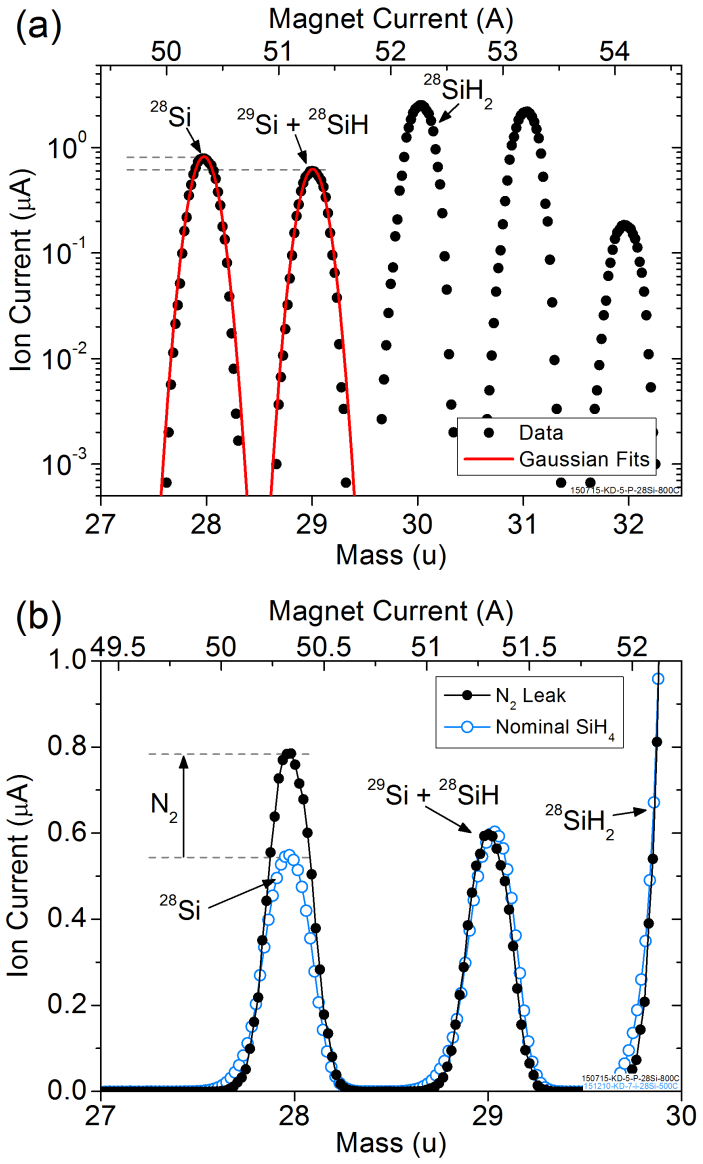

Figure 5.45: SiH_4 ion beam mass spectrum for N-contaminated ^{28}Si samples deposited at DC–3 using the low pressure plasma mode of the ion source. The ion currents (open and closed circles) are recorded while sweeping the mass analyzer current, and thus the magnetic field (top axes). (a) Mass spectrum for samples contaminated with large amounts of N shown on a semi-log scale with current peaks typical of SiH_4. The 28 u peak is ^{28}Si and the 29 u peak is both ^{28}SiH and ^{29}Si, assumed to be $\approx$ 5 % of the peak. Several higher order hydrides are also shown. Gaussian fits (line, Eq. (2.14)) to the 28 u and 29 u peaks are shown superimposed on the data. The 28 u peak appears higher than the 29 u peak, which is atypical. (b) Comparison between the spectrum in (a) (closed circles and line) and a nominal SiH_4 spectrum (open circles and line) plotted on a linear scale. The difference in signal of the 28 u peaks of the two spectra relative to the 29 u peak is clear. The additional current in the 28 u peak beyond the nominal ^{28}Si current is presumed to be mostly N_2.

higher order hydride peaks are also shown. Gaussian fits (line, Eq. (2.14)) to the 28 u and 29 u peaks are shown superimposed on the data. Unlike a typical SiH_4 mass spectrum for the low pressure mode such as the one acquired before depositing a ^{28}Si sample shown in Fig. 5.4, the 28 u peak appears higher than the 29 u peak here, indicated by the horizontal dashed lines. The increased current in the 28 u peak is due to the contaminants.

The difference between the spectra is highlighted in panel (b) of Fig. 5.45, which compares the contaminated mass spectrum (closed circles and line) to a nominal SiH_4 mass spectrum (open circles and line) from Fig. 5.4 on a linear current scale. These two spectra are comparable because the current levels at the 29 u peak are nearly identical. The difference in the current peak height of the contaminated spectrum compared to the nominal spectrum is clear here. The additional current in the 28 u peak beyond the nominal ^{28}Si current is presumed to be mostly N_2. This contamination comprises approximately 30 % of the 28 u current. For a contaminant beam of only N_2, this would actually amount to approximately 46 % contamination in the sample because each N_2 ion contains two N atoms.

A ^{28}Si sample was then deposited using a contaminated ion beam similar to that represented by Fig. 5.45, and it was analyzed by SIMS for chemical contaminants. This SIMS analysis was done in collaboration with Dr. David Simons (NIST). SIMS depth profiles of the atomic concentrations of ^{14}N, ^{12}C, ^{16}O, (lines) and ^{13}C (circles and line) in the N-contaminated ^{28}Si sample deposited with a substrate temperature of approximately 712 °C at DC–3 are shown vs. sputter depth in Fig. 5.46. Also shown is a depth profile of the ^{29}Si isotope fractions (squares

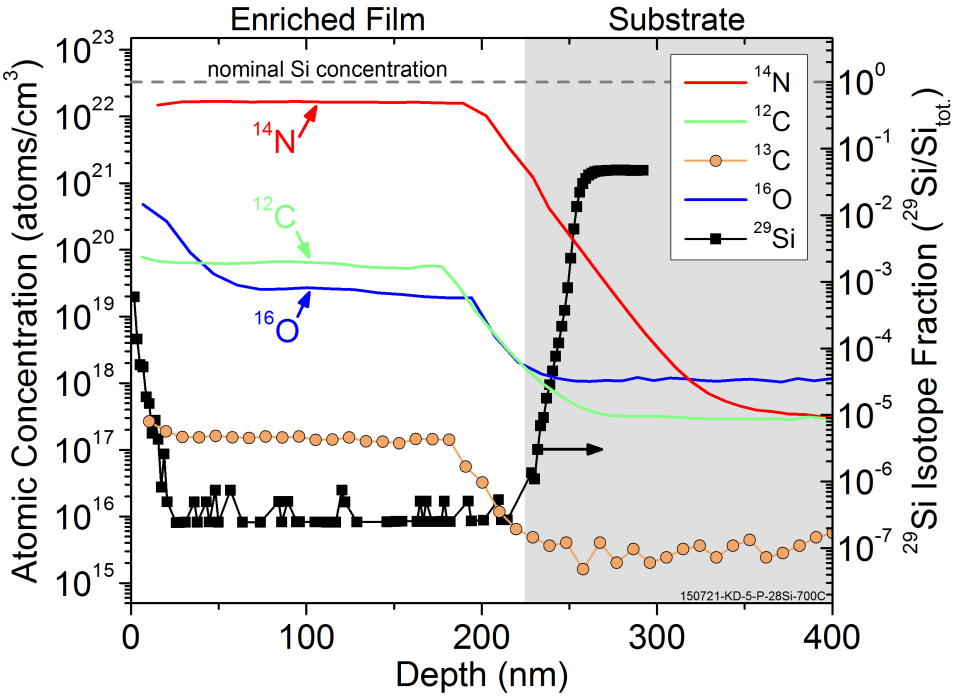

Figure 5.46: SIMS depth profiles showing the atomic concentration of ^{14}N, ^{12}C, ^{16}O, (lines) and ^{13}C (circles and line) vs. sputter depth in a ^{28}Si sample deposited at 712 °C at DC–3. Also shown is a depth profile of the ^{29}Si isotope fraction (squares and line) vs. sputter depth on the right axis as an indicator of the enriched film. The average ^{29}Si isotope fraction in the film is about 0.132(27) ppm. At a depth of about 256 nm, the ^{29}Si isotope fraction returns to the natural abundance value in the Si(100) substrate (shaded region), which gives a value for the film thickness. The atomic concentration of N in the ^{28}Si film is greater than 1 $\times 10^{22}$ cm^{-3}. This value is not quantitatively accurate, but shows that N is present in the film at a concentration of roughly 30 %. The tail of the N profile into the substrate is an artifact of the SIMS measurement. The measurements of C and O are accurate and show that the concentration of ^{12}C in the film is 6.1(1) $\times 10^{19}$ cm^{-3}, the concentration of ^{13}C in the film is 1.46(3) $\times 10^{17}$ cm^{-3}, and the concentration of ^{16}O in the film is 2.3(1) $\times 10^{19}$ cm^{-3}. The signals for these elements in the substrate are due to the measurement background.

and line) vs. sputter depth, which corresponds to the right axis as an indicator of the deposited enriched film. The average measured ^{29}Si isotope fraction in the film is 0.132(27) ppm. At a depth of approximately 256 nm, the ^{29}Si isotope fractions return to the natural abundance value in the Si(100) substrate, which is indicated by the shaded region and gives a value for the film thickness. The atomic concen-

tration of ^{14}N detected in this film is extremely high. The measurement of such a high concentration is not quantitatively accurate for the measurement conditions used here, but it appears greater than 1 $\times 10^{22}$ cm^{-3}. This measurement does show that ^{14}N is present in the film at a likely concentration of roughly 30 %. This rough SIMS value for the N contamination is supported by other measurements of similar N-contaminated films including XPS and energy dispersive x-ray spectroscopy (EDX), which give similar values. With this much N present in the ^{28}Si film, it is likely that a significant amount of silicon nitride (Si_3N_4) forms. The long tail of the ^{14}N profile that extends into the substrate is an artifact of the SIMS measurement. ^{12}C and ^{16}O have concentrations much lower than that of ^{14}N. The average atomic concentration of ^{16}O in the film was measured to be 2.3(1) $\times 10^{19}$ cm^{-3}, or 470(20) ppm. This concentration of O is only slightly higher than that of the previous ^{28}Si sample, which was not deposited with a contaminated beam. The average atomic concentration of ^{12}C in the film was measured to be 6.1(1) $\times 10^{19}$ cm^{-3}, or 1240(20) ppm, and the average atomic concentration of ^{13}C in the film was measured to be 1.46(3) $\times 10^{17}$ cm^{-3}, or 2.98(6) ppm. This concentration of C increased over that of the previous ^{28}Si sample by roughly the same amount that the concentration of O increased, which is about 2 $\times 10^{19}$ cm^{-3}. The signals for N, C, and O in the substrate are due to the background level of the measurement.

The ratio of ^{12}C to ^{13}C in this sample can indicate its origin because only ^{12}C is selected through the ion beam while both isotopes are present in their natural abundance coming from the vacuum. In this sample, the C ratio is measured to be ^{12}C/^{13}C $\approx$ 420. This ratio is larger than the natural abundance ratio of ap-

proximately 89.9, meaning that the C is being enriched and thus must be at least partially coming from the ion beam. Assuming that all the ^{13}C originates from the background pressure in the vacuum and using the C natural abundance ratio, it is determined that the atomic concentration of ^{12}C from the vacuum is approximately 1.3 $\times 10^{19}$ cm^{-3}, and the atomic concentration of ^{12}C from the ion beam is approximately 4.8 $\times 10^{19}$ cm^{-3} in this sample.

In order to produce ^{28}Si film with higher purities, several experimental improvements were made to the system, including the aforementioned switch to using Ar to purge the gas manifold instead of N_2. First, the Al deposition source was relocated to another part of the chamber and away from the manipulator where the sample sits during deposition at DC–3. Next, some in-vacuum components that outgas F, specifically PTFE-coated wires on the manipulator and the STM tip preparation tool, were removed from the system. These wires were replaced with Kapton-coated wires. Then, the background pressure in both the deposition chamber and the ion beam chamber were reduced to minimize contaminants adsorbing from the vacuum during deposition. In the ion beam chamber, a gate valve that was not rated for UHV was removed from the system. This resulted in a reduction in the base pressure of the ion beam chamber from approximately 1.3 $\times 10^{-5}$ Pa (9.4 $\times 10^{-8}$ Torr) when the previously analyzed ^{28}Si sample was deposited (Fig. 5.41) to approximately 3.9 $\times 10^{-6}$ Pa (2.9 $\times 10^{-8}$ Torr) when the first ^{28}Si sample was deposited after these changes were made. The base pressure in the deposition chamber was reduced by installing a new TSP to add more pumping capacity. Also, it was baked more thoroughly than what was previously done and

at higher temperatures of 150 °C to 200 °C. These factors resulted in a reduction in the base pressure from approximately 2.3 $\times 10^{-8}$ Pa (1.7 $\times 10^{-10}$ Torr) for the previously analyzed sample to 8.3 $\times 10^{-9}$ Pa (6.2 $\times 10^{-11}$ Torr) for the next sample deposited after these changes. Finally, for samples deposited after these experimental improvements, the high pressure plasma mode of the ion source was used. This mode produces higher ^{28}Si ion fluxes which resulted in increased growth rates of samples. Depositing with higher growth rates should reduce the concentration of contaminants adsorbed from the vacuum. Also, the higher cracking efficiency of the high pressure mode may result in cracking of some N_2 molecules in the ion source, which would eliminate them from the 28 u ion beam.

After enacting these changes, another ^{28}Si sample was deposited and analyzed for chemical contaminants by SIMS. This sample was deposited with a substrate temperature of approximately 460 °C at DC–3 using the high pressure mode of the ion source. SIMS depth profiles of the atomic concentrations of N, C, O, F, Cl, Al, and Mo (lines) in this ^{28}Si sample are shown vs. sputter depth in Fig. 5.47. Mo was analyzed in this sample to check for signs of contamination due to the Mo sample holder that contacts the substrate. Also shown are depth profiles of ^{28}Si (circles and line), ^{29}Si (squares and line), and ^{30}Si (triangles and line), which correspond to the right axis in arbitrary units related to the count rate that are roughly aligned to the atomic concentrations on the left axis, as an indicator of the ^{28}Si film. At a depth of approximately 293 nm, the concentrations of the Si isotopes increase and return to their natural abundance values in the Si(100) substrate, indicated by the shaded region, and giving a value for the film thickness. The minimum detected ^{29}Si and

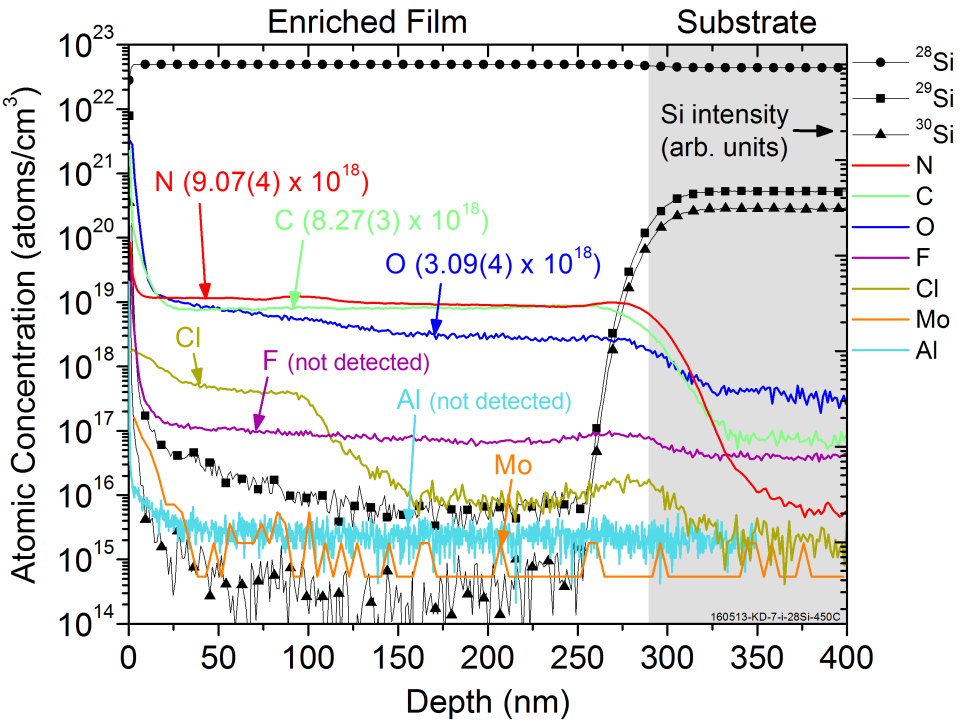

Figure 5.47: SIMS depth profiles of the concentration of contaminants in a ^{28}Si film deposited at 460 °C at DC–3 using the high pressure mode of the ion source. Atomic concentrations of ^{28}Si (circles and line), ^{29}Si (squares and line), and ^{30}Si (triangles and line) are also shown vs. sputter depth as an indicator of the ^{28}Si film. The Si concentrations correspond to the right axis, displayed in arbitrary units. The minimum detected ^{29}Si and ^{30}Si concentrations are limited by the measurement noise floor. At a depth of about 292 nm they return to their natural abundance values in the Si(100) substrate (shaded region), indicating the film thickness. Depth profiles of the atomic concentrations of N, C, O, F, Cl, Al, and Mo (lines) are shown vs. sputter depth. N, C, O, and Cl were detected in the film. F and Al were not detected and their signals are at the measurement detection limit. The concentration of N in the film is 9.07(4) $\times 10^{18}$ cm^{-3}, the concentration of C in the film is 8.27(3) $\times 10^{18}$ cm^{-3}, and the concentration of O in the film is 3.09(4) $\times 10^{18}$ cm^{-3}. The signals for these elements drop to the measurement detection limit in the substrate. It is unclear why Cl is detected at two different concentrations in the film.

^{30}Si concentrations are taken as bounds on the enrichment because they are limited by the measurement noise floor, which for ^{29}Si is approximately 20 ppm.

In this ^{28}Si sample, N, C, O, and Cl are all detected in the film, while F and Al are not detected. The signals for F and Al are at the detection limit of the measurement in the film and substrate, which is approximately 1 $\times 10^{17}$ cm^{-3} for F

and 3 $\times 10^{15}$ cm^{-3} for Al. The elimination of Al in this sample compared to the previous sample is likely due to moving the Al deposition source away from the sample location. The elimination of F in this sample compared to the previous sample may be due in part to the removal of PTFE-coated wires in the chamber, although the partial pressure of F in the chamber was still present after removing them. It was unclear if the concentration of F in the vacuum was reduced because a different RGA was used to measure residual gases after these experimental changes were made, and it is difficult to compare the absolute values of the partial pressures to those of the previous instrument. It is unclear why Cl is detected at two different concentrations within the film. From the surface down to a depth of approximately 100 nm, the average atomic concentration of Cl is 4.11(4) $\times 10^{17}$ cm^{-3}, or 8.24(8) ppm. The atomic concentration of Cl then drops to 8.6(3) $\times 10^{15}$ cm^{-3}, or 0.172(6) ppm in the remainder of the film. This indicates that something changed roughly midway through the deposition. It may be that part of the sample holder started heating slowly during the deposition which caused increased outgassing including a Cl compound, as mentioned previously. Throughout most of the film the Mo signal is also at the detection limit, although there may be a slight increase between a depth of 50 nm and 100 nm to an atomic concentration of 36(8) ppb.

The atomic concentrations of N, C, and O in this ^{28}Si sample are clearly reduced from those of the previous sample shown in Fig. 5.41. Note that the scale of the vertical axis of that figure and Fig. 5.47 are the same to facilitate easier comparisons. The average atomic concentration of N in the film was measured to be 9.07(4) $\times 10^{18}$ cm^{-3}, or 181.8(8) ppm. N was reduced compared to the previ-

ous sample by a factor of roughly 78. The average atomic concentration of C in the film was measured to be 8.27(3) $\times 10^{18}$ cm^{-3}, or 165.7(6) ppm. C was reduced compared to the previous sample by a factor of roughly 5. Finally, the average atomic concentration of O in the film was measured to be 3.09(4) $\times 10^{18}$ cm^{-3}, or 61.9(8) ppm, which is reduced by almost a factor of 10 compared to the previous sample. The total purity for this ^{28}Si sample determined from these measurements is approximately 99.96(2) %. The atomic concentrations of N and C in this sample are above their solid solubility limits, similar to the previous sample. Additionally, the atomic concentration of O in this sample is also slightly over its solid solubility limit in Si. This indicates that Si_3N_4, SiC, and SiO are all likely present in the ^{28}Si film.

The reduction of N in the second sample compared to the first seems likely due to changes in the ion beam. This is because the partial pressure of N_2 in the deposition chamber during deposition appears to be similar for both of the samples, although it is difficult to determine precisely because of the overlap of N_2 and ^{28}Si at 28 u in the residual gas mass spectrum of the RGA as well as other uncertainties. The deposition rate of the final sample deposited using the high pressure mode (2.21 nm/min) was roughly six times higher than that of the first sample (0.37 nm/min), which could account for some of the decrease in the N concentration if the N originated from the background vacuum. However, the reduction in the N concentration is still more than an order of magnitude lower than what would be expected just due to the increased deposition rate. So, the remaining reduction may be due to the ion beam. Use of the high pressure mode of the ion source for

the final sample may lead to a lower concentration of N in the 28 u beam relative to ^{28}Si. If the N_2 ion flux for both the low pressure and high pressure modes is similar, then the roughly factor of five increase in ^{28}Si beam flux (ion current) for the final sample compared to the first would result in a lower concentration of N relative to ^{28}Si. Additionally, the possibility of N_2 molecules being cracked more efficiently by the high pressure mode into atomic N and thus eliminated from the 28 u beam would also reduce the relative N concentration. The results from several samples do seem to support this hypothesis showing that the atomic concentration of N measured in the samples is inversely related to the ^{28}Si ion beam current, although only one of those samples was deposited using the high pressure mode. This inverse relationship can be seen in Fig. 5.48 showing the atomic concentration of N as well as C and O vs. the total 28 u ion current used for deposition. The data with ion currents around 0.5 μA correspond to the first two samples deposited using the low pressure mode discussed above, while the data with an ion current of roughly 2.8 μA corresponds to the final sample discussed in this section, which was deposited using the high pressure mode. The uncertainties in the atomic concentrations (most are smaller than the data symbols) are the standard deviations of the means, and an uncertainty of 50 nA was assigned to the values of the ion current. The atomic concentration of N (open squares) appears to have a strong inverse relationship to the ion current, decreasing roughly a factor of 80 while the 28 u ion beam current increases roughly a factor of five. This trend suggests that the higher concentrations of N measured in the first samples are likely due to ballistic incorporation from the ion beam. This also indicates that both increasing the ^{28}Si ion current and use of

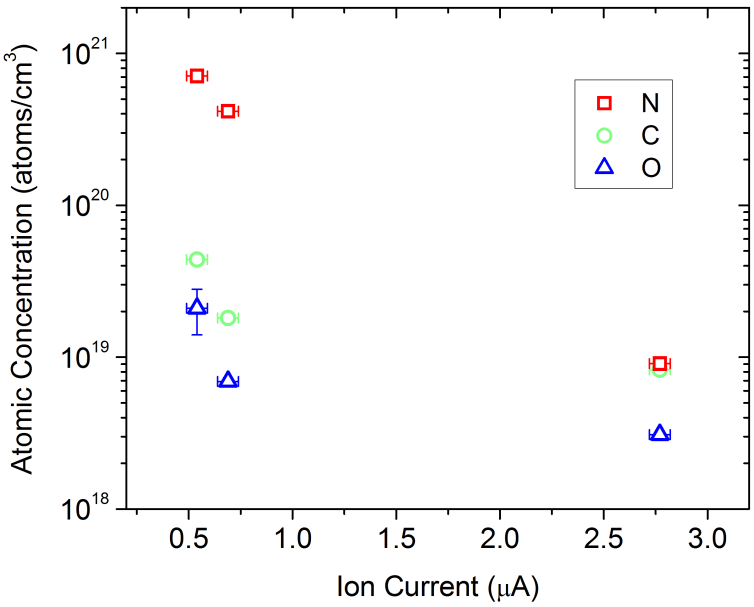

Figure 5.48: Atomic concentrations of N (open squares), C (open circles), and O (open triangles) for three ^{28}Si samples vs. the ion current used for deposition of the samples. The data with ion currents around 0.5 μA correspond to the samples deposited using the low pressure mode, while the data with an ion current of 2.8 μA corresponds to the sample deposited using the high pressure mode. The concentrations of N, C, and O all show an inverse relationship to the ion current, but N varies much more strongly than C and O, indicating that N contamination is more likely due to N_2 in the ion beam.

the high pressure mode do reduce the relative N_2 concentration in the beam. The atomic concentrations of C (open circles) and O (open triangles) are also inversely related to the ion current, but more weakly so than N. The decrease in the concentrations of C and O are likely mostly due to the increased deposition rates resulting from the increased ion current, similar to the result discussed above for the three measurements of the second analyzed sample.

The remaining N, C, and O in the final sample are difficult to attribute to either adsorption from the vacuum or deposition from the ion beam, and their presence is likely due to a combination of both. Either way, the solution to reducing

them further is a reduction of the partial pressures of these elements in the vacuum because the contaminants in the ion beam ultimately originate from the vacuum in the ion source. There also seems to be a significant amount of N_2 or CO entering the chamber with the SiH_4 gas from the gas manifold, probably more than what is due to the base pressures of the two chambers. Reducing N, C, and O concentration in the deposition chamber, ion beam chamber, and the gas manifold is required to reliably improve the purity of ^{28}Si films deposited with this system in order to achieve the third materials goal discussed here.

5.8 Crystallinity: Film Inspection via TEM

The ^{28}Si samples deposited at elevated temperatures at sample location DC–3 exhibit different morphologies depending on the deposition temperature, as discussed previously in this chapter. Rough films produced with deposition temperatures above 600 °C and smooth films produced with deposition temperatures below 600 °C both appear crystalline and epitaxially aligned to the underlying substrate based on observations with RHEED and STM. While defects at the surface of a depositing film will both cause and develop from step pinning and step bunching, it is not clear what crystalline defects are formed in the bulk of the films for the two deposition temperature ranges. Here, TEM is used to image and characterize crystalline defects in ^{28}Si films. TEM micrographs presented here were acquired in collaboration with Dr. Alline Myers and Dr. Vladimir Oleshko.

TEM is a common analysis tool used for inspecting the epitaxial quality of

and defects in films produced by low temperature Si deposition including MBE and IBE. A common type of defect observed in Si films deposited on Si(100) substrates is {111} stacking faults. As seen in the TEM micrographs of a Si film deposited by IAD in Fig. 5.17, {111} stacking faults and defects start building up in the epitaxial layer until an amorphous phase develops. IBE experiments have demonstrated epitaxial ^{28}Si films and used TEM to show, depending on the deposition conditions, both defective films with {111} stacking faults and microtwins, as well as higher quality epitaxial films without visible stacking faults or obvious dislocations. However, TEM inspection shows that these films likely still contain defects and strain [43, 51].

Chemical contaminants can not only affect the morphology of a depositing film through surface defect formation, they can also cause structural defects and amorphization in the bulk of a film when incorporated during deposition. Several ^{28}Si IBE experiments have been done showing the effects of chemical contaminants introduced through the ion beam during deposition on the epitaxial quality of the film. One experiment found that introducing approximately 1 % N_2 into the ^{28}Si ion beam during deposition caused the resulting film to be amorphous at a deposition temperature of 350 °C [169]. Others found that N_2 and CO in the ion beam resulted in highly defective or amorphous films using a range of deposition temperatures [49, 50]. Finally, an experiment found that using ^{30}Si ions to deposit a film resulted in epitaxial growth that was less defective than ^{28}Si, and concluded that trace amounts of CO present in the ^{28}Si beam, which are very difficult to eliminate, were the cause [134]. These experiments show the importance of reducing the concentration of N_2 and CO in the ion beam, as discussed in the previous section.

The lattice constant mismatch between natural abundance Si and ^{28}Si may also introduce dislocations into the film, which may be observed by TEM. As mentioned previously, however, the effect of the roughly 1×10^{-6} relative difference in lattice constants is likely too small compared to other defect causing mechanisms in these films.

Initially, TEM was used to inspect the bulk crystallinity of rough ^{28}Si films deposited at higher substrate temperatures above 600 °C to determine the effect on the crystallinity of the surface roughness. Additionally, it was used to confirm the observations made using RHEED and STM that, despite the rough surface, the films are still crystalline and epitaxially aligned to the Si(100) substrate. TEM cross-sectional micrographs of a rough ^{28}Si sample deposited with a substrate temperature of approximately 708 °C at DC–3 are shown in Fig. 5.49. The substrate used for this sample was not cleaned *ex situ* and was flashed annealed before deposition. The TEM specimen was prepared using a FIB, and these images were taken on the ⟨110⟩ zone axis. Panel (a) is a bright field image showing the ^{28}Si film above the Si(100) substrate at the bottom of the micrograph. A protective, thin layer of C (light) and a thicker layer of Pt (dark) are seen above the film. The ^{28}Si film consists of large mounds resulting in a very rough surface, as previously observed in the SEM micrographs of this and other rough samples (Fig. 5.22). The maximum film thickness (of the central mound) seen in this micrograph is approximately 116 nm and the minimum thickness is approximately 31 nm. The surface of the mounds comprising the film are faceted with predominately {113} and {111} microfacets visible, indicated by the arrows. The surfaces of the {113} microfacets make an

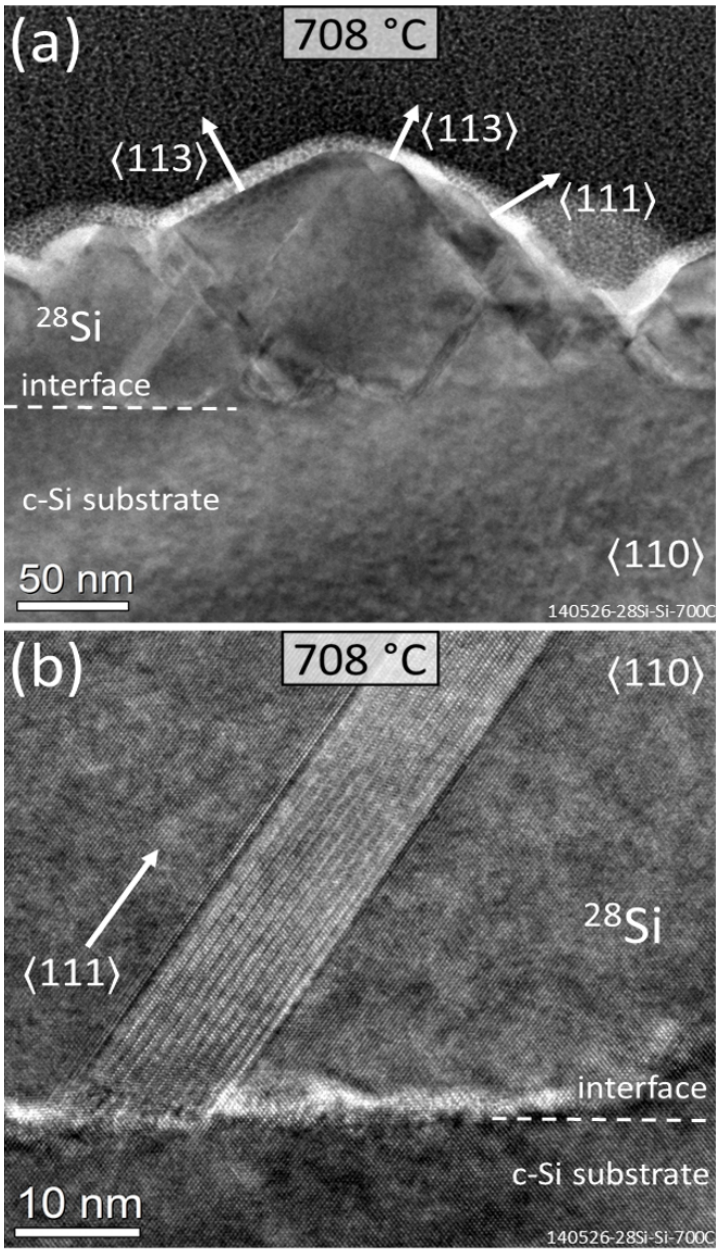

Figure 5.49: TEM cross-sectional micrographs of a rough ^{28}Si sample deposited at 708 °C at DC–3. This image was taken on the ⟨110⟩ zone axis. (a) Bright field image with the Si(100) substrate is visible at the bottom of the image and the ^{28}Si film above it, which consists of large mounds. Protective layers of C (light) and Pt (dark) were deposited on the ^{28}Si film. The surface of the mounds are faceted with {113} and {111} microfacets visible (arrows). Within the mounds, {111} stacking faults are seen. (b) HR-TEM image of a group of {111} stacking faults and microtwins that run from the interface of the film and the substrate up through the film. The ^{28}Si film is seen to be crystalline and epitaxially aligned to the substrate, evidenced by the continuation of ⟨111⟩ lattice rows across the interface.

angle with the surface of the substrate, or the substrate interface that matches the expected angle between the ⟨113⟩ and ⟨100⟩ planes of approximately 25.2°. Likewise, surface of the {111} microfacets make an angle with the surface of the substrate that matches the expected angle between the ⟨111⟩ and ⟨100⟩ planes of approximately 54.7°. These microfacets match those that were observed in the RHEED diffraction patterns for similar samples shown in Fig. 5.20. Also, within the mounds, multiple stacking faults are visible running through the film along the ⟨111⟩ planes.

Panel (b) of Fig. 5.49 is an HR-TEM image that shows another region of the same film in (a) at a higher magnification. The substrate is seen at the bottom of the micrograph with the ^{28}Si film above it. The ^{28}Si film is crystalline and epitaxially aligned to the substrate, as evidenced by the continuation of ⟨111⟩ lattice rows across the substrate interface into the film. A group of {111} stacking faults and microtwins are seen originating at the substrate interface and running through the film. The presence of microtwins is evidenced by the dark fringes inside the stacking fault appearing with a periodicity of three times the normal ⟨111⟩ lattice row spacing, as is often observed for microtwins [173]. These are possibly due to defects or contaminants such as SiC present on the surface at the beginning of the growth that cause step bunching and defects to form on {111} planes.

Some areas of this sample appear with fewer stacking fault defects, and the crystallinity can be inspected further and compared with that of the substrate using fast fourier transform (FFT) analysis. Figure 5.50 shows an HR-TEM cross-sectional micrograph of another area of the 708 °C sample analyzed using FFTs. Like with the previous micrographs of this sample, this image was taken on the ⟨110⟩ zone

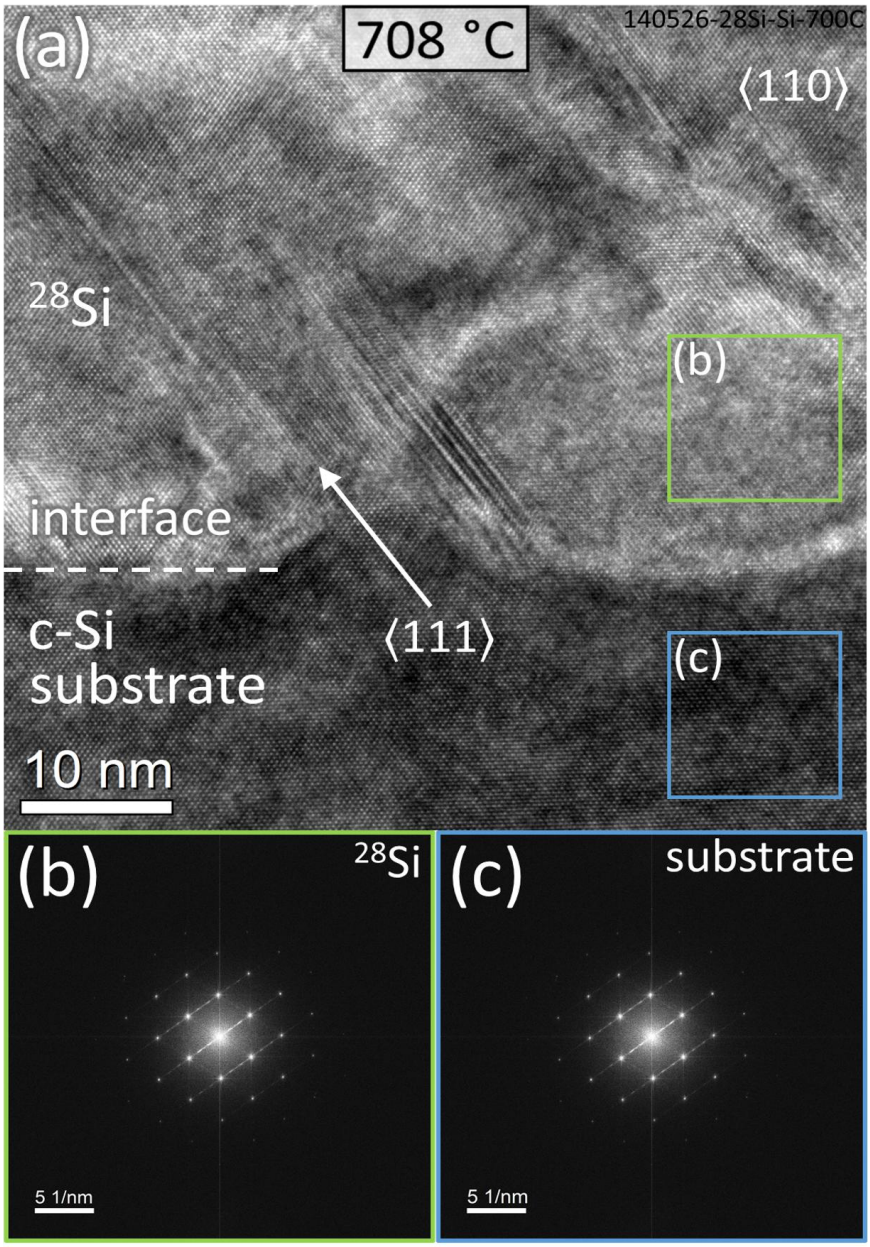

Figure 5.50: HR-TEM cross-sectional micrograph of a rough ^{28}Si sample deposited at 708 °C at DC–3. This image was taken on the ⟨110⟩ zone axis. (a) The Si(100) substrate is at the bottom of the image, and the ^{28}Si film is above it. Several {111} stacking faults are visible running through the film. The ^{28}Si film is seen to be crystalline and epitaxially aligned to the substrate, evidenced by the continuation of ⟨111⟩ lattice rows across the interface. (b) and (c) FFTs of the regions in the boxes for the ^{28}Si film and the substrate, respectively. The FFT of the film and substrate show the same crystal pattern indicating that the film is aligned to the substrate.

axis. Panel (a) shows the sample with the Si(100) substrate appearing dark at the bottom of the micrograph and the ^{28}Si film above it. Again, film appears epitaxially aligned to the substrate, as evidenced by the continuation of ⟨111⟩ lattice rows across the substrate interface into the film, indicated by the arrow. A few {111} stacking faults are seen in the film as well. Panels (b) and (c) are FFTs of the regions marked by the boxes in the substrate and ^{28}Si film, respectively. These FFTs appear nearly identical showing the sample crystal pattern and orientation, indicating again that the film is epitaxially aligned to the substrate.

^{28}Si samples made with lower deposition temperatures that were below 600 °C were observed to be much smoother than those with high deposition temperatures, and TEM was used to inspect these low deposition temperature samples for differences in the crystallinity compared to the samples with higher deposition temperatures. Samples with lower deposition temperatures were also prepared using the revised cleaning procedures discussed previously in the chapter, which may affect the bulk crystalline defects that develop in the film. TEM cross-sectional micrographs at two magnifications of a smooth ^{28}Si sample deposited with a substrate temperature of approximately 460 °C at DC–3 are shown in Fig. 5.51. This sample was prepared *ex situ* using the CMOS cleaning procedure and was flashed annealed before being deposited using the low pressure mode of the ion source. These images were taken on the ⟨110⟩ zone axis. Panel (a) shows a bright field image at lower magnification with the Si(100) substrate in the lower left of the image appearing lighter and the ^{28}Si film to the right of that. The ^{28}Si appears quite different from the substrate with varying contrast and dark patches throughout the film. These

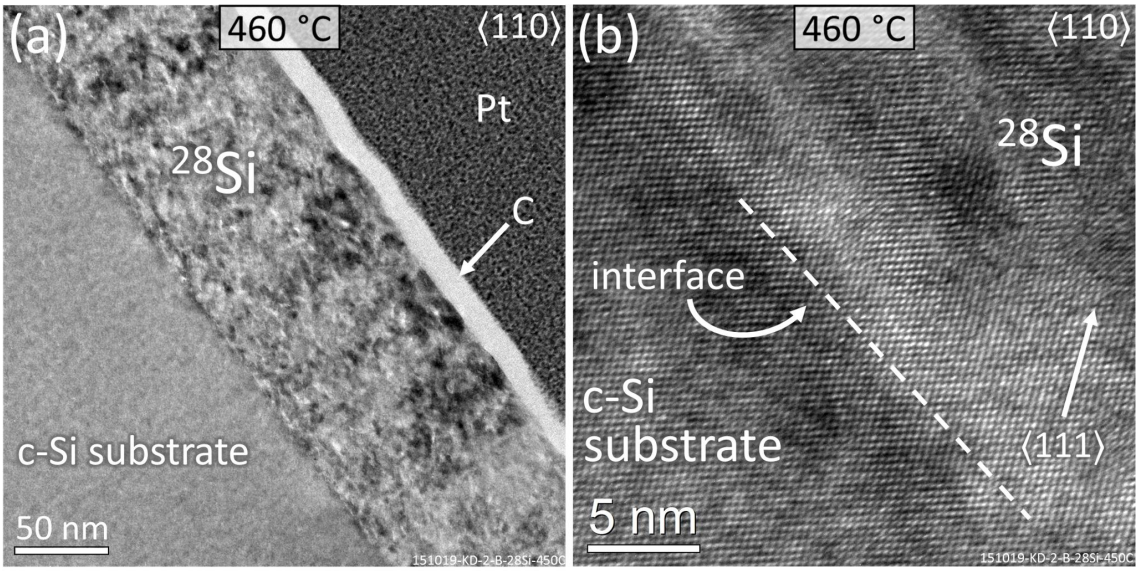

Figure 5.51: TEM cross-sectional micrographs of a smooth ^{28}Si sample deposited at 460 °C at DC–3 using the low pressure mode. These images were taken on the ⟨110⟩ zone axis. (a) Bright field image showing the Si(100) substrate in the lower left appearing lighter and the ^{28}Si film to the right of that with varied contrast. To the upper right of the ^{28}Si film are protective C (bright) and Pt (dark) layers. The ^{28}Si film thickness varies between about 105 nm and 110 nm here. (b) HR-TEM image showing the substrate in the lower left and the ^{28}Si film in the upper right. The ^{28}Si film is seen to be crystalline and epitaxially aligned to the substrate, evidenced by the continuation of ⟨111⟩ lattice rows across the interface.

are likely defects causing local strain in the film. To the upper right of the ^{28}Si are layers of C (light) and Pt (dark) which were deposited to protect the sample during preparation of the specimen, which was done using a FIB. The ^{28}Si film thickness varies between approximately 105 nm and 110 nm in this region of the film, meaning there is a roughly 5 nm surface width here. Panel (b) shows an HR-TEM image taken at much higher magnification (790 times). The crystalline Si(100) substrate is seen in the lower left of the image and the ^{28}Si film is in the upper right. The dashed line representing the interface is only approximate because the true interface is not clear at this magnification, and the ^{28}Si appears similar to the substrate, un-

like in panel (a). The ^{28}Si film in panel (b) is seen to be crystalline and epitaxially aligned to the substrate, evidenced by the continuation of individual ⟨111⟩ lattice rows throughout the image.

Another HR-TEM cross-sectional micrograph of this ^{28}Si sample from Fig. 5.51 is shown in Fig. 5.52 and the crystallinity is analyzed using FFTs. This image was taken on the ⟨110⟩ zone axis. Panel (a) shows the Si(100) substrate in the lower left of the micrograph with the ^{28}Si film in the upper right. The interface between the substrate and the film is indicated by the dashed line and is less clear than in the TEM micrographs of the previous sample. The film in this sample is crystalline and epitaxially aligned to the substrate, which is evidenced by the continuation of ⟨111⟩ lattice rows across the interface, indicated by the arrow. No obvious stacking faults are visible in the film in this micrograph or in any other areas of this film. Several dark areas appear in the film but not the substrate, probably indicating the presence of dislocation and other defects causing local strain fields in the film. Also, the lattice rows in some areas of the film are not as clear as others or those of the substrate, but these areas do not appear amorphous. Panels (b) and (c) are FFTs of the regions marked by the boxes in the substrate and ^{28}Si film, respectively. These FFTs appear very similar showing the sample crystal pattern and orientation, indicating that the film is, again, epitaxially aligned to the substrate.

This same 460 °C sample was analyzed by SIMS for chemical contaminants, which was shown in Fig. 5.41, and found to have an atomic concentration of N of approximately 7.1(1) $\times 10^{20}$ cm^{-3}, or 1.42(2) %. It is thus surprising that the ^{28}Si film is not more defective given that it likely contains Si_3N_4 and SiC crystallites and

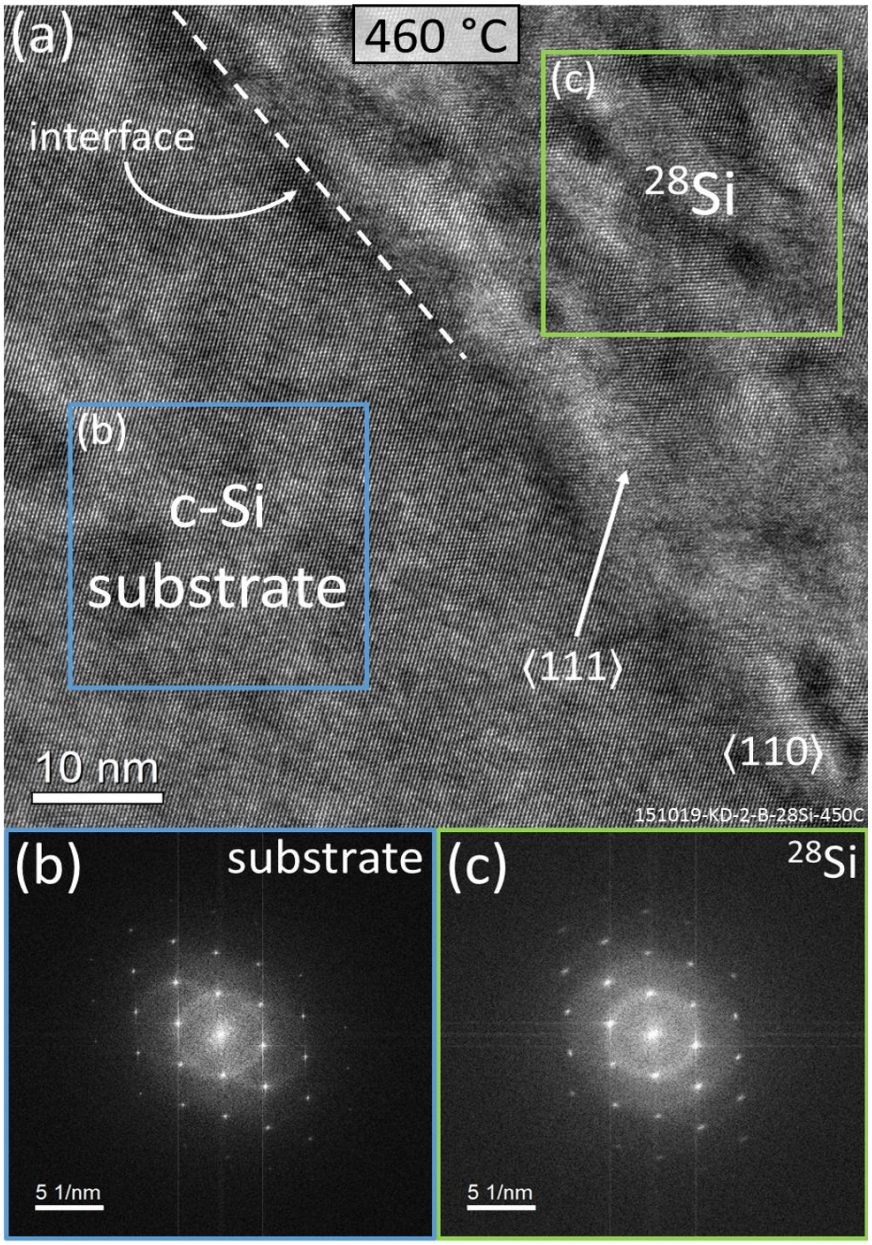

Figure 5.52: HR-TEM cross-sectional micrograph of a smooth ^{28}Si sample deposited at 460 °C at DC–3 using the low pressure mode. This image was taken on the ⟨110⟩ zone axis. (a) The Si(100) substrate is seen in the lower left and the ^{28}Si film in the upper right. The dashed line indicates the interface. The ^{28}Si film is seen to be crystalline and epitaxially aligned to the substrate, evidenced by the continuation of ⟨111⟩ lattice rows across the interface. Several dark patches appear in the film but not the substrate. (b) and (c) FFTs of the regions in the boxes for the substrate and the ^{28}Si film, respectively. The FFT of the film and substrate show the same crystal pattern indicating that the film is aligned to the substrate.

that, as mentioned previously, 1 % N contamination can lead to an amorphous Si film, although for a lower deposition temperature. The dark areas and other contrast changes observed in the ^{28}Si film may be related the Si_3N_4 and SiC compounds present in the film and their related structural defects.

A reduction in the amount of contaminants was then achieved in the next 460 °C sample analyzed in Fig. 5.47 due to having lower background pressures in the chambers and use of the high pressure mode of the ion source. A subsequent sample deposited after these experimental changes and after analyzing the second 460 °C sample was then inspected using TEM. This was to determine if the reduction in contaminants, particularly N and thus Si_3N_4 in the film, resulted in a reduction of the dark patches in the film, seen in the TEM micrograph in Fig. 5.52. An HR-TEM micrograph of this later ^{28}Si sample deposited with a substrate temperature of approximately 421 °C at DC–3 is shown in Fig. 5.53. This sample was prepared *ex situ* using the CMOS cleaning procedure and was flashed annealed before being deposited using the high pressure mode of the ion source. The TEM specimen was prepared using a FIB, and this image was taken on the ⟨110⟩ zone axis. Panel (a) shows the Si(100) substrate at the bottom of the micrograph and the ^{28}Si film at the top. The interface between the substrate and the film is roughly indicated by the dashed line. Like the previous sample, the film in this sample is crystalline and epitaxially aligned to the substrate, which is evidenced by the continuation of ⟨111⟩ lattice rows across the interface, indicated by the arrow. However, despite the presumed reduction in chemical contaminants in this sample compared to that shown in the previous TEM micrograph, this film appears much more defective.

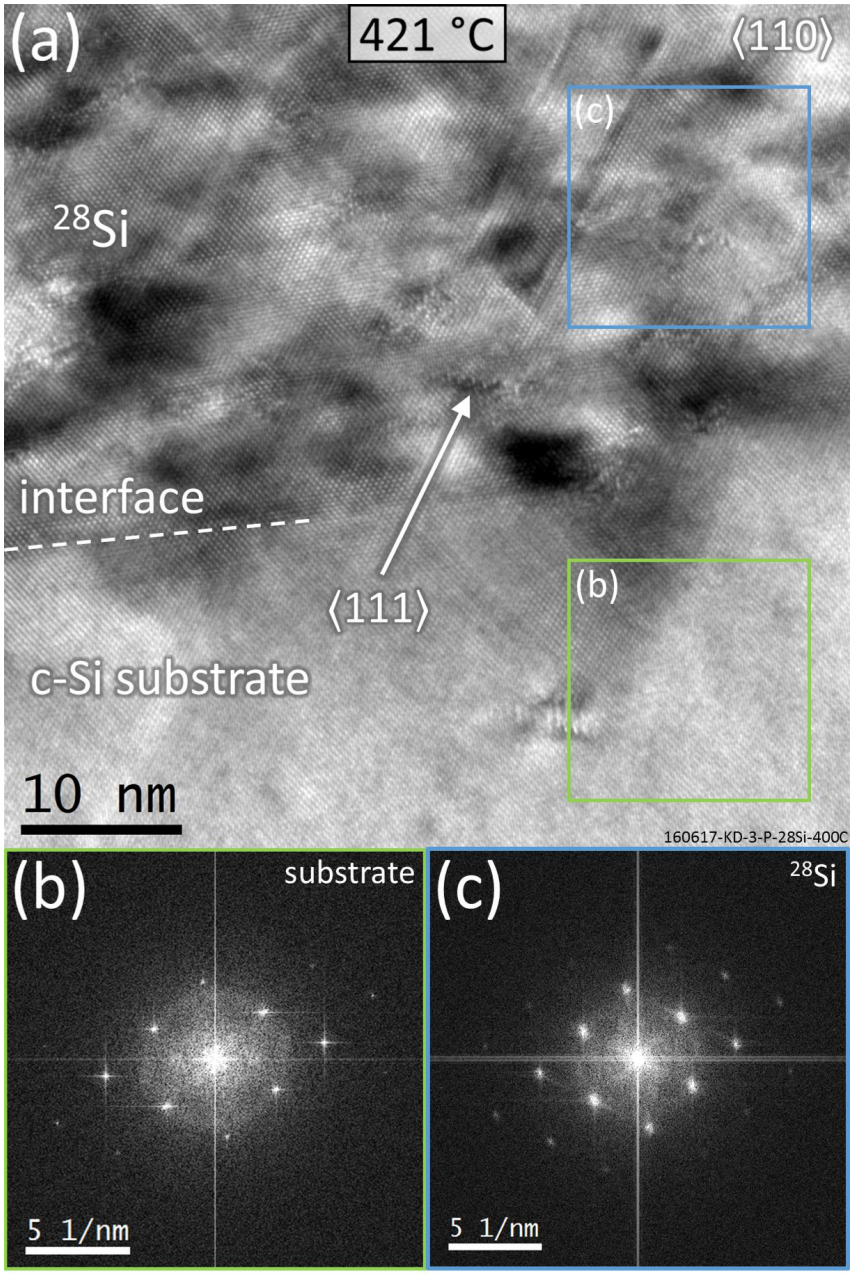

Figure 5.53: HR-TEM cross-sectional micrograph of a smooth ^{28}Si sample deposited at 421 °C at DC–3 using the high pressure mode. This image was taken on the ⟨110⟩ zone axis. (a) The Si(100) substrate is seen at the bottom of the image and the ^{28}Si film is above it. The nearly horizontal dashed line roughly indicates the interface. The ^{28}Si film is seen to be crystalline and epitaxially aligned to the substrate, evidenced by the continuation of ⟨111⟩ lattice rows across the interface. {111} stacking faults are seen running through the film along with several dark patches. (b) and (c) FFTs of the regions in the boxes for the substrate and the ^{28}Si film, respectively. The FFT of the film and substrate show the same crystal pattern indicating that the film is aligned to the substrate.

Several {111} stacking faults are seen running through the film in this micrograph, and further inspection of different areas of the film show that there are many more stacking faults and other dislocations throughout the film. Dark patches are also seen in this film, likely due to strain from defects. Panels (b) and (c) are FFTs of the regions marked by the boxes in the substrate and ^{28}Si film, respectively. These FFTs appear very similar showing the sample crystal pattern and orientation, indicating that the film is, again, epitaxially aligned to the substrate.

The more defective structure of the 421 °C sample compared to the previous 460 °C sample may be due to the deposition rate increasing from approximately 0.37 nm/min for the 460 °C sample to approximately 4.56 nm/min for the later 421 °C sample due to use of the high pressure deposition mode. These two factors may move the quality of the film growth closer to the defective and strained region of the epitaxy phase diagram for IBE, although there is no evidence of an amorphous layer developing in this sample. In fact, none of the ^{28}Si samples inspected with TEM showed signs of a critical thickness, h_{epi}, or an amorphous phase developing, and they were always observed to be crystalline throughout the film including up to the top surface. While the ^{28}Si films inspected by TEM were crystalline and epitaxially aligned to the substrate, the density of crystalline defects was too high to meet the second materials goal stated at the beginning of this chapter. A reduction in crystalline defects will likely require a reduction in chemical contaminants in these film.

5.9 Chapter 5 Summary

The ^{28}Si samples discussed in this chapter showed that ^{28}Si films could be deposited in the deposition chamber at sample location DC–3 while maintaining residual ^{29}Si and ^{30}Si isotope fractions well below 1 ppm. Measurements also shows that extremely high enrichments are achievable for samples deposited both with elevated substrate temperatures and while using the high pressure plasma mode of the ion source. In total, 40 ^{28}Si samples were produced at DC–3 with 39 of them being deposited with elevated substrate temperatures. Additionally, seven of those samples were deposited using the high pressure mode of the ion source. The residual ^{29}Si isotope fraction of the most highly enriched sample deposited at DC–3 was reduced by more than a factor of five compared to that of the previous most highly enriched sample deposited at LC–2, going from 0.691(74) ppm to 127(29) ppb. This progression can be seen in the enrichment progression timeline in Fig. 4.2.

The isotope reduction factor of ^{29}Si for the most highly enriched sample deposited at DC–3 is $3.7(8) \times 10^5$. This value of the reduction factor along with the values from all the other most highly enriched ^{28}Si samples deposited at IC–1, LC–2, and DC–3 are shown in an isotope reduction timeline, which is a progression of the Si isotope reduction factors $a_z/(^z\mathrm{Si}/\mathrm{Si}_{\mathrm{tot.}})$, in Fig. 5.54. This timeline is a modified version of the enrichment progression timeline, showing the isotope reduction factors vs. deposition date, where a larger reduction factor means a higher enrichment, instead. Nine ^{28}Si samples out of a total of 61 produced in this work are represented on this timeline. As with the enrichment progression timeline, the nine samples

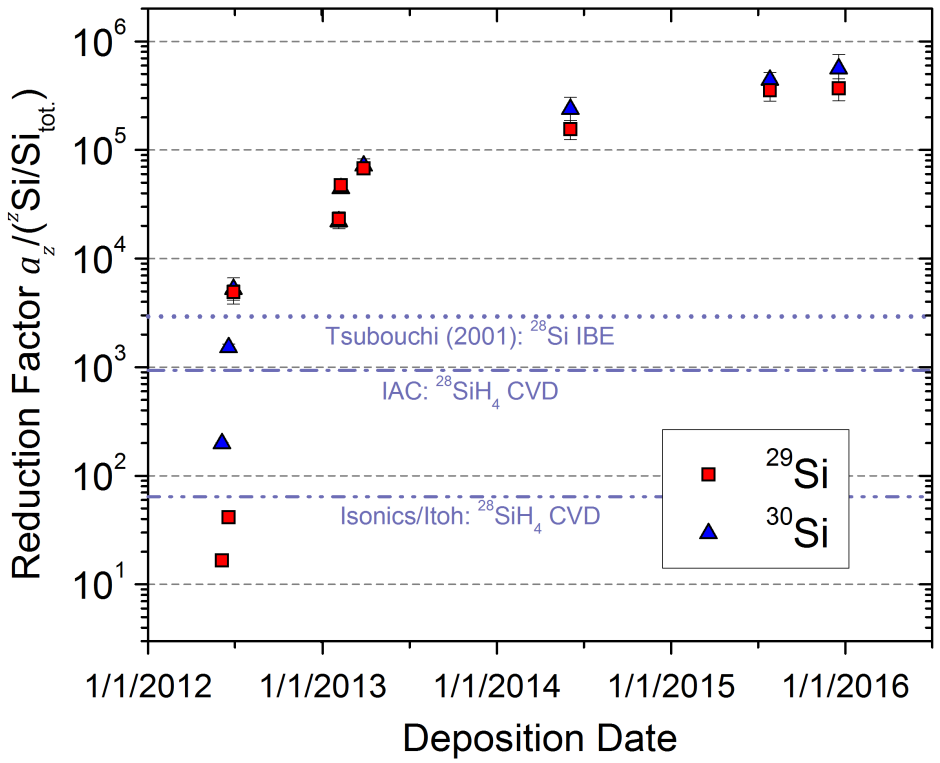

Figure 5.54: Isotope reduction timeline. A timeline of the progression of the isotope reduction factors of the lowest residual isotope fractions of ^{29}Si (squares) and ^{30}Si (triangles), as measured by SIMS. These were achieved for ^{28}Si samples deposited over approximately three and one half years. These results encompass samples produced at IC–1, LC–2, and DC–3. Shown for comparison are the ^{29}Si isotope reduction factors of the ^{28}Si epilayers and crystals produced by Isonics and Itoh using $^{28}SiH_4$ CVD (dash-double dotted line) from Ref. [36,37], the bulk ^{28}Si material produced by the IAC using $^{28}SiH_4$ CVD (dash-dotted line) from Ref. [32], and the ^{28}Si thin films produced by Tsubouchi *et al.* using ^{28}Si IBE (dotted line) from Ref. [43].

presented are those that achieved the best enrichment, or reduction factors of the minor isotopes, of any sample deposited up to that point. Both the reduction factor for ^{29}Si (squares) and ^{30}Si (triangles) are shown to increase in different samples over time from 16.6(1) for the initial sample deposited at LC–1 to the afore mentioned $3.7(8) \times 10^5$ for the most highly enriched sample produced at DC–3. Uncertainties in the reduction factors are derived from the uncertainties in the SIMS measurements

of the isotope fractions. Also shown for comparison are the ^{29}Si isotope reduction factors of three other sources of ^{28}Si. The ^{28}Si epilayers and crystals produced by Isonics and Itoh using $^{28}SiH_4$ CVD have a ^{29}Si reduction factor of approximately 64 (dash-double dotted line), which is larger than only the first two ^{28}Si samples produced here at IC–1 [36, 37]. The bulk ^{28}Si material produced by the IAC using $^{28}SiH_4$ CVD has a ^{29}Si reduction factor of 937 (dash-dotted line) [32], and the ^{28}Si thin films produced by Tsubouchi *et al.* using ^{28}Si IBE has a ^{29}Si reduction factor of approximately 2.9 $\times 10^3$ (dotted line) [43]. Both of these values are still below the most highly enriched ^{28}Si sample deposited at IC–1.

The overall ^{28}Si isotope fraction of this most highly enriched sample deposited at DC–3 and in this entire work was 99.9999819(35) %. These sample are more highly enriched than any other known source of ^{28}Si, including the IAC. These samples also demonstrate enrichments sufficient to enable a robust measurement of the dependance of electron coherence time on ^{29}Si concentration in the single spin regime and compare it to theoretical predictions (see Fig. 1.9), as proposed in Chapter 1 [12].

The achieved reduction in ^{29}Si and ^{30}Si isotope fractions in samples deposited at DC–3 was likely due to several factors. The deposition chamber had significantly lower background pressures than the lens chamber at LC–2 resulting in less SiH_4 adsorption during deposition. Also, higher deposition rates were generally achieved for samples deposited at DC–3, including the highest rates achieved using the high pressure mode of the ion source.

Depositing samples at DC–3 allowed for sample heating which was crucial in

achieving epitaxial deposition. Crystalline, epitaxial ^{28}Si films were produced using elevated deposition temperatures between 349 °C and 1041 °C, although samples deposited above 600 °C were very rough. This was due to chemical contaminants such as SiC at the growth surface that result in step pinning sites and lead to step bunching, faceting on {111} and {113} planes, and large mound formation. ^{28}Si samples deposited at lower temperatures between approximately 349 °C and 460 °C were found to be smooth with typical surface widths of $\Delta z = 2$ nm.

Chemical contaminants in these ^{28}Si films were measured by SIMS, which detected N, C, O, F, Al, and Cl. The N, C, and O were detected at especially high concentrations, initially all above 1×10^{19} cm^{-3}. F and Al were eliminated from a second sample due to experimental alterations. By improving the vacuum in both the deposition chamber and the ion beam chamber, and by using a higher ^{28}Si ion beam current generated in the high pressure mode of the ion source, N, C, and O were all able to be reduced in the final sample analyzed by SIMS. The average atomic concentration of N in the film was measured to be 9.07(4) $\times 10^{18}$ cm^{-3}, or 181.8(8) ppm, the average atomic concentration of C in the film was measured to be 8.27(3) $\times 10^{18}$ cm^{-3}, or 165.7(6) ppm, and the average atomic concentration of O in the film was measured to be 3.09(4) $\times 10^{18}$ cm^{-3}, or 61.9(8) ppm. Based on these concentrations and the solid solubility of these elements in Si, it is likely that Si_3N_4, SiC, and SiO exist within the ^{28}Si films. The resulting total best purity for a ^{28}Si sample deposited at DC–3 and overall in this work is approximately 99.96(2) %.

Finally, TEM was used to confirm that ^{29}Si films produced with both the higher and lower deposition temperatures were crystalline and epitaxially aligned to the

substrates. All samples deposited with substrate temperatures above 600 °C were observed to have {111} stacking faults and twinning present in the films. For lower deposition temperature samples, one sample deposited using the low pressure mode did not have any visible stacking faults but probably still contained other crystalline defects. Another sample deposited with a slightly lower substrate temperature and using the high pressure mode to generate a much higher deposition rate was observed to have a lot of {111} stacking faults and likely other defects. Reduction of these crystalline defects likely requires reduction of the chemical contaminants within the ^{28}Si films. Overall, samples deposited at DC–3 enabled improvements and new understanding regarding the second and third materials goals mentioned at the beginning of this chapter in support of the broader ^{28}Si effort, of which this work is a part.

Chapter 6

Pressure and Temperature Dependent Adsorption of ^{29}Si and ^{30}Si During ^{28}Si Deposition

6.1 Introduction

It was shown in Chapters 4 and 5 that an extremely high level of enrichment was achieved for ^{28}Si films deposited both amorphously at room temperature and epitaxially at elevated temperatures. However, despite the fact that the ^{28}Si ion beam is well resolved and separated from the ^{29}Si and ^{30}Si ions, the residual ^{29}Si and ^{30}Si isotope fractions in these samples were not zero. Understanding this discrepancy and how the concentration of isotopic contaminants are affected by different deposition parameters, such as substrate temperature, is necessary for the further development of ^{28}Si ion beam deposition. The objectives of the experiments and analysis discussed in this chapter are as follows:

(1) understand the source of residual ^{29}Si and ^{30}Si in the ^{28}Si films,

(2) determine the dependance of the residual isotope fractions on deposition tem-

perature, and

(3) understand the mechanism by which the residual isotope fractions depend on temperature.

These objectives are part of the larger goals of this work set forth in Chapter 1, which is to be able to produce ^{28}Si samples with targeted levels of enrichment (^{29}Si isotope fractions). Targeting specific enrichments would facilitate a study of spin coherence time as a function of ^{29}Si concentration. Electron and nuclear T_2 times of single implanted ^{31}P measured for a range of ^{29}Si concentrations could be compared to theoretical predictions (see Fig. 1.9), as mentioned in Chapter 1 [12].

The experiments described in this chapter were designed to test the hypothesis that the source of ^{29}Si and ^{30}Si, measured in the samples by SIMS, is the natural abundance SiH_4 gas which diffuses from the ion source to the sample location during deposition. This diffusion results in a partial pressure of SiH_4 at the surface of the ^{28}Si sample. The SiH_4 molecules (some of which are $^{29}SiH_4$ and $^{30}SiH_4$) will stick to the Si surface where they can be incorporated either through physisorption or in a chemisorption reaction similar to that of CVD. The sticking and growth behavior of SiH_4 in Si CVD processes, described by the so-called reactive sticking coefficient, has been studied extensively. The literature on this subject, however, is quite large and diverse and results are often difficult to compare or reconcile because they depend heavily on experimental conditions such as pressure, temperature, surface condition, specific SiH_4 species, and various systematic experimental uncertainties. Also, the reaction describing the conversion of gaseous SiH_4 to solid incorporated Si atoms is more complex than one might naively guess because it can occur through multiple

decomposition channels. Several review articles by Comfort and Reif [174], Jasinski and Gates [137], and Onischuk and Panfilov [175] have given summaries of both reaction mechanisms of SiH_4 CVD processes and experimental work measuring reactive sticking coefficients and the associated activation energies for these processes. The dominant reaction expected for SiH_4 CVD at pressures ≤ 0.1 Pa (as is the case in this work) is described by Jasinski and Gates to be

$$SiH_4(g) \rightarrow Si(s) + 2H_2(g), \tag{6.1}$$

where (g) represents the gaseous phase and (s) represents the solid phase [137]. This reaction is exothermic producing about 8.2 kcal/mol (0.36 eV), but energy in the form of heat is required to overcome the kinetic barriers to the decomposition, which is the activation energy. Figure 6.1 illustrates the reaction sequence and the role of dangling bond sites (_) in CVD reactions on the Si(100) surface. SiH_4 initially adsorbs on the surface at a double dangling bond site. The SiH_4 then decomposes into SiH_3 on one dangling bond site and H on the other. By encountering further dangling bond sites on the surface, the SiH_3 decomposes further until a Si atom is left along with four H atoms, which recombine into two H_2 molecules and desorb. The lone Si atom then becomes incorporated into the film. The desorption of H_2 frees three dangling bond sites that are then cycled back into the reaction sequence for the decomposition of other SiH_4 molecules.

There are several differences between SiH_4 based CVD and the sticking and/or reaction of SiH_4 being incorporated into the ^{28}Si films discussed here. These differences offer several advantages for this work over the typical experiments in the

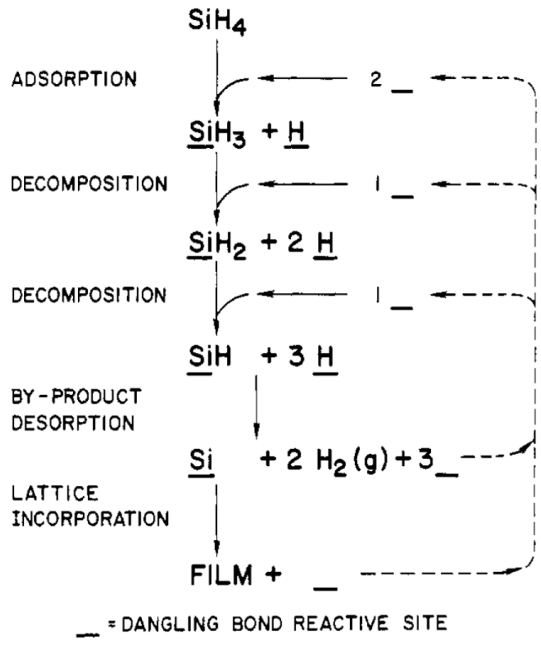

Figure 6.1: SiH_4 surface decomposition sequence during CVD growth for low pressures. The SiH_4 interacts with dangling bond sites (_) on the Si(100) surface to sequentially dissociate H which can then evaporate. (from Ref. [137])

literature, however these differences can make comparisons between the literature and this work more difficult. Unlike the data presented here for samples deposited with substrate temperatures ranging from room temperature up to 800 °C, CVD is not typically studied with a growth temperature below 500 °C to 600 °C because the growth rate drops dramatically below this range, depending on specific experimental conditions. This is partially due to increased H coverage at lower temperatures which inhibits the CVD reaction. CVD typically uses high pressures of H_2 with SiH_4 partial pressures as high as 130 Pa (975 mTorr) for UHV CVD, although some experiments have used pressures as low as 1.3×10^{-5} Pa (9.8×10^{-8} Torr) [176]. These pressures are orders of magnitude higher than what is used for the samples described in this chapter, and so H coverage is not believed to significantly influence the results reported here. The other major difference between CVD and the

ion beam deposited samples, is the ^{28}Si ion beam itself, which could interact with adsorbed SiH_4. The deposition rate due to the ion beam is typically much larger, i.e. > 10 times larger, than the growth rate due to the adsorbed species, therefore a SiH_4 molecule will (almost) always encounter a bare Si surface. Consequently, rate limiting effects seen in CVD such as surface diffusion, SiH_4 interaction with other adsorbates like H, and surface reaction rates would not occur [177, 178]. Energetic ions are also known to desorb H from Si(100) surfaces [121]. Finally, a unique feature of monoisotopic ion beam deposition in this context is that very small numbers of adsorbed species can be measured. As seen in the analysis of the enrichment of ^{28}Si samples in Chapters 4 and 5, SIMS is extremely sensitive to isotope ratios and so trace amounts of ^{29}Si and ^{30}Si adsorbed in the ^{28}Si films can be easily detected.

Section 6.2 of this chapter describes the experimental methods used to collect and analyze the relevant sample parameters discussed in the remainder of the chapter. In section 6.3, a model that describes the proposed SiH_4 adsorption process is introduced, and in section 6.4, it is used to analyze the data. Sections 6.5 and 6.6 explore the role of substrate temperature on the enrichment and calculated SiH_4 incorporation fractions, respectively. Section 6.7 uses the incorporation fractions to determine an activation energy for SiH_4 adsorption. Section 6.8 provides a brief summary. Analysis of some of the data discussed in this chapter was previously published in Ref. [84].

6.2 Experimental Methods

6.2.1 ^{28}Si Samples and Enrichment Values

The general deposition parameters for ^{28}Si samples similar to and including the samples used in the analysis of this chapter were described in detail Chapters 4 and 5. These samples were deposited on a variety of natural abundance Si(100) substrates including p-type, n-type, and undoped (intrinsic) wafers, discussed in Chapters 4 and 5. For most samples discussed here and deposited at room temperature, substrates were prepared *ex situ* by an HF etch to remove the native oxide and were not prepared further in vacuum. These samples were deposited at sample location LC–2 in the lens chamber. One room temperature sample was deposited at DC–3 in the deposition chamber, and was not prepared *ex situ* and were loaded with a native oxide. For most of the samples deposited at elevated temperatures, substrates were cleaned *ex situ* using the standard CMOS cleaning procedure described in Chapter 5. Three samples deposited above 600 °C were not cleaned *ex situ* and were loaded in the vacuum chamber with a native oxide. Substrates were then prepared for deposition *in situ* by flash annealing them to 1200 °C for $\approx$ 10 s several times to produce a clean (2×1) reconstructed Si(100) surface on which to deposit ^{28}Si epitaxially. These samples were all deposited at sample location DC–3 in the deposition chamber. As mentioned previously, the gas used in these experiments to generate a ^{28}Si ion beam was natural abundance SiH_4 with a purity of 99.999 % according to the gas vendor (Matheson Tri-Gas). To map out the temperature

dependance of the enrichment, samples were deposited with substrate temperatures including room temperature ($\approx$ 21 °C), 249 °C, 349 °C, 357 °C, 421 °C, 502 °C, 610 °C, 705 °C, 708 °C, and 812 °C.

^{28}Si ions were deposited onto the substrates with an average ion energy, E_i, at the sample of typically about 100 eV for the room temperature samples and approximately 35 eV for the samples deposited at elevated temperatures. Typical ^{28}Si ion beam currents, I_i, of around 500 nA were achieved over an area on the substrate between about 3 mm^2 and 16 mm^2. For one sample deposited at 421 °C, a higher ion beam current of approximately 3 μA was achieved. The resulting thicknesses, d, of the deposited films were inferred from the calibration of the SIMS depth profiles and ranged from $\approx$ 50 nm to 350 nm. Dividing the thicknesses by the deposition time for each sample gives an estimate for the deposition rates, R, of around 0.32 nm/min to 3.94 nm/min. Based on these rates, the corresponding average ion flux,F_i, was then calculated for each sample. F_i varied from 2.70×10^{13} cm$^{-2} \cdot$ s^{-1} to 3.4×10^{14} cm$^{-2} \cdot$ s^{-1}.

For the samples discussed in the analysis of this chapter, the total pressure rise during deposition after subtracting the chamber base pressure ranged from approximately 9.9×10^{-7} Pa to 4.9×10^{-6} Pa (7.5×10^{-9} Torr to 3.7×10^{-8} Torr) for the samples deposited at room temperature, and it ranged from approximately 4.9×10^{-7} Pa to 3.4×10^{-6} Pa (3.7×10^{-9} Torr to 2.5×10^{-8} Torr) for the samples deposited with elevated substrate temperatures. These pressures equate to a total gas flux, $F_g^{tot.}$, on the surface of the sample during deposition. A more relevant flux in this analysis is the flux due to the SiH_4 partial pressure, F_g, which will be

discussed in a later section.

The ^{29}Si and ^{30}Si isotope fractions for these samples were measured by SIMS in collaboration with Dr. David Simons (NIST) as described in Chapter 4. Isotope fractions of a particular isotope of Si are defined in a SIMS measurement as the detected average counts of that isotope divided by the total average counts of the measurement and are written as $^{z}\mathrm{Si}/\mathrm{Si}_{\mathrm{tot.}}$ for an isotope with mass number z, as previously discussed in Chapter 4. Measurements were performed by Dr. Simons and the analysis presented here was done by myself. The raw measurements show that at the low end of the deposition temperature range, the 249 °C sample had a residual ^{29}Si isotope fraction of $0.79(12) \times 10^{-6}$ or 0.79(12) ppm. For the sample deposited at the highest temperature, 812 °C, the ^{29}Si isotope fraction was 4.32(46) ppm. This increase in isotope fraction with increasing substrate temperature is the focus of this discussion. The sample with the best enrichment and lowest ^{29}Si isotope fractions in this study was deposited at 502 °C, as previously reported in Chapter 5 (see Fig. 5.11). The measured ^{28}Si isotope fraction of the most highly enriched portion of this sample is 99.9999819(35) %, the average residual ^{29}Si isotope fraction is 127(29) ppb, and the average residual ^{30}Si isotope fraction is 55(19) ppb. The uncertainty of the isotope ratios was determined from the standard deviation of the mean of the measurements. A list of the samples discussed in this chapter, their deposition parameters, and measurement and analysis results can be found in Tables D.10 to D.13 in Appendix D.

For the samples deposited at 705 °C, 708 °C, and 812 °C, the measured isotope fractions have to be taken as an upper bound. This is because during deposition,

the samples deposited above 600 °C developed a large amount of surface roughness on the order of the film thickness itself. As discussed in Chapter 5, this roughness had the effect of artificially inflating the isotope fractions measured by SIMS (see Fig. 5.12 and Fig. 5.14). The 610 °C sample is excluded from this caveat because the SIMS measurement of it was found to be more trustworthy. Nominally the SIMS depth profiles show a clear extended minimum in ^{29}Si and ^{30}Si isotope fractions through the thickness of the film, but instead, in these higher deposition temperature samples there is a gradual increase in isotope fractions up to the natural abundance values in the substrate. This effect is a measurement artifact caused by the SIMS sputter beam sampling the ^{28}Si film and substrate at the sample time. The stated enrichment values for the effected samples are considered upper bounds because the measurement artifact would only increase the apparent isotope fractions but never decrease them. Care was taken to exclude data that was clearly influenced by this effect, however, it is possible that this artifact still played a small role in determining the isotope ratios of the highest temperature samples.

6.2.2 SiH_4 Mass Spectrum and Mass Selectivity

A key component of the analysis of SiH_4 adsorption discussed in this chapter is the assumption that the ion beam is 100 % pure ^{28}Si. This assumption can be justified in part by analysing the isolation of the ^{28}Si ion beam as measured in the SiH_4 mass spectrum that is collected during operation of the ion beam with SiH_4 gas. A portion of a SiH_4 mass spectrum, representative of the ion beam conditions used in Chapter 4 to deposit room temperature samples at sample location LC–2,

is presented in Fig. 6.2. Qualitatively similar mass spectrums were obtained for samples deposited at elevated temperatures, as can be seen in Fig. 5.4 in Chapter 5. In Fig. 6.2, the ion current peaks corresponding approximately to 28 u (^{28}Si), 29 u (^{29}Si and ^{28}SiH), 30 u (predominately $^{28}SiH_2$), and 31 u (predominately $^{28}SiH_3$) are observed. Gaussian fits (Eq. (2.14)) to the 28 u (dashed line) and 29 u (solid line) peaks are shown superimposed on the data. The 95 % confidence bands of the two fits are also shown (dash-dotted lines). The applied current corresponding to the sweep of the magnetic field of the mass analyzer is shown on the top axis. This mass spectrum indicates a mass resolving power $\frac{m}{\Delta m} \approx 80$ (measured at 10 % of the peak height). The Gaussian fits give a separation of the 28 u peak from the 29 u peak of about 11 σ (standard deviation). The Gaussian fits are used to determine the approximate geometric mass selectivity (i.e. the amount of mass separation) of the ion beam system to estimate the amount of ^{29}Si potentially contaminating the ^{28}Si beam. This is done by calculating the overlap of the 29 u and 28 u peaks using the parameters $G_{28}(m)$ and $G_{29}(m)$, which are the values (calculated at mass m in units of u) of the Gaussian fits to the current peaks at 28 u and 29 u respectively. The overlap of the 29 u peak on the 28 u peak is then determined from

$$\frac{G_{29}(28)}{G_{28}(28) + G_{29}(28)} \ , \tag{6.2}$$

where $m = 28$ for the above parameters signifying that the values of the Gaussian fits are calculated at a mass of 28 u. The 95 % confidence band of the fit to the 28 u peak is used to calculate $G_{28}(m)$, and the 95 % upper confidence band of the fit to the 29 u peak is used to calculate $G_{29}(m)$. When also taking into account

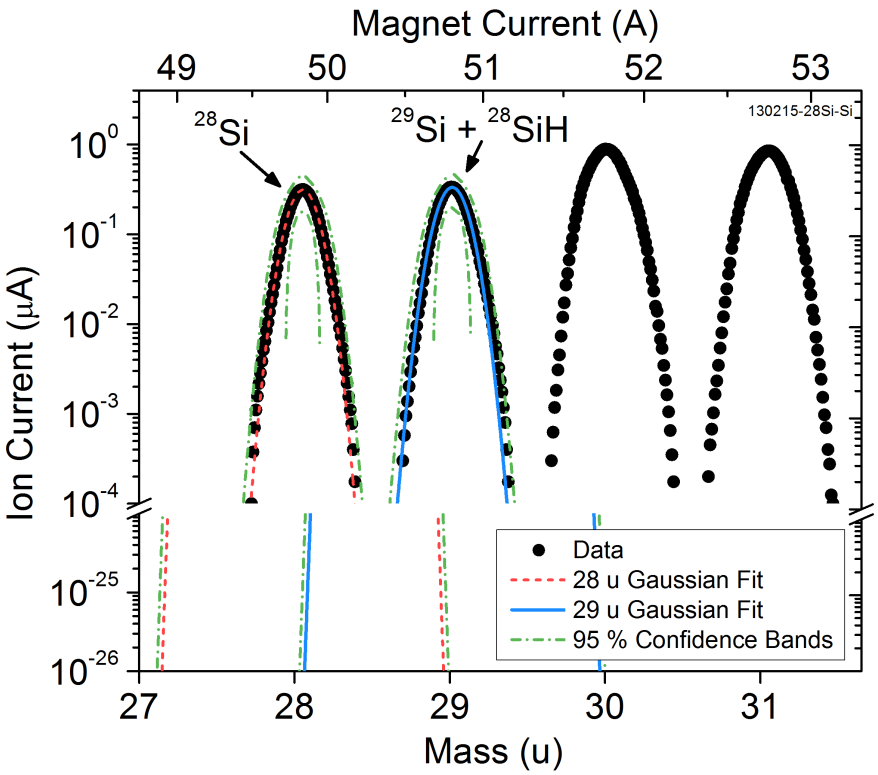

Figure 6.2: SiH_4 ion beam mass spectrum (circles) showing the ^{28}Si ion current peak at 28 u, ^{29}Si ion current at 29 u ($\approx$ 5 % of the total current at 29 u), and two higher mass Si hydride peaks. The top axis shows the corresponding current applied to the magnetic sector mass analyzer to sweep the field. Gaussian fits (Eq. (2.14)) to the 28 u (dashed line) and 29 u (solid line) peaks along with 95 % confidence bands (dash-dotted lines) are plotted to calculate the overlap of the 29 u peak onto the 28 u peak. The centers of the 28 u and 29 u fits are separated by $\approx 11\ \sigma$.

that the 29 u peak consists of approximately 5 % ^{29}Si (95 % ^{28}SiH), as discussed in Chapter 4, the ^{29}Si contamination fraction of the 28 u ion current is calculated to be $\approx 5 \times 10^{-26}$. This extreme estimate of the contamination fraction of the ^{28}Si peak from the ^{29}Si peak is unphysical and is purely a measure of the geometric mass selectivity of the ion beam system.

To get an estimate of the potential realized mass selectivity due to the ^{29}Si peak overlap, a gas scattering mechanism is considered that would likely be a dominant contributing factor to the ^{29}Si beam contamination. Inelastic scattering between ions

and gas molecules occurs along the flight path of the ions as they travel down the beamline. This causes an ion at mass 29 u to lose sufficient energy to be incorporated into the 28 u trajectory and pass through the mass-selecting aperture. This so-called scattering tail effect, referred to as the abundance selectivity when considering the tail contribution to an adjacent mass current peak, I_S/I_0, can be estimated from

$$\frac{I_S}{I_0} \propto P\Delta x \left(\frac{m}{\Delta m}\right)^n, \tag{6.3}$$

which was adapted from Ref. [179]. I_S is the scattered ion current from a peak at mass m to a peak at mass $m + \Delta m$, where Δm is an integer. For the scattering contribution of an ion current peak to a current peak at an adjacent mass, $\Delta m = \pm 1$. I_0 is the total ion current at mass m, P is the background gas pressure in the beamline, Δx is the width of the mass-selecting aperture, and n is a parameter corresponding to the scattering cross sections and is ≈ 1.7 for similar ion beam systems [179]. Figure 6.3 shows an experimental example of the scattering tail and abundance selectivity for a mass spectrum of ThO^+ from Ref. [180]. The current of the ThO peak at mass 248 u drops quickly on either side of the peak, but then levels off, illustrating the scattering tail effect, which contributes roughly 10^{-6} of the 248 u peak at 247 u and 249 u.

From Eq. (6.3) and literature values of the abundance selectivity for a single magnet system with an operating pressure within the beamline of approximately 1.3×10^{-4} Pa (1.0×10^{-6} Torr), a contribution of roughly 4×10^{-6} of the higher mass peak to the lower mass peak is expected at a mass of 28 u [180, 181]. This peak tail current is not measurable in this ion beamline because the mass resolu-

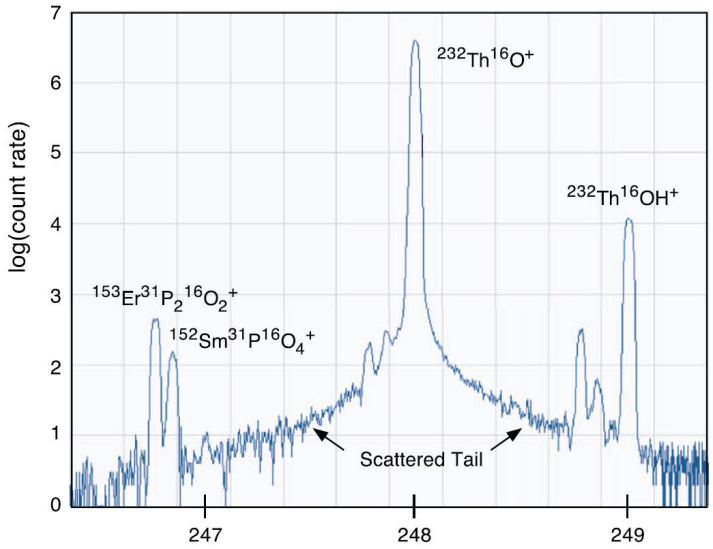

Figure 6.3: ThO^+ ion beam mass spectrum illustrating the scattering tail and abundance selectivity at mass 248 u. The main peak initially drops quickly on either side of the peak before leveling off as the ion current signal begins to be dominated by the scatter tail. This tail decreases more gradually and contributes approximately 10^{-6} of the 248 u peak at $\Delta m = 1$ u. (from Ref. [180])

tion and current sensitivity are too low. Combining the scattering fraction with the ^{29}Si natural abundance and the fact that the 29 u peak is typically about the same magnitude as the 28 u peak gives an estimate for an upper bound on the ^{29}Si concentration in the ^{28}Si beam of roughly 2×10^{-7}, or 200 ppb. This concentration may be significant for a few samples discussed here with the lowest ^{29}Si isotope fractions around 200 ppb, although the true value may be lower making it less significant. Further, there is no evidence, e.g. significant and consistent attenuation of the ^{30}Si isotope fractions compared to ^{29}Si, that this scattering limit is having a significant effect on the measured enrichment. For example, the 502 °C sample with a measured ^{29}Si isotope fraction of 127(29) ppb has a ^{29}Si/^{30}Si ratio of 2.31 ± 0.96. This value agrees within the uncertainty with the natural abundance value of approximately 1.52. Further, the expected ^{29}Si/^{30}Si ratio of the scatter tails from Eq. (6.3)

is larger than the measured ratio at ≈ 4.6. Based on this analysis, the scattering tail contribution is considered to be negligible of the purposes of the analysis discussed in this chapter, and the ion beam is assumed to be pure ^{28}Si. For the discussion of the following sections, the difference between the expected (100 % enriched) and measured enrichment is considered by identifying only the natural abundance SiH_4 gas diffusing from the ion beam into the deposition chamber as the source of ^{29}Si and ^{30}Si.

6.2.3 Determination of SiH_4 Partial Pressures

An accurate estimate of the partial pressure of SiH_4, present at the sample location during ^{28}Si deposition, is required to determine any correlations between this partial pressure and enrichment levels (i.e. ^{29}Si and ^{30}Si isotope fractions). Total pressure measurements were made using several different ion gauges in the system located in two of the three sample deposition locations (the lens chamber, LC–2, and the deposition chamber, DC–3) as described in Chapters 2 and 4. Comparing samples with pressure readings taken from different gauges introduces some error in the analysis because gauges may be calibrated differently. For the samples deposited at room temperature, and some samples deposited with elevated substrate temperatures, the raw ion gauge readings from different gauges are assumed to be comparable in this analysis, although with different known uncertainties in the readings of different gauges, because a direct conversion was not performed at the time. Another gauge used for some of the samples deposited at elevated temperatures had a known offset which could be compared to a more accurate gauge at the same loca-

tion. A conversion was used to translate the pressure reading from this gauge to the equivalent readings for the more accurate gauge. Typically the readings from these types of ion gauges have a relative uncertainty of ≈ 20 %, while the more accurate gauge has a relative uncertainty of ≈ 5 %. After determining the appropriate total pressure during deposition for each sample, the base pressure at the relevant sample location immediately prior to deposition was subtracted out to get the total pressure increase due to gas diffusion from the ion source, which was typically a factor of 50 to 100 times higher than that base pressure. Pressure increases due to sample heating were also taken into account.

To determine the SiH_4 partial pressure component of the total pressure readings, the RGA in the deposition chamber was used to take partial pressure measurements from the residual gas mass spectrum while flowing SiH_4 gas from the ion source. Because the RGA is not necessarily calibrated the same way as the ion gauges in the chamber, and the readings are influenced by the electron multiplier settings in the detector of the RGA, the absolute partial pressure readings are not reliable. Instead, the partial pressure readings of SiH_4 were used to calculate the approximate fraction of the total sum of partial pressure peaks in the residual gas spectrum. Determining this SiH_4 fraction is complicated by the fact that when the ion source is in operation, it cracks SiH_4 into lower order Si hydrides, SiH_x ($1 < x < 4$), and H_2. The RGA filament itself further cracks SiH_x. Figure 6.4 shows RGA residual gas mass spectra for the base pressure of the deposition chamber, which was about 8.3×10^{-9} Pa (6.2×10^{-11} Torr) (diagonal line fill), during SiH_4 gas flow (horizontal line fill), and when the ion beam is on (solid line). When SiH_4

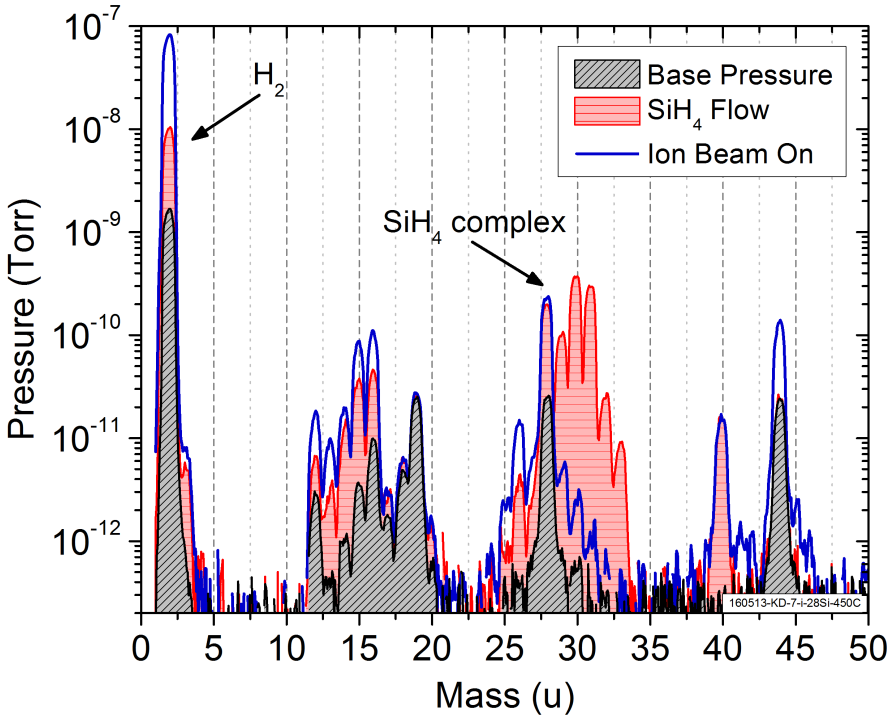

Figure 6.4: Residual gas mass spectra collected from the RGA in the deposition chamber for the chamber base pressure (diagonal line fill), while flowing SiH_4 (horizontal line fill), and with the ion beam in operation (solid line). The complex of SiH_x peaks are observed from 28 u to 33 u during SiH_4 gas flow. H_2 is also observed to increase.

is flowed into the chamber with the ion source off, the SiH_x peaks are observed between 28 u and 33 u due to gas cracking from the RGA itself. The increased H_2 signal is partially due to this process. When the ion source is operating, the SiH_4 is initially cracked before diffusing to the RGA where the resulting SiH_x is cracked further so that the residual gas mass spectrum does not show any significant Si hydride peaks. This is accompanied by an additional increase in H_2 signal. This reduction in SiH_x signal with the ion beam on precludes a direct measurement of the SiH_4 partial pressure.

To get an estimate of the SiH_4 partial pressure during ion beam operation, the cracking efficiency of the ion source and RGA are assumed to be similar and

then measure the total SiH_4 partial pressure fraction with the ion beam off. This assumption is supported by the fact that the ratios of Si hydride peaks seen in the ion beam mass spectrum above (Fig. 6.2) and the RGA residual gas mass spectrum (Fig. 6.4) are similar. From these measurements and estimates for the H_2 and SiH_4 gas sensitivity factors [182, 183], the SiH_x partial pressures is estimated to be roughly 28 % ± 5 % of the total pressure increase. This gives SiH_x partial pressures, P_{SiH_x}, that range from 2.8×10^{-7} Pa to 1.4×10^{-6} Pa (2.1×10^{-9} Torr to 1.1×10^{-8} Torr) for the room temperature samples, and from 1.4×10^{-7} Pa to 9.6×10^{-7} Pa (1.1×10^{-9} Torr to 7.2×10^{-9} Torr) for the samples deposited at elevated temperatures.

The SiH_x gas flux, F_g, which impinges on the sample during deposition is a critical parameter to the analysis of this chapter. F_g is derived from the SiH_x partial pressures using the Hertz-Knudsen equation for gas flux [184, 185],

$$F_g = \frac{P_{SiH_x}}{\sqrt{2\pi m k_B T_g}} \ , \tag{6.4}$$

where P_{SiH_x} is the SiH_x partial pressure, m is the molecular mass of SiH_4 ($\approx$ 32 u), k_B is the Boltzmann constant, and T_g is the temperature of the gas ($\approx$ 21 °C). This calculation gives SiH_4 gas fluxes between 7.6×10^{11} cm$^{-2} \cdot$ s^{-1} and 3.7×10^{12} cm$^{-2} \cdot$ s^{-1} for the room temperature samples. For the higher temperature samples, the SiH_4 gas fluxes are calculated to be between 3.7×10^{11} cm$^{-2} \cdot$ s^{-1} and 2.6×10^{12} cm$^{-2} \cdot$ s^{-1}. The relative uncertainty of these estimates is $\approx$ 15 % to 20 %.

6.2.4 Substrate Temperature Calibration

The temperature of the samples were carefully measured during deposition to ensure an accurate mapping of enrichment vs. temperature and determination of the temperature dependance of the incorporation fraction, s, discussed in the following sections. As explained in Chapter 2, the samples were heated using direct current heating (DH) through the substrate for all samples except the one deposited at 249 °C, which was heated using the tungsten radiative back heater (RH). The substrate temperatures were measured by the two previously discussed infrared pyrometers. The Process Sensors pyrometer, which was calibrated for this system as discussed in Chapter 2, was used for most samples discussed in this chapter, but the un-calibrated Omega pyrometer was used for four of the samples. A correction was applied to the Omega pyrometer readings, which can differ from the Process Sensors readings by ≈ 25 °C. Including the uncertainties from the pyrometer calibration, the temperature readings of the substrate are estimated to have a 5 % relative uncertainty due to fluctuations in the current used for sample heating as well as temperature gradients across the sample. The exact temperatures of the samples deposited at room temperature were not measured but instead assumed to be similar to the typical measured ambient temperature outside of the vacuum chamber, which was 21 °C $\pm$ 2 °C. For the analysis of these room temperature samples, this value was used.

6.3 Temperature Dependent Gas Incorporation Model

To correlate the effect of SiH_x partial pressure on the incorporation or adsorption of ^{29}Si and ^{30}Si during deposition of ^{28}Si films at different temperatures, a gas sticking deposition model is formulated that describes the different contributing sources to the film deposition. The sticking of gaseous species is based simply on the idea of idealized Langmuir adsorption for a flat surface with equivalent adsorption sites [186]. This model is later compared to the sample enrichments measured by SIMS.

The model describes two sources of Si atoms that contribute to deposition at the substrate:

(1) the ion beam, which is presumed to be pure ^{28}Si, deposits ions onto the substrate, and

(2) the partial pressure of SiH_x, which contains all three Si isotopes in their natural abundance, can stick and become incorporated into the film.

Figure 6.5 is a cartoon representation of this two source deposition model. In this model, the isotopic concentrations measured by SIMS is the fraction of the total Si deposited that is due to ^{29}Si or ^{30}Si sticking from the SiH_x background partial pressure. The isotope fraction of ^{29}Si and ^{30}Si in a sample is described by the gas sticking deposition model, c_z (with z denoted as 29 for ^{29}Si and 30 for ^{30}Si), given by

$$c_z = \frac{F_g a_z s}{F_g s + F_i} \ , \tag{6.5}$$

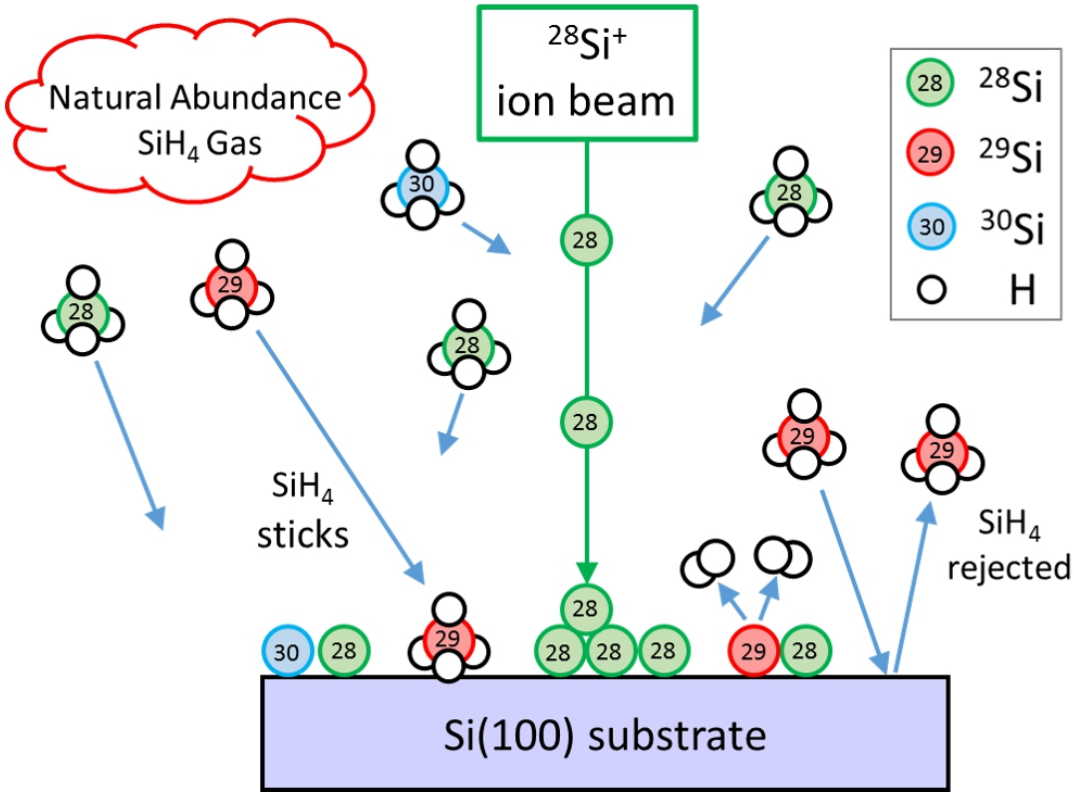

Figure 6.5: Cartoon illustrating the ^{28}Si thin film deposition process described by the gas sticking deposition model. Two sources contributing Si to the deposition are the ^{28}Si ion beam and the SiH_4 gas which diffuses from the ion source and contains a natural abundance of isotopes. SiH_4 can adsorb and react with the Si surface with different probabilities.

where F_g is the SiH_x gas flux, F_i is the ^{28}Si ion flux, a_z is the isotopic abundance of ^{29}Si or ^{30}Si in the SiH_4, which is assumed to have a natural abundance, and s is an effective incorporation fraction (or sticking coefficient) for an average SiH_x species to be adsorbed into the surface. c_z gives the calculated isotope fraction for a given set of deposition conditions. c_z can be re-written as a function that correlates the isotope concentrations to the deposition conditions using a convenient deposition parameter; the SiH_4 flux ratio, $k = F_g/F_i$. c_z written as a function of k is then

$$c_z = \frac{a_z s k}{1 + s k} \ . \tag{6.6}$$

Notice that c_z increases with increasing SiH_4 gas flux, and it decreases with increasing ion beam flux. Additionally, when $F_g \ll F_i$, then $c_z \propto k$, and when $F_g \gg F_i$, then $c_z \approx a_z$. Another convenient transformation of c_z is to convert the isotope specific model of Eq. (6.6) into a general model for SiH_4 sticking by dividing by each isotope's natural abundance so that ^{29}Si and ^{30}Si data can be fit together within the same model. Dividing the measured isotope fraction of a sample by its natural isotopic abundance gives an expected total adsorbed SiH_4 fraction, which is then described by the gas sticking deposition model giving the calculated SiH_4 fraction, $c_{tot.}$, for the total adsorbed SiH_4 where

$$c_{tot.} = \frac{c_z}{a_z} = \frac{sk}{1+sk} \ . \tag{6.7}$$

Equation (6.7) allows the full statistical weight of all the data to be used for determining the incorporation fraction, s, for each sample deposited at different temperatures and get the trend of s vs. temperature, T.

Next, to describe the behavior of s vs. T, a temperature dependent incorporation model, $s(T)$, is defined that is described by two gas sticking terms; a sticking probability resulting from physisorption, s_c, and a higher temperature reactive sticking coefficient, s_r, resulting from chemisorption. s_c and s_r are both expected to be activated by temperature, but s_c decreases with increasing temperature, and s_r increases with increasing temperature. These components are defined to be

$$s_c = 1 - \exp\left(\frac{-E_p}{k_B T}\right) \tag{6.8}$$

and

$$s_r = A_r \exp\left(\frac{-E_c}{k_B T}\right) \ , \tag{6.9}$$

where E_p is the activation energy for physisorption, E_c is the activation energy for chemisorption, k_B is the Boltzmann constant, and T is the substrate temperature during deposition. The exponential prefactor A_r is left as a free parameter to account for experimental uncertainties which may introduce a constant shift in the data, and it will be discussed further in the following sections. The prefactor for s_c is set to 1 because the sticking probability is expected to be close to unity as T approaches zero. The total incorporation fraction at a given temperature is then described by the temperature dependent incorporation model, which is the sum of the two sticking components,

$$s(T) = s_c + s_r = 1 - \exp\left(\frac{-E_p}{k_B T}\right) + A_r \exp\left(\frac{-E_c}{k_B T}\right). \tag{6.10}$$

6.4 Correlating Enrichment to SiH_4 Partial Pressure

To demonstrate the correlation between the SiH_x partial pressure and the ^{28}Si sample enrichment, the raw SIMS isotope fraction data ($^{z}Si/Si_{tot.}$) for the room temperature samples are plotted as a function of the SiH_4 flux ratio, $k = F_g/F_i$ in Fig. 6.6, with ^{29}Si (squares) and ^{30}Si (triangles) isotope fractions plotted together. The top axis in panel (a) shows the total gas flux ratio, $F_g^{tot.}/F_i$, using the gas flux corresponding to the total measured pressure increase during deposition without subtracting out the estimated H_2 fraction in the gas. This difference only shifts the axis laterally, and both the ^{29}Si and ^{30}Si isotope fractions have a strong linear correlation with k, representing the deposition conditions. The resulting Pearson

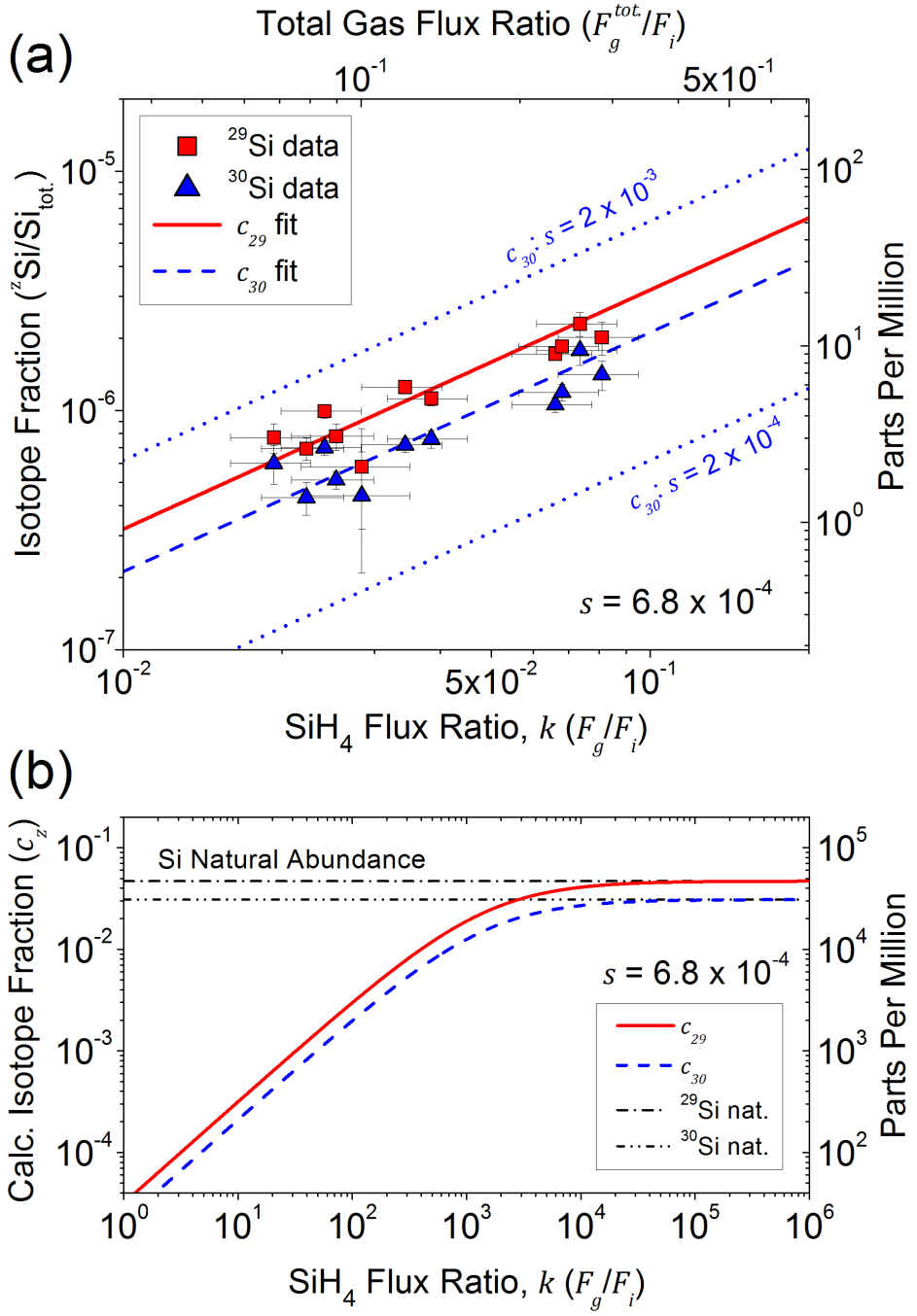

Figure 6.6: Correlation plot of isotope fraction vs. k for ^{28}Si samples deposited at room temperature ($\approx$ 21 °C). (a) SIMS measurements of ^{29}Si (squares) and ^{30}Si (triangles) are shown. The top axis shows the total gas flux during deposition after subtracting the background pressure flux. c_z is fit (Eq. (6.6)) to the ^{29}Si (solid line) and ^{30}Si (dashed line) data giving $s = 6.8(3) \times 10^{-4}$. c_{30} is also shown calculated for two other values of s (dotted lines) to show the sensitivity of the model to s. (b) c_z fits from (a) asymptote to the natural abundance values (dash-dotted lines) at large k ($F_g \gg F_i$).

correlation coefficient for the ^{29}Si data is $r = 0.95$, and for the ^{30}Si data $r = 0.92$. This shows that an increase in SiH_4 flux corresponds to an increased isotope fraction in the sample.

The correlation between enrichment and k is modeled using Eq. (6.6) to get c_{29} and c_{30}, which are fit to the data with s as the only free parameter. These fits are shown in Fig. 6.6 as solid and dashed lines respectively, and they are approximately linear over the range of the data with a slope proportional to s. In panel (b), the fits are plotted in an extended range to show the crossover to a_z at high values of k. Above a k value of about 10^4, c_z starts to asymptote to the natural abundance values of 4.7 % for ^{29}Si and 3.1 % for ^{30}Si (dash-dotted lines). In other words, when $F_g/F_i \gg 1$, the contribution from the ^{28}Si ion beam becomes negligible compared to the gas flux, and so the film composition approaches the composition of the gas, which is assumed in the model and expected in reality to have a natural abundance of Si isotopes. The fits to the data give a room temperature incorporation fraction of $s = 6.8(3) \times 10^{-4}$. The uncertainty in this value is the standard error from the fit. Also plotted for reference is c_{30} calculated for two other values of s (dotted lines), 2×10^{-4} and 2×10^{-3}, which span an order of magnitude around the data. This is to illustrate the sensitivity of the fit to s. Note that when viewed as a log-log plot as in Fig. 6.6, c_z does not change apparent slope as s is varied, it only changes vertical offset.

To investigate this correlation over a larger range of k values and specifically a larger range of SiH_4 fluxes, i.e. pressures, samples deposited in the ion beam chamber at sample location IC–1 were also analyzed. These samples, which were

described in Chapter 4, were also deposited at room temperature and with much higher background pressures during deposition. These additional data are shown in Fig. 6.7, which is an expanded version of Fig. 6.6. The ^{29}Si and ^{30}Si data for the samples deposited at IC–1 (open squares and open triangles, respectively) exhibit similar qualitative behavior to the data for the samples mostly deposited at LC–2 (closed squares and closed triangles, respectively) at lower k values from Fig. 6.6. The fits of c_z (Eq. (6.6)) from Fig. 6.6 are again shown, which are only fit to the LC–2 sample ^{29}Si and ^{30}Si data (solid and dashed lines, respectively). The IC–1 samples generally increase in isotope fraction with increasing k, however, they tend to deviate from the fit of c_z exhibiting an apparently lower incorporation fraction. This deviation can possibly be explained as due to several factors. First, because there was no gas outlet via a vacuum pump at the sample location for these samples, there is an unknown and likely large uncertainty on the total pressure at the sample and its composition in terms of H_2 and SiH_x. The ion beam itself delivers gaseous species to the location of the mass-selecting aperture, which is relatively close to the sample, in the form of ionized SiH_x that may locally increase the pressure around the sample. This pressure increase can be roughly estimated to increase the H_2 partial pressure to $\approx$ 85 % of the total pressure, which is an increase from 70 % in the other experimental configurations. This correction cannot totally account for the discrepancy between the data and the model fit, however.

Additionally, these samples were deposited with a total background pressure increase during deposition between approximately 1.5 $\times 10^{-4}$ Pa and 2.1 $\times 10^{-4}$ Pa (1.2 $\times 10^{-6}$ Torr to 1.6 $\times 10^{-6}$ Torr), which is at least a factor of 30 times higher

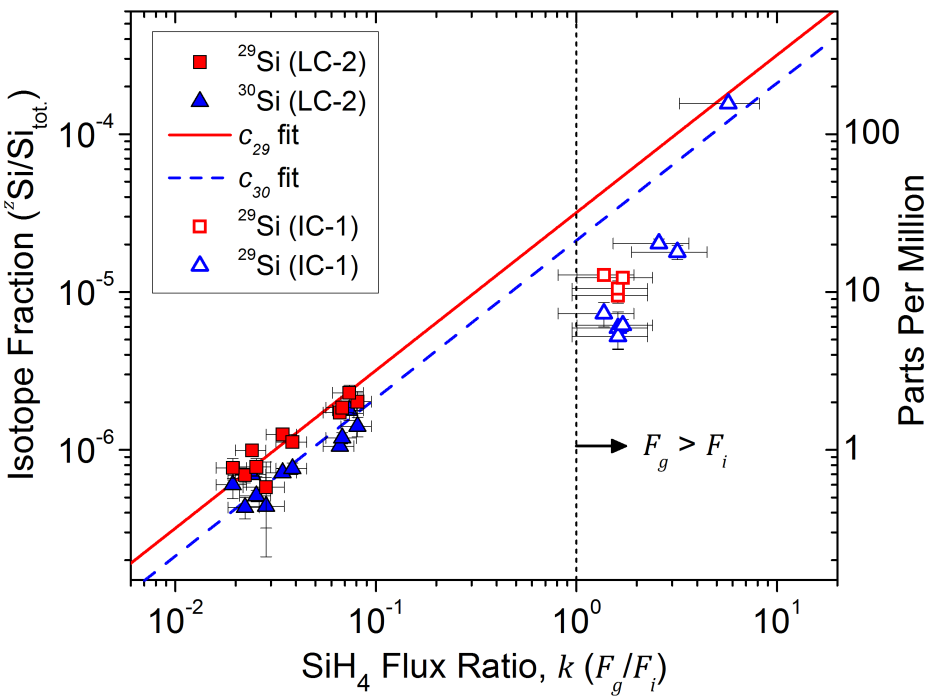

Figure 6.7: Correlation plot of isotope fraction vs. k for ^{28}Si samples deposited at room temperature ($\approx$ 21 °C). The data from Fig. 6.6 of samples deposited mostly at LC–2 (closed squares and closed triangles) are shown as well as SIMS measurements of ^{29}Si (open squares) and ^{30}Si (open triangles) from samples deposited at IC–1 with higher background pressures and thus larger F_g and k values. c_z is fit (Eq. (6.6)) to only the LC–2 ^{29}Si and ^{30}Si data (solid and dashed lines, respectively). The vertical dashed line indicates the boundary where $k = 1$. The LC–1 data lie to the right of this where $F_g > F_i$ in a different deposition regime than the LC–2 data.

than the other room temperature samples deposited at LC–2 and at most a factor of 220 times higher. These pressures and corresponding higher gas flux results in these samples being deposited in a regime where $F_g > F_i$. This is represented by the vertical dashed line in Fig. 6.7. When $F_g > F_i$, an incident SiH_x molecule may not find an area of the surface with bare Si, and instead it may encounter another adsorbed SiH_x or H_2 molecule, blocking further adsorption. H_2 coverage is known to decrease the effective reactive sticking coefficient of SiH_4 [178], although with a small sticking coefficient of $\approx 10^{-4}$ on Si, H_2 coverage may not be significant

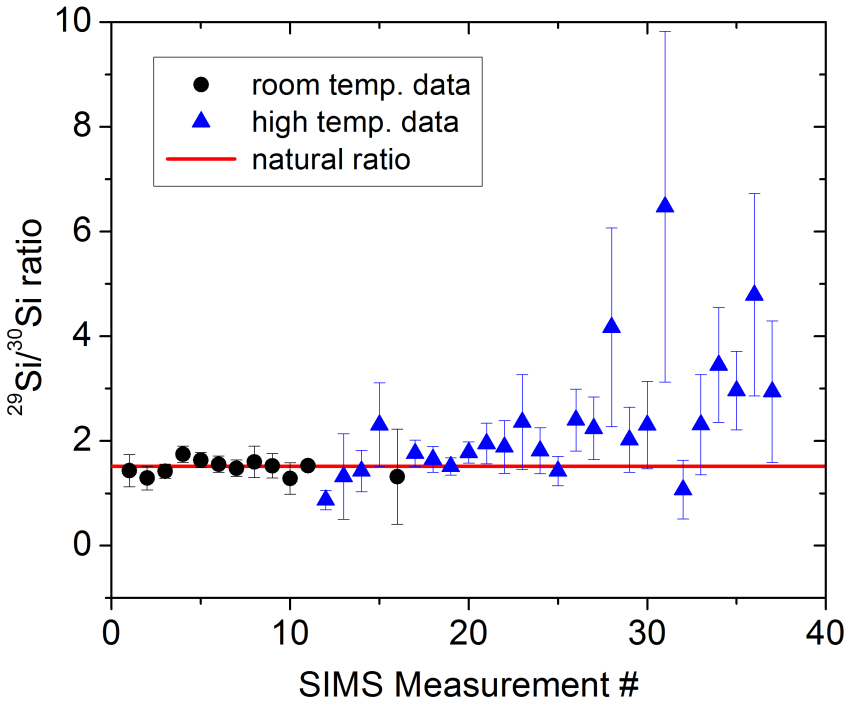

Figure 6.8: ^{29}Si/^{30}Si isotope ratios for all measured samples deposited at room temperature (circles) and elevated temperatures (triangles). The ratios of these samples agree with the natural abundance ratio of 1.52 (line) indicating that the source of ^{29}Si and ^{30}Si is naturally abundant, probably the SiH_4 gas.

here [169]. Energetic ions can also desorb H from Si(100) surfaces [121]. It is difficult to accurately account for these high pressure effects and so the samples deposited at IC–1 are excluded from the analysis of this chapter.

Further strong evidence that the SiH_4 partial pressure is the source of the measured residual isotope fraction of ^{29}Si and ^{30}Si can be derived from the measured isotope ratios, ^{29}Si/^{30}Si, for each sample. If these isotopes were originating from the ion beam, one would expect an attenuation of ^{30}Si compared to ^{29}Si which would increase the ^{29}Si/^{30}Si ratio above the natural value. Instead, the measured isotope ratios are found to be very close to the natural value of approximately 1.52. Figure 6.8 shows the ^{29}Si/^{30}Si isotope ratios for a large number of room

temperature (circles) and elevated temperature (triangles) samples. Also shown is a line representing the natural abundance ratio. All of the data lie close to the natural ratio within their error bars. This indicates that the source of ^{29}Si and ^{30}Si has a natural abundance of Si isotopes, e.g., the SiH_4 source gas. Measurement number 28 and 31, which lie above a ^{29}Si/^{30}Si ratio of four, suffer from discrete counting noise in the SIMS measurements due to a total ^{30}Si count < 10 through the entire enriched film, which makes the ratio highly sensitive to single count fluctuations.

6.5 Temperature Dependence of ^{29}Si and ^{30}Si Adsorption

The previous section showed that a strong correlation exists between the relative SiH_4 flux at the sample and the measured enrichment. This pressure dependance indicates that the natural abundance SiH_4 gas diffusing from the ion beam is the source of residual ^{29}Si and ^{30}Si in the samples. Next, because substrate deposition temperature is a key parameter for facilitating and controlling the quality of epitaxial deposition as this work progresses further, it is important to understand the effect of different substrate temperatures on the correlation between enrichment and gas flux.

As reported previously in this chapter, the raw SIMS data show that the ^{29}Si isotope fractions increase rapidly in the deposition temperature range from 502 °C (127 ppb) to 812 °C (4.32 ppm). However, the room temperature correlation plot (Fig. 6.6) showed that the isotope fractions also depend on k, the SiH_4 flux ratio

(i.e. the deposition conditions). In order to extract an accurate temperature dependence of the enrichment, the raw SIMS measurements are adjusted to a common set of deposition conditions (F_g and F_i). To perform this adjustment, the k value matching the sample deposited at 502 °C is chosen, i.e. the sample with the lowest measured isotope fractions of ^{29}Si and ^{30}Si. This adjustment suppresses the effect on enrichment of varying deposition conditions across samples. By using the 502 °C sample as a benchmark against which to compare the other samples, the change in isotope fraction is mapped against temperature for the conditions that produced the best measured enrichment.

To find the adjusted isotope fractions from the raw SIMS values, Eq. (6.6) is first solved for s, using subscript T to denote the resulting value, s_T, for a specific data point with deposition temperature T (in °C). Equation (6.6) is then used along with each calculated s_T value to generate the gas sticking deposition model curve, $c_z(s_T)$, for each data point. The k value of the 502 °C sample, which is the reference to which the raw SIMS data will be adjusted, is denoted as k_{502}. To get these adjusted values, $c_z(s_T)$ at $k = k_{502}$ is then evaluated for each data point. This gives $c_z(s_T, k_{502})$, which is thus the isotope fraction of a sample with deposition temperature T adjusted to the deposition conditions (SiH_4 flux ratio) of the 502 °C sample. For example, the adjusted isotope fraction of the 812 °C sample is calculated as $c_z(s_{812}, k_{502})$. In Fig. 6.9, the adjusted isotope fractions given by $c_z(s_T, k_{502})$ are plotted as a function of temperature showing the temperature dependence of the enrichment, independent of variations in deposition conditions. More specifically, the values in Fig. 6.9 are the expected isotope fractions of ^{29}Si

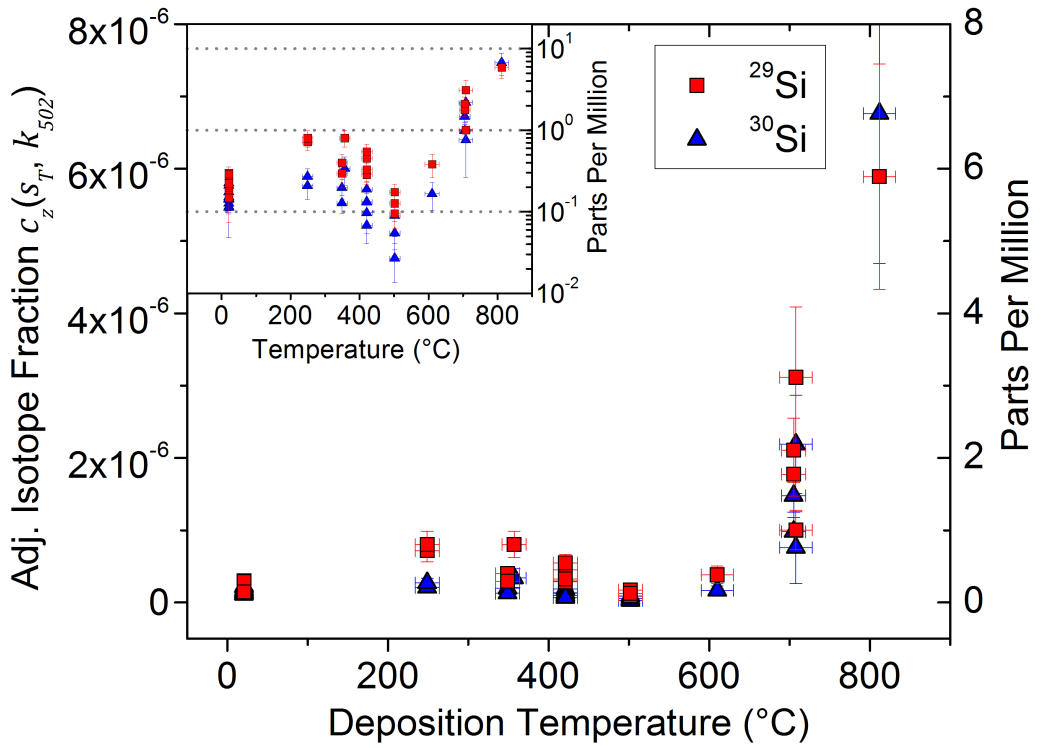

Figure 6.9: Adjusted isotope fraction, $c_z(s_T, k_{502})$, vs. temperature for ^{29}Si (squares) and ^{30}Si (triangles). The raw isotope fractions are adjusted to the deposition conditions (F_g and F_i) of the 502 °C sample. The inset shows the same data on a semi-log scale to highlight the behavior of the data below 500 °C.

(squares) and ^{30}Si (triangles) for all samples had they been deposited with the same SiH_4 partial pressure and ion beam flux as the 502 °C sample. The adjusted isotope fractions are shown to trend downwards slightly from the 249 °C sample average of about 0.76 ppm ^{29}Si to a minimum at the 502 °C average of about 0.13 ppm ^{29}Si. This implies that if the substrate temperature of a sample similar to the 502 °C sample is lowered to 249 °C during deposition, the ^{29}Si isotope fraction is expected to increase to approximately 0.76(17) ppm.

The room temperature samples do not seem to follow this trend and instead have adjusted isotope fractions that are lower than expected. The deposition pressure for these samples was measured using a different ion gauge configuration than

the later high temperature samples, which may affect the adjustment of these data. Another difference is that the room temperature samples were all grown as amorphous films while the samples deposited at elevated temperatures were crystalline. Surface orientation and crystallinity affect the adsorption of SiH_4 on Si surfaces as described by Comfort and Reif who note that for Si CVD, the growth rate on a Si(100) surface is generally higher than on a Si(111) surface, which is itself higher than the growth rate on a polycrystalline surface [174]. These effects may lead to a lower effective sticking coefficient on the amorphous samples compared to that of the crystalline samples.

Above 502 °C, the adjusted ^{29}Si isotope fraction sharply increases up to a value of 5.9 ppm ^{29}Si at 812 °C. Again, this shows that if the substrate temperature of a sample similar to the 502 °C sample was increased to 812 °C during deposition, the ^{29}Si isotope fraction is expected to increase to 5.9(16) ppm. This increase is posited to be due to an increase in s as a process similar to a CVD reaction becomes more active, and the reactive sticking coefficient begins to dominate the total incorporation fraction. To examine this hypothesis, the values of s at each temperature need to be determined and compared to the temperature dependent incorporation model (Eq. (6.10)).

6.6 Temperature Dependence of the Incorporation Fraction, s

The gas incorporation fraction, s, is determined at each sample temperature using Eq. (6.6) shown in Fig. 6.6. It should be noted that the incorporation fractions determined here are a total net sticking probability; i.e. a molecule was incorporated into the growing film, and remained there until detected by SIMS. A convenient transformation in the analysis of this gas sticking deposition model is to convert each isotope fraction for a given sample by dividing by their respective natural abundance values, a_z, so both ^{29}Si and ^{30}Si can contribute statistical weight together when fit with the model. This conversion follows the model of Eq. (6.7) for calculating $c_{tot.}$ and gives the converted isotope fraction, i.e. the expected total SiH_4 fraction adsorbed in the sample, $(^z\mathrm{Si}/\mathrm{Si}_{\mathrm{tot.}})/a_z$. Figure 6.10 (a) is a correlation plot of the converted isotope fractions for several deposition temperatures: 812 °C (diamonds), 705 °C (left-pointing triangles), 249 °C (hexagons), 421 °C (right-pointing triangles), and 502 °C (down-pointing triangles). These data are plotted vs. the SiH_4 flux ratio, k. Also plotted is $c_{tot.}$ (Eq. (6.7)), which is fit to each temperature set with s as the only free parameter. The fits reported in this chapter are achieved using an orthogonal distance regression method which accounts for uncertainty in both coordinate values of each datum. Uncertainties reported with the fit values are the standard error from the fits. Within the range of Fig. 6.10, $c_{tot.}$ is approximately linear with a slope equal to s. Note that when $c_{tot.}$ is plotted on a linear scale, it runs through the origin because zero SiH_4 flux results in a calculated SiH_4

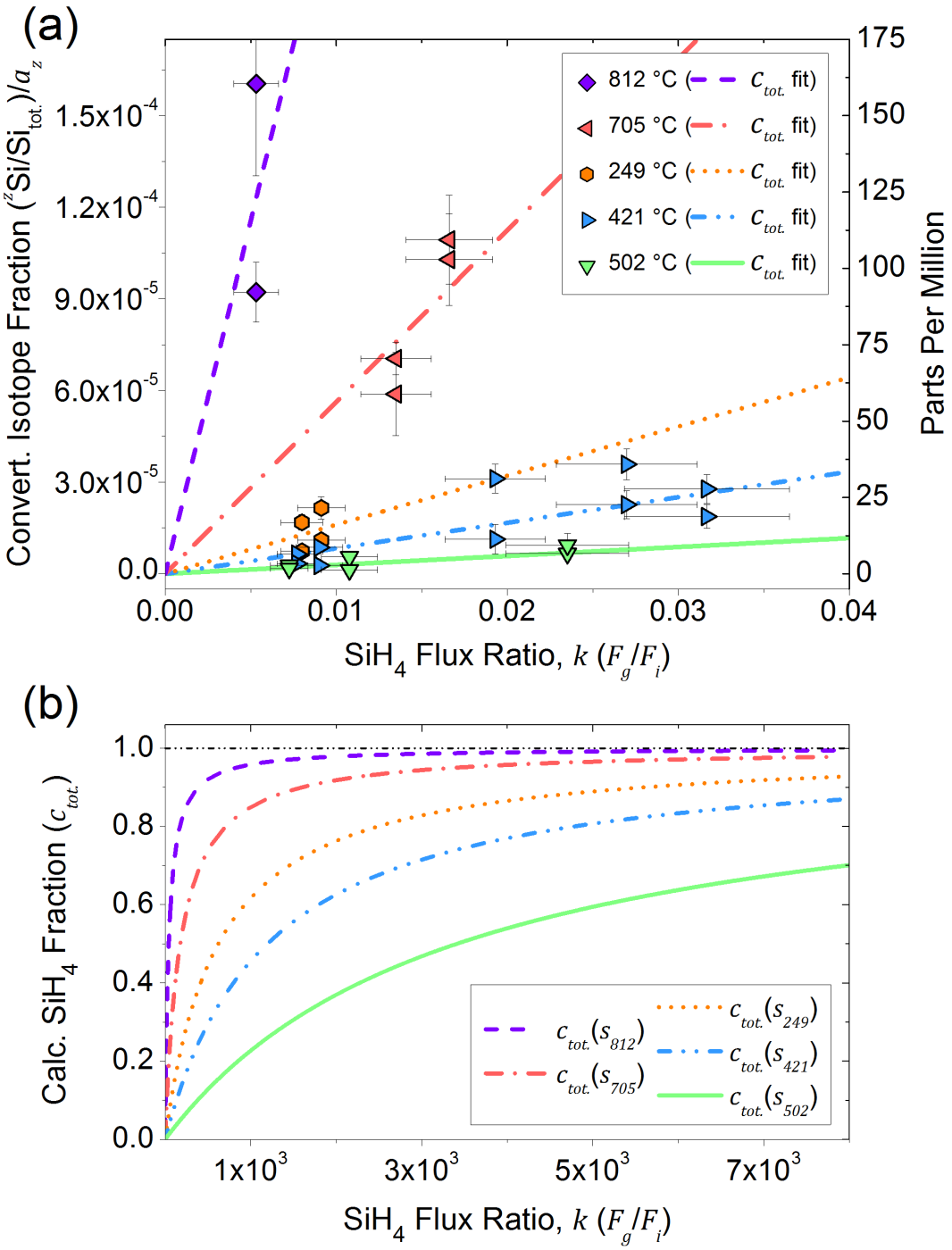

Figure 6.10: Correlation plot of the converted isotope fractions vs. SiH_4 flux ratio, k, shown on a linear scale for samples deposited at several elevated temperatures. (a) The raw SIMS isotope fractions for ^{29}Si and ^{30}Si are each converted to an expected SiH_4 fraction using their natural abundance, a_z. $c_{tot.}$, is fit (Eq. (6.7)) to the data for each deposition temperature (solid, dashed, dotted lines) and is approximately linear over this range with a slope of s. (b) $c_{tot.}$ fits from (a) asymptote to unity at large values of k.

fraction (adsorbed SiH_4) of zero. Figure 6.10 (b) illustrates the functional form of the calculated SiH_4 fraction, $c_{tot.}$, at large values of $k = F_g/F_i$ where the SiH_4 gas flux dominates the ratio and $c_{tot.}$ asymptotes to unity.

From the fit values of $c_{tot.}$ at each temperature, the temperature dependence of s is plotted in Fig. 6.11, which shows that s follows a similar trend to the ^{29}Si and ^{30}Si isotope fractions in Fig. 6.9. In panel (a) of Fig. 6.11, s trends downwards slightly from a value of $1.6(2) \times 10^{-3}$ at 249 °C to a minimum of $2.9(4) \times 10^{-4}$ at 502 °C. In this temperature range, the data appears to behave in a similar manner to the sticking probability term resulting from physisorption, s_c, which decreases with increasing temperature. Then as T is increased more, s rapidly increases to $2.3(5) \times 10^{-2}$ at 812 °C. This increase is expected qualitatively for the reactive sticking coefficient term resulting from chemisorption, s_r, which increases with increasing temperature. A list of the samples discussed in this chapter, their deposition parameters, and measurement and analysis results can be found in Tables D.10 to D.13 in Appendix D. These values of s are consistent with previously reported values of the reactive sticking coefficient of silane species on Si surfaces, although there is a large variation in the literature. Si CVD studies have shown s_r to range from 5×10^{-4} to 5×10^{-3} for polycrystalline Si deposition at 600 °C to 800 °C [177], and it ranges from 1×10^{-3} to 3×10^{-5} for Si(111) surfaces below 500 °C [187, 188].

Next, the data in Fig. 6.11 is fit to the temperature dependent incorporation model of Eq. (6.10), $s(T)$, which is the sum of the sticking terms, $s_c + s_r$. E_p, E_c, and A_r are set as free parameters in the fit, which is shown in Fig. 6.11 (a) (line). Also plotted separately are the s_c (Eq. (6.8)) and s_r (Eq. (6.9)) terms (dotted and dashed

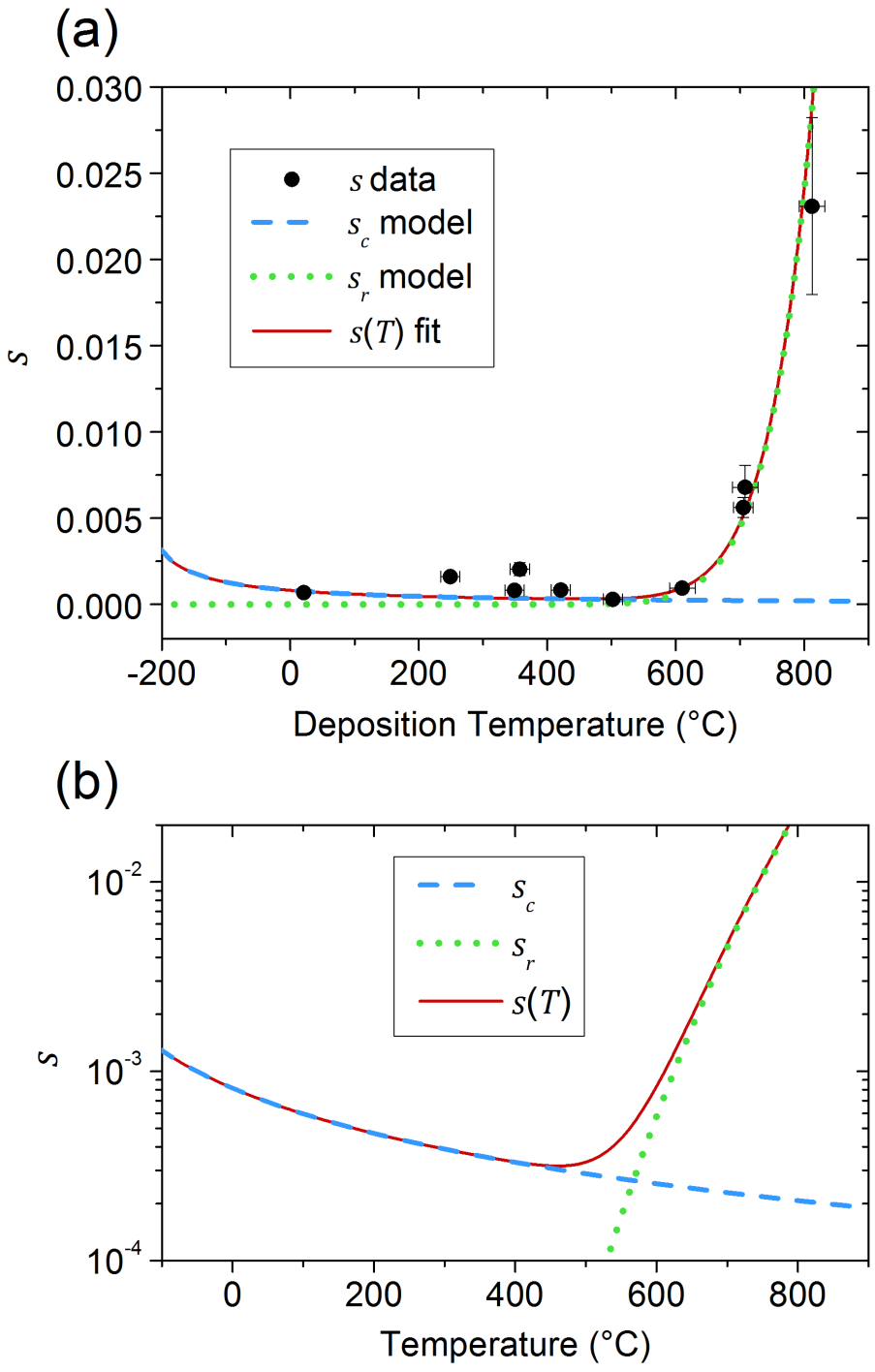

Figure 6.11: (a) s (circles) vs. deposition temperature. The temperature dependent incorporation model, $s(T)$, is fit to the data (Eq. (6.10)) and plotted (line) along with the individual sticking terms calculated from the fit; s_c (dotted line, Eq. (6.8)), representing physisorption, and s_r (dashed line, Eq. (6.9)), representing reactive chemisorption. (b) Semi-log plot of the fits from (a) showing the crossover from $s(T)$ dominated by s_c to s_r where s increases rapidly above 600 °C.

lines, respectively), which are calculated from the fit parameters. Panel (b) shows the fit and its modeled components on a semi-log plot to illustrate the crossover from $s(T)$ being dominated by s_c to $s(T)$ being dominated by s_r. The fit of $s(T)$ matches the data fairly well at higher temperatures, while there is some deviation in the lower temperature range. The fit also matches the minimum of s in the data around 500 °C. The value of the activation energy for chemisorption, E_c, given by this fit of Eq. (6.10) is 1.5(2) eV. The uncertainty in this value is the standard error from the fit. The value of E_p generated by the fit, however, has a large uncertainty indicating that the fit is under-constrained for the low temperature region, and so the value is not necessarily reliable. Because the fit's choice of E_p parameter can also affect the high temperature part of the fit, the data dominated by E_c needs to be isolated and analyzed separately, which will be discussed in the next section.

6.7 Determination of the Reactive Sticking Activation Energy, E_c

To isolate the incorporation fraction data that is most sensitive to the value of E_c, the data from Fig. 6.11 is plotted in an Arrhenius form for thermally activated processes [189, 190], and the higher temperature data is fit to a line. This analysis involves taking the natural log of $s(T)$ (Eq. (6.10)), the temperature dependent incorporation model, giving

$$\ln(s(T)) = \ln\left(1 - \exp\left(\frac{-E_p}{k_B T}\right) + A_r \exp\left(\frac{-E_c}{k_B T}\right)\right) \ . \tag{6.11}$$

This equation in this form is not useful for this analysis because a linear term cannot easily be extracted. However, for the higher temperature data, the reactive sticking coefficient is expected to dominate, which means $s \approx s_r$, and so taking the natural log of only the s_r term (Eq. (6.9)) yields

$$\ln(s_r) = \ln(A_r) - E_c \left(\frac{1}{k_B T} \right), \tag{6.12}$$

which is the equation for a line with intercept $\ln(A_r)$ and slope E_c. Figure 6.12 is a plot of $\ln(s)$ (circles) vs. inverse deposition temperature, $\frac{1}{k_B T}$, modified by the Boltzmann constant to have units of inverse energy. Also plotted is the natural log of $s(T)$ (dotted line, Eq. (6.11)). The room temperature data resides outside the graph window of Fig. 6.12 for clarity and to highlight the higher temperature data, but it is included in the $s(T)$ fit. Using a linear fit to determine E_c is accurate within the uncertainties in the linear region of the higher temperature data where s_r dominates. This linear fit (Eq. (6.12)) is also shown in Fig. 6.12 (solid line) for the data between 502 °C and 812 °C. This fit gives a value for the chemisorption activation energy of $E_c = 1.1(1)$ eV. The uncertainty of this value is the standard error from the fit. This value differs from the value of E_c obtained in the previous section of 1.5(2) eV from the $s(T)$ fit. As was mentioned previously, the Arrhenius fit is an alternative fitting method that gives a comparison to the previous fit of $s(T)$ and is possibly more accurate because it allows analysis of E_c separate from E_p and avoids convolution with the large uncertainty in the fit value of E_p. Both of these values, however, are consistent with reported activation energies of SiH_4 CVD between 600 °C and 800 °C. The literature values for SiH_4 CVD activation

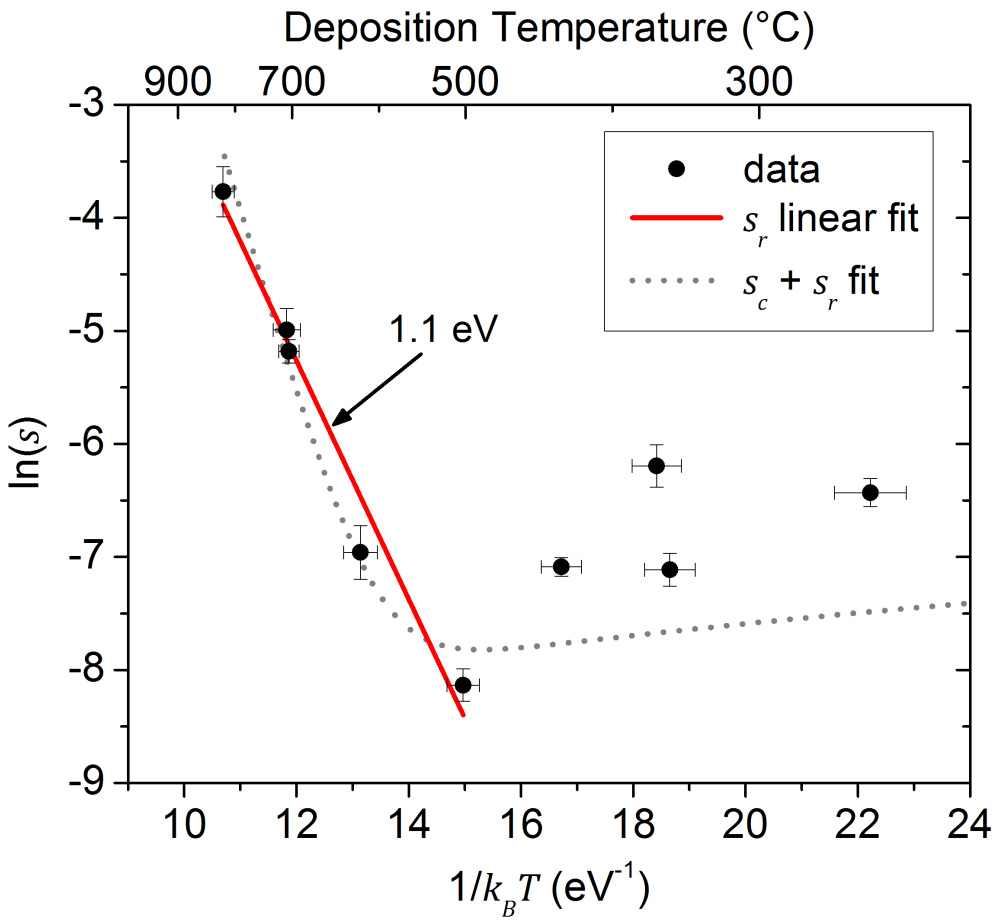

Figure 6.12: Arrhenius plot of $\ln(s)$ (circles) vs. inverse temperature in energy units. The top axis shows the equivalent deposition temperature in °C. The data between the 502 °C sample and the 812 °C sample are fit to a line (Eq. (6.12)) whose slope gives an activation energy, $E_c = 1.1(1)$ eV. Also plotted is the natural log of the fit of $s(T)$ (dotted line, Eq. (6.11)).

energy can vary from about 0.4 eV to 2.2 eV depending heavily on experimental conditions such as surface orientation, gas pressure, and hydride species [177, 187, 191–194]. An average value of the activation energies derived from data in Ref. [174] for lower pressure CVD experiments with deposition temperatures between 500 °C and 900 °C is approximately 1.1 eV.

The exponential prefactor, A_r, is required in the model for s_r because it accounts for the vertical offset of the data in the Arrhenius plot (Fig. 6.12) from the

expected intercept of zero. Leaving A_r as a free parameter allows for experimental uncertainties that cannot reasonably be predicted such as the method used for estimating the SiH_4 partial pressure having a systematic shift that propagates to the calculated incorporation fraction values, which would affect A_r but not E_c. The presence of different silicon hydrides, (SiH_x) or possibly disilane (Si_2H_6) which is known to contaminate commercial silane and have higher sticking coefficients [188, 195], in the background gas could also introduce errors because they may have different reactive sticking coefficients leading to an average value being measured. Gates has shown that the activation energy of Si CVD increases from around 1.17 eV to 2.04 eV for SiH_3 and SiH respectively [194]. As stated previously, the prefactor for s_c is set to 1 because it is more reasonable that s_c approaches unity at zero temperature. Also, differences in reactive sticking of different molecules should not affect the physisorption term as much, making it not as critical for the prefactor to be left free.

6.8 Chapter 6 Summary

In this chapter, the measured enrichment (i.e. residual ^{29}Si and ^{30}Si isotope fractions) of samples grown at both room temperature and with elevated substrate temperatures ranging from 249 °C to 812 °C was analyzed to understand how enrichment changes as a function of pressure and temperature due to SiH_4 incorporation. The ^{29}Si and ^{30}Si isotope fraction were found to be highly correlated to the background partial pressure of SiH_4 during deposition. This showed that the

dominant, if not only, source of residual minor isotopes in ^{28}Si samples is the natural abundance SiH_4 gas which adsorbs into samples during growth with a room temperature incorporation fraction, $s = 6.8(3) \times 10^{-4}$. From further analysis, the temperature dependence of the incorporation fraction is determined and modeled using two sticking terms in the temperature dependent incorporation model. A physisorption sticking probability decreases weakly with increasing temperature while a reactive sticking coefficient due to CVD-like chemisorption increases more strongly with increasing temperature from a minimum of $2.9(4) \times 10^{-4}$ for the 502 °C sample up almost two orders of magnitude to $2.3(5) \times 10^{-2}$ for the 812 °C sample. These competing terms lead to a minimum in residual ^{29}Si and ^{30}Si isotopic concentration at around 500 °C. The lowest ^{29}Si isotopic concentration for a sample deposited in that range was 127(29) ppb. As an alternative to the temperature dependent incorporation model, an Arrhenius formalism was used to determine the activation energy of the reactive sticking coefficient and found that $E_c = 1.1(1)$ eV. Understanding the role of SiH_4 gas sticking for a range of deposition temperatures allows for better prediction of, and control over, the resulting enrichment. This knowledge enables production of ^{28}Si samples with targeted levels of enrichment (^{29}Si isotope fractions), which could facilitate a study of T_2 coherence times as a function of ^{29}Si concentration.

Chapter 7

Summary of Results and Future Experiments

7.1 Summary and Conclusions

In this work, a mass selected, hyperthermal energy ion beam deposition system was used to achieve *in situ* isotopic enrichment of a total of three ^{22}Ne samples, three ^{12}C samples, and 61 ^{28}Si samples. Very high levels of enrichment were achieved, especially for ^{28}Si, which was also successfully deposited as epitaxial thin films.

Chapter 3 demonstrated successful proof of principle enrichment by implanting the minor isotope ^{22}Ne enriched with an isotope fraction of 99.455(36) % into Si as well as depositing thin films of ^{12}C enriched to an isotope fraction of 99.9961(4) % using the mass selected ion beam system. Realized mass selectivities of 1785:1 for ^{22}Ne and 276:1 for ^{12}C were achieved. While these selectivities are not directly translatable to ^{28}Si enrichment, these experiments do show that very high levels of *in situ* enrichment are possible in thin film deposition using this system.

Chapters 4 and 5 demonstrated that ^{28}Si films could be deposited with residual

^{29}Si and ^{30}Si isotope fractions consistently below 1 ppm with both elevated substrate temperatures and while using the high pressure plasma mode of the ion source. The enrichment values of these samples meet the enrichment materials goal laid out at the beginning of this thesis to achieve ^{28}Si enrichments that surpass those of any other known sources of ^{28}Si including the IAC. The isotope reduction factor of ^{29}Si for the most highly enriched sample deposited at DC–3 is $3.7(8) \times 10^5$. This means that there is approximately 3.7×10^5 times less ^{29}Si in that sample than in natural abundance Si. This value of the reduction factor along with the reduction factor values of the excluded isotopes from all the most highly enriched samples of ^{28}Si, ^{22}Ne, ^{12}C are shown in the isotope reduction timeline of isotope reduction factors in Fig. 7.1. A version of this figure was previously shown for Si samples in Fig. 5.54 in Chapter 5.

Like that figure, Fig. 7.1 shows the isotope reduction factors vs. the sample deposition date for samples with the highest enrichments achieved up to that point, where a larger reduction factor is equivalent to a higher level of enrichment. As previously discussed, the isotope reduction factors are defined as the natural abundance of an isotope of an element, a_z, divided by the measured isotope fraction of that isotope. Here, the isotope fractions are written generally as $^z\mathrm{X}/\mathrm{X}_{\mathrm{tot.}}$, where $^z\mathrm{X}$ refers to the counts of a particular isotope in the measurement of a particular element, and $\mathrm{X}_{\mathrm{tot.}}$ is the sum of the counts of all isotopes being measured, as discussed in Chapter 1. The isotope reduction factors are therefore written here as $a_z/(^z\mathrm{X}/\mathrm{X}_{\mathrm{tot.}})$. The isotope reduction factors for ^{22}Ne (diamonds), ^{12}C (circle), ^{29}Si (squares) and ^{30}Si (triangles) in Fig. 7.1 are shown to increase for samples deposited throughout

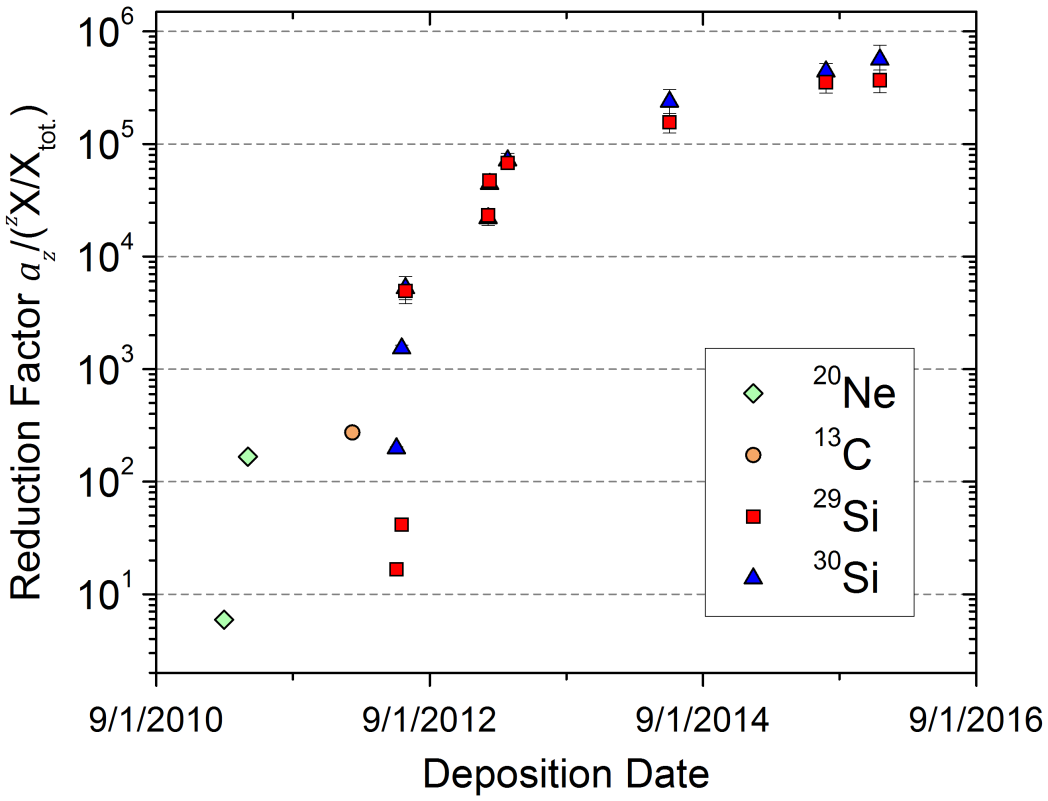

Figure 7.1: Isotope reduction timeline. Timeline of the progression of the isotope reduction factors for the lowest residual isotope fractions of ^{22}Ne (diamonds), ^{12}C (circle), ^{29}Si (squares) and ^{30}Si (triangles), as measured by SIMS. These were achieved for ^{22}Ne, ^{12}C, and ^{28}Si samples deposited over approximately five years.

this work. Uncertainties in the reduction factors are shown for all samples and are derived from the SIMS measurements of the isotope fractions.

The overall ^{28}Si isotope fraction of the most highly enriched ^{28}Si sample deposited at DC–3 and in this entire work was 99.9999819(35) %. This demonstrates an improvement over the initial ^{28}Si sample deposited at IC–1 in the form of a reduction in ^{29}Si of approximately 2.2 $\times 10^4$ times. This and other similar samples are more highly enriched than any other known source of ^{28}Si, including that of the IAC. These samples also demonstrate enrichments sufficient to enable a robust measurement of the dependance of electron coherence times on ^{29}Si concentration

in the single spin regime and compare it to theoretical predictions [12], as proposed in Chapter 1 (see Fig. 1.9). The overall decrease in isotope fractions for isotopes rejected during production of ^{22}Ne, ^{12}C, and ^{28}Si samples can be seen in the enrichment progression timeline for ^{20}Ne (diamonds), ^{13}C (circles), ^{29}Si (squares) and ^{30}Si (triangles) in Fig. 7.2. As mentioned previously, this timeline shows the SIMS measurements of the isotope fractions vs. deposition date for the samples that were the most highly enriched of any samples deposited up to that point. These are the record enrichments of samples produced in this work. As previously discussed, the isotope fractions are written generally here as $^{z}\mathrm{X}/\mathrm{X}_{\mathrm{tot.}}$. Uncertainties in the isotope fractions are shown for all samples and are derived from the SIMS measurements, as previously discussed. Also shown for comparison are the ^{29}Si isotope fractions of the ^{28}Si epilayers and crystals produced by Isonics and Itoh using $^{28}SiH_4$ CVD (dash-double dotted line) from Ref. [36,37], the bulk ^{28}Si material produced by the IAC using $^{28}SiH_4$ CVD (dash-dotted line) from Ref. [32], and the ^{28}Si thin films produced by Tsubouchi *et al.* using ^{28}Si IBE (dotted line) from Ref. [43]. The ^{28}Si samples produced in this work have residual ^{29}Si and ^{30}Si isotope fraction that are far less than those of these other sources.

Some of the key experimental changes that led to the improvements in enrichment include improving the ion beam geometric mass selectivity through beam tuning, depositing in a lower background pressure of SiH_4, and achieving higher deposition rates and smaller ion beam spot sizes through beam tuning. Most of these factors relate to the adsorption of natural abundance SiH_4 gas from the vacuum during deposition, which lowers the resulting ^{28}Si enrichment.

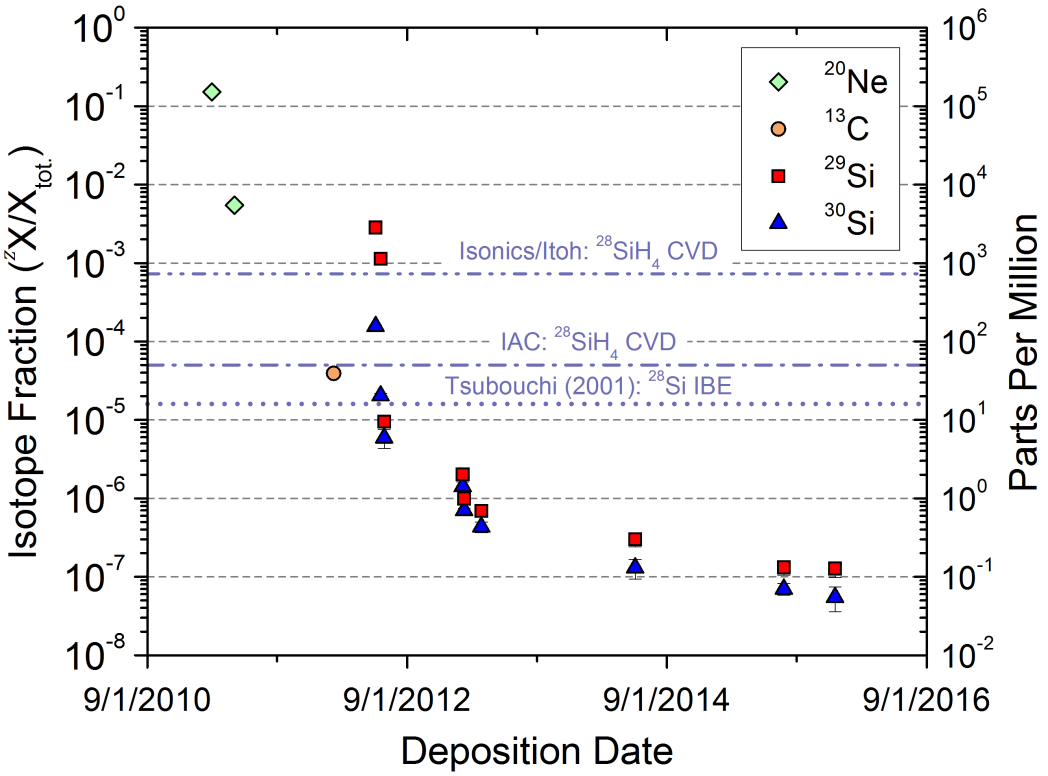

Figure 7.2: Enrichment progression timeline. A timeline of the progression of the best residual isotope fractions of ^{20}Ne (diamonds), ^{13}C (circle), ^{29}Si (squares), and ^{30}Si (triangles), as measured by SIMS. These were achieved for ^{22}Ne, ^{12}C, and ^{28}Si samples deposited over approximately five years. Also shown for comparison are the ^{29}Si isotope fractions of the ^{28}Si epilayers and crystals produced by Isonics and Itoh using $^{28}SiH_4$ CVD (dash-double dotted line) from Ref. [36, 37], the bulk ^{28}Si material produced by the IAC using $^{28}SiH_4$ CVD (dash-dotted line) from Ref. [32], and the ^{28}Si thin films produced by Tsubouchi *et al.* using ^{28}Si IBE (dotted line) from Ref. [43].

Chapter 5 also demonstrated that sample heating was critical for achieving epitaxy. Crystalline, epitaxial ^{28}Si films were produced using elevated deposition temperatures between 349 °C and 1041 °C, although samples deposited above 600 °C were very rough. This was due to chemical contaminants such as SiC at the growth surface that result in step pinning sites that lead to step bunching, faceting on {111} and {113} planes, and large mound formation. Smooth, epitaxial ^{28}Si films with typical surface widths of $\Delta z = 2$ nm were achieved by depositing at lower

temperatures between 349 °C and 460 °C.

Chemical contaminants in these ^{28}Si films were measured by SIMS, which detected N, C, O, F, Al, and Cl. The N, C, and O were detected at especially high concentrations, initially all above 1×10^{19} cm^{-3}. The dominant source of the N, C, and O for this sample was the ion beam. N_2 and CO ions were likely introduced ballistically into the film from the 28 u beam. F and Al contamination were eliminated for a later sample due to experimental alterations. By improving the vacuum in both the deposition chamber and the ion beam chamber, and by using a higher ^{28}Si ion beam current generated in the high pressure mode of the ion source, N, C, and O were reduced in the final sample. The average atomic concentration of N in the film was measured to be 9.07(4) $\times 10^{18}$ cm^{-3}, or 181.8(8) ppm, the average atomic concentration of C in the film was measured to be 8.27(3) $\times 10^{18}$ cm^{-3}, or 165.7(6) ppm, and the average atomic concentration of O in the film was measured to be 3.09(4) $\times 10^{18}$ cm^{-3}, or 61.9(8) ppm. Based on these concentrations and the solid solubility of these elements in Si, it is likely that Si_3N_4, SiC, and SiO exist within the ^{28}Si films. These remaining atomic concentrations were likely the result of both adsorption from the background vacuum and ballistic transport from the ion beam. The resulting best total chemical purity for a ^{28}Si sample deposited at DC–3 and overall in this work is approximately 99.96(2) %.

Finally, TEM was used to confirm that ^{29}Si films produced with both the higher and lower deposition temperatures were crystalline and epitaxially aligned to the substrates. All samples deposited with substrate temperatures above 600 °C were observed to have {111} stacking faults and twinning present in the films. For

lower deposition temperature samples, one sample deposited using the low pressure mode did not have any visible stacking faults but probably still contained other crystalline defects. Another sample deposited using the high pressure mode to generate a much higher deposition rate was observed to have a lot of {111} stacking faults and likely other defects. This increased defect concentration may have been due to the deposition rate for the second sample being over a factor of 12 larger while the deposition temperature was slightly lower. In general, the crystalline defects in these films are likely related to the presence of clusters of chemical contaminant. Reduction of these crystalline defects likely requires reduction of the chemical contaminants within the ^{28}Si films. The second and third materials goals for chemical purity and crystallinity described in Chapter 1 were not pursued further within the experiments depositing ^{28}Si samples at DC–3, although improvements and new understanding regarding the source of both chemical and crystalline defects were made.

Chapter 6 explored and quantified the relation between the natural abundance gas in the chamber and the resulting sample enrichments. The measured enrichment (i.e. residual ^{29}Si and ^{30}Si isotope fractions) of samples grown at both room temperature and with elevated substrate temperatures ranging from 249 °C to 812 °C was analyzed to understand how enrichment changes as a function of pressure and temperature due to SiH_4 incorporation. The ^{29}Si and ^{30}Si isotope fractions were found to be highly correlated to the background partial pressure of SiH_4 during deposition. This showed that the dominant, if not only, source of residual minor isotopes in ^{28}Si samples is the natural abundance SiH_4 gas which adsorbs into sam-

ples during deposition with an incorporation fraction, s. From further analysis, the temperature dependence of s is determined and modeled using two sticking terms in a temperature dependent incorporation model. A physisorption sticking probability decreases weakly with increasing temperature while a reactive sticking coefficient due to CVD-like chemisorption increases more strongly with increasing temperature from a minimum of $2.9(4) \times 10^{-4}$ for the 502 °C sample up almost two orders of magnitude to $2.3(5) \times 10^{-2}$ for the 812 °C sample. These competing terms lead to a minimum in residual ^{29}Si and ^{30}Si isotopic concentrations at around 500 °C. The lowest ^{29}Si isotopic concentration for a sample deposited in that range was 127(29) ppb. As an alternative to the temperature dependent incorporation model, an Arrhenius formalism was used to determine that the activation energy of the reactive sticking coefficient is $E_c = 1.1(1)$ eV. Understanding the role of SiH_4 gas sticking for a range of deposition temperatures allows for better prediction of, and control over, the resulting enrichment. This knowledge can aid in enabling production of ^{28}Si samples with targeted levels of enrichment (^{29}Si isotope fractions) that could facilitate a study of T_2 coherence times as a function of ^{29}Si concentration, as discussed in the next section.

The main impact of this work on the field of Si-based solid state quantum computing is the demonstration of ^{28}Si produced with extremely high levels of enrichment that have never been produced before. This was achieved in a laboratory setting as opposed to an industrial scale effort and was comparatively cheap. Effectively, a new material was engineered using a particular processing method, i.e. ion beam *in situ* enrichment and deposition. Overall, the highest quality ^{28}Si films

produced in this work, in terms of the materials goals stated in Chapter 1, were deposited with varied deposition conditions. However, ^{28}Si films deposited using the high pressure mode of the ion source with a deposition temperature of approximately 450 °C are most likely to result in the highest quality films. This temperature is optimal for both enrichment and smooth epitaxial growth, and the high ion current achieved in the high pressure mode should lead to a minimization of chemical contaminants. The high growth rate however, may lead to diminished crystalline quality.

7.2 Proposals for Future Experiments

7.2.1 Targeted Levels of Enrichment

One of the advantages of enriching material *in situ* nearly simultaneously with deposition is the ability to more easily modulate the enrichment level throughout the sample by switching the magnetic field of the sector mass analyzer to modulate the isotope being deposited. As a demonstration of modulating the isotopic concentration of a material throughout its thickness, an isotope heterostructure that alternates between layers of enriched ^{28}Si and layers of near natural abundance Si was produced. This sample was deposited at room temperature at LC–2. By switching the magnetic field of the sector mass analyzer from the 28 u beam to the 29 u beam (which is composed of both ^{29}Si and ^{28}SiH), one can control which isotope or combination of isotopes is deposited. In a typical SiH_4 mass spectrum produced when using the low pressure mode of the ion source, the ion current peak height at

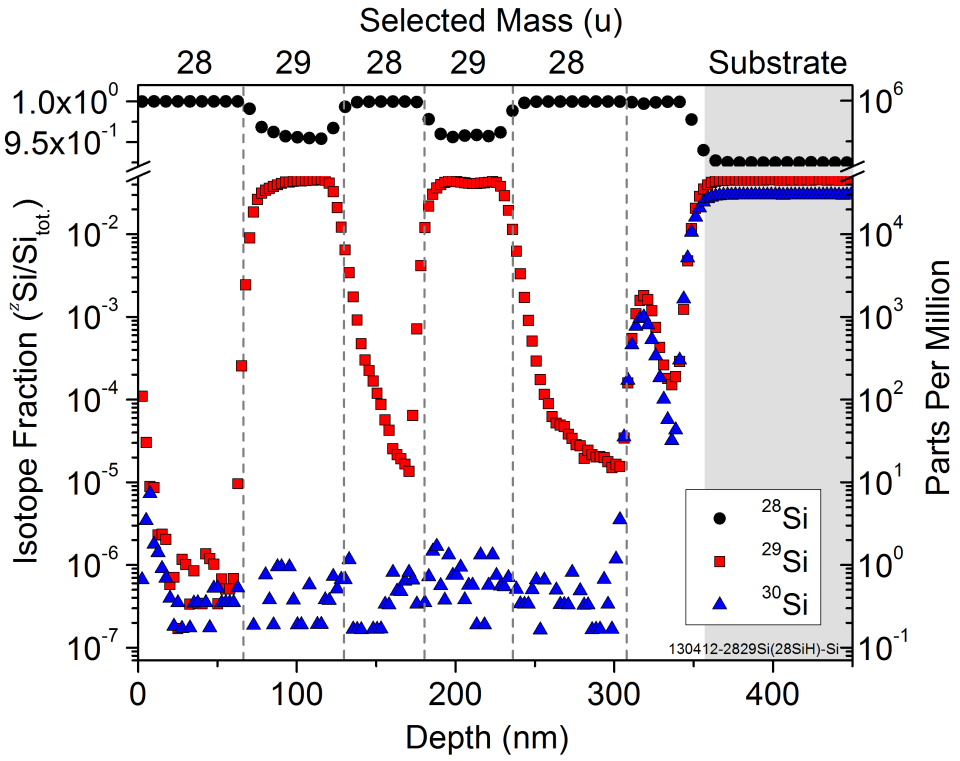

Figure 7.3: SIMS depth profile of a Si isotope heterostructure deposited at room temperature at LC–2. The isotope fractions are shown as a function of depth for ^{28}Si (circles), ^{29}Si (squares), and ^{30}Si (triangles) in an isotope heterostructure. The magnetic field of the sector mass analyzer was modulated to select 28 u or 29 u at different depths, as noted on the top axis of the figure. The ^{29}Si isotope fractions are seen to be roughly the natural abundance within the 29 u regions and much lower within the 28 u regions. The ^{29}Si tail in 28 u regions is a measurement artifact. The peak below a depth of 300 nm is due to ion beam tuning during the beginning of the deposition. At a depth of about 351 nm, the isotope fractions return to their natural abundance values, indicating the interface with the Si(100) substrate (shaded region).

29 u is similar to the ^{28}Si peak height, suggesting about 95 % of the 29 u peak is composed of ^{28}SiH, as previously discussed. The ^{29}Si concentration when depositing from the 29 u peak is then expected to be similar to the natural abundance value at roughly 5 %. No ^{30}Si is expected whether the analyzer is set to mass 28 u or 29 u.

SIMS was used to measure the isotope fractions of the isotope heterostructure. A SIMS depth profile of this sample is shown in Fig. 7.3. Isotope fractions of ^{28}Si

(circles), ^{29}Si (squares), and ^{30}Si (triangles) are shown as a function of sputter depth into the film. The ^{29}Si isotope fractions are seen to be roughly the natural abundance within the 29 u regions and much lower within the 28 u regions. The ^{29}Si tail in 28 u regions is a measurement artifact, and the true ^{29}Si isotope fractions in these regions is expected to be roughly 1×10^{-6} (1 ppm), as seen at a depth of 50 nm. The ^{30}Si isotope fraction remains below roughly 1×10^{-6} (1 ppm) throughout the entire film, as expected. The peak in ^{29}Si and ^{30}Si below a depth of 300 nm is due to ion beam tuning during the beginning of the deposition. At a depth of about 351 nm, the isotope fractions return to their natural abundance values, indicating the interface with the Si(100) substrate, which is marked by the shaded region.

The ability to switch between ^{28}Si and ^{29}Si can enable deposition of ^{28}Si samples with targeted enrichments, i.e. different isotopic concentrations of ^{29}Si. To produce a desired isotopic concentration of ^{29}Si in a sample, one could deposit ^{28}Si normally and then during deposition, mass select for the 29 u ion beam for the appropriate fraction of the total deposition time, taking into account the ^{28}SiH in the 29 u peak. A duty cycle would be chosen to ensure sufficient mixing of the two isotopes, depending on the deposition rate. Samples with specific enrichments ranging from natural abundance down to less than 1 ppm ^{29}Si isotopic concentrations would enable a measurement of T_2 as a function of ^{29}Si concentration for a wide range of enrichment values, as discussed in Chapter 1. These measurements would begin to address the question of "how good is good enough?" for the enrichment of ^{28}Si in a Si-based quantum computing architecture.

7.2.2 Enriched Si/Ge Deposition

Quantum wells in Si/SiGe heterostructures are a promising system for solid state quantum information. Although ^{28}Si has been used by several research groups to produce quantum coherent devices, including a ^{28}Si quantum well in SiGe [**?**], fully enriched Si/SiGe devices have not yet been demonstrated. Like ^{28}Si, ^{74}Ge has no net nuclear spin and is the most abundant of the Ge isotopes comprising approximately 37 % of natural abundance Ge. The critical isotope to be removed is ^{73}Ge, which does have a nuclear spin of $I = 9/2$ and a natural abundance of approximately 8 %.

The ability described previously to switch between different masses in the ion beam during deposition enables the growth of heterostructures from isotopic materials. This is achieved by cycling between the constituents of compound materials where both components are enriched, e.g. ^{28}Si/^{28}Si^{74}Ge. To produce Ge ions, Ge cathodes could be used in the solids-mode ion source designed for sputtering the cathode material. The source of Si could either be SiH_4 or a Si cathodes with Ar being used as the working gas.

Magnetic peak switching could then be used, as described previously, to control the relative concentrations of Si and Ge needed for SiGe deposition. A duty cycle would be chosen to ensure that the compound is sufficiently mixed during deposition to produced enriched ^{28}Si^{74}Ge. During deposition, a layer of pure ^{28}Si would be deposited as the quantum well layer followed by a capping layer of ^{28}Si^{74}Ge. Control gates would then need to be patterned on the top surface of the heterostructure.

7.2.3 ^{28}Si sublimation

In order to facilitate collaborations with other research groups interested in using enriched ^{28}Si to fabricate quantum coherent devices, a useful experimental technique would be thermal re-deposition of ^{28}Si from a deposited thin film onto a fabricated device as a capping layer. Quantum dot devices can benefit from not only having a ^{28}Si substrate, onto which the device is fabricated, but also a ^{28}Si cap to further isolate the qubit spins from ^{29}Si. A demonstration of the re-deposition of ^{28}Si was attempted in this work by heating a ^{28}Si thin film sample using the DH method of heating to approximately 1100 °C to cause sublimation of the ^{28}Si. Another Si(100) substrate with a thermal oxide surface layer was used as a deposition target. In order to attempt this transfer of ^{28}Si, the sublimation rate needed to be calibrated.

A calibration for three different sublimation temperatures was performed and is shown in Fig. 7.4. The measured sublimation rates (triangles) at approximately 1100 °C, 1150 °C, and 1200 °C were determined from ellipsometry measurements of the film thicknesses. Also shown are calculations for the expected sublimation rate based on the Si vapor pressure at different temperatures (line). Taking into account geometric factors of the deposition, a correction to the raw calculation was applied. The corrected calculation (dashed line) has values that are 25 % of the raw calculation and matches the measured rates well. The target substrate in the ^{28}Si sublimation test was measured by SIMS to detect the transferred ^{28}Si film. However, the presence of the thermal oxide and the fact that the film was very thin resulted

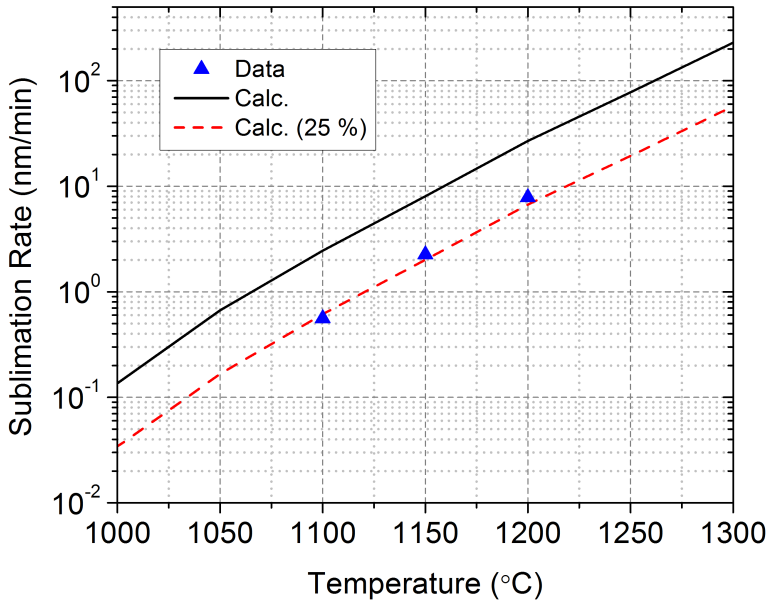

Figure 7.4: Si sublimation rates for a ^{28}Si chip and calculated values. Measured rates (triangles) at 1100 °C, 1150 °C, and 1200 °C are compared to calculations based on Si vapor pressures (line) and a modified calculation (dashed line) whose values are 25 % of the raw calculation to account for geometric factors of the deposition.

in a null measurement with no ^{28}Si being detected.

7.2.4 Al Dopant Devices with Hydrogen Lithography

STM hydrogen lithography is a promising technique for fabricating single atom ^{31}P dopant devices for quantum information. A STM probe is used to selectively remove H atoms from a H-terminated Si surface thus defining a lithographic pattern. This surface is then exposed to phosphene gas which incorporates into the bare Si within the pattern forming a single atom thick delta layer. Using this technique, conducting wires and quantum dot islands comprised of ^{31}P atoms, as well as single atom islands can be fabricated [5]. Instead of using ^{31}P, which is an electron donor, it may be interesting to use an acceptor atom to create quantum coherent devices based on the physics of hole transport. One candidate acceptor atom is Al. If Al

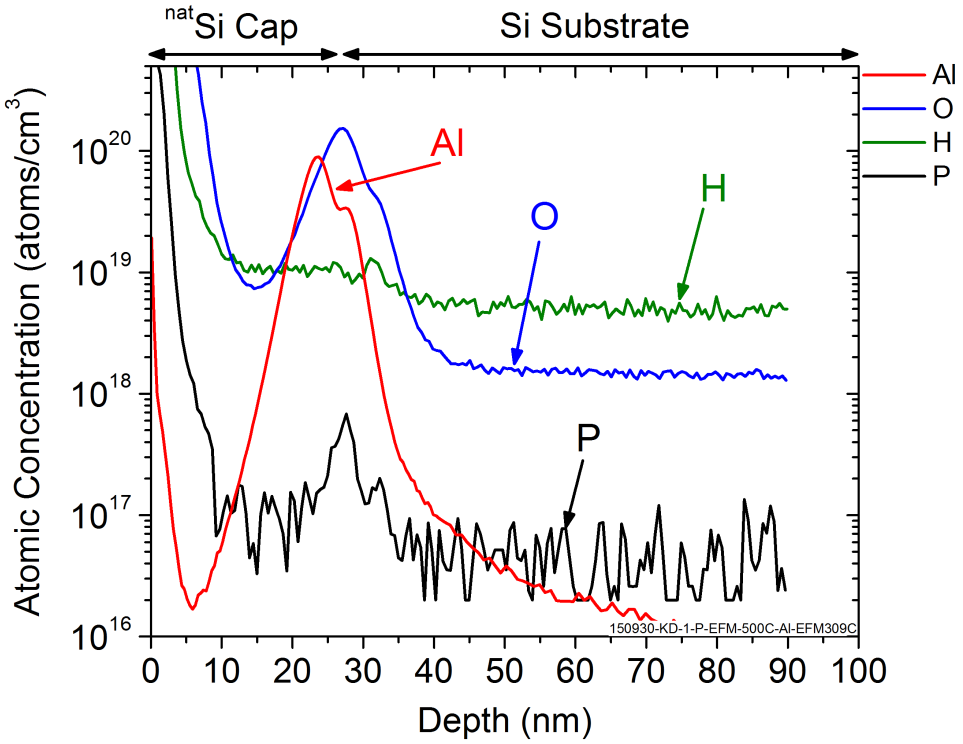

Figure 7.5: SIMS depth profile of an Al delta layer in Si showing atomic concentrations of Al, O, H, and P (lines) in the sample. Al is clearly concentrated in a layer roughly 25 nm below the surface. Above this depth is the ^{nat}Si capping layer and below it is the Si(100) substrate. The peak atomic concentration of Al is about 1×10^{20} cm^{-3}. The high concentration of O at the Al layer is likely due to outgassing of the Al thermal deposition source.

can be selectively deposited in a delta layer onto Si(100) with a H pattern, then an acceptor device may be possible.

To demonstrate the capability to deposit an Al delta layer, Al was deposited on a Si(100) substrate with a roughly monolayer coverage and then overgrown with natural abundance Si, ^{nat}Si, from the evaporation source. The composition of this sample was measured by SIMS in a depth profile, which is shown in Fig. 7.5. The atomic concentrations of Al, O, H, and P (lines) are shown vs. the sputter depth into the sample. One can see that there is a clear Al rich layer roughly 25 nm below the surface. This first 25 nm represents the ^{nat}Si capping layer. It is difficult to

determine from this measurement if the Al resides in a true delta layer, but the Al likely spread out to some extent, possibly due to heating the sample during ^{nat}Si deposition. Beyond 25 nm represents the Si(100) substrate. The peak atomic concentration of Al is approximately 1×10^{20} cm^{-3}, which is approximately 20 % of the nominal density of crystalline Si. A large concentration of O is also observed at the delta layer with a similar concentration as the Al, possibly due to the Al thermal deposition source outgassing. This successful demonstration producing a confined Al layer in Si is the first step towards patterned Al dopant devices defined by STM hydrogen lithography. Selectivity of Al atoms deposited in a H pattern would need to be tested further before production of a device.

7.2.5 Electrical Measurements and T_2 in ^{28}Si

Ultimately, the quality and usefulness of ^{28}Si material produced in this work to quantum information research will be determined by the T_2 time of spins within the material. Additionally, the electrical quality of the material is important for the operation of quantum coherent devices. Several types of devices can be used to test parameters related to the electrical quality including Schottky diodes, capacitors, and transistors in Hall and Van der Pauw measurement geometries. A cartoon schematic of a capacitor structure and measurement for a ^{28}Si sample is shown in Fig. 7.6. A ^{28}Si film is seen on top of a natural abundance Si substrate. An isolation gate oxide is grown from the ^{28}Si film and then an Al gate 300 nm thick is deposited on top of the oxide. Then, to perform measurements, a metal probe contacts the top gate while the substrate contacts metal on the back side of the sample, and

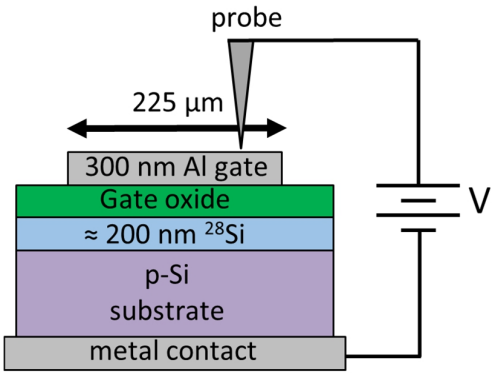

Figure 7.6: Cartoon schematic of a ^{28}Si capacitor. An isolating gate oxide is grown on a ^{28}Si film and an Al top gate is deposited on top of that, forming a capacitor. A voltage sweep can then be applied between a metal probe contacting the gate and a back metal contact behind the Si(100) wafer.

a voltage sweep is applied to perform a capacitance-voltage, C-V, measurement. This measurement can determine the interface trap density and free charge carrier density in the ^{28}Si oxide. Transistors can also be fabricated on ^{28}Si and used for measuring electron mobility and carrier type within the enriched film.

While the ^{28}Si films produced in this work typically do not comprise a large enough volume of ^{28}Si material to contain enough spins for traditional ESR measurements, other specialized measurements can be used to measure T_2 in these films. For a sample implanted with ^{31}P atoms, a small ESR probe can be fabricated onto the surface of a ^{28}Si thin film. Such a μm scale probe greatly increases the sensitivity of the measurement and can measure a much smaller number of spins, potentially as few as 10s of spins. A group led by Aharon Blank has tested this technique [40] and has already made test devices on ^{28}Si samples produced in this work. The primary impediment of these measurements at the moment is the concentrations of chemical contaminants within the ^{28}Si samples. The concentration of N spins in

these samples exceeds that of the implanted ^{31}P atoms, making a T_2 measurement impossible. Therefore, to enable these measurements, the purity of ^{28}Si samples must be improved and potentially can be by switching to a UHV compatible ion source and a high purity gas feed line.

Appendix A: Ion Source and Beamline: Additional Operating Parameters

This appendix gives additional operating parameters and analysis for the ion source and ion beamline. A circuit diagram and schematic of the lens elements of the beamline before the magnetic sector mass analyzer showing the relationship between the controlling power supplies and measured currents is shown in Fig. A.1. Operating parameter scans of the ion source and beamline using Ne in the gas mode ion source are shown in Fig. A.2. These give the ^{20}Ne ion current as a function of source magnetic field, gas flow, arc voltage, and extractor voltage. Finally, the operating parameters used for producing the most highly enriched ^{22}Ne, ^{12}C, and ^{28}Si samples are given in Tables A.1 to A.3, respectively.

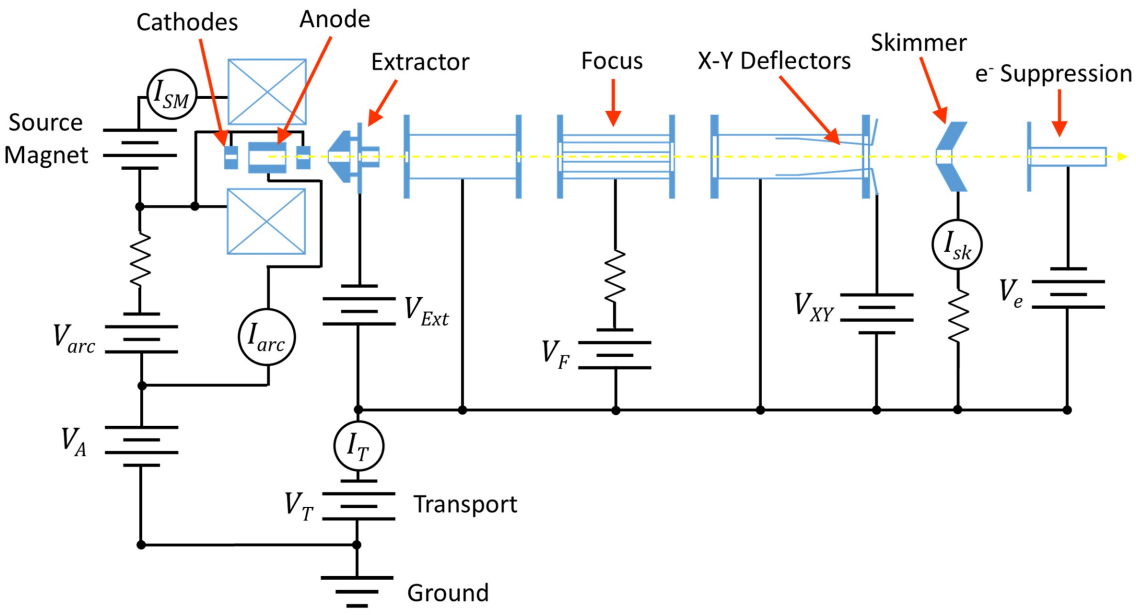

Figure A.1: Circuit diagram and schematic of the electrostatic lenses of the ion beamline before the magnetic sector mass analyzer. Elements of the ion source including the anode, cathodes and the source electromagnet coil are shown at the left. The lens elements that form the potential landscape of the ion beam, depicted from left to right, are the extractor, at negative voltage, V_{Ext}, a transport tube, at negative transport voltage, V_T, the focus, at negative voltage, V_F, another transport tube with X-Y deflectors biased positively with V_{XY}, the skimmer, and the electron suppressor, at negative voltage, V_e, which is set to a potential about 100 V more negative than V_T. V_{Ext}, V_F, V_{XY}, and V_e all float on top of V_T. V_A applies a positive voltage to the anode, and V_{arc} floats on top of the anode potential to apply a negative voltage to the cathodes. The source electromagnet drives current I_{SM} through the solenoid and it floats on top of V_{arc} due to the magnet housing not being well isolated from the cathode housing. I_{arc} is the measured current flowing between the anode and cathodes. All ion current that is neutralized on these lens elements or the vacuum chamber is recorded as I_T.

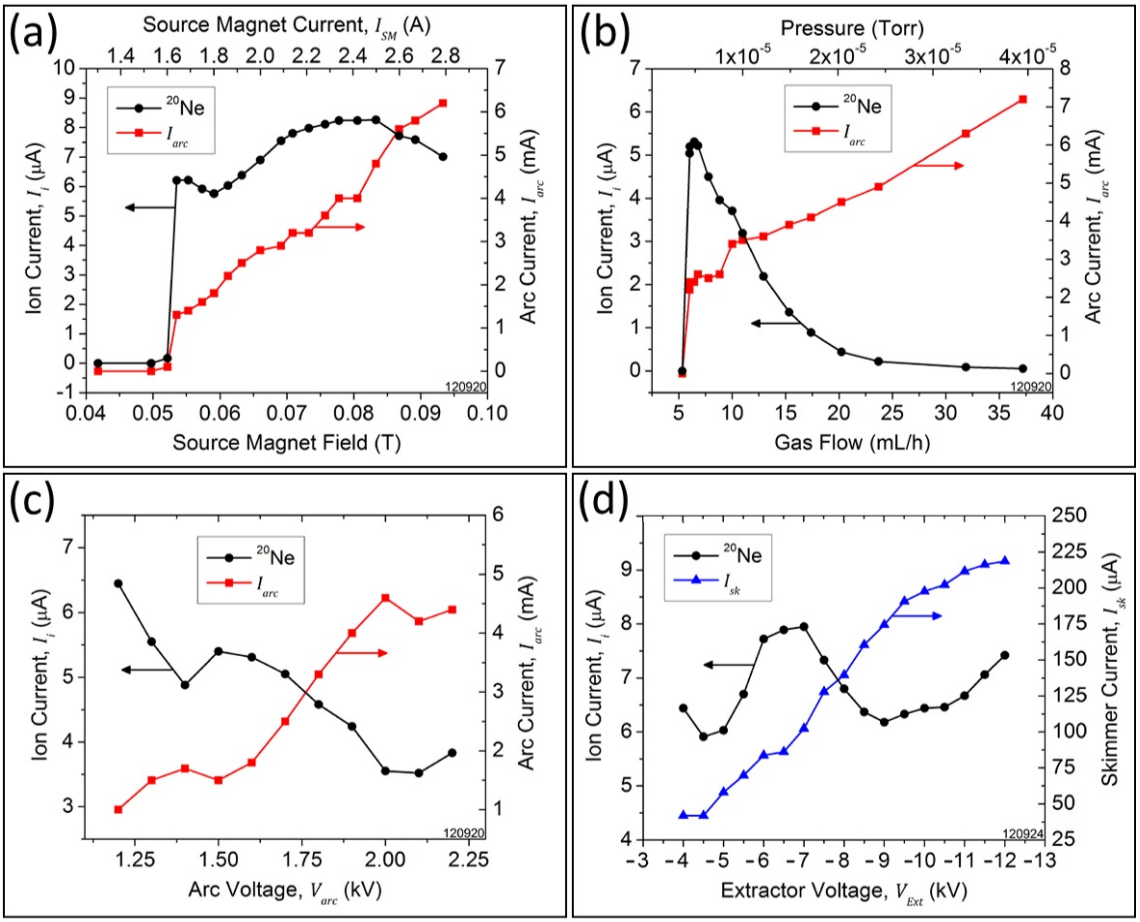

Figure A.2: Operating parameter scans of the gas mode ion source using Ne. (a) The ^{20}Ne ion current, I_i, and the arc current, I_{arc}, are shown as a function of the source magnet field. The corresponding current, I_{SM}, applied to the electromagnet is shown on the top axis. The plasma ignites above 0.05 T and two peaks are observed. (b) I_i and I_{arc} for ^{20}Ne are shown as a function of the Ne gas flow, with the corresponding pressure in the ion beam chamber displayed on the top axis. The highest ion current is observed at a flow of about 6 mL/h. (c) I_i and I_{arc} for ^{20}Ne are shown as a function of the arc voltage, V_{arc}. I_i and I_{arc} appear inversely related. (d) I_i and the ion current on the skimmer, Isk, for ^{20}Ne are shown as a function of the extractor voltage, V_{Ext}. I_i was optimized at each value of V_{arc} by tuning the other lens elements. A peak in I_i at about -6.5 kV is observed.

^{22}Ne Ion Beam Parameters
for 110504-22Ne-OxSi on 5/4/11

Source P (Pa)	V_A (V)	V_{arc} (V)	V_C (V)	V_T (kV)
1.0×10^{-2}	501	500	0	-4.006

Sample Bias (kV)	V_{Ext} (kV)	V_F (kV)	I_{SM} (A)	I_{arc} (mA)
-4.00	-7.0	-13.0	1.1	22

Table A.1: Ion source and beamline operating parameters for implanting ^{22}Ne sample 110504-22Ne-OxSi on 5/4/11 using the solids-mode ion source. This sample was the most highly enriched ^{22}Ne sample produced in this work. Ne was used as the working gas for this sample. V_A is the anode voltage, and V_{arc} is the arc voltage applied in reference to V_A to get the resulting cathode voltage, V_C. V_T is the transport voltage. A Si(100) substrate was biased negatively for implantation. V_{Ext} is the extractor voltage and V_F is the focus voltage. The ion source plasma is ignited by setting the source electromagnet current, I_{SM}, producing an arc current, I_{arc}.

^{12}C Ion Beam Parameters
for 120207-12C-OxSi on 2/7/12

Source P (Pa)	V_A (V)	V_{arc} (kV)	V_C (V)	V_T (kV)
3.1×10^{-3}	608	1.147	-539	-4.00

V_{Ext} (kV)	V_F (kV)	I_{SM} (A)	I_{arc} (mA)	I_{sk} (μA)
-7.50	-15.0	1.45	25	32

Table A.2: Ion source and beamline operating parameters for depositing ^{12}C sample 120207-12C-OxSi on 2/7/12 using the solids-mode ion source. This sample was the most highly enriched ^{12}C sample produced in this work. CO_2 was used as the working gas for this sample. V_A is the anode voltage, and V_{arc} is the arc voltage applied in reference to V_A to get the resulting cathode voltage, V_C. V_T is the transport voltage. V_{Ext} is the extractor voltage and V_F is the focus voltage. The ion source plasma is ignited by setting the source electromagnet current, I_{SM}, producing an arc current, I_{arc}. I_{sk} is the ion current measured on the skimmer.

^{28}Si Ion Beam Parameters
for 151210-KD-7-i-28Si-500C on 12/18/15

Source P (Pa)	V_A (V)	V_{arc} (kV)	V_C (kV)	V_T (kV)
2.1×10^{-4}	50	3.420	-3.370	-4.00

V_{Ext} (kV)	V_F (kV)	I_{SM} (A)	I_{arc} (mA)	I_T (mA)	I_{sk} (μA)
-11.0	-12.5	1.69	0.7	0.6	190

Deceleration Lenses

A2 (kV)	A3 (kV)	B2 (kV)	B3 (kV)	B4 (kV)	X (V)
-2.50	-0.49	-3.04	-0.70	-1.34	-14

Table A.3: Ion source and beamline operating parameters for depositing ^{28}Si sample 151210-KD-7-i-28Si-500C on 12/18/15 using the gas-mode ion source. This sample was the most highly enriched ^{28}Si sample produced in this work. SiH_4 was used as the working gas for this sample. V_A is the anode voltage, and V_{arc} is the arc voltage applied in reference to V_A to get the resulting cathode voltage, V_C. V_T is the transport voltage. V_{Ext} is the extractor voltage and V_F is the focus voltage. The ion source plasma is ignited by setting the source electromagnet current, I_{SM}, producing an arc current, I_{arc}. I_T is the ion current measured on the transport voltage line, and I_{sk} is the ion current measured on the skimmer. A2, A3, B2, B3, B4, and X refer to deceleration lens elements.

Appendix B: Experimental Apparatus Photographs

This appendix shows photographs of various experimental apparatus used for producing enriched samples in this work including the hyperthermal energy ion beam deposition system as a whole, the gas manifold, the two ion sources, the electrostatic and magnetic lens elements comprising the beamline, the three mass-selecting apertures, a gas aperture, experimental setups and sample stages for samples produced at IC–1 in the ion beam chamber, LC–2 in the deceleration lens chamber, and DC–3 in the deposition chamber, and finally the sample apertures used for monitoring the ion beam current.

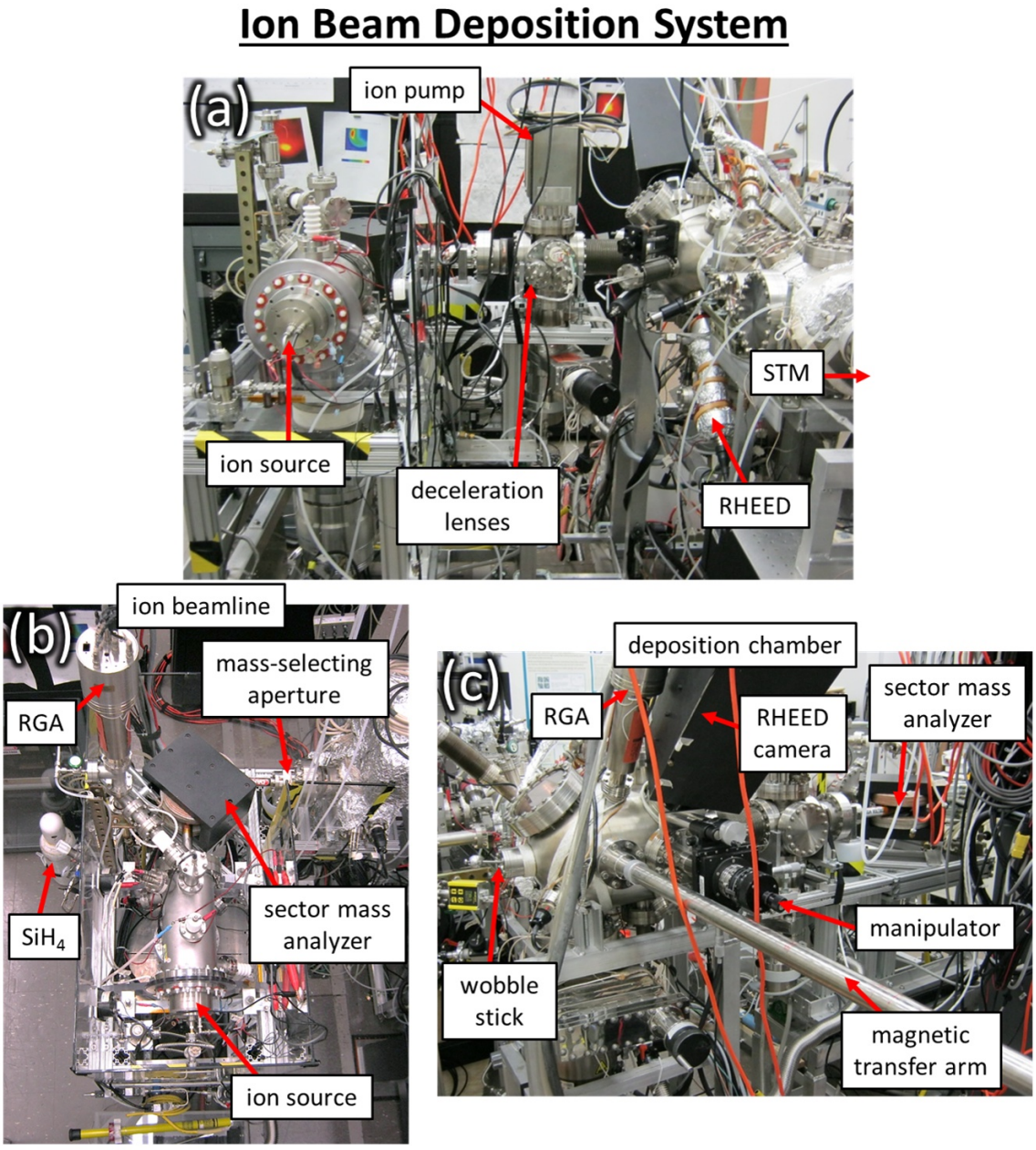

Figure B.1: Photographs of the ion beam deposition system (a) Side view of the ion beamline and deposition system. (b) Top-down view of the ion beamline. (c) Side view of the deposition and analysis chamber showing the manipulator where samples are located at DC–3.

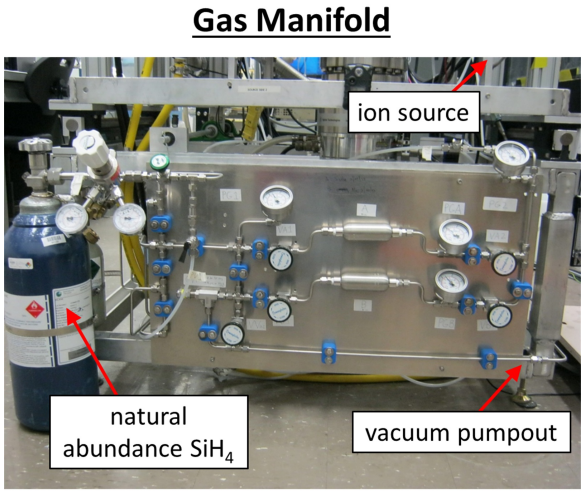

Figure B.2: Photograph of the gas manifold. The natural abundance SiH_4 gas source used for depositing ^{28}Si is connected at the left. The manifold contains two gas reservoir tanks in the middle and a vacuum pumpout at the bottom. The manifold connects to the ion source inlet out of view at the top right.

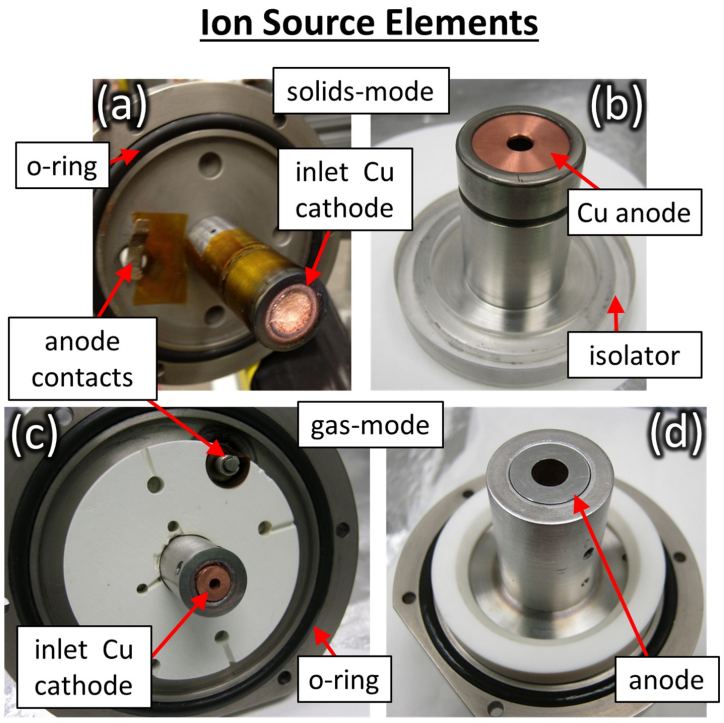

Figure B.3: Photographs of the ion source elements. (a) Inlet cathode housing of the solids- mode ion source with a Cu cathode. (b) Anode housing of the solids-mode ion source with a Cu anode disk. This housing fits over the cathode in (a). (c) Inlet cathode housing of the gas-mode ion source with a Cu cathode. (d) Anode housing of the gas-mode ion source with a cylindrical steel anode. The anode housing is seen fitted over the cathode in (c).

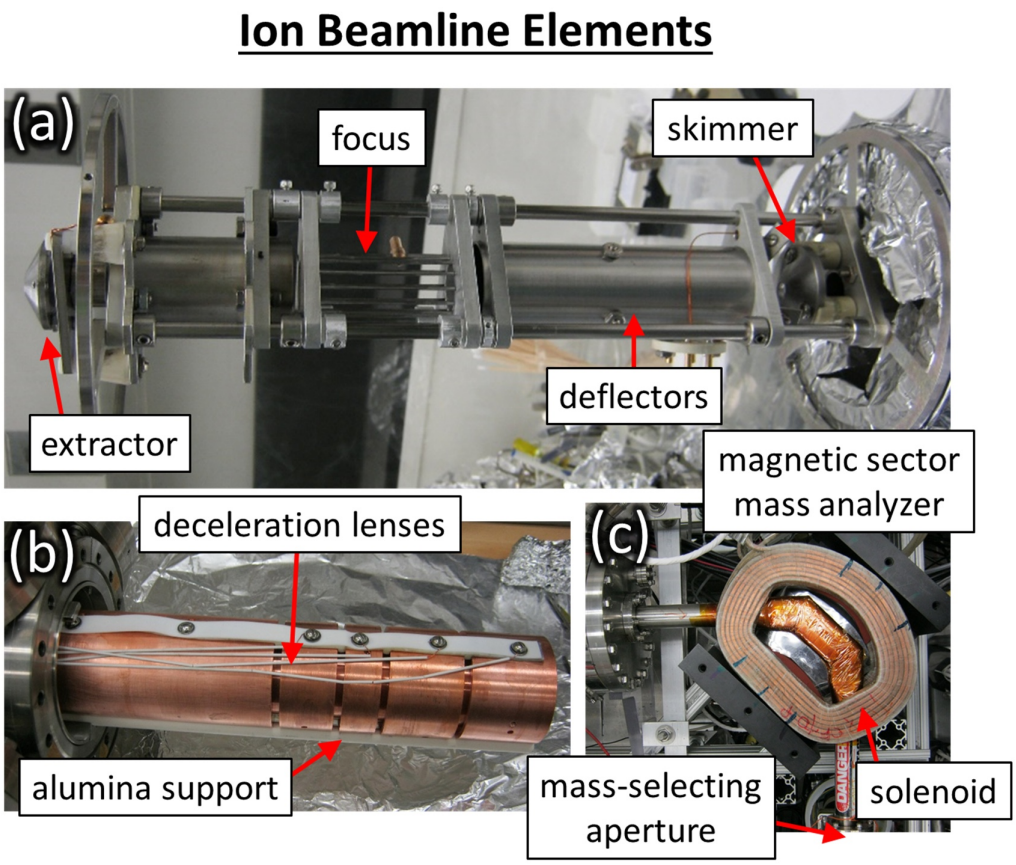

Figure B.4: Ion beamline electrostatic elements and magnetic sector mass analyzer. (a) The electrostatic elements used to generate an ion beam from the source are seen with the extractor at the left, focus and X-Y deflectors in the middle, and skimmer at the right. These reside between the ion source and the mass analyzer. (b) Deceleration lenses after the mass analyzer focus ions onto the sample are seen with alumina support rods and a teflon separator on top. (c) The bottom pole piece and solenoid of the magnetic sector mass analyzer is seen with the entrance from the beamline at the left and the exit leading to the mass-selecting aperture at the bottom. There is a 90° bend in the vacuum pipe of the beamline.

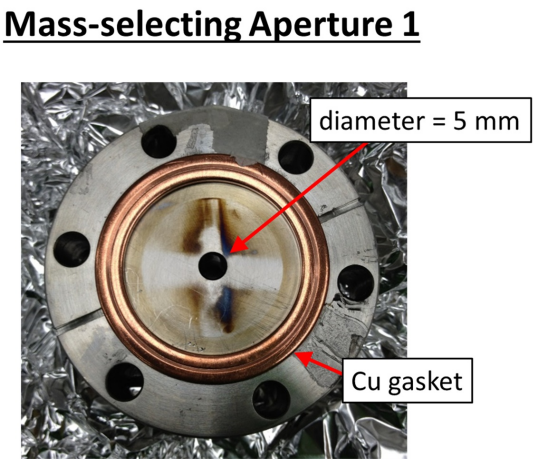

Figure B.5: Photograph of the mass-selecting aperture used for ^{22}Ne and ^{12}C samples. The aperture consists of a 5 mm diameter hole in a standard 2.75 in size (69.85 mm vacuum flange spacer 16 mm thick.

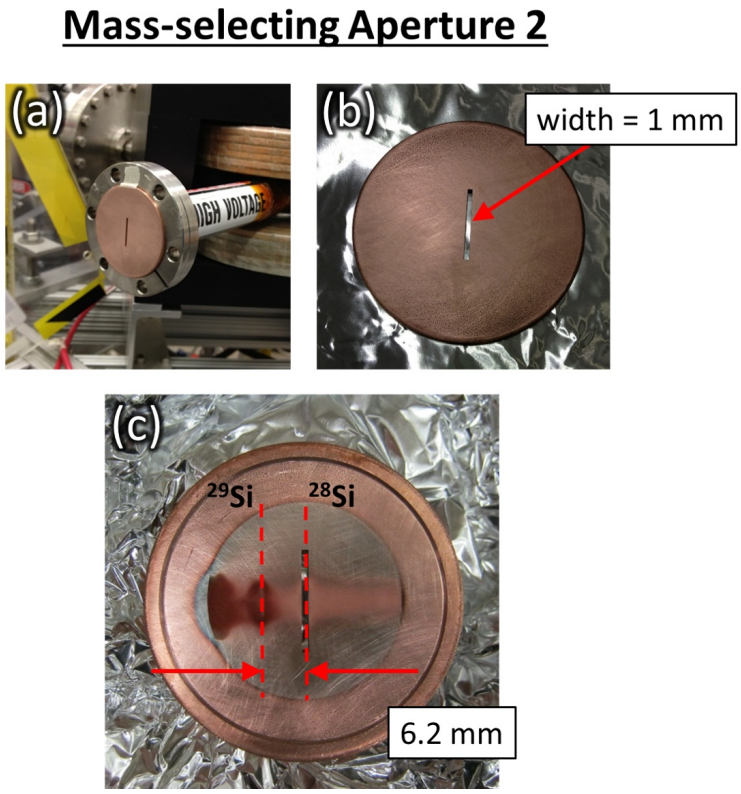

Figure B.6: Photographs of the mass-selecting aperture used for ^{28}Si samples at IC–1 and LC–2. The aperture consists of a 1 mm wide slit that is 15.25 mm tall and 2 mm thick in a Cu gasket. (a) A new aperture is seen at the exit of the magnetic mass selecting magnet. (b) Closeup of a new aperture. (c) A used aperture had dark deposited spots from the 30 u (far left of the aperture) and 29 u (left of the aperture) ion beams. The separation between the ^{28}Si beam centered on the aperture and the ^{29}Si beam is about 6.2 mm.

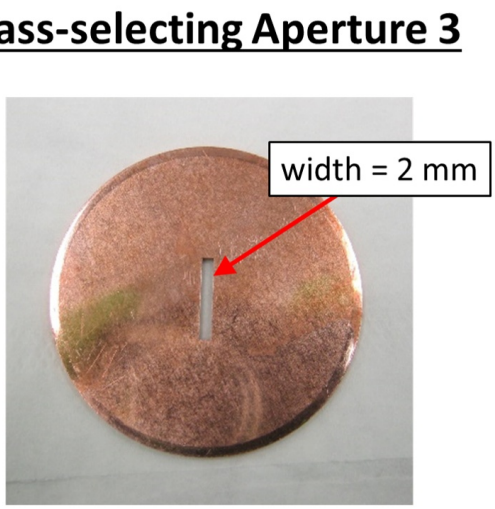

Figure B.7: Photograph of the mass-selecting aperture used for ^{28}Si samples at DC–3. The aperture consists of a 2 mm wide slit that is 12 mm tall with a beveled edge in a Cu gasket. The beveled edge is on the back side with the side shown facing the ion beam.

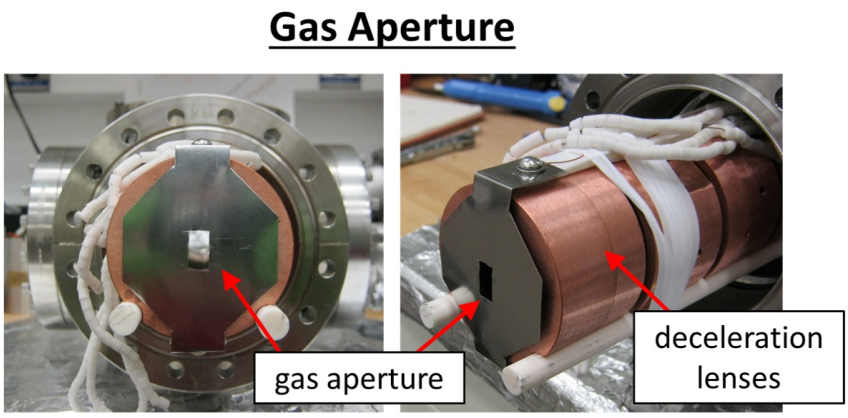

Figure B.8: Photograph of a gas aperture on the inlet to the deceleration lenes in the ion beam. The aperture consists of a 12.7 mm by 6.4 mm rectangular opening in a stainless steel shim. The purpose of this gas aperture is to direct gas diffusing from the ion beam chamber around the lenses to then be pumped away.

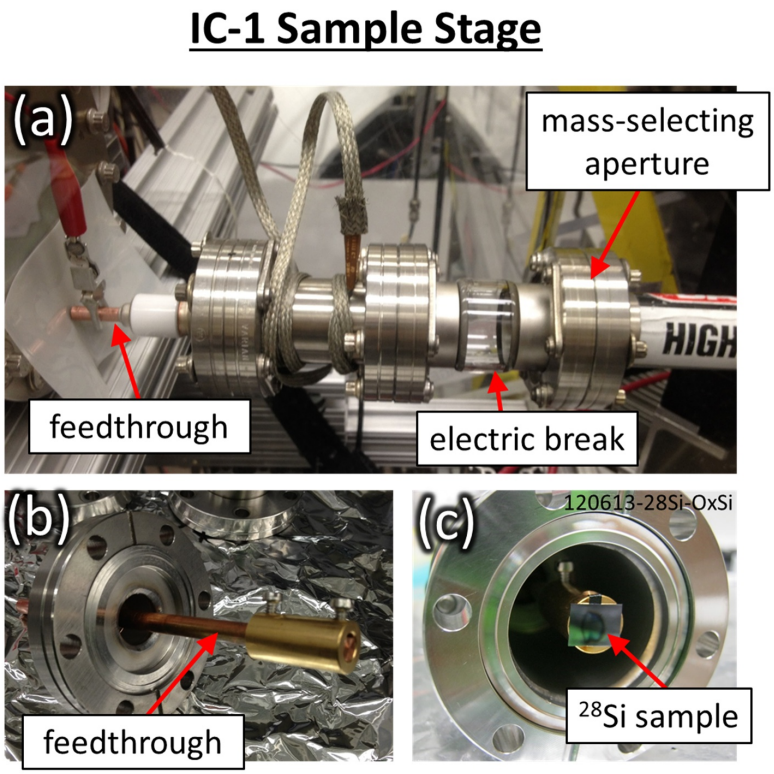

Figure B.9: Photographs of the experimental setup and sample stage for ^{28}Si samples deposited at IC–1 in the ion beam chamber. (a) An electrical vacuum feedthrough at the left serves as a sample stage and is connected to an electric break at the exit of the magnetic sector mass analyzer. (b) The feedthrough flange is seen. (c) A ^{28}Si sample is mounted on the end of the feedthrough using carbon tape.

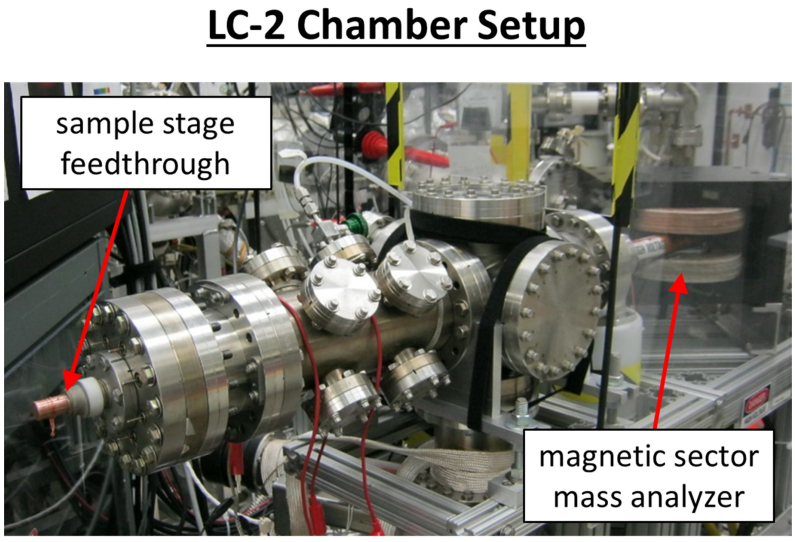

Figure B.10: Photograph of the experimental setup of the deceleration lens chamber for samples produced at LC–2. The ion beam enters the lens chamber from the right. An electrical vacuum feedthrough serves as a sample stage at the right.

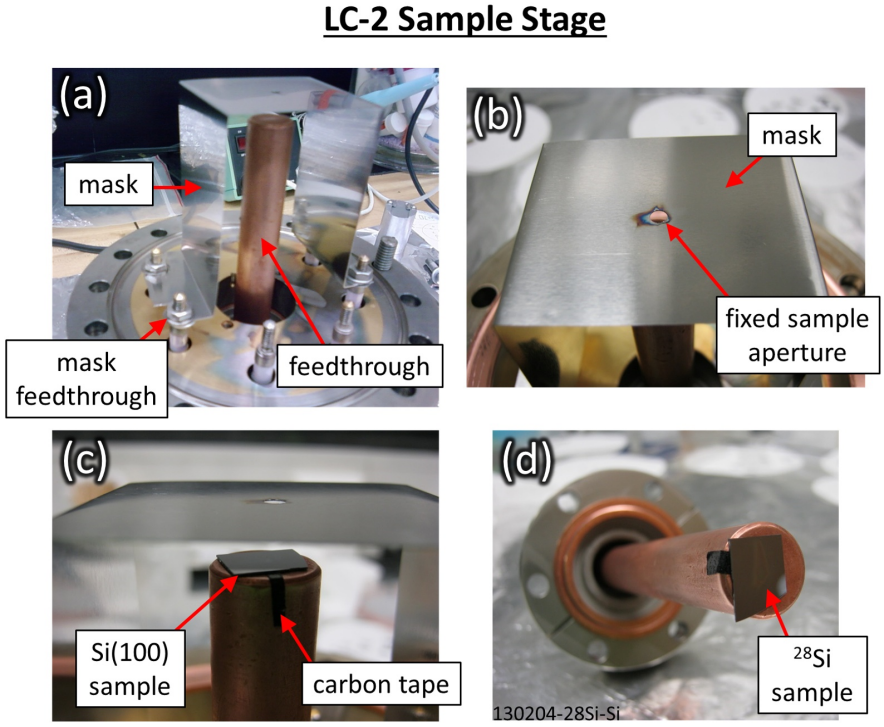

Figure B.11: Photographs of the sample stage for producing sample at LC–2. (a) The sample stage flange with Cu electrical vacuum feedthrough for mounting samples is seen in the middle. Additional electrical feedthroughs are seen to the left and right connected to the fixed sample aperture in the metal mask. (b) A stainless steel shim makes up the mask that covers the sample on the feedthrough. The fixed sample aperture consists of a hole about 3 mm in diameter centered over the feedthrough. (c) A Si(100) substrate is seen mounted on the end of the feedthrough using carbon tape. (d) The Cu feedthrough is separated from the rest of the sample stage with a ^{28}Si sample mounted on the end.

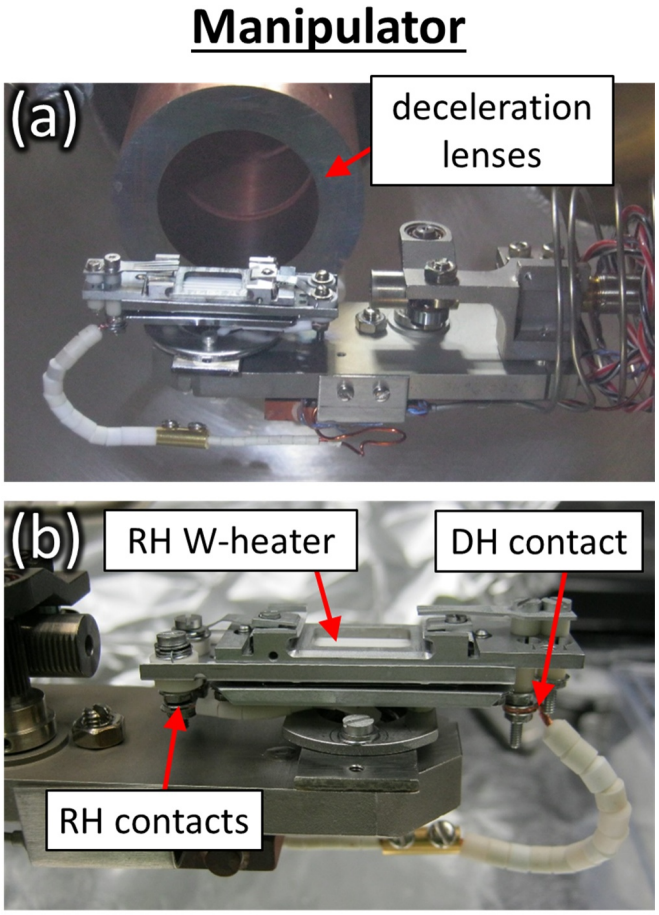

Figure B.12: Photographs of the manipulator used for heating substates and samples and depositing ^{28}Si samples at DC–3 in the deposition chamber. (a) The manipulator with the sample stage is seen in the deposition chamber with the ion beam deceleration lenses behind it. (b) A closeup of the sample stage outside of the chamber with the RH contacts visible at the left, the RH tungsten wire heater in the middle below where the sample sits, and the DH contact visible at the right.

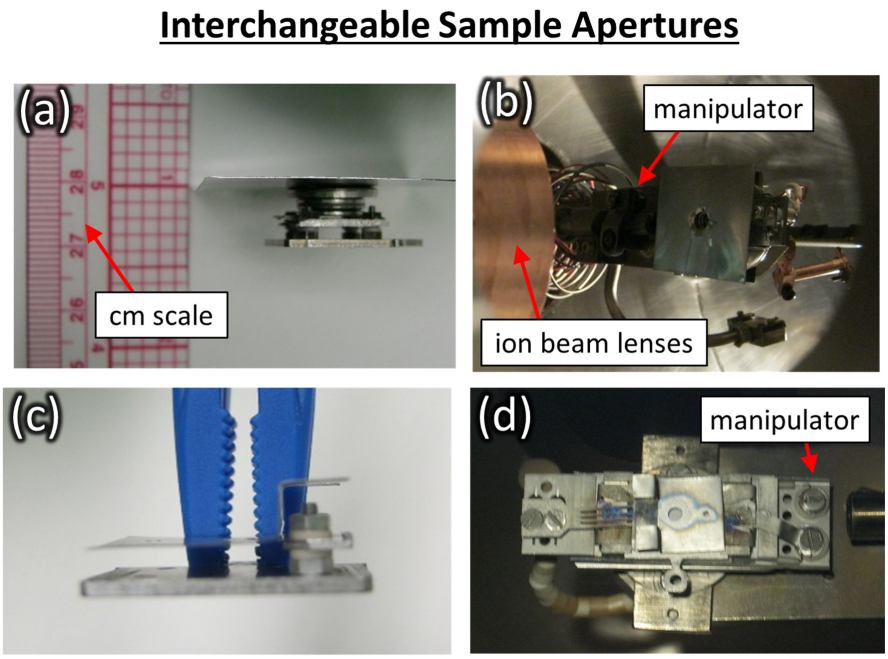

Figure B.13: Photographs of interchangeable sample apertures used to measure ion beam currents prior to depositing ^{28}Si samples at DC–3. (a) The side view of an initial sample aperture consisting of a 2.2 mm diameter hole in a stainless steel shim mounted on a sample holder. (b) The aperture in (a) sits on the manipulator and faces the ion beamline to measure ion current. (c) The side view of a later sample aperture consisting of a 2.5 mm diameter hole, and a 1 mm diameter hole in a Mo shim mounted on a sample holder. (d) The aperture in (c) sits on the manipulator to measure ion current. The 2.5 mm diameter aperture is at the center of the shim and the 1 mm diameter aperture is offset to the right. Both apertures are electrically isolated from the sample holders and connect to the DH contact.

Appendix C: Substrate Catalog

The table shown here gives the specifications and source of the various substrates used for producing enriched samples in this work.

#	Material	Dopant	ρ ($\Omega \cdot$ cm)	Thickness (μm)	Supplier	Identifier
(1)	Si(100)			200*		lightly doped
(2)	Ag			25	Kurt J. Lesker Company	Pure Al Foil
(3)	Si(100)	boron	1 to 10	380	University Wafer	Prime lot 12/0604
(4)	Si(100) SOI	boron	10 to 30	0.035†	Dr. Neil Zimmerman (NIST)	NIST-2
(5)	Si(100)	phosphorous	5 to 10	600	Dr. Mike Stewart (NIST)	55 nm thermal Ox
(6)	Si(100)	phosphorous	1 to 5	300	University Wafer	20141231-12
(7)	Si(100)	boron	7 to 20	340	University Wafer	4/15/15
(8)	Si(100)	undoped (intrinsic)	2×10^4	380	University Wafer	FZ SEMI Prime L849
(9)	Si(100)	boron	5 to 10	300	ITME	3611/110057
(10)	Si(100)	phosphorous	7 to 20	300	Virginia Semiconductor	$\pm$ 0.05° 15-10973

Table C.1: Substrate catalog for substrates used for depositing enriched films. Substrate numbers are referenced in the sample catalogs. *The wafer thickness of substrate (1) is an estimate. †The thickness of substrate (4) is the thickness of the Si device layer in the SOI stack. This SOI wafer also possessed a 400 nm buried oxide layer. A 55 nm thermal oxide was grown on the surface of the wafer for substrate (5). The wafer for substrate (10) was specified to have a miscut tolerance of $\pm$ 0.05° with the {100} surface.

Appendix D: Sample Catalogs

The sample catalogs presented here list all of the enriched samples produced in this work and are organized several ways. The ^{22}Ne sample implantation parameters and measured enrichments are summarized in Table D.1. The ^{12}C sample deposition parameters and measured enrichments are summarized in Table D.2. ^{28}Si samples are organized by their deposition location, IC–1, the ion beam chamber, LC–2, the deceleration lens chamber, and DC–3, the deposition and analysis chamber. ^{28}Si sample deposition parameters for samples deposited at IC–1 are summarized in Table D.3. ^{28}Si sample deposition parameters for samples deposited at LC–2 are summarized in Tables D.4 and D.5. Finally, the ^{28}Si sample deposition parameters for samples deposited at DC–3 are summarized in Tables D.6 to D.9. Enrichment measurements and parameters used in the modeling analysis discussed in Chapter 6 are presented for ^{28}Si samples deposited at room temperature in Tables D.10 and D.11. Similarly, the enrichment measurements and modeling parameters for samples deposited with elevated temperatures are presented in Tables D.12 and D.13.

#	Sample Name	Load Date	Dep. Date	Substrate Type	Aperture (mm)	Base P (Pa)	Implant P (Pa)	V_A (V)	V_T (kV)	E_i (eV)
1	110301-22Ne-OxSi	2/28/11	3/1/11	Si(100):Ox (1)	5	1.1×10^{-5}		404	-3.885	≈ 3000
2	110418-22Ne-OxSi	3/1/11	4/18/11	Si(100):Ox (1)	5	7.6×10^{-7}	3.3×10^{-5}	500	-4.002	4460
3	110504-22Ne-OxSi	4/28/11	5/4/11	Si(100):Ox (1)	5	3.1×10^{-6}		501	-4.006	4460

#	Sample Name	I_i (μA)	Ion Dose (cm^{-2})	Spot Size (mm^2)	Implant (nm)	Primary Measurement	Isotope Fraction (^{z}Ne/Ne$_{tot.}$) ^{22}Ne (%)	^{20}Ne (%)
1	110301-22Ne-OxSi	0.14*	7.7×10^{16}*	2*	9	SIMS	88.4(10)	15.2(10)
2	110418-22Ne-OxSi	0.14*	7.7×10^{16}*	5*	12.5			
3	110504-22Ne-OxSi	0.14	7.7×10^{16}	2*	12.5	SIMS	99.455(36)	0.545(36)

Table D.1: ^{22}Ne Sample Catalog (3/1/11–5/4/11). ^{22}Ne samples were implanted at room temperature ($\approx$ 21 °C) using Ne in the solids-mode ion source at LC–2, the deceleration lens chamber. Substrates had a native oxide and were not prepared *ex situ* or *in situ*. Aperture gives the diameter of the circular mass-selecting aperture. Pressures are raw reading of the lens chamber base and with the ion source on. V_A is the anode voltage and V_T is the transport voltage. E_i is the average ion energy at the sample, and I_i is the average ion current. Implant refers to the peak implantation depth. Isotope fraction measurements assume no ^{21}Ne is present. Items marked with * are estimates.

#	Sample Name	Load Date	Dep. Date	Substrate Type	Aperture (mm)	Base P (Pa)	Dep. P (Pa)	V_A (V)	V_T (kV)	E_i (eV)	I_i (μA)
1	120125-12C-OxSi	1/24/12	1/25/12	Si(100):Ox (1)	5	4.4×10^{-6}		596	-4.00	543	0.55
2	120206-12C-OxSi	2/1/12	2/6/12	Si(100):Ox (1)	5			608	-4.00	554	0.40
3	120207-12C-OxSi	2/6/12	2/7/12	Si(100):Ox (1)	5	1.7×10^{-6}	2.1×10^{-5}	608	-4.00	554	0.70

#	Sample Name	C. I. (C)	Ion Dose (cm^{-2})	Spot Size (mm^2)	R (nm/min)	d (nm)	Film Mass (μg)	Primary Measurement(s)	Isotope Fraction ($^z C/C_{tot.}$) ^{12}C (%)	^{13}C (ppm)
1	120125-12C-OxSi	0.01	2.7×10^{18}	2.3	0.68*	206*	0.95	SIMS	99.996107(88)	38.93(88)
2	120206-12C-OxSi	0.00012	4.7×10^{16}	1.6	0.77*	4*	0.01	SEM		
3	120207-12C-OxSi	0.00555	2.9×10^{18}	1.2	0.76	100	0.52	SIMS, SEM	99.99608(13)	39.2(13)

Table D.2: ^{12}C Sample Catalog (1/25/12–2/7/12). ^{12}C samples were deposited at room temperature ($\approx$ 21 °C) using CO_2 in the solids-mode ion source at LC–2, the deceleration lens chamber. Substrates had a native oxide and were not prepared *ex situ* or *in situ*. Aperture gives the diameter of the circular mass-selecting aperture. Pressures are raw reading of the lens chamber base with the ion source on. V_A is the anode voltage and V_T is the transport voltage. E_i is the average ion energy at the sample, and I_i is the average ion current. C. I. is the ion current integral. R is the deposition rate, and d is the film thickness. Isotope fraction measurements of sample #1 were not corrected for instrumental error. Items marked with * are estimates.

#	Sample Name	Load Date	Dep. Date	Substrate Type	Aperture (mm)	Base P (Pa)	Dep. P (Pa)	V_A (V)	V_T (kV)
1	120604-28Si-OxSi	6/1/12	6/4/12	Si(100):Ox (1)	1	6.5×10^{-6}	1.6×10^{-4}	514	-4.00
2	120613-28Si-OxSi	6/4/12	6/13/12	Si(100):Ox (1)	1	1.2×10^{-5}	1.7×10^{-4}	106	-4.315
3	120618-28Si-OxSi	6/14/12	6/18/12	Si(100):Ox (1)	1	1.3×10^{-5}	2.3×10^{-4}	106	-4.314
4	120627-28Si-Ag	6/19/12	6/27/12	Ag foil (2)	1	1.3×10^{-5}	2.1×10^{-4}	106	-4.312
5	120628-28Si-OxSi	6/27/12	6/28/12	Si(100):Ox (1)	1	1.3×10^{-5}	1.8×10^{-4}	106	-4.311

#	Sample Name	E_i (eV)	I_i (μA)	C. I. (C)	Ion Dose (cm^{-2})	Spot Size (mm^2)	R (nm/min)	d (nm)	Film Mass (μg)	Primary Measurement
1	120604-28Si-OxSi	455	0.95	0.0102	3.4×10^{17}	19	0.07	12	1.36	SIMS
2	120613-28Si-OxSi	64	1.10	0.0136	3.2×10^{17}	27	0.42	86	3.63	SEM
3	120618-28Si-OxSi	64	0.77	0.0114	4.8×10^{17}	15	0.40	92	3.04	TOF-SIMS
4	120627-28Si-Ag	64	0.95	0.0109	2.5×10^{17}	27	0.24*	46*	2.90	
5	120628-28Si-OxSi	64	0.85	0.0075	2.9×10^{17}	16	0.59	86	1.98	SIMS

Table D.3: ^{28}Si Sample Catalog: IC–1 (6/4/12–6/28/12). ^{28}Si samples were deposited at room temperature ($\approx$ 21 °C) using SiH_4 with the low pressure mode of the gas-mode ion source at IC–1, the ion beam chamber. Substrates had a native oxide and were not prepared *ex situ* or *in situ*. Aperture gives the width of the mass-selecting aperture slit. Pressures are raw reading of the ion beam chamber base and with the ion source on. V_A is the anode voltage and V_T is the transport voltage. E_i is the average ion energy at the sample, and I_i is the average ion current. C. I. is the ion current integral. R is the deposition rate, and d is the film thickness. Thicknesses and rates correspond to the thickest measured film area. Items marked with * are estimates.

#	Sample Name	Load Date	Dep. Date	Substrate Type	Substrate Prep. (*ex situ*)	Aperture (mm)	Base P (Pa)	Dep. P (Pa)	V_A (V)
6	130204-28Si-Si	2/1/13	2/4/13	Si(100) (1)	HF etch	1	3.2×10^{-7}	5.9×10^{-6}	100
6a	151109-KD-2-P-Ox-28SiSub	11/9/15	1/1/16	Si(100):P:Ox (5)			2.3×10^{-8}	2.7×10^{-7}	
7	130206-28Si-Si	2/5/13	2/6/13	Si(100) (1)	HF etch	1	7.5×10^{-7}	7.2×10^{-6}	113
8	130208-28Si-Si	2/7/13	2/8/13	Si(100) (1)	HF etch	1	1.3×10^{-6}	6.1×10^{-6}	150
9	130213-28Si-Si	2/11/13	2/13/13	Si(100) (1)	HF etch	1	4.5×10^{-7}	6.4×10^{-6}	100
10	130215-28Si-Si	2/14/13	2/15/13	Si(100) (1)	HF etch	1	7.6×10^{-7}	4.8×10^{-6}	150
11	130221-28Si-Si	2/19/13	2/21/13	Si(100) (1)	HF etch	1	3.7×10^{-7}	4.9×10^{-6}	150
12	130227-28Si-Si	2/22/13	2/27/13	Si(100) (1)	HF etch	1	2.0×10^{-7}	5.7×10^{-6}	100
13	130304-28Si-Si	3/1/13	3/4/13	Si(100) (1)	HF etch	1	6.7×10^{-7}	6.0×10^{-6}	300

#	Sample Name	V_T (kV)	E_i (eV)	I_i (μA)	C. I. (C)	Ion Dose (cm^{-2})	Spot Size (mm^2)	R (nm/min)	d (nm)	Film Mass (μg)	Primary Measurement
6	130204-28Si-Si	-4.000	74	0.57	0.0067	2.6×10^{17}	16	0.56	110	1.76	SIMS
6a	151109-KD-2-P-Ox-28SiSub						22	0.56	50		SIMS
7	130206-28Si-Si	-3.941	86	0.50			8	0.40*	80*		
8	130208-28Si-Si	-4.000	121	0.56	0.0081	7.6×10^{17}	7	1.49	384	1.96	SIMS
9	130213-28Si-Si	-4.000	76	0.36	0.0046	2.9×10^{17}	10	0.17	37	1.20	TEM
10	130215-28Si-Si	-3.997	122	0.36	0.0058	4.0×10^{17}	9	0.25*	67*	1.38	XPS
11	130221-28Si-Si	-4.000	124	0.26	0.0035	3.1×10^{17}	7	0.23*	51*	0.83	SEM
12	130227-28Si-Si	-3.998	74	0.5*	0.0021	5.4×10^{17}	2	1.41*	97*	0.54	
13	130304-28Si-Si	-4.000	160	0.65	0.0054	6.0×10^{17}	6	0.67	92*	1.20	SEM

Table D.4: ^{28}Si Sample Catalog: LC–2: I (2/4/13–3/4/13). ^{28}Si samples were deposited at room temperature ($\approx$ 21 °C) using SiH_4 with the low pressure mode of the gas-mode ion source at LC–2, the deceleration lens chamber. Substrates were etched with HF *ex situ* but not prepared *in situ*. Aperture gives the width of the mass-selecting aperture slit. Pressures are raw reading of the lens chamber base and with the ion source on. V_A is the anode voltage and V_T is the transport voltage. E_i is the average ion energy at the sample, and I_i is the average ion current. C. I. is the ion current integral. R is the deposition rate, and d is the film thickness. Thicknesses and rates correspond to the thickest measured film area. Items marked with * are estimates. Sample #6a was deposited at DC–3 by sublimating sample #6 at about 1100 °C.

#	Sample Name	Load Date	Dep. Date	Substrate Type	Substrate Prep. (*ex situ*)	Aperture (mm)	Base P (Pa)	Dep. P (Pa)	V_A (V)
14	130307-28Si-OxSi	3/4/13	3/7/13	Si(100) (1)	HF etch	1	2.4×10^{-7}	4.0×10^{-6}	325*
15	130311-28Si-Si	3/8/13	3/11/13	Si(100) (1)	HF etch	1	2.5×10^{-7}	5.5×10^{-6}	325*
16	130328-28Si(dP)-Si	3/25/13	3/28/13	Si(100) (1)	HF etch	1	2.3×10^{-7}	3.7×10^{-6} (low) 1.9×10^{-4} (high)	142*
17	130404-28Si(dP)-Si	4/1/13	4/4/13	Si(100) (1)	HF etch	1	2.4×10^{-7}	3.9×10^{-6} (low) 3.1×10^{-4} (high)	130*
18	130412-2829Si(28SiH)-Si	4/8/13	4/12/13	Si(100):B (3)	HF etch	1	1.9×10^{-7}	3.6×10^{-6}	116
19	130520-28Si-SOI	4/15/13	5/20/13	Si(100) SOI (4)	HF etch	1	1.1×10^{-7}	3.7×10^{-6}	229
20	130920-28Si(dP)-SOI	8/2/13	9/20/13	Si(100) SOI (4)	HF etch	1	3.6×10^{-8}	5.1×10^{-6} (low) 5.3×10^{-5} (high)	100
21	130924-28Si-Si-550C	9/23/13	9/24/13	Si(100):B (3)	HF etch	1	1.1×10^{-6}	2.1×10^{-5}	200

#	Sample Name	V_T (kV)	E_i (eV)	I_i (μA)	C. I. (C)	Ion Dose (cm^{-2})	Spot Size (mm^2)	R (nm/min)	d (nm)	Film Mass (μg)	Primary Measurement
14	130307-28Si-OxSi	-4.000	230*	0.54	0.0089	6.0×10^{17}	9	1.52	415	1.94	SEM
15	130311-28Si-Si	-4.000	230*	0.60	0.0066	4.3×10^{17}	10	0.35*	64*	1.45	
16	130328-28Si(dP)-Si	-3.995	64*	0.42	0.0070	2.7×10^{17}	6	0.93	249	2.00	SIMS
17	130404-28Si(dP)-Si	-3.995	55*	0.43	0.0073	8.8×10^{17}	5	0.62*	175*	2.10	TOF-SIMS
18	130412-2829Si(28SiH)-Si	-3.993	50	0.37	0.0070	9.1×10^{17}	5	0.84	351	1.92	SIMS
19	130520-28Si-SOI	-4.000	179*	0.48	0.0040	3.8×10^{16}	7	1.07	149	0.89	SIMS
20	130920-28Si(dP)-SOI	-4.000	80	0.62	0.0075	8.8×10^{17}	5	1.41	285	1.92	SIMS
21	130924-28Si-Si-550C	-4.000	75	0.41	0.0007	1.5×10^{17}	3	0.74	22	0.19	

Table D.5: ^{28}Si Sample Catalog: LC–2: II (3/7/13–9/24/13). ^{28}Si samples were deposited at room temperature ($\approx$ 21 °C) using SiH_4 with the low pressure mode of the gas-mode ion source at LC–2, the deceleration lens chamber. Sample #21 was deposited at about 550 °C. Substrates were etched with HF *ex situ* but not prepared *in situ*. Aperture gives the width of the mass-selecting aperture slit. Pressures are raw reading of the lens chamber base and with the ion source on. For samples #16, #17, and #20, the pressure was modulated from low to high to low. V_A is the anode voltage and V_T is the transport voltage. E_i is the average ion energy at the sample, and I_i is the average ion current. C. I. is the ion current integral. R is the deposition rate, and d is the film thickness. Thicknesses and rates correspond to the thickest measured film area. Items marked with * are estimates.

#	Sample Name	Load Date	Dep. Date	Substrate Type	Substrate Prep. (*ex situ*)	Aperture (mm)	Base P (Pa)	Dep. P (Pa)	V_A (V)	V_T (kV)
22	140224-28Si-Si-750C	2/7/14	2/24/14	Si(100):B (3)		2	2.4×10^{-8}	2.1×10^{-7}	40	-4.000
23	140521-28Si-Si-800C	3/25/14	5/21/14	Si(100):B (3)		2	4.9×10^{-9}	2.4×10^{-7}	35	-4.000
24	140526-28Si-Si-700C	5/20/14	5/26/14	Si(100):B (3)		2	2.9×10^{-9}	2.0×10^{-7}	35	-4.000
25	140603-28Si-Si-700C	2/22/14	6/3/14	Si(100):B (3)		2	3.7×10^{-9}	2.0×10^{-7}	35	-4.000
26	140604-28Si-Si-600C	2/22/14	6/4/14	Si(100):B (3)		2	5.7×10^{-9}	2.0×10^{-7}	35	-4.000
27	140610-28Si-Si-900C	5/23/14	6/10/14	Si(100):B (3)		2	2.8×10^{-9}	2.0×10^{-7}	35	-4.000
28	140619-28Si-Si-700C	6/5/14	6/19/14	Si(100):B (3)		2	2.5×10^{-9}	2.0×10^{-7}	35	-4.001
29	140627-28Si-Si-1050C	5/28/14	6/27/14	Si(100):B (3)		2	2.8×10^{-9}	2.7×10^{-7}	35	-4.000
30	140710-28Si-Si-1010C	6/26/14	7/10/14	Si(100):B (3)		2	4.9×10^{-9}	1.5×10^{-7}	36	-4.000
31	140716-28Si-Si-1000C	6/26/14	7/16/14	Si(100):B (3)		2	5.1×10^{-9}	1.9×10^{-7}	50	-4.000

#	Sample Name	T (°C)	E_i (eV)	I_i (μA)	C. I. (C)	Ion Dose (cm^{-2})	Spot Size (mm^2)	R (nm/min)	d (nm)	Film Mass (μg)	Primary Measurement(s)
22	140224-28Si-Si-750C	759	50	0.18	0.0012		28*	0.21*	22		SIMS, SEM
23	140521-28Si-Si-800C	812	33	0.42	0.0044	3.7×10^{17}	7	0.90	158	1.20	SIMS, SEM, XPS
24	140526-28Si-Si-700C	708	33	0.58	0.0054	4.1×10^{17}	8	0.77	120	1.50	SEM, TEM
25	140603-28Si-Si-700C	708	33	0.51	0.0032	4.5×10^{17}	4	1.20	126	0.90	SIMS, SEM, XPS
26	140604-28Si-Si-600C	610	33	0.50	0.0063	5.3×10^{17}	7	0.77	162	1.77	SIMS, SEM
27	140610-28Si-Si-900C	920	33	0.53	0.0049	8.3×10^{17}	4	2.60*	400*	1.38	SEM
28	140619-28Si-Si-700C	708	34	0.53	0.0057	9.9×10^{17}	4	0.84	150	1.60	SIMS, SEM, TEM
29	140627-28Si-Si-1050C	1085	33	0.60	0.0054		1*			1.50	
30	140710-28Si-Si-1010C	1041	33	0.57	0.0060			0.29	50	1.77	SIMS, SEM, TEM
31	140716-28Si-Si-1000C	1030	31	0.55	0.0060					1.69	

Table D.6: ^{28}Si Sample Catalog: DC–3: I (2/7/14–6/26/14). ^{28}Si samples were deposited using SiH_4 with the low pressure mode of the gas-mode ion source at DC–3, the deposition chamber. Substrates were not prepared *ex situ* but were flash annealed *in situ*. Aperture gives the width of the mass-selecting aperture slit. Pressures are raw reading of the deposition chamber base and with the ion source on. V_A is the anode voltage and V_T is the transport voltage. E_i is the average ion energy at the sample, and I_i is the average ion current. T is the substrate deposition temperature. C. I. is the ion current integral. R is the deposition rate, and d is the film thickness. Thicknesses and rates correspond to the thickest measured film area. Items marked with * are estimates.

#	Sample Name	Load Date	Dep. Date	Substrate Type	Substrate Prep. (*ex situ*)	Aperture (mm)	Base P (Pa)	Dep. P (Pa)	V_A (V)	V_T (kV)
32	140828-28Si-Si	6/30/14	8/28/14	Si(100):B (4)		2	2.4×10^{-9}	1.2×10^{-7}	85	-4.00
33	150202-28Si-Si-800C	1/27/15	2/2/15	Si(100):P (5)	HF etch	2	2.1×10^{-8}	1.0×10^{-7}	100	-4.00
34	150323-28Si-Si-700C	3/17/15	3/23/15	Si(100):B (4)	HF etch	2	1.9×10^{-8}	3.2×10^{-7}	100	-4.00
35	150627-KD-7-P-28Si-600C	6/27/15	7/6/15	Si(100):P (6)	CMOS clean	2	2.7×10^{-8}	6.5×10^{-7}	100	-4.00
36	150627-KD-3-P-28Si-700C	6/27/17	7/9/15	Si(100):P (6)	CMOS clean	2	2.1×10^{-8}	5.5×10^{-7}	120	-4.00
37	150707-KD-1-P-28Si-800C	7/7/15	7/14/15	Si(100):P (6)	CMOS clean	2	1.5×10^{-8}	7.6×10^{-7}	108	-4.00
38	150715-KD-5-P-28Si-800C	7/15/15	7/17/15	Si(100):P (6)	CMOS clean	2	1.6×10^{-8}	1.2×10^{-6}	100	-4.00
39	150719-KD-2-B-28Si-700C	7/19/15	7/22/15	Si(100):B (7)	CMOS clean	2	1.5×10^{-8}	1.0×10^{-6}	100	-4.00
40	150715-KD-9-B-28Si-700C	7/15/15	7/22/15	Si(100):B (7)	CMOS clean	2	1.5×10^{-8}	1.0×10^{-6}	100	-4.00
41	150721-KD-5-P-28Si-700C	7/21/15	7/27/15	Si(100):P (6)	CMOS clean	2	1.5×10^{-8}	1.0×10^{-6}	120	-4.00

#	Sample Name	T (°C)	E_i (eV)	I_i (μA)	C. I. (C)	Ion Dose (cm^{-2})	Spot Size (mm^2)	R (nm/min)	d (nm)	Film Mass (μg)	Primary Measurement(s)
32	140828-28Si-Si	21*	38	0.25	0.0025	6.0×10^{17}	3	0.32	53	0.69	SIMS
33	150202-28Si-Si-800C	804	33	0.41*			2	1.4*	170*		SIMS, SEM
34	150323-28Si-Si-700C	709	20	0.32	0.0002				8	0.06	
35	150627-KD-7-P-28Si-600C	619	12	0.64	0.0004					0.11	
36	150627-KD-3-P-28Si-700C	712	24	0.65	0.0101	1.3×10^{18}	5	0.54	140	2.89	SIMS, TEM, XPS
37	150707-KD-1-P-28Si-800C	808	34*	0.85	0.0071	1.1×10^{18}	4	1.57*	217*	1.97	SEM
38	150715-KD-5-P-28Si-800C	808	19	0.64*	0.0077*	2.3×10^{18}	2	0.60	120	2.13*	SIMS, SEM
39	150719-KD-2-B-28Si-700C	712	18	0.72	0.0002				5*	0.05	
40	150715-KD-9-B-28Si-700C	712	18	0.67	0.0001				5	0.04	
41	150721-KD-5-P-28Si-700C	712	37	0.74	0.0093	1.4×10^{18}	4	1.22	256	2.60	SIMS

Table D.7: ^{28}Si Sample Catalog: DC–3: II (8/28/14–7/27/15). ^{28}Si samples were deposited using SiH_4 with the low pressure mode of the gas-mode ion source at DC–3, the deposition chamber. Substrates were flash annealed *in situ*. Aperture gives the width of the mass-selecting aperture slit. Pressures are raw reading of the deposition chamber base and with the ion source on. V_A is the anode voltage and V_T is the transport voltage. E_i is the average ion energy at the sample, and I_i is the average ion current. T is the substrate deposition temperature. C. I. is the ion current integral. R is the deposition rate, and d is the film thickness. Thicknesses and rates correspond to the thickest measured film area. Items marked with * are estimates. Samples #35 to #41 contain roughly 30 % N.

#	Sample Name	Load Date	Dep. Date	Substrate Type	Substrate Prep. (*ex situ*)	Aperture (mm)	Base P (Pa)	Dep. P (Pa)	V_A (V)	V_T (kV)
42	150920-KD-3-P-28Si-308C	9/20/15	10/2/15	Si(100):P (6)	CMOS clean	2	1.7×10^{-8}	1.1×10^{-6}	45	-4.00
43	150926-KD-4-P-28Si-312C	9/26/15	10/5/15	Si(100):P (6)	CMOS clean	2	1.6×10^{-8}	1.5×10^{-6}	50	-4.00
44	151020-KD-9-B-28Si-700C	10/20/15	10/22/15	Si(100):B (7)	CMOS clean	2	2.3×10^{-8}	1.3×10^{-6}	50	-4.00
45	151019-KD-2-B-28Si-450C	10/19/15	10/22/15	Si(100):B (7)	CMOS clean	2	2.3×10^{-8}	1.3×10^{-6}	50	-4.00
46	151025-KD-4-B-28Si-400C	10/25/15	11/2/15	Si(100):B (7)	CMOS clean	2	1.6×10^{-8}	9.6×10^{-7}	50	-4.00
47	151028-KD-1-B-28Si-700C	10/28/15	11/20/15	Si(100):B (7)	CMOS clean	2	1.5×10^{-8}	1.3×10^{-6}	50	-4.00
48	151102-KD-7-i-28Si-400C	11/2/15	11/30/15	Si(100):i (8)	CMOS clean	2	1.5×10^{-8}	1.2×10^{-6}	50	-4.00
49	151202-KD-7-i-28Si-400C	12/2/15	12/7/15	Si(100):i (8)	CMOS clean	2	1.5×10^{-8}	1.5×10^{-6}	50	-4.00
50	151109-KD-9-B-28Si-400C	11/9/15	12/10/15	Si(100):B (9)	CMOS clean	2	1.7×10^{-8}	1.3×10^{-6}	50	-4.00
51	151109-KD-4-B-28Si-300C	11/9/15	12/14/15	Si(100):B (9)	CMOS clean	2	1.5×10^{-8}	1.3×10^{-6}	50	-4.00

#	Sample Name	T (°C)	E_i (eV)	I_i (μA)	C. I. (C)	Ion Dose (cm^{-2})	Spot Size (mm^2)	R (nm/min)	d (nm)	Film Mass (μg)	Primary Measurement(s)
42	150920-KD-3-P-28Si-308C	355	40	0.53	0.0003			1.14*	9*	0.07	
43	150926-KD-4-P-28Si-312C	357	46	0.55	0.0050	1.1×10^{18}	3	0.33	50	1.36	SIMS, XPS
44	151020-KD-9-B-28Si-700C	712	43	0.54	0.0003		1	1.11*	11*	0.09	
45	151019-KD-2-B-28Si-450C	460	43	0.54	0.0097	1.6×10^{18}	4	0.53	160	2.69	SIMS, TEM
46	151025-KD-4-B-28Si-400C	721	42	0.47*	0.0036	6.2×10^{17}	4	0.21	44	0.99*	SIMS
47	151028-KD-1-B-28Si-700C	705	39	0.55	0.0058	4.6×10^{17}	8	0.82	144	1.62	SIMS, SEM
48	151102-KD-7-i-28Si-400C	417	40	0.55	0.0079	6.8×10^{17}	7	0.63	150	2.20	ESR
49	151202-KD-7-i-28Si-400C	417	40	0.54	0.0087	1.1×10^{18}	5	0.93	250	2.42	ESR
50	151109-KD-9-B-28Si-400C	421	38	0.54	0.0082	5.6×10^{17}*	9*	0.60	151	2.29	SIMS
51	151109-KD-4-B-28Si-300C	349	37	0.51	0.0074	8.5×10^{17}	5	0.87	210	2.05	SIMS

Table D.8: ^{28}Si Sample Catalog: DC–3: III (9/20/15–11/9/15). ^{28}Si samples were deposited using SiH_4 with the low pressure mode of the gas-mode ion source at DC–3, the deposition chamber. Substrates were flash annealed *in situ*. Aperture gives the width of the mass-selecting aperture slit. Pressures are raw reading of the deposition chamber base and with the ion source on. V_A is the anode voltage and V_T is the transport voltage. E_i is the average ion energy at the sample, and I_i is the average ion current. T is the substrate deposition temperature. C. I. is the ion current integral. R is the deposition rate, and d is the film thickness. Thicknesses and rates correspond to the thickest measured film area. Items marked with * are estimates.

#	Sample Name	Load Date	Dep. Date	Substrate Type	Substrate Prep. (*ex situ*)	Aperture (mm)	Base P (Pa)	Dep. P (Pa)	Plasma Mode	V_A (V)
52	151210-KD-7-i-28Si-500C	12/10/15	12/18/15	Si(100):i (8)	CMOS clean	2	1.5×10^{-8}	1.2×10^{-6}	low P	50
53	151218-KD-4-i-28Si-200C	12/18/15	12/21/15	Si(100):i (8)	CMOS clean	2	1.7×10^{-8}	1.2×10^{-6}	low P	57
54	151218-KD-9-B-28Si-400C	12/18/15	12/29/15	Si(100):B (9)	CMOS clean	2	1.7×10^{-8}	1.2×10^{-6}	low P	69
55	160113-KD-4-P-28Si-400C	1/13/16	2/8/16	Si(100):P (10)	CMOS clean	2	2.4×10^{-8}	5.3×10^{-6}	high P	55
56	160202-KD-7-P-28Si-400C	2/2/16	2/10/16	Si(100):P (10)	CMOS clean	2	2.1×10^{-8}	5.2×10^{-6}	high P	55
57	160210-KD-1-P-28Si-400C	2/10/16	2/12/16	Si(100):P (10)	CMOS clean	2	2.1×10^{-8}	5.1×10^{-6}	high P	55
58	160217-KD-7-P-28Si-450C	2/17/16	2/29/16	Si(100):P (10)	CMOS clean	2	1.7×10^{-8}	5.5×10^{-6}	high P	55
59	160513-KD-7-i-28Si-450C	5/13/16	6/9/16	Si(100):i (8)	CMOS clean	2	8.3×10^{-9}	3.6×10^{-6}	high P	52
60	160617-KD-3-P-28Si-400C	6/17/16	6/24/16	Si(100):P (10)	CMOS clean	2	7.1×10^{-9}	3.4×10^{-6}	high P	52
61	160617-KD-7-P-28Si-403C	6/17/16	6/24/16	Si(100):P (10)	CMOS clean	2	7.1×10^{-9}	2.9×10^{-6}	high P	50

#	Sample Name	V_T (kV)	T (°C)	E_i (eV)	I_i (μA)	C. I. (C)	Ion Dose (cm^{-2})	Spot Size (mm^2)	R (nm/min)	d (nm)	Film Mass (μg)	Primary Measurement(s)
52	151210-KD-7-i-28Si-500C	-4.00	502	37	0.52	0.0071	7.4×10^{17}	6	0.95	321	1.99	SIMS
53	151218-KD-4-i-28Si-200C	-4.00	249	38	0.63	0.0091	6.6×10^{17}	9	1.27	305	2.54	SIMS
54	151218-KD-9-B-28Si-400C	-4.00	421	40	0.69	0.0110	1.0×10^{18}	7	0.87	232	3.06	SIMS
55	160113-KD-4-P-28Si-400C	-4.70	421	35	2.29	0.0178	1.5×10^{18}	7	2.48*	322*	4.99	
56	160202-KD-7-P-28Si-400C	-4.70	421	35	2.27	0.0190	1.4×10^{18}	9	2.57	359*	5.33	
57	160210-KD-1-P-28Si-400C	-4.70	421	36	2.28	0.0178	1.3×10^{18}	9	2.65*	345*	4.98	
58	160217-KD-7-P-28Si-450C	-4.70	460	37	2.15	0.0006			2.60*	13*	0.18	
59	160513-KD-7-i-28Si-450C	-4.70	460	34	2.77	0.0220	1.4×10^{18}	10	2.21	292	6.18	SIMS
60	160617-KD-3-P-28Si-400C	-4.70	421	31	3.00	0.0144	2.4×10^{18}	4	4.56	365	4.07	SIMS, TEM
61	160617-KD-7-P-28Si-403C	-4.70	423	32	2.50	0.0150	6.2×10^{18}	2	2.33*	233*	4.23	

Table D.9: ^{28}Si Sample Catalog: DC–3: IV (12/18/15–6/24/16). ^{28}Si samples were deposited using SiH_4 with the gas-mode ion source at DC–3, the deposition chamber. Substrates were flash annealed *in situ*. Aperture gives the width of the mass-selecting aperture slit. Pressures are raw reading of the deposition chamber base and with the ion source on. V_A is the anode voltage and V_T is the transport voltage. E_i is the average ion energy at the sample, and I_i is the average ion current. T is the substrate deposition temperature. C. I. is the ion current integral. R is the deposition rate, and d is the film thickness. Thicknesses and rates correspond to the thickest measured film area. Items marked with * are estimates.

Sample Name	Data Set	Dep. Location	E_i (eV)	I_i (μA)	R (nm/min)	P_{SiH_x} (Pa)	F_i ($cm^{-2} \cdot s^{-1}$)	F_g ($cm^{-2} \cdot s^{-1}$)
120604-28Si-OxSi	1	IC–1	455	0.95	0.07	2.4×10^{-5}	1.1×10^{13}	6.6×10^{13}
120618-28Si-OxSi	Ar SF5	IC–1	64	0.77	0.40 0.33	3.4×10^{-5}	3.5×10^{13} 2.8×10^{13}	9.2×10^{13}
120628-28Si-OxSi	4 5 7 8	IC–1	64	0.85	0.5 0.5 0.47 0.59	2.6×10^{-5}	4.4×10^{13} 4.4×10^{13} 4.2×10^{13} 5.2×10^{13}	7.2×10^{13}
130204-28Si-Si	1 2	LC–2	74	0.57	0.51 0.56	1.4×10^{-6}	4.6×10^{13} 5.1×10^{13}	3.7×10^{12}
130208-28Si-Si	1 2 3 4 5	LC–2	121	0.56	1.49 1.05 0.54 0.53 0.94	1.4×10^{-6}	1.5×10^{14} 1.1×10^{14} 5.6×10^{13} 5.4×10^{13} 9.6×10^{13}	3.7×10^{12}
130328-28Si(dP)-Si	low-P	LC–2	60	0.33	0.93	6.8×10^{-7}	8.3×10^{13}	1.8×10^{12}
130412-2829Si(28SiH)-Si	dip/film	LC–2	50	0.31	0.84	6.8×10^{-7}	7.3×10^{13}	1.8×10^{12}
130520-28Si-SOI	1	LC–2	180	0.48	1.07	8.3×10^{-7}	1.2×10^{14}	2.3×10^{12}
140828-28Si-Si	1	DC–3	38	0.25	0.32	2.8×10^{-7}	2.7×10^{13}	7.6×10^{11}

Table D.10: Deposition parameters of ^{28}Si samples deposited at room temperature ($\approx$ 21 °C) for the gas sticking deposition model analysis discussed in Chapter 6. Samples deposited at IC–1 were excluded in that analysis. Some samples have multiple SIMS data sets that are grouped together. E_i is the average ion energy at the sample. I_i is the average ^{28}Si ion beam current. R is the deposition rate. P_{SiH_x} is the SiH_x partial pressure at the sample during deposition. F_i is the ^{28}Si ion flux. F_g is the SiH_x molecular flux at the sample.

Sample Name	Data Set	Dep. Location	d (nm)	Isotope Fraction (^{z}Si/Si$_{\text{tot.}}$) ^{28}Si (%)	^{29}Si (ppm)	^{30}Si (ppm)	$c_z(s_T, k_{502})$ ^{29}Si (ppm)	^{30}Si (ppm)
120604-28Si-OxSi	1	IC–1	12	99.702(12)	2822(18)	156.1(38)		0.112
120618-28Si-OxSi	Ar	IC–1	92	99.8850(14)	1130(14)	20.3(14)		0.032
	SF5		75	99.8448(21)	1534(21)	17.9(19)		0.0228
120628-28Si-OxSi	4	IC–1	73	99.99846(19)	9.5(10)	5.9(16)	0.043	0.027
	5		73	99.99842(16)	10.5(13)	5.23(87)	0.047	0.024
	7		69	99.99816(11)	12.3(10)	6.15(52)	0.052	0.026
	8		86	99.99799(16)	12.8(10)	7.3(13)	0.068	0.039
130204-28Si-Si	1	LC–2	100	99.999657(38)	2.02(32)	1.41(20)	0.181	0.126
	2		110	99.999592(36)	2.30(26)	1.78(24)	0.227	0.176
130208-28Si-Si	1	LC–2	384	99.9998308(82)	0.993(64)	0.699(51)	0.299	0.210
	2		270	99.9998031(86)	1.252(72)	0.717(48)	0.265	0.152
	3		140	99.999722(12)	1.724(97)	1.055(74)	0.189	0.116
	4		136	99.999696(15)	1.85(11)	1.189(96)	0.197	0.127
	5		241	99.999812(10)	1.122(76)	0.760(64)	0.212	0.144
130328-28Si(dP)-Si	low-P	LC–2	249	99.999888(10)	0.691(74)	0.432(67)	0.225	0.141
130412-2829Si(28SiH)-Si	dip/film	LC–2	351	99.999889(11)	0.78(10)	0.512(42)	0.223	0.147
130520-28Si-SOI	1	LC–2	149	99.999863(16)	0.77(11)	0.60(11)	0.289	0.225
140828-28Si-Si	1	DC–3	53	99.99990(11)	0.58(26)	0.44(23)	0.148	0.113

Table D.11: Enrichment measurements and gas sticking deposition model model analysis results for ^{28}Si samples deposited at room temperature ($\approx$ 21 °C) discussed in Chapter 6. Some samples have multiple SIMS data sets that are grouped together. d is the ^{28}Si film thickness. The raw SIMS isotope fractions as well as those adjusted to the deposition conditions of the 502 °C sample, $c_z(s_T, k_{502})$, are listed.

Sample Name	Data Set	T (°C)	E_i (eV)	I_i (μA)	R (nm/min)	$P_{\mathrm{SiH_x}}$ (Pa)	F_i ($\mathrm{cm^{-2} \cdot s^{-1}}$)	F_g ($\mathrm{cm^{-2} \cdot s^{-1}}$)
151218-KD-4-i-28Si-200C	1 2	249	38	0.63	1.27 1.11	3.2×10^{-7}	1.1×10^{14} 9.6×10^{13}	8.7×10^{11}
151109-KD-4-B-28Si-300C	3 4	349	37	0.51	0.80 0.87	3.6×10^{-7}	6.9×10^{13} 7.5×10^{13}	9.8×10^{11}
150926-KD-4-P-28Si-312C	1	357	46	0.55	0.33	4.1×10^{-7}	2.9×10^{13}	1.1×10^{12}
151109-KD-9-B-28Si-400C	1 4 6	421	38	0.54	0.43 0.36 0.60	3.7×10^{-7}	3.7×10^{13} 3.1×10^{13} 5.1×10^{13}	9.9×10^{11}
160617-KD-3-P-28Si-400C	1 2	421	31	3.00	3.94 3.36	9.6×10^{-7}	3.4×10^{14} 2.9×10^{14}	2.6×10^{12}
151210-KD-7-i-28Si-500C	2 3 4	502	37	0.52	0.95 0.43 1.41	3.3×10^{-7}	8.1×10^{13} 3.7×10^{13} 1.2×10^{14}	8.8×10^{11}
140604-28Si-Si-600C	1	610	33	0.50	0.77	1.4×10^{-7}	6.6×10^{13}	3.7×10^{11}
151028-KD-1-B-28Si-700C	1 2	705	39	0.55	0.82 0.66	3.5×10^{-7}	7.0×10^{13} 5.7×10^{13}	9.5×10^{11}
140603-28Si-Si-700C	1 2	708	33	0.51	1.20 0.98	2.2×10^{-7}	1.0×10^{14} 8.3×10^{13}	6.0×10^{11}
140521-28Si-Si-800C	1	812	33	0.42	0.90	1.5×10^{-7}	7.7×10^{13}	4.1×10^{11}

Table D.12: Deposition parameters of ^{28}Si samples deposited at elevated temperature for the gas sticking deposition model analysis discussed in Chapter 6. Some samples have multiple SIMS data sets that are grouped together. T is the substrate deposition temperature. E_i is the average ion energy at the sample. I_i is the average ^{28}Si ion beam current. R is the deposition rate. $P_{\mathrm{SiH_x}}$ is the $\mathrm{SiH_x}$ partial pressure at the sample during deposition. F_i is the ^{28}Si ion flux. F_g is the $\mathrm{SiH_x}$ molecular flux at the sample.

Sample Name	Data Set	T (°C)	d (nm)	Isotope Fraction (^{z}Si/Si$_{\text{tot.}}$) ^{28}Si (%)	^{29}Si (ppm)	^{30}Si (ppm)	$c_z(s_T, k_{502})$ ^{29}Si (ppm)	^{30}Si (ppm)	s
151218-KD-4-i-28Si-200C	1	249	305	99.999898(13)	0.79(12)	0.229(64)	0.72	0.208	1.6×10^{-3}
	2		267	99.999865(18)	1.01(17)	0.341(65)	0.80	0.271	
151109-KD-4-B-28Si-300C	3	349	193	99.999884(18)	0.78(16)	0.386(88)	0.40	0.197	8×10^{-4}
	4		210	99.999924(17)	0.53(16)	0.230(46)	0.29	0.128	
150926-KD-4-P-28Si-312C	1	357	50	99.999405(93)	4.18(70)	1.77(61)	0.80	0.34	2.0×10^{-3}
151109-KD-9-B-28Si-400C	1	421	108	99.999762(27)	1.68(24)	0.70(14)	0.452	0.188	8.4×10^{-4}
	4		92	99.999812(25)	1.30(22)	0.58(12)	0.298	0.133	
	6		151	99.999818(26)	1.46(22)	0.35(15)	0.55	0.132	
160617-KD-3-P-28Si-400C	1	421	315	99.9999594(72)	0.303(58)	0.103(43)	0.285	0.097	
	2		269	99.9999446(67)	0.407(59)	0.058(32)	0.327	0.068	
151210-KD-7-i-28Si-500C	2	502	216	99.9999701(57)	0.259(53)	0.040(19)	0.174	0.027	2.9×10^{-4}
	3		99	99.999940(16)	0.31(10)	0.29(12)	0.096	0.089	
	4		321	99.9999819(35)	0.127(29)	0.055(19)	0.127	0.055	
140604-28Si-Si-600C	1	610	162	99.9999570(70)	0.300(60)	0.130(37)	0.38	0.166	9×10^{-4}
151028-KD-1-B-28Si-700C	1	705	144	99.999488(48)	3.30(25)	1.82(42)	1.77	0.98	5.6×10^{-3}
	2		117	99.999181(83)	4.82(70)	3.38(45)	2.11	1.48	
140603-28Si-Si-700C	1	708	126	99.99986(11)	0.806(97)	0.61(37)	1.00	0.76	7×10^{-3}
	2		102	99.99947(18)	3.09(61)	2.17(42)	3.12	2.19	
140521-28Si-Si-800C	1	812	158	99.99907(25)	4.32(46)	4.96(93)	5.9	6.8	2.3×10^{-2}

Table D.13: Enrichment measurements and temperature dependant gas incorporation model analysis results for ^{28}Si samples deposited at elevated temperature discussed in Chapter 6. Some samples have multiple SIMS data sets that are grouped together. T is the substrate deposition temperature. d is the ^{28}Si film thickness. The raw SIMS isotope fractions as well as those adjusted to the deposition conditions of the 502 °C sample, $c_z(s_T, k_{502})$, are listed. s is the incorporation fraction at each deposition temperature.

Appendix E: SIMS Measurement Settings

^{22}Ne:

The following is a statement of the SIMS measurement settings and techniques used for assessing the enrichment of ^{22}Ne samples implanted at LC–2. This statement was adapted from one provided by Dr. Dave Simons (NIST) for sample 110504-22Ne-OxSi.

A Cameca IMS-1280 magnetic sector secondary ion mass spectrometer was used to make the measurements. The primary ion beam was composed of Cs^+ ions with a current of 40 nA and an energy with respect to ground of 10 keV. The beam was raster-scanned over a nominal 280 μm by 430 μm in size, and the ions were only accepted for counting from a central region that represented about 40 % of the area of the crater. At implantation doses used for these samples, it is expected that the peak concentration of implanted species would occur at the surface and would be constant roughly up to the range of the implanted ions. The maximum concentration is governed by a balance between implantation and sputter removal rates.

The most sensitive method to detect noble gases by SIMS is via Cs attachment ions CsM^+, where M is the noble gas isotope. Thus positive secondary ions

of $^{133}Cs^{20}Ne^+$, $^{133}Cs^{22}Ne^+$, and $^{133}Cs^{29}Si^+$ were accelerated to 5 keV, separated by mass, and detected with a secondary electron multiplier operating in a pulse-counting mode. These species were detected sequentially and repetitively over 50 cycles, with the Ne species being detected for 5 s each per cycle and the Si for 1 s. The sequence of data constitutes a depth profile since the sample surface is eroded with time by ion sputtering. Depth profile data were taken both in the area designated as having been implanted, as well as far from that area to serve as a control.

^{12}C:

The following is a statement of the SIMS measurement settings and techniques used for assessing the enrichment of ^{12}C samples deposited at LC–2. This statement was adapted from one provided by Dr. David Simons (NIST) for sample 120207-12C-OxSi.

The isotopic composition of deposited carbon films were measured with a Cameca IMS-1270 large geometry secondary ion mass spectrometer. A Cs^+ primary ion beam with an impact energy of 20 keV was raster-scanned over a 150 μm by 150 μm area on the sample in the center of the deposited region. Secondary negative ion signals of ^{12}C and ^{13}C were extracted from a gated area of 125 μm by 125 μm into the mass spectrometer and alternately directed by magnetic peak-switching into a secondary electron multiplier where their count rates were recorded. A mass resolving power $\frac{m}{\Delta m}$ of 5000 at 10 % of peak amplitude was set by a combination of entrance and exit slits so that a spectral interference of ^{12}CH on ^{13}C was effectively

excluded. A set of measurements were made by pre-sputtering the area for 90 s or 360 s with an 8 nA primary ion current and then recording 40 isotopic ratio pairs with a beam current of 23 pA. The count rates were corrected for the dead time of the electron multiplier.

The isotope profiles are the results of 8 successive sets of measurements of $^{13}C/^{12}C$ ratios from the same area of the carbon film. These values do not take into account an instrumental mass fractionation for carbon that would make measured ratios smaller by about 5 %. A stylus profilometry is used to measure the sputtered crater depth. To assess the degree of enrichment of ^{12}C in the films, a ratio measurement of a pyrolytic graphite disk with isotopically natural carbon was made under similar analysis conditions. In this case the measured $^{13}C/^{12}C$ ratio was 1.046×10^{-2}.

^{28}Si at IC–1:

The following is a statement of the SIMS measurement settings and techniques used for assessing the enrichment of ^{28}Si samples deposited at IC–1. This statement was adapted from one provided by Dr. Dave Simons (NIST) for sample 120604-28Si-OxSi.

The mass spectrometer was set to exclude ^{28}SiH from the ^{29}Si signal and was used to first measure isotopic ratios in the Si substrate far from the film deposit. The primary beam species was O^- with an impact energy of 23 keV and a current of about 0.4 nA. The analyzed area was 25 μm by 25 μm, defined by an aperture in the ion optics. The beam was not rastered and the spot had an elliptical shape

about 50 μm on the major axis. The measured ratio of $^{29}Si/^{28}Si$ was 0.0497 and the measured ratio of $^{30}Si/^{28}Si$ was 0.0323 in the Si substrate. These values are smaller than the known ratios of 0.0508 for $^{29}Si/^{28}Si$ and 0.03353 for $^{30}Si/^{28}Si$ but that result is expected since SIMS is known to ionize the lighter isotope with higher efficiency. These measured values are used to calculate the degree to which the minor isotopes have been reduced in the deposited film.

The film area was then analyzed in a region that appeared to be the center, assumed to have the greatest thickness. 20 sequential analytical runs were made on the same area, sputtering in total for nearly 4 h. The count rates of ^{28}Si, ^{29}Si and ^{30}Si were recorded sequentially. The count rates were corrected to account for detector dead time. The crater depth was later measured with a stylus profilometer.

^{28}Si at LC–2:

The following is a statement of the SIMS measurement settings and techniques used for assessing the enrichment of ^{28}Si samples deposited at LC–2. This statement was adapted from one provided by Dr. Dave Simons (NIST) for sample 130208-28Si-Si.

Isotopic measurements were made in a CAMECA IMS-1280 large geometry secondary ion mass spectrometer. The sample was bombarded with a primary ion beam of O_2^+ at an impact energy of 8 keV and a current of 0.3 nA. The beam was focused to a probe size of a few micrometers diameter and it was raster-scanned over a 50 μm by 50 μm area. Positive secondary ions were accepted for detection from the central 25 μm by 25 μm portion of the rastered area. The secondary ions passed

through an entrance slit of 20 μm and an exit slit of 200 μm. These conditions produce a mass resolving power of about 6000 ($\frac{m}{\Delta m}$ at 10 % of peak maximum). This resolving power is necessary to separate the ^{29}Si peak from the ^{28}SiH peak that is produced during the SIMS process. The ^{28}SiH signal is normally about 0.05 % to 0.1 % of the ^{28}Si signal and the ratio can vary depending on the analytical conditions. For one sample the ^{28}SiH signal within the film was about 4000 times larger than the ^{29}Si signal demonstrating why very good separation between these peaks is needed to measure the ^{29}Si/^{28}Si ratio accurately.

Data were taken over 100 to 360 cycles in which the ^{28}Si was measured for 1 s, the ^{29}Si for 10 s, ^{28}SiH for 1 s and the ^{30}Si for 10 s sequentially during each cycle by switching the magnetic field. The runs took between 50 min and 100 min to sputter through the film depending on the thickness of the film at the analysis location.

Quantitative isotopic ratio calculations were made by averaging the cycle-by-cycle ratio measurements in the part of the profiles where the ratios were at a minimum. These values were then corrected for instrumental mass fractionation based on the differences between the measured ratios of the wafer silicon and the accepted natural values. Uncertainties were determined from the standard deviation of the mean of the measurements and were compared with a Poisson estimation based on the total number of detected counts of the minor isotopes. The depths of each crater were measured with a stylus profilometer and the film thickness was defined as the depth where the ^{29}Si/^{28}Si ratio had risen to half of its natural value.

Carbon isotopic signals were monitored in a separate depth profile of the film. ^{30}Si was also monitored as a marker of the film-substrate interface and as a normal-

ization signal for concentration estimates. The concentrations of the carbon isotopes in the film were estimated by averaging their count rates over the cycles within the film and applying a value obtained from literature of 0.007 for the relative sensitivity factor of carbon to silicon by SIMS under similar analytical conditions. The SIMS instrumental background for carbon analyzed under similar conditions is unknown but it must be at least an order of magnitude lower than what is measured since the carbon signals typically decrease by more than a factor of 10 in the Si substrate. Trace carbon is not normally analyzed by SIMS under these conditions of oxygen ion bombardment and positive ion detection but rather with cesium ion bombardment and negative ion detection. In the present case the conditions were not changed to simplify the measurement process.

^{28}Si at DC–3:

The following is a statement of the SIMS measurement settings and techniques used for assessing the enrichment of ^{28}Si samples deposited at DC–3. This statement was adapted from one provided by Dr. Dave Simons (NIST) as a general procedure for measuring samples deposited at elevated temperatures.

Isotopic measurements of Si were made in a CAMECA IMS-1270E7 large geometry secondary ion mass spectrometer. The samples were bombarded with a primary ion beam of O_2^+ ions at an impact energy of 8 keV and a current of 1 nA. The beam was focused to a probe size of a few micrometers diameter and it was raster-scanned over a 50 μm by 50 μm area. Positive secondary ions were accepted for detection from the central 20 μm by 20 μm portion of the rastered area as

defined by a field aperture in a focal plane of the mass spectrometer. The entrance and exit slits of the spectrometer were selected to produce a mass resolving power of about 6000 ($\frac{m}{\Delta m}$ at 10 % of peak maximum). This resolving power is necessary to separate cleanly the ^{29}Si peak from the ^{28}SiH peak that is produced during the SIMS process. Under these conditions we estimate that less than 10^{-5} of the ^{28}SiH signal contributes to the ^{29}Si measurement.

Depth profiles of the Si isotopes ^{28}Si, ^{29}Si and ^{30}Si through deposited films were acquired by monitoring ^{28}Si for 1 s, ^{29}Si for 10 s, ^{28}SiH for 1 s and ^{30}Si for 10 s in each data cycle and collecting a sufficient number of data cycles until the profile penetrated into the silicon substrate. The sputter rate as determined by measuring the final crater depths with a stylus profilometer was approximately 0.15 nm/s under these conditions.

Isotope ratios of ^{29}Si/^{28}Si and ^{30}Si/^{28}Si were calculated on a cycle-by-cycle basis. Average isotopic ratios for a film were calculated by averaging the cycle-by-cycle ratio measurements in the portion of a profile where the ratios were at a relatively constant minimum value. These values were then corrected for instrumental mass fractionation based on the differences between the measured ratios from a Si wafer and the accepted natural values. Uncertainties were determined from the standard deviation of the mean of the measurements and were usually similar to Poisson estimations based on the total number of detected counts of the minor isotopes.

Appendix F: ^{28}Si Deposition Fun Facts

(1) the total mass of ^{28}Si deposited in this work: ≈ 112 μg

(2) the total area deposited for ^{28}Si samples: ≈ 460 mm^2

(3) the total number of ^{28}Si atoms deposited in this work: $\approx 2.6 \times 10^{18}$

(4) the total time depositing ^{28}Si: ≈ 169 h ≈ 7 days

(5) the resulting film thickness if all ^{28}Si samples were deposited at once with a spot size of 7.5 mm^2: ≈ 6.5 μm

(6) the average distance between ^{28}Si ions along the beamline with an energy of 4050 eV for 0.5 μA of ion current: ≈ 54 nm

(7) the mean free path of SiH_4 molecules at 21 °C for a pressure of 1.3×10^{-4} Pa (1.0×10^{-6} Torr): $\lambda \approx 200$ m

Bibliography

[1] Jonathan Wood. "The top ten advances in materials science". *Mater. Today*, **11**(1-2):40–45, 2008.

[2] Floris A. Zwanenburg, Andrew S. Dzurak, Andrea Morello, Michelle Y. Simmons, Lloyd C. L. Hollenberg, Gerhard Klimeck, Sven Rogge, Susan N. Coppersmith, and Mark A. Eriksson. "Silicon quantum electronics". *Rev. Mod. Phys.*, **85**(3):961–1019, 2013.

[3] B. E. Kane. "A silicon-based nuclear spin quantum computer". *Nature*, **393**(6681):133–137, 1998.

[4] VeldhorstM, J. C. C. Hwang, C. H. Yang, A. W. Leenstra, B. de Ronde, J. P. Dehollain, J. T. Muhonen, F. E. Hudson, K. M. Itoh, MorelloA, and A. S. Dzurak. "An addressable quantum dot qubit with fault-tolerant control-fidelity". *Nat. Nano.*, **9**(12):981–985, 2014.

[5] M. Fuechsle, S. Mahapatra, F. A. Zwanenburg, M. Friesen, M. A. Eriksson, and M. Y. Simmons. "Spectroscopy of few-electron single-crystal silicon quantum dots". *Nat. Nanotechnol.*, **5**(7):502–505, 2010.

[6] M. Veldhorst, C. H. Yang, J. C. C. Hwang, W. Huang, J. P. Dehollain, J. T. Muhonen, S. Simmons, A. Laucht, F. E. Hudson, K. M. Itoh, A. Morello, and A. S. Dzurak. "A two-qubit logic gate in silicon". *Nature*, **526**(7573):410–414, 2015.

[7] Keiichi Edamatsu. "Quantum physics: swift control of a single spin". *Nature*, **456**(7219):182–183, 2008.

[8] John P. Ridgway. "Cardiovascular magnetic resonance physics for clinicians: part I". *J. Cardiovasc. Magn. Reson.*, **12**(1):71, 2010.

[9] M. Steger, K. Saeedi, M. L. W. Thewalt, J. J. L. Morton, H. Riemann, N. V. Abrosimov, P. Becker, and H. J. Pohl. "Quantum information storage for

over 180 s using donor spins in a Si-28 'Semiconductor Vacuum'". *Science*, **336**(6086):1280–1283, 2012.

[10] Juha T. Muhonen, Juan P. Dehollain, Arne Laucht, Fay E. Hudson, Rachpon Kalra, Takeharu Sekiguchi, Kohei M. Itoh, David N. Jamieson, Jeffrey C. McCallum, Andrew S. Dzurak, and Andrea Morello. "Storing quantum information for 30 seconds in a nanoelectronic device". *Nat. Nano.*, **9**(12):986–991, 2014.

[11] Eisuke Abe, Alexei M. Tyryshkin, Shinichi Tojo, John J. L. Morton, Wayne M. Witzel, Akira Fujimoto, Joel W. Ager, Eugene E. Haller, Junichi Isoya, Stephen A. Lyon, Mike L. W. Thewalt, and Kohei M. Itoh. "Electron spin coherence of phosphorus donors in silicon: Effect of environmental nuclei". *Phys. Rev. B*, **82**(12), 2010.

[12] Wayne M. Witzel, Malcolm S. Carroll, Łukasz Cywiński, and S. Das Sarma. "Quantum decoherence of the central spin in a sparse system of dipolar coupled spins". *Phys. Rev. B*, **86**(3):35452, 2012.

[13] Alexei M. Tyryshkin, Shinichi Tojo, John J. L. Morton, Helge Riemann, Nikolai V. Abrosimov, Peter Becker, Hans-Joachim Pohl, Thomas Schenkel, Michael L. W. Thewalt, Kohei M. Itoh, and S. A. Lyon. "Electron spin coherence exceeding seconds in high-purity silicon". *Nat. Mater.*, **11**(2):143–147, 2012.

[14] Kamyar Saeedi, Stephanie Simmons, Jeff Z. Salvail, Phillip Dluhy, Helge Riemann, Nikolai V. Abrosimov, Peter Becker, Hans-Joachim Pohl, John J. L. Morton, and Mike L. W. Thewalt. "Room-temperature quantum bit storage exceeding 39 minutes using ionized donors in silicon-28". *Science*, **342**(6160):830–833, 2013.

[15] S. Meiboom and D. Gill. "Modified spin-echo method for measuring nuclear relaxation times". *Rev. Sci. Instrum.*, **29**(8):688–691, 1958.

[16] Terry Gullion, David B. Baker, and Mark S. Conradi. "New, compensated Carr-Purcell sequences". *J. Magn. Reson.*, **89**(3):479–484, 1990.

[17] B. Weber, S. Mahapatra, T. F. Watson, and M. Y. Simmons. "Engineering independent electrostatic control of atomic-scale (similar to 4 nm) silicon double quantum dots". *Nano Letters*, **12**(8):4001–4006, 2012.

[18] B. Weber, S. Mahapatra, H. Ryu, S. Lee, A. Fuhrer, T. C. G. Reusch, D. L. Thompson, W. C. T. Lee, G. Klimeck, L. C. L. Hollenberg, and M. Y. Simmons. "Ohm's law survives to the atomic scale". *Science*, **335**(6064):64–67, 2012.

[19] H. Buch, S. Mahapatra, R. Rahman, A. Morello, and M. Y. Simmons. "Spin readout and addressability of phosphorus-donor clusters in silicon". *Nature Commun.*, **4**:1038, 2013.

[20] J. A. Miwa, J. A. Mol, J. Salfi, S. Rogge, and M. Y. Simmons. "Transport through a single donor in p-type silicon". *Appl. Phys. Lett.*, **103**(4):043106, 2013.

[21] J. J. Pla, K. Y. Tan, J. P. Dehollain, W. H. Lim, J. J. L. Morton, F. A. Zwanenburg, D. N. Jamieson, A. S. Dzurak, and A. Morello. "High-fidelity readout and control of a nuclear spin qubit in silicon". *Nature*, **496**(7445):334–338, 2013.

[22] C. H. Yang, A. Rossi, R. Ruskov, N. S. Lai, F. A. Mohiyaddin, S. Lee, C. Tahan, G. Klimeck, A. Morello, and A. S. Dzurak. "Spin-valley lifetimes in a silicon quantum dot with tunable valley splitting". *Nature Commun.*, **4**:3069, 2013.

[23] L. A. Tracy, T. M. Lu, N. C. Bishop, G. A. Ten Eyck, T. Pluym, J. R. Wendt, M. P. Lilly, and M. S. Carroll. "Electron spin lifetime of a single antimony donor in silicon". *Appl. Phys. Lett.*, **103**(14):143115, 2013.

[24] A. Wild, J. Kierig, J. Sailer, J. W. Ager, E. E. Haller, G. Abstreiter, S. Ludwig, and D. Bougeard. "Few electron double quantum dot in an isotopically purified Si-28 quantum well". *Appl. Phys. Lett.*, **100**(14):143110, 2012.

[25] J. Y. Li, C. T. Huang, L. P. Rokhinson, and J. C. Sturm. "Extremely high electron mobility in isotopically-enriched Si-28 two-dimensional electron gases grown by chemical vapor deposition". *Appl. Phys. Lett.*, **103**(16):162105, 2013.

[26] C. C. Lo, A. Persaud, S. Dhuey, D. Olynick, F. Borondics, M. C. Martin, H. A. Bechtel, J. Bokor, and T. Schenkel. "Device fabrication and transport measurements of FinFETs built with Si-28 SOI wafers toward donor qubits in silicon". *Semicond. Sci. Technol.*, **24**(10):105022, 2009.

[27] John J. L. Morton, Alexei M. Tyryshkin, Richard M. Brown, Shyam Shankar, Brendon W. Lovett, Arzhang Ardavan, Thomas Schenkel, Eugene E. Haller, Joel W. Ager, and S. A. Lyon. "Solid-state quantum memory using the (31)P nuclear spin". *Nature*, **455**(7216):1085–1088, 2008.

[28] L. A. Tracy, D. R. Luhman, S. M. Carr, N. C. Bishop, G. A. Ten Eyck, T. Pluym, J. R. Wendt, M. P. Lilly, and M. S. Carroll. "Single shot spin readout using a cryogenic high-electron-mobility transistor amplifier at sub-Kelvin temperatures". *Appl. Phys. Lett.*, **108**(6):63101, 2016.

[29] A. Yang, H. J. Lian, M. L. W. Thewalt, M. Uemura, A. Sagara, K. M. Itoh, E. E. Haller, J. W. Ager, and S. A. Lyon. "Isotopic mass dependence of the lattice parameter in silicon determined by measurement of strain-induced splitting of impurity bound exciton transitions". *Phys. B-Condensed Matter*, **376**:54–56, 2006.

[30] O. E. Dial, M. D. Shulman, S. P. Harvey, H. Bluhm, V. Umansky, and A. Yacoby. "Charge Noise Spectroscopy Using Coherent Exchange Oscillations in a Singlet-Triplet Qubit". *Phys. Rev. Lett.*, **110**(14):146804, 2013.

[31] M. L. W. Thewalt, A. Yang, M. Steger, D. Karaiskaj, M. Cardona, H. Riemann, N. V. Abrosimov, A. V. Gusev, A. D. Bulanov, I. D. Kovalev, A. K. Kaliteevskii, O. N. Godisov, P. Becker, H. J. Pohl, E. E. Haller, J. W. Ager, and K. M. Itoh. "Direct observation of the donor nuclear spin in a near-gap bound exciton transition: ^{31}P in highly enriched ^{28}Si". *J. Appl. Phys.*, **101**(8):081724, 2007.

[32] P. Becker, H. J. Pohl, H. Riemann, and N. Abrosimov. "Enrichment of silicon for a better kilogram". *Phys. Status Solidi a-Applications Mater. Sci.*, **207**(1):49–66, 2010.

[33] T. Ruf, R.W. Henn, M. Asen-Palmer, E. Gmelin, M. Cardona, H.-J. Pohl, G.G. Devyatych, and P.G. Sennikov. "Thermal conductivity of isotopically enriched silicon". *Solid State Commun.*, **115**(5):243–247, 2000.

[34] P. Becker, H. Friedrich, K. Fujii, W. Giardini, G. Mana, A. Picard, H. J. Pohl, H. Riemann, and S Valkiers. "The Avogadro constant determination via enriched silicon-28". *Meas. Sci. Technol.*, **20**(9), 2009.

[35] P. Becker and D. Schiel. "The Avogadro constant and a new definition of the kilogram". *Int. J. Mass Spectrometry*, **349**:219–226, 2013.

[36] Shigeto Fukatsu, Tomonori Takahashi, Kohei M. Itoh, Masashi Uematsu, Akira Fujiwara, Hiroyuki Kageshima, Yasuo Takahashi, Kenji Shiraishi, and Ulrich Gösele. "Effect of the Si/SiO2 interface on self-diffusion of Si in semiconductor-grade SiO2". *Appl. Phys. Lett.*, **83**(19):3897–3899, 2003.

[37] K. Takyu, K. M. Itoh, K. Oka, N. Saito, and V. I. Ozhogin. "Growth and characterization of the isotopically enriched Si-28 bulk single crystal". *Jpn. J. Appl. Phys.*, **38**(12B):L1493–L1495, 1999.

[38] S. A. Lyon, A. M. Tyryshkin, T. Schenkel, J. Bokor, J. Chu, W. Jantsch, F. Schaffler, J. L. Truitt, S. N. Coppersmith, and M. A. Eriksson. "Electron spin coherence in Si". *Physica E*, **35**(2), 2006.

[39] C. C. Lo, M. Urdampilleta, P. Ross, M. F. Gonzalez-Zalba, J. Mansir, S. A. Lyon, M.L.W. Thewalt, and J. J. L. Morton. "Hybrid opticalelectrical detection of donor electron spins with bound excitons in silicon". *Nature Mater.*, **14**(5):490–494, 2015.

[40] Yaron Artzi, Ygal Twig, and Aharon Blank. "Induction-detection electron spin resonance with spin sensitivity of a few tens of spins". *Appl. Phys. Lett.*, **106**(8):84104, 2015.

[41] A. Bienfait, J. J. Pla, Y. Kubo, M. Stern, X. Zhou, C. C. Lo, C. D. Weis, T. Schenkel, M. L. W. Thewalt, D. Vion, D. Esteve, B. Julsgaard, K. Mølmer, J. J. L. Morton, and P. Bertet. "Reaching the quantum limit of sensitivity in electron spin resonance". *Nature Nanotech.*, **11**(3):253–257, 2015.

[42] Kevin G. Orrman-Rossiter, D. R. G. Mitchell, S. E. Donnelly, C. J. Rossouw, S. R. Glanvill, P. R. Miller, Amir H. Al-Bayati, J. A. van den Berg, and D. G. Armour. "Evidence for competing growth phases in ion-beam-deposited epitaxial silicon films". *Philos. Mag. Lett.*, **61**(6):311–318, 1990.

[43] N. Tsubouchi, A. Chayahara, Y. Mokuno, A. Kinomura, and Y. Horino. "Epitaxial growth of pure Si-28 thin films using isotopically purified ion beams". *Jpn. J. Appl. Phys. Part 2-Letters*, **40**(12A):L1283–L1285, 2001.

[44] Richard G. Hewlett and Oscar E. Jr. Anderson. *The New World 1939/1946: A History of the United States Atomic Energy Commission.* The Pennsylvania State University Press, University Park, Pa, volume 1 edition, 1962.

[45] Richard B. Fair. "Analysis and design of ion-beam deposition apparatus". *J. Appl. Phys.*, **42**(8):3176, 1971.

[46] Sol Aisenberg and Ronald Chabot. "Ion-Beam Deposition of Thin Films of Diamondlike Carbon". *J. Appl. Phys.*, **42**(7):2953, 1971.

[47] S. Shimizu, N. Sasaki, S. Ogata, and O. Tsukakoshi. "Ion beam deceleration characteristics of a high-current, mass-separated, low-energy ion beam deposition system". *Rev. Sci. Instrum.*, **67**(10):3664–3671, 1996.

[48] N. Herbots, B.R. Appleton, T.S. Noggle, R.A. Zuhr, and S.J. Pennycook. "Ion-solid interactions during ion beam deposition of 74Ge and 30Si on Si at very low ion energies (0-200 eV range)". *Nucl. Instrum. Meth. Phys. Res. Sect. B*, **13**(1):250–258, 1986.

[49] P. C. Zalm and L. J. Beckers. "Ion-beam epitaxy of silicon on Ge and Si at temperatures of 400–K". *Appl. Phys. Lett.*, **41**(2):167–169, 1982.

[50] K. Yagi, S. Tamura, and T. Tokuyama. "Germanium and silicon film growth by low-energy ion-beam deposition". *Jpn. J. Appl. Phys.*, **16**(2):245–251, 1977.

[51] J. W. Rabalais, A. H. Albayati, K. J. Boyd, D. Marton, J. Kulik, Z. Zhang, and W. K. Chu. "Ion-energy effects in silicon ion-beam epitaxy". *Phys. Rev. B*, **53**(16):10781–10792, 1996.

[52] A. H. Albayati, D. Marton, S. S. Todorov, K. J. Boyd, J. W. Rabalais, D. G. Armour, J. S. Gordon, and G. Duller. "Performance of mass-analyzed, low-energy, dual-ion beam system for materials research". *Rev. Sci. Instrum.*, **65**(8):2680–2692, 1994.

[53] Y. Horino, N. Tsubouchi, B. Enders, C. Heck, A. Chayahara, A. Kinomura, and K. Fujii. "Development of a new ion-beam deposition technology for ultra-high-purity film fabrication". *Phys. Status Solidi a-Applied Res.*, **160**(2):583–589, 1997.

[54] J. P. Zhao, D. X. Huang, Z. Y. Chen, W. K. Chu, B. Makarenkov, A. J. Jacobson, B. Bahrim, and J. W. Rabalais. "Amorphous Ge quantum dots embedded in SiO_2 formed by low energy ion implantation". *J. Appl. Phys.*, **103**(12):124304, 2008.

[55] A. H. Al-Bayati, S. S. Todorov, K. J. Boyd, D. Marton, J. W. Rabalais, and J. Kulik. "Homoepitaxy and controlled oxidation of silicon at low temperatures using low-energy ion beams". *J. Vac. Sci. Technol. B Microelectron. Nanom. Struct.*, **13**(4):1639, 1995.

[56] N. Tsubouchi, A. Chayahara, Y. Mokuno, A. Kinomura, and Y. Horino. "3C-SiC thin epilayer formation at low temperature using ion beams". *Appl. Surf. Sci.*, **212**:920–925, 2003.

[57] N. Tsubouchi, B. Enders, A. Chayahara, A. Kinomura, C. Heck, and Y. Horino. "Optical properties of carbon and carbon nitride films prepared by mass-separated energetic negative carbon and carbon nitrogen ions". *J. Vac. Sci. Technol. A*, **17**(4):2384–2388, 1999.

[58] J. M. Pomeroy, J. Jacobsen, C. C. Hill, B. H. Cooper, and J. P. Sethna. "Kinetic Monte Carlo-molecular dynamics investigations of hyperthermal copper deposition on Cu(111)". *Phys. Rev. B*, **66**(23):235411–235412, 2002.

[59] J. M. Pomeroy, A. J. Couture, M. V. R. Murty, E. N. Butler, and B. H. Cooper. "Hyperthermal ion beam system optimized for studying the effects of kinetic energy on thin-film growth". *Rev. Sci. Instrum.*, **73**(11):3846–3852, 2002.

[60] R. C. Newman. "Defects in silicon". *Rep. Prog. Phys.*, **45**(10):1163–1210, 1982.

[61] Stanley Wolf and Richard N. Tauber. *Silicon Processing for the VLSI Era: Volume 1 - Process Technology*. Lattice Press, 2000.

[62] H. Baumann and K. Bethge. "The Frankfurt PIG ion source". *Nucl. Instrum. Meth. Phys. Res.*, **189**(1):107–110, 1981.

[63] P. Rohwer, H. Baumann, K. Bethge, and W. Schütze. "Ion energy analysis of a penning ion source using a high resolution mass spectrometer". *Nucl. Instrum. Meth. Phys. Res.*, **204**(1):245–248, 1982.

[64] P. Rohwer, H. Baumann, W. Schütze, and K. Bethge. "Studies of the center potential in a penning discharge". *Nucl. Instrum. Meth. Phys. Res.*, **211**(2-3):543–546, 1983.

[65] H. Baumann and K. Bethge. "PIG ion source with end extraction for multiply charged ions". *Nucl. Instrum. Meth.*, **122**:517–525, 1974.

[66] Z. Nouri, R. Li, R. A. Holt, and S. D. Rosner. "A Penning sputter ion source with very low energy spread". *Nucl. Instrum. Meth. Phys. Res. Sect. A*, **614**(2):174–178, 2010.

[67] Bernhard H. Wolf. *Handbook of Ion Sources*. CRC Press, 1995.

[68] C. E. S. Phillips. "The action of magnetised electrodes upon electrical discharge phenomena in rarefied gases. Preliminary note". *Proc. R. Soc. Lond.*, **64**(1):172–176, 1898.

[69] J. P. Biersack and W. Eckstein. "Sputtering studies with the Monte Carlo program TRIM.SP". *Appl. Phys. A Solids Surfaces*, **34**(2):73–94, 1984.

[70] V. I. Rudakov, V. V. Ovcharov, and V. P. Prigara. "Influence of optical properties of the SOI structure on the wafer temperature during rapid thermal annealing". *Russ. Microelectron.*, **41**(1):15–24, 2012.

[71] J. Nulman, S. Antonio, and W. Blonigan. "Observation of silicon wafer emissivity in rapid thermal processing chambers for pyrometric temperature monitoring". *Appl. Phys. Lett.*, **56**(25):2513, 1990.

[72] C. Y. Kuo and C. Gau. "Vaporsolidsolid growth of crystalline silicon nanowires using anodic aluminum oxide template". *Thin Solid Films*, **519**(11):3603–3607, 2011.

[73] P. C. Maurer, G. Kucsko, C. Latta, L. Jiang, N. Y. Yao, S. D. Bennett, F. Pastawski, D. Hunger, N. Chisholm, M. Markham, D. J. Twitchen, J. I. Cirac, and M. D. Lukin. "Room-temperature quantum bit memory exceeding one second". *Science*, **336**(6086):1283–1286, 2012.

[74] K. D. Jahnke, B. Naydenov, T. Teraji, S. Koizumi, T. Umeda, J. Isoya, and F. Jelezko. "Long coherence time of spin qubits in C-12 enriched polycrystalline chemical vapor deposition diamond". *Appl. Phys. Lett.*, **101**(1), 2012.

[75] G. Balasubramanian, P. Neumann, D. Twitchen, M. Markham, R. Kolesov, N. Mizuochi, J. Isoya, J. Achard, J. Beck, J. Tissler, V. Jacques, P. R. Hemmer, F. Jelezko, and J. Wrachtrup. "Ultralong spin coherence time in isotopically engineered diamond". *Nature Mater.*, **8**(5):383–387, 2009.

[76] K. J. Dwyer, J. M. Pomeroy, and D. S. Simons. "99.996 % C-12 films isotopically enriched and deposited in situ". *Appl. Phys. Lett.*, **102**(25), 2013.

[77] K. Ohno, F. J. Heremans, L. C. Bassett, B. A. Myers, D. M. Toyli, A. C. B. Jayich, C. J. Palmstrom, and D. D. Awschalom. "Engineering shallow spins in diamond with nitrogen delta-doping". *Appl. Phys. Lett.*, **101**(8), 2012.

[78] T. Teraji, T. Taniguchi, S. Koizumi, K. Watanabe, M. Y. Liao, Y. Koide, and J. Isoya. "Chemical vapor deposition of C-12 isotopically enriched polycrystalline diamond". *Jpn. J. Appl. Phys.*, **51**(9), 2012.

[79] M. L. Markham, J. M. Dodson, G. A. Scarsbrook, D. J. Twitchen, G. Balasubramanian, F. Jelezko, and J. Wrachtrup. "CVD diamond for spintronics". *Diamond Relat. Mater.*, **20**(2):134–139, 2011.

[80] W. M. Lau, I. Bello, X. Feng, L. J. Huang, F. G. Qin, Z. Y. Yao, Z. Z. Ren, and S. T. Lee. "Direct ion-beam deposition of carbon-films on silicon in the ion energy-range of 15–500 eV". *J. Appl. Phys.*, **70**(10):5623–5627, 1991.

[81] J. S. Hodges, L. Li, M. Lu, E. H. Chen, M. E. Trusheim, S. Allegri, X. Yao, O. Gaathon, H. Bakhru, and D. Englund. "Long-lived NV-spin coherence in high-purity diamond membranes". *New J. Phys.*, **14**, 2012.

[82] F. Kuemmeth, H. O. H. Churchill, P. K. Herring, and C. M. Marcus. "Carbon nanotubes for coherent spintronics". *Materials Today*, **13**(3):18–26, 2010.

[83] D. A. Alman and D. N. Ruzic. "Molecular dynamics calculation of carbon/hydrocarbon reflection coefficients on a hydrogenated graphite surface". *J. Nucl. Mater.*, **313**:182–186, 2003.

[84] K. J. Dwyer, J. M. Pomeroy, D. S. Simons, K. L. Steffens, and J. W. Lau. "Enriching ^{28}Si beyond 99.9998% for semiconductor quantum computing". *J. Phys. D. Appl. Phys.*, **47**(34):345105, 2014.

[85] J. K. Rath. "Low temperature polycrystalline silicon: a review on deposition, physical properties and solar cell applications". *Sol. Energy Mater. Sol. Cells*, **76**(4):431–487, 2003.

[86] Siegfried Hofmann. "Atomic mixing, surface roughness and information depth in high-resolution AES depth profiling of a GaAs/AlAs superlattice structure". *Surf. Interface Anal.*, **21**(9):673–678, 1994.

[87] T. de Jong, W. A. S. Douma, L. Smit, V. V. Korablev, and F. W. Saris. "The use of pulsed laser irradiation in silicon molecular beam epitaxy: A comparative low energy electron diffraction study". *J. Vac. Sci. Technol. B*, **1**(4):888, 1983.

[88] J. S. Williams. "Solid phase epitaxial regrowth phenomena in silicon". *Nucl. Instrum. Meth. Phys. Res.*, **209**:219–228, 1983.

[89] F. A. Stevie and R. G. Wilson. "Relative sensitivity factors for positive atomic and molecular ions sputtered from Si and GaAs". *J. Vac. Sci. Technol. A*, **9**(6):3064, 1991.

[90] J. S. Custer, Michael O. Thompson, D. C. Jacobson, J. M. Poate, S. Roorda, W. C. Sinke, and F. Spaepen. "Density of amorphous Si". *Appl. Phys. Lett.*, **64**(4):437, 1994.

[91] Donald Long and John Myers. "Ionized-impurity scattering mobility of electrons in silicon". *Phys. Rev.*, **115**(5):1107–1118, 1959.

[92] Dimitrie Culcer and Neil M. Zimmerman. "Dephasing of Si singlet-triplet qubits due to charge and spin defects". *Appl. Phys. Lett.*, **102**(23):232108, 2013.

[93] K. Oura, M. Katayama, A. V. Zotov, V. G. Lifshits, and A. A. Saranin. *Surface Science: An Introduction*. Springer, Berlin, 2003.

[94] M. Volmer and A. Weber. "Keimbildung in übersättigten Gebilden". *Z. Phys. Chem.*, **119**(277):227–301, 1926.

[95] F. C. Frank and J. H. van der Merwe. "One-dimensional dislocations. II. Misfitting monolayers and oriented overgrowth". *Proc. R. Soc. London A Math. Phys. Eng. Sci.*, **198**(1053), 1949.

[96] Helmut Alexander. *Dislocations in Solids*. Pages 115–118. North-Holland, Amsterdam, 1980.

[97] R. G. Humphreys, S. Brand, and M. Jaros. "Electronic structure of the divacancy in silicon". *J. Phys. C Solid State Phys.*, **16**(12):L337–L343, 1983.

[98] V. V. Kveder, T. Sekiguchi, and K. Sumino. "Electronic states associated with dislocations in p-type silicon studied by means of electric-dipole spin resonance and deep-level transient spectroscopy". *Phys. Rev. B. Condens. Matter*, **51**(23):16721–16727, 1995.

[99] C. A. Londos. "Defect states in electron-bombarded n-type silicon". *Phys. Status Solidi*, **113**(2):503–510, 1989.

[100] Niklas Lehto. "Shallow electron states of bounded intrinsic stacking faults in silicon". *Phys. Rev. B*, **55**(23):15601–15607, 1997.

[101] Ted Thorbeck and Neil M. Zimmerman. "Formation of strain-induced quantum dots in gated semiconductor nanostructures". *AIP Adv.*, **5**(8):087107, 2015.

[102] A.J. Sigillito, A.M. Tyryshkin, and S.A. Lyon. "Anisotropic Stark effect and electric-field noise suppression for phosphorus donor qubits in silicon". *Phys. Rev. Lett.*, **114**(21):217601, 2015.

[103] Giuseppe Pica, Gary Wolfowicz, Matias Urdampilleta, Mike L. W. Thewalt, Helge Riemann, Nikolai V. Abrosimov, Peter Becker, Hans-Joachim Pohl, John J. L. Morton, R. N. Bhatt, S. A. Lyon, and Brendon W. Lovett. "Hyperfine Stark effect of shallow donors in silicon". *Phys. Rev. B*, **90**, 2014.

[104] Dimitrie Culcer, Xuedong Hu, and S. Das Sarma. "Interface roughness, valley-orbit coupling, and valley manipulation in quantum dots". *Phys. Rev. B*, **82**(20):205315, 2010.

[105] John King Gamble, M. A. Eriksson, S. N. Coppersmith, and Mark Friesen. "Disorder-induced valley-orbit hybrid states in Si quantum dots". *Phys. Rev. B*, **88**(3):035310, 2013.

[106] Xiaojie Hao, Rusko Ruskov, Ming Xiao, Charles Tahan, and HongWen Jiang. "Electron spin resonance and spinvalley physics in a silicon double quantum dot". *Nat. Commun.*, **5**:344–347, 2014.

[107] S. Srinivasan, G. Klimeck, and L. P. Rokhinson. "Valley splitting in Si quantum dots embedded in SiGe". *Appl. Phys. Lett.*, **93**(11):112102, 2008.

[108] Neil Zimmerman, Peihao Huang, and Dimitrie Culcer. "Valley phase, interface roughness and voltage control, and coherent manipulation in Si quantum dots". arXiv:1608.06881, 2016.

[109] M. Nerding, L. Oberbeck, T. A. Wagner, R. B. Bergmann, and H. P. Strunk. "Single to polycrystalline transition in silicon growth by ion-assisted deposition at low temperatures". *J. Appl. Phys.*, **93**(5):2570, 2003.

[110] G. Xue, H. Z. Xiao, M.-A. Hasan, J. E. Greene, and H. K. Birnbaum. "Critical epitaxial thicknesses for low-temperature (20-100 °C) Ge(001)2x1 growth by molecular-beam epitaxy". *J. Appl. Phys.*, **74**(4):2512, 1993.

[111] Werner Kern. *Handbook of Semiconductor Wafer Cleaning Technology: Science, Technology, and Applications*. Page 623. Noyes Publications, 1993.

[112] J. A. Mol, S. P. C. Beentjes, and S. Rogge. "A low temperature surface preparation method for STM nano-lithography on Si(100)". *Appl. Surf. Sci.*, **256**(16):5042–5045, 2010.

[113] R. J. Hamers, R. M. Tromp, and J. E. Demuth. "Scanning tunneling microscopy of Si(001)". *Phys. Rev. B*, **34**(8):5343–5357, 1986.

[114] K. Hata, T. Kimura, S. Ozawa, and H. Shigekawa. "How to fabricate a defect free Si(001) surface". *J. Vac. Sci. Technol. A*, **18**(4):1933, 2000.

[115] E. Kasper, M. Bauer, and M. Oehme. "Quantitative secondary ion mass spectrometry analysis of SiO2 desorption during in situ heat cleaning". *Thin Solid Films*, **321**(1):148–152, 1998.

[116] V. A. Ukraintsev and John T. Yate. "The role of nickel in Si(001) roughening". *Surf. Sci.*, **346**(1):31–39, 1996.

[117] H. Bracht, E. E. Haller, and R. Clark-Phelps. "Silicon self-diffusion in isotope heterostructures". *Phys. Rev. Lett.*, **81**(2):393–396, 1998.

[118] D. Eaglesham, H.-J. Gossmann, and M. Cerullo. "Limiting thickness h_{epi} for epitaxial growth and room-temperature Si growth on Si(100)". *Phys. Rev. Lett.*, **65**(10):1227–1230, 1990.

[119] D. J. Eaglesham. "Semiconductor molecular-beam epitaxy at low temperatures". *J. Appl. Phys.*, **77**(8):3597, 1995.

[120] N.E. Lee, G. Xue, and J. E. Greene. "Epitaxial Si(001) grown at 80-750 °C by ion-beam sputter deposition: crystal growth, doping, and electronic properties". *J. Appl. Phys.*, **80**(2):769–780, 1996.

[121] M. V. Ramana Murty, Harry A. Atwater, A. J. Kellock, and J. E. E. Baglin. "Very low temperature (400 °C) silicon molecular beam epitaxy: the role of low energy ion irradiation". *Appl. Phys. Lett.*, **62**(20):2566, 1993.

[122] M. V. Ramana Murty and Harry A. Atwater. "Crystal-stateamorphous-state transition in low-temperature silicon homoepitaxy". *Phys. Rev. B*, **49**(12):8483–8486, 1994.

[123] Jack Thiesen, Howard M. Branz, and Richard S. Crandall. "Explanation of the limiting thickness observed in low-temperature silicon epitaxy". *Appl. Phys. Lett.*, **77**(22):3589, 2000.

[124] D. J. Eaglesham, G. S. Higashi, and M. Cerullo. "370°C clean for Si molecular beam epitaxy using a HF dip". *Appl. Phys. Lett.*, **59**(6):685, 1991.

[125] H. Jorke, H.-J. Herzog, and H. Kibbel. "Kinetics of ordered growth of Si on Si(100) at low temperatures". *Phys. Rev. B*, **40**(3):2005–2008, 1989.

[126] D.J. Eaglesham, H.-J. Gossmann, M. Cerullo, L.N. Pfeiffer, and K.W. West. "Limited thickness epitaxy of semiconductors and Si MBE down to room temperature". *J. Cryst. Growth*, **111**(1):833–837, 1991.

[127] E. Chason, P. Bedrossian, K. M. Horn, J. Y. Tsao, and S. T. Picraux. "Ion beam enhanced epitaxial growth of Ge(001)". *Appl. Phys. Lett.*, **57**(17):1793, 1990.

[128] C.-H. Choi, R. Ai, and S. Barnett. "Suppression of three-dimensional island nucleation during GaAs growth on Si(100)". *Phys. Rev. Lett.*, **67**(20):2826–2829, 1991.

[129] N.-E. Lee, G. A. Tomasch, and J. E. Greene. "Low-temperature Si(001) epitaxy using low-energy (E $\simeq$ 18 eV) Si atoms". *Appl. Phys. Lett.*, **65**(25):3236, 1994.

[130] Morito Matsuoka and Shun-ichi Tohno. "Ion beam epitaxy of silicon films in an ultrahigh vacuum using a sputtering-type metal ion source". *J. Vac. Sci. Technol. A*, **13**(2):305, 1995.

[131] K. Miyake and T. Tokuyama. "Germanium and silicon ion-beam deposition". *Thin Solid Films*, **92**(1-2):123–129, 1982.

[132] K. J. Boyd, D. Marton, J. W. Rabalais, S. Uhlmann, and Th. Frauenheim. "Semiquantitative subplantation model for low energy ion interactions with solid surfaces. III. Ion beam homoepitaxy of Si". *J. Vac. Sci. Technol. A*, **16**(2):463, 1998.

[133] M. Kitabatake, P. Fons, and J. E. Greene. "Molecular dynamics and quasidynamics simulations of low-energy ion/surface interactions leading to decreased epitaxial temperatures and increased dopant incorporation probabilities during Si MBE". *J. Cryst. Growth*, **111**(1):870–875, 1991.

[134] Kevin G. Orrman-Rossiter, Amir H. Al-Bayati, D.G. Armour, S.E. Donnelly, and J.A. van den Berg. "Ion beam deposited epitaxial thin silicon films". *Nucl. Instrum. Meth. Phys. Res. Sect. B*, **59**:197–202, 1991.

[135] L. A. Miller, D. K. Brice, A. K. Prinja, and S. T. Picraux. "Displacement-threshold energies in Si calculated by molecular dynamics". *Phys. Rev. B*, **49**(24):16953–16964, 1994.

[136] K. A. Jackson, L. Csepregi, W. K. Chu, H. Muller, J. W. Mayer, T. W. Sigmon, G.L. Olson, S.A. Kokorowski, J.A. Roth, L.D. Hess, J. S. Williams, R. G. Elliman, W. L. Brown, T. E. Seidel, J. Linnros, R. G. Elliman, W. L. Brown, Jan Linnros, W. L. Brown, R. G. Elliman, J.P. Biersack, and L.G. Haggmark. "A defect model for ion-induced crystallization and amorphization". *J. Mater. Res.*, **3**(06):1218–1226, 1988.

[137] Joseph M. Jasinski and Stephen M. Gates. "Silicon chemical vapor deposition one step at a time: fundamental studies of silicon hydride chemistry". *Acc. Chem. Res.*, **24**(1):9–15, 1991.

[138] W. C. T. Lee, N. Bishop, D. L. Thompson, K. Xue, G. Scappucci, J. G. Cederberg, J. K. Gray, S. M. Han, G. K. Celler, M. S. Carroll, and M. Y. Simmons. "Thermal processing of strained silicon-on-insulator for atomically precise silicon device fabrication". *Appl. Surf. Sci.*, **265**:833–838, 2013.

[139] E. Massa, G. Mana, L. Ferroglio, E. G. Kessler, D. Schiel, and S. Zakel. "The lattice parameter of the ^{28}Si spheres in the determination of the Avogadro constant". *Metrologia*, **48**(2):S44–S49, 2011.

[140] A. Yang, M. Steger, H. J. Lian, M. L. W. Thewalt, M. Uemura, A. Sagara, K. M. Itoh, E. E. Haller, J. W. Ager III, S. A. Lyon, M. Konuma, and M. Cardona. "High-resolution photoluminescence measurement of the isotopic-mass dependence of the lattice parameter of silicon". *Phys. Rev. B*, **77**(11), 2008.

[141] Yu-Nong Yang and Ellen D. Williams. "The role of carbon in the faceting of silicon surfaces on the (111) to (001) azimuth". *J. Vac. Sci. Technol. A*, **8**(3):2481, 1990.

[142] Hiroyuki Hirayama, Masayuki Hiroi, and Takashi Ide. "{311} facets of selectively grown epitaxial Si layers on SiO2–patterned Si(100) surfaces". *Phys. Rev. B*, **48**(23):17331–17337, 1993.

[143] Atsushi Oshiyama. "Structures of steps and appearances of {311} facets on Si(100) surfaces". *Phys. Rev. Lett.*, **74**(1):130–133, 1995.

[144] P. Ashu, C. C. Matthai, and T.-H. Shen. "Dynamics of atoms on silicon substrates". *Surf. Sci.*, **251**:955–959, 1991.

[145] P. Becker, P. Scyfried, and H. Siegert. "The lattice parameter of highly pure silicon single crystals". *Zeitschrift für Phys. B Condens. Matter*, **48**(1):17–21, 1982.

[146] O. Madelung, U. Rossler, and M. Schulz. "Silicon carbide (SiC), lattice parameters, thermal expansion". In *Gr. IV Elem. IV-IV III-V Compd. Part b - Electron. Transp. Opt. Other Prop.* Pages 1–11. Springer-Verlag, Berlin/Heidelberg, 41a1b edition, 2002.

[147] F. Bozso, J. T. Yates, W. J. Choyke, and L. Muehlhoff. "Studies of SiC formation on Si (100) by chemical vapor deposition". *J. Appl. Phys.*, **57**(8):2771, 1985.

[148] L. Moro, A. Paul, D. C. Lorents, R. Malhotra, R. S. Ruoff, P. Lazzeri, L. Vanzetti, A. Lui, and S. Subramoney. "Silicon carbide formation by annealing C_{60} films on silicon". *J. Appl. Phys.*, **81**(9):6141, 1997.

[149] James P. Becker, Robert G. Long, and John E. Mahan. "Reflection high-energy electron diffraction patterns of carbide-contaminated silicon surfaces". *J. Vac. Sci. Technol. A*, **12**(1):174, 1994.

[150] R. C. Henderson, R. B. Marcus, and W. J. Polito. "Carbide contamination of silicon surfaces". *J. Appl. Phys.*, **42**(3):1208, 1971.

[151] J. R. Engstrom, M. M. Nelson, and T. Engel. "Thermal decomposition of a silicon-fluoride adlayer: evidence for spatially inhomogeneous removal of a single monolayer of the silicon substrate". *Phys. Rev. B*, **37**(11):6563–6566, 1988.

[152] M. Maeder, A. Ramírez, and A. Zehe. "A RHEED study of as-received and atomically clean silicon surfaces in UHV-environment". *Superf. y vacío*, 9:242–244, 1999.

[153] Jun-Zhong Wang, Jin-Feng Jia, Hong Liu, Jian-Long Li, Xi Liu, and Qi-Kun Xue. "Spontaneous vacancy array formation on $FeSi_2$ and $CoSi_2$ formed on Si(100) 2xn surface". *Appl. Phys. Lett.*, **80**, 2002.

[154] Ja-Yong Koo, Jae-Yel Yi, Chanyong Hwang, Dal-Hyun Kim, Sekyung Lee, and Dong-Hyuk Shin. "Dimer-vacancy defects on the Si(001)–2x1 and the Ni-contaminated Si(001)–2xn surfaces". *Phys. Rev. B*, **52**(24):17269–17274, 1995.

[155] B. Kolditz and K. R. Roos. "Effect of ambient pressure and nickel contamination on the dimer-dangling-bond surface state of Si(001)2x1". *J. Vac. Sci. Technol. A*, **25**(4):721–725, 2007.

[156] Masamichi Yoshimura, Izumi Ono, and Kazuyuki Ueda. "Initial stages of Ni reaction on Si(100) and H-terminated Si(100) surfaces". *Appl. Surf. Sci.*, **130**:276–281, 1998.

[157] W. Koczorowski, M. Bazarnik, and R. Czajka. "SPM characterization of titanium disilicide nanostructures grown on a Ni-modified Si(100) substrate". *ACTA Phys. Pol. A*, **120**(3):480–484, 2011.

[158] H. J. W. Zandvliet, H. K. Louwsma, P. E. Hegeman, and Bene Poelsema. "Energetics of Ni-induced vacancy line defects on Si(001)". *Phys. Rev. Lett.*, **75**(21):3890–3893, 1995.

[159] Yoichiro Yamaguchi, Masayuki Yoshida, and Hiroyuki Aoki. "Solid solubility of nickel in silicon determined by use of ^{63}Ni as a tracer". *Jpn. J. Appl. Phys.*, **2**(11):714–718, 1963.

[160] Y.-W. Mo, R. Kariotis, B. S. Swartzentruber, M. B. Webb, and M. G. Lagally. "Scanning tunneling microscopy study of diffusion, growth, and coarsening of Si on Si(001)". *J. Vac. Sci. Technol. A*, **8**(1):201, 1990.

[161] Y. W. Mo, J. Kleiner, M. B. Webb, and M. G. Lagally. "Activation energy for surface diffusion of Si on Si(001): a scanning-tunneling-microscopy study". *Phys. Rev. Lett.*, **66**(15):1998–2001, 1991.

[162] G. Brocks, P. J. Kelly, and R. Car. "Binding and diffusion of a Si adatom on the Si(100) surface". *Phys. Rev. Lett.*, **66**(13):1729–1732, 1991.

[163] Takahisa Doi, Masakazu Ichikawa, Shigeyuki Hosoki, and Ken Ninomiya. "Anisotropic diffusion between the step-up and the step-down directions on a Si(001) surface". *Phys. Rev. B*, **53**(24):16609–16614, 1996.

[164] Chris Richardson. Document: "MBE and UHV component etchants". *Private communication*, 2015.

[165] P. Asoka-Kumar, S. Szpala, B. Nielsen, Cs. Szeles, K. G. Lynn, W. A. Lanford, C. A. Shepard, and H.-J. Gossmann. "Hydrogen-induced breakdown of low-temperature molecular-beam epitaxy of Si". *Phys. Rev. B*, **51**(7):4630–4632, 1995.

[166] J. A. Roth, G. L. Olson, D. C. Jacobson, and J. M. Poate. "Kinetics of solid phase epitaxy in thick amorphous Si layers formed by MeV ion implantation". *Appl. Phys. Lett.*, **57**(13):1340, 1990.

[167] L. Oberbeck, N. J. Curson, T. Hallam, M. Y. Simmons, G. Bilger, and R. G. Clark. "Measurement of phosphorus segregation in silicon at the atomic scale using scanning tunneling microscopy". *Appl. Phys. Lett.*, **85**(8):1359–1361, 2004.

[168] R. J. Hamers, U. K. Köhler, and J. E. Demuth. "Epitaxial growth of silicon on Si(001) by scanning tunneling microscopy". *J. Vac. Sci. Technol. A*, **8**(1):195, 1990.

[169] A. H. Albayati, K. J. Boyd, D. Marton, S. S. Todorov, J. W. Rabalais, Z. H. Zhang, and W. K. Chu. "Substrate-temperature dependence of homoepitaxial growth of Si using mass-selected ion-beam deposition". *J. Appl. Phys.*, **76**(7):4383–4389, 1994.

[170] M. Wang, G. Audi, A.H. Wapstra, F.G. Kondev, M. MacCormick, X. Xu, and B. Pfeiffer. "The Ame2012 atomic mass evaluation". *Chinese Phys. C*, **36**(12):1603–2014, 2012.

[171] Y. Yatsurugi, N. Akiyama, Y. Endo, and T. Nozaki. "Concentration, solubility, and equilibrium distribution coefficient of nitrogen and oxygen in semiconductor silicon". *J. Electrochem. Soc.*, **120**(7):975, 1973.

[172] Tadashi Nozaki, Yoshifumi Yatsurugi, and Nobuyuki Akiyama. "Concentration and behavior of carbon in semiconductor silicon". *J. Electrochem. Soc.*, **117**(12):1566, 1970.

[173] M. I. den Hertog, C. Cayron, P. Gentile, F. Dhalluin, F. Oehler, T. Baron, and J. L. Rouviere. "Hidden defects in silicon nanowires". *Nanotechnology*, **23**(2):025701, 2012.

[174] James H. Comfort and Rafael Reif. "Chemical vapor deposition of epitaxial silicon from silane at low temperatures". *J. Electrochem. Soc.*, **136**(8):2386, 1989.

[175] Andrei A. Onischuk and Viktor N. O. Panfilov. "Mechanism of thermal decomposition of silanes". *Russ. Chem. Rev.*, **70**(4):321–332, 2001.

[176] B. A. Joyce, R. R. Bradley, and G. R. Booker. "A study of nucleation in chemically grown epitaxial silicon films using molecular beam techniques III. Nucleation rate measurements and the effect of oxygen on initial growth behaviour". *Philos. Mag.*, **15**(138):1167–1187, 1967.

[177] R. J. Buss, P. Ho, W. G. Breiland, and M. E. Coltrin. "Reactive sticking coefficient for silane and disilane on polycrystalline silicon". *J. Appl. Phys.*, **63**(8):2808–2819, 1988.

[178] M. Liehr, C. M. Greenlief, S. R. Kasi, and M. Offenberg. "Kinetics of silicon epitaxy using SiH4 in a rapid thermal chemical vapor deposition reactor". *Appl. Phys. Lett.*, **56**(7):629, 1990.

[179] F. G. Ruedenauer. "Gas scattering as a limit to trace sensitivity in analytical mass spectrometers". *Rev. Sci. Instrum.*, **41**(10):1487, 1970.

[180] Trevor R. Ireland. "Invited Review Article: Recent developments in isotope-ratio mass spectrometry for geochemistry and cosmochemistry". *Rev. Sci. Instrum.*, **84**(1):011101, 2013.

[181] N. J. Freeman, N. R. Daly, and R. E. Powell. "Retardation lens used to improve the abundance sensitivity of a mass spectrometer". *Rev. Sci. Instrum.*, **38**(7):945, 1967.

[182] R. L. Summers. "Empirical observations on the sensitivity of hot cathode ionization type vacuum gauges". Technical report, National Aeronautics and Space Administration, NASA TN D-5285, Washington, D.C., 1969.

[183] C. Y. Peng, A. A. Woodworth, and C. D. Stinespring. "Method for rapid determination of ion gauge sensitivity factors". *Rev. Sci. Instrum.*, **78**(11):113908, 2007.

[184] H. Hertz. "On the evaporation of liquids, especially mercury, in vacuo". *Ann. Phys. (N. Y.)*, **17**:177, 1882.

[185] M. Knudesn. "Maximum rate of vaporization of mercury". *Ann. Phys. (N. Y.)*, **47**:697, 1915.

[186] Irving Langmuir. "The adsorption of gases on plane surfaces of glass, mica, and platinum". *J. Am. Chem. Soc.*, **40**(9):1361–1403, 1918.

[187] S. M. Gates, C. M. Greenlief, D. B. Beach, and R. R. Kunz. "Reactive sticking coefficient of silane on the Si(111)-(7x7) surface". *Chem. Phys. Lett.*, **154**(6):505–510, 1989.

[188] Stephen M. Gates. "Adsorption kinetics of SiH4, Si2H6 and Si3H8 on the Si(111)-(7x7) surface". *Surf. Sci.*, **195**(1):307–329, 1988.

[189] S. R. Logan. "The origin and status of the Arrhenius equation". *J. Chem. Educ.*, **59**(4):279, 1982.

[190] Keith J. Laidler. "The development of the Arrhenius equation". *J. Chem. Educ.*, **61**(6):494, 1984.

[191] B. A. Scott, R. D. Estes, and J. M. Jasinski. "The role of surface reactions in monosilane pyrolysis". *J. Chem. Phys.*, **89**(4):2544–2549, 1988.

[192] Karl F. Roenigk, Klavs F. Jensen, and Robert W. Carr. "Rice-Ramsperger-Kassel-Marcus theoretical prediction of high-pressure Arrhenius parameters by nonlinear regression: application to silane and disilane decomposition". *J. Phys. Chem.*, **91**(22):5732–5739, 1987.

[193] F. Hirose. "Modeling growth in Si gas-source molecular beam epitaxy using Si2H6". *J. Cryst. Growth*, **179**(1):108–114, 1997.

[194] S. M. Gates, C. M. Greenlief, S. K. Kulkarni, and H. H. Sawin. "Surface reactions in Si chemical vapor deposition from silane". *J. Vac. Sci. Technol. A Vacuum, Surfaces, Film.*, **8**(3):2965, 1990.

[195] D. S. Lin, E. S. Hirschorn, T. C. Chiang, R. Tsu, D. Lubben, and J. E. Greene. "Scanning-tunneling-microscopy studies of disilane adsorption and pyrolytic growth on Si(100)-(2X1)". *Phys. Rev. B*, **45**(7):3494–3498, 1992.